DESIGN-ORIENTED ROBUSTNESS ASSESSMENT OF REINFORCED CONCRETE BUILDING STRUCTURES

João Filipe Ângelo Sio

Thesis submitted in fulfilment of the requirements for

the degree of Doctor of Philosophy

and the Diploma of Imperial College London

Department of Civil and Environmental Engineering

Imperial College London

London SW7 2AZ, United Kingdom

January 2023

To my parents and sister,

for their love and support.

Declaration of Originality

I hereby declare that this thesis entails my own original work. Any published and unpublished content of others are appropriately acknowledged and referenced.

Copyright Declaration

The copyright of this thesis rests with the author. Unless otherwise indicated, its contents are licensed under a Creative Commons Attribution-Non Commercial-No Derivatives 4.0 International Licence (CC BY-NC-ND).

Under this licence, you may copy and redistribute the material in any medium or format on the condition that; you credit the author, do not use it for commercial purposes and do not distribute modified versions of the work.

When reusing or sharing this work, ensure you make the licence terms clear to others by naming the licence and linking to the licence text.

Please seek permission from the copyright holder for uses of this work that are not included in this licence or permitted under UK Copyright Law.

Abstract

This thesis proposes enhancements to the rational robustness assessment frameworks recently developed at Imperial College London, namely the performance-based ductility-centred framework for disproportionate collapse assessment under 'notional member removal', and the novel horizontal tying force method to replace current 'prescriptive tying force' requirements.

Within the option provided by the ductility-centred framework to assess building structures under sudden column loss by simply providing the nonlinear static response of a planar beam sub-system, the first part of the research involves the development of a practical numerical modelling approach for reinforced concrete planar beam sub-systems. Compared to modelling approaches available in literature, the proposed approach benefits from representing, at a relatively low computational cost, the bond-slip between the concrete and the reinforcement throughout the structural member. The proposed modelling approach is demonstrated to predict, with reasonable accuracy, the development of cracks and the ductility limit of reinforced concrete beam sub-systems.

The second part of the research addresses some of the current limitations of the recently developed novel horizontal tying force method, including i) the proposal of a simplified analytical approach to predict the planar restraint stiffness of floor systems under column loss, including the influence of compressive ring action in the affected floor slab; and ii) the adaptation of the horizontal tying force method to floor systems under corner column loss.

The conservatism of the current tying method is successfully reduced with the analytical approach considering the influence of the compressive ring. Furthermore, the method developed for corner floor systems demonstrates a more significant mobilisation of tensile membrane action than anticipated in current flexure-based assessment methods, offering a novel view on the research and design of corner floor systems against disproportionate collapse.

Acknowledgements

This is it! The end of the journey I set myself out on since my undergraduate days. I would have never foreseen writing these acknowledgements as the conclusion to years of 'sweat and tears' for the fulfilment of one of my dreams – pursuing a PhD, but most importantly learning so much more within the field that I love! Evidently, none of this would have been possible without the remarkable group of people who supported me along the way, and whom I am greatly indebted to:

First and foremost, my supervisor Prof. Bassam A. Izzuddin, for his dedicated guidance and constant encouragement throughout the duration of this research. A great deal of what has been achieved is due to his invaluable suggestions and clear sense of direction. In addition to his eagerness in 'getting to the bottom' of things yet somehow achieving it with such simplicity, I admire, and will always strive for, the sincerity and fairness that Prof. Izzuddin has shown. I am immensely grateful for his teachings, and it was an absolute pleasure working with him.

The research presented in this thesis is sponsored by Fundação para a Ciência e a Tecnologia, Portugal through the grant SFRH/BD/137612/2018. Their financial support is greatly acknowledged.

Prof. Beatrice Belletti and Dr. Simone Ravasini, for the fruitful discussions and collaboration on the validation paper of the horizontal tying force method.

Dr. Teresa M. Bodas Freitas, for seeding me into the idea of pursuing the PhD at Imperial College London and for her continued encouragement even when I am no longer her student.

The amazing friends and colleagues I have met during the PhD. Ayse, whom I have shared a lot of my happy and difficult moments with during long (very long) coffee breaks. Deema, who cheered up my afternoons by teasingly catching me napping in front of the computer! Carlos, *meu amigão*, for the endless and pleasant conversations. Andri and Luís, for showing me the ropes in the beginning of the PhD. Stanyslav, Matthew and Qili, for the fruitful discussions and joy we had during the CST trip in Montpellier. Moemen and Haochen, for the crispy duck dinners! And others who I did not mention here.

My friends beyond Imperial College London. Stefano, Nuno and João Paulo, whom I have fought through my undergraduate with, and who have kept calling me from time to time for hour-long sessions of catching up. My mates back in Macau, for the online gaming sessions as

short but much-needed breakaways from my work. Hugo, my childhood friend and flatmate during the PhD, for his incessant yet playful annoyance right from the morning of everyday! This PhD would have been much harder to get through with without his company, specifically during the periods of covid lockdown.

Tio Artur, Tia Ivone, Tia Bebe and Tio Mario, for their care and for making me feel at home throughout my undergraduate and PhD studies in Lisbon and London, respectively.

Lastly, my family whom I dearly miss. My sister Jaquelina, for always being there for me, offering koala hugs and making funny cute faces whenever I feel down and helpless. My Mom and Dad, for their unconditional love, care, support and understanding. I am immensely grateful to you for raising me into the person I am today and for the things that I have achieved. I love you and thank you for believing that I could do this right from the start.

Table of Contents

Declaration of Originality **1**

Copyright Declaration **3**

Abstract **5**

Acknowledgements **7**

Table of Contents **9**

List of Tables **15**

List of Figures **17**

Notation **23**

Chapter 1: Introduction **25**

1.1 Disproportionate collapse and structural robustness 25

1.2 Properties of structural robustness 27

1.3 Past occurrences and context 28

1.3.1 Notional member removal and key element provisions 30

1.3.2 Prescriptive tying forces 32

1.4 Research aims 33

1.5 Thesis outline 34

Chapter 2: Literature Review **37**

2.1 Introduction 37

2.2 Design regulations for structural robustness 37

2.2.1 The UK and Europe 37

2.2.2 The US 39

2.3 Prescriptive tying force requirements 40

2.4 Notional member removal and key element provisions 45

2.4.1 Linear analysis 47

2.4.2 Nonlinear analysis 48

2.4.3 Simplified assessment framework 50

2.5 Behaviour and characterisation of RC planar frame sub-systems 54
2.5.1 Typical behaviour 54
2.5.2 Modelling 60
2.6 Behaviour and characterisation of RC floor systems 65
2.6.1 Typical behaviour and membrane action 65
2.6.2 Modelling 69
2.7 Nonlinear structural analysis program ADAPTIC 70
2.7.1 Material models and section types 71
2.7.2 Elements 72
2.8 Conclusion 73

Chapter 3: Enhancement of fibre-beam elements with bond-modelling feature 75
3.1 Introduction 75
3.2 Fibre-beam elements with bond-modelling feature 75
3.2.1 Concrete element 76
3.2.2 Steel-bond element 83
3.3 Steel material model with tensile softening 86
3.3.1 Standard bilinear kinematic strain hardening model 88
3.3.2 Formulation of the newly developed model 89
3.3.3 Verification 94
3.4 Strain-dependent bond-slip model 99
3.4.1 Formulation 104
3.4.2 Verification 110
3.5 I- and T-shaped cross sections 115
3.5.1 Formulation 115
3.5.2 Verification 117
3.6 Consistent mass matrix (CMM) 121
3.6.1 Definition of CMM 123
3.6.2 CMM formulation for the concrete element 125
3.6.3 CMM formulation for the steel-bond element 127
3.6.4 Diagonally lumped mass matrix (DLMM) 129
3.6.5 Finite element response 129
3.6.6 Verification 131
3.7 Conclusion 135

Chapter 4: Modelling of RC planar frame sub-systems under column loss scenario 137
4.1 Introduction 137
4.2 Modelling considerations 137
4.2.1 Description of typical models 138
4.2.2 Representation of the surrounding structure 139
4.2.3 Material models 142
4.2.4 Mesh refinement 144
4.3 Validation against experimental tests 145
4.3.1 General validation 146
4.3.2 Beam models with T-shaped section 164
4.3.3 Beam models with sophisticated detailing 173
4.4 Sensitivity assessment 174
4.4.1 Boundary restraint 175
4.4.2 Reinforcement and span-to-depth ratio 176
4.4.3 Concrete strength 179
4.4.4 Bond strength and anchorage length 180
4.4.5 Enhancement solutions 181
4.5 Conclusion 184

Chapter 5: Rational horizontal tying force method for practical robustness design of building structures 187
5.1 Introduction 187
5.2 General tying formulation 188
5.3 Tying via double-span beams 190
5.4 Tying via floor system 192
5.4.1 Two-way tying 192
5.4.2 One-way tying 193
5.5 Dynamic amplification 194
5.6 Interaction with the surrounding structure 196
5.6.1 Planar interaction 196
5.6.2 Amplification of redistributed gravity loads 199
5.7 Contributions additional to tying 200
5.8 Validation and verification 201
5.8.1 Validation of numerical models for floor systems 201

5.8.2 Verification of tying via beams 204
5.8.3 Verification of tying via floor system 210
5.9 Validation against experimental tests 217
5.9.1 Tying via beams 218
5.9.2 Tying via floor system 221
5.10 Conclusion 223

Chapter 6: Planar interaction with compressive ring 225
6.1 Introduction 225
6.2 General formulation for circular slabs 225
6.2.1 Main assumptions 226
6.2.2 Formulation 227
6.2.3 Verification of the formulation and its applicability to square slabs 229
6.3 General formulation for square slabs 232
6.3.1 Main assumptions 233
6.3.2 Formulation 234
6.4 Verification against square models 235
6.5 Application to rectangular slabs 242
6.5.1 Generalisation of the proposed formulation 243
6.5.2 Verification against rectangular models 243
6.6 Conclusion 248

Chapter 7: Rational horizontal tying force method for corner column loss scenario 249
7.1 Introduction 249
7.2 General formulation 252
7.2.1 Rational basis and main assumptions 252
7.2.2 Tying mechanism 254
7.2.3 Bending mechanism 265
7.3 Verification of the proposed tying method 266
7.3.1 Verification cases and model description 267
7.3.2 Pull-in at the free tip and average reinforcement strains 268
7.3.3 Verification of the load-deflection response of the control models 275
7.3.4 Sensitivity to equal variation of top and bottom reinforcement 279
7.3.5 Sensitivity to variation of bottom or top reinforcement alone 280

7.3.6 Sensitivity to depth and span length of floor slab 287
7.4 An alternative planar displacement approximation 289
7.5 Applicability of proposed method to conventional reinforcement layout 291
7.6 Potential formulation including resistance contribution from beams 297
7.7 Conclusion 301

Chapter 8: Summary and conclusions 303
8.1 Summary 303
8.1.1 Notional member removal 303
8.1.2 Rational horizontal tying force method 305
8.2 Recommendations for future research 308
8.2.1 Modelling approach for RC planar frame sub-systems under a column loss 308
8.2.2 Tying force method for column loss scenarios with adequate planar restraint 309
8.2.3 Tying force method for other column loss scenarios 310

References 313

Appendix A: Properties of structural robustness 325

Appendix B: Background of prescriptive tying requirements 329

Appendix C: Modelling considerations for beam sub-systems with sophisticated reinforcement detailing 337

Appendix D: Supplementary information for the sensitivity assessment of the system response on the bond strength and anchorage length 339

Appendix E: Supplementary tables for the rational horizontal tying force method 341

Appendix F: Average strain contours at initial stages of tensile membrane action 349

Appendix G: Permission to reuse figures from other publications 351

List of Tables

Table 2.1 – Horizontal tying for framed structures....41
Table 2.2 – Horizontal tying for load-bearing wall constructions....41
Table 3.1 – Steel properties for the sketch of cyclic response....94
Table 3.2 – Concrete properties for the verification beam (element size: 100mm)....98
Table 3.3 – Steel and concrete properties for the verification specimen....111
Table 3.4 – Steel and concrete properties for the verification beam....118
Table 3.5 – Periods and mode types from eigenvalue analysis....131
Table 4.1 – Yu and Tan (2012, 2013a): beam geometry and reinforcement....147
Table 4.2 – Properties for spring and contact elements....147
Table 4.3 – Concrete properties....148
Table 4.4 – Steel properties....148
Table 4.5 – Reference bond properties....148
Table 4.6 – Reduced bond strengths....157
Table 4.7 – Symmetric properties for the single spring element and the contact element....161
Table 4.8 – T-beam geometry (in mm)....165
Table 4.9 – Reinforcement detailing (in mm)....166
Table 4.10 – Reinforcement anchorage and curtailment lengths (in mm)....166
Table 4.11 – Stiffness of boundary springs (assumed values)....166
Table 4.12 – Concrete properties....166
Table 4.13 – Steel properties....167
Table 4.14 – Bond properties....167
Table 4.15 – T-section RC sub-systems: fracture of reinforcement....172
Table 4.16 – Anchorage lengths and bond strengths....180
Table 5.1 – Mechanical properties for the steel reinforcement and the concrete....202
Table 5.2 – Main boundary spring properties....204
Table 5.3 – RC beam properties....205
Table 5.4 – Steel beam properties....205
Table 5.5 – Verification cases for RC beam example....207
Table 5.6 – Verification cases for steel beam example....207
Table 5.7 – Model modification scheme....211
Table 5.8 – Validation of tying via beams against experimental tests....219

Table 5.9 – Validation of tying via floor system against experimental tests 222
Table 6.1 – Geometric and reinforcement details for the slab models 230
Table 6.2 – Concrete and steel properties 230
Table 6.3 – Geometric and reinforcement details for the control square slab models.....236
Table 6.4 – Concrete and steel material properties for the control square slab models 237
Table 6.5 – Numerical models for the verification of the square formulation 238
Table 6.6 – Numerical models for the verification of the rectangular formulation.....244
Table 7.1 – Geometric and reinforcement details for the control corner floor systems 267
Table 7.2 – Concrete and steel properties 267
Table 7.3 – Stress contours at approximately 900mm tip displacement for the corner slab with 6500mm span length 283
Table B.1 – Horizontal tying for framed structures 329
Table B.2 – Horizontal tying for load-bearing wall constructions 329
Table C.1 – Stiffness of boundary springs (assumed values) 338
Table C.2 – Concrete properties 338
Table C.3 – Steel properties.....338
Table C.4 – Bond properties 338
Table D.1 – Damage mechanism and corresponding vertical displacement (in mm) 339
Table E.1 – Tying parameters for double-span beams 341
Table E.2 – Tying parameters for two-way floor tying 342
Table E.3 – Tying parameters for one-way floor tying 343
Table E.4 – Amplification of redistributed vertical gravity loading for double-span beams 344
Table E.5 – Amplification of redistributed vertical gravity loading for two-way floor tying 345
Table E.6 – Amplification of redistributed vertical gravity loading for one-way floor tying346
Table E.7 – Properties of the specimens selected for the validation of tying via beams.....347
Table E.8 – Properties of the specimens selected for the validation of tying via floor system 347

List of Figures

Fig. 1.1 – Partial collapse of the Ronan Point Tower (source: The National Archives) 28
Fig. 1.2 – Historic collapses in the US (source: Encyclopædia Britannica – images a) and b) reproduced with permission of the rights holders, AP Images and Chao Soi Cheong/AP Images, respectively) 29
Fig. 2.1 – Sub-structural levels for progressive collapse (source: Izzuddin *et al.*, 2008) 52
Fig. 2.2 – Simplified dynamic assessment and definition of pseudo-static response (source: Izzuddin *et al.*, 2008) 53
Fig. 2.3 – Typical RC beam sub-system 55
Fig. 2.4 – Schematic illustration of a typical static load-displacement response under the loss of a column 56
Fig. 2.5 – Response comparison between beam sub-systems with deformed and smooth reinforcement bars (experimental data from Lim *et al.*, 2017b) 59
Fig. 2.6 – Typical bond-modelling approaches currently available in literature 64
Fig. 2.7 – Tensile membrane action (source: Dat and Hai, 2013) 66
Fig. 2.8 – Load-deflection response from different column loss scenarios (source: Pham *et al.*, 2017a) 68
Fig. 3.1 – Local DOFs of the concrete element (adapted from Khalid, 2011) 76
Fig. 3.2 – Shape functions over the cross-section depth (adapted from Khalid, 2011) 78
Fig. 3.3 – Determination of local from global displacements 81
Fig. 3.4 – Local DOFs of the steel-bond element (adapted from Khalid, 2011) 84
Fig. 3.5 – Schematic illustration of the standard and new steel models 87
Fig. 3.6 – Significance of effective stiffness modulus and damage strain state variable 92
Fig. 3.7 – Strain history for the verification of the new steel model 94
Fig. 3.8 – Stress-strain cyclic response of new steel model 95
Fig. 3.9 – Significance of the tensile softening parameter 95
Fig. 3.10 – Input histories for the assessment of the new steel model in ADAPTIC 96
Fig. 3.11 – Verification of the new steel model in ADAPTIC: axial loading 97
Fig. 3.12 – Verification of the new steel model in ADAPTIC: flexural loading I 98
Fig. 3.13 – Verification of the new steel model in ADAPTIC: flexural loading II 99
Fig. 3.14 – Influence of yield penetration within the embedded reinforcement on the ductility limit of the system 101

Fig. 3.15 – Mechanic of the strain-independent bond-slip model 104
Fig. 3.16 – Flowchart describing the logic of the strain-independent bond-slip model 109
Fig. 3.17 – Test specimen for the verification of the strain-dependent bond-slip model 110
Fig. 3.18 – Verification of reinforcement strain-distribution over the embedment length 113
Fig. 3.19 – Influence of reinforcement strains on the bond-slip behaviour 114
Fig. 3.20 – Verification for orthogonal shape functions: rectangular beam 119
Fig. 3.21 – Verification for orthogonal shape functions: beam with T-shaped section (load-displacement response) 120
Fig. 3.22 – Verification for orthogonal shape functions: beam with T-shaped section (local stress response) 121
Fig. 3.23 – Convergence assessment: static analysis 122
Fig. 3.24 – Convergence assessment: dynamic analysis with applied constant velocity 123
Fig. 3.25 – Verification with eigenvalue analysis: first six mode shapes 132
Fig. 3.26 – Verification with dynamic analysis (implicit HHT) 133
Fig. 3.27 – Verification with dynamic analysis (Newmark scheme) 134
Fig. 3.28 – Verification with dynamic analysis (HHT explicit scheme) 134
Fig. 4.1 – Typical model for RC planar beam sub-systems 138
Fig. 4.2 – Representation of the surrounding structure (values in mm) 140
Fig. 4.3 – Constitutive relationship for spring and contact elements 141
Fig. 4.4 – Trilinear concrete material model 142
Fig. 4.5 – Steel and bond-slip material models 143
Fig. 4.6 – Half model example for mesh refinement 144
Fig. 4.7 – Determination of the fracture displacement: 7.5mm mesh size 145
Fig. 4.8 – Convergence of fracture displacement with mesh refinement 145
Fig. 4.9 – Typical setup of the specimens tested by Yu and Tan (2012, 2013a) 146
Fig. 4.10 – Predictions of *cbp2* vs *bme* models 149
Fig. 4.11 – *bme* model: bond strength calibration 151
Fig. 4.12 – Influence of reinforcement strain on the bond-slip behaviour 152
Fig. 4.13 – Reinforcement stress distribution of specimen S4 154
Fig. 4.14 – Specimen S4: yield penetration process of MJBR 155
Fig. 4.15 – *sd* model: calibration of the parameter *b* 156
Fig. 4.16 – Validation of the proposed modelling approach: specimens S1-S4 158
Fig. 4.17 – Validation of the proposed modelling approach: specimens S5-S8 159
Fig. 4.18 – Assessment of *sjm* for the modelling of the boundary restraint 161

Fig. 4.19 – Assessment of full models 163
Fig. 4.20 – Influence of material imperfection 164
Fig. 4.21 – Typical specimen with T-shaped section: plan view 164
Fig. 4.22 – Typical specimen with T-shaped section: elevation view 165
Fig. 4.23 – Validation of the proposed modelling approach: specimens with T-shaped section 168
Fig. 4.24 – Development of local flexural hinge in specimen S3 169
Fig. 4.25 – *shell* model of specimen S3 169
Fig. 4.26 – Damage mechanisms predicted for specimen S6 at its ductility limit 171
Fig. 4.27 – Experimental damage mechanisms from specimen S6 (data adapted from Ren *et al.*, 2016) 172
Fig. 4.28 – Specimens with sophisticated detailing (MJ – middle joint; EC – end-column; BR, TR and CR – bottom, top and curtailed reinforcement) 174
Fig. 4.29 – Sensitivity of the system response to the level of restraint stiffness 175
Fig. 4.30 – Sensitivity of the system response to varying reinforcement and span-to-depth ratios 177
Fig. 4.31 – Sensitivity of the system response to the concrete strength 179
Fig. 4.32 – Sensitivity of the pseudo-static resistance to the bond strength and anchorage length 181
Fig. 4.33 – Detailing scheme for the three cases of mid-layer reinforcement 182
Fig. 4.34 – Load response of the control model and the three cases of mid-layer reinforcement 183
Fig. 5.1 – General case of tying via double-span beams 190
Fig. 5.2 – General case of tying via floor system: two-way tying 192
Fig. 5.3 – General case of tying via floor system: one-way tying 194
Fig. 5.4 – Development of flexural and tying resistance 195
Fig. 5.5 – Interaction of tying beam with surrounding structure 197
Fig. 5.6 – Influence of residual bending resistance in catenary stage (source: Izzuddin, 2022) 201
Fig. 5.7 – Geometry and detailing illustration of specimen SE1 202
Fig. 5.8 – Schematic representation of the finite element model 203
Fig. 5.9 – Validation of static response under concentrated load condition 204
Fig. 5.10 – Typical geometry and reinforcement detailing of beam examples 205

Fig. 5.11 – Static and dynamic responses of the beam examples under concentrated loading 208
Fig. 5.12 – Redistribution of vertical gravity loads of the beam examples 210
Fig. 5.13 – Static response of case models under applied concentrated load 212
Fig. 5.14 – Static response of case models under applied uniformly distributed load 212
Fig. 5.15 – Verification of minimum chord rotation for the activation of tying.....214
Fig. 5.16 – Verification with initial model under applied concentrated load 216
Fig. 5.17 – Verification with model NM3 under uniformly distributed load 217
Fig. 5.18 – Validation of tying via beams against experimental tests 220
Fig. 5.19 – Validation of tying via floor system against experimental tests.....222
Fig. 6.1 – Circular formulation for compressive ring 226
Fig. 6.2 – Force equilibrium of the circular formulation 228
Fig. 6.3 – Verification of circular slabs (dimensions in mm) 230
Fig. 6.4 – Verification of the circular formulation considering $t.E_c$ 231
Fig. 6.5 – Verification of the circular formulation considering $0.01(t.E_c)$ 231
Fig. 6.6 – Idealisation of the compressive ring as a square hollow boundary region.....232
Fig. 6.7 – Models associated with the compressive ring formulation for square slabs 233
Fig. 6.8 – Verification of compressive ring model for square slabs 236
Fig. 6.9 – Predicted and numerical outcomes for control model (1) with $1.00k_s$ 238
Fig. 6.10 – Predicted and numerical outcomes for control model (2) with $1.00k_s$ 239
Fig. 6.11 – Verification of analytical compressive ring formulation for square slabs.....241
Fig. 6.12 – Idealisation of the compressive ring as a rectangular hollow section 242
Fig. 6.13 – Verification of analytical compressive ring formulation for rectangular slabs: response in the *x*-direction 246
Fig. 6.14 – Verification of analytical compressive ring formulation for rectangular slabs: response in the *y*-direction 247
Fig. 7.1 – Dominant mechanism for different loading conditions.....250
Fig. 7.2 – Dominant deformation modes/mechanisms involved in the proposed method.....251
Fig. 7.3 – General case under tying mechanism 255
Fig. 7.4 – Tying contribution from the top reinforcement.....256
Fig. 7.5 – Tying contribution from the bottom reinforcement within the supported region..260
Fig. 7.6 – Tying contribution from bottom reinforcement within the unsupported region ...262
Fig. 7.7 – General case under bending mechanism 266
Fig. 7.8 – Boundary assumptions for the numerical models.....268

Fig. 7.9 – Verification of the planar pull-in at the free tip for the control specimens 269
Fig. 7.10 – Control specimen 6500mm: Sensitivity of the pull-in to the equal variation of the top and bottom reinforcement.....269
Fig. 7.11 – Control specimen 6500mm: Sensitivity of the pull-in to the variation of the bottom reinforcement only.....270
Fig. 7.12 – Control specimen 6500mm: Sensitivity of the pull-in to the variation of the top reinforcement only.....270
Fig. 7.13 – Control specimen 6500mm: Sensitivity of the pull-in to the depth and span length of the slab.....271
Fig. 7.14 – Supplementary illustrations for the assessment of predicted and numerical outcomes 272
Fig. 7.15 – Average reinforcement strains at 668mm tip displacement of the control specimen with 4500mm span length.....273
Fig. 7.16 – Average reinforcement strains at 906mm tip displacement of the control specimen with 6500mm span length.....274
Fig. 7.17 – Verification of the load-deflection response of the control models 276
Fig. 7.18 – Evolution of the bottom reinforcement stresses with tip displacement.....277
Fig. 7.19 – Equal variation of top and bottom reinforcement.....279
Fig. 7.20 – Variation of the bottom reinforcement only.....281
Fig. 7.21 – Displacement profile along the diagonal AD with 6500mm span length.....284
Fig. 7.22 – Variation of the top reinforcement only 286
Fig. 7.23 – Models with 6500mm span length: comparison of load-deflection responses between equal increase of bottom and top reinforcement (As,bt), increase of bottom reinforcement only (As,b), and increase of top reinforcement only (As,t).....287
Fig. 7.24 – Sensitivity of the load-deflection response to the depth of the slab 288
Fig. 7.25 – Sensitivity of the load-deflection response to the span length of the slab.....288
Fig. 7.26 – Sensitivity of the displacement approximation to the equal variation of the top and bottom reinforcement.....290
Fig. 7.27 – Sensitivity of the displacement approximation to the variation of the bottom reinforcement only.....290
Fig. 7.28 – Sensitivity of the displacement approximation to the variation of the top reinforcement only.....291
Fig. 7.29 – Diagonal and conventional reinforcement layout.....292
Fig. 7.30 – Equivalence between diagonal and conventional reinforcement layouts.....293

Fig. 7.31 – Yield line analysis for ULS design of the corner slab 294
Fig. 7.32 – Load-deflection response of the diagonal and conventional reinforcement layouts 295
Fig. 7.33 – Load-deflection response of the conventional layout with curtailed top reinforcement 296
Fig. 7.34 – Verification of the planar pull-in at the free tip for the beam-slab floor model 299
Fig. 7.35 – Comparison of transverse deformation between the slab-only model and the beam-slab model at approximately 1000mm of tip displacement 300
Fig. 7.36 – Verification of the analytical and numerical load-deflection responses of the beam-slab model 301
Fig. B.1 – Equilibrium model considered for the tying force requirement in the UK National Annex of Eurocode 2 331
Fig. B.2 – Equilibrium model considered for the tying force requirement in the Eurocode 1: Part 1-7 for framed structures (adapted from Vrouwenvelder, 2008b) 333
Fig. C.1 – Specimens with sophisticated reinforcement detailing 337
Fig. F.1 – Average reinforcement strains at 400mm tip displacement of the control specimen with 4500mm span length 349
Fig. F.2 – Average reinforcement strains at 611mm tip displacement of the control specimen with 6500mm span length 350

Notation

Symbols

All symbols used in this thesis are defined where they first appear in the text. When the symbols denote more than one quantity, their meaning should be clear when read in context.

Abbreviations

1/2/3D	one/two/three-dimension(al)
CA (TCA)	catenary action (tensile catenary action)
CAA	compressive arching action
CL	concentrated load
CMA	compressive membrane action
CMM	consistent mass matrix
DOF(s)	degree(s) of freedom
EC	end column
ECBR	end column bottom reinforcement
ECMR	end column mid-layer reinforcement
ECTR	end column top reinforcement
MJ	middle joint
MJBR	middle joint bottom reinforcement
MJMR	middle joint mid-layer reinforcement
RC	reinforced concrete
TMA	tensile membrane action
UDL	uniformly distributed load

Chapter 1: Introduction

1.1 Disproportionate collapse and structural robustness

Instigated by several historic collapses, the concepts of disproportionate collapse and structural robustness have gained international significance over the last few decades. Despite the general low probability of occurrence of unforeseen events leading to the disproportionate collapse of structures, there is undeniable interest in mitigating such a collapse owed to the severeness of its consequences, usually involving significant human and economic losses.

This chapter provides an overview on disproportionate collapse and structural robustness, as well as the motivation and aims of this thesis. The chapter commences with the definitions of disproportionate collapse and structural robustness, along with the description of properties related to structural robustness, providing further insight into the key aspects influencing the resistance of structures against disproportionate collapse. A selection of past occurrences related to the field is then presented, followed by a discussion regarding the context to the work of this thesis, highlighting a summary of features and limitations of existing design regulations and assessment methods for structural robustness. The chapter culminates with the research aims and the outline of this thesis.

A consensus has emerged recently on the terminologies of progressive collapse, disproportionate collapse and structural robustness. Progressive collapse was commonly regarded as the phenomenon in which an initial local/limited damage caused by an unforeseen event triggers a sequence of structural component failures, ultimately leading to the widespread collapse of the structure (e.g. Gross and McGuire, 1983; GSA, 2003). Such a definition implicitly suggests that the final damage resulting from progressive collapse is always disproportionate to the original cause. However, a clearer distinction between progressive collapse and disproportionate collapse has been recently highlighted (Agarwal and England, 2008; Starossek and Haberland, 2010; Adam *et al.*, 2018), where these terminologies denote two different aspects of the evolution of structural damage, with progressive collapse providing

the concept of damage propagation and disproportionate collapse comparing the extent of the initial and final damage.

In this regard, progressive collapse simply assesses how damage is spread, in a chain reaction manner, from an initial damage to other parts of the structure that are not directly affected by said initial damage. As an example related to this definition, the different types of progressive collapse identified by Starossek (2007a) can be classified in terms of damage propagation mechanism into redistribution- and impact-type collapses. In the former type of collapse, damage is propagated through successive redistribution of forces within the structure, whereas in the latter type of collapse damage propagates via the interchange between potential and kinetic energies during the fall/overturning of elements and their subsequent impact on others (Adam *et al.*, 2018). Propagation of damage can also be classified in terms of its direction, whether collapse progresses horizontally, vertically or a combination of both. On the other hand, disproportionate collapse simply refers to the disproportion of the final damage of the structure relative to the initial local damage, without providing any consideration to how damage is spread within the structure.

Based on these definitions, a progressive collapse is also disproportionate if the initial damage is limited in size but spreads to a large portion of the structure, resulting in its partial or total collapse. Conversely, a progressive collapse is considered proportionate if either the initial damage is already extensive (and proportionate to the final damage) or the propagation of damage is limited to a small portion of the structure. On the other hand, a disproportionate collapse can be immediate or progressive, where an example for the former can be the collapse of a statically determinate structure originating from the failure of a single member (Adam *et al.*, 2018). Though, since most structures are designed to be statically indeterminate, disproportionate collapse is commonly deemed as also progressive.

This thesis mainly involves the concept of disproportionate collapse as the associated work aims to propose design-oriented methods to assess the resistance of building structures against widespread collapses originating from the loss of a single column/load-bearing member. Notwithstanding, the concepts related to progressive collapse also merit appreciation, for example to ensure that the improvement of the structure against a specific type of collapse would not induce others.

Structural robustness is defined in related design regulations, such as the Eurocode 1 – Part 1-7 (CEN, 2006) and the GSA code (GSA, 2003), as “the ability of the structure to withstand

events like fire, explosions, impact or consequences of human error, without being damaged to an extent disproportionate to the original cause". However, it is recently preferred to view the aforementioned definition as collapse resistance (Starossek, 2006) and to define structural robustness instead as the ability of the structure to withstand an initial local damage, independently on whichever the cause, without being damaged to an extent disproportionate to the initial local damage (e.g. Starossek, 2006; Biondini *et al.*, 2008; Vrouwenvelder, 2008a). Defined in this way, structural robustness is considered as a property of the structure alone (Starossek, 2006), hence allowing for a broader application of the concept to actions other than those considered as extreme, which may also expose the structure to disproportionate collapse. An example of such actions is the ageing and deterioration of the structure over its lifetime. The preferred definition also enables the direct association of structural robustness with disproportionate collapse, in the sense that mitigating disproportionate collapse necessarily leads to an enhancement in structural robustness.

1.2 Properties of structural robustness

It is commonly identified from the observation of past disproportionate collapses that mitigation usually involves the provision of ductility, continuity, redundancy, energy absorption and local load resistance. Specifically, ductility, continuity, redundancy and energy absorption are properties thought to be beneficial for the development of alternative load paths within the structure, promoting the redistribution of the gravity load following an initial local damage, whilst local load resistance, notwithstanding a property more related to collapse resistance (Starossek, 2007b), derives from the idea of preventing the initial local damage instead. Improvement in structural robustness requires careful consideration of the aforementioned properties, depending on the design objectives, configuration and exposure of the structure (Starossek, 2007b).

Importantly, the above noted properties should not be contemplated as a measure for structural robustness alone as it can be shown that enhancing any of these properties alone for certain structural configurations can be rather detrimental to the robustness of the structure (Starossek, 2006; Izzuddin *et al.*, 2008). In recognition of this, Izzuddin *et al.* (2008) proposes the system pseudo-static capacity under the sudden loss of a column/load-bearing member as the appropriate single measure of structural robustness, with its comparison against the applied gravity loading establishing the required limit state. The system pseudo-static capacity can be determined with the multi-level assessment framework also proposed by Izzuddin *et al.* (2008),

detailed in Section 2.4.3, which accounts for all the previously discussed properties in a rational manner. Further review on the properties of structural robustness is provided in Appendix A.

1.3 Past occurrences and context

The most iconic disproportionate collapse event which first prompted research interest and the proposal of design regulations related to the field is the partial collapse of the Ronan Point Tower in London, UK (Pearson and Delatte, 2005). In the early morning of 16 May 1968, a small gas explosion occurred on the 18th floor of the 22-storey large panel precast building and blasted out a load-bearing wall located at one of its corners. The floors above collapsed with such a loss in vertical support and the ensuing debris fell and impacted onto the 18th floor. The damage continued to propagate downwards until it reached the ground, leading to the collapse of the entire corner bay of the building, as illustrated in Fig. 1.1.



Fig. 1.1 – Partial collapse of the Ronan Point Tower (source: The National Archives)

The design regulations used at the time of construction did not provide any provisions regarding structural robustness, with the structure generally lacking continuity between the floor panels and the load-bearing walls, thereby not able to develop alternative load paths for the redistribution of the gravity loads.

Initial recommendations following the collapse of the Ronan Point Tower were mainly aimed at precast structures, e.g. Griffiths *et al.* (1968) in the UK and Fintel and Schultz (1976, 1979) in the US, subsequently encouraging the prescription of ties in view of improved monolithic

behaviour, structural ductility and continuity, thus increasing the likelihood of the structure to develop alternative load paths. Notwithstanding, in recognition that the issues related to disproportionate collapse are not limited to precast constructions, the concepts of disproportionate collapse and structural robustness have later been extended also to monolithic structures (Russell *et al.*, 2019). The UK led with the first design requirements for structural robustness, as embodied in the Code of Practice 110 (BSI, 1972), which have since been adapted in the material specific standards of concrete (BSI, 1985b) and steel (BSI, 1985a); in the Approved Document A of the UK building regulations (MHCLG, 2013); and most recently in the Eurocodes (CEN, 2004b, 2006).

In the US (Fig. 1.2), the bombing and collapse of the Alfred P. Murrah Federal Building in 1995 (Corley *et al.*, 1996; Corley *et al.*, 1998; Sozen *et al.*, 1998; Osteraas, 2006; Kazemi-Moghaddam and Sasani, 2015), and the events of 11 September 2001 which led to the catastrophic collapse of the WTC Twin Towers are examples of occurrences that brought the consideration of structural robustness back to the forefront at the international level. Notwithstanding, the collapse of the Twin Towers could not be classified as disproportionate because the initial damage caused by the impact of the aircraft was already extensive and deemed proportionate to the final damage.



(a) Alfred P. Murrah Federal Building (b) WTC Twin Towers

Fig. 1.2 – Historic collapses in the US (source: Encyclopædia Britannica – images a) and b) reproduced with permission of the rights holders, AP Images and Chao Soi Cheong/AP Images, respectively)

The US have since developed their own regulations for structural robustness design and assessment, specifically the GSA code for governmental buildings (GSA, 2003, 2013) and the

UFC code for military buildings (DoD, 2005, 2009). These codes were influenced by the UK building regulations but adopted a more rational treatment, including a performance-based assessment of the structure for alternative load paths under the scenario of sudden column/load-bearing member loss, with the objective of ensuring that the maximum dynamic deformations are within the ductility limit of the affected part of the structure.

The publication of robustness design regulations over the past decades undeniably provided pioneering guidance for the mitigation of disproportionate collapse, a phenomenon which was not considered actively in design before the partial collapse of Ronan Point. Yet, major shortcomings can be identified in the corresponding design requirements. In general terms, the requirements of the current design regulations can be broken down into 'notional member removal', 'key element provisions' and 'prescriptive tying forces', the application of which depends on the level of robustness intended for the structure under consideration, with the requisite level of robustness defined based on the building class provisions termed as 'consequence classes' in the UK building regulation and the Eurocode, and as 'risk requirements' in the UFC guidelines.

1.3.1 Notional member removal and key element provisions

The requirements of 'notional member removal' and 'key element provisions' are grouped into a single assessment strategy so-called 'alternative load path method', which first involves the removal of a notional member, generally referring to a column or a load-bearing member. If the damage of the structure exceeds specified limits under such a scenario, the notional member which has been removed is then classified as a key element and should be designed to resist the unforeseen event. Current US regulations allow linear static, nonlinear static and nonlinear dynamic analyses for the structural assessment under the sudden loss of a load-bearing member. Notwithstanding, as detailed in Section 2.4, these approaches are either overly impractical for common engineering practices or overly simplistic, such as with the use of linear static analysis, with the exclusion of nonlinear dynamic effects of sudden member loss and ductility limits.

In recognition of these shortcomings, a ductility-centred multi-level assessment framework has been developed at Imperial College London (Izzuddin *et al.*, 2008), addressing the usual measures advocated for structural robustness in a rational manner whilst benefiting from practical applicability. The framework allows the use of practical nonlinear static analysis but with the remarkable feature of not relying on forced-based factors for dynamic amplification. The dynamic response is instead determined from the transformation of the nonlinear static

response into a so-called pseudo-static response based on principles of energy balance. The framework also allows for the incremental assessment over successive levels of structural idealisation in the sense that the response of a building structure can be obtained from the assemblage of its individual sub-systems and/or components. With such features, the application of the framework can be initiated at any given level of structural idealisation, simply requiring simplified or detailed models to generate the corresponding nonlinear structural response. Further details of the framework are provided in Section 2.4.3.

The framework has been extensively validated and enhanced over recent years, with specific focus on steel and steel-concrete composite building structures. Notable contributions include: (i) the development of simplified models to predict the ductility limit of steel connections and assessment of its effects on higher-level structural idealisations (Vlassis *et al.*, 2008); (ii) the assessment of debris impact on the lower floor if the floor(s) above the lost column fail(s) (Vlassis, 2007; Vlassis *et al.*, 2009); (iii) correlation of the framework with real extreme events such as blasts and impacts (Gudmundsson and Izzuddin, 2010); (iv) practicality and accuracy comparison between different levels of structural idealisation (Jahromi, 2009; Jahromi *et al.*, 2013); (v) rate-sensitivity and multiple column loss assessment (Pereira, 2012); and (vi) interaction with masonry infill panels (Xavier *et al.*, 2014).

Yet, contributions to the framework related to reinforced concrete (RC) building structures are still relatively limited, importantly in relation to the development of simplified models to predict the nonlinear static response and ductility limit of RC components and sub-systems, thus establishing the clear need for further research. As detailed in Sections 2.5 and 2.6, the characterisation of RC components and sub-systems should involve considerations such as axial-flexural interaction, boundary restraint, reinforcement fracture and bond-slip between the reinforcement and the concrete. Specifically, the latter two considerations primarily define the ductility limit of RC components and sub-systems. Despite recently published models that are capable of characterising the fracture of the reinforcement and the bond-slip between the reinforcement and concrete, the treatment of bond-slip behaviour mostly involves either its local characterisation using force-slip springs located at the beam-column connections (e.g. Bao *et al.*, 2008; Yu and Tan, 2014a) or its implicit consideration within the constitutive relationship of the steel reinforcement (Sadek *et al.*, 2011; Bao *et al.*, 2012). An explicit and more generalised approach for the characterisation of bond-slip behaviour over the whole length of the RC members should be developed for an accurate yet practical assessment of ductility limits, crack development and sophisticated reinforcement detailing schemes.

1.3.2 Prescriptive tying forces

The requirements of 'prescriptive tying forces' are viewed as an indirect design method for structural robustness. These requirements entail, as the name suggests, the prescription of reinforcement and its improved detailing to enhance the continuity of the affected system and thus its capability to bridge over the loads via catenary/membrane tying action following the loss of a load-bearing member. The rationale of these requirements is not, however, entirely clear and consistent across the design regulations, and they do not consider the ductility limit of the structure and its direct influence on the resistance of the gravity load via catenary/membrane tying action (Izzuddin *et al.*, 2008; Izzuddin and Sio, 2022). Indeed, the specified levels of tying forces in these requirements, as detailed in Section 2.3, are far too low to achieve the requisite resistance at typical levels of ductility as often determined by the joint rotational capacity (Byfield and Paramasivam, 2007; Izzuddin *et al.*, 2007). Furthermore, dynamic amplification is not explicitly considered, not even in the UFC guidance (DoD, 2009) which does consider a so-called dynamic increase factor (DIF) for the requirements of notional member removal (alternative load path method). Provisions are also prescriptive, if not inexistent, for the interaction of the affected system with the surrounding structure.

In recognition of the need to replace the current prescriptive tying force requirements, a rational horizontal tying force method has been recently developed by Izzuddin (Izzuddin and Sio, 2022) as a member of the project team WG6.T2 commissioned under mandate M515 of CEN/TC 250 to develop robustness guidance for the next generation of the Eurocodes. The novel method, with the formulation, validation, verification and application presented in Chapter 5 of this thesis, benefits from a rational association with local damage scenarios consisting of the sudden loss of a column or a load-bearing wall, addressing the aforementioned shortcomings of current prescriptive tying force requirements and allowing for a systematic combination of various types of loading and sources of tying. Importantly, all the relative benefits are still realised within a practical application framework that is comparable in simplicity to the prescriptive tying rules, rendering the novel tying method suitable for codification.

Under the consideration of common slab reinforcement detailing, consisting in a reinforcement arrangement parallel to the edges of the floor system, the novel tying method would not be applicable to corner, penultimate exterior and penultimate interior column removal scenarios simply because the surrounding structure does not typically provide adequate horizontal restraint to the affected system. Notwithstanding, alternative resistance mechanisms may exist which redirect the tying forces within the affected system to parts of the surrounding structure

where such horizontal restraint becomes adequate. In this case, the novel tying method should be accordingly adapted to cover the aforementioned scenarios of column/load-bearing member loss.

1.4 Research aims

In light of the discussion in the previous section, the main aim of this thesis is to provide enhancements to the rational methods recently developed for the assessment of structural robustness, specifically the simplified assessment framework under the sudden loss of a column/load-bearing member and the novel tying force method, progressively moving the prescriptive and qualitative treatment of robustness in design regulations towards the quantifiable. In this respect, the present thesis involves two main lines of research work focused on RC building structures: (i) the development of a simplified numerical method for the assessment of RC planar frame sub-systems which can explicitly model the fracture of the reinforcement determined by the bond-slip between the reinforcement and the concrete along the RC member; and (ii) validation, verification and application of the tying force method developed by Izzuddin (Izzuddin and Sio, 2022), along with important extensions covering aspects which are not considered in the current method.

An extensive review is first carried out, identifying the relevant basis for the proposed lines of research work. Specifically, for the first line of research work, the review focuses on the behaviour of RC planar frame sub-systems under the loss of a column/load-bearing member and on the limitations of corresponding numerical models currently available in literature. For the second line of research work, emphasis is given to the discussion of current tying force requirements, the limitations of which encouraged the development of the novel tying force method. The review also covers the role of the RC slab in floor systems under the scenario of column/load-bearing member loss, which helps in identifying the enhancements proposed herein for the novel method.

Aiming at the development of a simplified numerical method to predict the nonlinear static response and ductility limit of RC planar frame sub-systems, the first line of research work refers to the objective RC modelling approach previously developed by Khalid (2011). This approach explicitly characterises the bond-slip behaviour via the definition of individual fibre-beam elements for the concrete and the reinforcement, where the bond-slip interface is encapsulated within the element. Additional contributions are proposed in this thesis to enable the application of these elements in robustness assessment. The proposed numerical method is

then validated against published experimental tests to assess its effectiveness in establishing ductility limits for RC members/planar frame sub-systems.

The second line of research work commences with presenting the formulation of the novel tying force method developed by Izzuddin (Izzuddin and Sio, 2022), along with its validation, verification and application undertaken in the present work. In the current method, the supplementary formulation for the minimum planar restraint stiffness to mobilise the requisite tying forces, detailed in Chapter 5, considers the planar restraint provided from the surrounding structure alone, even though planar restraint may also be realised via compressive ring action equilibrating the tensile membrane forces. Therefore, as an important contribution to the current method, the second line of research work also entails the extension of the supplementary formulation to include the planar restraint contribution from the compressive ring.

Lastly, in recognition of alternative resistance mechanisms where tensile membrane action can be mobilised within floor systems under corner, penultimate exterior and penultimate interior column/load-bearing member loss, the second line of research work culminates with the extension of the novel tying force method to corner floor systems, laying the foundation for future research in this area.

1.5 Thesis outline

This thesis is divided into three main parts based on the research aims presented in Section 1.4: (i) a literature review for the two main lines of research work, (ii) the development, validation and verification of the simplified numerical method for the assessment of RC planar frame sub-systems, and (iii) presentation of the novel tying force method (Izzuddin and Sio, 2022), along with its enhancement to include the planar restraint contribution from the compressive ring and its extension to corner floor systems.

Chapter 1 (the present chapter) is the introductory chapter involving the definitions of disproportionate collapse and structural robustness, along with a brief discussion on the measures advocated for structural robustness. The chapter concludes with the context and research aims of this thesis.

As the first part of this thesis, an extensive literature review is presented in Chapter 2, commencing with a detailed discussion on current robustness requirements and assessment methods, followed by a review of the behaviour and characterisation of RC planar frame sub-

systems and floor systems, and culminating with a description of the adopted nonlinear structural analysis program ADAPTIC along with the elements relevant to the work of this thesis.

The third and fourth chapters form the second part of this thesis. Chapter 3 presents the formulation and verification of the enhancements proposed for the fibre-beam elements developed by Khalid (2011), while Chapter 4 details the development and validation of the simplified numerical method proposed for the nonlinear static assessment of RC planar frame sub-systems. The sensitivity of the ductility limit predicted from the proposed method is then assessed to parameters such as reinforcement ratio, bond strength, anchorage length and others.

Chapters 5 to 7 form the third and final part of this thesis, with the chapters respectively detailing and validating the novel tying force method (Chapter 5), the contribution of the compressive ring to the planar restraint stiffness of the affected system (Chapter 6), and the extension of the tying method to corner floor systems (Chapter 7).

Chapter 8 is the concluding chapter of this thesis, summarising the main outcomes of the present research and provides recommendations for future research.

Chapter 2: Literature Review

2.1 Introduction

This chapter provides a literature review relevant to the two main lines of research work discussed in Section 1.4. The chapter begins with the exposition of current design regulations and assessment methods for structural robustness, first involving the general framework of the regulations, then proceeding with the requirements of prescriptive tying forces, notional member removal and key element provisions. This is followed by a review on reinforced concrete planar frame sub-systems and floor systems under the loss of a load-bearing member, highlighting the key aspects in the modelling of such structural systems, along with a discussion on the features and limitations of published numerical models. The chapter then concludes with an overview of the adopted nonlinear structural analysis program ADAPTIC (Izzuddin, 1991), describing the material models and elements relevant for the work of this thesis.

2.2 Design regulations for structural robustness

Consideration is given to the framework of current design regulations for structural robustness in the UK, Europe and the US, involving the definition of the design situation and the subsequent recommendation of corresponding robustness strategies/requirements.

2.2.1 The UK and Europe

The framework for robustness design provided in the Approved Document A of the UK building regulations (MHCLG, 2013) and the Eurocodes (CEN, 2006) presents considerable similarities and overlapping provisions since not only the Eurocodes have mirrored the robustness provisions from the UK building regulations, but also compliance of the UK building regulations currently refers to the Eurocodes, supplemented by additional requirements not covered in such regulation. In this respect, exposition of the design framework is herein based on the Eurocodes, where reference is made to the Approved Document A for overlaps and differences in provisions.

Robustness provisions in the Eurocodes commence with Eurocode 0 (CEN, 2002), involving general statements which, upon inspection, basically refer to the requirements of 'prescriptive tying forces', 'notional member removal' and 'key element provision' detailed in Eurocode 1 – Part 1-7 (CEN, 2006). In turn, the main text of Eurocode 1 – Part 1-7 expands the same narrative, differentiating the design of structures against identified and unidentified accidental actions. Notwithstanding, despite some additional considerations recommended for the design of structures against identified actions, the main text ultimately refers both design scenarios to Annex A of the same document. Annex A follows up on the design objectives set out in the main text of Eurocode 1 – Part 1-7, with the application of recommended strategies depending on the consequence class determined for the building structure, and with more stringent requirements applied for higher consequence classes:

- For buildings in Consequence Class 1, no additional robustness provision is required beyond those applied for satisfying structural safety in normal use.
- For buildings in Consequence Class 2a, only horizontal ties are required in addition to the strategies recommended for Consequence Class 1.
- For buildings in Consequence Class 2b, both horizontal and vertical ties should be provided in addition to the strategies recommended for Consequence Class 1, or alternatively, the building structure should be assessed under the scenario of notional member loss, where the ensuing extent of damage should not exceed a specified limit. Otherwise, such notional members should be designed as key elements, withstanding a notional accidental action A_d of 34kN/m^2.
- For buildings in Consequence Class 3, a systematic risk assessment of the building should be undertaken considering both foreseeable and unforeseeable hazards. Provisions of risk assessment are outside the scope of this thesis, and thus not detailed hereinafter.

For buildings in Consequence Class 2a/b, Annex A provides explicit quantification of horizontal and vertical ties, as discussed later in Section 2.3. Under the alternative strategy for buildings in Consequence Class 2b, Annex A recommends an admissible extent of damage up to 15% of the floor area or 100m^2, whichever is smaller, and limited within the two storeys immediately adjacent to the removed notional member. The annex does not, however, provide detailed guidance on how to quantify the extent of damage, specifically in the recommendation of assessment methods, which are discussed in Section 2.4, and the consideration of ductility

limits to determine the failure of components within the building structure. The provisions also ignore dynamic effects as the notional member removal appears to be static.

The current Approved Document A of the UK building regulations (MHCLG, 2013) presents essentially identical categorisation of Consequence Classes and application of suitable strategies as those outlined in the Annex A of Eurocode 1 – Part 1-7, with the difference of referring the design of horizontal and vertical ties also to the material specific documents of the Eurocode, along with the corresponding UK national annexes.

2.2.2 The US

The current UFC code (DoD, 2009) presents a layout similar to the UK building regulations and the Eurocodes, where it also involves the requirements of 'prescriptive tying forces', 'alternative load paths' and 'enhanced local resistance', the application of which follows a building classification procedure termed as 'risk category'. Contrary to the UK building regulations and the Eurocodes, where requirements of 'prescriptive tying forces' and 'alternative load paths' are to be employed as alternative strategies, 'risk category' IV in the UFC code requires the simultaneous application of these strategies.

Tying force requirements within the initial UFC code (DoD, 2005) were material specific, largely adopting the requirements from the first iterations of the UK building regulations for structural robustness. Tying was also considered to be mainly realised within the beams or near the column lines. The material specific requirements have, however, been replaced by a more generic approach in the subsequent revision of the code (DoD, 2009). Moreover, in recognition that primary load carrying members (i.e. beams) may not be able to develop the requisite tying forces due to significant rotational demands, the 2009 revision of the code also recommends that tying should instead be realised within the floor system unless the primary members are shown to develop a rotational capacity exceeding 0.20rad. Further discussion and comparison of the tying force requirements from the UK, Europe and the US regulations are provided in Section 2.3.

Unlike the current UK building regulations and the Eurocodes, the UFC code explicitly specifies assessment methods and acceptance criteria for alternative load paths. Adapting the initial proposal in the GSA code (GSA, 2003), the UFC code allows for linear static, nonlinear static and nonlinear dynamic analyses, with the consideration of load and dynamic increase factors in linear static and nonlinear static analyses, respectively. These factors approximately accounts for the inertial and nonlinear effects of sudden column/load-bearing member loss in

linear static analyses and for the inertial effects alone in nonlinear static analyses. The first iteration of the GSA code (GSA, 2003) and the UFC code (DoD, 2005) adopted an identical dynamic increase factor of 2.0, which was later shown to be inconsistent and unrealistic (Stevens *et al.*, 2008; McKay *et al.*, 2012), and was replaced in the revision of both codes (DoD, 2009; GSA, 2013) by improved factors determined considering structural deformation as the best metric for adjustment of damage (Stevens *et al.*, 2008). Still, as further detailed in Section 2.4, these improved factors are only suitable for elastic-perfectly plastic structural responses, and general application can lead to unsafe assessments and/or designs (Izzuddin and Nethercot, 2009).

2.3 Prescriptive tying force requirements

Consideration is given to the current tying force requirements in the UK, European and US regulations, along with a discussion on the corresponding background in Appendix B to identify the shortcomings of such requirements. Limitations are then highlighted for closed-form analytical methods available in literature, which are often considered as practical yet more rational alternatives to the tying force requirements. The section culminates with a summary of key aspects to be addressed considering the identified shortcomings, which later motivated the proposal of the novel tying force method detailed in Chapter 5. With RC building structures being the primary building typology involved in this thesis, the narrative is herein focused on tying requirements and analytical methods mainly applicable for RC systems.

The background of currently mandated tying force requirements is generally unclear. The first proposals of prescriptive tying applied for structural robustness appear to be provided by the Institution of Structural Engineers in the UK following the collapse of Ronan Point and, in parallel, by the Portland Cement Association in the US dealing with large panel constructions (Adam *et al.*, 2018). Prescriptive tying force requirements were intended to enhance bridging capability, continuity and ductility of a structure by means of added reinforcement and improved reinforcement detailing, although, as the name suggests, such measures are rather prescriptive and often not associated to a sound rationale. The requirements entail the prescription of horizontal tying in the floor panels and beams, and vertical tying in the columns and walls.

Tables 2.1 and 2.2 summarise the current horizontal tying requirements respectively for framed structures and load-bearing wall constructions, with the Eurocode and the UFC code also providing recommendations for the detailing/placement of the resulting reinforcement ties.

Table 2.1 – Horizontal tying for framed structures

Regulation	Internal ties	Peripheral ties
Eurocode 1 – Part 1-7	$0.8(g_k + \psi q_k)sL \geq 75\,\text{kN}$	$0.4(g_k + \psi q_k)sL \geq 75\,\text{kN}$
Eurocode 2	$q_3(L_1 + L_2)/2 \geq Q_4$ $q_3 = 20\,\text{kN/m}$, $Q_4 = 70\,\text{kN}$	$L_i\, q_1 \geq Q_2$ $q_1 = 10\,\text{kN/m}$, $Q_2 = 70\,\text{kN}$
Eurocode 2 + UK National Annex	$\frac{(g_k + q_k)}{7.5}\frac{L_r}{5}F_t \geq F_t$ (kN/m) $F_t = 20 + 4n_0 \leq 60\,\text{kN/m}$	$L_i\, q_1 \geq Q_2$ $q_1 = (20 + 4n_0)L_i$ kN/m, $Q_2 = 60\,\text{kN}$
UFC 4-023-03:2009	$F_i = 3w_f L_r$ (kN/m)	$F_p = 6w_f s_p L_r + 3W_c$ (kN)

Table 2.2 – Horizontal tying for load-bearing wall constructions

Regulation	Internal ties	Peripheral ties
Eurocode 1 – Part 1-7	$\frac{(g_k + \psi q_k)}{7.5}\frac{z}{5}F_t \geq F_t$ (kN/m) $F_t = 20 + 4n_0 \leq 60\,\text{kN/m}$ $z = \min(5h_w, L)$	$20 + 4n_0 \leq 60\,\text{kN/m}$
UFC 4-023-03:2009	Two-way panels $F_i = 3w_f L_r$ (kN/m) One-way panel $F_i = 3w_f L_3$ (kN/m)	Two-way panels $F_p = 6w_f s_p L_r + 3W_c$ (kN) One-way panel $F_p = 6w_f s_p L_4 + 3W_c + 3W_w$ (kN)

where:

s is the spacing of ties (m)

L is the span of the tie (m)

g_k is the characteristic dead load (kN/m^2)

q_k is the characteristic live load (kN/m^2)

ψ is the combination factor for accidental actions

L_1, L_2 are the span lengths of the floor slabs on either side of the beam (m)

L_i is the length of the end span (m)

L_r is the greater of the distances between the centres of the columns, frames or walls supporting any two adjacent floor spans in the direction of the tie under consideration (m)

n_0 is the number of storeys

w_f is the design load and is equal to $1.2DL + 0.5LL$, where DL and LL are the dead and live load, respectively (kN/m^2)

L_3 is the longest span for ties perpendicular to the load-bearing walls or $5h_w$ for ties parallel to the load-bearing walls (m)

L_4 is the longest span for ties perpendicular to the load-bearing walls or $2h_w$ for ties parallel to the load-bearing walls (m)
h_w is the clear storey height (m)
s_p is the considered width to place the peripheral ties and is taken as 1.0 m
W_c is 1.2 times the dead load of cladding over the length of L_r (kN)
W_w is 1.2 times the dead load of wall over the length of h_w (kN)

An initial inspection of the above horizontal tying expressions reveals that most of these expressions can be rearranged in the following general form:

$$F = i_f wL \tag{2.1}$$

where F is the required tying force; i_f is denoted as the force intensity factor; and L is the longest span in the direction of tying. Considering the distributed area load w to be expressed in kN/m^2, the tying force F as presented in (2.1) is expressed in kN/m.

In this respect, along with the background information presented in Appendix B, the current tying requirements are demonstrated to be inconsistent across existing regulations despite these having evolved from similar backgrounds. This is primarily due to the assumption, often without any rational justification, of different reference applied loads, span lengths and demonstrated levels of central deflection, even though such levels of central deflection are not explicitly considered in the UK building regulations and the Eurocodes – see Appendix B, Vrouwenvelder (2008b) and Smith (2016). Moreover, horizontal tying requirements between current regulations are shown to be derived even from different procedures: the requirements in the UFC code and the UK National Annex of Eurocode 2 are likely established with a planar moment equilibrium between the imposed distributed load and the tying force under an assumed central deflection, as demonstrated in Appendix B and in Smith (2016), whilst the requirements applied in Eurocode 1 – Part 1-7 for framed structures likely use equivalent 1D beam systems to determine the tying resistance developed within a 2D system, as demonstrated in Vrouwenvelder (2008b). Note that because the equilibrium is established based on two equivalent 1D beam systems the considered approach only represents the tie forces developed within the 2D system in an approximate way.

As a result of these inconsistencies, both the required tying force and the force ratio of internal to peripheral ties differ between requirements of existing regulations. The requirements in Eurocode 1 – Part 1-7 for framed structures present intensity factors i_f of 0.8 and 0.4 for

internal and peripheral ties, respectively, whilst the UFC code adopts more conservative values of 3.0 and 6.0 (see Table 2.1). Furthermore, all the presented European regulations including the UK National Annex of Eurocode 2 have the required tying force reduced, if not halved, from internal to peripheral ties, whilst peripheral tying requirements in the UFC code not only require double the tying force of the internal ties but also explicitly specify additional cladding and wall loads. These observations suggest that peripheral ties, as specified in the Eurocode, may not be intended to bridge over the gravity loads under the double-span configuration or, if considered otherwise, it is doubtful that such ties can effectively bridge over the gravity loads given the low design tying forces. The UFC code provides, on the other hand, more reasonable recommendations.

More important is the concern for the rotation capacity of the structural members under tying. It is deduced from the derivation procedures – Appendix B and Smith (2016) – that structural members under horizontal tying should develop a rotation capacity exceeding 0.2rad to mobilise the tie force specified in all requirements except those applied in Eurocode 1 – Part 1-7 for framed structures, where the demonstration in Vrouwenvelder (2008b) suggests that an i_f of 0.75 (approximate to 0.8) for internal ties requires a rotation capacity of 0.33rad instead. Moreover, the reduction of i_f to 0.4 for peripheral ties suggests that the required rotation should be even higher than 0.33rad. In this respect, the Eurocode does not provide any guidance on the minimum rotation capacity required from the structural members under tying. The UFC code tentatively addresses this limitation by providing a statement on the rotation capacity of beam members, ensuring that horizontal ties should be placed only in beam members which can develop a rotation capacity of 0.2rad, otherwise tying should be realised within the floor panels. However, no further information is given to the rotation capacity of the floor panels. Indeed, the level of mobilised tying force directly depends on the deflection the bridging structural system can achieve, which in turn is often determined by the joint rotation capacity. For rotation capacities lower than 0.2rad, the bridging system must provide higher tying resistance to withstand the same gravity loads under tensile catenary action. In such a case, the level of tying forces specified in the requirements that are derived based on a rotation capacity of 0.2rad become far too low to achieve the requisite resistance at the level of rotation under consideration, let alone the requirements that are derived based on a rotation equal or greater than 0.33rad, thus rendering the requirements unsafe. Tying force requirements should be made explicitly dependent on the level of deflection/chord rotation of the structure to ensure that the required tying force is effectively mobilised.

Further to the considerations of rotation capacity, mobilisation of tying forces also requires adequate boundary restraint from the surrounding structure. Limited guidance is, however, provided in the current regulations and is mostly in the form of general statements. For example, the UFC code requires both framed structures and load bearing-wall constructions to have a minimum number of neighbouring bays so as to ensure adequate restraint stiffness. Fulfilling this requirement though is based on engineering judgement, expecting compliance of the surrounding structure over the whole range of restraint demand from the affected system. Instead, the demand in planar restraint should be explicitly quantified since it depends on the level of tying force and rotation of the affected system, the combination of which could render a restraint demand exceeding the capacity provided by the recommended number of neighbouring bays in the UFC code. Another shortcoming of current regulations is that tying requirements are formulated under static loading condition when the sudden loss of a column/load-bearing member is a dynamic event. Dynamic amplification is not reflected in the current prescriptive tying requirements, not even in the UFC code, which does consider a so-called dynamic increase factor (DIF) for the requirements of notional member removal (i.e. alternative load path method).

As alternative methods close to the context of prescriptive tying forces, recently published closed-form analytical solutions for double-span beams primarily aim at addressing the lack of rotation capacity and planar restraint considerations in current tying force requirements (e.g. Jian and Zheng, 2014; Stylianidis *et al.*, 2016; Pham and Tan, 2017; Wang and Kang, 2019; Kang *et al.*, 2020). Formulation of the analytical methods is usually based on either detailed cross-section analysis to establish equilibrium and compatibility equations (Jian and Zheng, 2014; Wang and Kang, 2019; Kang *et al.*, 2020) or semi-empirical expressions defined via extensive sensitivity assessment of the double-span beam response to pre-established parameters (Pham and Tan, 2017). Accordingly, these methods generally account for the interaction of flexural and axial forces for the entirety of the loading response, including compressive arching/membrane action and tensile catenary/membrane action. Notwithstanding, the resulting analytical expressions are typically too complex for the objectives set out for the use of prescriptive tying forces and, for methods formulated under a semi-empirical framework, the physical meaning of the corresponding expressions can be even unclear. Furthermore, similarly to the current tying force requirements, the application of such analytical methods is also limited to: (i) specific and individual loading conditions (typically a concentrated load applied at the location of the lost column/load-bearing member), (ii) 1D assessments neglecting

the consideration of redistribution of forces within 2D systems and (iii) assessment under static conditions.

Li and co-workers (Li *et al.*, 2011, 2014) proposed an improved tying force formulation, partially addressing some of the aforementioned shortcomings, including (i) further simplification to the analytical expressions, where the gravity loads are assumed to be resisted via tying of the double-span beam alone under the tensile catenary stage, (ii) development of analytical expressions for double-span beams under uniformly distributed load conditions (Li *et al.*, 2014), (iii) acknowledgement of tying within 2D systems considering a system of orthogonal double-span beams as the equivalent model (Li *et al.*, 2011) and (iv) recovery of dynamic load response via the application of dynamic amplification factors similar to DIFs in the UFC code. Still, the range of applicable loading conditions remains limited, and the tying formulation proposed by Li *et al.* (2011) is primarily focused on the catenary action of beams where, despite initial efforts in recognising redistribution of forces via tying action in 2D systems, the formulation assimilates the derivation procedure of the requirements in Eurocode 1 – Part 1-7 for framed structures.

There is experimental evidence (e.g. Qian *et al.*, 2014; Lu *et al.*, 2017) that floor slabs also contribute significant load resistance via tensile membrane action. In this respect, there are existing analytical methods predicting the entire loading response of floor systems under column/load-bearing member loss scenario (e.g. Bailey, 2001; Foster *et al.*, 2004; Pham and Tan, 2019a). However, these methods present similar shortcomings as those discussed for double-span beams in the sense that the ensuing formulation may not be suitable for practical application and that the models are limited to concentrated load and uniformly distributed load conditions. A rational yet practical approach suitable for codification has not yet been developed for the quantification of tying resistance via the floor system. Importantly, such an approach should allow for a practical combination of different sources of tying (i.e. catenary action of beams and tensile membrane action via distributed ties within the floor slab) and different loading conditions (i.e. concentrated loads applied at any given location of the floor system and generic floor loads).

2.4 Notional member removal and key element provisions

The alternative load path method offers a more performance-based approach for the robustness assessment of structures compared to the tying force requirements. The method presumes an initial local damage and assess whether the structure can develop alternative load paths to

prevent further propagation of damage leading to disproportionate collapse. A selection of localised damage scenarios can be considered such as explosions, impacts and instantaneous column/load-bearing member loss. Importantly, sudden member removal has further significance in relation to the structural response under local damage scenarios associated with explosions, where the consideration of sudden member removal is a realistic and typically conservative event-independent assumption as it can be shown to offer a upper bound on the building response in comparison with column damage due to blast event (Gudmundsson and Izzuddin, 2010).

The robustness assessment of the building structure can in principle proceed beyond the initial assessment with alternative load path method, where consideration is given to the impact of the failed upper floors, which exceeded the limits required by the alternative load path method, on the lower floors of the building structure. Disproportionate collapse is avoided if the lower floors can resist the impact of the debris from the failed upper floors. In this respect, however, Vlassis *et al.* (2009) have shown that even the collapse of just one floor leads to onerous demands in the lower floors. Therefore, allowing for the failure of bridged floors subsequent to the sudden loss of a column consists in an unrealistic robustness limit state (Izzuddin, 2010). Accordingly, the robustness limit state should focus on the compliance of alternative load path requirements within the affected system and to ensure that the surrounding structure can withstand the redistributed gravity loads. Exceedance of such robustness limit state would imply the consideration of the removed member as a key element, which should then be designed to resist a pressure load of $34kN/m^2$ as per the UK building regulation and the Eurocode. This pressure load corresponds to the estimated pressure of the gas explosion that led to the partial collapse of the Ronan Point Tower. In this respect, however, the key element provision can be unconservative as it presumes that all pressure loads originating from blasts would necessary be equal if not lower than $34kN/m^2$.

Consideration is subsequently given to the methods allowed in current regulations for the assessment of sudden member loss, namely linear analysis, nonlinear static analysis and nonlinear dynamic analysis, with emphasis on the corresponding limitations, culminating in the presentation of the simplified assessment framework proposed by Izzuddin *et al.* (2008) as a practical alternative addressing the shortcomings of such conventional approaches within a rational framework.

2.4.1 Linear analysis

Linear analysis excludes the consideration of material and geometric nonlinearity, hence is mostly suitable for the assessment of non-ductile building structures where member/component failure is often associated to the exceedance of strength limit rather than the exceedance of ductility/deformation limit. It also requires that resistance is mobilised i) in the range of small displacement, ii) without significant material nonlinearity, and iii) without local and global structural instabilities.

Notwithstanding, the GSA code and the UFC code still allow for the use of linear procedures to represent the dynamic and nonlinear effects associated to sudden member removal via the application of force-based factors, where the design action and the expected capacity of the components within the affected system are scaled by a dynamic multiplier and a resistance factor, respectively. Thus, the ratio of the dynamic multiplier to the resistance factor establishes an equivalent dynamic load amplification, which implicitly considers the nonlinear response of the system. Accordingly, it can be shown that the dynamic multiplier (2.0) and resistance factor (so-called 'capacity increase factor', CIF) recommended in the first version of both codes (GSA, 2003; DoD, 2005) can result in an equivalent dynamic load amplification lower than 1.0 (McKay *et al.*, 2012). This is clearly unsafe as it suggests that the applied loads considered for the analysis are lower than the gravity loads. The subsequent revision of the GSA code (GSA, 2013) and the UFC code (DoD, 2009) tentatively improved the provisions by replacing the CIF and the dynamic multiplier of 2.0 respectively with the so-called 'm-factor' m_{LIF} and a dynamic amplification dependent on such 'm-factor' Ω_{LD}, thereby resulting in an equivalent dynamic amplification which varies between 1.0 and 2.0 (McKay *et al.*, 2012).

$$\Omega_{LD} = \begin{cases} 1.2m_{LIF} + 0.80 & \text{for RC framed structures} \\ 0.9m_{LIF} + 1.10 & \text{for steel structures} \end{cases} \tag{2.2}$$

Nonetheless, neither version of the codes accurately addresses the equivalent dynamic amplification, as the proposed scaling factors do not explicitly account for a general nonlinear response and ductility limit of the system.

On the other hand, the optional limitation of the system response to linear elastic for a more accurate and typically conservative analysis leads to an unrealistic and economically inviable design of structures against disproportionate collapse as it does not take advantage of the available ductility of the components and the mobilisation of secondary resistance mechanisms.

As such, linear static analysis is often not considered as an attractive approach for general robustness assessment.

2.4.2 Nonlinear analysis

Nonlinear analysis offers major advantages compared to linear static analysis, specifically in its ability to account for material and geometric nonlinear behaviour of the structure, hence the analysis is specifically appealing to structures in which components can develop significant plastic deformation before failing by fracture. The analysis typically considers the modelling of large displacements, structural instability and inelastic material response (e.g. cracking of concrete, yielding and fracture of steel). Accordingly, depending on the sophistication of the model in considering the aforementioned modelling features, the nonlinear response preceding component failure/structural collapse can be represented to various degrees of accuracy including flexural strength, compressive arching/membrane action and tensile catenary/membrane action. This posits nonlinear analysis as a more suitable procedure for general robustness assessment since a more realistic and economically viable design, exceeding the conventional strength-based norms, can be achieved. In this respect, the main consideration for nonlinear analysis is to ensure that, under the sudden loss of a column, the maximum dynamic deformation of the components due to the applied gravity loads is within their corresponding deformation limit. The nonlinear response can conservatively terminate at first component failure (fracture) if the response following such failure is not accounted by the nonlinear analysis model. Otherwise, with the use of more sophisticated models that can realistically reproduce successive component failures, the nonlinear analysis can take advantage of the residual strength of the structure following initial component failure.

For nonlinear static analysis, the dynamic nature of sudden column loss can be again reflected via amplification of the gravity loads within the affected system. Notwithstanding, similarly to linear analysis, the revised version of the GSA code and UFC code utilise force-based dynamic increase factors as per (2.3) for such scaling purpose (McKay *et al.*, 2012), which is an improvement from the rotation-independent factor of 2.0 used in the first iteration of the codes. A dynamic amplification of 2.0 is appropriate for structural responses limited to the linear elastic range. For nonlinear structural responses, dynamic amplification is generally reduced via hysteretic damping resulting from the development of significant plastic deformation in the components, rendering the amplification factor of 2.0 generally overconservative in nonlinear static analysis (Tsai and Lin, 2009; McKay *et al.*, 2012).

$$\text{DIF} = \begin{cases} 1.04 + \dfrac{0.45}{\dfrac{\theta_{pra}}{\theta_{yield}} + 0.48} & \text{for RC framed structures} \\ 1.08 + \dfrac{0.76}{\dfrac{\theta_{pra}}{\theta_{yield}} + 0.83} & \text{for steel structures} \end{cases} \tag{2.3}$$

where θ_{pra} is the plastic rotation angle and θ_{yield} is the rotation at yield.

Equation (2.3) indicates that the DIF decreases from 2.0 to 1.0 with increasing plastic deformations, hence suggesting the influence of dynamic effects to be progressively dampened by the development of plastic deformations. It is worth noting though that (2.3) was obtained based on structures exhibiting an elastic-perfectly plastic response, thus ignoring contributions to load resistance enhancement such as material strain hardening and mobilisation of compressive arching/membrane action and tensile catenary/membrane action. It can be shown that, in the presence of hardening effects, the dynamic amplification factor commonly varies from 2.0 to a minimum value (always above 1.0) following yielding of the components but then increases again with progressive hardening, approaching back to the value of 2.0 with significant development of tensile catenary/membrane action (Izzuddin and Nethercot, 2009; Naji and Irani, 2012; Li *et al.*, 2014; Ferraioli, 2016). Therefore, despite the relative realism achieved by the dynamic increase factors presented in (2.3) compared to the amplification factor of 2.0, the use of such DIFs can lead to unsafe assessments, specifically for structures with significant hardening behaviour.

Nonlinear dynamic analysis, on the other hand, can reproduce the influence of sudden loss of a column without making assumptions regarding dynamic amplification. Robustness assessment is undertaken using time history dynamic analysis under loading representing the loss of a column. The most effective representation is to first apply gravity loads statically to the undamaged structure or, alternatively, to the locally damaged structure along with initial loading representing the reactions from the lost column. Once static equilibrium is reached for the initial state of the structure, the column or, alternatively, the initial loading representing the reactions from the lost column can then be removed over a very short duration to simulate sudden loss of the column, usually in a few milli-seconds. This is the loading procedure adopted by the current GSA and UFC codes, requiring the duration for removal of the column to be less than "one tenth of the period associated with the structural response mode for the vertical motion of the bays above the removed column". A simpler but less accurate procedure is to

consider the model of the locally damaged structure and apply the gravity loads over a very short duration, but only in the parts of the structure directly affected by the local damage. The gravity loads on the remote parts of the structure should be applied statically, otherwise the internal forces in the remote parts would be significantly overestimated.

Nonlinear dynamic analysis also requires mass and damping considerations in addition to the nonlinear resistance and deformations properties of the components. The treatment for viscous damping can follow the Rayleigh assumption of proportionality to stiffness and/or mass in accordance with a specific damping ratio in the lowest governing vibration modes.

Rate-sensitivity is another feature of material response that can be effectively reproduced with nonlinear dynamic analysis. However, Pereira (2012) has shown that the effects of loading-rate for building structures under the sudden loss of a column can generally be neglected, as the associated loading rates are often much slower compared to blast and impact loadings.

Amongst the analysis procedures currently recommended in design regulations, nonlinear dynamic analysis provides the most realistic robustness assessment under the sudden loss of a column. Although, the use of this analysis procedure comes at a significant computational expense, even more than the nonlinear static procedure, as it requires iterative procedures for equilibrium convergence as well as time stepping. Furthermore, the analysis considers a specific level of gravity load for each analysis run, demanding for multiple simulations if robustness of the structure is to be assessed under different levels of gravity loading.

2.4.3 Simplified assessment framework

Clearly, the analysis procedures currently allowed in design regulations present their own limitations, where either the sophistication of the approach does not comply with the practicality required for common engineering practice or the assumptions made for the use of more simplified approaches are unrealistic and even unconservative. As a tentative proposal to provide some redundancy for these analysis procedures, Marjanishvili (2004) suggested a sequential design approach involving the assessment of the structure via analysis procedures of increasing levels of sophistication and accuracy, from linear static analysis to nonlinear dynamic analysis, until a satisfactory design is achieved. Nevertheless, the practicality and accuracy of this approach remain questionable due to its repetitive nature and to the limitations inherent of each analysis. Furthermore, it is not guaranteed that the simpler analysis procedures are more conservative (Marjanishvili and Agnew, 2006; Izzuddin, 2010).

The ductility-centred robustness assessment approach recently developed at Imperial College London (Izzuddin *et al.*, 2008), which makes use of the nonlinear static response of the building structure or its sub-systems, can effectively address the inaccuracies and limitations of the analysis procedures currently recommended in the regulations whilst providing a practical framework for common engineering practice. Instead of employing force-based dynamic amplification factors, the dynamic response is determined from the transformation of the nonlinear static response into a so-called pseudo-static response based on principles of energy balance. As such, the framework rationally considers the effects of system ductility on the dynamically amplified response, as the applied amplification directly depends on the determined nonlinear static response instead of a pre-established response (such as the elastic-perfectly plastic response assumed in the current GSA and UFC codes).

On the other hand, because the framework is applicable at various levels of structural idealisation, consideration of highly detailed models for nonlinear static analysis can be computationally less prohibitive compared to those used in analysis procedures currently recommended in the regulations, as modelling can be simply limited to planar or grillage beam sub-systems instead of representing the whole building bay. The assessment proceeds in three main stages:

- Determination of the nonlinear static response of the damaged structure under gravity loading, encapsulated within a multi-level assessment framework;
- Simplified dynamic assessment to establish the maximum dynamic response, so-called pseudo-static response, under the sudden loss of a column/load-bearing member;
- Ductility assessment of components leading to the determination of the pseudo-static capacity.

2.4.3.1 Multi-level application and nonlinear static response

For the assessment of the building structure under the sudden loss of a column/load-bearing member, the simplified framework is applicable at several levels of structural idealisation, allowing for successive model reduction depending on the regularity of the structure, from the building bay directly affected by the loss of the column/load-bearing member to a grillage system comprised of individual beams, as illustrated in Fig. 2.1.

Considering the assessment to begin at the highest level of model reduction, emphasis should be given to the accurate representation of the nonlinear static response of beam sub-systems. This involves the modelling of large displacements and inelastic material response, taking full

advantage of the ductility supply of the system. For concrete structures, as detailed later in Section 2.5, further to the use of fibre-beam elements for the representation of axial-flexural interaction, modelling of beam sub-systems should involve the fracture of the reinforcement and the bond-slip between the concrete and the reinforcement as these features govern the ductility limit of the beam sub-system.

Then, provided that the building structure undergoes a dominant deformation mode governed by a single degree of freedom (SDOF), the response of individual floors (and subsequently the response of the affected building bay) can be determined from the assembly of the individual beams (and subsequently the assembly of the individual floors) based on the equivalence of energy absorption (Izzuddin *et al.*, 2008).

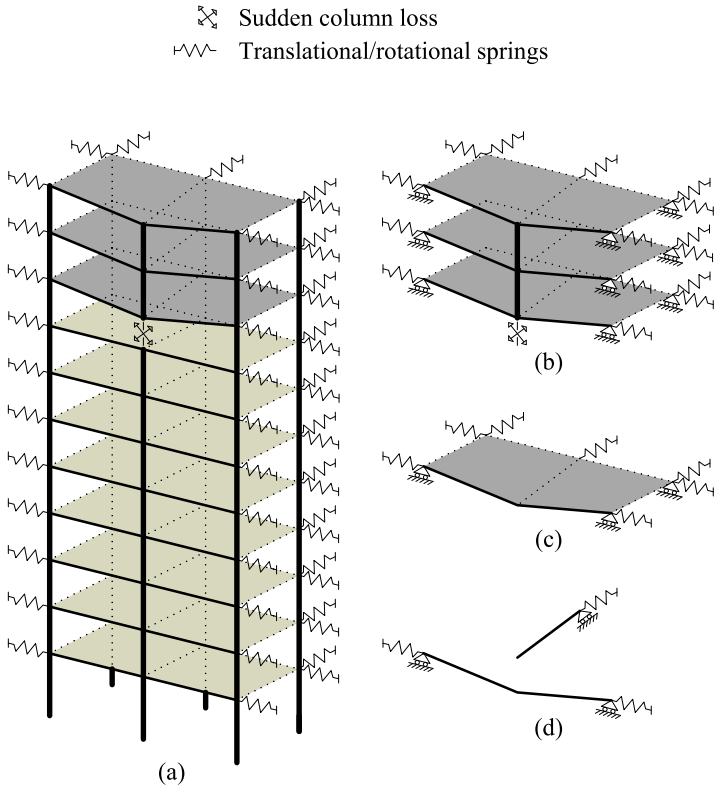
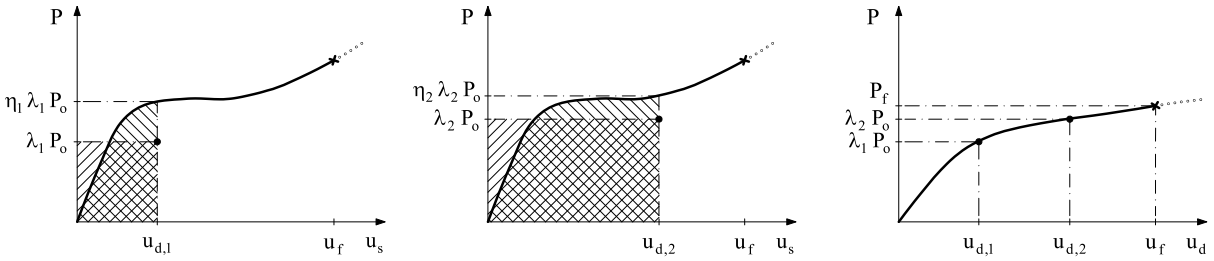


Fig. 2.1 – Sub-structural levels for progressive collapse (source: Izzuddin *et al.*, 2008)

2.4.3.2 Simplified dynamic assessment

The conversion of the nonlinear static response into the pseudo-static response based on energy balance considerations again requires the affected structure to undergo a dominant deformation mode such that it can be treated as a nonlinear single degree of freedom (SDOF) system. Fig. 2.2 illustrates the basis for such a response conversion.



(a) Dynamic response ($P=\lambda_1 P_o$) (b) Dynamic response ($P=\lambda_2 P_o$) (c) Pseudo-static response

Fig. 2.2 – Simplified dynamic assessment and definition of pseudo-static response (source: Izzuddin *et al.*, 2008)

When the column is suddenly removed, which is similar to a sudden application of a gravity load $\lambda_n P_0$ on the affected structure (where λ_n is the load factor and P_0 is the nominal load), the gravity load exceeds the static structural resistance. The differential work done over the incremental deformation is transformed into kinetic energy, leading to increasing velocities. As deformation increases, the structural resistance surpasses the gravity load, beyond which the differential work accounts for a reduction in kinetic energy instead, leading to decreasing velocities. The affected structure reaches its maximum dynamic displacement $u_{d,n}$ when the kinetic energy of the system is reduced back to zero.

According to Fig. 2.2, this corresponds to the condition occurring at displacement $u_{d,n}$, in which the area delimited by the nonlinear static resistance of the system becomes equal to the rectangular area defined by the product of $u_{d,n}$ and the applied gravity load $\lambda_n P_0$. The pseudo-static response can be obtained for different levels of applied load $\lambda_n P_0$, where the corresponding maximum dynamic displacement $u_{d,n}$ is determined as (Izzuddin *et al.*, 2008):

$$P_n = \lambda_n P_0 = \frac{1}{u_{d,n}} \int_0^{u_{d,n}} P \, du \tag{2.4}$$

in which P is the nonlinear static resistance of the system.

2.4.3.3 Ductility assessment of components and robustness measure

The final step of the assessment is to define the ductility limit and robustness measure of the system. The ductility limit of the system, herein represented by the failure displacement limit u_f, can be established based on simplified or detailed models of the system with appropriate consideration of the features detailed in Section 2.4.3.1. Once the failure displacement limit of

the system u_f is defined, the limit gravity load that can be sustained under sudden column loss is determined as the maximum value P_f from the pseudo-static response such that:

$$P_f = \max(P_n) \text{ for } 0 \le u_{d,n} \le u_f \tag{2.5}$$

where P_n and $u_{d,n}$ follow identical definitions as in (2.4).

It is worth noting that P_f is not necessarily associated with u_f if the nonlinear static response is not monotonically increasing, requiring the determination of the full pseudo-static response (Izzuddin, 2012). This is typically the case for analyses allowing for successive component failures or for static responses where the resistance within a compressive arching stage governs.

2.5 Behaviour and characterisation of RC planar frame sub-systems

Considering the applicability of the ductility-centred framework proposed by Izzuddin *et al.* (2008) to the highest level of model reduction, emphasis is placed on the development of simplified numerical models capable of accurately predicting the nonlinear static response and ductility limit of planar frame/beam sub-systems. In this respect, despite notable outcomes from the research work affiliated to Imperial College London, most of the developed models have been focused on steel and steel-concrete composite structures (e.g. Vlassis *et al.*, 2008; Pereira, 2012; Jahromi *et al.*, 2013), with limited contributions concerning the prediction of ductility limit of reinforced concrete structures. Part of the research from this thesis therefore involves the development of a simplified numerical modelling approach for RC beam sub-systems.

For such a purpose, this section provides a review on the aspects relevant for the modelling of RC beam sub-systems along with modelling strategies currently available in literature. Importantly, the limitations of such strategies are herein highlighted as motivation for the innovative extensions proposed in this thesis.

2.5.1 Typical behaviour

A typical RC beam sub-system extracted from the building structure usually comprises of a double-span beam, a middle joint representing the removed column and two boundary column stubs, as illustrated in Fig. 2.3.

Considering the case where the surrounding structure provides adequate levels of axial and rotational restraint, the beam sub-system develops secondary mechanisms at large

displacements, enhancing its load carrying resistance beyond the flexural capacity. These secondary mechanisms are denoted as compressive arching action (CAA) and catenary action (CA) depending on whether the internal axial force of the beam sub-system is compressive or tensile.

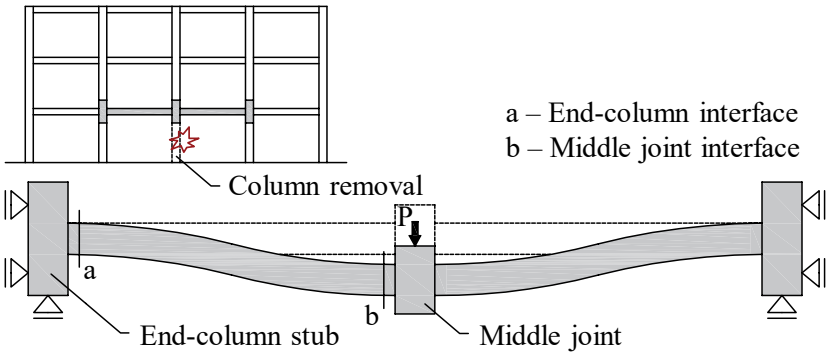


Fig. 2.3 – Typical RC beam sub-system

Fig. 2.4 illustrates the typical loading response of adequately restrained beam sub-systems under the loss of a column. In essence, following the removal of the column, the beam sub-system undergoes flexural deflection under a double-span beam configuration. Flexural cracks and the yield of reinforcement can be observed at the interfaces between the beams and the columns. These, in turn, cause the beams to elongate (Xiao and Hedegaard, 2017), but with the beam sub-system axially and rotationally restrained at the boundaries, the elongation is prevented, and a compressive force is generated instead, marking the onset of the compressive arching action phase.

The interaction between flexural and compressive axial forces has a two-fold effect on the load resistance of the beam sub-system (Su *et al.*, 2009; Yu and Tan, 2013a). On one hand, the axial-flexural interaction increases the load resistance of the beam sub-system via enhancement of the flexural resistance at the beam ends. On the other hand, the compressive axial force generates a second-order effect detrimental to the load resistance of the beam sub-system. Initially, the enhancement due to the increased flexural resistance subsumes the detrimental effects associated to the second order effects, hence the load resistance of the beam sub-system exceeds its flexural capacity. As the detrimental-second order effects overcome the enhancement of flexural resistance, the load resistance of the beam sub-system reaches a peak and decreases with further vertical displacement.

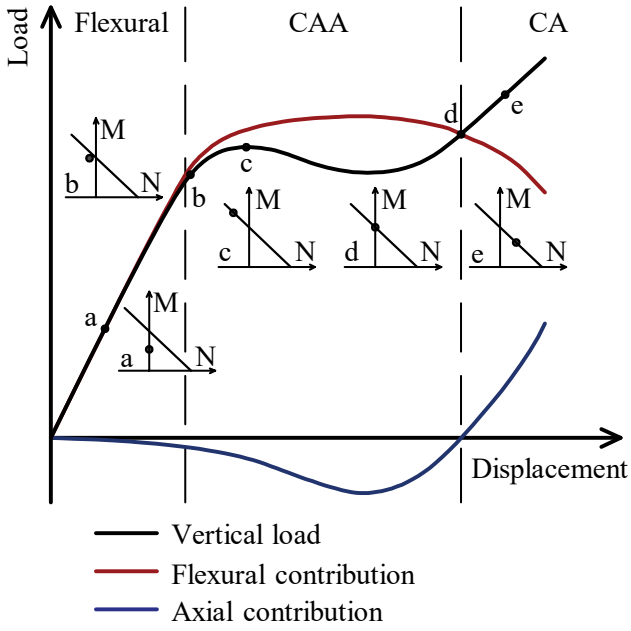


Fig. 2.4 – Schematic illustration of a typical static load-displacement response under the loss of a column

The decrease in load starts to level out when the double-span beam begins to pull-in the boundary columns. The compressive force is gradually nullified and transitioned into a tensile axial force, marking the onset of the catenary action phase. With further vertical displacement, the resistance of the beam sub-system increases again. This resistance is essentially offered by the axial tensile force within the beams since the contribution of flexural resistance becomes negligible as a result of axial-flexural interaction. If no further component failure is observed (such as the fracture of the reinforcement), the increase in load resistance with vertical displacement approximates to a linear relationship (e.g. Yu and Tan, 2012; Lim *et al.*, 2017b), with the slope primarily dependent on the amount of reinforcement to tying.

Notwithstanding the above, apart from the effects of axial-flexural interaction, the ductility of the beam sub-systems, as mainly reflected by the fracture of the reinforcement, also assumes a fundamental role in the load resistance. Note that shear failure modes are unlikely since the span-to-depth ratio of the beam sub-system under a column loss is twice the ratio under service conditions.

Each occurrence of reinforcement fracture corresponds to a sudden load drop in the load resistance of the beam sub-system. Generally, as a result of common design requirements and application of concentrated load in experiments, fracture begins with the bottom reinforcement at the middle joint (Choi and Kim, 2011; Sadek *et al.*, 2011; Yu and Tan, 2012, 2013a). This

is because the bottom reinforcement at this location is not designed to resist a sagging moment, let alone an augmented sagging moment arising from the double-span beam configuration. Subsequent to the fracture of this reinforcement, the load resistance of the beam sub-system may or may not surpass, with further vertical displacement, the resistance attained before the fracture. Eventually, the top reinforcement at the end columns also fractures, and the load resistance undergoes a sudden drop again. The residual load resistance following this load drop is usually very low, at which point the beam sub-system is considered to have failed. Notwithstanding, the order of reinforcement fracture can be inverted, with fracture of reinforcement first occurring at the end columns, as typically shown in experiments under uniformly distributed loads (Pham and Tan, 2019b).

The load-deflection response of a RC beam sub-system under the loss of a column is demonstrated based on published experimental, numerical and analytical outcomes to be sensitive to parameters such as the reinforcement ratio, span-to-depth ratio, boundary restraint stiffness, the contribution of the slab as part of a T-shaped beam cross-section, seismic design and detailing, and others. In summary, the following can be concluded from the variation of such parameters:

- Reinforcement ratio (Su *et al.*, 2009; Yu and Tan, 2012; Alogla *et al.*, 2016b) – the increase in reinforcement ratio leads to a resistance enhancement of the beam sub-system within the flexural/CAA stage, but also within the CA stage if the additional reinforcement is continuous throughout the beam sub-system.
- Span-to-depth ratio (Su *et al.*, 2009; Yu and Tan, 2012; Tsai and Chang, 2015) – the ratio primarily defines the dominant mechanism (CAA or CA) via which the beam sub-system arrests disproportionate collapse, as a higher ratio enhances resistance within the CAA stage, whilst a lower ratio increases the transverse displacement of the system, thus allowing for an extended gain in resistance under catenary action.
- Boundary restraint stiffness (Yu and Tan, 2013a, 2014b; Lim *et al.*, 2017b; Diao *et al.*, 2020) – the mobilisation of CAA necessitates adequate axial and rotational restraint stiffness, whilst the mobilisation of CA primarily requires adequate axial restraint only. Once the minimum requisite restraint stiffness level is reached, further increase in such stiffness leads to a negligible increase in load resistance, under which the boundary restraints can be simply idealised as rigid supports.
- T-shaped beam cross-sections (Ren *et al.*, 2016) – the addition of one-way slab strip enhances the resistance within both the CAA and CA stages. Under the former stage,

enhancement is primarily flexural, associated to an increased geometry of the beam cross-section, whilst under the latter stage the slab reinforcement provides additional resistance via tying. It is worth noting, however, the resistance enhancement within the CAA stage is shown limited to the effective flange width of the T-section due to the phenomenon of shear lag, whilst catenary action can benefit from the whole width of the additional slab strip (Ren *et al.*, 2016).

- Seismic design – some researchers (Baldridge and Humay, 2003; Choi and Kim, 2011; Sadek *et al.*, 2011; Marchis *et al.*, 2013) argued that beam sub-systems designed for seismic regions should yield better robustness performance given the improvement in overall ductility and added amount of reinforcement. Others (Li and Sasani, 2015; Livingston *et al.*, 2015) questioned the applicability of the ductility treatment in seismic provisions for disproportionate collapse mitigation, such as the behaviour factor in Eurocode 8 (CEN, 2004a), noting that while deformation capacity is the critical measure of structural performance in seismic loading scenarios, load-carrying capacity can be a more important measure in structural robustness (Li and Sasani, 2015). Indeed, it can be demonstrated based on the pseudo-static resistance (Izzuddin *et al.*, 2008), which is herein considered as the appropriate measure for robustness, that seismic design does not necessarily lead to an improvement in structural robustness.
- Seismic detailing – Yu and Tan (2013a) suggest negligible influence of reinforcement splices and curtailments on the static resistance of beam sub-systems provided these splices and curtailments are adequately designed according to the regulations. Lim *et al.* (2017b) also report negligible influence on the static resistance of beam sub-systems for increasing number of stirrups, as the ductility limit under tensile catenary action, defined by the fracture of the reinforcement, differs from the deformation capacity under flexure.

Another important parameter which influences the ductility limit of RC beam sub-systems is the fracture of the reinforcement. This, in turn, depends on the ductility of the reinforcement and its bond-slip interaction with the concrete, where for the case of lightly reinforced concrete beams (below 1% reinforcement ratio) under the development of a single crack at the beam ends for the whole loading scenario, weaker bonds are demonstrated to improve the ductility limit of the system (Elghazouli and Izzuddin, 2004; Izzuddin and Elghazouli, 2004).

This is because, with the concentration of reinforcement strains within such cracks, at a level close to the ultimate strain, a lower bond strength leads to a less effective transmission of

stresses from the reinforcement to the concrete, resulting in higher averaged reinforcement strains along the beam sub-system. Considering that the integration of these average strains establishes the reinforcement end-slip at the single cracks, which in turn promotes the end-rotation/transverse displacement of the beam sub-system, it follows that the sub-system can undergo higher displacements prior to the fracture of the reinforcement. This delay in reinforcement fracture benefits the development of catenary action, potentially enhancing the robustness performance of the beam sub-system.

Notwithstanding the above, with the application of more common reinforcement ratios, the effects of bond-slip can be less straightforward given the possible development of additional cracks along the beam member prior to the fracture of the reinforcement at the beam ends. In this case, a stronger bond between the reinforcement and the concrete, which leads to a more frequent development of cracks, could result in an averaged reinforcement strain higher than the case with weaker bond. Despite such observations, experimental comparison performed by Lim *et al.* (2017b) between beam sub-systems using deformed and smooth reinforcement (with reinforcement ratios of 1% to 2%) suggest that the beam sub-system using the latter type of reinforcement, which is associated with a lower bond strength, presents a significantly better robustness performance, as evidenced in Fig. 2.5.

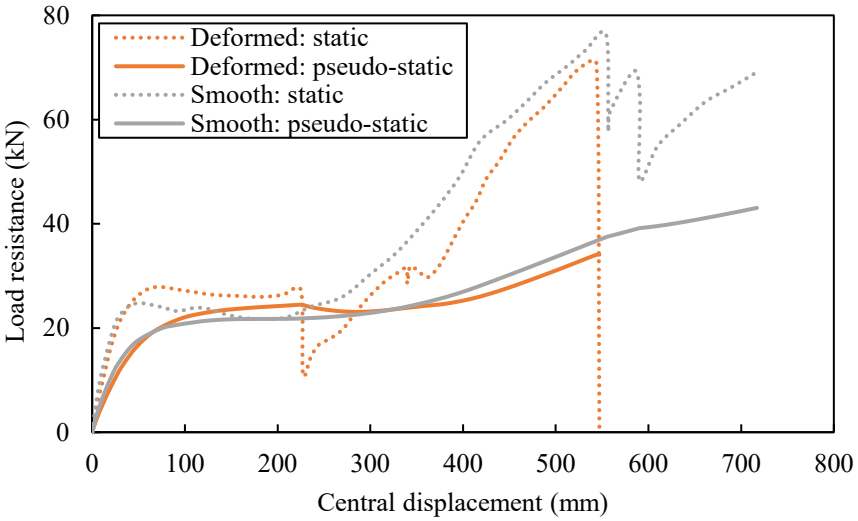


Fig. 2.5 – Response comparison between beam sub-systems with deformed and smooth reinforcement bars (experimental data from Lim *et al.*, 2017b)

It is worth noting that the experimental test of the beam sub-system with smooth reinforcement bars was terminated only with the fracture of the bottom reinforcement, and it is expected that the sub-system still presents significant residual resistance to withstand loading under much

further deflections. Although, it is also worth noting that the corresponding reinforcement ratio of this sub-system was slightly higher to compensate for the loss of flexural resistance due to reduced bond strength. Further investigation should be carried out considering the individual variation of the relevant parameters (such as reinforcement ratio and bond strength) so as to confirm whether weaker bond necessarily leads to a better robustness performance.

2.5.2 Modelling

Several types of numerical models have been published to reproduce the behaviour of RC beam sub-systems under the loss of a column. These models can be grouped into detailed finite element models and simplified beam macro models. Detailed finite element models (e.g. Bao *et al.*, 2008; Lew *et al.*, 2011; Sadek *et al.*, 2011; Bao *et al.*, 2012; Pham *et al.*, 2017b) usually employ solid and beam elements to represent the concrete and the reinforcement, respectively, whereas the bond-slip between reinforcement and concrete can be accounted by 1D contact elements. Detailed finite element models can reproduce the behaviour of the beam sub-system with high precision, but the inherent computational demand is impractical, if not prohibitive, for common design practices. In this sense, detailed finite element models are commonly preferred in academic research and for validating simplified beam macro models.

Beam macro models generally entail 1D fibre beam elements, which represent the beam members of the sub-system, along with a selection of joints and links, which represent the boundaries of the sub-system (e.g. Bao *et al.*, 2008; Sadek *et al.*, 2011; Bao *et al.*, 2012; Yu and Tan, 2013a, 2014a; Livingston *et al.*, 2015). The aim of these models is to provide practical means to assess structures under a column loss. Evidently, compared to detailed finite element models, some loss in prediction accuracy is expected due to the assumptions undertaken in model simplification. Notwithstanding, an acceptable level of accuracy can be achieved if the simplified model effectively reproduces the dominant effects and the expected damage mechanisms of the beam sub-system. The review on the behaviour of beam sub-systems under a column loss suggests that the following effects are essential and should be captured by the simplified model: i) axial-flexural interaction; ii) joint panel behaviour; iii) boundary restraints; iv) fracture of the reinforcement; and v) bond-slip between the reinforcement and the concrete.

2.5.2.1 Axial-flexural interaction

Axial-flexural interaction can be represented using 1D fibre-beam elements. The cross-section of these elements is divided into several fibres, within which a uniaxial constitutive relationship is assigned (e.g. Bao *et al.*, 2008; Sadek *et al.*, 2011; Bao *et al.*, 2012; Yu and Tan, 2013a,

2014a; Livingston *et al.*, 2015). The cross-sectional response (i.e. the axial and flexural forces) is then determined by integrating the response of each fibre over the cross-section.

2.5.2.2 Joint panel behaviour

The simplified representation of joint panel behaviour usually follows two approaches: either the various phenomena occurring within the joint panel are encapsulated within a single rotational and/or axial joint element, or the various phenomena are individually described by spring and link elements via a component-based method. Further to the characterisation of joint panel behaviour, if the bond-slip behaviour between the reinforcement and concrete is represented locally at the beam ends, the modelling of joint panels should include the bond-slip between reinforcement and concrete.

For the modelling approach involving a single rotational joint element, all relevant effects occurring within the joint should be addressed by the constitutive relationship describing the joint element. This is usually achieved by identifying the governing joint behaviour for each characteristic point of the constitutive relationship. An example of such an approach is the rotational joint element developed by Favvata *et al.* (2008).

For the component-based approach, the effects occurring within the joint panel are addressed individually by link elements, associated with different constitutive relationships. This typically entails i) a joint panel spring, representing its shear distortion; ii) a joint interface shear spring, representing the shear transfer from the beam to the joint; and iii) bar force-slip springs placed near the top and bottom part of the joint panel, representing the pair of longitudinal forces transferred from the beam to the joint, within which the bond-slip between the reinforcement and the concrete is also encapsulated. The global joint panel response is then obtained by the assembly of the individual link elements. A selection of published component-based joint panel models can be found in Lowes and Altoontash (2003), Bao *et al.* (2008), Sadek *et al.* (2011), Bao *et al.* (2012), Xu (2013), Yu and Tan (2013a, 2014a).

These typical component-based models can be further simplified under the following conditions. First, the interface shear can be assumed rigid if the beams do not develop shear damage and shear deformations are already represented via a Timoshenko-formulated fibre-beam element. The next level of simplification considers that bond-slip is not represented as part of the joint panel behaviour, with which the model of the panel reduces to the spring representing the joint panel shear. Finally, the last level of simplification can be assumed for beam sub-systems with adequate restraint, where the shear deformation in joint panels is

typically negligible. Accordingly, the joint panel shear spring can also be assumed rigid, rendering unnecessary the modelling of the joint panel altogether.

2.5.2.3 Boundary restraints

The axial and rotational restraint offered by the surrounding structure can be modelled respectively via axial and rotational springs with a linear elastic response provided that the surrounding structure remains elastic. Rotational restraint offered by the boundary structure primarily relates to the flexural stiffness of the beams and the floor slab adjacent to the beam sub-system, whilst the stiffness of the axial restraint is governed by the in-plane shear of the neighbouring slab (Wang *et al.*, 2011). Such stiffness parameters can be estimated numerically with a simplified model of the surrounding structure (Yu, 2012), or alternatively via analytical approaches.

2.5.2.4 Reinforcement fracture and bond-slip between reinforcement and concrete

As noted before, along with the ductility of the reinforcement, the bond-slip between reinforcement and concrete defines the level of beam deflection preceding the fracture of the reinforcement. Accordingly, the uniaxial steel material model should consider a tensile softening branch for the representation of reinforcement fracture.

The modelling of bond-slip is, on the other hand, less straightforward since common 1D fibre beam elements assume the reinforcement and the concrete to be fully bonded, hence not predicting any slip at the beam ends. The assumption of full bond usually leads to the prediction of premature fracture of the reinforcement, hence significantly underestimating the ductility limit of beam sub-systems. To overcome such an issue, most numerical models available in literature for the representation of beam sub-systems under column loss scenario employ a localised approach, under the backdrop that the slippage and the fracture of the reinforcement are most critical near the beam ends. This involves the modelling of bond-slip via the component-based approach described in Section 2.5.2.2 (e.g. Lowes and Altoontash, 2003; Yu and Tan, 2014a), where the stress-slip relationship of the reinforcement is commonly determined using the analytical bond model proposed by Lowes and co-workers (Lowes and Altoontash, 2003; Lowes *et al.*, 2004a). Under the assumption of piece-wise constant bond strengths, the model first considers the possible strain that the reinforcement can develop along its embedment length. The model then determines the stress-slip relationship of the embedded reinforcement by integrating the reinforcement strains $\varepsilon(x)$ along the considered embedment length l:

$$s = \int_0^l \varepsilon(x)\, dx \tag{2.6}$$

As an alternative to representing bond-slip with force-slip springs, Sadek *et al.* (2011) and Bao *et al.* (2012) altered the steel constitutive relationship in 'critical' fibre beam elements (i.e. elements located at the critical parts of the beam) to address the influence of bar slippage on the reinforcement strains:

$$\varepsilon' = \frac{L - L_0}{L_0} = \frac{s(\sigma) + \varepsilon(\sigma) L_0}{L_0} = \frac{s(\sigma)}{L_0} + \varepsilon(\sigma) \tag{2.7}$$

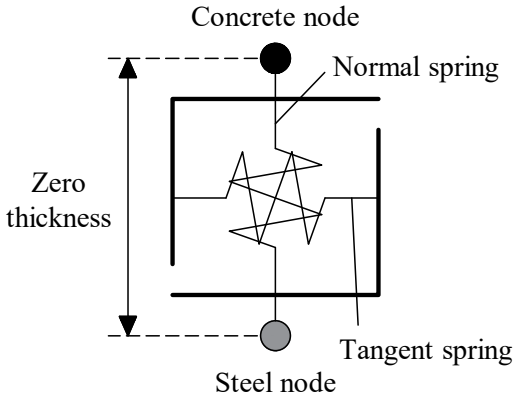
where L_0 and L are the original and deformed length of the reinforcement; $s(\sigma)$ and $\varepsilon(\sigma)$ are respectively the slip and the original reinforcement strain under stress σ, with $s(\sigma)$ again established via the approach proposed by Lowes and co-workers (Lowes and Altoontash, 2003; Lowes *et al.*, 2004a).

Despite its relatively practical application, localised modelling of bond-slip, involving force-slip springs or alteration of the steel constitutive relationship in 'critical' fibre beam elements, is limited to rather simple bond-slip and steel reinforcement relationships, treating bond stress as average values and assuming a bilinear curve for the reinforcement. The formulation of these approaches becomes increasingly complex when more sophisticated material laws are considered, under which the determination of a closed-form solution is no longer possible.

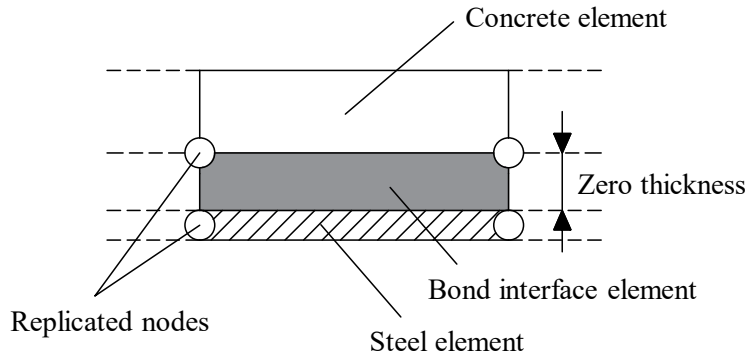
Another limitation of localised bond-slip modelling is that it fails to provide an accurate representation of crack development along the beams of the sub-system. Accordingly, the approach can only assess scenarios where a single crack is developed at the beam ends; and would not be able to model bond-slip and crack development for more sophisticated reinforcement detailing schemes, involving reinforcement curtailments and splices.

Generalised modelling of bond-slip along the whole member length would generally involve the separate modelling of the steel reinforcement and the concrete, with the corresponding elements presenting separate but coincident set of nodes. These nodes are then connected based on the considered bond modelling approach, either employing discrete bond link elements or continuous bond interface elements (Khalid, 2011; Casanova *et al.*, 2012). The former approach, illustrated in Fig. 2.6a, utilises link elements to couple the nodes of the concrete and the steel discretely. These elements have no physical dimensions, with the coupled nodes having the same coordinates in the undeformed state. Given the discrete nature of the coupling, the link properties are sensitive to the mesh size and should be readjusted upon mesh refinement.

The latter approach, illustrated in Fig. 2.6b, couples the concrete and the steel elements using interface elements with zero thickness, leading to a continuous interaction between steel and concrete (e.g. Lowes *et al.*, 2004b). It requires, however, the interface element to be compatible with the order of the concrete and reinforcement elements (Khalid, 2011). Despite the relative sophistication achieved with generalised bond modelling approaches, the need for duplicate nodes to connect the steel and concrete elements via bond links/interfaces imposes not only increased modelling demands, specifically with the use of discrete bond link elements, but also computational demands due to a significant increase in the number of degrees of freedom when the model involves many beam elements.



(a) Discrete bond link elements



(b) Continuous bond interface elements

Fig. 2.6 – Typical bond-modelling approaches currently available in literature

In recognition of the limitations of existing localised and generalised bond modelling strategies, Khalid (2011) developed a modelling approach for RC members which is capable of representing the influence of bond-slip and crack development for the whole member whilst realising such relative sophistication at a reduced computational expense by avoiding the need for duplicate nodes. In this approach, the concrete and the reinforcement are still modelled with

their dedicated fibre-beam elements. However, bond-slip is encapsulated in the reinforcement element as a layer of the fibre-beam approach, without requiring any additional bond elements. Consequently, there is no need to define separate nodes to be connected by these bond elements. In this approach, the concrete and the reinforcement elements are overlaid with each other and share the same nodes, and the treatment of bond-slip as a layer of the fibre-beam approach also allows for a straightforward consideration of uniaxial nonlinear bond-slip laws. Other features of the approach include its ability to model each reinforcement bar individually, enabling the assessment of RC members with a wide variety of reinforcement detailing, and the ability to represent nonlinear cross-sectional deformations (beyond the assumption of plane sections remaining plane), which is important for realistic modelling of concrete cracking. Considering such benefits, the present thesis proposes a novel modelling approach for beam sub-systems under the loss of a column, making use of the fibre-beam elements proposed by Khalid (2011). Further details on these elements are provided in Section 3.2.

2.6 Behaviour and characterisation of RC floor systems

This section provides a review on the behaviour and characterisation of RC floor systems as a basis for the validation and verification of the novel horizontal tying force method, along with its extension involving the planar restraint stiffness contribution from the compressive ring and the floor system response under corner column loss scenario.

2.6.1 Typical behaviour and membrane action

Similar to beam sub-systems, floor systems can develop secondary mechanisms under large displacements which are additional to the compressive arching action and catenary action of beams. These mechanisms are denoted as the compressive and tensile membrane actions of the slab. Membrane action was first studied in the 1960s (Park, 1964a, 1964b, 1965; Taylor, 1965; Taylor *et al.*, 1966; Hayes, 1968) and is recently researched more extensively due to the wider interest in structural robustness, including 1-way membrane action (e.g. Gouverneur *et al.*, 2013; Gouverneur *et al.*, 2015; Lu *et al.*, 2017; Yu *et al.*, 2020a) and 2-way membrane action (e.g. Dat and Hai, 2013; Qian *et al.*, 2014).

In essence, with adequate restraints to mobilise compressive arching/membrane action (CAA/CMA) and tensile catenary/membrane action (TCA/TMA), the floor system would follow a similar load history as the beam-only sub-system, characterised by an initial local peak within the CAA/CMA stage and by an approximately linear load increase within the TCA/TMA stage. Although, a more substantial increase in load resistance is achieved within

both stages due to the additional resistance contribution from the slab. The load enhancement within the CAA/CMA stage of a floor system, compared to a beam-only sub-system, is primarily due to the increase of flexural resistance from the T-beam effect and to a more extensive mobilisation of CAA as a result of the increased beam depth, with similar findings also reported in Ren *et al.* (2016). Furthermore, the slab also offers resistance contribution via bending and compressive membrane effects.

Of greater interest to the current research work is the mechanism occurring within the TCA/TMA stage, where the slab enhances the load resistance of the floor system primarily via the contribution of additional reinforcement to tying. It is also worth noting that a self-equilibrated restraint mechanism is mobilised within the floor slab, which is additional to the usual restraint provided from the surrounding structure, though this effect is reduced for peripheral floor systems.

Such a self-equilibrated mechanism (Fig. 2.7) involves the development of a compressive ring along the perimeter of the affected floor system, equilibrating the pull-in due to the tensile forces developed within the central region of the system. Thus, this self-equilibrium can offer a certain level of horizontal restraint to mobilise the tying of the reinforcement even if the floor system is not restrained in the plane by its surrounding structure (Taylor, 1965; Dat and Tan, 2013).

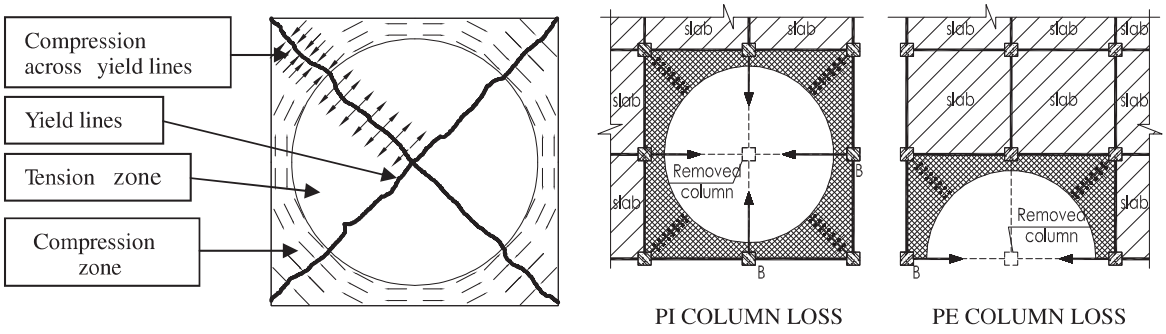


Fig. 2.7 – Tensile membrane action (source: Dat and Hai, 2013)

Consistently, the self-equilibrating system can also reduce the demand of tensile catenary/membrane action on the restraint stiffness from the surrounding structure (Dat and Hai, 2013; Dat and Tan, 2013), specifically benefitting floor systems under edge or corner removal scenarios, where the restraint stiffness from the surrounding structure is usually inadequate. In such scenarios, the generated compressive ring delays the excessive inward displacement of the peripheral beams and columns, which would otherwise fail prematurely.

The less stringent restraint stiffness demand due to the contribution of the compressive ring also indicates that TCA/TMA is less sensitive to boundary restraints than CAA/CMA (Mitchell and Cook, 1984). Indeed, typical load-deflection responses of floor systems under peripheral and corner column loss scenarios do not usually exhibit an initial load peak within the flexural loading stage. Instead, the load response directly transitions from the flexural stage to the tensile catenary/membrane action stage.

Further to the effects already discussed in Section 2.5.1 for beams, the load-deflection response of RC floor systems under the loss of a column is demonstrated based on published literature to depend on parameters such as the thickness of the slab, the slab reinforcement ratio, the aspect ratio of the slab, the loading condition and the location of column loss.

2.6.1.1 Slab thickness, reinforcement ratio and slab aspect ratio

Experimental tests from Yu *et al.* (2020a) suggest that structural resistance of floor systems increases with the slab thickness and the reinforcement ratio, with the former parameter primarily enhancing the system response via flexure, whilst the latter led to a more substantial increase in tying forces within the TCA/TMA stage.

Comparison of axially unrestrained floor systems experimented by Dat and Tan (2013) suggest that the slab aspect ratio (i.e. length-to-width ratio) alters the formation of yield lines and the damage sequence of the components of the floor systems. Dat and Tan (2013) also note that the load increase due to tensile catenary/membrane action is more significant in square floor systems than in the rectangular floor systems with equivalent material and geometric characteristics. An elliptical compression ring forms in rectangular floor systems under tensile membrane action, which is less effective than a circular ring in equilibrating the pull-in forces from the horizontal ties, as the elliptical geometry would lead to an equilibrium mechanism where the ring is simultaneously under compression and bending.

2.6.1.2 Loading condition

Pham *et al.* (2017a) and Yu *et al.* (2020a) presented similar findings on the load resistance of floor systems under applied concentrated load (CL) and uniformly distributed load (UDL), concluding that floor systems under the latter load condition develops a higher load resistance under the loss of a column (approximately four-fold of the resistance under CL). This can be demonstrated based on the larger extent of yielding within the central part of the slab under UDL, as opposed to the localisation of damage within the vicinity where the CL is applied.

2.6.1.3 Location of column loss

As noted before, activation of compressive and tensile membrane forces depend on the level of boundary restraint provided to the affected floor system. In this respect, only under the scenarios of internal and edge column loss that the load-deflection response of floor systems usually presents an initial load peak within the flexural stage and with tying fully activated within the TCA/TMA stage. For the remaining column loss scenarios (i.e. corner, penultimate interior and penultimate exterior), there is negligible activation of CAA/CMA and, despite some self-restraint developed by the compression ring, the total planar restraint stiffness is generally inadequate to fully activate tensile membrane action. Pham *et al.* (2017a) assessed the resistance performance of floor systems subject to internal, corner, edge, penultimate-interior (PI) and penultimate-exterior (PE) column removal scenarios, which comparison of the load-deflection responses (Fig. 2.8) confirms the above observation.

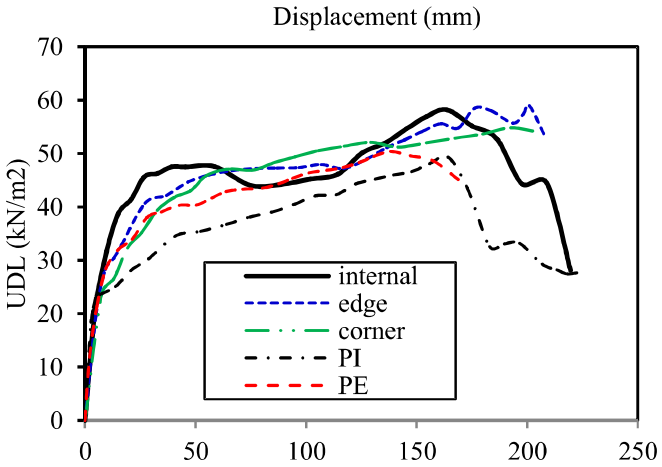


Fig. 2.8 – Load-deflection response from different column loss scenarios (source: Pham *et al.*, 2017a)

For corner, penultimate interior and penultimate exterior column loss scenarios, the anchorage of slab reinforcement under typical arrangement layouts (i.e. reinforcement placed parallel to the edges of the floor system) locates along the peripheral beams. The activation of tying within the slab reinforcement tends to pull-in the peripheral beams, damaging the beams by torsion and/or in-plane bending, which in turn lose their ability to provide the requisite planar restraint. As a result, floor systems under corner, penultimate interior and penultimate exterior column loss scenarios are typically considered to mitigate disproportionate collapse primarily via flexural resistance of beams and the slab (Qian and Li, 2012; Dat and Tan, 2013, 2014; Yu *et al.*, 2020b) and/or via Vierendeel action of frames when considering the assessment of multiple floors (Yi *et al.*, 2008; Li *et al.*, 2016; Diao *et al.*, 2020).

Given that the successful activation of tying would potentially enhance the resistance of the floor system beyond its flexural capacity, it is worth considering structural solutions where the activation of tying becomes possible for corner, penultimate interior and penultimate exterior column loss scenarios. There are, however, limited research for such a purpose. Yu *et al.* (2020b) note that the consideration of slab flanges at the free ends of the floor system (slab cantilevers) can enhance the torsional and pull-in resistance of the peripheral beams, thus providing the required axial restraint for mobilisation of TCA/TMA, even though the consideration of slab cantilevers is not always feasible, specifically in dense urban areas where buildings are commonly built immediately adjacent to each other. Furthermore, since the occurrence of disproportionate collapse of structures is generally very unlikely, this also leads to a substantial increase in construction cost if slab cantilevers are designed only with the purpose of promoting the activation of tying.

The research work of this thesis explores tensile membrane action under an alternative slab reinforcement layout, involving the arrangement of reinforcement bars diagonally to the edges of the floor system. With such an arrangement, the horizontal ties are anchored within the adjacent floor panels instead, which can provide the requisite planar restraint for mobilisation of tensile membrane action.

2.6.2 Modelling

The modelling of floor systems follows similar procedures described for the modelling of beam sub-systems. Continuum models provide a high-fidelity assessment of floor systems, utilising solid and beam elements respectively for the representation of the concrete and the reinforcement bars (e.g. Bermejo *et al.*, 2017; Pham *et al.*, 2017a; Li *et al.*, 2019; Yu *et al.*, 2020a), though the inclusion of slabs renders the approach even more prohibitive for common engineering practice. The more practical approach is to model the beams of the floor system with 1D fibre-beam models, considering the aspects already discussed for the modelling of beam sub-systems (Section 2.5.2). The slabs can then be modelled using 2D shell elements involving a fibre-layered approach (Izzuddin *et al.*, 2004; Dat and Hai, 2013; Bermejo *et al.*, 2017; Li *et al.*, 2019), with the corresponding concrete constitutive relationship accounting for stress states under biaxial bending (Izzuddin *et al.*, 2004; Dat and Hai, 2013).

The effects of bond-slip may be less critical in the current slab reinforcement because this is less likely to fracture compared to the reinforcement placed near the beams of the floor system. Given that the latter reinforcement can be modelled as part of the beam elements instead, the

treatment of bond-slip effects within the shell element can be disregarded for model simplification. Notwithstanding, consideration of bond-slip effects within the shell elements potentially provides a better understanding on the local effects associated with the detailing of slab reinforcement and may be necessary for the assessment of flat-slab structures under the loss of a column.

2.7 Nonlinear structural analysis program ADAPTIC

It clearly follows from the discussion in the preceding sections that the determination of the structural response under the sudden loss of a column/load-bearing member necessitates a powerful structural analysis software which can explicitly account for geometric and material nonlinearity. In this respect, the nonlinear structural analysis program ADAPTIC (Izzuddin, 1991) is herein adopted to assist the proposal of the novel modelling strategy for beam sub-systems under the loss of a column/load-bearing member, and also to numerically verify the various design-oriented methodologies proposed in this thesis for horizontal tying.

The initial development of ADAPTIC incorporates pioneering adaptive nonlinear analysis for steel framed structures, accounting for geometric and material nonlinearity. Available analysis procedures include static analysis under proportional loading, static analysis under time history loading, dynamic analysis and eigenvalue analysis, where loading can be either applied forces or prescribed displacements/velocities/accelerations at nodal points, the variation of which can be proportional under static conditions (via the use of a load factor), or can vary in the time or pseudo-time domains.

Inelastic analysis of steel frames may be performed by either of two approaches. The first is an approximate approach using ideal plastic hinge elements (Izzuddin and Elnashai, 1993a), while the second is a more accurate approach employing layered/fibre elements, with plasticity spreading over the section depth and along the member length (Izzuddin and Elnashai, 1993b). The program then offers an adaptive analysis, with which significant computational savings can be achieved (Izzuddin, 1991). The aforementioned approaches are considered in the context of an automatic mesh refinement process, where the analysis begins with the use of a single elastic quartic element per member, with subsequent insertion of elasto-plastic elements where and when necessary during the analysis.

The program has since been extended to deal with other structural forms and materials such as RC beams as well as RC and steel-deck composite slabs, where inelastic analysis is performed exclusively via the layered/fibre approach. Furthermore, with material models capable to

reproduce concrete damage (compressive crushing and tensile cracking), the influence of elevated temperature and material rate-sensitivity, application of the program has also extended beyond the initial focus of nonlinear analysis under earthquake loading to deal with other extreme loading scenarios such as fire and blast. The available library of elements and material models are readily suitable for the research work conducted in this thesis. Importantly, the RC beam elements with explicit bond-modelling capability, which were recently developed by Khalid (2011) and implemented in ADAPTIC, form the basis of the novel modelling strategy proposed in this thesis for beam sub-systems under the loss of a column/load-bearing member. Considering these features, ADAPTIC presents itself as the preferential analysis program for this research.

2.7.1 Material models and section types

Considering that the effects of material rate-sensitivity can be neglected for robustness assessment involving the sudden loss of a column/load-bearing member, as concluded by Pereira (2012), rate-independent material models are adopted for the work of this thesis.

Accordingly, with the representation of RC beam members via a fibre/layered-beam approach, uniaxial material models are employed for the concrete and the steel reinforcement, involving a trilinear concrete model, with optional tensile response and quadratic initial compressive response (Izzuddin, 2016), and a bilinear elasto-plastic steel model with kinematic strain hardening (Izzuddin, 1991). Whilst the concrete model is readily suitable for the modelling of concrete crushing and cracking, the bilinear steel model is enhanced in the present work, via the inclusion of a tensile softening branch, to reproduce the fracture of the reinforcement whenever necessary, as detailed in Section 3.3. Also, for beam elements with bond-modelling capability, the current research initially adopts the nonlinear bond-slip model proposed by Khalid (2011), where further developments are then proposed to deal with the dependency of bond-strength on the strain of the reinforcement (Section 3.4). For the response of RC floor slabs, given that typical RC slab elements available in ADAPTIC treats the slab reinforcement in each direction as separate layers smeared within the element, the steel response within such layers can be simply described by a uniaxial steel model, and therefore the bilinear steel model with kinematic strain hardening is again considered. On the other hand, biaxial concrete models considering compressive and tensile softening are assumed for the nonlinear response of the concrete slab (Izzuddin *et al.*, 2004; Izzuddin, 2016).

With respect to cross-sections, ADAPTIC provides a number of pre-defined cross-section types, amongst which rectangular solid sections, solid I-sections and reinforced concrete T-sections are primarily employed herein for beam elements, whereas the slab elements consider a slab section capable to represent composite floors with steel deck.

2.7.2 Elements

Where the assessment of the ductility limit is not of concern, the nonlinear response of RC beam sub-systems can be obtained using cubic elasto-plastic beam-column elements considering full-bond interaction (Karayannis *et al.*, 1994; Izzuddin and Lloyd Smith, 2000). The corresponding formulation assumes cubic shape functions for the transverse displacements, employs a constant centroidal axial strain criterion and considers the section to remain plane after deformations. Two Gauss points are considered for the integration of the virtual work equation, at each of which the cross-section is divided into a number of monitoring areas where strain and stresses are evaluated. This element is primarily employed in the present work to demonstrate the limitations of full-bond interaction on the modelling of beam sub-systems under the loss of a column/load bearing member. Conversely, where assessment of the ductility limit is of concern, the RC beam elements developed by Khalid (2011) are employed, the benefits of which have been discussed in Section 2.5.2.4, with the underlying formulation detailed in Section 3.2.

The nonlinear response of RC floor slabs is obtained via either of the two 2D flat shell elements for composite and reinforced concrete floor slabs: a 4-noded quadrilateral element (Izzuddin *et al.*, 2004) or a 3-noded triangular element (Grosman and Izzuddin, 2018), where the latter element presents the advantage of allowing for arbitrary slab shapes and rebar orientations, a feature which is required for the assessment of floor systems with diagonally arranged reinforcement. Both elements consider the reinforcement layers to be fully bonded to the concrete. The quadrilateral element divides a composite slab into cover and rib regions, each with a corresponding element formulation. Specifically, the cover region assumes the conventional Reissner-Mindlin hypothesis (Zienkiewicz and Taylor, 2000a), whilst the rib region incorporates higher-order hierarchic degrees of freedom for the treatment of problems associated with the geometric orthotropy of composite floor slabs (Izzuddin *et al.*, 2004). On the other hand, formulation of the triangular element is limited to the cover region, also assuming the conventional Reissner-Mindlin hypothesis. Notwithstanding, only the cover region is herein utilised for the assessment of RC floor systems since it does not require the consideration of the rib region. Further hierarchic degrees of freedom are assigned for the

planar and rotational displacement fields, where the elements are readily employed in the basic form or in the hierarchic quadratic form. In dealing with geometric nonlinearity, the elements are formulated in a local co-rotational framework (Izzuddin, 2002, 2005; Izzuddin and Liang, 2016), enabling the use of linear strain-displacement relationships, with the influence of geometric nonlinearity addressed through transformations between the local and global systems.

Lastly, joint elements with uncoupled axial, shear and moment actions allow for the modelling of link components connecting the beams and the slab as well as for the idealisation of boundary restraints.

2.8 Conclusion

An extensive review has been provided in this chapter discussing the limitations of current robustness design regulations and strategies with respect to notional member removal and prescriptive tying forces.

For notional member removal, the ductility-centred assessment framework (Izzuddin *et al.*, 2008) is shown to be a suitable candidate for replacement of existing methods, where the assessment of an entire building structure simply requires the nonlinear static response of beam sub-systems, with the global response of the structure subsequently determined via an assemblage procedure and the dynamic response determined based on principles of energy balance. Following a review of the critical aspects influencing the nonlinear static response of RC beam sub-systems under a column/load-bearing member loss, the limitations of simplified modelling approaches currently available in literature have been highlighted, specifically their inability to explicitly represent bond-slip between the reinforcement and the concrete throughout the whole structural member. In this respect, a novel modelling strategy is proposed herein to address such a limitation within a practical framework and with relatively low computational demands. The RC elements previously developed by Khalid (2011) are employed for this purpose, with appropriate extensions proposed in this thesis for structural assessment under a column/load-bearing member loss.

For prescriptive tying forces, the review highlights significant inconsistencies in the requisite tying resistance across robustness regulations. Importantly, the lack of ductility limit considerations, dynamic amplification and requirements for the surrounding structure render the current tying force provisions unsafe. In recognition of this, a rational horizontal tying force method has been recently developed, along with its supplementary methods for dynamic

amplification and interaction with the surrounding structure (Izzuddin and Sio, 2022), with the formulation, validation and verification presented in Chapter 5 of this thesis. Under such a backdrop, the present thesis proposes an extension to the supplementary method assessing the interaction of the affected floor system with the surrounding structure, considering the additional restraint stiffness from the compressive ring.

A brief review on the behaviour and characterisation of RC floor systems has been provided as supplementary background for the abovementioned research work. This review has also highlighted the lack of horizontal restraint in floor systems with typical reinforcement arrangements (i.e. parallel to the edges of the floor system) under corner, penultimate interior and penultimate exterior column loss scenarios, thus inhibiting the full activation of tensile membrane action. This has motivated the consideration of alternative resistance mechanisms with diagonal slab reinforcement under which the mobilisation of tying could be more significant. Considering the proposed reinforcement arrangement, the rational horizontal tying force method is accordingly extended in Chapter 7 to cover corner column loss scenarios.

Chapter 3: Enhancement of fibre-beam elements with bond-modelling feature

3.1 Introduction

Following a formulation review of the fibre-beam elements developed by Khalid (2011), this chapter details the enhancements proposed in this thesis such that the elements become readily suitable for the assessment of (sudden) loss of a column/load-bearing member. These enhancements entail:

- At the material level, i) a modified bilinear steel model with kinematic strain hardening which includes a tensile softening branch to model the fracture of reinforcement, and ii) an enhanced bond-slip model considering the dependency of bond strength on the reinforcement strains;
- At the section level, extension of the element formulation to cover I- and T-shaped sections;
- At the element level, formulation of the corresponding consistent mass matrices for more accurate dynamic assessment and better numerical convergence stability.

3.2 Fibre-beam elements with bond-modelling feature

As previously noted, the RC beam-column modelling approach developed by Khalid (2011) employs two separate 1D beam-column elements to model the concrete and the reinforcement, respectively. A fibre-based approach is utilised, where cross-sections are divided into layers. Further to bond-modelling considerations, these elements are also formulated based on a modified Timoshenko beam theory, involving hierarchic degrees of freedoms (DOFs) for the allowance of nonlinear strain distributions over the cross-section depth. As shown by Khalid (2011), such a feature ensures the objectivity of the elements with mesh refinement.

3.2.1 Concrete element

3.2.1.1 Kinematics and local response of the element

The element is formulated under a local co-rotational reference system, where the *x*-axis originates at node 1 and passes through node 2, as shown in Fig. 3.1. This reference axis is chosen as the centroidal line passing through the centroid of the cross-section.

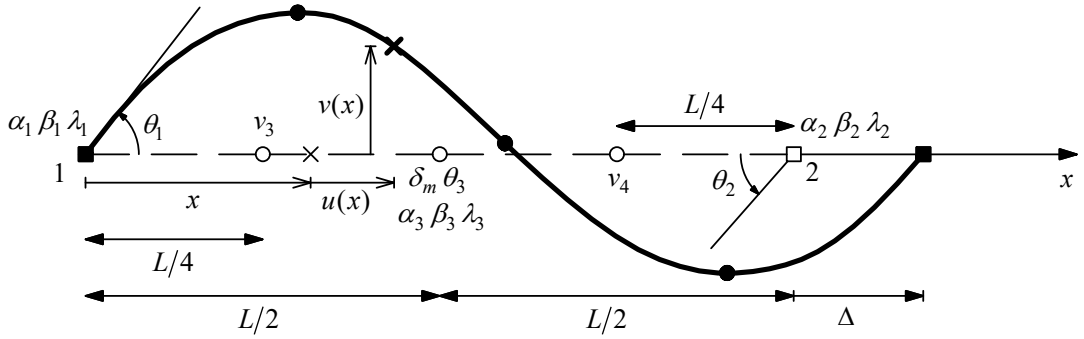


Fig. 3.1 – Local DOFs of the concrete element (adapted from Khalid, 2011)

Under this system, which excludes rigid-body translations, the element has three basic local DOFs: two rotations relative to the chord of the element (θ_1, θ_2) respectively at nodes 1 and 2, and an axial elongation of the element (Δ) at node 2. Further hierarchic DOFs are used not only for the enrichment of the axial, transverse and rotation fields (u, v, θ) but also to relax the condition of plane sections remain plane. Accordingly, an additional axial hierarchic DOF (δ_m) is used to approximate the axial displacement field along the reference centroidal axis $u_c(x)$ to a quadratic function of x.

$$u_c(x) = \frac{\Delta x}{L} + \frac{4\delta_m x(L-x)}{L^2} \tag{3.1}$$

For consistency with the assumed axial displacement field, the rotation field $\theta(x)$ as well as the displacements fields associated with the relaxation of plane sections remain plane condition $\alpha(x), \beta(x), \lambda(x)$ are also chosen as quadratic functions of x. This requires a rotational DOF (θ_3), in addition to the basic rotations of (θ_1, θ_2), for the rotation field $\theta(x)$ and three DOFs for each of the displacement fields associated to the nonlinear displacement distribution over the cross-section $(\alpha_1, \alpha_2, \alpha_3, \beta_1, \beta_2, \beta_3, \lambda_1, \lambda_2, \lambda_3)$.

$$\theta(x)=\left(1-\frac{3x}{L}+\frac{2x^2}{L^2}\right)\theta_1+\left(-\frac{x}{L}+\frac{2x^2}{L^2}\right)\theta_2+\left(\frac{4x}{L}-\frac{4x^2}{L^2}\right)\theta_3 \tag{3.2}$$

$$\alpha(x)=\left(1-\frac{3x}{L}+\frac{2x^2}{L^2}\right)\alpha_1+\left(-\frac{x}{L}+\frac{2x^2}{L^2}\right)\alpha_2+\left(\frac{4x}{L}-\frac{4x^2}{L^2}\right)\alpha_3 \tag{3.3}$$

$$\beta(x)=\left(1-\frac{3x}{L}+\frac{2x^2}{L^2}\right)\beta_1+\left(-\frac{x}{L}+\frac{2x^2}{L^2}\right)\beta_2+\left(\frac{4x}{L}-\frac{4x^2}{L^2}\right)\beta_3 \tag{3.4}$$

$$\lambda(x)=\left(1-\frac{3x}{L}+\frac{2x^2}{L^2}\right)\lambda_1+\left(-\frac{x}{L}+\frac{2x^2}{L^2}\right)\lambda_2+\left(\frac{4x}{L}-\frac{4x^2}{L^2}\right)\lambda_3 \tag{3.5}$$

A cubic shape function is used for the transverse displacement field along the reference centroidal axis $v_c(x)$, which is consistent with a quadratic approximation for $\theta(x)$.

$$v_c(x)=\left(\frac{8x}{L}-\frac{56x^2}{3L^2}+\frac{32x^3}{3L^3}\right)v_3+\left(-\frac{8x}{3L}+\frac{40x^2}{3L^2}-\frac{32x^3}{3L^3}\right)v_4 \tag{3.6}$$

The corresponding approximation of axial and transverse displacement fields for the element, which also depends on the distance y to the centroidal axis, are then expressed as:

$$u(x,y)=u_c(x)+f_1(y)\,\theta(x)+f_2(y)\,\alpha(x)+f_3(y)\,\beta(x)+f_4(y)\,\lambda(x) \tag{3.7}$$

$$v(x,y)=v_c(x) \tag{3.8}$$

where $f_1(y)$, $f_2(y)$, $f_3(y)$ and $f_4(y)$ in (3.7) are shape functions over the cross-section depth and are chosen to form an orthogonal set, the condition of which is required to avoid any local influence of the higher-order approximation fields on the axial centroidal extension. The exact shape functions for a rectangular cross-section are determined by Khalid (2011) as:

$$\begin{aligned}
f_1(y)&=-y\\
f_2(y)&=\frac{\sqrt{15}}{h}y^2-\frac{\sqrt{15}}{12}h\\
f_3(y)&=\frac{10\sqrt{21}}{3h^2}y^3-\frac{\sqrt{21}}{2}y\\
f_4(y)&=\frac{35\sqrt{3}}{h^3}y^4-\frac{15\sqrt{3}}{2h}y^2+\frac{3\sqrt{3}}{16}h
\end{aligned} \tag{3.9}$$

where h is the height of the rectangular cross-section.

Under such a formulation, the first two terms of the axial displacement field $u(x,y)$, as described in (3.7), represent the conventional constant/linear variation of $u(x,y)$ over the cross-section, encapsulated within the Timoshenko beam theory, whereas the latter terms enrich the approximation of the axial displacement field up to the fourth order, as illustrated in Fig. 3.2.

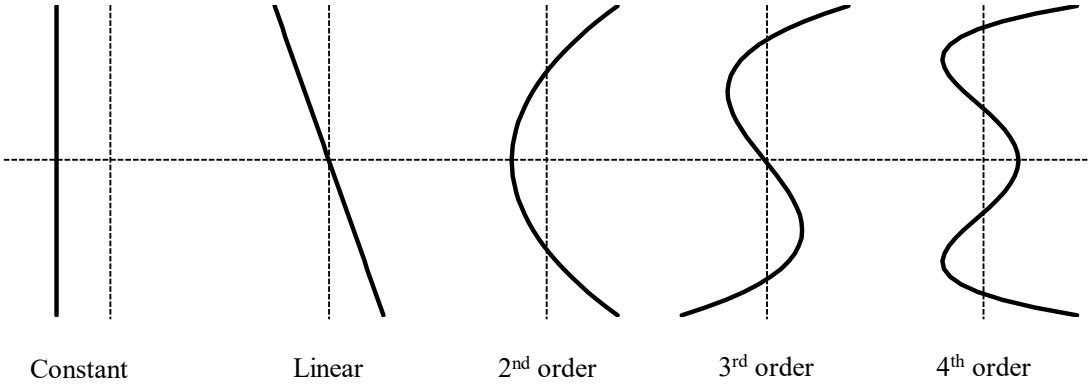


Fig. 3.2 – Shape functions over the cross-section depth (adapted from Khalid, 2011)

Given the restriction of (3.9) to rectangular cross-sections, the cross-sectional shape functions are extended in this chapter to include other types of cross-section, such as I- and T-shaped sections, as further detailed in Section 3.5.

Equations (3.7) and (3.8) can also be expressed in matrix form as:

$$\begin{Bmatrix} u(x,y) \\ v(x,y) \end{Bmatrix} = [\mathbf{N}]\{\mathbf{u}\} \tag{3.10}$$

where $\{\mathbf{u}\}$ is the vector for the 3 basic and 13 hierarchic local DOFs of the element,

$$\{\mathbf{u}\} = \langle \theta_1, \theta_2, \Delta, \delta_m, v_3, v_4, \theta_3, \alpha_1, \alpha_2, \alpha_3, \beta_1, \beta_2, \beta_3, \lambda_1, \lambda_2, \lambda_3 \rangle^{\mathbf{T}} \tag{3.11}$$

and $[\mathbf{N}]$ is the matrix for the associated shape functions, the terms of which can be easily worked out with (3.1)-(3.9).

The two components of the considered strain tensor can be established from (3.10) by derivation of the axial and transverse displacement fields with respect to the local coordinates (x,y) as follows:

$$\begin{Bmatrix} \varepsilon_x(x,y) \\ \gamma_{xy}(x,y) \end{Bmatrix} = \begin{Bmatrix} \dfrac{\partial u(x,y)}{\partial x} \\ \dfrac{\partial u(x,y)}{\partial y} + \dfrac{\partial v(x,y)}{\partial x} \end{Bmatrix} = [\mathbf{B}]\{\mathbf{u}\} \tag{3.12}$$

where $[\mathbf{B}]$ can be determined by accordingly deriving the shape functions within the matrix $[\mathbf{N}]$.

After each incremental step, the strains of each layer of the concrete element can be determined according to (3.12), the evaluation of which is performed at the Gauss points defined for the subsequent numerical integration of the local nonlinear response of the element. The corresponding stresses $\{\sigma\}$ at the considered Gauss points can then be established based on the multiplication of the strain tensor with the material tangent stiffness matrix $[\mathbf{D}_t]$. This is a 2×2 matrix with diagonal terms only, where the first term represents the material response related to the normal strains, which is determined based on a chosen uniaxial concrete model (Izzuddin, 2016), whilst the second diagonal term represents the material response related to the shear strains, which is established with an adjusted shear modulus G':

$$G' = G \cdot SF \tag{3.13}$$

where G is the elastic shear modulus and SF is a shear retention factor accounting for the reduction of the shear resistance with cracking of the concrete (Khalid, 2011). The local element forces $\{\mathbf{f}_c\}$ and tangent stiffness matrix $[\mathbf{k}_t]$ can then be obtained via numerical integration over the element domain:

$$\{\mathbf{f}_c\} = \sum_{j=1}^{n} w_{g,j} \sum_{i=1}^{m} A_i \left([\mathbf{B}]^{\mathrm{T}} \{\sigma\} \right) \Big|_{x=x_{g,j},\, y=y_i} \tag{3.14}$$

$$[\mathbf{k}_t] = \sum_{j=1}^{n} w_{g,j} \sum_{i=1}^{m} A_i \left([\mathbf{B}]^{\mathrm{T}} [\mathbf{D}_t][\mathbf{B}] \right) \Big|_{x=x_{g,j},\, y=y_i} \tag{3.15}$$

where m is the number of layers considered for the cross-section of the element; A_i and y_i are respectively the area and distance to the centroidal axis of layer i; n is the number of Gauss points considered for the numerical integration, whereas $w_{g,j}$ and $x_{g,j}$ respectively represent the weighting factor and the location of the Gauss point j. Three Gauss points are considered herein $(n = 3)$, which is deemed adequate if the RC member is represented with several

elements. Accordingly, the weighting factors and the locations of the three Gauss points are given as:

$$
\begin{aligned}
w_{g,1} &= w_{g,3} = \frac{5L}{18} \\
w_{g,2} &= \frac{8L}{18} \\
x_{g,1} &= \frac{L}{2}\left(1-\sqrt{\frac{3}{5}}\right) \\
x_{g,2} &= \frac{L}{2} \\
x_{g,3} &= \frac{L}{2}\left(1+\sqrt{\frac{3}{5}}\right)
\end{aligned}
\tag{3.16}
$$

3.2.1.2 Global element response

At the global element level, the global element resistance and the associated global element tangent stiffness should be determined with respect to the global element parameters. This requires three transformations between the local and global systems: i) the geometric transformation establishing the local element displacements from the global displacements, ii) the determination of global from local element forces and iii) transformation of the local to global tangent stiffness matrix.

<u>*Determination of local from global displacements.*</u> Under the geometric considerations illustrated in Fig. 3.3 and with a total of six global displacement parameters, $\left(U_1, V_1, \phi_1\right)$ for node 1 and $\left(U_2, V_2, \phi_2\right)$ for node 2, the following geometric transformation applies between the global displacement parameters and the basic local DOFs $\left(\theta_1, \theta_2, \Delta\right)$, which is a subset of $\left\{\mathbf{u}\right\}$ as per (3.11).

$$\left\{\mathbf{u}_b\right\} = \left\langle \theta_1, \theta_2, \Delta \right\rangle^{\mathbf{T}} \tag{3.17}$$

$$\left\{\mathbf{U}_b\right\} = \left\langle U_1, V_1, \phi_1, U_2, V_2, \phi_2 \right\rangle^{\mathbf{T}} \tag{3.18}$$

$$\hat{X}_E = X_E + U_2 - U_1 \tag{3.19}$$

$$\hat{Y}_E = Y_E + V_2 - V_1 \tag{3.20}$$

$$\hat{L} = \sqrt{\hat{X}_E^2 + \hat{Y}_E^2} \; ; \quad \hat{\rho} = \arctan\left(\hat{Y}_E / \hat{X}_E\right) + n\pi \quad (n = 0, \pm 1) \tag{3.21}$$

$$\theta_1 = \phi_1 + \rho - \hat{\rho} \; ; \quad \theta_2 = \phi_2 + \rho - \hat{\rho} \; ; \quad \Delta = \hat{L} - L \tag{3.22}$$

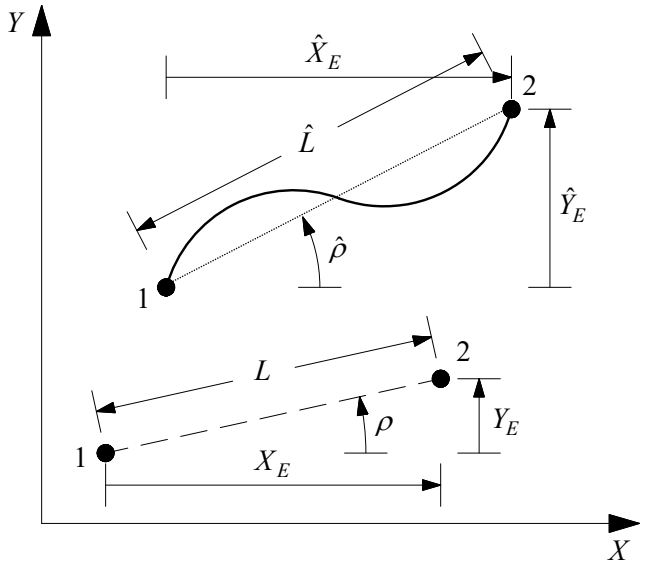


Fig. 3.3 – Determination of local from global displacements

The global additional DOFs are simply its local DOFs, thus the global nodal displacement vector $\{\mathbf{U}^e\}$ entails 19 degrees of freedom (6 basic DOFs and 13 additional DOFs):

$$\{\mathbf{U}^e\} = \langle U_1, V_1, \phi_1, U_2, V_2, \phi_2, \delta_m, v_3, v_4, \theta_3, \alpha_1, \alpha_2, \alpha_3, \beta_1, \beta_2, \beta_3, \lambda_1, \lambda_2, \lambda_3 \rangle^{\mathrm{T}} \tag{3.23}$$

Determination of global from local forces. The global element resistance forces $\{\mathbf{R}^e\}$ are determined from its local forces $\{\mathbf{f}_c\}$ as follows:

$$\{\mathbf{R}^e\} = [\mathbf{T}]\{\mathbf{f}_c\} \tag{3.24}$$

where $[\mathbf{T}]$ is a 19×16 transformation matrix (considering the size of the local and global element force vectors) and can be expressed in a partitioned form separating the terms related to the basic and additional element DOFs:

$$[\mathbf{T}] = \begin{bmatrix} \mathbf{T}_{bb} & \mathbf{T}_{ba} \\ \mathbf{T}_{ab} & \mathbf{T}_{aa} \end{bmatrix} \tag{3.25}$$

Considering that there is no coupling between the basic and additional DOFs and that the global additional DOFs directly correspond to its local DOFs, the subset matrices $[\mathbf{T}_{ab}]$ and $[\mathbf{T}_{ba}]$ are

13×3 and 6×13 zero matrices, respectively, whilst $\left[\mathbf{T}_{aa}\right]$ is a 13×13 identity matrix. The subset matrix $\left[\mathbf{T}_{bb}\right]$ is a 6×3 matrix relating the local and global basic DOFs, the terms of which are shown to be expressed as (Izzuddin, 1991):

$$\left[\mathbf{T}_{bb}\right]=\begin{bmatrix} -\frac{\hat{s}}{\hat{L}} & -\frac{\hat{s}}{\hat{L}} & -\hat{c} \\ \frac{\hat{c}}{\hat{L}} & \frac{\hat{c}}{\hat{L}} & -\hat{s} \\ 1 & 0 & 0 \\ \frac{\hat{s}}{\hat{L}} & \frac{\hat{s}}{\hat{L}} & \hat{c} \\ -\frac{\hat{c}}{\hat{L}} & \frac{\hat{c}}{\hat{L}} & \hat{s} \\ 0 & 1 & 0 \end{bmatrix} \tag{3.26}$$

where $\hat{c}$ and $\hat{s}$ are the direction cosines in the deformed configuration.

$$\hat{c}=\frac{\hat{X}_E}{\hat{L}} \;;\quad \hat{s}=\frac{\hat{Y}_E}{\hat{L}} \tag{3.27}$$

Determination of global from local tangent stiffness. The global element stiffness $\left[\mathbf{K}_T^e\right]$ is a 19×19 matrix also partitioned to separate the terms related to the basic and additional DOFs:

$$\left[\mathbf{K}_T^e\right]=\begin{bmatrix} \left[\mathbf{K}_T\right]_{bb} & \left[\mathbf{K}_T\right]_{ba} \\ \left[\mathbf{K}_T\right]_{ab} & \left[\mathbf{K}_T\right]_{aa} \end{bmatrix} \tag{3.28}$$

where $\left[\mathbf{K}_T\right]_{aa}$ is simply established from the subset of the local tangent stiffness matrix related to the additional DOFs $\left[\mathbf{k}_t\right]_{aa}$. On the other hand, $\left[\mathbf{K}_T\right]_{ab}$ and $\left[\mathbf{K}_T\right]_{ba}$ are established from the corresponding subsets of the local tangent stiffness matrix $\left(\left[\mathbf{k}_t\right]_{ab},\left[\mathbf{k}_t\right]_{ba}\right)$ as follows:

$$\left[\mathbf{K}_T\right]_{ba}=\left[\mathbf{K}_T\right]_{ab}^{\mathbf{T}}=\left[\mathbf{T}_{bb}\right]\left[\mathbf{k}_t\right]_{ba} \tag{3.29}$$

Lastly, $\left[\mathbf{K}_T\right]_{bb}$ can be determined from the subset of the local tangent stiffness matrix related to the basic DOFs $\left[\mathbf{k}_t\right]_{bb}$ as follows (Izzuddin, 1991):

$$\left[\mathbf{K}_T\right]_{bb} = \left[\mathbf{T}_{bb}\right]\left[\mathbf{k}_t\right]_{bb}\left[\mathbf{T}_{bb}\right]^{\mathrm{T}} + \left[\frac{\partial^2\left\langle\theta_1,\theta_2,\Delta\right\rangle}{\partial\left\{\mathbf{U}^e\right\}\partial\left\langle\mathbf{U}^e\right\rangle}\begin{Bmatrix}M_1\\M_2\\F\end{Bmatrix}\right]$$

$$\left[\frac{\partial^2\theta_1}{\partial\left\{\mathbf{U}^e\right\}\partial\left\langle\mathbf{U}^e\right\rangle}\right] = \left[\frac{\partial^2\theta_2}{\partial\left\{\mathbf{U}^e\right\}\partial\left\langle\mathbf{U}^e\right\rangle}\right] = \begin{bmatrix} -g_1 & g_2 & 0 & g_1 & -g_2 & 0\\ g_2 & g_1 & 0 & -g_2 & -g_1 & 0\\ 0 & 0 & 0 & 0 & 0 & 0\\ g_1 & -g_2 & 0 & -g_1 & g_2 & 0\\ -g_2 & -g_1 & 0 & g_2 & g_1 & 0\\ 0 & 0 & 0 & 0 & 0 & 0 \end{bmatrix} \tag{3.30}$$

$$\left[\frac{\partial^2\Delta}{\partial\left\{\mathbf{U}^e\right\}\partial\left\langle\mathbf{U}^e\right\rangle}\right] = \begin{bmatrix} g_5 & -g_4 & 0 & -g_5 & g_4 & 0\\ -g_4 & g_3 & 0 & g_4 & -g_3 & 0\\ 0 & 0 & 0 & 0 & 0 & 0\\ -g_5 & g_4 & 0 & g_5 & -g_4 & 0\\ g_4 & -g_3 & 0 & -g_4 & g_3 & 0\\ 0 & 0 & 0 & 0 & 0 & 0 \end{bmatrix}$$

where $\left(M_1, M_2, F\right)$ are the local element forces associated to the local basic DOFs $\left(\theta_1,\theta_2,\Delta\right)$ and the terms $\left(g_1,g_2,g_3,g_4,g_5\right)$ are expressed as:

$$g_1 = \frac{2\hat{c}\hat{s}}{\hat{L}^2}\ ;\ g_2 = \frac{\hat{c}^2-\hat{s}^2}{\hat{L}^2}\ ;\ g_3 = \frac{\hat{c}^2}{\hat{L}}\ ;\ g_4 = \frac{\hat{c}\hat{s}}{\hat{L}}\ ;\ g_5 = \frac{\hat{s}^2}{\hat{L}} \tag{3.31}$$

3.2.2 Steel-bond element

3.2.2.1 Kinematics and local element response of the element

The steel-bond element considers contributions to the element response from two constituents: the reinforcement bar and the interface between the reinforcement bar and the concrete. The element formulation follows a similar procedure as that of the concrete element but considering three additional DOFs for the determination of bond-slip and with the response established at the local coordinate $y = d$, where d is the distance of the reinforcement bar with respect to the centroidal axis, as illustrated in Fig. 3.4.

Accordingly, the element DOFs for the steel-bond element are as follows:

$$\left\{\mathbf{u}\right\} = \left\langle\theta_1,\theta_2,\Delta,\Delta_1,\Delta_2,\Delta_3,\delta_m,v_3,v_4,\theta_3,\alpha_1,\alpha_2,\alpha_3,\beta_1,\beta_2,\beta_3,\lambda_1,\lambda_2,\lambda_3\right\rangle^{\mathbf{T}} \tag{3.32}$$

where the subset $\left\langle\Delta_1,\Delta_2,\Delta_3\right\rangle^{\mathbf{T}}$ correspond to the slip DOFs of the bond-slip interface.

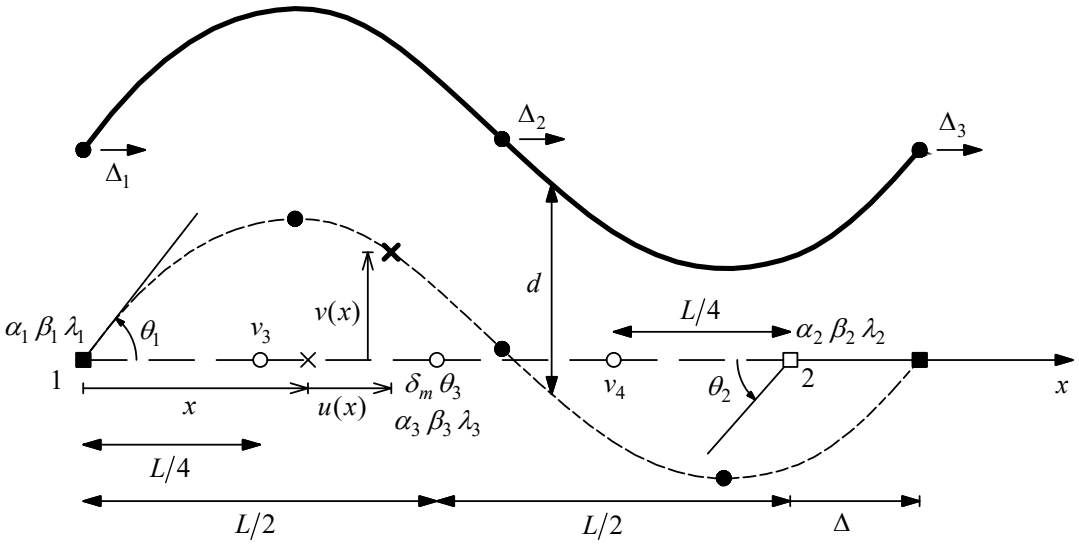


Fig. 3.4 – Local DOFs of the steel-bond element (adapted from Khalid, 2011)

The axial displacement field of a reinforcement bar at a distance d from the centroidal axis follows a similar expression as per (3.7) but considering $y = d$ and with the additional contribution from the slip field.

$$u(x,d) = u_c(x) + f_1(d)\,\theta(x) + f_2(d)\,\alpha(x) + f_3(d)\,\beta(x) + f_4(d)\,\lambda(x) + \Delta(x) \tag{3.33}$$

where $u_c(x)$, $\theta(x)$, $\alpha(x)$, $\beta(x)$ and $\lambda(x)$ remain the same as described for the concrete element. The additional slip field $\Delta(x)$, which also represents the displacement field of the bond-slip interface, can be approximated by a quadratic function similar to $\theta(x)$, $\alpha(x)$, $\beta(x)$ and $\lambda(x)$.

$$\Delta(x) = \left(1 - \frac{3x}{L} + \frac{2x^2}{L^2}\right)\Delta_1 + \left(-\frac{x}{L} + \frac{2x^2}{L^2}\right)\Delta_2 + \left(\frac{4x}{L} - \frac{4x^2}{L^2}\right)\Delta_3 \tag{3.34}$$

Equations (3.33)-(3.34) can be expressed in matrix form as follows:

$$\begin{Bmatrix} u(x,d) \\ \Delta(x) \end{Bmatrix} = [\mathbf{N}]\{\mathbf{u}\} \tag{3.35}$$

where the terms of $[\mathbf{N}]$ can again be easily worked out from (3.33)-(3.34).

The generalised strains of the reinforcement $\varepsilon_s(x,d)$ and the bond-slip interface $\varepsilon_b(x)$ are then established as follows:

$$\begin{Bmatrix} \varepsilon_s(x,d) \\ \varepsilon_b(x) \end{Bmatrix} = \begin{Bmatrix} \dfrac{\partial u(x,d)}{\partial x} \\ \Delta(x) \end{Bmatrix} = \left[\mathbf{B}\right]\{\mathbf{u}\} \tag{3.36}$$

with the terms of $\left[\mathbf{B}\right]$ accordingly determined from the terms of $[\mathbf{N}]$. It is worth noting that the generalised strain for the bond-slip interface is directly the slip and that the steel-bond element is assumed to not contribute any shear resistance, hence the neglect of shear strains. The corresponding stresses $\{\sigma\}$ can be obtained by multiplying the generalised strains in (3.36) by the material tangent stiffness matrix $\left[\mathbf{D}_t\right]$. Once again, this is a 2×2 matrix with diagonal terms only but with the first term representing the response of the reinforcing steel, which in the work of Khalid (2011) is established from a bilinear kinematic strain hardening model without tensile softening. The second term, on the other hand, represents the nonlinear response of the bond-slip interface, where in the work of Khalid (2011) the defined bond-slip law does not account for the reduction of bond strength with reinforcement strains. Such limitations for the assessment of RC beam sub-systems under the loss of a column are herein addressed with appropriate enhancements to both steel reinforcement and bond-slip material models.

The local element forces $\{\mathbf{f}_c\}$ and tangent stiffness matrix $\left[\mathbf{k}_t\right]$ can then be obtained via numerical integration over the element domain:

$$\{\mathbf{f}_c\} = \sum_{j=1}^{n} w_{g,j} \left(\left[\mathbf{B}\right]^{\mathrm{T}} \left[\mathbf{G}\right]\{\sigma\} \right)\Big|_{x=x_{g,j}} \tag{3.37}$$

$$\left[\mathbf{k}_t\right] = \sum_{j=1}^{n} w_{g,j} \left(\left[\mathbf{B}\right]^{\mathrm{T}} \left[\mathbf{G}\right]\left[\mathbf{D}_t\right]\left[\mathbf{B}\right] \right)\Big|_{x=x_{g,j}} \tag{3.38}$$

where n is again the number of Gauss points considered for the element $(n=3)$; $w_{g,j}$ and $x_{g,j}$ respectively represent the weighting factor and the location of the Gauss point j, expressed as per (3.16). It is worth noting that the contribution of the two constituents to the element response (i.e. reinforcement bar and bond-slip interface) is established from different geometric considerations in the sense that the resultant forces of the reinforcement bar are determined from the stresses applied over the bar area whilst the resultant forces of the bond-slip interface are determined from the bond stresses applied along the bar perimeter. Hence, this requires an additional diagonal matrix $\left[\mathbf{G}\right]$ to assemble the local element forces and tangent stiffness matrix via only a single expression as per (3.37)-(3.38).

$$[\mathbf{G}]=\begin{bmatrix} A_s & 0 \\ 0 & p_s \end{bmatrix} \tag{3.39}$$

where A_s and p_s are respectively the area and perimeter of the reinforcement bar.

3.2.2.2 Global element response

The global element resistance and the associated global element tangent stiffness with respect to the global element parameters are established following an identical procedure described for the concrete element.

Given that the DOFs $(\Delta_1,\Delta_2,\Delta_3)$ do not form part of the basic DOFs, the determination of local from global displacements follows again the same procedure, relating the basic local DOFs $(\theta_1,\theta_2,\Delta)$ to the basic global DOFs $(U_1,V_1,\phi_1,U_2,V_2,\phi_2)$. There is no transformation for the additional DOFs.

The global element resistance forces $\{\mathbf{R}^e\}$ are determined from its local forces $\{\mathbf{f}_c\}$ as follows:

$$\{\mathbf{R}^e\}=[\mathbf{T}]\{\mathbf{f}_c\} \tag{3.40}$$

where $[\mathbf{T}]$ is now a 22×19 transformation matrix.

$$[\mathbf{T}]=\begin{bmatrix} \mathbf{T}_{bb} & \mathbf{T}_{ba} \\ \mathbf{T}_{ab} & \mathbf{T}_{aa} \end{bmatrix} \tag{3.41}$$

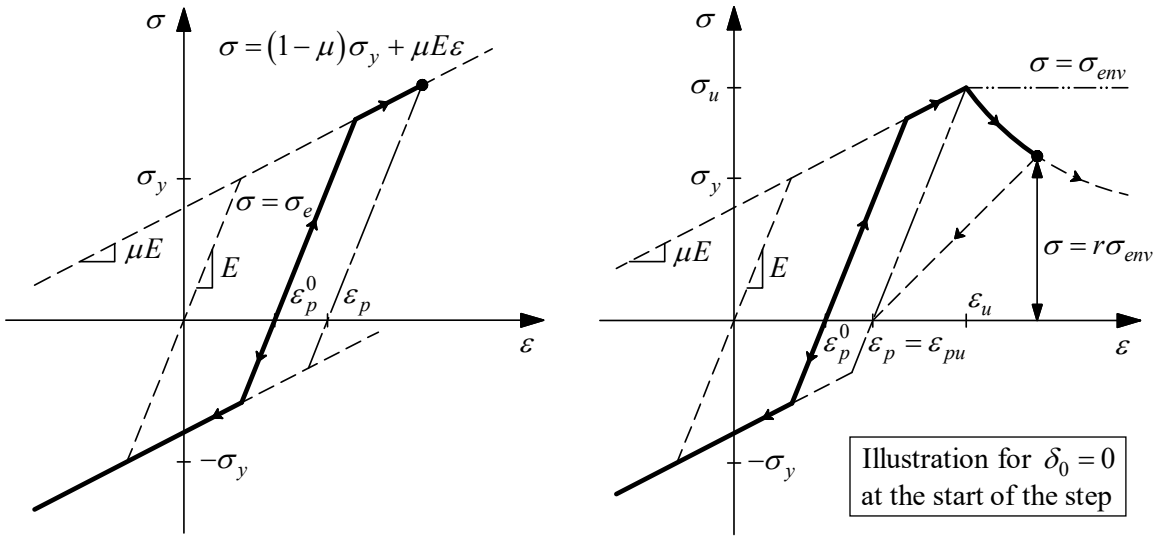
$[\mathbf{T}_{bb}]$ is the same 6×3 matrix described in (3.26), whilst $[\mathbf{T}_{ab}]$ and $[\mathbf{T}_{ba}]$ are now 16×3 and 6×16 zero matrices, respectively, and $[\mathbf{T}_{aa}]$ is a 16×16 identity matrix. Lastly, the global element stiffness $[\mathbf{K}_T^e]$ is now a 22×22 matrix, where the subset $[\mathbf{K}_T]_{bb}$ is established as per (3.30), whilst subsets $[\mathbf{K}_T]_{aa}$, $[\mathbf{K}_T]_{ab}$ and $[\mathbf{K}_T]_{ba}$ are respectively given as:

$$\begin{aligned} [\mathbf{K}_T]_{aa} &= [\mathbf{k}_t]_{aa} \\ [\mathbf{K}_T]_{ba} &= [\mathbf{K}_T]_{ab}^{\mathrm{T}} = [\mathbf{T}_{bb}][\mathbf{k}_t]_{ba} \end{aligned} \tag{3.42}$$

3.3 Steel material model with tensile softening

Consideration is given herein to the development of an uniaxial steel material model with representation of tensile softening, replacing the standard bilinear kinematic strain hardening

model originally used in the work of Khalid (2011) (Fig. 3.5a) so as to allow for the modelling of fracture of reinforcement. Specifically, the new model (Fig. 3.5b) follows the response of the standard bilinear model up to a specified ultimate tensile strain. Due consideration is then proposed for the representation of the stress decay under tensile softening and to the accumulation of tensile strain damage with increasing strains beyond the ultimate limit, which subsequently influences the reloading response of the steel material.



(a) Standard bilinear kinematic model (b) Newly developed model

Fig. 3.5 – Schematic illustration of the standard and new steel models

Accordingly, the new steel model is formulated with the following damage plasticity considerations:

- The nominal (scaled) tensile response is obtained from an effective (unscaled) tensile stress by scaling with a damage reduction factor r.
- The damage reduction factor r is related to a tensile damage strain state variable δ via the exponential function:

$$r = e^{-a\delta} \tag{3.43}$$

where a is a function parameter representing the rate of tensile softening. The damage strain state variable δ varies from zero to a positive value with the accumulation of damage.

- As illustrated in Fig. 3.5b, the tensile yield envelope σ_{env} initially follows that of the standard bilinear model (Fig. 3.5a) but is then limited to the maximum ultimate tensile strength σ_u, which is the stress evaluated at the ultimate strain ε_u.
- The plastic strain ε_p is limited to the ultimate plastic strain limit ε_{pu}.

3.3.1 Standard bilinear kinematic strain hardening model

The standard bilinear kinematic strain hardening model does not present any tensile damage accumulation, under which the yield envelope can extend to infinite strains. For a given accumulated plastic strain ε_p^0 at the start of the increment step, the current stress σ corresponding to the current strain ε can be initially estimated by a trial stress:

$$\sigma_e = E\left(\varepsilon - \varepsilon_p^0\right) \tag{3.44}$$

where E is the elastic stiffness modulus.

The trial stress σ_e is the current stress σ if the trial stress is within the yield envelope σ_{env}. The response is purely elastic in such a case, with the tangent stiffness modulus E_t equal to E and the current plastic strain remaining as the initial plastic strain.

$$\sigma_{env} = \pm\left(1-\mu\right)\sigma_y + \mu E\varepsilon \tag{3.45}$$

$$\left|\sigma_e - \frac{\mu E\varepsilon_p^0}{1-\mu}\right| \le \sigma_y \Rightarrow \begin{cases} \sigma = \sigma_e \\ E_t = \dfrac{\partial\sigma}{\partial\varepsilon} = E \\ \varepsilon_p = \varepsilon_p^0 \end{cases} \tag{3.46}$$

where σ_y is the yield strength and μ is the ratio of plastic-to-elastic stiffness modulus.

Otherwise, if the trial stress exceeds the yield envelope, the current stress is the yield envelope stress at strain ε. The behaviour is plastic, with the tangent stiffness equal to μE. Since further plastic strains are developed with the yield of the steel, these should be updated as per (3.47).

$$\pm\left(\sigma_e-\frac{\mu E\varepsilon_p^0}{1-\mu}\right)>\sigma_y \Rightarrow \begin{cases} \sigma=\pm(1-\mu)\sigma_y+\mu E\varepsilon \\ E_t=\dfrac{\partial\sigma}{\partial\varepsilon}=\mu E \\ \varepsilon_p=\varepsilon-\dfrac{\sigma}{E} \end{cases} \tag{3.47}$$

3.3.2 Formulation of the newly developed model

The response of the newly developed model depends on five model input properties – the elastic stiffness modulus E, the yield strength σ_y, the ratio of plastic-to-elastic stiffness modulus μ, the ultimate tensile strain ε_u and the softening parameter a; and two state variables at the start of the increment step – the accumulated plastic strain ε_p^0 and the accumulated damage strain δ_0.

3.3.2.1 Compressive behaviour

The compressive response of the newly developed model, occurring when $\varepsilon\le\varepsilon_p^0$, follows the same trial increment and stress verification procedure as in the standard model, independently on the damage strain state variable at the start of the increment step δ_0. This indicates that the fracture of the reinforcement does not affect the steel behaviour under compression. It is also worth noting that the damage strain state at the start of the step δ_0 is directly carried forward as the state at the end of the step δ.

$$\text{Elastic response}\quad -\sigma_e+\frac{\mu E\varepsilon_p^0}{1-\mu}\le\sigma_y \Rightarrow \begin{cases} \sigma=\sigma_e \\ \varepsilon_p=\varepsilon_p^0 \\ \delta=\delta_0 \\ E_t=\dfrac{\partial\sigma}{\partial\varepsilon}=E \end{cases}$$

$$\text{Plastic response}\quad -\sigma_e+\frac{\mu E\varepsilon_p^0}{1-\mu}>\sigma_y \Rightarrow \begin{cases} \sigma=-(1-\mu)\sigma_y+\mu E\varepsilon \\ \varepsilon_p=\varepsilon-\dfrac{\sigma}{E} \\ \delta=\delta_0 \\ E_t=\dfrac{\partial\sigma}{\partial\varepsilon}=\mu E \end{cases} \tag{3.48}$$

where σ_e is the trial stress established as per (3.44).

3.3.2.2 Tensile behaviour

The tensile behaviour of the newly developed model, occurring when $\varepsilon > \varepsilon_p^0$, is established by scaling an effective stress by the reduction factor r, which depends on the considered damage strain state δ. As such, considering the general case of a damage strain state at the start of the step δ_0, the effective trial stress is determined from the current strain ε based on an adjusted elastic stiffness E' as follows:

$$\sigma_e = E'\left(\varepsilon - \varepsilon_p^0\right) \tag{3.49}$$

with:

$$E' = \frac{\sigma_u}{\varepsilon_u - \varepsilon_{pu} + \delta_0} \tag{3.50}$$

where ε_u is the ultimate tensile strain and ε_{pu} is the ultimate tensile plastic strain.

$$\varepsilon_{pu} = \varepsilon_u - \frac{\sigma_u}{E} \tag{3.51}$$

The effective trial stress determined in (3.49) is then compared to the effective tensile yield envelope σ_{env}, which is herein limited to the ultimate tensile strength σ_u.

$$\sigma_{env} = \min\begin{Bmatrix}\left(1-\mu\right)\sigma_y + \mu E\varepsilon \\ \sigma_u\end{Bmatrix} \tag{3.52}$$

If the effective trial stress is within the effective yield envelope, there is by default no further accumulation of tensile strain damage. Hence, the current damage state δ remains the same as the state at the start of the step δ_0 and the nominal response is determined from the effective trial stress by scaling with the damage reduction factor r_0.

$$r_0 = e^{-a\delta_0}$$

$$\sigma_e \le \sigma_{env} \Rightarrow \begin{cases} \sigma = r_0\sigma_e \\ \varepsilon_p = \varepsilon_p^0 \\ \delta = \delta_0 \\ E_t = \dfrac{\partial\sigma}{\partial\varepsilon} = r_0 E' \end{cases} \tag{3.53}$$

If the effective trial stress exceeds the effective yield envelope, the nominal response is further dependent on a comparison plastic strain ε_p', which provides information on whether the stress state is under tensile softening.

$$\varepsilon_p' = \varepsilon - \frac{\sigma_{env}}{E'} \tag{3.54}$$

where E' is determined according to (3.50).

If $\varepsilon_p' \le \varepsilon_{pu}$, the stress state is on the nominal yield envelope with no further accumulation of tensile strain damage $(\delta = \delta_0)$. The nominal yield envelope is determined from the effective yield envelope σ_{env} by scaling with the damage reduction factor r_0. The plastic strain at the end of the step ε_p is then the comparison plastic strain ε_p'. Finally, the tangent stiffness depends on whether the effective yield envelope has reached the ultimate tensile strength.

$$\begin{matrix}\sigma_e > \sigma_{env} \\ \varepsilon_p' \le \varepsilon_{pu}\end{matrix} \Rightarrow \begin{cases} \sigma = r_0 \sigma_{env} \\ \varepsilon_p = \varepsilon_p' \\ \delta = \delta_0 \\ E_t = \dfrac{\partial \sigma}{\partial \varepsilon} = \begin{cases} r_0 \mu E & \sigma_{env} < \sigma_u \\ 0 & \sigma_{env} = \sigma_u \end{cases} \end{cases} \tag{3.55}$$

If $\varepsilon_p' > \varepsilon_{pu}$, stress state is on the softening branch, where further strain damage is introduced, hence the damage strain state variable should be updated to $\delta = \delta_0 + \varepsilon_p' - \varepsilon_{pu}$. The nominal stress is then obtained from the effective yield envelope σ_{env} by scaling with the updated damage reduction factor r. It is worth noting that the effective yield envelope would have reached the ultimate tensile strength for comparison plastic strains exceeding the ultimate value, hence σ_{env} is taken as σ_u. The plastic strains at the end of the step ε_p is set to the ultimate value ε_{pu}, whilst the tangent stiffness is established from the derivative of the nominal stress with respect to the strain.

$$r = e^{-a\delta}$$

$$\begin{matrix}\sigma_e > \sigma_{env} \\ \varepsilon'_p > \varepsilon_{pu}\end{matrix} \Rightarrow \begin{cases} \sigma = r\sigma_u \\ \varepsilon_p = \varepsilon_{pu} \\ \delta = \delta_0 + \varepsilon'_p - \varepsilon_{pu} \\ E_t = \dfrac{\partial\sigma}{\partial\varepsilon} = \dfrac{\partial\left(r\sigma_u\right)}{\partial\varepsilon} = -a\left(r\sigma_u\right) \end{cases} \tag{3.56}$$

3.3.2.3 Significance of E' and δ

Further explanation is provided herein to understand the mechanics behind the newly developed model. It is worth noting that the effective tensile trial stress, as per (3.49), is established based on an adjusted effective stiffness modulus E' instead of the usual elastic stiffness modulus E, suggesting that even the effective elastic response is dependent on the damage strain state variable at the start of the step δ_0. By inspection of Fig. 3.6, it follows that such an adjusted modulus ensures the compliance of the material response with the condition in which the plastic strain is limited to the ultimate value ε_{pu}. In other words, this adjusted stiffness ensures that the elastic unloading from any effective stress state at the level of σ_u to zero stress would strictly pass through the ultimate plastic strain limit.

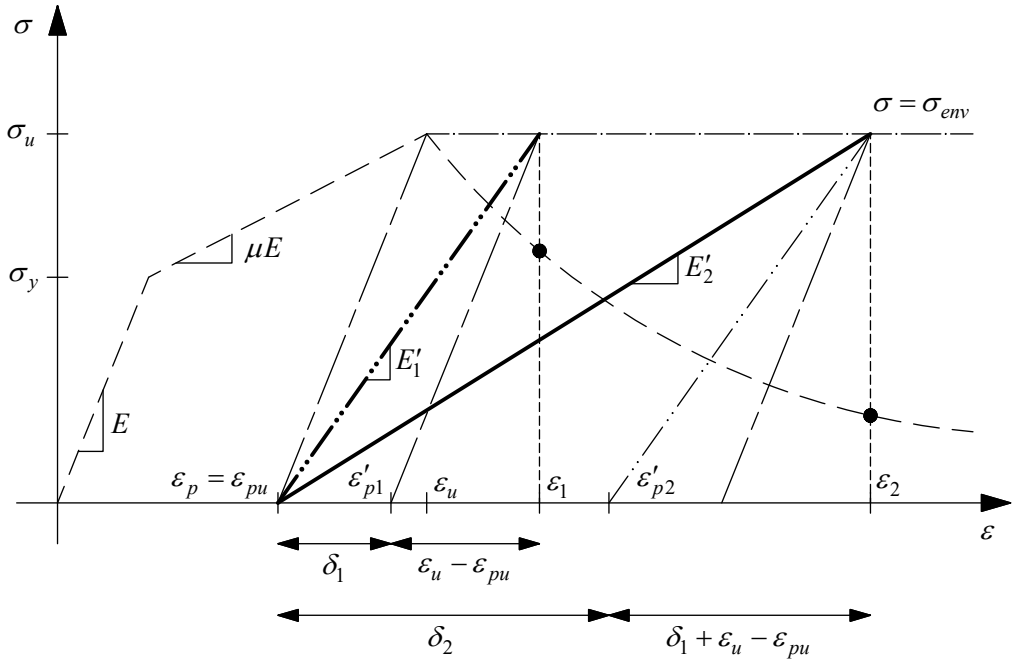


Fig. 3.6 – Significance of effective stiffness modulus and damage strain state variable

Furthermore, Fig. 3.6 also illustrates how the effective stiffness modulus helps determine whether further tensile strain damage is being accumulated, as per (3.54), and how the damage

strain state variable δ would update the adjusted stiffness modulus in case there is further accumulation of strain damage. Considering the highest tensile strain previously experienced by the material response as ε_1, where the associated accumulated damage strain state δ_1 and adjusted stiffness modulus E_1' can be deduced by inspection of Fig. 3.6, and that the response is currently loaded up to a strain $\varepsilon_2 > \varepsilon_1$, a comparison plastic strain ε_{p2}' is determined from (3.54) with the stiffness modulus E_1'. This comparison strain clearly exceeds the ultimate plastic strain limit ε_{pu}, hence further strain damage is accumulated, and the effective stiffness modulus should be accordingly updated. Given that δ_1 is the accumulated damage strain state at the start of the step (i.e. δ_0), the accumulated damage strain state at the end of the step for ε_2 is established as $\delta = \delta_1 + \varepsilon_{p2}' - \varepsilon_{pu} = \delta_1 + \delta_2$. The effective stiffness modulus E_2' can then be determined from (3.50) with the updated damage strain state variable. Such procedure is graphically represented in Fig. 3.6 as follows: the previous effective stiffness modulus is established from the double dot-dashed line, whilst the updated modulus is determined from the full line.

3.3.2.4 Significance of E_t under tensile behaviour

According to (3.53), (3.55) and (3.56), the tangent stiffness modulus within the tensile elastic, plastic and softening ranges is respectively established as:

$$\begin{aligned}
&\text{Elastic} \quad E_t = \frac{\partial \sigma}{\partial \varepsilon} = r_0 E' \\
&\text{Plastic} \quad E_t = \frac{\partial \sigma}{\partial \varepsilon} = \begin{cases} r_0 \mu E & \sigma_{env} < \sigma_u \\ 0 & \sigma_{env} = \sigma_u \end{cases} \\
&\text{Softening} \quad E_t = \frac{\partial \sigma}{\partial \varepsilon} = \frac{\partial \left(r\sigma_u \right)}{\partial \varepsilon} = -a\left(r\sigma_u \right)
\end{aligned} \tag{3.57}$$

with:

$$r_0 = e^{-a\delta_0} \;\; ; \;\; E' = \frac{\sigma_u}{\varepsilon_u - \varepsilon_{pu} + \delta_0} = \frac{E}{1 + \dfrac{E\,\delta_0}{\sigma_u}} \tag{3.58}$$

It follows from (3.57) that the tangent stiffness within the tensile elastic and plastic range reduces with increasing damage strain state variable δ_0, as reflected by the exponential reduction of r_0 and, specifically within the elastic range, also by the reduction of the effective

stiffness modulus as previously demonstrated. On the other hand, if no previous strain damage has been accumulated, then the stiffness modulus within the elastic and plastic ranges would be the standard values of E and μE, respectively. Lastly, within the tensile softening range, the tangent stiffness modulus presents a negative slope varying from $-a\sigma_u$ to zero, where the constant a dictates the rate of stress decay.

3.3.3 Verification

A cyclic stress-strain curve of the newly developed model is first sketched with a MATLAB algorithm, which serves to verify the correct implementation of the FORTRAN code for ADAPTIC (Izzuddin, 1991). Table 3.1 presents the assumed steel properties for the sketch of the cyclic response under the strain history illustrated in Fig. 3.7.

Table 3.1 – Steel properties for the sketch of cyclic response

E (MPa)	σ_y (MPa)	μ (-)	ε_u (-)	a (-)
185873	494	4.998×10^{-3}	1.092×10^{-1}	10

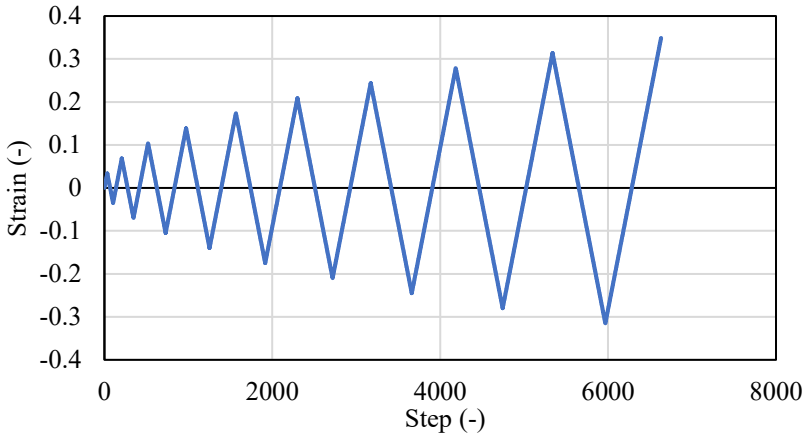


Fig. 3.7 – Strain history for the verification of the new steel model

Fig. 3.8 demonstrates identical cyclic stress-strain responses predicted from the MATLAB and FORTRAN algorithms. Furthermore, the initial loading cycles for strain levels lower than the ultimate strain follows the response of the standard bilinear kinematic strain hardening model. With increasing strains beyond the ultimate limit, the stress decays according to the considered exponential decreasing function and the subsequent elastic unloading from any point of the softening curve to zero stress passes through the ultimate plastic strain limit ε_{pu}. This is consistent with the model mechanics discussed in Section 3.3.2.3, noting that the slope of the

unloading branches simply represents the effective stiffness modulus E' scaled down by the reduction factor r.

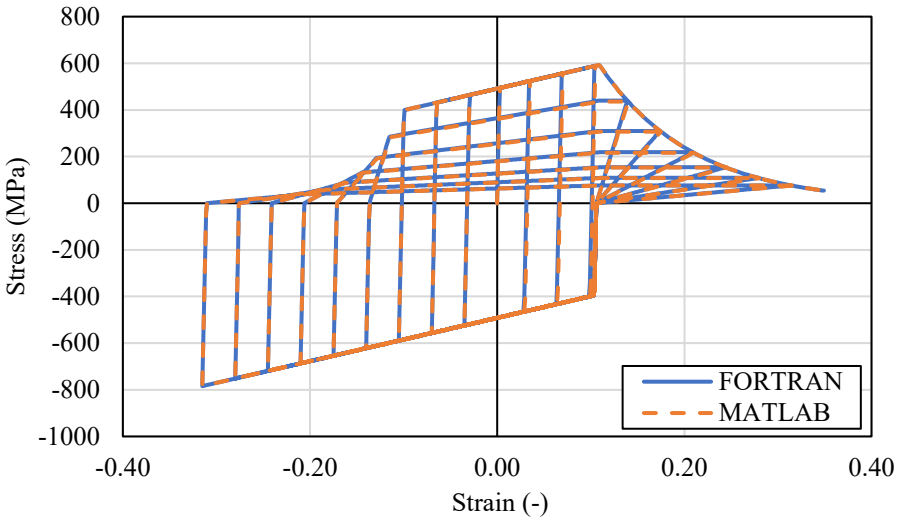


Fig. 3.8 – Stress-strain cyclic response of new steel model

The compressive response remains unaffected by the accumulated tensile strain damage, where the reloading behaviour is established based on the standard elastic stiffness modulus and yield envelope, whilst the tensile response is progressively scaled down with the accumulated tensile strain damage. Such observations confirm the correct implementation of the FORTRAN code for the newly developed model.

Fig. 3.9 highlights the significance of the function parameter a, with higher values leading to a faster rate of stress decay.

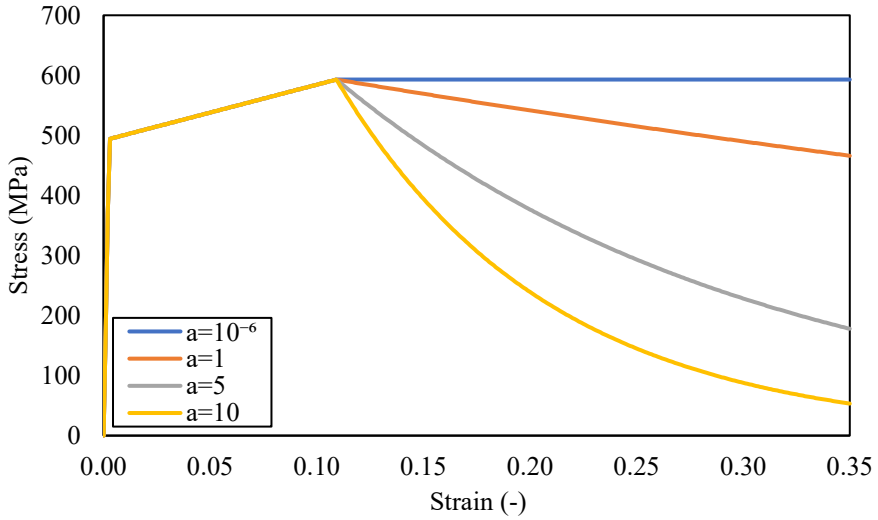
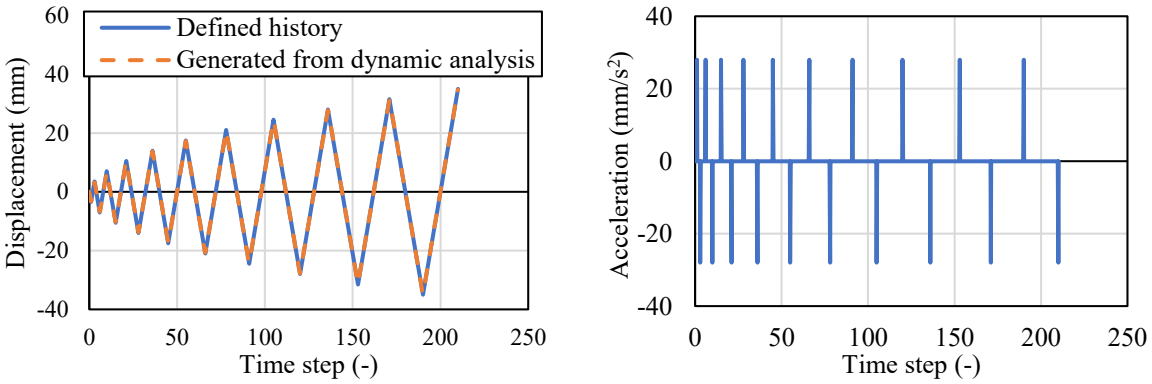


Fig. 3.9 – Significance of the tensile softening parameter

It is also worth noting that setting the parameter a to a very small value approximately reproduces a trilinear steel model where the last branch represents a perfectly plastic response associated with a strength of σ_u, which can be useful for models neglecting steel fracture to prevent infinite stress increase with tensile strain hardening.

The material model implemented in ADAPTIC is then verified under axial and bending loading of steel and RC members considering the displacement history curve illustrated in Fig. 3.10. Such a displacement history curve has been established to provide an identical strain history illustrated in Fig. 3.7 for an axially loaded steel member measuring 100mm in length, hence providing a direct comparison between the results of ADAPTIC and the FORTRAN algorithm. Furthermore, since model verification under bending loading conditions is carried out with a dynamic solution procedure, requiring an acceleration history curve instead, an equivalent acceleration curve is generated from the established displacement history curve (Fig. 3.10b). The resulting displacement response from the dynamic analysis is then verified against the established displacement history curve as illustrated in Fig. 3.10a.

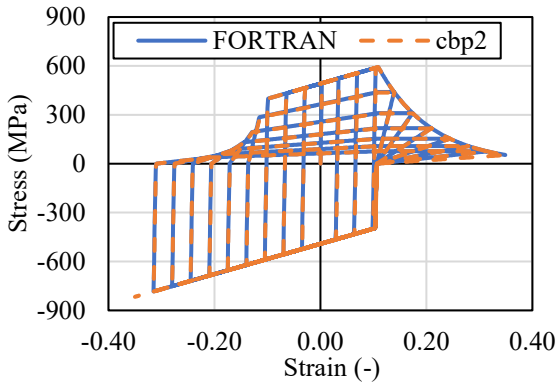


(a) Load-displacement history (b) Acceleration history

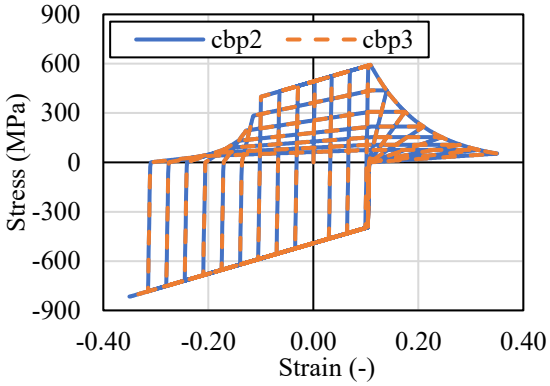
Fig. 3.10 – Input histories for the assessment of the new steel model in ADAPTIC

The verification under axial loading considers a steel truss member measuring 100mm in length and with a cross section of 100×5mm^2, which has identical material properties as those given in Table 3.1 and is axially displaced at its free end according to the established displacement history curve. The truss member is modelled with a single elasto-plastic cubic beam-column element. Both 2- and 3-dimensional cubic beam-column elements are used for the verification: cbp2 and cbp3, respectively (Izzuddin, 1991, 2016). The response is determined via a static time-history solution procedure.

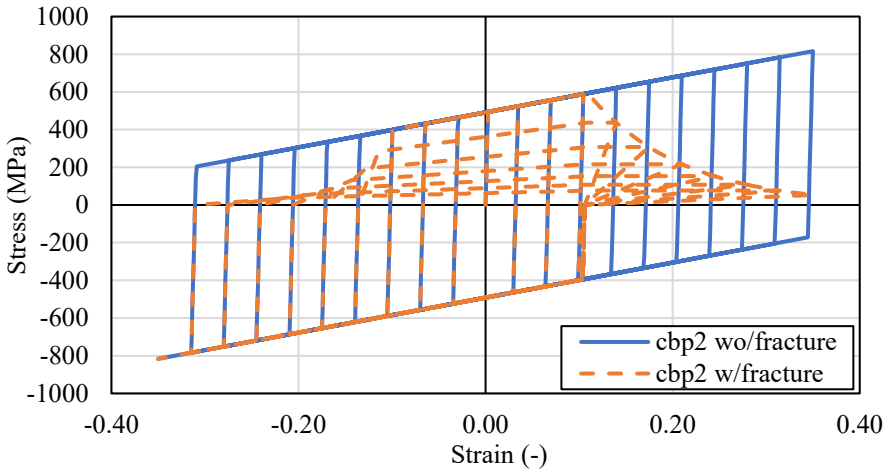
Fig. 3.11a indicates that the strain response of the steel truss member modelled with the cbp2 element matches the stress-strain response previously sketched by the FORTRAN algorithm, hence verifying the correct implementation of the FORTRAN code into ADAPTIC. Furthermore, such a verification is also extended to the truss member modelled with the cbp3 element as illustrated in Fig. 3.11b. Lastly, Fig. 3.11c provides the comparison between the response of the standard bilinear kinematic strain hardening model and the newly developed model. The compressive response is identical between the two models whilst the difference in tensile response becomes evident beyond the ultimate tensile strain, with the subsequent tensile reloading response of the new model also differing from the standard model following the accumulation of tensile strain damage.



(a) Verification for ADAPTIC



(b) cbp2 vs cbp3



(c) Response with and without fracture of reinforcement

Fig. 3.11 – Verification of the new steel model in ADAPTIC: axial loading

The verification under bending considers a fully fixed and axially unrestrained RC beam member with an applied vertical acceleration at mid-span, which follows the history curve defined in Fig. 3.10b. The RC beam measures 1000mm in length, presents a cross-section of

150mm in width and 250mm in depth, and is detailed with $3\phi13$ top reinforcement and $2\phi10$ bottom reinforcement. Material properties for the steel is provided in Table 3.1, whilst properties for the trilinear concrete model is provided in Table 3.2. The mass density of the RC beam is considered as 2500kg/m^3.

Table 3.2 – Concrete properties for the verification beam (element size: 100mm)

E_{c1} (MPa)	f_{c1} (MPa)	E_{c2} (MPa)	f_{cu} (MPa)	E_{t1} (MPa)	f_t (MPa)	E_{t2} (MPa)
13300	38.20	-2386.50	1.00	13000	3.50	-5008.52

where:

E_{c1} is the secant compressive stiffness

f_{c1} is the compressive strength

E_{c2} is the compressive softening stiffness

f_{cu} is the residual compressive stiffness

E_{t1} is the initial tensile stiffness

f_t is the tensile strength

E_{t2} is the tensile softening stiffness

Verification first proceeds based on two models using 10 cbp2 elements (100mm element size), comparing the sensitivity of the central load-displacement response to the consideration of reinforcement fracture (Fig. 3.12). Once again, both responses are initially identical up to the onset of concrete softening, which occurs around 10mm of central displacement. The responses then differ for displacements beyond 10-15mm due to the fracture of the reinforcement.

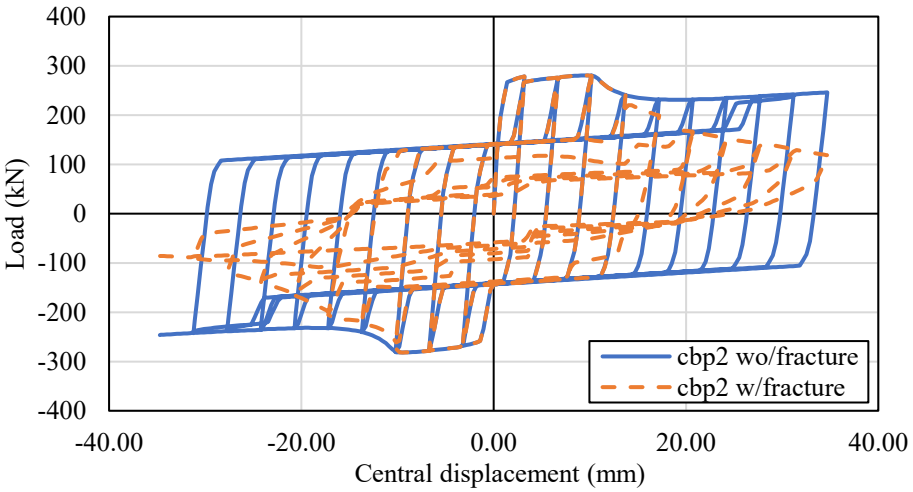


Fig. 3.12 – Verification of the new steel model in ADAPTIC: flexural loading I

The central load-displacement response predicted using cbp2 elements is then compared in Fig. 3.13 to the response predicted using the elements with bond-modelling capability (bme), the difference of which can be explained by the consideration of higher-order displacement modes over the cross-section and finite bond-slip in the latter elements.

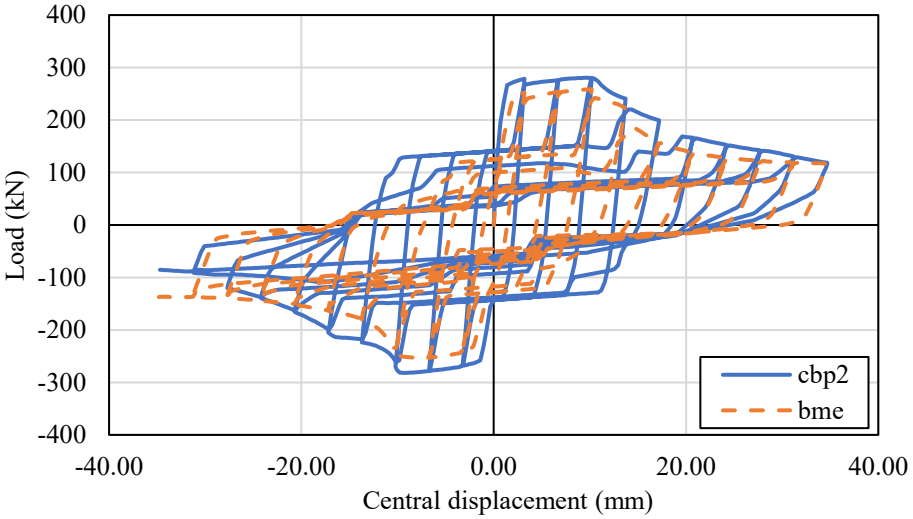


Fig. 3.13 – Verification of the new steel model in ADAPTIC: flexural loading II

3.4 Strain-dependent bond-slip model

One of the more common material models based on which researchers characterise the bond-slip between the reinforcement and the concrete is the model proposed by Eligehausen *et al.* (1983), as indeed it is later adapted by the CEB-FIP Model Code (fib, 2012b) and, with specific interest to the work of this thesis, also largely establishes the basis of the bond-slip model developed by Khalid (2011) for the bond-modelling elements. The bond-slip model by Eligehausen *et al.* (1983) is developed based on the outcomes of an extensive experimental investigation, also performed by the same researchers, involving more than 100 pull-out tests of a single Grade 60 deformed reinforcement (with minimum yield strength of 420MPa) embedded in an adequately confined concrete block (with a reference concrete compressive strength of 30MPa). The reference reinforcement bar measured 25.4mm in diameter (d_b) and was embedded within the concrete block for a length of five times its own diameter $(5d_b)$. These pull-out tests also involved the sensitivity assessment of the bond-slip behaviour to different loading histories, confining reinforcement, reinforcement bar diameters and deformation patterns, concrete compressive strengths, transverse pressures and loading rates. Eligehausen *et al.* (1983) notes that, with the short embedment length of $5d_b$ and the steel

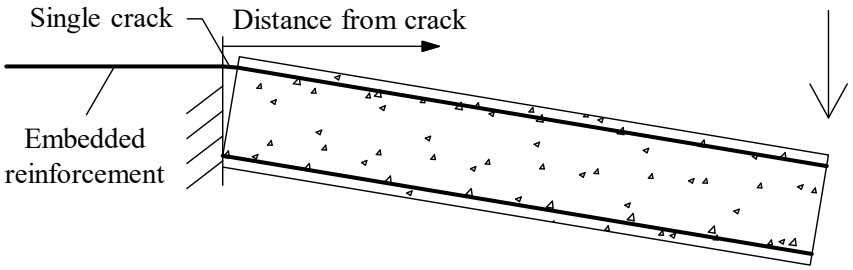
remaining elastic, the local bond-slip behaviour can be approximated by an average one with adequate accuracy, assuming that the bond stresses are evenly distributed along the bonded length. The approximated local bond-slip behaviour can then be easily determined from the forces and the corresponding slip at the loaded end of the reinforcement.

Notwithstanding, the local bond-slip behaviour established under such testing conditions is representative only for reinforcements with insufficient embedded lengths, under which pull-out occurs well before the reinforcement yields. In the context of disproportionate collapse assessment of actual RC structural systems, the reinforcement of such systems usually present adequate embedment lengths (Beconcini *et al.*, 2008), and hence the above-described reinforcement pull-out is unlikely to occur. Instead, the reinforcement yields and undergoes extensive tensile inelastic strains up to its fracture (Pham *et al.*, 2017b). Interestingly, even when the reinforcement is adequately embedded, there is evidence that slip also increases with the tensile inelastic strains of the reinforcement (Viwathanatepa *et al.*, 1979; Shima *et al.*, 1987). Such observation can be explained by the contraction of the cross-section area of the reinforcement due to the Poisson effect, leading to the detachment of the deformed reinforcement from the surface of the concrete and in turn further reducing the bond resistance over the reinforcement length which is under yielding (Viwathanatepa *et al.*, 1979; Zhou *et al.*, 2017). This dependency of the bond strength on the reinforcement strains, so-called yield penetration, is not considered in common bond-slip models such as that developed by Eligehausen *et al.* (1983).

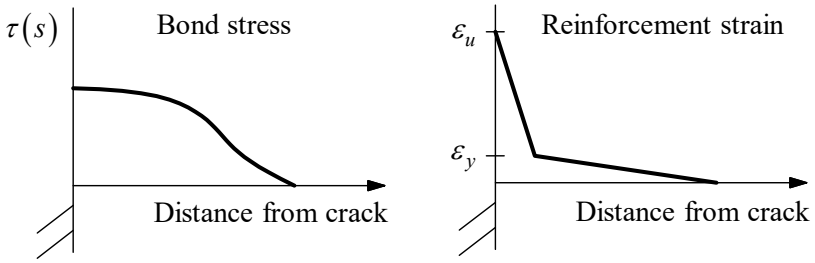
Nonetheless, the bond-slip model by Eligehausen *et al.* (1983) conservatively predicts the ductility limit of RC structures such as the beam sub-systems to be assessed in Chapter 4. Although, such an assumption can be overly conservative, specifically when a significant resistance gain can be achieved via tying of the reinforcement at large displacements, whilst a strain-dependent bond-slip model can provide a more realistic representation of the ductility limit and thus the load resistance of the system under the loss of a load-bearing member.

Fig. 3.14 provides an illustrative example on how the consideration of bond strength dependency on the reinforcement strains predicts an increased system ductility. The example entails a cantilever beam under an applied concentrated load at the free end and with the reinforcement at the fixed end anchored via an adequate embedment length to prevent its pull-out. Following the development of a single crack at the fixed end of the beam and the subsequent yielding of the top reinforcement, the slip along the reinforcement would be such

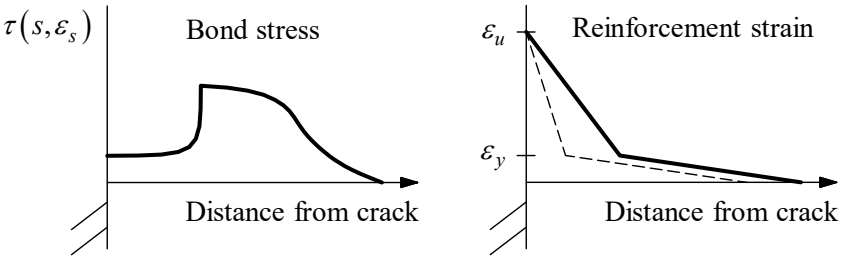
that the resulting bond stress profile for a strain-independent bond-slip model is given by Fig. 3.14b, which does not exhibit a decrease in bond strength within the inelastic region of the reinforcement.



(a) Cantilever example



(b) Bond stress and reinforcement strain for strain-independent bond-slip



(c) Bond stress and reinforcement strain for strain-dependent bond-slip

Fig. 3.14 – Influence of yield penetration within the embedded reinforcement on the ductility limit of the system

On the other hand, the strain-dependent bond-slip model predicts a drop in the bond strength within the same region (Fig. 3.14c). Such reduction in bond strength implies that the transfer of stresses from the reinforcement to the concrete is less effective, in turn leading to a slower decay of reinforcement strains. Accordingly, under the consideration that the fixed-end rotation, which largely defines the ductility limit of the cantilever, depends on the slip at the cracked location, and that this slip can be approximately determined from the integration of the reinforcement strains along the reinforcement length, it clearly follows that the strain-dependent model predicts a higher ductility limit for the cantilever.

In recognition of the influence of the reinforcement strains on the bond strength, Shima *et al.* (1987) developed a model described by a unique bond stress-slip-strain relationship based on curve-fitting of experimental data obtained with specimens ranging from $2d_b$ to $50d_b$ embedment lengths.

$$\tau\left(s,\varepsilon_s\right)=0.73f_c\left[\ln\left(1+5000\frac{s}{d_b}\right)\right]^3\frac{1}{1+\varepsilon_s\cdot 10^5} \tag{3.59}$$

where τ is the bond stress (in MPa); f_c is the concrete compressive strength (in MPa); ε_s is the steel strain; s is the slip between the reinforcement and the concrete (in mm); and d_b is the reinforcement diameter (in mm). Equation (3.59) was validated under both pre- and post-yield stages of the reinforcement.

Aiming towards a more practical evaluation of bond behaviour in RC structures, Marti *et al.* (1998) developed the Tension Chord Model (TCM), which assumed a rigid plastic bond law associated with two mean bond stresses at pre- and post-yield stages of the reinforcement.

$$\tau\left(\varepsilon_s\right)=\begin{cases}0.6f_c^{2/3} & \varepsilon_s\le\varepsilon_y\\ 0.3f_c^{2/3} & \varepsilon_s>\varepsilon_y\end{cases} \tag{3.60}$$

where f_c is the concrete compressive strength (in MPa); ε_s is the steel strain and ε_y is the yield strain of the steel. As noted by Zhou *et al.* (2017), the two values of the constant mean bond stresses were derived from a nonlinear bond-slip law which does not consider the effect of reinforcement yielding on bond. It also follows that approaches similar to TCM have been considered in the component-based joint models for the representation of bond-slip behaviour in RC sub-systems under the loss of a load bearing member – see Section 2.5.2.4 of the present thesis, Lowes and Altoontash (2003) and Yu and Tan (2014a).

Fernández Ruiz *et al.* (2007) developed an approach where a strain-independent bond-slip model can be simply reduced by an established factor to account for the effects of reinforcement strain on the bond-strength:

$$\tau\left(s,\varepsilon_s\right)=\tau\left(s\right)\cdot\Omega_y\left(\varepsilon_s\right) \tag{3.61}$$

where $\tau\left(s\right)$ is the strain-independent bond-slip model and $\Omega_y\left(\varepsilon_s\right)$ is the strain-dependent reduction factor. The described approach presents the advantage in allowing for the direct use of common strain-independent bond-slip models such as that developed by Eligehausen *et al.*

(1983) with the simple requirement of determining an appropriate reduction factor $\Omega_y(\varepsilon_s)$ for the representation of bond strength reduction with reinforcement strains. Indeed, the practicality of such an approach led to its later adaptation in the CEB-FIP Model Code (fib, 2012b) with the following reduction factor:

$$\Omega_y(\varepsilon_s) = \begin{cases} 1.0 & \varepsilon_s \le \varepsilon_y \\ 1.0 - \left[0.85\left(1 - e^{-5a^b}\right)\right] & \varepsilon_s > \varepsilon_y \end{cases}$$
$$\text{with } a = \frac{\varepsilon_s - \varepsilon_y}{\varepsilon_u - \varepsilon_y} \text{ and } b = \left(2.0 - \frac{f_t}{f_y}\right)^2 \tag{3.62}$$

where ε_s is the steel strain; ε_y and ε_u are respectively the yield and ultimate tensile strain of the steel; f_t is the tensile strength of the concrete (in MPa); and f_y is the yield strength of the steel reinforcement (in MPa).

In the context of this thesis, i.e. the use of the bond-modelling elements for the assessment of RC sub-systems under the loss of a load-bearing member, given that a strain-independent nonlinear bond-slip model has already been developed in the work of Khalid (2011), the most straightforward approach to implement a strain-dependent bond-slip model in ADAPTIC is to scale the model by Khalid (2011) with a given strain-dependent reduction factor $\Omega_y(\varepsilon_s)$. Indeed, the consideration of other bond stress-slip-strain models such as that of Shima *et al.* (1987) would require the implementation of the entire formulation into ADAPTIC instead of a simple modification, whilst the approaches similar to the Tension Chord Model (e.g. Marti *et al.*, 1998; Lowes and Altoontash, 2003; Yu and Tan, 2014a) would simply not be as accurate as nonlinear models in the local representation of bond behaviour. Furthermore, this approach would also require prior knowledge of the location at which reinforcement yields. Accordingly, an option is herein implemented for ADAPTIC to select the type of bond-slip model intended for the assessment of bond behaviour, where the strain-independent bond-slip model is directly used or alternatively reduced by the factor expressed in (3.62) depending whether the influence of reinforcement strain on the bond behaviour is considered for the analysis. The formulation of the bond-slip model developed by Khalid (2011) is thus subsequently reviewed and improved for model stability. This is then followed by the extension of the model to include the influence of reinforcement strains on the bond behaviour.

3.4.1 Formulation

The extended bond-slip model to include the influence of reinforcement strains on the bond behaviour is expressed as:

$$\tau\left(s,\varepsilon_s\right)=\tau\left(s\right)\cdot\Omega_y\left(\varepsilon_s\right) \tag{3.63}$$

where $\tau\left(s\right)$ is the strain-independent bond-slip model adapted from Khalid (2011) and $\Omega_y\left(\varepsilon_s\right)$ is the strain-dependent bond reduction factor.

3.4.1.1 Strain-independent bond-slip model

As noted before, the strain-independent bond-slip model developed by Khalid (2011) is largely based on the model by Eligehausen *et al.* (1983), where due modifications have been introduced to achieve a piece-wise linear model. Such model is herein improved for model stability during unloading and reloading phases.

Considering the bond stress-slip state to initiate at the origin and with all subsequently described state variables as zero, the response of a loading history involving two slip reversals (i.e. positive-negative-positive slip) is shown in Fig. 3.15. Under this loading history, the stress state passes through four types of branches: i) the monotonic and reduced envelopes – paths ABC, FGH and KLM; ii) the elastic loading/unloading branch – paths CD and HI; iii) the frictional branch – paths DE and IJ; and iv) the reloading branch – paths EF and JK.

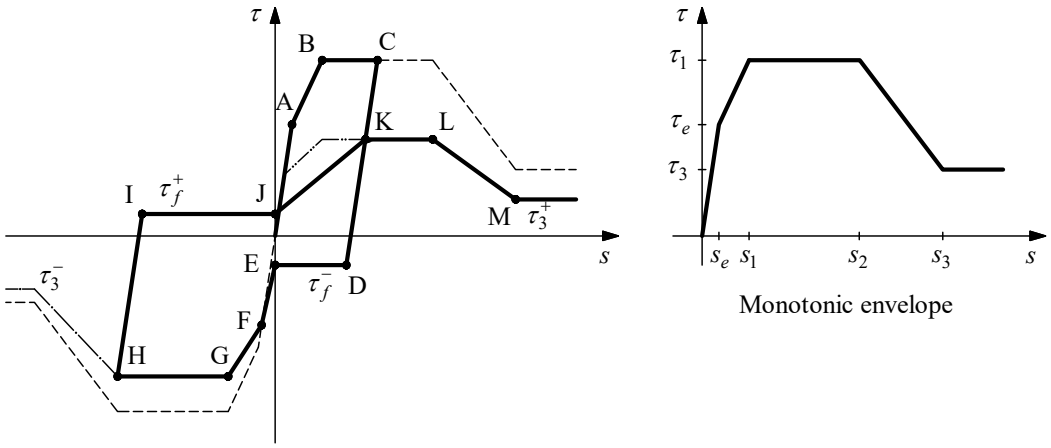


Fig. 3.15 – Mechanic of the strain-independent bond-slip model

Such branches can be fully defined with seven model input properties $\left(s_e,s_1,s_2,s_3,\tau_e,\tau_1,\tau_3\right)$ associated to the monotonic envelope of the model, which is also illustrated in Fig. 3.15, and five state variables – the largest positive and smallest negative plastic slip experienced from

the loading history $\left(s_{pl}^{+}, s_{pl}^{-}\right)$, the current plastic slip s_{pl} and the total energy dissipated in the positive and negative slip direction $\left(E^{+}, E^{-}\right)$. The former three state variables primarily help determining the loading branch of the current step and the corresponding dissipated energy. This dissipated energy is then added to the state variable E^{+} or E^{-}, depending on the slip direction the current step is following ($s \geq 0$ or $s < 0$, respectively). The total dissipated energies $\left(E^{+}, E^{-}\right)$ primarily define the reduction of the negative and positive monotonic envelopes, respectively.

Monotonic and reduced envelopes. The monotonic envelope follows a piece-wise linear function defined by the input properties $\left(s_e, s_1, s_2, s_3, \tau_e, \tau_1, \tau_3\right)$, which are recommended by Khalid (2011) as follows:

$$\begin{aligned} s_1 &= \sqrt{\frac{f_c'}{30}} \text{ mm} \\ s_2 &= 3 \text{ mm} \\ s_3 &= S_{lug} \end{aligned} \tag{3.64}$$

$$\begin{aligned} \tau_1 &= \left(20 - \frac{d_b}{4}\right)\sqrt{\frac{f_c'}{30}} \text{ MPa} \\ \tau_3 &= \left(5.5 - \frac{0.07 S_{lug}}{H_{lug}}\right)\sqrt{\frac{f_c'}{27.6}} \text{ MPa} \end{aligned} \tag{3.65}$$

where f_c' is the compressive strength of the concrete in MPa; and d_b is the diameter of the reinforcement bar in mm. On the other hand, S_{lug} and H_{lug} represent the clear spacing and height of lugs on the reinforcement bar, respectively, in mm.

The reduced envelopes are determined from scaling of the monotonic envelope via a damage parameter D which reflects the energy dissipated in previous slip cycles:

$$\begin{aligned} \tau_e^{+(-)} &= \tau_e\left(1 - D\right) \\ \tau_1^{+(-)} &= \tau_1\left(1 - D\right) \\ \tau_3^{+(-)} &= \tau_3\left(1 - D\right) \\ D &= 1 - e^{-1.2\left(E_0^{-(+)}/E_R\right)^{1.1}} \\ s_e^{+(-)} &= \tau_e^{+(-)}/E \end{aligned} \tag{3.66}$$

where E_R is the reference dissipated energy, which is determined with the monotonic envelope up to slip s_3:

$$E_R = \frac{\tau_e s_e}{2} + \frac{\tau_e + \tau_1}{2}\left(s_1 - s_e\right) + \tau_1\left(s_2 - s_1\right) + \frac{\tau_1 + \tau_3}{2}\left(s_3 - s_2\right) \tag{3.67}$$

Considering the total dissipated energies at the start of the step $\left(E_0^+, E_0^-\right)$, it is worth noting that the bond-slip model is formulated in such a way that the positive monotonic envelope (i.e. envelope for $s \geq 0$) is reduced based solely on the energy dissipated under negative slips (i.e. $s < 0$) and vice-versa, hence the representation of superscript signs to highlight this correspondence in the expressions of (3.66). It is also worth noting that only the elastic slip $s_e^{+(-)}$ is readjusted for the reduced envelope to maintain the same elastic stiffness modulus $E = \tau_e / s_e$, with the remaining slip values remain unchanged from the reference values $\left(s_1, s_2, s_3\right)$.

The state variables E^+ and E^- only accumulates dissipated energy respectively when $s_{pl} > s_{pl,0}^+$ and $s_{pl} < s_{pl,0}^-$, with $s_{pl,0}^{+(-)}$ representing the maximum positive (minimum negative) plastic slip at the start of the step and s_{pl} representing the current plastic slip at the end of the step:

$$s_{pl} = s - \frac{\tau}{E} \tag{3.68}$$

where τ and s are the current bond stress and slip.

Such limiting conditions correspond to a stress state developing further inelastic slips on the monotonic/reduced envelope, with the total dissipated energy accumulated at the end of the step determined as follows:

$$E^{+(-)} = E_0^{+(-)} + \tau \cdot \left(s_{pl} - s_{pl,0}^{+(-)}\right) \tag{3.69}$$

The conditions for further accumulation of dissipated energy also implies that the current plastic slip s_{pl} would have exceeded the maximum positive (minimum negative) plastic slip previously experienced by the loading history. Hence, s_{pl}^+ and s_{pl}^- should be updated at the end of the step as:

$$s_{pl}^{+(-)} = s_{pl} \tag{3.70}$$

Elastic loading/unloading branch. Considering a given current plastic slip at the start of the step $s_{pl,0}$, the elastic loading/unloading response of the current slip s is established as:

$$\tau_{eld} = E\left(s - s_{pl,0}\right) \tag{3.71}$$

The above equation provides a trial elastic stress which is subsequently compared with the stress determined from the other branches so as to establish the actual stress corresponding to the current slip via the logic of the model formulation. If stress state is indeed on the elastic loading/unloading branch, all state variables at the start of the step are directly carried forward at end of the step.

Frictional branch. The resistance of the frictional branch is determined as follows:

$$\begin{aligned} \tau_f^- &= -\frac{\min\left(s_{pl}^+, u^+\right)}{u^+}\tau_3^- \\ \tau_f^+ &= \frac{\min\left(-s_{pl}^-, u^-\right)}{u^-}\tau_3^+ \end{aligned} \tag{3.72}$$

with:

$$\begin{aligned} u^+ &= s_3 - \frac{\tau_3^+}{E} \\ u^- &= s_3 - \frac{\tau_3^-}{E} \end{aligned} \tag{3.73}$$

Equation (3.72) indicates that the resistance of the frictional branch is limited by the residual resistance of the current reduced envelope, i.e. the frictional resistance under positive slip τ_f^- is limited by the residual resistance of the reduced envelope under negative slip τ_3^- and vice-versa (see Fig. 3.15). The frictional resistance is also a function of the ratio between the maximum plastic slip experienced in the previous monotonic/reduced envelope (from which unloading initiated) and the corresponding reference value established as per (3.73) (Eligehausen *et al.*, 1983; Khalid, 2011). For a stress state within the frictional branch, only the current plastic slip needs to be updated at the end of the step.

$$s_{pl} = s - \frac{\tau}{E} \quad \text{with } \tau = \tau_f^{-(+)} \tag{3.74}$$

Reloading branch. The reloading branch is determined with two points. The first one is simply the frictional resistance at zero slip, whereas the second point is defined by the intersection of the current reduced envelope with the elastic loading/unloading branch associated to the maximum (minimum) plastic slip $s_{pl}^{+(-)}$. It is worth noting that for the first slip reversal (i.e. first transition from positive to negative slip or vice-versa) it is assumed that the reloading branch directly connects the frictional resistance at zero slip to the point $\left(s_e^{+(-)}, \tau_e^{+(-)}\right)$ as a result of the elastic loading/unloading branch coinciding with the elastic response of the reduced envelope. Considering the reloading branches illustrated in Fig. 3.15 as examples, the reloading branch under negative slip is established as:

$$\tau_{rld}^{-} = \tau_f^{-} + \frac{s}{s_{\mathrm{F}}}\left(\tau_{\mathrm{F}} - \tau_f^{-}\right) \tag{3.75}$$

whilst the reloading branch under positive slip is established as:

$$\tau_{rld}^{+} = \tau_f^{+} + \frac{s}{s_{\mathrm{K}}}\left(\tau_{\mathrm{K}} - \tau_f^{+}\right) \tag{3.76}$$

The above equations are valid for a current slip $s > s_{\mathrm{F}}$ and $s < s_{\mathrm{K}}$, respectively, under which only the current plastic slip is updated at the end of the step.

$$s_{pl} = s - \frac{\tau}{E} \quad \text{with } \tau = \tau_{rld}^{+(-)} \tag{3.77}$$

Otherwise, the stress state is on the reduced envelope, where the state variables should be accordingly updated following the procedure described for the monotonic/reduced envelope.

Logic of the model formulation. Fig. 3.16 illustrates the flowchart for the selection of the loading branch corresponding to a given current slip and state variables at the start of the step. The logic for negative slip $\left(s < 0\right)$ is omitted for conciseness since it mirrors the logic for positive slip. Furthermore, all variables can be determined from the equations provided throughout this section, including the comparative stress on the monotonic envelope τ_{mr}, which is determined with the current slip s and (3.64)-(3.66), and the slip of the second point for the definition of the reloading branch s_{rld}. Once the type of loading branch is identified for the current slip, the state variables should be updated following the procedure presented for such loading branch.

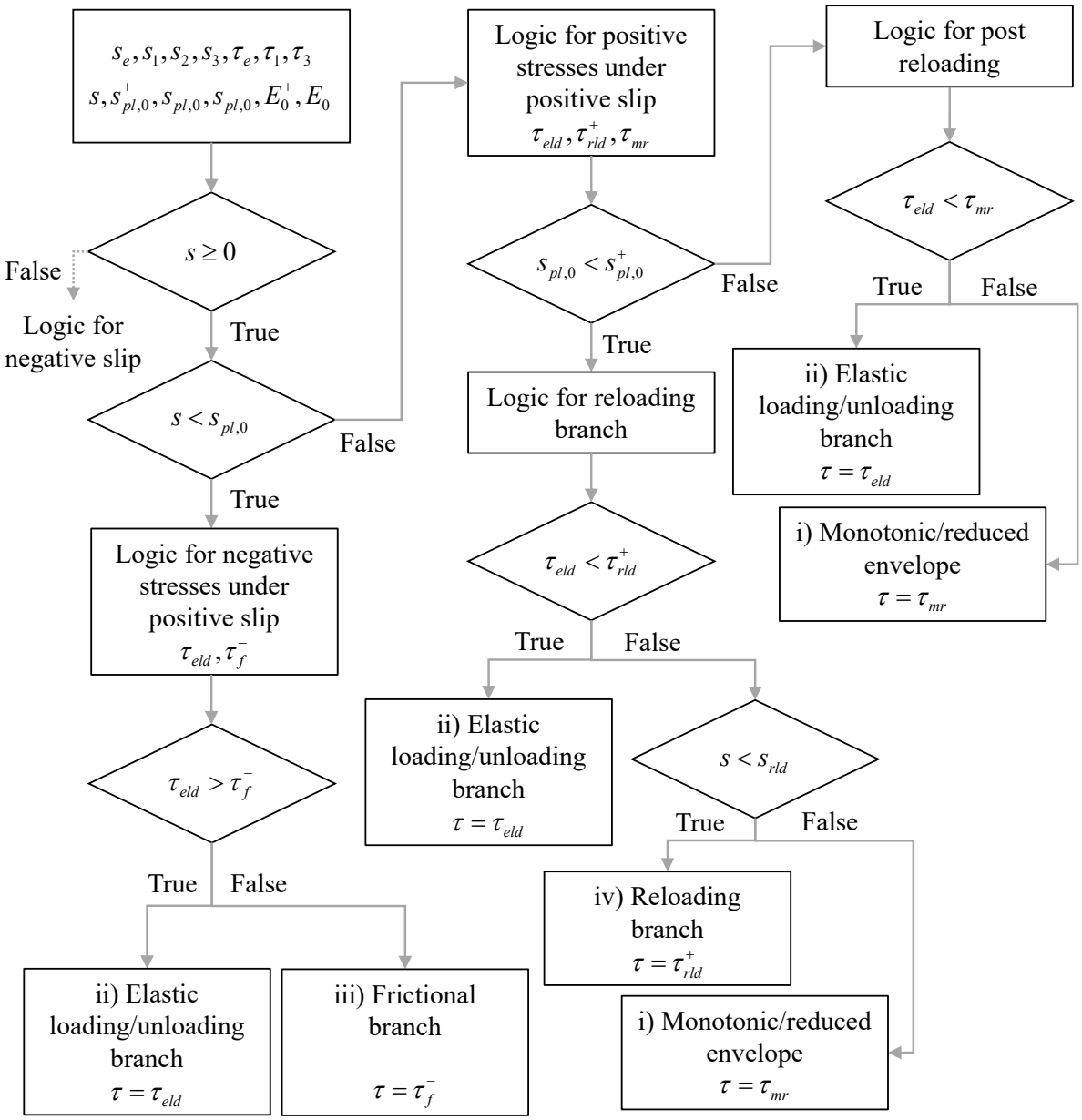


Fig. 3.16 – Flowchart describing the logic of the strain-independent bond-slip model

3.4.1.2 Strain-dependent reduction factor

The strain-dependent reduction factor $\Omega_y(\varepsilon_s)$ follows the expression given in the CEB-FIP Model Code (fib, 2012b):

$$\Omega_y(\varepsilon_s) = \begin{cases} 1.0 & \varepsilon_s \leq \varepsilon_y \\ 1.0 - \left[0.85\left(1 - e^{-5a^b}\right)\right] & \varepsilon_s > \varepsilon_y \end{cases} \quad \text{with } a = \frac{\varepsilon_s - \varepsilon_y}{\varepsilon_u - \varepsilon_y} \text{ and } b = \left(2.0 - \frac{f_t}{f_y}\right)^2 \tag{3.78}$$

where ε_s is the tensile reinforcement strain, ε_y and ε_u are respectively the yield and ultimate tensile strain of the steel, f_t is the tensile strength of the concrete (in MPa) and f_y is the yield strength of the steel reinforcement (in MPa). The reduction factor $\Omega_y(\varepsilon_s)$ is implemented as a state variable for the bond stress-slip-strain model given in (3.63) with the parameter b defined as a material model input. It is worth noting that the reduction factor is formulated in such a way that when $b \leq 0$ the reduction factor is equal to 1.0, hence recovering the strain-independent model. It is also worth noting that the reduction factor at the current step is calculated based on the tensile reinforcement strain ε_s from the previous step and is only updated for the next step if the reduction factor determined with the current reinforcement strain results in a lower value. This implies that bond strength only reduces with increasing tensile strain of the reinforcement.

3.4.2 Verification

The proposed bond stress-slip-strain model is herein verified based on the monotonic pull-out response of an adequately embedded reinforcement. In this respect, a pull-out test specimen from Shima *et al.* (1987) is replicated in ADAPTIC. The specimen entails a reinforcement measuring 19.5mm in diameter and embedded in a concrete cylinder for a length of 50ϕ, as illustrated in Fig. 3.17. As noted by Shima *et al.* (1987), this embedment length is adequately long to cause the yield of the reinforcement. The concrete cylinder measures 500mm in diameter and is represented with an equivalent squared section in ADAPTIC. The remaining modelling considerations (e.g. boundary conditions and mesh) are also illustrated in Fig. 3.17, whilst the material properties for the concrete, reinforcement and bond are given in Table 3.3.

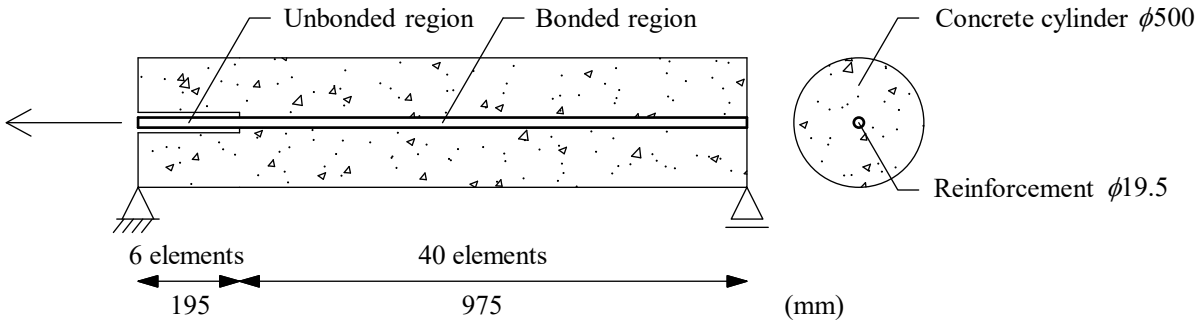


Fig. 3.17 – Test specimen for the verification of the strain-dependent bond-slip model

Table 3.3 – Steel and concrete properties for the verification specimen

Steel properties				
E (MPa)	σ_y (MPa)	μ (-)	ε_u (-)	a (-)
190000	820	1.220×10^{-2}	0.043	10^{-6}

Concrete properties (element size: 25mm)						
E_{c1} (MPa)	f_{c1} (MPa)	E_{c2} (MPa)	f_{cu} (MPa)	E_{t1} (MPa)	f_t (MPa)	E_{t2} (MPa)
11132	19.60	-154.01	1.00	26922	1.537	-236.86

Bond properties						
s_e (mm)	s_1 (mm)	s_2 (mm)	s_3 (mm)	τ_e (MPa)	τ_1 (MPa)	τ_3 (MPa)
0.02	0.525	3.00	9.90	5.50	6.00	2.83

where for the steel properties:
E is the stiffness
σ_y is the yield strength
μ is the ratio of hardening stiffness to elastic stiffness modulus
ε_u is the ultimate strain
a is the tensile softening parameter

and for the concrete properties:
E_{c1} is the secant compressive stiffness
f_{c1} is the compressive strength
E_{c2} is the compressive softening stiffness
f_{cu} is the residual compressive stiffness
E_{t1} is the initial tensile stiffness
f_t is the tensile strength
E_{t2} is the tensile softening stiffness

Note that the input properties defined for the monotonic envelope of the bond model are not those recommended in (3.64) and (3.65) but are instead chosen for a closer fitting of the numerically predicted bond response to the experimental data. Three models are considered for the current verification, involving i) BM1 – the strain-independent bond-slip model, where $\Omega_y(\varepsilon_s)=1.0$, ii) BM2a – the strain-dependent model with $\Omega_y(\varepsilon_s)$ exactly defined as per (3.78), thus following the values recommended in the CEB-FIP Model Code, and iii) BM2b – the same strain-dependent model but allowing more generic parameters for (3.78):

$$\Omega_y\left(\varepsilon_s\right)=\begin{cases}1.0 & \varepsilon_s \le \varepsilon_y \\ 1.0-\left[b_2\left(1-e^{-b_3 \cdot a^{h}}\right)\right] & \varepsilon_s > \varepsilon_y\end{cases} \tag{3.79}$$

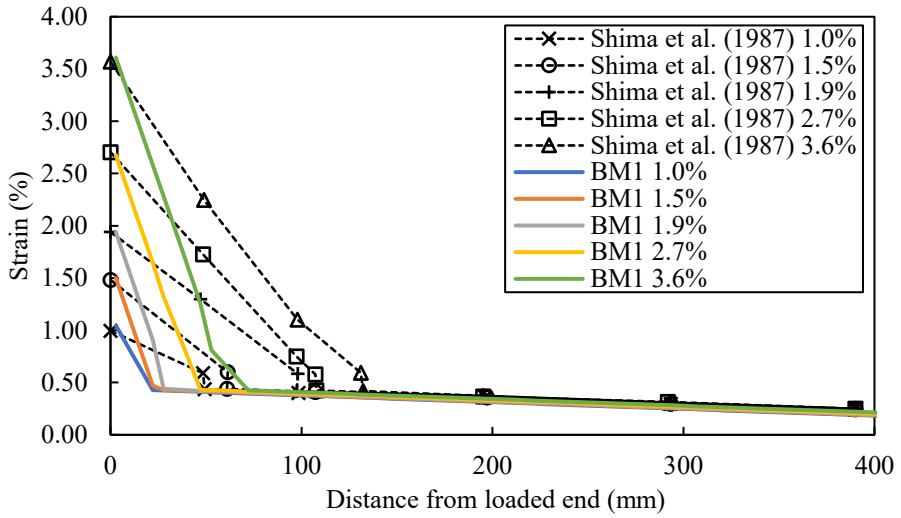
where a remains unchanged and $\left(b_1, b_2, b_3\right)$ are now freely defined. Specifically for model BM2b, along with the parameters defining the monotonic envelope of the bond model, the parameters $\left(b_1, b_2, b_3\right)$ are curve-fitted to the experimental data via an optimisation algorithm.

$$b_1 = 0.15 \; ; \quad b_2 = 0.65 \; ; \quad b_3 = 5.0 \tag{3.80}$$

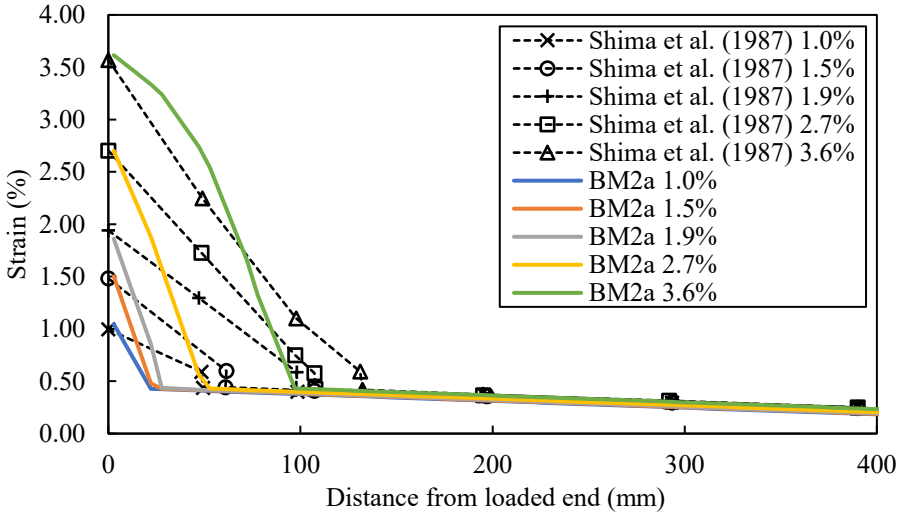
Fig. 3.18 illustrate the comparison of the numerical predictions and the experimental data based on the development of reinforcement strains over the first 400mm of embedment length from the loaded end (approximately corresponding to 20ϕ). The numerical predictions and the experimental data are compared at five levels of reinforcement strain at the loaded end (1.0%, 1.5%, 1.9%, 2.7% and 3.6%) which have all exceed the yield strain.

A satisfactory fit is verified for all three models for reinforcement strains below yield (0.43%). For strains above yield, however, model BM1 clearly predicts a faster reduction of reinforcement strains over the embedment length, and thus a more efficient transfer of reinforcement stresses to the concrete, a result primarily due to the higher bond strengths predicted within this embedment region, noting that there is no reduction of bond strength with reinforcement strains for model BM1. Furthermore, given that the slip at the loaded end can be established from the integration of reinforcement strains over the embedded length, it follows that model BM1 largely underestimates the experimental slip for the considered strain levels.

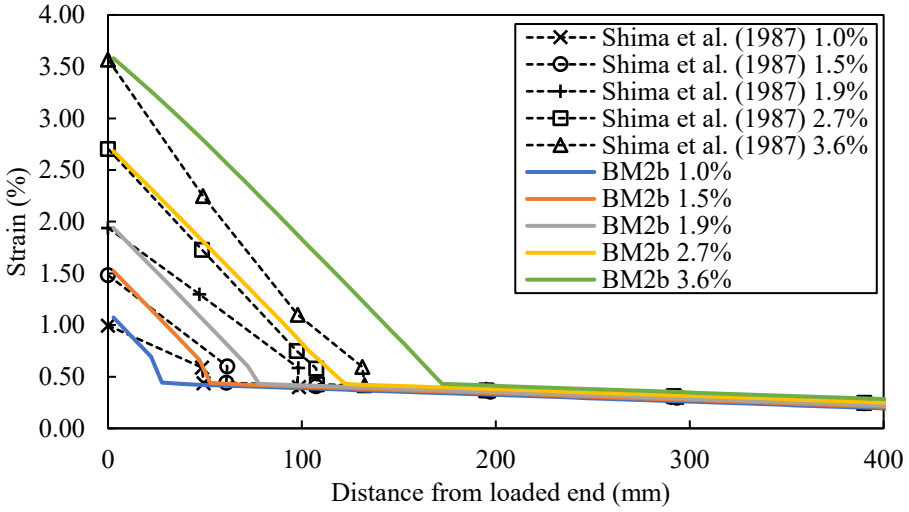
The improvement achieved with model BM2a compared to model BM1 is not significant for the considered strain levels except for 3.6%, where the model predicts an extended region of high reinforcement strains. Such conclusions are subsequently explained via the assessment of bond stresses over the embedment length. Lastly, with the optimised parameters for the decay of bond strength, model BM2b provides a reasonable fit between numerical predictions and the experimental data, thus highlighting the benefit of the proposed bond stress-slip-strain model to represent bond behaviour of adequately embedded reinforcements provided that the parameters from the strain-dependent reduction factor are appropriately calibrated with respect to the experimental data.



(a) Strain-independent bond-slip model



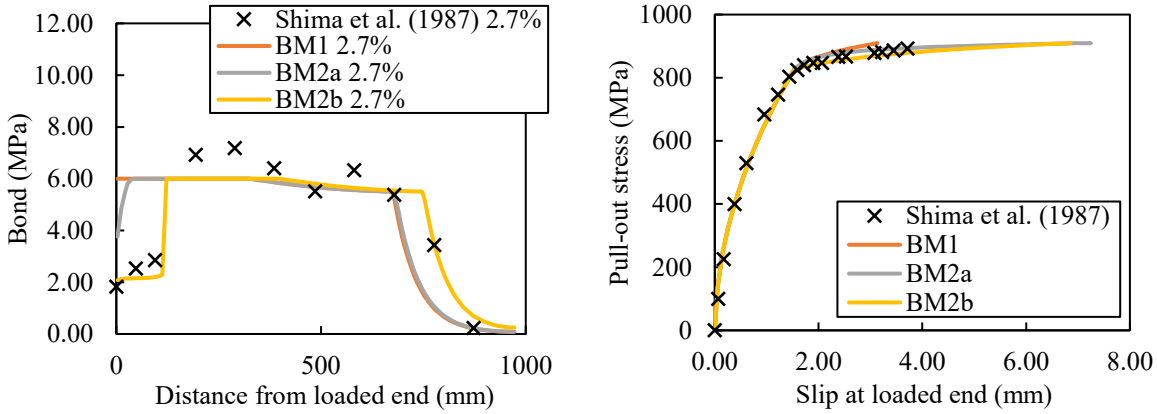
(b) Reference strain-dependent bond-slip model



(c) Optimised strain-dependent bond-slip model

Fig. 3.18 – Verification of reinforcement strain-distribution over the embedment length

Fig. 3.19a compares the distribution of bond stress over the embedment length predicted by the three models for a strain level of 2.7% at the loaded end. Such comparison explains why the improvement achieved with model BM2a with reference to model BM1 is not significant for strain levels up to 2.7% at the loaded end. At the considered strain level, the reduction in bond strength achieved with model BM2a due to the yield of the reinforcement is not significant yet. Indeed, the experimental data suggest that yield penetration have already developed approximately for an embedment length of 175mm from the loaded end, whilst bond stress is just starting to reduce for the response predicted by the BM2a model. This underestimation on the reduction of bond strength by model BM2a can be related to the defined rate at which bond strength decreases with increasing strains, i.e. the parameters b_1 and b_3 from (3.79), thus suggesting that the combination of parameters recommended in the CEB-FIP Model Code does not result in a sufficiently high rate of bond stress decay to match the considered set of experimental data. The rate of bond stress decay with increasing strains is substantially faster following optimisation of the parameters b_1 and b_3, as shown by the numerical prediction from model BM2b.



(a) Bond stress distribution (b) Stress-slip response

Fig. 3.19 – Influence of reinforcement strains on the bond-slip behaviour

Notwithstanding, despite not satisfactorily predicting the increase in slip due to reinforcement strains at lower strain levels (1.0%-2.7%), model BM2a still predicts a significant increase of slip at the ultimate strength of the reinforcement, as evidenced in Fig. 3.19b. At this level of reinforcement stress, the corresponding strains are sufficiently high such that model BM2a effectively predicts a significant decay in bond strength due to the reinforcement strains. As such, for the context of this thesis, where the primary aim is to assess the ductility supply of RC sub-systems at fracture of the reinforcement (associated to high levels of reinforcement

strain), the strain-dependent reduction factor expressed in (3.78) is deemed acceptable for the representation of strain-dependent bond behaviour. Indeed, given the usual scatter of data and uncertainties related to the experimental tests, a bond model adopting the optimised parameters for the reduction factor may not be applicable for embedment scenarios involving general geometric and mechanical considerations.

3.5 I- and T-shaped cross sections

As discussed in Section 3.2, the feature involving nonlinear displacement distribution over the cross-section depth is achieved based on a set of orthogonal shape functions, which in the work of Khalid (2011) have been limited to square/rectangular cross-sections. Extending the applicability of the bond-modelling elements also to I- and T-shaped sections present the advantage in considering the additional contribution of the slab for compressive arching action and tensile catenary action, with the slab acting as the flange of the beam. Such benefit is appreciated in the application of the elements as part of a grillage model representing an entire floor system, though it is worth noting that the mechanisms associated to membrane effects (i.e. compressive and tensile membrane actions) would still not be addressed, the consideration of which would require the explicit modelling of the floor slab with shell elements instead. Furthermore, given that the bond-modelling elements are currently formulated for planar assessments, these elements would require further development to be readily suitable for its application in a 3-dimensional grillage model. Nonetheless, further to establishing the basis for such a future application of the elements, the inclusion of I- and T-shaped sections still benefits the assessment of planar frames, potentially achieving a more economical robustness design. In this respect, this section extends the application of the bond-modelling elements to beam-column members with a cross-section which is symmetric about its vertical axis. The formulation of the corresponding orthogonal shape function is first presented followed by verification examples to assess its correct implementation into ADAPTIC.

3.5.1 Formulation

Two functions f and g are orthogonal if the inner product over the considered domain is equal to zero.

$$\langle f, g \rangle = \int_{\Omega} f\, g\, d\Omega = 0 \tag{3.81}$$

As such, to ensure that an order n cross-sectional shape function $f_n(y)$ belongs to a defined set of orthogonal functions, $f_n(y)$ should be orthogonal to all of the lower order functions in

sequence, from $f_{n-1}(y)$ to $f_0(y)$, with $f_0(y)$ being a constant function independent of y. Considering the shape functions over the cross-section depth as polynomial functions, this leads to:

$$\begin{aligned} &f_n(y) = a_{n+1}\left(y^n + ... + a_{n-1}y + a_n\right) \\ &\langle f_n, f_{n-1}\rangle = \int_A f_n(y)\, f_{n-1}(y)\, dA = 0 \\ &\langle f_n, f_{n-2}\rangle = \int_A f_n(y)\, f_{n-2}(y)\, dA = 0 \\ &\qquad\qquad ... \\ &\langle f_n, f_1\rangle = \int_A f_n(y)\, f_1(y)\, dA = 0 \\ &\langle f_n, f_0\rangle = \int_A f_n(y)\, f_0(y)\, dA = 0 \end{aligned} \tag{3.82}$$

where A is the area of the cross-section; $f_0(y)$ and $f_1(y)$ represent the constant and linear kinematic functions, respectively.

With the previous determination of all polynomials up to $f_{n-1}(y)$, (3.82) presents a system of n equations but with $n+1$ unknows (i.e. the coefficients of the shape function $f_n(y)$). An additional equation is required such that the system of equations becomes solvable. The last equation represents a normalisation condition, in which the self inner product of all the shape functions to be determined must be identical.

$$\langle f_i, f_i\rangle = \int_A f_i(y)\, f_i(y)\, dA = c \quad \text{with } i = 0,1,...,n \tag{3.83}$$

where c is the normalising term for all the shape functions to be determined.

Thus, the construction of the set of orthogonal shape functions initiates with an assumed normalising term c, with which the shape functions are then sequentially determined from $f_0(y)$ up to $f_n(y)$ as per (3.82). In this respect, to recover the same functions presented in (3.9) when a rectangular cross-section is considered, c is herein defined as:

$$c = \int_A y^2 dA \tag{3.84}$$

Such a normalising term implies that $f_1(y) = -y$, whereas $f_0(y)$ is assumed as 1.

The explicit resolution of the integrations in (3.82)-(3.84) is less straightforward for cross-sections with more complex forms, where numerical integration based on the layered cross-section approach is preferable to solve the systems of equations. Considering up to fourth-order

shape functions, the corresponding coefficients of the polynomials can be determined with the following systems of equations:

$$
\begin{aligned}
&f_2(y) = a_3\left(y^2 + a_1 y + a_2\right)\\
&\left\langle f_2, f_1\right\rangle = \sum_{i=1}^{m} A_i\, f_2(d_i)\, f_1(d_i) = 0\\
&\left\langle f_2, f_0\right\rangle = \sum_{i=1}^{m} A_i\, f_2(d_i) = 0\\
&\left\langle f_2, f_2\right\rangle = \sum_{i=1}^{m} A_i\, f_2(d_i)\, f_2(d_i) = \sum_{i=1}^{m} A_i\left(-d_i\right)^2
\end{aligned}
\tag{3.85}
$$

$$
\begin{aligned}
&f_3(y) = b_4\left(y^3 + b_1 y^2 + b_2 y + b_3\right)\\
&\left\langle f_3, f_2\right\rangle = \sum_{i=1}^{m} A_i\, f_3(d_i)\, f_2(d_i) = 0\\
&\left\langle f_3, f_1\right\rangle = \sum_{i=1}^{m} A_i\, f_3(d_i)\, f_1(d_i) = 0\\
&\left\langle f_3, f_0\right\rangle = \sum_{i=1}^{m} A_i\, f_3(d_i) = 0\\
&\left\langle f_3, f_3\right\rangle = \sum_{i=1}^{m} A_i\, f_3(d_i)\, f_3(d_i) = \sum_{i=1}^{m} A_i\left(-d_i\right)^2
\end{aligned}
\tag{3.86}
$$

$$
\begin{aligned}
&f_4(y) = c_5\left(y^4 + c_1 y^3 + c_2 y^2 + c_3 y + c_4\right)\\
&\left\langle f_4, f_3\right\rangle = \sum_{i=1}^{m} A_i\, f_4(d_i)\, f_3(d_i) = 0\\
&\left\langle f_4, f_2\right\rangle = \sum_{i=1}^{m} A_i\, f_4(d_i)\, f_2(d_i) = 0\\
&\left\langle f_4, f_1\right\rangle = \sum_{i=1}^{m} A_i\, f_4(d_i)\, f_1(d_i) = 0\\
&\left\langle f_4, f_0\right\rangle = \sum_{i=1}^{m} A_i\, f_4(d_i) = 0\\
&\left\langle f_4, f_4\right\rangle = \sum_{i=1}^{m} A_i\, f_4(d_i)\, f_4(d_i) = \sum_{i=1}^{m} A_i\left(-d_i\right)^2
\end{aligned}
\tag{3.87}
$$

where m is the number of layers over the cross-section; A_i and d_i are respectively the area of layer i and its distance to the centroidal axis.

3.5.2 Verification

The corresponding FORTRAN code is first verified by comparing the coefficients of the polynomial functions determined via numerical integration to the exact values generated for a

square/rectangular cross-section, with the outcomes suggesting the correct implementation of the code.

The implementation of the FORTRAN code into ADAPTIC is subsequently verified with a simply supported and axially unrestrained rectangular beam, measuring 2400mm in span length, 85mm in width and 170mm in height. The beam is under a constant downward displacement applied at its mid-span and entails 2ϕ8 top reinforcement and 2ϕ8 bottom reinforcement. Table 3.4 provides the steel and concrete properties for the verification beam.

Table 3.4 – Steel and concrete properties for the verification beam

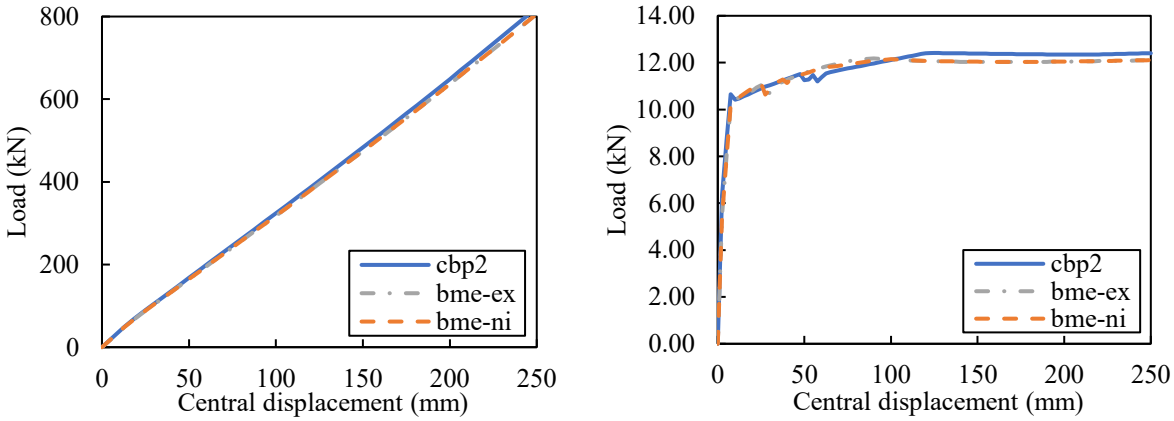
Steel properties						
E (MPa)	σ_y (MPa)	μ (-)	ε_u (-)	a (-)		
200000	390	3.300×10^{-3}	0.12	10^{-6}		
Concrete properties (element size: 80mm)						
E_{c1} (MPa)	f_{c1} (MPa)	E_{c2} (MPa)	f_{cu} (MPa)	E_{t1} (MPa)	f_t (MPa)	E_{t2} (MPa)
19448	44.00	-2147.24	1.00	34313	3.27	-2966.39

where for the steel properties:
E is the stiffness
σ_y is the yield strength
μ is the ratio of hardening stiffness to elastic stiffness modulus
ε_u is the ultimate strain
a is the tensile softening parameter

and for the concrete properties:
E_{c1} is the secant compressive stiffness
f_{c1} is the compressive strength
E_{c2} is the compressive softening stiffness
f_{cu} is the residual compressive stiffness
E_{t1} is the initial tensile stiffness
f_t is the tensile strength
E_{t2} is the tensile softening stiffness

Comparison proceeds with three models of the simply supported beam using: i) the conventional cubic elasto-plastic beam elements, ii) the bond-modelling elements based on the exact solution for the polynomial functions over the cross-section and iii) the same elements as ii) but based on the integration procedure for the polynomial functions instead. These models,

which are herein termed as cbp2, bme-ex and bme-ni, respectively, present identical number of elements and discretised layers over the cross-section (30 elements and 100 layers, respectively). Fig. 3.20 illustrates the central load-displacement response of the models considering elastic and nonlinear behaviour of the concrete.



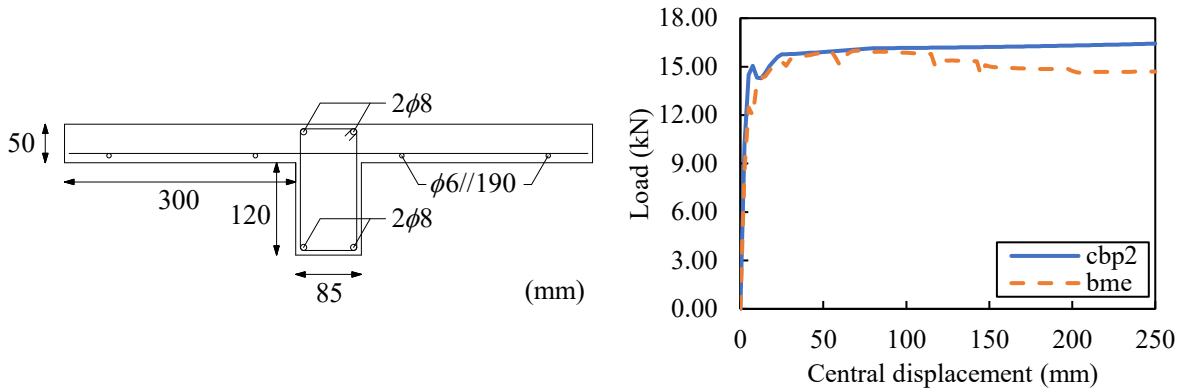
(a) Elastic concrete response (b) Nonlinear concrete response

Fig. 3.20 – Verification for orthogonal shape functions: rectangular beam

The central load-displacement responses predicted by the models bme-ni and bme-ex are approximately identical and both with a slightly lower resistance compared to the response of the cbp2 model. This latter observation agrees well with the assumption of higher-order displacement distributions over the cross-section in the bme models, which inherently leads to a more flexible loading response.

The final verification assesses the advantage of the bond-modelling elements, with reference to the conventional cbp2 elements, in representing the response of beam-column members with a T-shaped cross-section. The simply supported beam from the previous verification is again utilised but considering the T-shaped section illustrated in Fig. 3.21a.

The beam is herein modelled with 120 elements (element size: 20mm) and with the cross-section divided into 100 layers. Fig. 3.21b illustrates the load-displacement response predicted by the models using cbp2 and bond-modelling elements, where the response predicted by the latter model is again slightly less resistant than the response of the former model.

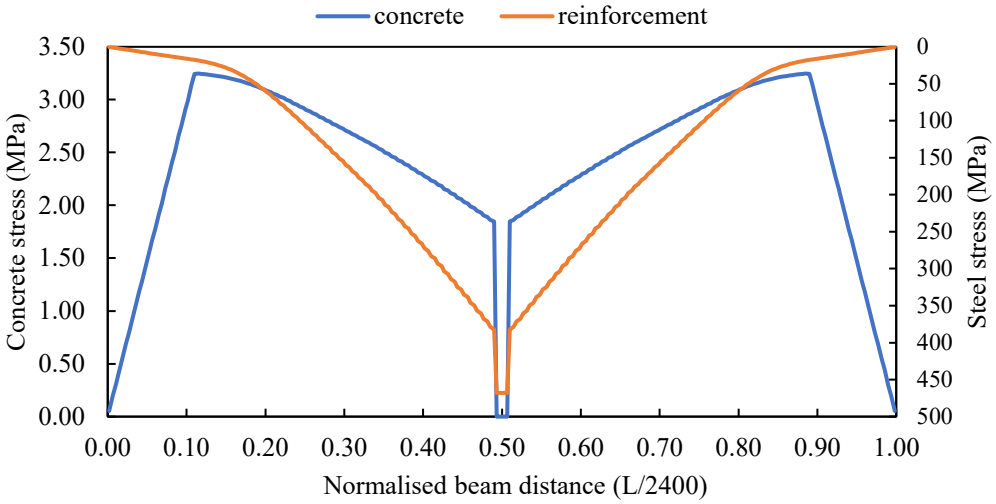


(a) Beam cross-section (b) Central load-displacement response

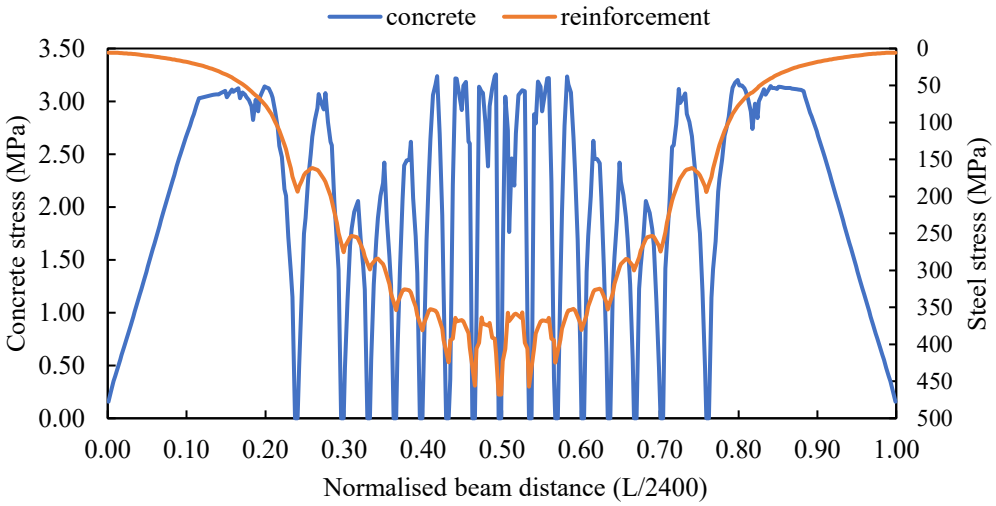
Fig. 3.21 – Verification for orthogonal shape functions: beam with T-shaped section (load-displacement response)

Importantly, Fig. 3.22 shows significant difference in the local stress response predicted by the two models at 50mm central displacement. With the bending moment diagram varying linearly from zero at the support to the maximum bending moment resistance at mid-span, the normalised distance from the supports of the beam beyond which the bending moment exceeds the cracking resistance can be shown to be approximately 0.10. This indicates that concrete cracks are expected to develop between 0.10 and 0.90 normalised beam distance, with the number of cracks depending on the characteristics of the bond interface.

In this respect, given that full-bond condition is assumed for both models, multiple cracks are expected to develop within the established region. Fig. 3.22a shows, however, that the model using conventional cbp2 elements (cbp2) fail to reproduce such a behaviour. Not only does the model predict the spread of concrete cracking beyond a single element at mid-span, hence failing to localise the crack, but it also predicts the reinforcement and concrete strains in an average sense due to the smearing of the reinforcement under the assumption of infinite bond, thus failing to represent further crack development within the expected crack region. Such an observation agrees well with the outcomes noted by Khalid (2011) for beam-column members with a rectangular cross-section. On the other hand, the model using the bond-modelling elements (bme) effectively addresses the limitations of the conventional cbp2 elements, as illustrated in Fig. 3.22b.



(a) Local stress response predicted by the cbp2 model at 50mm central displacement



(b) Local stress response predicted by the bme model at 50mm central displacement

Fig. 3.22 – Verification for orthogonal shape functions: beam with T-shaped section (local stress response)

3.6 Consistent mass matrix (CMM)

Although the present thesis primarily focuses on the representation of the nonlinear static response of RC sub-systems under the loss of a load-bearing member, which simply requires a static procedure for the assessment of the numerical model, determination of the nonlinear static response via a dynamic analysis procedure involving the application of a constant velocity or very slow load increments can result in a better solution convergence compared to static analysis procedures, specifically in load responses with significant softening and snap-through phenomena. Such an observation is demonstrated with a 4000mm fully fixed and axially restrained RC beam example with identical concrete and steel material properties of the

beam example presented for the verification of the steel material model (see Section 3.3.3, Tables 3.1 and 3.2), except that the tensile softening parameter a is defined as 10^{-6} to reproduce a steel response limited to the ultimate tensile strength σ_u and with negligible tensile softening. The assessment of solution procedures proceeds with models using cbp2 elements (cbp2) and models employing the bond-modelling elements (bme). It is also worth noting that in both types of models, the mass of the beam, which is required for dynamic analyses, is represented via the superposition of mass-specific elements cbm2 (Izzuddin, 1991, 2016) to the cbp2 and bond-modelling elements. Thus, the abovementioned models are respectively termed as cbp2-cbm2 and bme-cbm2 for dynamic analysis.

Initial static analysis of the beam example (Fig. 3.23) shows that, despite prior consideration of a wide range of step sizes to search for the furthest solution up to which the procedure would converge, the static solution procedure rarely converges up to the specified displacement (approximately 500mm), regardless of the type of element used to model the beam. Significantly, the solution procedure is prematurely interrupted at very small displacements for the model employing the bond-modelling elements.

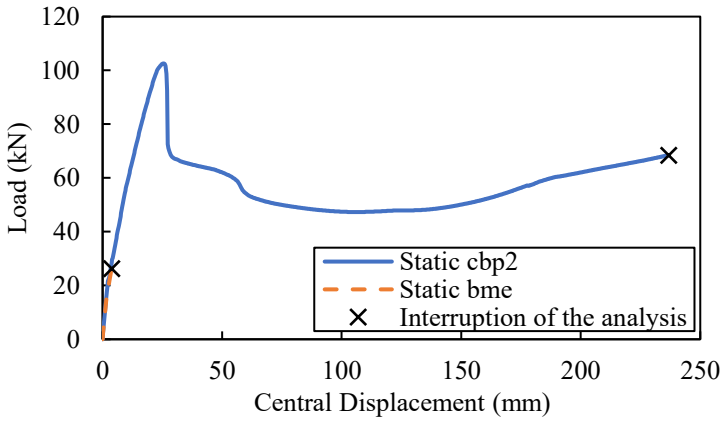


Fig. 3.23 – Convergence assessment: static analysis

The solution procedure converges up to further displacements with a dynamic analysis procedure involving the application of constant velocity (cv), where a solution is found for displacements up to 500mm with the model using the cbp2 elements (Fig. 3.24a). For the model employing the bond-modelling elements, although convergence of the solution procedure has improved with reference to the static procedure, the analysis remains prematurely interrupted well before reaching the specified displacement, as illustrated in Fig. 3.24b.

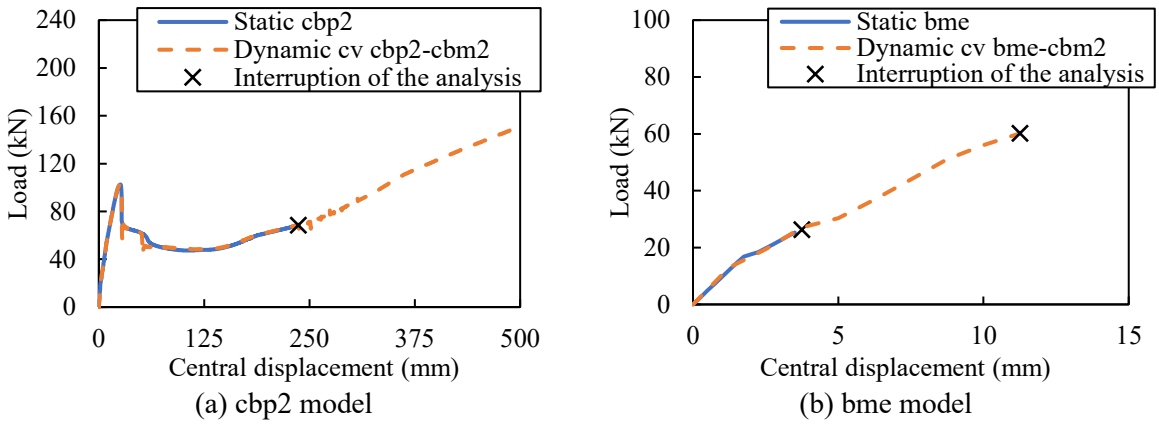


Fig. 3.24 – Convergence assessment: dynamic analysis with applied constant velocity

It follows that the bond-modelling elements developed by Khalid (2011) do not include the formulation of the consistent mass matrix of the elements, hence requiring the said superposition of additional mass-specific elements for dynamic analysis. These mass-specific elements (termed as cbm2), which have also been considered for the dynamic analysis of the model using the conventional cbp2 elements, attribute the mass distributed over the element length to its own nodal DOFs. In this respect, whilst such an approach works reasonably well with the conventional cbp2 elements, given that the cbp2 elements present identical global nodal DOFs as the mass-specific elements, the mass-specific elements fail to attribute any mass to the additional DOFs of the bond-modelling elements, rendering the global mass matrix of the corresponding beam model with a significant amount of zero diagonal terms, thus increasing the likelihood of the analysis procedure to numerical instability.

The consideration of the consistent mass matrix of the elements should mitigate such a convergence issue by accurately attributing mass also to the additional DOFs. Furthermore, for structural assessments where the influence of inertia and damping forces are of interest, such as seismic and impact assessments, the consideration of the consistent mass matrix of the elements should also increase the accuracy of the predicted response. Therefore, to address the abovementioned limitations, the bond-modelling elements are herein completed with the formulation of the corresponding CMM, along with a mass diagonalisation procedure so as to also allow for explicit dynamic analyses.

3.6.1 Definition of CMM

A mass matrix is a discrete representation of the continuum mass distribution, where the global mass matrix follows a similar assembly procedure as that applied for the global stiffness matrix.

Mass matrices are first determined for the individual elements in local coordinates, transformed into global coordinates and are then assembled into the global matrix of the system. The mass matrix of an individual element can be established either via the direct lumping of the mass or based on the kinetic energy over the domain of the element.

In direct mass lumping, the total mass of an element is directly apportioned to the nodal DOFs based on symmetry and conservation, neglecting any cross coupling between the nodal DOFs. Since mass lumping is achieved based on the observation of symmetry, it is only applicable to a limited number of simple elements, where lumping is physically obvious (Zienkiewicz and Taylor, 2000b). The resulting matrix is a diagonally lumped mass matrix (DLMM), which allows for the use of explicit time integration schemes. It is worth noting that explicit time integration schemes present reduced computational demands since these schemes do not require an iterative procedure in solving the governing system of equations within each time step. Though, explicit integration schemes require the specification of a much smaller time step compared to implicit schemes.

The other alternative is to determine the mass matrix based on the kinetic energy over the domain of the element (Felippa, 2004):

$$T = \frac{1}{2}\int_{\Omega} \rho \{\dot{u}\}^{\mathrm{T}} \{\dot{u}\}\, d\Omega \tag{3.88}$$

where ρ is the mass density of the element; Ω is the domain of the element; and $\{\dot{u}\}$ is the velocity field. The resulting matrix can present non-diagonal terms, in which case implicit time integration schemes must be used. Notwithstanding, the non-diagonal mass matrix can be subsequently transformed into a DLMM via a diagonalisation procedure, thus taking advantage of the reduced computational demand from explicit time integration schemes. Under the context of Finite Element Method, the approximation of the displacement field $\{u\}$ by the discrete nodal displacements $\{\mathbf{u}\}$ is established by means of the shape functions $[\mathbf{N}]$:

$$\{u\} = [\mathbf{N}]\{\mathbf{u}\} \tag{3.89}$$

Thus, the velocity is simply the derivative of the displacement field with respect to time. It is worth noting that matrix $[\mathbf{N}]$ entails functions which are independent to time, hence $\partial[\mathbf{N}]/\partial t$ results in a matrix of zeros.

$$\{\dot{u}\} = \frac{\partial \{u\}}{\partial t} = [\mathbf{N}]\{\dot{\mathbf{u}}\} \tag{3.90}$$

Substituting (3.90) into (3.88) gives:

$$T = \frac{1}{2}\{\dot{\mathbf{u}}\}^{\mathrm{T}} \left(\int_{\Omega} \rho [\mathbf{N}]^{\mathrm{T}} [\mathbf{N}] d\Omega \right) \{\dot{\mathbf{u}}\} \tag{3.91}$$

Comparing (3.91) to the scalar kinetic energy expression, it follows that the discrete mass matrix is established as:

$$[\mathbf{m}] = \int_{\Omega} \rho [\mathbf{N}]^{\mathrm{T}} [\mathbf{N}] d\Omega \tag{3.92}$$

If the shape functions $[\mathbf{N}]$ in (3.92) are chosen as identical functions for the determination of the stiffness matrix, the discrete mass matrix $[\mathbf{m}]$ is denoted as a Consistent Mass Matrix (CMM). As noted before, a CMM can present non-diagonal terms (i.e. cross coupling between the nodal DOFs). A CMM is also positive definite and must at least conserve the total mass of the element (Felippa, 2004).

3.6.2 CMM formulation for the concrete element

3.6.2.1 Kinematics and local response of the element

The basic local Lagrangian nodal parameters are considered for the definition of the CMM $(u_1, v_1, \theta_1, u_2, v_2, \theta_2)$ rather than the co-rotational parameters to account for the inertia forces associated to rigid body movements, whilst the additional DOFs remain unchanged $(\delta_m, v_3, v_4, \theta_3, \alpha_1, \alpha_2, \alpha_3, \beta_1, \beta_2, \beta_3, \lambda_1, \lambda_2, \lambda_3)$. Since the kinematics considered for the definition of the CMM and the stiffness matrix are largely identical, exposition of the CMM formulation focuses herein on the details which differ from the stiffness matrix, referring the remaining considerations to Section 3.2.

Once again, the axial displacement field, considering the Timoshenko and higher-order kinematics, is established as:

$$u(x,y) = u_c(x) + f_1(y)\,\theta(x) + f_2(y)\,\alpha(x) + f_3(y)\,\beta(x) + f_4(y)\,\lambda(x) \tag{3.93}$$

where $f_1(y)$, $f_2(y)$, $f_3(y)$ and $f_4(y)$ are the orthogonal shape functions over the cross-section, which are expressed in (3.9) for a rectangular cross-section or numerically determined following the procedure described in Section 3.5.1. $\theta(x)$, $\alpha(x)$, $\beta(x)$, $\lambda(x)$ remain

unchanged and are given in (3.2)-(3.5), whilst the function describing the axial displacement along the reference centroidal axis $u_c(x)$ is now:

$$u_c(x) = \left(1 - \frac{x}{L}\right)u_1 + \left(\frac{x}{L}\right)u_2 + \left[\frac{4x(L-x)}{L^2}\right]\delta_m \tag{3.94}$$

The transverse displacement field is also modified as follows:

$$v(x,y) = \left(1 - \frac{x}{L}\right)v_1 + \left(\frac{x}{L}\right)v_2 + \left(\frac{8x}{L} - \frac{56x^2}{3L^2} + \frac{32x^3}{3L^3}\right)v_3 + \left(-\frac{8x}{3L} + \frac{40x^2}{3L^2} - \frac{32x^3}{3L^3}\right)v_4 \tag{3.95}$$

Accordingly, the displacement fields can be expressed in matrix form as:

$$\begin{Bmatrix} u(x,y) \\ v(x,y) \end{Bmatrix} = [\mathbf{N}]\{\mathbf{u}\} \tag{3.96}$$

where $\{\mathbf{u}\}$ is the vector containing the 19 DOFs of the element,

$$\{\mathbf{u}\} = \langle u_1, v_1, \theta_1, u_2, v_2, \theta_2, \delta_m, v_3, v_4, \theta_3, \alpha_1, \alpha_2, \alpha_3, \beta_1, \beta_2, \beta_3, \lambda_1, \lambda_2, \lambda_3 \rangle^{\mathbf{T}} \tag{3.97}$$

and $[\mathbf{N}]$ is the matrix of the associated shape functions, the terms of which can be easily worked out with (3.93)-(3.95).

With the matrix of the shape functions $[\mathbf{N}]$ determined, (3.92) can then be numerically evaluated based on the same integration procedure for the stiffness matrix:

$$[\mathbf{m}] = \sum_{j=1}^{n} w_{g,j} \sum_{i=1}^{m} \rho_c A_i \left([\mathbf{N}]^{\mathbf{T}} [\mathbf{N}] \right)\Big|_{x=x_{g,j}, y=y_i} \tag{3.98}$$

where ρ_c is the mass density of the concrete. m is the number of layers considered for the cross-section of the element, whereas A_i and y_i are respectively the area and distance to the centroidal axis of layer i. n is the number of Gauss points considered for the numerical integration $(n = 3)$, whereas $w_{g,j}$ and $x_{g,j}$ respectively represent the weighting factor and the location of the Gauss point j, which are given in (3.16).

3.6.2.2 Global element response

For structural level assessment, the mass matrix of the element should be transformed from the local reference system to the global reference system prior to the final assembly of the global mass matrix and dynamic forces of the structure. Under the consideration of the basic local

Lagrangian nodal parameters, only the local DOFs (u_1, v_1, u_2, v_2) necessitates transformation to the corresponding global DOFs, whilst the basic rotation DOFs (θ_1, θ_2) and the additional DOFs $(\delta_m, v_3, v_4, \theta_3, \alpha_1, \alpha_2, \alpha_3, \beta_1, \beta_2, \beta_3, \lambda_1, \lambda_2, \lambda_3)$ are identical in both local and global reference systems. Accordingly, the global mass matrix of the element is established as:

$$\left[\mathbf{M}^e\right] = \left[\mathbf{T}\right]^{\mathrm{T}} \left[\mathbf{m}\right] \left[\mathbf{T}\right] \tag{3.99}$$

The transformation matrix $\left[\mathbf{T}\right]$ involves the direction cosines of the last equilibrium configuration of the element (Izzuddin, 1991) and is divided into subsets separating the basic and additional DOFs:

$$\left[\mathbf{T}\right] = \begin{bmatrix} \mathbf{T}_{bb} & \mathbf{T}_{ba} \\ \mathbf{T}_{ab} & \mathbf{T}_{aa} \end{bmatrix} \tag{3.100}$$

where $\left[\mathbf{T}_{ba}\right]$ and $\left[\mathbf{T}_{ab}\right]$ are 6×13 and 13×6 zero matrices, respectively, whereas $\left[\mathbf{T}_{aa}\right]$ is a 13×13 identity matrix. Lastly, the subset $\left[\mathbf{T}_{bb}\right]$ is given as:

$$\left[\mathbf{T}_{bb}\right] = \begin{bmatrix} c & s & 0 & 0 & 0 & 0 \\ -s & c & 0 & 0 & 0 & 0 \\ 0 & 0 & 1 & 0 & 0 & 0 \\ 0 & 0 & 0 & c & s & 0 \\ 0 & 0 & 0 & -s & c & 0 \\ 0 & 0 & 0 & 0 & 0 & 1 \end{bmatrix} \tag{3.101}$$

where c and s are the direction cosines established based on the last equilibrium configuration of the element.

$$c = \frac{X_E}{L} \;\; ; \;\; s = \frac{Y_E}{L} \tag{3.102}$$

3.6.3 CMM formulation for the steel-bond element

3.6.3.1 Kinematics and local element response

The determination of the mass matrix for the steel-bond element follows a similar procedure described for the concrete element, where the basic local Lagrangian nodal parameters are again considered. Thus, the axial displacement field of a reinforcement bar at a distance d from the reference centroidal axis is established as:

$$u(x,d) = u_c(x) + f_1(d)\,\theta(x) + f_2(d)\,\alpha(x) + f_3(d)\,\beta(x) + f_4(d)\,\lambda(x) + \Delta(x) \tag{3.103}$$

where all terms except $\Delta(x)$ remains unchanged from (3.93); and $\Delta(x)$ is the additional slip field, which is given in (3.34).

Unlike the derivation of the stiffness mass matrix, where the axial displacement field of the reinforcement and the slip field of the bond-slip interface are of interest, the CMM of the element is established based on the axial and transverse displacement field of the reinforcement instead. The contribution from the bond-slip interface is not considered simply because the interface is fictitious and should not present any mass. The transverse displacement field considered herein follows the expression given in (3.95), thus the relevant displacement fields can be expressed in matrix form as:

$$\begin{Bmatrix} u(x,d) \\ v(x,d) \end{Bmatrix} = [\mathbf{N}]\{\mathbf{u}\} \tag{3.104}$$

where $\{\mathbf{u}\}$ is the vector containing the 22 DOFs of the element:

$$\{\mathbf{u}\} = \langle u_1, v_1, \theta_1, u_2, v_2, \theta_2, \Delta_1, \Delta_2, \Delta_3, \delta_m, v_3, v_4, \theta_3, \alpha_1, \alpha_2, \alpha_3, \beta_1, \beta_2, \beta_3, \lambda_1, \lambda_2, \lambda_3 \rangle^{\mathbf{T}} \tag{3.105}$$

and $[\mathbf{N}]$ is the matrix of the associated shape functions, the terms of which can be easily worked out with (3.95), (3.103) and (3.104). The local element mass matrix can then be determined via numerical integration:

$$[\mathbf{m}] = \sum_{j=1}^{n} w_{g,j} \rho_s A_s \left([\mathbf{N}]^{\mathbf{T}} [\mathbf{N}] \right) \Big|_{x=x_{g,j}} \tag{3.106}$$

where ρ_s and A_s are respectively the mass density and area of the steel reinforcement; n, $w_{g,j}$ and $x_{g,j}$ are again the number of Gauss integration points and the associated weights and locations given in (3.16).

3.6.3.2 Global element response

The transformation of local to global element mass matrix follows the same procedure described for the concrete element except that the three additional slip DOFs $(\Delta_1, \Delta_2, \Delta_3)$ are herein considered.

$$\left[\mathbf{M}^e\right] = [\mathbf{T}]^{\mathbf{T}} [\mathbf{m}][\mathbf{T}] \tag{3.107}$$

In this case, the transformation matrix $[\mathbf{T}]$ is a 22×22 matrix:

$$[\mathbf{T}] = \begin{bmatrix} \mathbf{T}_{bb} & \mathbf{T}_{ba} \\ \mathbf{T}_{ab} & \mathbf{T}_{aa} \end{bmatrix} \tag{3.108}$$

where $[\mathbf{T}_{ba}]$ and $[\mathbf{T}_{ab}]$ are now 6×16 and 16×6 zero matrices, respectively, whereas $[\mathbf{T}_{aa}]$ is a 16×16 identity matrix and the subset $[\mathbf{T}_{bb}]$ remains the same as (3.101).

3.6.4 Diagonally lumped mass matrix (DLMM)

The Consistent Mass Matrix of the bond-modelling elements are herein diagonalised based on the procedure employed in Gu (2018). The diagonal terms corresponding to the basic DOFs are added up with respect to the translational and rotational masses, which are then equally distributed back to such diagonal terms. The diagonal terms corresponding to the additional DOFs remain unchanged from the initial CMM. Lastly, all non-diagonal terms are set to zero.

$$M_{1,1}^{DLMM} = M_{2,2}^{DLMM} = M_{4,4}^{DLMM} = M_{5,5}^{DLMM} = \frac{\sum_{i=1,2,4,5} M_{i,i}}{2\times 2} \tag{3.109}$$

$$M_{3,3}^{DLMM} = M_{6,6}^{DLMM} = \frac{\sum_{i=3,6} M_{i,i}}{2} \tag{3.110}$$

$$M_{i,i}^{DLMM} = M_{i,i} \text{ for } i \neq 1:6 \tag{3.111}$$

$$M_{i,j}^{DLMM} = 0 \text{ for } i \neq j \tag{3.112}$$

Equations (3.109) and (3.110) express respectively the equal proportioning of the masses corresponding to the basic translation and rotation DOFs, whilst (3.111) states that the diagonal terms corresponding to the additional DOFs remain unchanged and (3.112) sets the non-diagonal terms of the DLMM to zero.

3.6.5 Finite element response

For dynamic analysis, the dynamic equilibrium of a discrete system as per (3.113) needs to be discretised also with respect to time. This is achieved using step-by-step integration methods evaluating the equilibrium in (3.113) at a specific instant of time t_{n+1}, which solution can be determined with the displacement, velocity and acceleration histories corresponding to the previous time instant t_n.

$$\{\mathbf{G}\} = [\mathbf{M}]\{\ddot{\mathbf{U}}\} + [\mathbf{C}]\{\dot{\mathbf{U}}\} + \{\mathbf{R}\} - \{\mathbf{P}\} = \{\mathbf{0}\} \tag{3.113}$$

where $[\mathbf{M}]$ is the mass matrix; $[\mathbf{C}]$ is the damping matrix; $\{\mathbf{R}\}$ is the resistance forces; and $\{\mathbf{P}\}$ is the equivalent loading. On the other hand, $\{\ddot{\mathbf{U}}\}$ and $\{\dot{\mathbf{U}}\}$ respectively represent the accelerations and velocities of the system parameters $\{\mathbf{U}\}$.

Considering the Newmark time integration scheme (Bathe, 1996) as demonstration example, (3.113) can be shown to give:

$$\{\mathbf{G}_{n+1}\} = \{\tilde{\mathbf{R}}_{n+1}\} - \{\tilde{\mathbf{P}}_{n+1}\} = \{\mathbf{0}\} \tag{3.114}$$

where:

$$\{\tilde{\mathbf{R}}_{n+1}\} = \left(\frac{1}{\beta\Delta t^2}[\mathbf{M}] + \frac{\gamma}{\beta\Delta t}[\mathbf{C}]\right)\{\mathbf{U}_{n+1}\} + \{\mathbf{R}_{n+1}\} \tag{3.115}$$

$$\{\tilde{\mathbf{P}}_{n+1}\} = \{\mathbf{P}_{n+1}\} - [\mathbf{M}]\{\hat{\ddot{\mathbf{U}}}_n\} - [\mathbf{C}]\{\hat{\dot{\mathbf{U}}}_n\} \tag{3.116}$$

β and γ are the parameters of the Newmark time integration method; $\{\mathbf{U}_{n+1}\}$ is the displacement vector of the current time step, whilst $\{\hat{\ddot{\mathbf{U}}}_n\}$ and $\{\hat{\dot{\mathbf{U}}}_n\}$ are established as:

$$\{\hat{\ddot{\mathbf{U}}}_n\} = -\frac{1}{\beta\Delta t^2}\left(\{\mathbf{U}_n\} + \Delta t\{\dot{\mathbf{U}}_n\} + (1/2-\beta)\Delta t^2\{\ddot{\mathbf{U}}_n\}\right) \tag{3.117}$$

$$\{\hat{\dot{\mathbf{U}}}_n\} = \{\dot{\mathbf{U}}_n\} + \Delta t\left((1-\gamma)\{\ddot{\mathbf{U}}_n\} + \gamma\{\hat{\ddot{\mathbf{U}}}_n\}\right) \tag{3.118}$$

where Δt is the time step increment; $\{\ddot{\mathbf{U}}_n\}$, $\{\dot{\mathbf{U}}_n\}$ and $\{\mathbf{U}_n\}$ are respectively the acceleration, velocity and displacement vectors of the previous time step.

Equations (3.115) and (3.116) indicate that, under dynamic analysis, the time integration scheme transforms the dynamic equilibrium problem into a static one by adding the inertia and damping force contributions to both the static resistance vector $\{\mathbf{R}_{n+1}\}$ and the static equivalent load vector $\{\mathbf{P}_{n+1}\}$. The solution of the nonlinear system of equations expressed in (3.114) can then be determined with iterative procedures for static analysis but considering the modified tangent stiffness matrix.

$$\left[\tilde{\mathbf{K}}_T\right]=\left[\frac{\partial\left\{\mathbf{G}_{n+1}\right\}}{\partial\left\langle\mathbf{U}_{n+1}\right\rangle}\right] \tag{3.119}$$

Assuming $\left[\mathbf{M}\right]$ and $\left[\mathbf{C}\right]$ independent of $\left\{\mathbf{U}_{n+1}\right\}$, and considering (3.114)-(3.119), $\left[\tilde{\mathbf{K}}_T\right]$ can be expressed as:

$$\left[\tilde{\mathbf{K}}_T\right]=\left[\mathbf{K}_T\right]+\frac{1}{\beta\Delta t^2}\left[\mathbf{M}\right]+\frac{\gamma}{\beta\Delta t}\left[\mathbf{C}\right] \tag{3.120}$$

3.6.6 Verification

For the verification of the Consistent Mass Matrix in ADAPTIC, consideration is again given to the 4000mm fixed and axially restrained RC beam presented in the beginning of this section, which is modelled with 40 elements. Three predicted responses of the RC beam are respectively established with: i) the updated element considering the optional CMM (bme-cmm), ii) same element as i) but considering the overlay of mass-specific elements instead (bme-cbm2) and iii) conventional elasto-plastic cbp2 elements (cbp2-cbm2). The predicted responses are compared under eigenvalue and dynamic analyses, with the latter analysis further divided into assessments under applied constant velocity and the sudden application of a vertical load at the mid-span of the RC beam.

Table 3.5 and Fig. 3.25 provide the first six eigenvalue periods and corresponding mode shapes predicted using the three modelling approaches, the comparison of which indicate a close fit between the three approaches.

Table 3.5 – Periods and mode types from eigenvalue analysis

Mode	bme-dens		bme-cbm2		cbp2-cbm2	
	Period (ms)	Type	Period (ms)	Type	Period (ms)	Type
1	24.30	y	24.20	y	23.40	y
2	9.12	y	9.10	y	8.51	y
3	4.84	y	4.84	y	4.34	y
4	3.18	x	3.16	x	3.16	x
5	3.06	y	3.07	y	2.63	y
6	2.15	y	2.17	y	1.76	y

The more flexible responses are predicted by the bme-cmm and bme-cbm2 models, whilst the opposite is predicted by the cbp2-cbm2 model. Such an observation can be explained by the consideration of a finite bond stiffness and higher-order displacement modes over the cross-section in the models utilising the bond-modelling elements, thus inherently increasing its

flexibility with respect to a model using the conventional cbp2 elements. Importantly, the response of the bme-cmm model follows very closely the response of the bme-cbm2 model, hence indicating the correct implementation of the CMM in ADAPTIC.

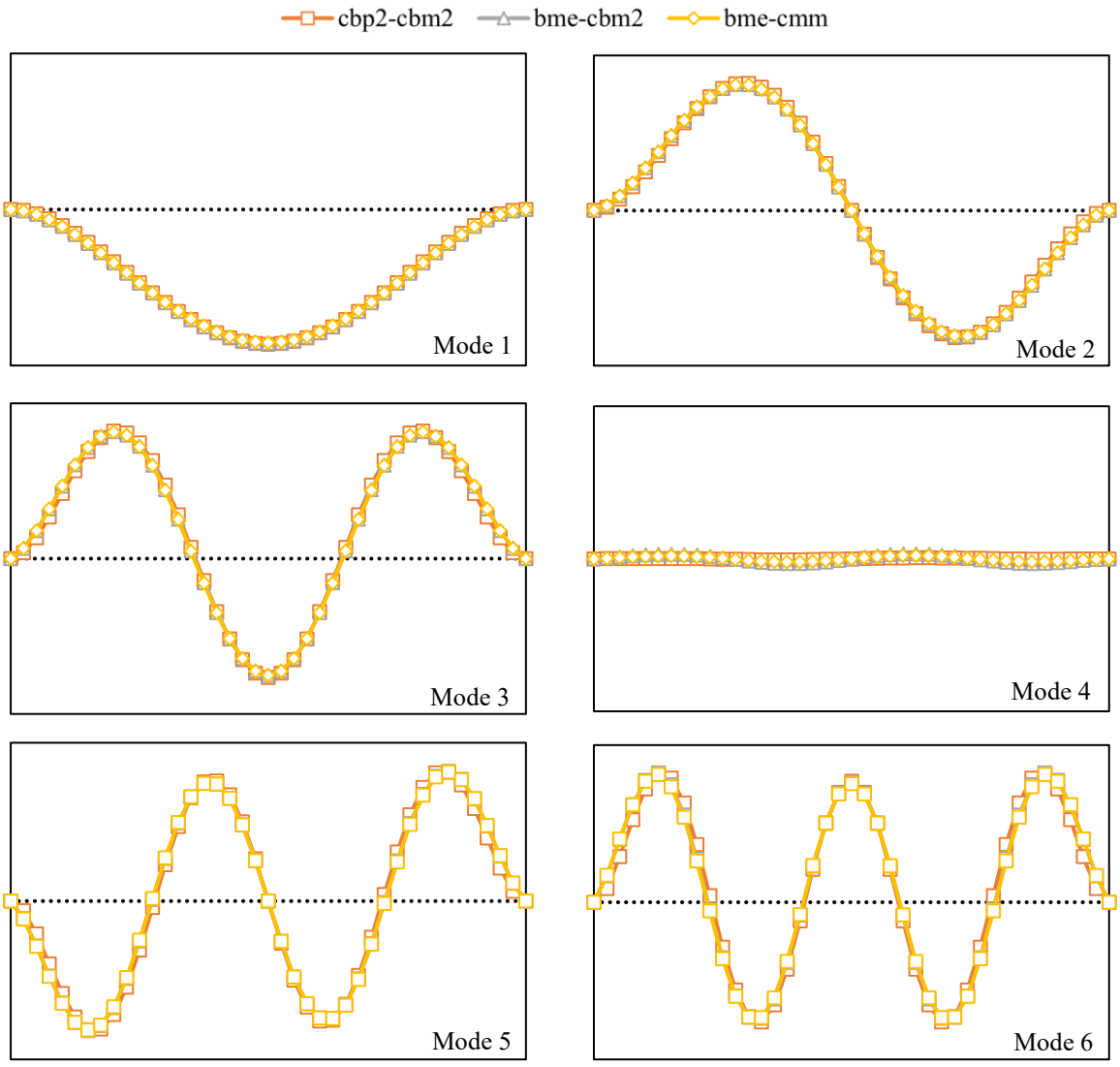
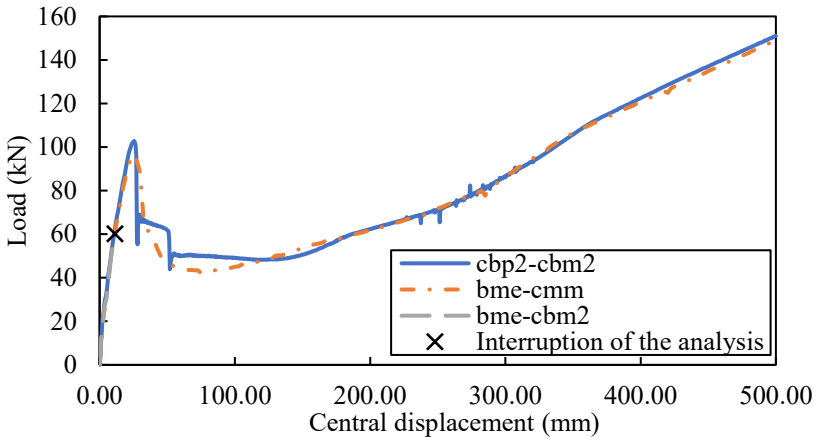
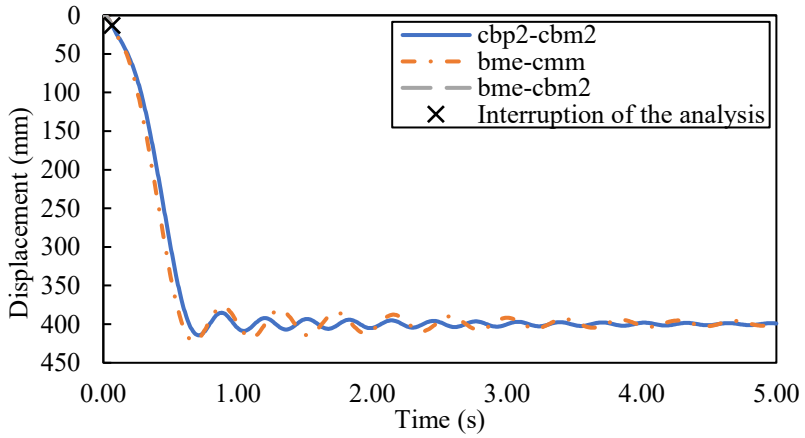


Fig. 3.25 – Verification with eigenvalue analysis: first six mode shapes

Fig. 3.26 illustrates the verification of the CMM for dynamic analysis under applied constant velocity and the sudden application of a vertical load of 80kN at mid-span of the RC beam. The dynamic analysis considers as reference time integration scheme the Hilber-Hughes-Taylor method (HHT).



(a) Applied constant velocity



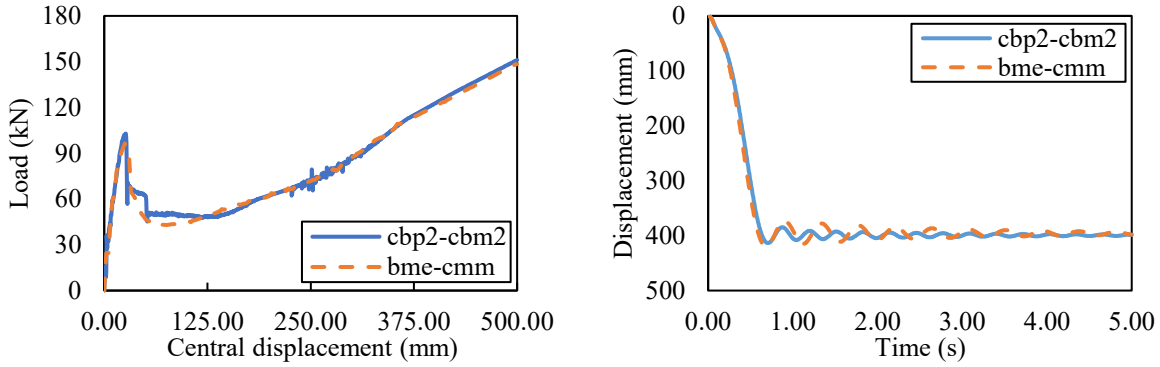
(b) Sudden application of P=80kN concentrated load

Fig. 3.26 – Verification with dynamic analysis (implicit HHT)

Clearly, with the use of the CMM, the dynamic analysis of the bme-cmm model can converge up to the specified displacement of 500mm in the assessment under applied constant velocity and to the specified time of 5s in the assessment under the sudden application of the vertical load of 80kN, whilst the analysis of the bme-cbm2 model fails to converge at a very premature displacement and time step in such assessments. It is worth noting that the convergence up to any specified displacement/time can now be frequently achieved with the modelling approach considering the CMM, irrespective of the parameters defined for the time integration (e.g. time step and mass proportional damping) and for the discretisation of the model (e.g. number of elements and layers over the cross-section). Indeed, the convergence improvement achieved with the bme-cmm model verifies even for a reduced number of time integration steps compared to the bme-cbm2 model. Although an appreciable comparison cannot be established with the responses predicted by the bme-cmm and bme-cbm2 model due to the premature interruption of the analysis of the latter model, the comparison of the bme-cmm model to the

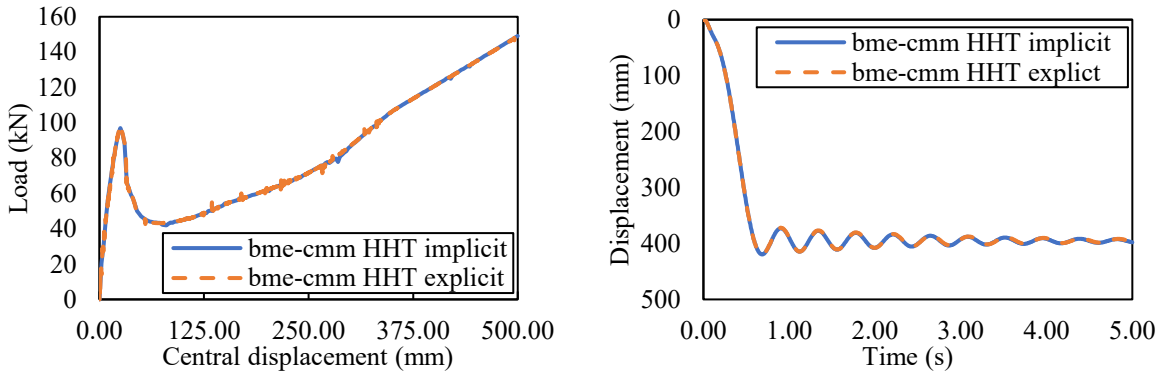
cbp2-cbm2 model still provides an approximate verification of the CMM for dynamic analysis. The two responses are very similar, with the differences largely attributed to the same reasons highlighted for the eigenvalue analysis. Specifically, following the sudden application of the vertical load of 80kN, the RC beam modelled with the bond-modelling elements (bme-cmm) oscillates at a lower frequency, which is in agreement with the outcomes from the eigenvalue analysis.

The verification of the CMM for dynamic analysis concludes with further assessment considering the Newmark time integration scheme (Fig. 3.27) and the explicit HHT time integration (Fig. 3.28) for the solution procedure of the analysis, with the figures indicating once again the correct implementation of the CMM, along with the mass diagonalisation procedure, for such time integration methods.



(a) Newmark: applied constant velocity (b) Newmark: sudden load application

Fig. 3.27 – Verification with dynamic analysis (Newmark scheme)



(a) Explicit: applied constant velocity (b) Explicit: sudden load application

Fig. 3.28 – Verification with dynamic analysis (HHT explicit scheme)

3.7 Conclusion

A selection of enhancements have been proposed in this chapter for the fibre-beam elements with bond-modelling capability (Khalid, 2011) so that these elements become readily applicable for disproportionate collapse assessment of RC planar frame sub-systems under the loss of a load-bearing member. These enhancements include, at the material level, a steel material model able to represent the tensile fracture of the reinforcement and a strain-dependent bond-slip model. At the section level, the elements with bond-modelling capability have been extended for the representation of RC beam-column members involving a generic cross-section that is symmetric about the vertical axis. Lastly, at the element level, the elements with bond-modelling capability are completed with the corresponding consistent mass matrices primarily aimed at improving the stability of the solution procedure under dynamic analysis. Implementation of the proposed enhancements in the nonlinear structural analysis program ADAPTIC has been verified with several simple truss and beam examples, where the relative benefits of each enhancement with respect to the initial formulation have also been highlighted.

Chapter 4: Modelling of RC planar frame sub-systems under column loss scenario

4.1 Introduction

This chapter details the application of the fibre-beam elements with bond-modelling capability (herein termed as *bme* elements) for the assessment of RC planar frame sub-systems under column loss scenario, where the enhancements proposed in the previous chapter are also validated within this backdrop against experimental data available in literature.

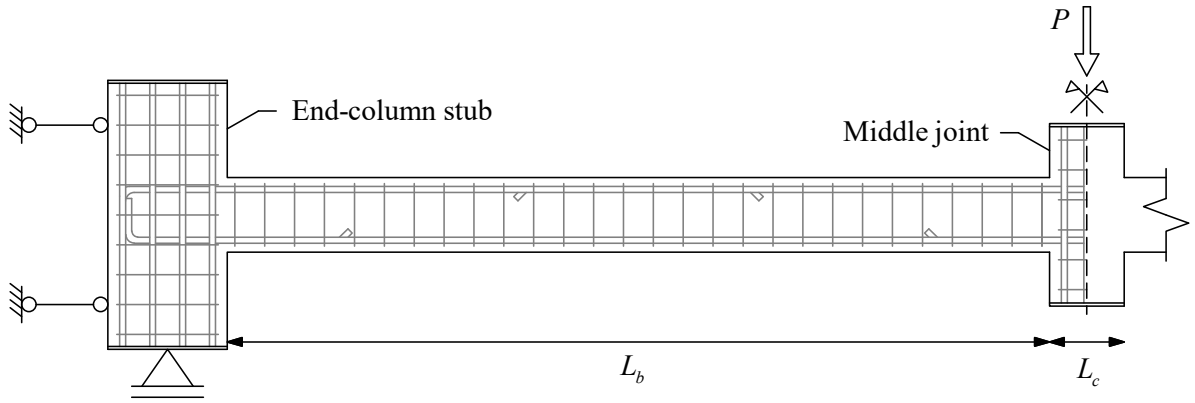
The modelling assumptions considered for the RC planar frame sub-systems are first presented, involving the considered strategy to represent the RC beams, joint panels and the surrounding structure, along with the calibration of the material models and the definition of the mesh refinement procedure. This chapter then proceeds with the validation of the proposed modelling strategy against experimental data available in literature. The proposed modelling strategy is also compared to the case using conventional fibre-beam elements with a formulation considering full bond between the reinforcement and the concrete (herein termed as *cbp2* elements). Finally, on the basis of the calibrated models, the sensitivity of the ductility limit of typical RC planar frame sub-systems is assessed for different reinforcement and span-to-depth ratios as well as for different bond strength, anchorage length and boundary conditions.

4.2 Modelling considerations

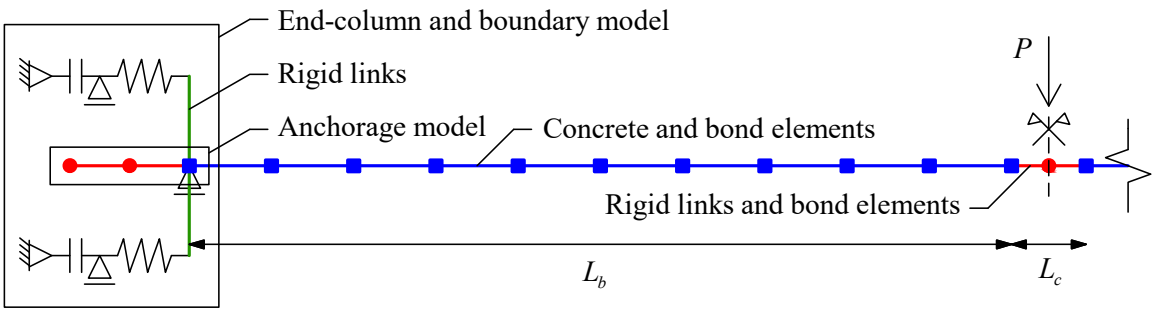
Consideration is specifically given herein to the modelling of RC planar frame sub-systems with adequate axial and rotational restraint from the surrounding structure (e.g. interior column loss scenario), although additional modelling considerations are stated whenever these are required for the representation of RC planar frame sub-systems under other column loss scenarios.

4.2.1 Description of typical models

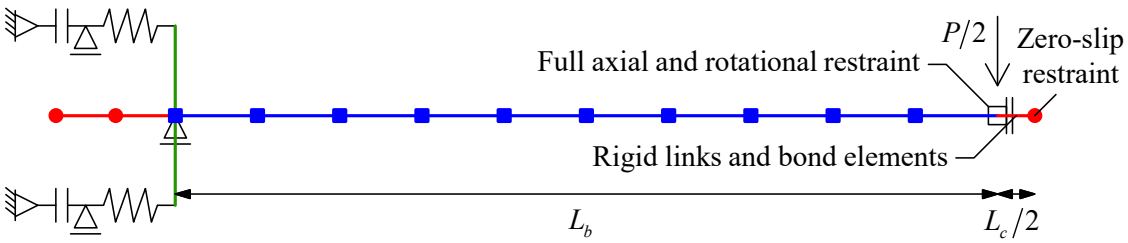
As noted before, a typical RC planar frame sub-system can be further simplified into a single RC planar beam sub-system, with the frame response subsequently established via the simplified assessment framework by Izzuddin *et al.* (2008). Alternatively, the planar frame sub-system can be fully modelled with similar considerations herein proposed for the beam sub-systems. A RC planar beam sub-system typically entails a double-span beam, a middle joint representing the removed column and two end-column stubs representing the connection of the double-span beam to the adjacent columns, as illustrated in Fig. 4.1a.



(a) Typical RC planar beam sub-system



(b) Typical full numerical model



(c) Typical half numerical model

Fig. 4.1 – Typical model for RC planar beam sub-systems

The modelling strategy proposed herein utilises the *bme* elements to represent the double-span beam, whilst the behaviour of joint panels (i.e. middle joint and end-column stubs) is assumed rigid. Such an assumption is deemed acceptable for planar beam sub-systems with adequate axial and rotational restraint from the surrounding structure as these prevent significant joint shear deformation and damage at the end-column stubs. Damage is instead primarily concentrated at the interface between the ends of the double-span beam and the joint panels, the behaviour of which can be effectively represented by the *bme* elements. Notwithstanding, for the assessment of RC beam sub-systems under other column removal scenarios, where the restraint from the surrounding structure may be negligible, or for joint panels exhibiting significant joint deformations, the joint behaviour of the end-column stubs as well as the middle joint can be modelled via a component-based approach, as discussed in Section 2.5.2.2.

Another limitation of the proposed modelling strategy is that the formulation of the *bme* elements does not provide a shear failure criterion, hence unable to detect shear-dominant beam damage. In this respect, the proposed modelling strategy is applicable only to flexure-dominant RC planar beam sub-systems associated with a sufficiently large beam span-to-depth ratio. It is worth noting, however, that such a condition is generally satisfied as the span of the beam doubles under the scenario of column loss.

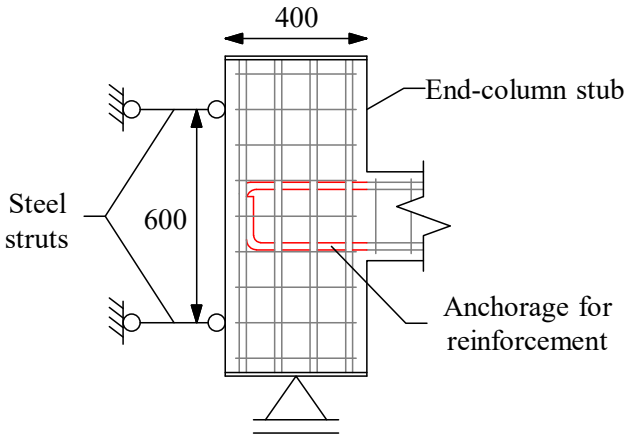
For the subsequent model validation and sensitivity assessment of ductility limit, the RC planar beam sub-systems are represented by full models (Fig. 4.1b) or by half models (Fig. 4.1c) if the beam sub-system satisfies symmetry conditions and presents a reinforcement detailing which allows for such model reduction. In the latter models, symmetry conditions are established at the symmetry axis via an axial and rotational restraint applied to the beam and by imposing a zero-slip boundary condition to the reinforcement.

4.2.2 Representation of the surrounding structure

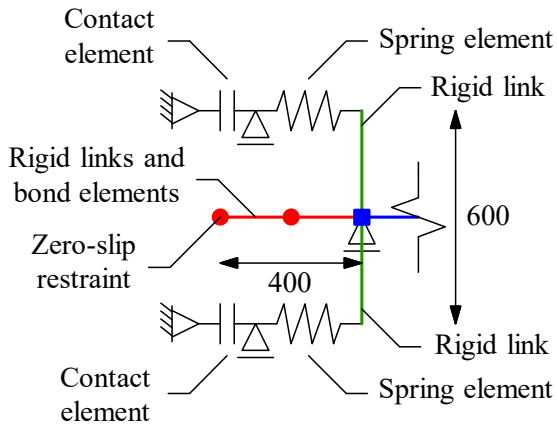
The proposed modelling strategy considers two approaches for the representation of the restraint from the surrounding structure. Consider the boundary example illustrated in Fig. 4.2a, where the axial and rotational restraints of the beam sub-system are achieved based on the connection of the end-column stubs to a rigid/reacting structure via a pair of parallel axial steel struts (e.g. Yu and Tan, 2012).

The first approach involves a detailed modelling of the restraints via a component-based method (similar to the modelling of joint panels), as illustrated in Fig. 4.2b, and is primarily employed herein to represent the boundary layout of specific experimental setups. Under this

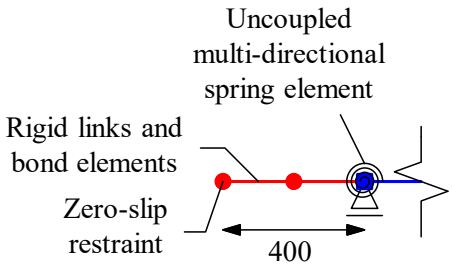
component-based approach, which is herein termed as the component-based method, the end-column stubs of the provided boundary example are represented with rigid links, whilst each steel strut connecting the end-column stubs to the rigid/reacting structure is modelled with a zero-length axial spring element. Furthermore, a zero-length contact element can be assembled in series with each axial spring to allow for possible gaps from the connections of the steel struts (e.g. Yu and Tan, 2012). Evidently, for the modelling of more general RC beam sub-systems, where the surrounding restraints are the adjacent beams and columns, the approach can instead employ the *bme* elements to represent such beams and columns.



(a) Boundary restraint of the experimental setup



(b) Component-based method



(c) Simplified method

Fig. 4.2 – Representation of the surrounding structure (values in mm)

The second is as simplified method (Fig. 4.2c) which encapsulates in its most basic form the boundary restraint behaviour within a single joint element with uncoupled constitutive laws for the joint axial displacement and rotation (Izzuddin, 2016). For the assessment of general RC beam sub-systems, provided that the surrounding structure behaves elastically, the single joint

element can be simply defined with linear elastic constitutive laws. Notwithstanding, more sophisticated constitutive laws can be easily utilised in such a joint element to characterise boundary restraints with a nonlinear response. Also, a further contact element can be assembled in series specifically to represent contact gaps from experimental setups.

In the current work, the behaviour of the surrounding restraints is assumed elastic, with the inclusion of contact gaps whenever this is required. In this respect, the spring and joint elements representing the restraint stiffness from the surrounding structure follow the linear elastic constitutive relationship illustrated in Fig. 4.3a, which allows for an asymmetric response under positive and negative displacements (rotations), with the slope of the linear branches defining the axial (or rotational) stiffness of the restraint. The contact elements follow the relationship illustrated in Fig. 4.3b, with the gap size defined by the displacements (or rotations) d_0^- and d_0^+.



(a) Spring element (b) Contact element

Fig. 4.3 – Constitutive relationship for spring and contact elements

The stiffness of the spring and joint elements as well as the limiting displacements (rotations) of the contact elements can be based on experimental outcomes or estimated via a numerical/analytical procedure in the absence of experimental data. The rotational restraint stiffness can be estimated based on the flexural stiffness of the beam and slab adjacent to the sub-system under consideration, whilst the axial stiffness can be estimated based on the in-plane shear stiffness of the neighbouring floor system.

Finally, for the anchorages of the beam reinforcement located within the end-column stubs, considering again the boundary example illustrated in Fig. 4.2a, the straight part of the anchorages is modelled by overlaying additionally assigned bond elements to rigid links, as illustrated in Figs. 4.2b-c, whereas the bent part is implicitly considered by imposing zero slip at the end of the straight anchorage.

4.2.3 Material models

So as to represent the behaviour of RC planar beam sub-systems under the scenario of column loss, which involves the resistance mechanisms of compressive arching action (CAA) and tensile catenary action (CA), the fibre-beam elements of the corresponding numerical model necessitate a concrete material model able to reflect the tensile cracking and the compressive crushing of the concrete. The steel and bond material models, on the other hand, need to be defined in such a way so as to predict the fracture of the reinforcement, which is crucial for the definition of the ductility limit of the sub-system.

In this respect, a trilinear concrete model including tensile and compressive softening branches (Izzuddin, 2016), as illustrated in Fig. 4.4, is utilised in the current work, requiring 7 input parameters. It is worth noting that, under the consideration of a stress-strain relationship for the material model, if the slopes of the tensile and compressive softening branches are assumed unique for different mesh sizes, the softening response of the concrete would be mesh sensitive. This can be avoided by assuming a unique fracture energy G_f, which is defined as the work of the softening stress over the crack width (crushing displacement) w, i.e. the area beneath the linear softening branch, as illustrated also in Fig. 4.4.

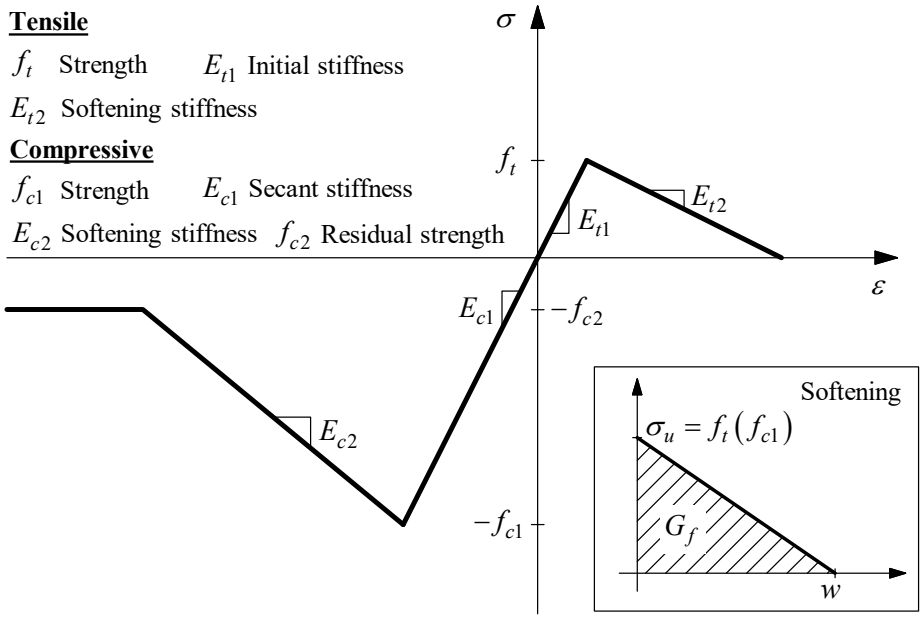


Fig. 4.4 – Trilinear concrete material model

$$G_f = \frac{\sigma_u w}{2} \tag{4.1}$$

where σ_u is the concrete tensile (compressive) stress at the start of softening.

Considering that the crack width (crushing displacement) is simply $w = s_m \varepsilon$, where s_m is the mesh size and ε is the strain, the slope of the linear softening branches can be shown given as:

$$E_{t2} = -\frac{s_m \left(f_t\right)^2}{2G_{ft}} \; ; \quad E_{c2} = -\frac{s_m \left(f_{c1}\right)^2}{2G_{fc}} \tag{4.2}$$

The tensile fracture energy follows the value recommend in the CEB-FIP Model Code (fib, 2012b):

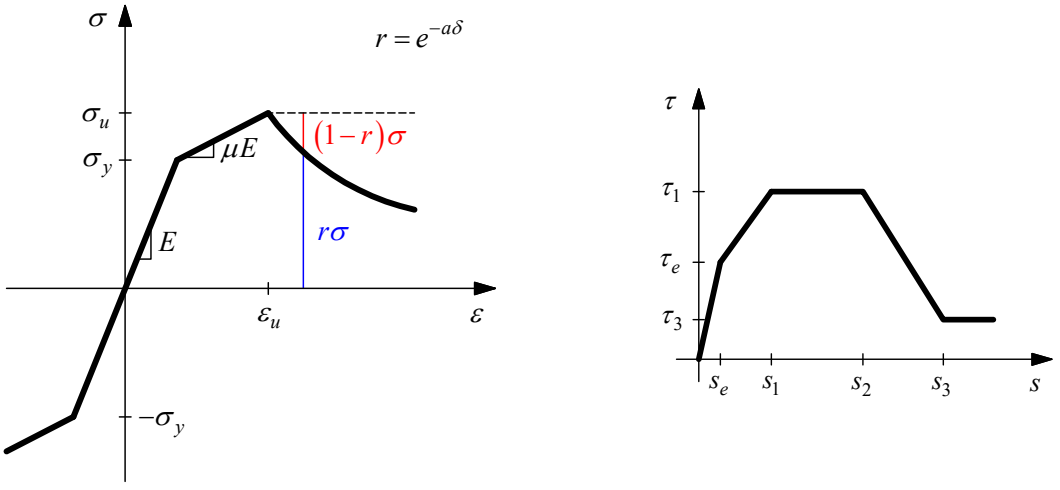
$$G_{ft} = 0.073\left(f_{cm}\right)^{0.18} \text{ N/mm} \tag{4.3}$$

where f_{cm} is the mean compressive strength of the concrete (in MPa). On the other hand, the compressive fracture energy is herein assumed as:

$$G_{fc} = 250n \cdot G_{ft} \tag{4.4}$$

where n is first defined as 1.0, thus recovering the value recommended by Nakamura and Higai (1999), with its subsequent calibration to account for material uncertainties and to implicitly allow for the increase in compressive ductility due to the possible confinement of the concrete.

The fracture of reinforcement, along with its interaction with the bond-slip behaviour, is modelled with the steel and bond material models proposed in Chapter 3. The general monotonic response of such models is respectively shown in Figs. 4.5a-b.



(a) Steel material model (b) Bond-slip material model

Fig. 4.5 – Steel and bond-slip material models

It is worth noting that where fracture of reinforcement is considered, a sufficiently high softening parameter a is assumed such that fracture is represented by a sharp drop in the resistance of the RC beam sub-system. Otherwise, the softening parameter is set to a very small value (in the order of 10^{-6}) for the cases where the fracture of reinforcement is to be neglected. Lastly, the input parameters for the bond model first follow the values recommended in Chapter 3, as per (3.64), (3.65) and (3.78). The input bond stresses are then scaled down under a calibration process to account for possible material uncertainties.

4.2.4 Mesh refinement

The main criterion chosen for the mesh refinement procedure is the convergence of the displacement at which the reinforcement fractures in the critical regions (i.e. the bottom reinforcement at the middle joint, MJBR, and the top reinforcement at the end-columns, ECTR). Fig. 4.6 provides a model example for the demonstration of the refinement procedure – specimen S4 (Yu and Tan, 2012), which involves a RC beam sub-system with a span equal to 2750mm. A sufficiently high softening parameter a is defined for the steel model to predict a sharp drop in resistance at the fracture of reinforcement, and the strain-independent bond-slip model is considered for the bond response, along with input parameters representing the full-bond condition. The critical region is assumed as 105mm from the beam-column interfaces, within which the mesh size is progressively reduced.

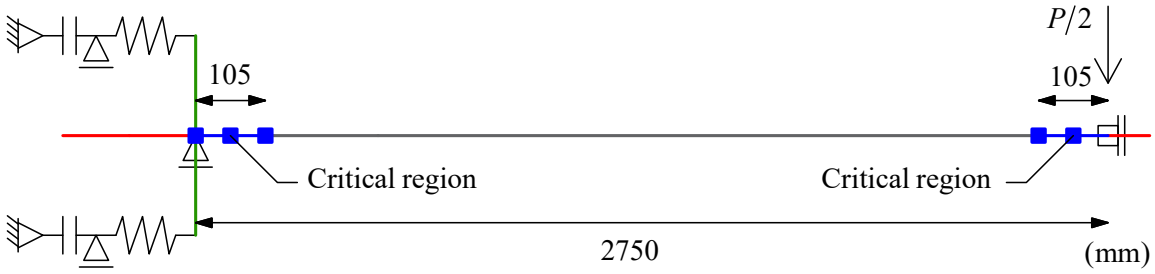


Fig. 4.6 – Half model example for mesh refinement

The load-displacement response of the sub-system corresponding to each mesh size is then obtained, on the basis of which the displacement at fracture of the reinforcement in the critical regions is established, as exemplified in Fig. 4.7 for the model with a mesh size of 7.5mm for the critical region.

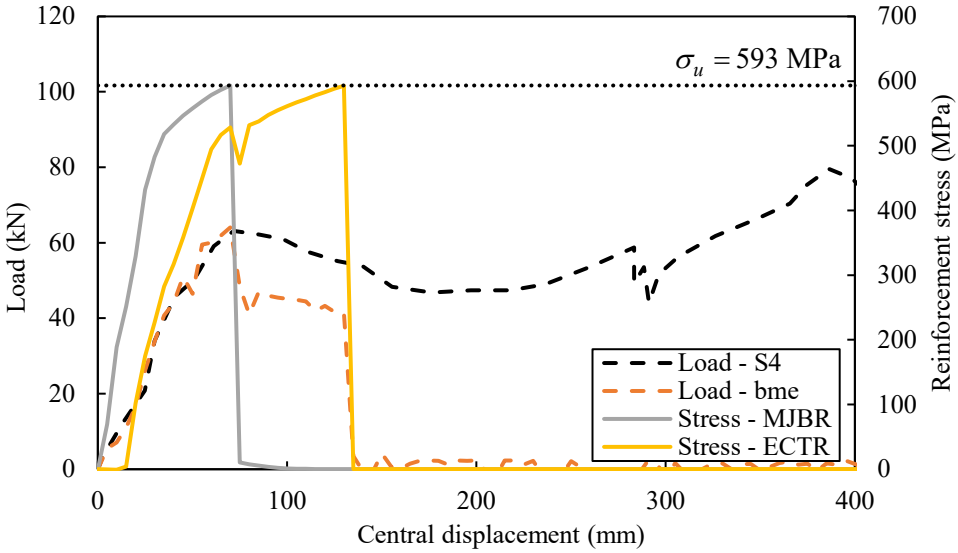


Fig. 4.7 – Determination of the fracture displacement: 7.5mm mesh size

The described mesh refinement procedure is carried out for the model using *cbp2* elements and for the model using the *bme* elements, with the outcomes illustrated in Fig. 4.8. It can be seen that, whilst the former model does not seem to converge, the latter model has already converged for the considered mesh sizes, which confirms the mesh objectivity of *bme* elements.

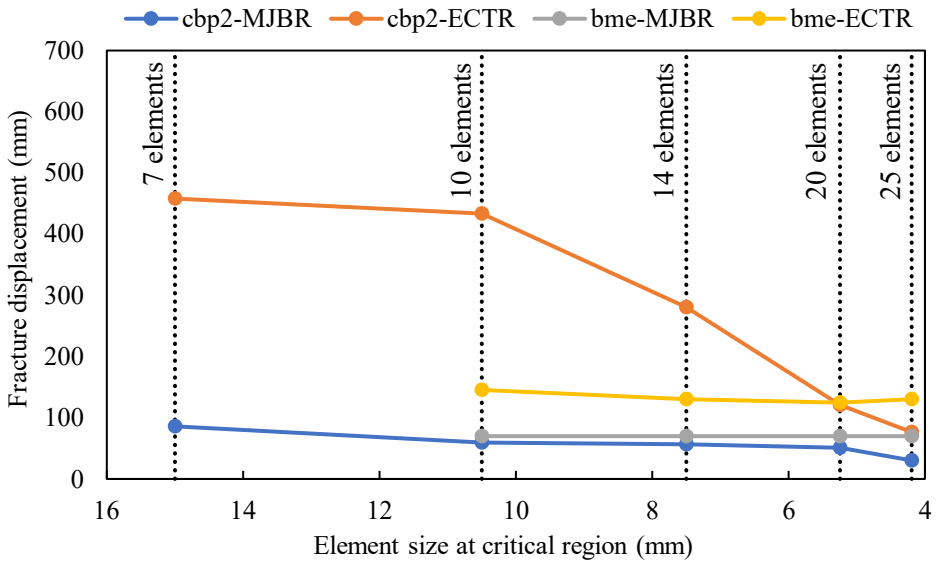


Fig. 4.8 – Convergence of fracture displacement with mesh refinement

4.3 Validation against experimental tests

This section presents the validation of the modelling approach proposed for RC planar beam sub-systems with adequate surrounding restraints, which is first aimed at demonstrating the

accuracy and relative benefits of the *bme* elements along with the newly developed steel and bond material models. Validation is then provided for beam models with T-shaped sections.

4.3.1 General validation

The general validation involves the assessment of i) the *bme* elements, ii) the newly developed steel and bond material models, iii) the two approaches considered for the representation of the boundary restraints and iv) the half and full models. The RC planar beam sub-systems experimentally tested by Yu and Tan (2012, 2013a) establish the basis for such validation, with the typical setup and reinforcement detailing illustrated in Fig. 4.9, and with the corresponding beam and reinforcement geometries provided in Table 4.1.

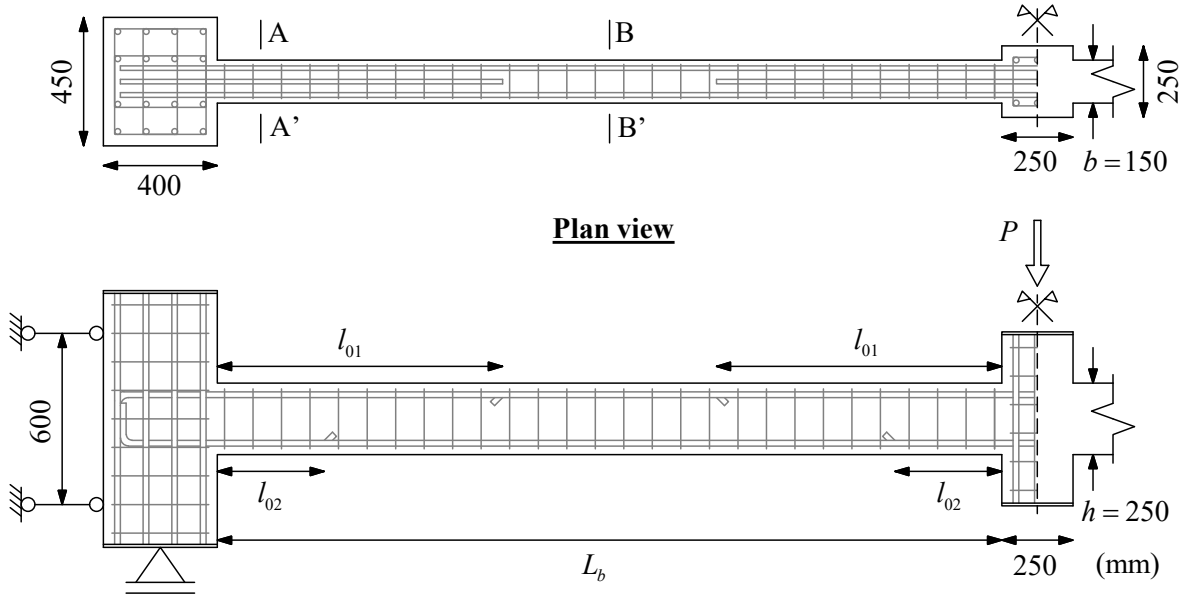


Fig. 4.9 – Typical setup of the specimens tested by Yu and Tan (2012, 2013a)

The typical numerical model for specimens S1 to S8 follows the considerations discussed in Section 4.2, employing the component-based method for the representation of the surrounding restraint, as illustrated in Fig. 4.2b, where the end-column stub is modelled with rigid links and each steel strut is represented by an axial spring element and a contact element configured in series.

Table 4.1 – Yu and Tan (2012, 2013a): beam geometry and reinforcement

Test	L_b (mm)	Position of curtailment (mm)		Longitudinal reinforcement (mm)				Bottom bars at the middle joint[a]
				A-A' section		B-B' section		
		l_{01}	l_{02}	Top	Bottom	Top	Bottom	
S1	2750	1000	-	$1\phi13+2\phi10$	$2\phi10$	$2\phi10$	$2\phi10$	Continuous
S2	2750	925	-	$3\phi10$	$2\phi10$	$2\phi10$	$2\phi10$	Lap splice
S3	2750	1000	345	$3\phi13$	$2\phi10$	$2\phi13$	$2\phi10+1\phi13$	Lap splice
S4	2750	1000	-	$3\phi13$	$2\phi13$	$2\phi13$	$2\phi13$	Continuous
S5	2750	1000	-	$3\phi13$	$3\phi13$	$2\phi13$	$3\phi13$	Continuous
S6	2750	1000	345	$3\phi16$	$2\phi13$	$2\phi16$	$2\phi13$	Lap splice
S7	2150	780	-	$3\phi13$	$2\phi13$	$2\phi13$	$2\phi13$	Continuous
S8	1550	560	-	$3\phi13$	$2\phi13$	$2\phi13$	$2\phi13$	Continuous

[a] The lap splice lengths for the bottom bars of specimens S2 and S3 are 410mm, whereas for the bottom bars of specimen S6 is 530mm.

Table 4.2 provides the properties for the axial spring elements and the contact elements. The stiffness and gap values are established based on the experimental data presented in Yu (2012). Notwithstanding, given that all specimens are initially assumed symmetric for model reduction, the values presented in Yu (2012) are averaged respectively for the top and bottom steel struts located at the two end-column stubs. Furthermore, all lap splices passing through the middle joint are assumed as continuous reinforcement instead, with a zero-slip restraint applied at the symmetry axis. The implications related to such assumptions are subsequently discussed in Section 4.3.1.5.

Table 4.2 – Properties for spring and contact elements

Test specimen	Top spring (10^4 N/mm)		Bottom spring (10^4 N/mm)		Top contact (mm)		Bottom contact (mm)	
	K^+	K^-	K^+	K^-	d_0^+	d_0^-	d_0^+	d_0^-
S1	4.32	0.01	4.26	12.30	3.00[a]	-10.00	1.20	-3.00[a]
S2	5.60	0.01	6.39	10.20	2.00[a]	-10.00	1.70	-2.00[a]
S3	10.30	0.01	4.08	16.00	2.50	-10.00	4.40	-1.35
S4	13.00	0.01	6.60	21.50	1.60	-10.00	3.80	-3.20
S5	13.20	0.01	8.26	19.50	2.10	-10.00	3.80	-1.95
S6	11.60	0.01	7.40	19.00	2.90	-10.00	2.00	-4.90
S7	9.22	0.01	7.21	23.50	2.05	-10.00	2.60	-4.20
S8	8.86	0.01	12.70	19.90	3.45	-10.00	3.45	-3.35

[a] Calibrated values

The properties for the concrete and steel models are respectively provided in Tables 4.3 and 4.4. The compressive damage energy is assumed as $1000G_{ft}$. The reference properties for the

bond model are given in Table 4.5, where the strength values are subsequently scaled down for the calibration of the central load-displacement response.

Table 4.3 – Concrete properties

Test specimen	Compressive				Tensile		
	Secant stiffness[b]	Strength[a]	G_{fc}	Residual strength[c]	Initial stiffness[a]	Strength[a]	G_{ft}
	MPa	MPa	N.mm	MPa	MPa	MPa	N.mm
S1-S2	15342	31.20	135.60	1.00	27663	3.20	0.1356
S3-S8	17641	38.20	140.64	1.00	29600	3.50	0.1406

[a] Values from Yu and Tan (2012, 2013a)
[b] Values determined based on Eurocode 2 (CEN, 2004b)
[c] Assumed values

Table 4.4 – Steel properties

Test specimen	Reinforcement diameter	Young's modulus	Yield strength	Ultimate strength	Ultimate strain	Softening parameter
	mm	MPa	MPa	MPa	-	-
S1-S2	10	182611	511	731	0.1232	5.00
	13	185763	527	640	0.1076	5.00
S3-S8	10	211020	511	622	0.1100	5.00
	13	185873	494	593	0.1092	5.00
	16	184423	513	612	0.1343	5.00

Table 4.5 – Reference bond properties

Test specimen	Reinforcement diameter	s_e	s_1	s_2	s_3	τ_e	τ_1	τ_3
	mm	mm	mm	mm	MPa	MPa	MPa	MPa
S1-S2	10	0.14	1.02	3.00	8.00	9.40	17.85	5.19
	13	0.14	1.02	3.00	10.40	9.00	17.08	5.19
S3-S8	10	0.16	1.13	3.00	8.00	10.50	19.75	5.74
	13	0.15	1.13	3.00	10.40	10.00	18.90	5.74
	16	0.14	1.13	3.00	12.80	9.20	18.05	5.74

4.3.1.1 Conventional elements versus fibre-beam elements with bond-modelling capability

Considering specimen S4 as the base validation example, Fig. 4.10 compares the responses predicted by the models using the *cbp2* elements and *bme* elements. The latter models consider the strain-independent bond-slip model with a maximum reference bond strength of 18.90MPa.

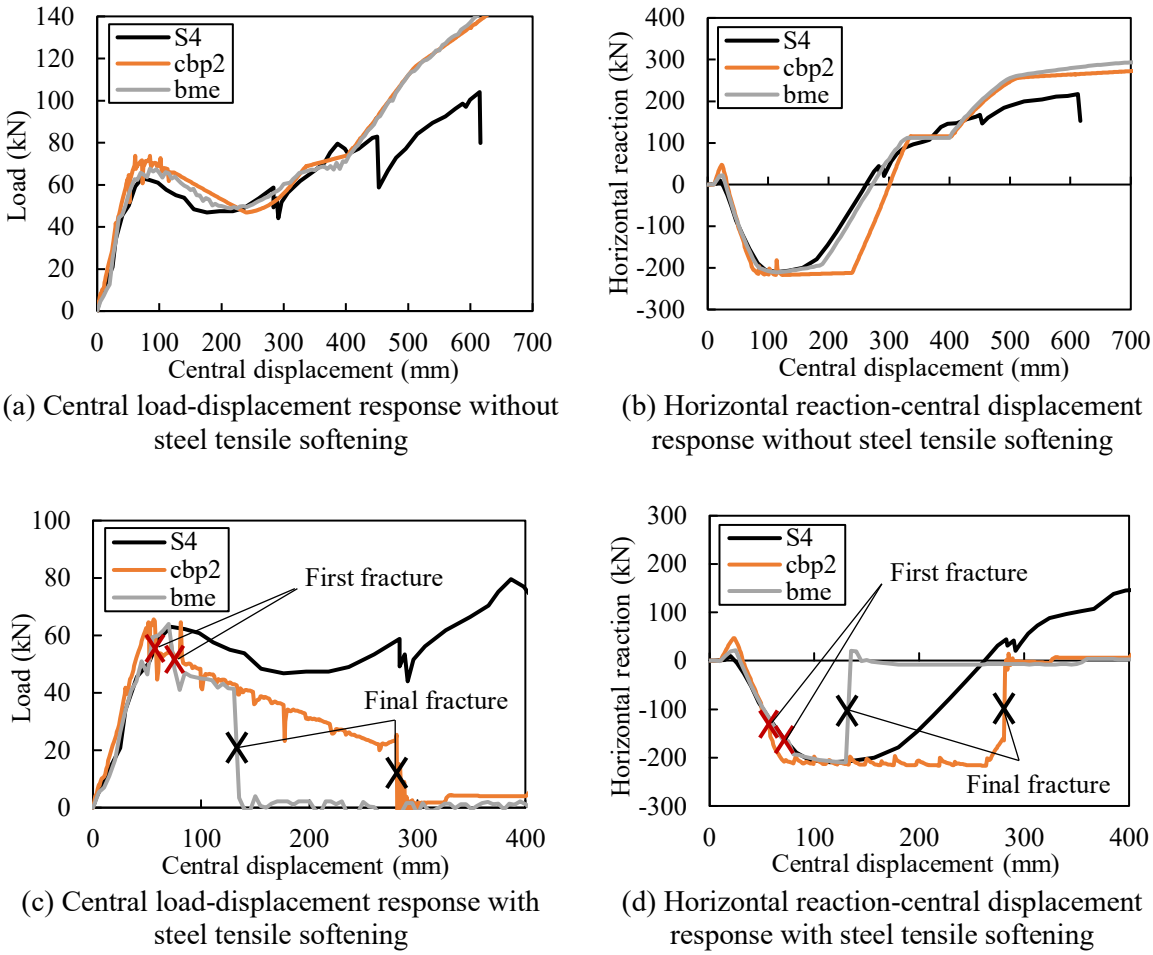


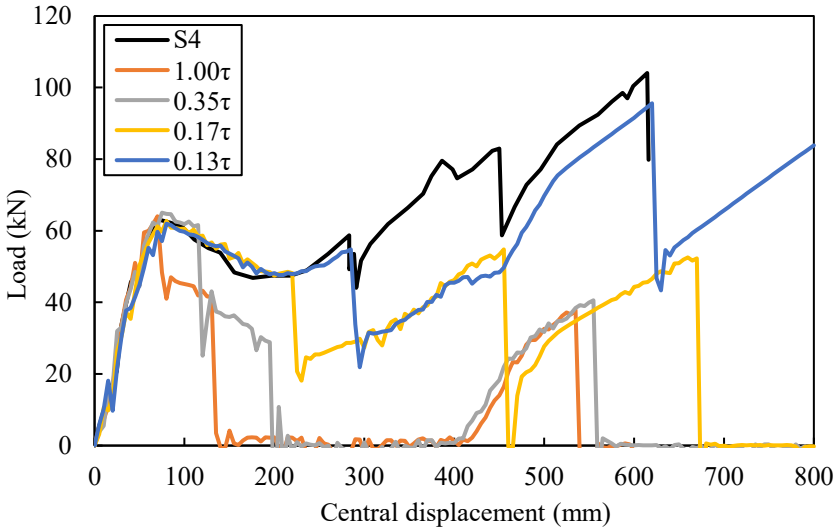
Fig. 4.10 – Predictions of *cbp2* vs *bme* models

Assessing the models without steel tensile softening (Figs. 4.10a-b), it follows that the predictions from the *cbp2* and *bme* models closely match the load-displacement response determined experimentally, except for not representing the fracture of reinforcement. This indicates that the effects related to the boundary restraints and the axial-flexural interaction of the beam forces are satisfactorily represented by the proposed boundary modelling approach and the selected beam-column elements.

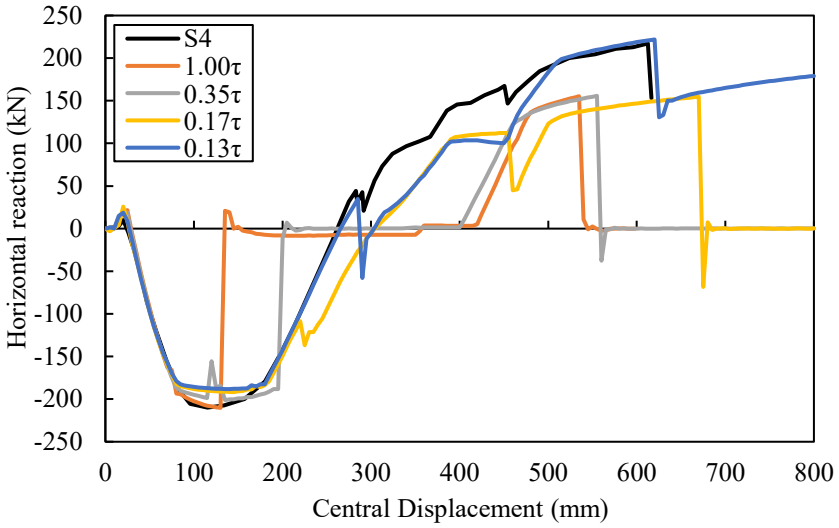
Significantly, the predictions from the *cbp2* and *bme* models are very similar, indicating that pull-out damage does not occur in the latter model. The load-displacement response predicted by the *bme* model up to the peak load within the CAA stage is slightly lower than the *cbp2* model, which is consistent with the assumption of a finite bond strength. The similarity in the load-displacement responses predicted by the two models seemingly suggests that the use of the *cbp2* elements would suffice for the modelling of RC planar beam sub-systems under a column loss scenario, provided a manual inspection of the reinforcement strains is carried out

to identify the ductility limit of the system. It is worth noting, however, that the predicted local distribution of concrete and reinforcement strains, which are not explicitly reflected in the load-displacement response, significantly differs between the *cbp2* and the *bme* models. Such differences are first evidenced in the horizontal reaction-central displacement response (Fig. 4.10b), where the *bme* model predicts more accurately the concrete crushing response primarily due to the consideration of higher-order cross-section kinematics. Importantly, once the fracture of the reinforcement is considered in the *cbp2* and the *bme* models (Figs. 4.10c-d), the differences in the local strain distribution are explicitly reflected in the load-displacement response. Compared to the *bme* model, the *cbp2* model consistently underestimates the earliest displacement at which reinforcement fractures, which can be attributed to the assumption of infinite bond between the concrete and the reinforcement. Notwithstanding, the *cbp2* model predicts a higher displacement for the subsequent fracture, i.e. the final load drop illustrated in Fig. 4.10c, though the final fracture displacement has not yet converged under the mesh refinement procedure detailed in Section 4.2.4 and will eventually be lower than the fracture displacement predicted by the *bme* model with further refinement of the mesh.

Despite considering the influence of bond-slip between the reinforcement and the concrete, the *bme* model still significantly underestimates the ductility limit of specimen S4, the difference of which can be due to the inability of the strain-independent bond-slip model to predict the additional slip arising from yield penetration. It is worth noting, however, that the considered reference bond strengths could also be significantly overestimated compared to the experimental values. In this respect, due to the absence of experimental bond data, validation proceeds to primarily highlight the benefits achieved with the *bme* model compared to the *cbp2* model. The load-displacement response predicted by the *bme* model is calibrated against the experimental response via reduction of the reference bond strengths initially defined for the strain-independent bond-slip material model, where the reference bond strength is uniformly reduced for the whole reinforcement length. Fig. 4.11 illustrates the responses considering 65%, 83% and 87% reduction of the reference bond strength (18.90 MPa), which indicate a significant improvement in the predicted ductility limit for specimen S4 with progressive reduction of the bond strength.



(a) Central load-displacement response



(b) Horizontal reaction-central displacement response

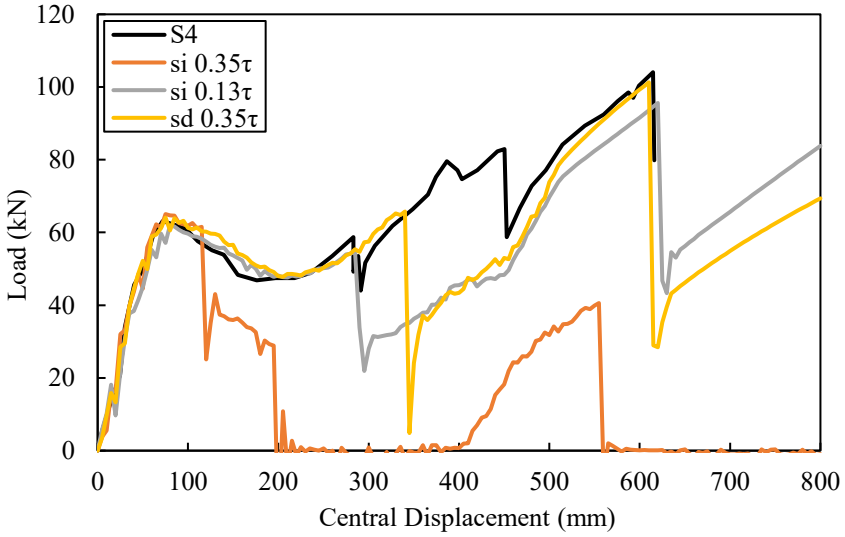
Fig. 4.11 – *bme* model: bond strength calibration

As such, whilst the *cbp2* model predicts by default a premature fracture of the reinforcement due to the assumption of infinite bond, the *bme* model addresses such a limitation in the sense that the model can predict a satisfactory response through calibration of the bond parameters.

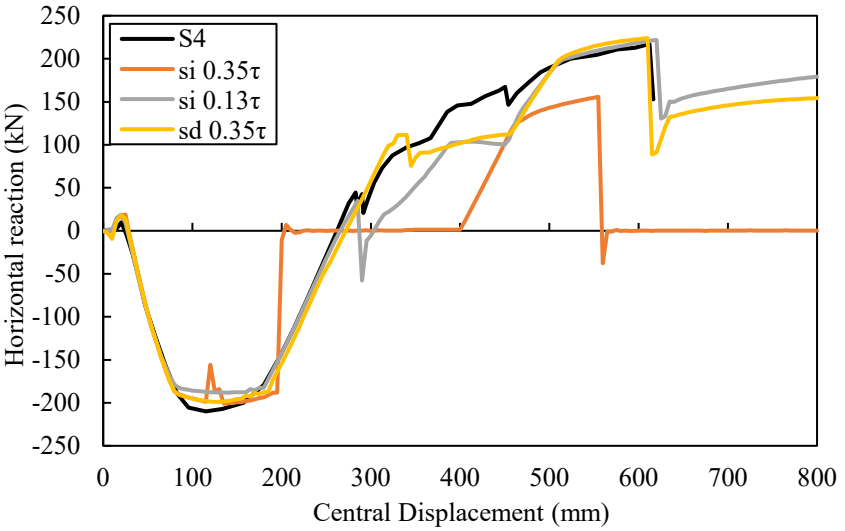
4.3.1.2 Strain-independent versus strain-dependent bond-slip model

Whilst reducing the bond strength of the strain-independent bond-slip model (*si*) may suffice, there are some limitations with this approach. The bond strength established from the calibration of the load-displacement response seems to be significantly lower compared to usual bond strengths, which in turn leads to underestimated bending resistances of the RC beam

sub-system. Though not significant, this is evidenced by the lower peak resistance within the CAA stage predicted with the model considering an 87% reduction in bond strength (Fig. 4.12, *si 0.13τ*). Furthermore, a parallel offset between the experimental and predicted responses can also be observed prior to the final load drop, which is primarily related to the difference in experimental and predicted residual bending resistances.



(a) Central load-displacement response



(b) Horizontal reaction-central displacement response

Fig. 4.12 – Influence of reinforcement strain on the bond-slip behaviour

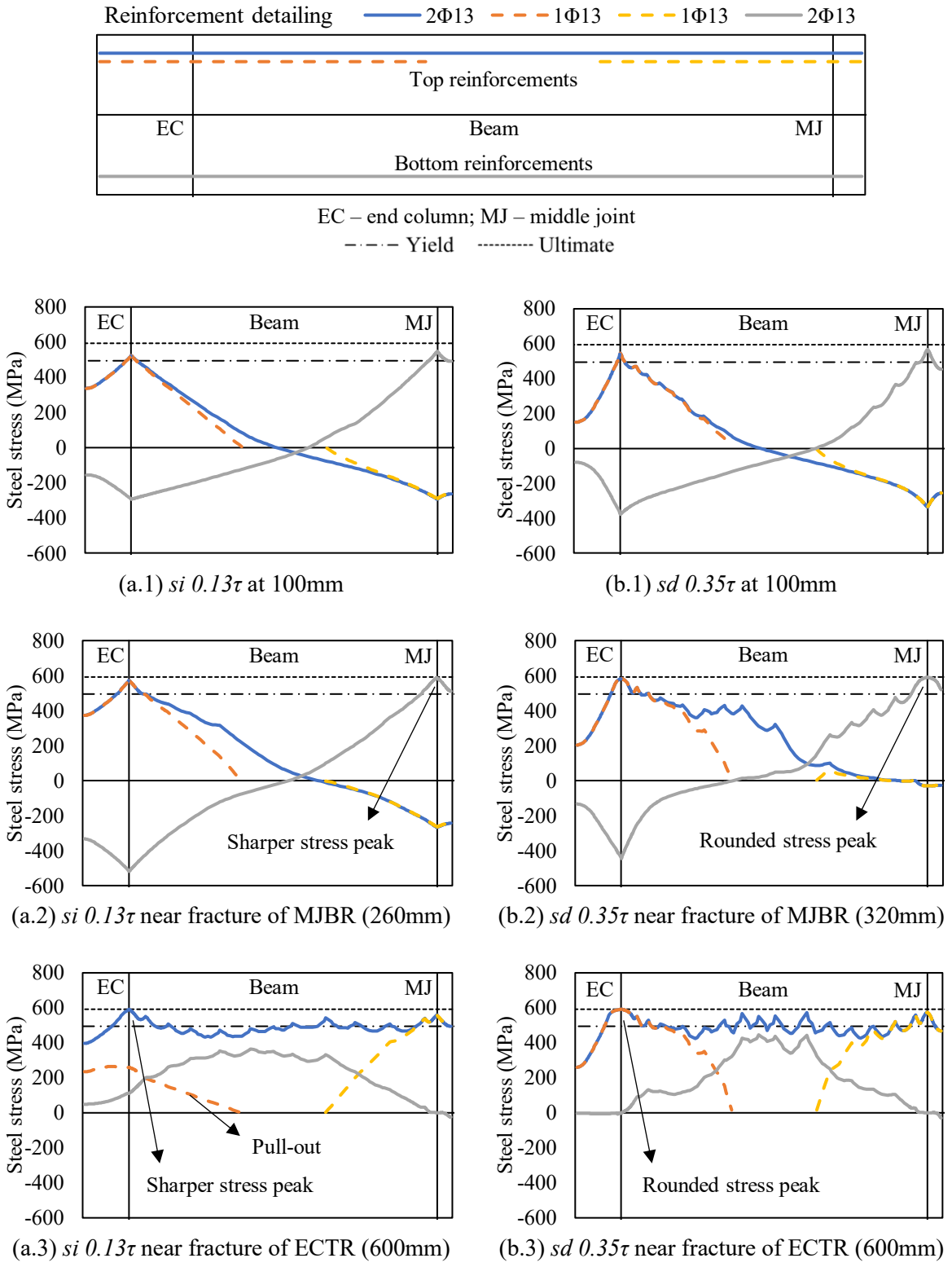
Another limitation is that the additional slip arising from yield penetration is not appropriately addressed as the bond reduction is applied over the whole reinforcement length rather than over the region that has yielded. This limitation can be circumvented by reducing the bond strength

over a pre-defined region, though its definition is only approximate and not straightforward, requiring an iterative assessment of the reinforcement strains and subsequent redefinition of the yielded region.

On the other hand, the proposed strain-dependent bond-slip model (*sd*) improves the accuracy of the predicted response by addressing such limitations. A close fit is achieved between the experimental and predicted load-displacement responses with only a 65% reduction in the bond strength over the whole reinforcement length (Fig. 4.12, *sd 0.35τ*), thus mitigating the underestimated bending resistances of the RC beam sub-system. Importantly, the satisfactory prediction is achieved with a lower global reduction because the resulting bond strength is further reduced via the strain-dependent bond-slip model over the yielded region. The distribution of the reinforcement stresses (Fig. 4.13) further evidences the noted differences between the models *si 0.13τ* and *sd 0.35τ*.

Since the *si* model requires a higher global bond strength reduction to fit the experimental load-displacement response, the resulting local stress gradient is not as high as that predicted with the *sd* model, and the stress profile presents a smaller number of local stress peaks, which implicitly represent concrete cracks. Indeed, concrete cracks are expected to be further spaced with lower bond strengths between the reinforcement and the concrete. Notwithstanding, both models predict reasonably well the variation of the reinforcement stresses with central displacement, as such a variation is in agreement with the transition of the resultant forces from the flexural/compressive arching action stage to the tensile catenary action stage.

Inspection of the reinforcement stresses near the fracture of the MJBR (Figs. 4.13a.2-b.2) and the ECTR (Figs. 4.13a.3-b.3) suggests that, with the *sd* model, the most significant reinforcement strain contributions to the end-slip/ductility limit are located near the beam-column interfaces, as illustrated by the stress distribution with a rounded/concave peak. The stresses (strains) within this region are generally greater than the stresses predicted with the *si* model, for which the stress distribution exhibits a sharper peak. On the other hand, the *si* model achieves a similar end-slip/ductility limit via an overall higher contribution of strains throughout the whole reinforcement instead, owed to the assumption of the lower global bond strength. This is specifically evident in the stress distribution along the reinforcements embedded within the end-column.



(a.1) *si 0.13τ* at 100mm

(b.1) *sd 0.35τ* at 100mm

(a.2) *si 0.13τ* near fracture of MJBR (260mm)

(b.2) *sd 0.35τ* near fracture of MJBR (320mm)

(a.3) *si 0.13τ* near fracture of ECTR (600mm)

(b.3) *sd 0.35τ* near fracture of ECTR (600mm)

Fig. 4.13 – Reinforcement stress distribution of specimen S4

Finally, also due to the lower global bond strength, the *si* model predicts near the fracture of the ECTR the pull-out of the top curtailed reinforcement, as illustrated in Fig. 4.13a.3, which explains the lower load resistance observed in Fig. 4.12a prior to the final load drop. On the

other hand, the rounded stress peak in the *sd* model results originates from the progressive yield penetration of the reinforcement strains from the crack along the beam-column interface to the beam and the embedded reinforcement, as illustrated in Fig. 4.14.

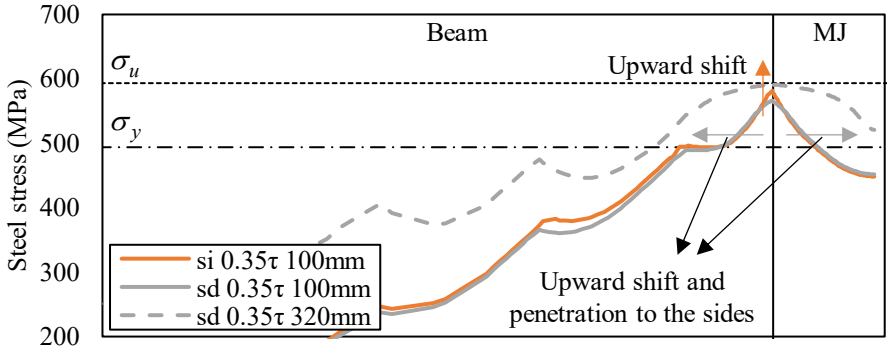
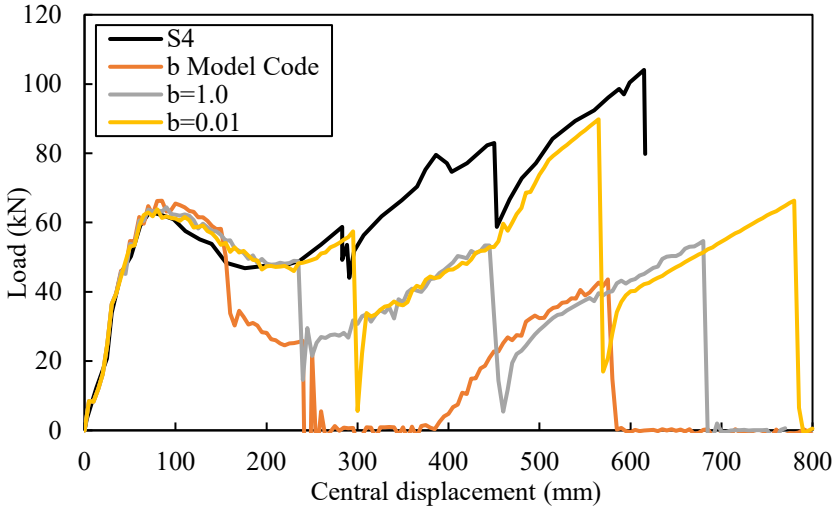


Fig. 4.14 – Specimen S4: yield penetration process of MJBR

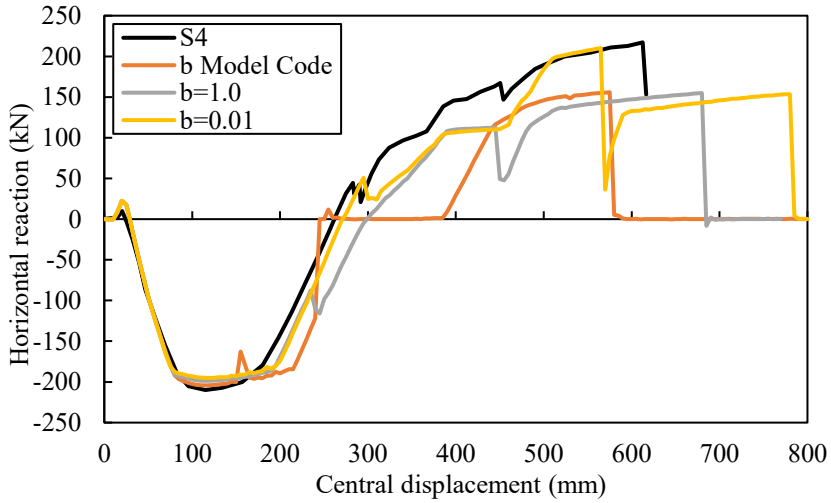
The figure compares the stress distribution of the MJBR predicted by the *si* and *sd* models, both considering a 0.35τ global reduced bond strength. The stress distribution of the two models is initially similar at a displacement level approximate to the fracture of the MJBR predicted by the *si* model (i.e. at 100mm central displacement), suggesting that the influence of the reinforcement strains on the bond-slip behaviour is still negligible. However, with further loading, the shape of the stress peak predicted by the *si* model remain practically unchanged, with the peak stress increasing up to the ultimate tensile stress. On the other hand, due to the assumption of strain-dependency, the *sd* model predicts an expansion of significant reinforcement stresses also to the neighbouring region of the cracked location, resulting in the rounded/concave peak when the peak stress reaches the ultimate tensile threshold.

Despite the lower bond strength reduction required by the *sd* model, it can be argued that a bond strength of 6.62MPa (35% of the reference value) may still be relatively low compared to the usual bond strength values. Due to the absence of corresponding experimental data, it is not clear whether the actual experimental bond strength is indeed within the range of the predicted value or if the decay in bond stresses due to the yield of the reinforcement is not accurately described by the proposed reduction factor. Nonetheless, calibration of the strain-dependent reduction factor can further limit the requisite global reduction in bond strength. Fig. 4.15 illustrates the sensitivity of the predicted response to the parameter b of the strain-dependent reduction factor, where the predicted response considers the global bond strength as 80% of the reference value (i.e. 20% reduction). It follows that for $b = 0.01$ a satisfactory response can also be achieved with a global reduction in bond strength of only 20%, with the

reduced bond strength of 15.12MPa again closer to the usual bond strength values. This demonstrates that, despite following the reduction factor from the CEB-FIP Model Code (fib, 2012b), the consideration of the *sd* model subsumes the *si* model as the former offers more flexibility to the calibration of the numerical response.



(a) Central load-displacement response



(b) Horizontal reaction-central displacement response

Fig. 4.15 – *sd* model: calibration of the parameter *b*

4.3.1.3 Validation of specimens S1-S8

Figs. 4.16 and 4.17 compare the predictions of the proposed modelling approach against the experimental responses of specimens S1-S4 and S5-S8, respectively, where the global reduction of the reference bond strength for each reinforcement diameter is applied according to Table 4.6.

Table 4.6 – Reduced bond strengths

Test	Strain-independent model (*si*)			Strain-dependent model (*sd*)		
	ϕ10	ϕ13	ϕ16	ϕ10	ϕ13	ϕ16
S1-S2	0.40τ	0.25τ	-	1.00τ	0.65τ	-
S3-S8	0.13τ	0.13τ	0.18τ	0.35τ	0.35τ	0.50τ

A very good fit between experimental and numerical responses is generally achieved irrespective of the considered bond-slip material model, except for some aspects related to specimens S1, S2 and S8. Once again, the outcomes indicate that the *sd* model is more realistic than the *si* model, as it minimises the requisite global bond strength reduction to achieve similar levels of ductility limit, thus mitigating possible underestimation of residual flexural resistances and pull-out of the top curtailed reinforcement, as illustrated at the end of the predicted response for specimens S3 and S4.

The proposed modelling approach also predicts with reasonable accuracy the locations and the sequence for the fracture of reinforcement, with the first significant load drop corresponding to the fracture of the MJBR and the subsequent drop corresponding to the fracture of the ECTR, approximately matching the sequence and locations observed in the experimental tests. Notwithstanding, the models do not reflect the possible staged fracture of the reinforcement at such locations mainly due to the neglect of material and geometric imperfections.

The most significant deviations observed between the experimental and predicted responses of specimens S1 and S2 are the local load peak and the subsequent softening response within the CAA stage. It is unclear to what factor this discrepancy may be attributed, although, given the good fit of the same responses within the CA stage, the resistance of which is governed by the tensile reinforcement, the observed discrepancy is likely associated with the uncertainty of the concrete material response (primarily compressive crushing) and the flexural boundary restraint.

The predicted response of specimen S8, on the other hand, follows closely the experimental response up to the first fracture of the MJBR. The prediction considering the *sd* model then differs from that of the *si* model, with the former predicting the fracture of the ECTR at a significantly greater central displacement (495mm as opposed to 320mm). This delay in fracture also leads to a load resistance within the CA stage surpassing the peak resistance within the CAA stage, a response which is not experimentally observed. In this respect, the *si* model seems to predict more accurately the fracture of the reinforcement, although it is worth noting that the second load drop of the predicted response is associated to the fracture of the ECTR,

whilst the second load drop determined experimentally still corresponds to the fracture of the MJBR.

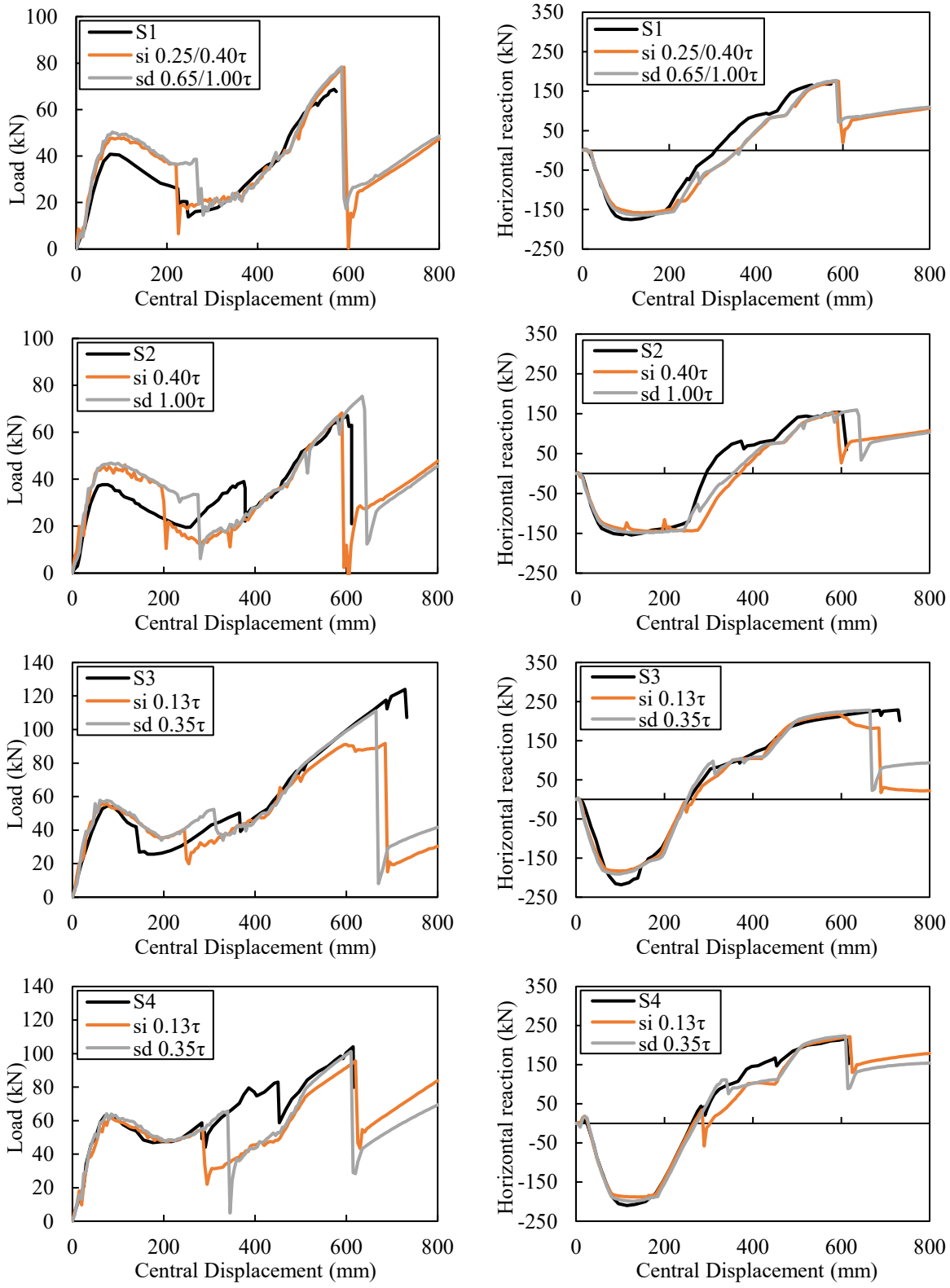


Fig. 4.16 – Validation of the proposed modelling approach: specimens S1-S4

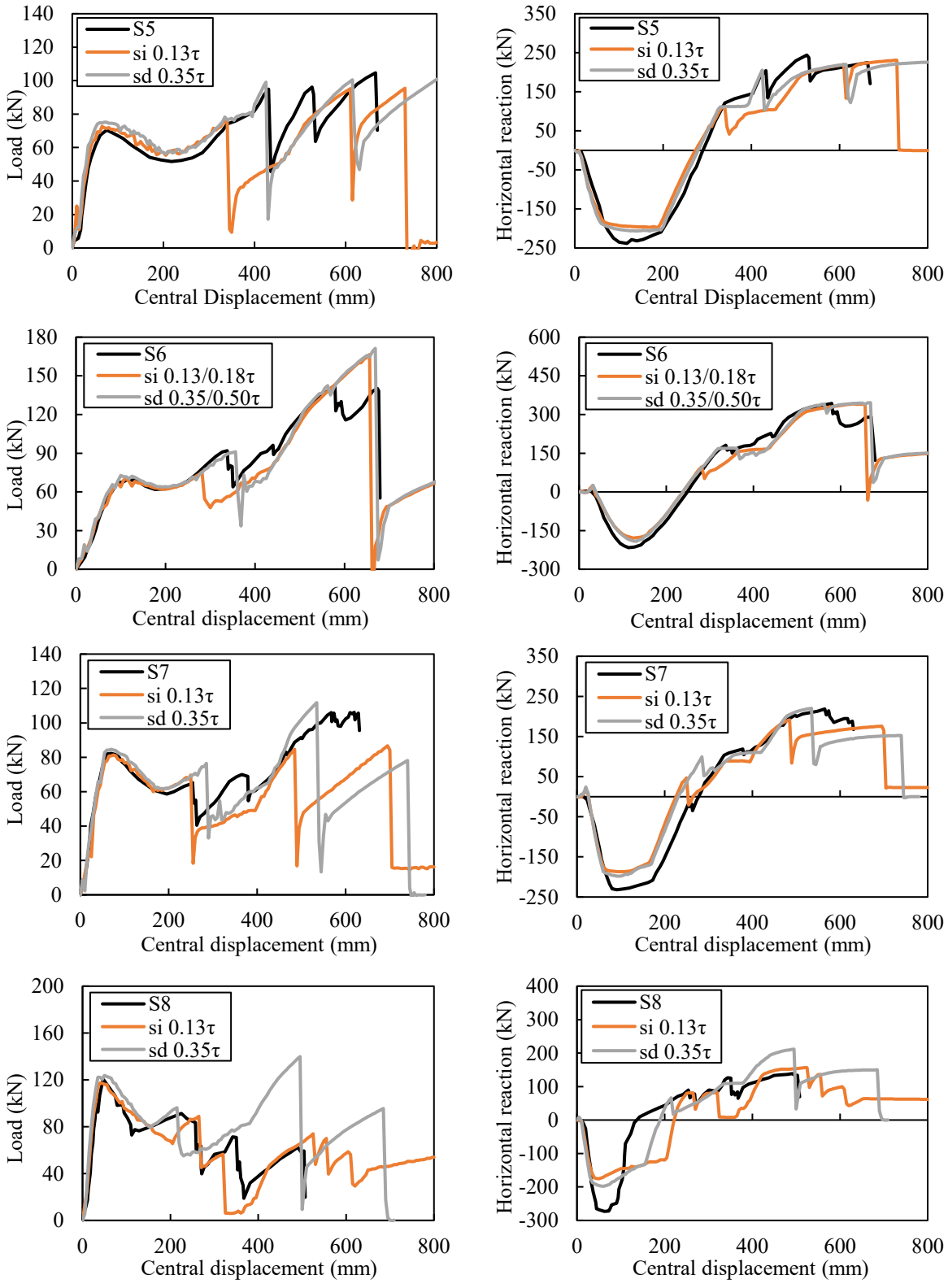


Fig. 4.17 – Validation of the proposed modelling approach: specimens S5-S8

Indeed, neither of the two predictions accurately represent the experimental response of specimen S8, specifically with respect to the horizontal reaction forces, where the predicted

responses within the CAA stage differ significantly from the experimental response. Noting that the proposed modelling approach is limited to flexure-dominant RC planar beam sub-systems, its inability to represent specimen S8 can be explained by the short span of the specimen, which led to a shear-dominant failure, associated with concrete shear cracks and the fracture of two stirrup reinforcements near the middle joint, as reported by Yu and Tan (2012). The proposed modelling approach would require an additional criterion to address such a failure mode.

Nonetheless, apart from specimens S1, S2 and S8, the remaining numerical predictions demonstrate good agreement with the experimental results for the whole loading response, thus reassuring the accuracy of the proposed modelling approach for RC planar beam sub-systems, specifically when considering the strain-dependent bond-slip model.

Lastly, it can also be established from the comparison between the *si* and *sd* models that the ductility limit of the specimens is highly influenced not only by the bond-slip between the reinforcement and the concrete but also by the ductility of the reinforcement. This suggests that uncertainty in the ductility of the reinforcement can significantly influence the requisite global bond strength reduction, though such an observation can only be confirmed with knowledge of the experimental reinforcement and bond data.

4.3.1.4 Representation of the boundary restraint: component-based versus simplified methods

Whilst the component-based method (*cjm*) involves a more sophisticated representation of the boundary restraint, the simplified method considering a single joint element (*sjm*) can be preferable for general and practical application of the proposed modelling approach. As such, the sensitivity of the load response to the simplified method is assessed herein, thus verifying whether such a method is also effective in representing the boundary restraint of RC planar beam sub-systems. A contact element is applied in series with the single spring element to account for the slip exhibited by the connections of the boundary restraint.

Table 4.7 summarises the symmetric properties for the single spring element and the contact element, which are established based on the experimental values reported in Yu (2012) as follows: the equivalent axial stiffness is determined from a system of two axial springs configured in series, where each spring represents the axial response at one of the ends of the specimen. The rotational response, on the other hand, is simply the lowest stiffness from the two ends of the beam specimen.

Table 4.7 – Symmetric properties for the single spring element and the contact element

Test	Single spring element			Single contact element			
	Axial (10^4 N/mm)		Rotation (10^{10} N.mm/rad)	Axial (mm)		Rotation[a] (10^{-1} rad)	
	K^+	K^-	K	d_0^+	d_0^-	d_0^+	d_0^-
S3	10.70	43.80	2.14	0.00	-1.00	0.00	0.00
S4	16.50	34.40	3.01	0.00	-0.80	0.00	-0.09
S6	14.20	37.50	1.95	0.00	-1.00	0.00	-0.09

[a] Assumed values

Fig. 4.18 confirms the effectiveness of the *sjm* approach in representing the boundary restraint of RC beam sub-systems, noting that the minor discrepancies observed with reference to the response predicted by the *cjm* approach are primarily due to differences in the input properties.

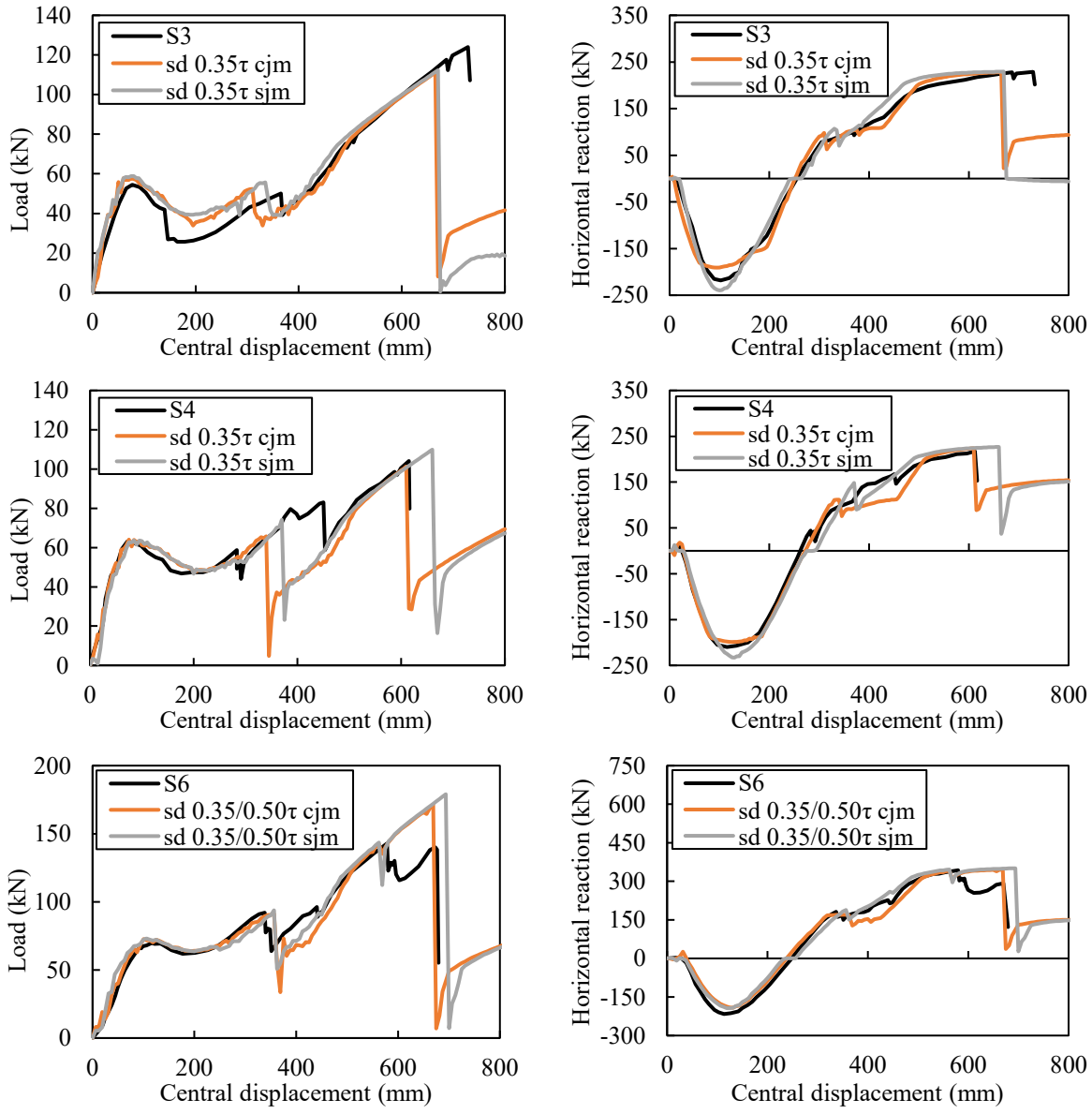


Fig. 4.18 – Assessment of *sjm* for the modelling of the boundary restraint

4.3.1.5 Symmetry versus full models

The implications of symmetry assumption are herein assessed via the comparison between the half and full models. In the latter models, all reinforcement splices are explicitly modelled and the properties of the spring and contact elements associated to the boundary restraints are directly provided from Yu (2012), noting that the corresponding values are not identical, but within the same order, at the two ends of the beam specimens.

As evidenced in Fig. 4.19, the responses predicted with the half and full models remain relatively similar, hence suggesting that the assumed symmetry conditions are acceptable for the presented specimens. Furthermore, such similarity in the predicted responses also suggest that the reinforcement splices at the middle joint are adequately long to mobilise the requisite reinforcement strength at the interfaces of the middle joint, thus acting as continuous reinforcement. It is worth noting though that symmetry conditions may no longer be applied if the properties of the restraints at each end of the beam specimens differ significantly, under which the specimens should be represented by full models.

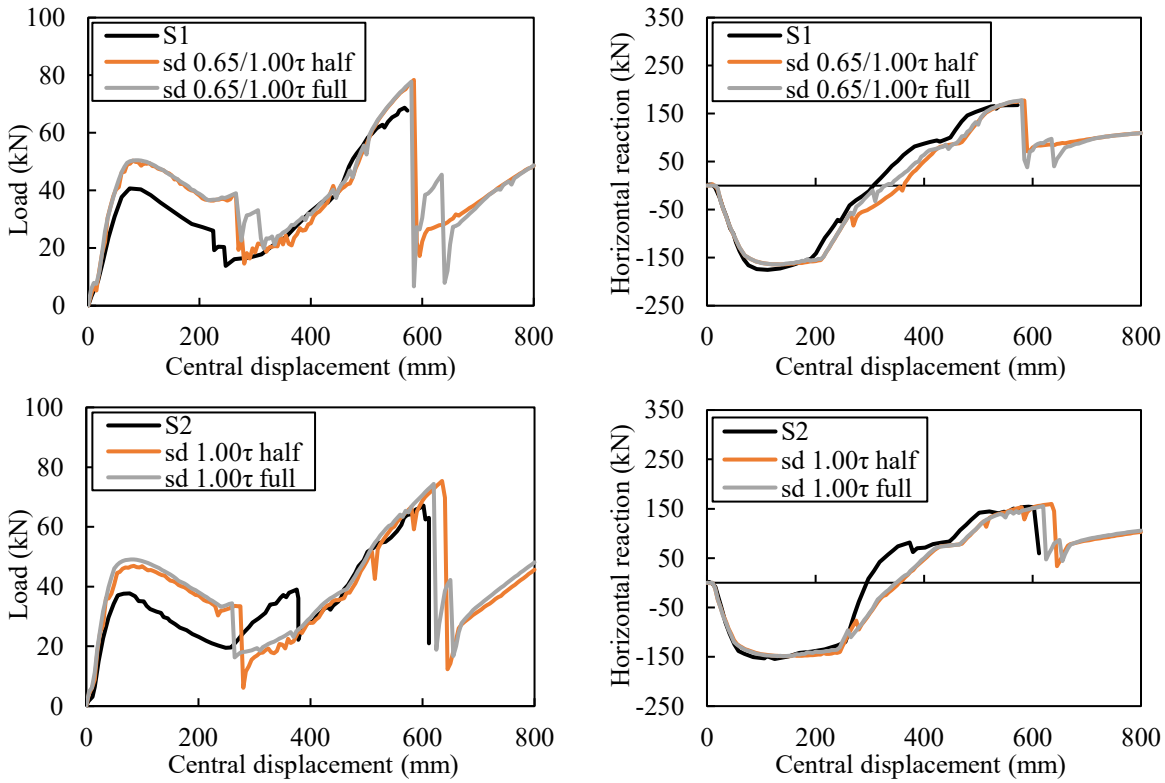


Fig. 4.19 – Assessment of full models (cont'd)

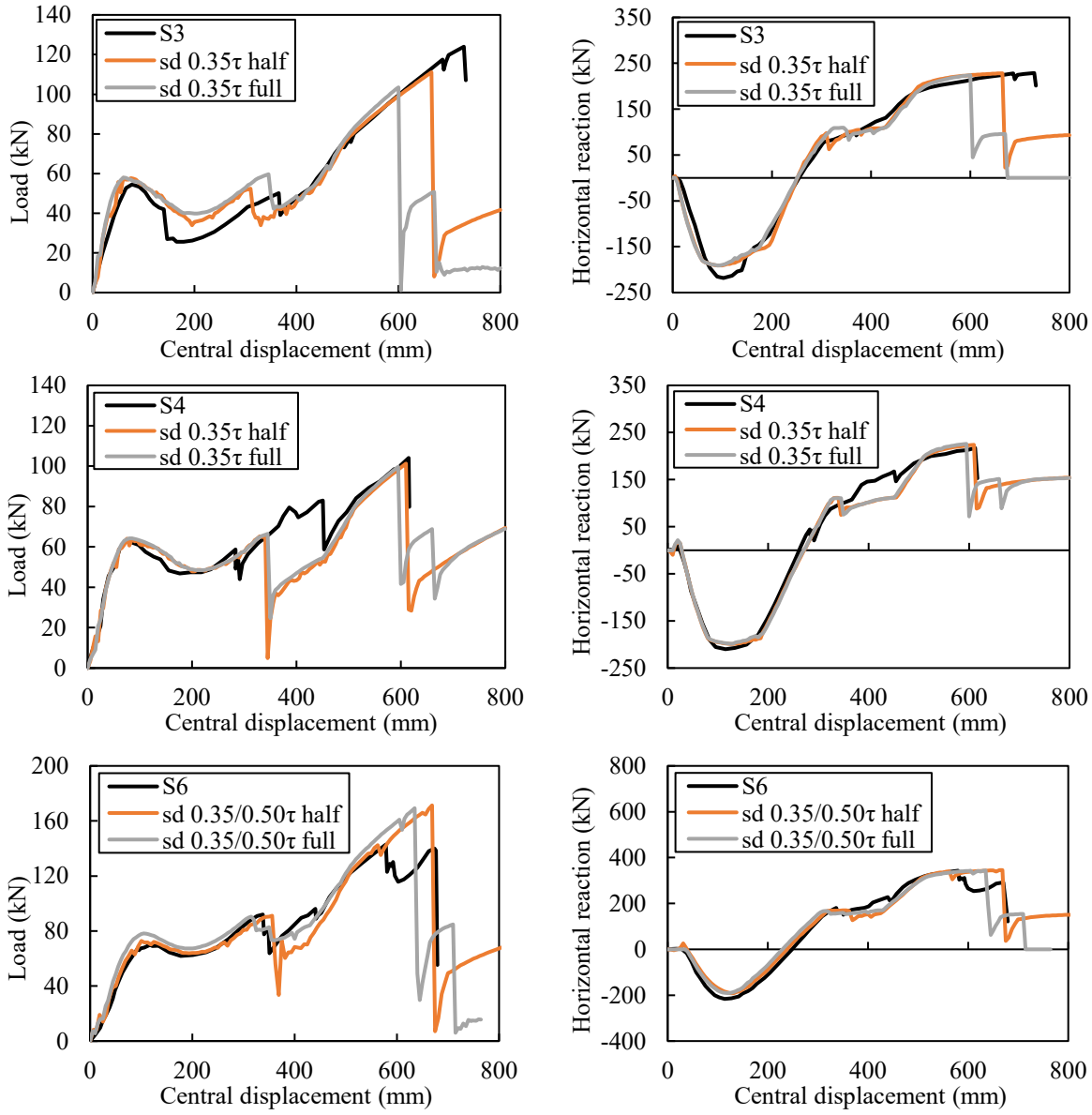
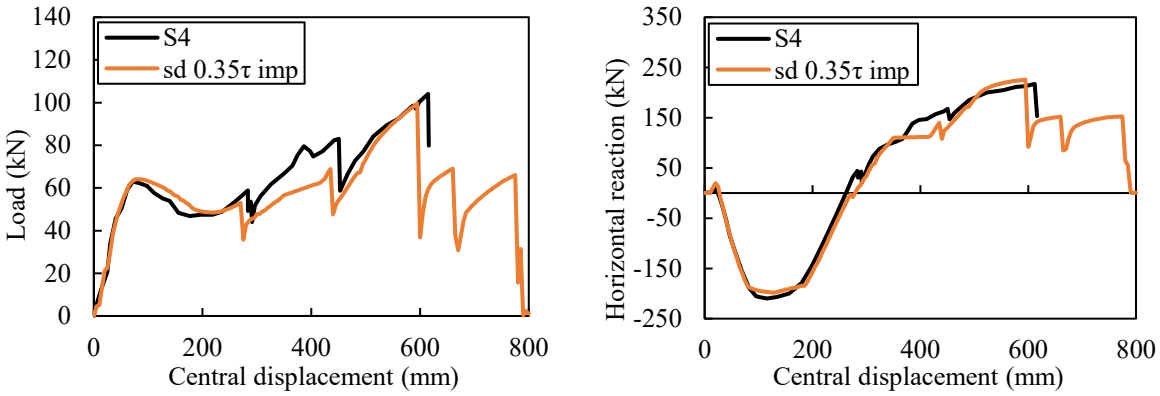


Fig. 4.19 – Assessment of full models

It is also worth noting that, despite the additional details, the full model is still unable to predict a clear phased fracture of the MJBR, which as noted before can be due to the assumption of perfect material properties and beam geometry. Considering the example of specimen S4, if different strain limits are assigned to each bar of the bottom layer of reinforcement passing through the middle joint, the ensuing response would be as illustrated in Fig. 4.20, demonstrating improved accuracy in the prediction of the load response.



(a) Central load-displacement response (b) Horizontal reaction-displacement response

Fig. 4.20 – Influence of material imperfection

4.3.2 Beam models with T-shaped section

Beam models with a T-shaped section are validated here against experimental test specimens from Ren *et al.* (2016) and Qiu *et al.* (2021), with the typical geometry and reinforcement detailing illustrated in Figs. 4.21 and 4.22. Tables 4.8-4.14 provide the corresponding model properties, including the assumed stiffness for the boundary springs as well as the concrete, steel and bond material properties. Note that specimen B3 from Ren *et al.* (2016) involves a rectangular cross-section and is herein presented to assess the contribution of the slab (specimen S3) to the resistance of the beam sub-system under column loss.

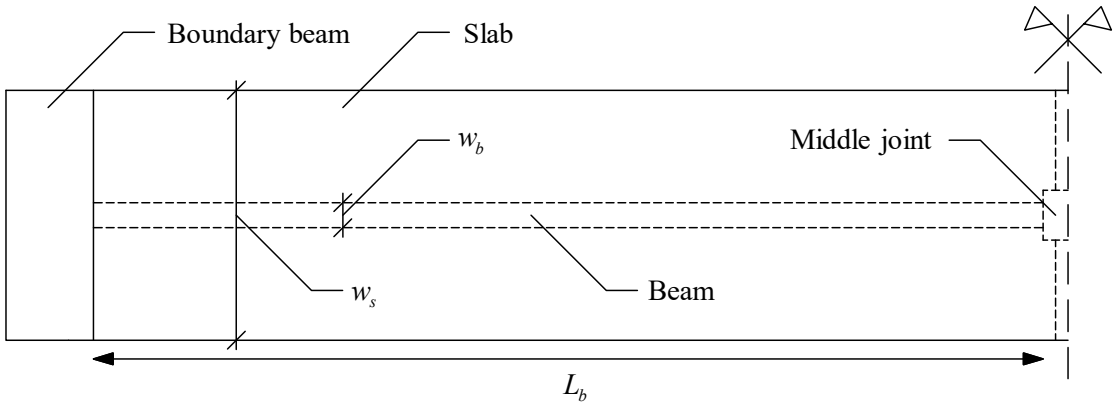


Fig. 4.21 – Typical specimen with T-shaped section: plan view

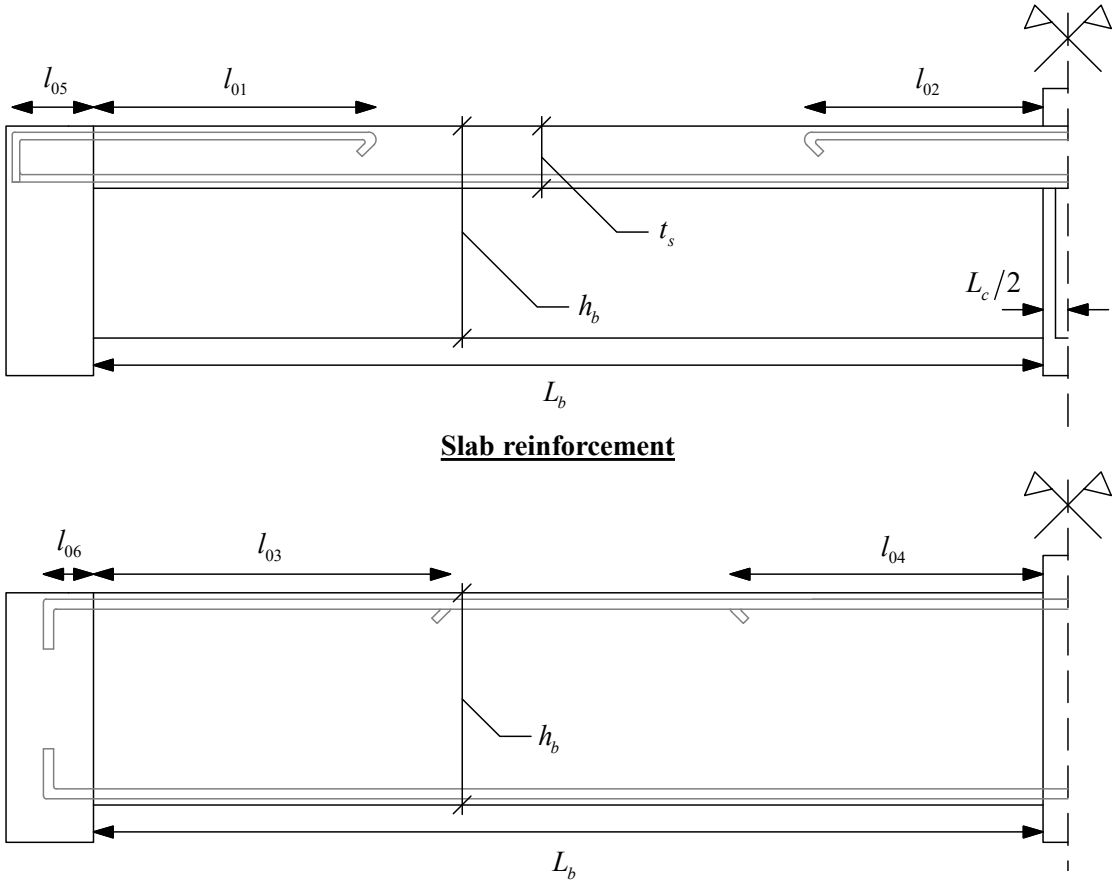


Fig. 4.22 – Typical specimen with T-shaped section: elevation view

Table 4.8 – T-beam geometry (in mm)

Test specimen		L_b	h_b	w_b	t_s	w_s	$L_c/2$
Ren *et al.* (2016)	B3	1900	200	85	-	-	100
	S3	1900	200	85	50	2000	100
	S4	1900	170	85	50	2000	100
	S6	1900	170	85	50	2000	100
Qiu *et al.* (2021)	S-F450	1800	150	100	40	450	75
	S-F1050	1800	150	100	40	1050	75

Table 4.9 – Reinforcement detailing (in mm)

Test specimen		Slab		Beam		
		Top	Bottom	Top continuous	Top curtailed	Bottom
Ren *et al.* (2016)	B3	-	-	2ϕ8	ϕ6	2ϕ8
	S3	ϕ6//190	ϕ6//190	2ϕ8	ϕ6	2ϕ8
	S4	ϕ6//190	ϕ6//190	2ϕ10	ϕ10	2ϕ10
	S6	ϕ6//190	ϕ6//190	2ϕ8	ϕ6	2ϕ8
Qiu *et al.* (2021)	S-F450	-	2ϕ3	2ϕ8	-	2ϕ8
	S-F1050	-	8ϕ3	2ϕ8	-	2ϕ8

Table 4.10 – Reinforcement anchorage and curtailment lengths (in mm)

Test specimen	l_{01}	l_{02}	l_{03}	l_{04}	l_{05}	l_{06}
Ren *et al.* (2016)	550	450	640	540	480	360
Qiu *et al.* (2021)	-	-	-	-	350	350

Table 4.11 – Stiffness of boundary springs (assumed values)

Test specimen		Spring stiffness	
		Axial (10^5 N/mm)	Rotation (10^{10} N.mm/rad)
Ren *et al.* (2016)	B3	10.00	3.00
	S3	10.00	3.00
	S4	10.00	1.00
	S6	10.00	1.00
Qiu *et al.* (2021)	S-F450	1.00	1.00
	S-F1050	1.00	1.00

Table 4.12 – Concrete properties

Test specimen	Compressive				Tensile		
	Secant stiffness[b]	Strength[a]	G_{fc}	Residual strength[c]	Initial stiffness	Strength[b]	G_{ft}
	MPa	MPa	N.mm	MPa	MPa	MPa	N.mm
Ren *et al.* (2016)	19448	44.00	144.26	1.00	34313[b]	3.27	0.1443
Qiu *et al.* (2021)	13814	26.80	131.94	1.00	30000[a]	2.12	0.1319

[a] Values from paper
[b] Values determined based on Eurocode 2 (CEN, 2004b)
[c] Assumed values

Table 4.13 – Steel properties

Test specimen	Reinforcement diameter	Young's modulus	Yield strength	Ultimate strength	Ultimate strain	Softening parameter[a]
	mm	MPa	MPa	MPa	-	-
Ren *et al.* (2016)	6	200000[a]	387	475	0.150[a]	10.00
	8	200000[a]	390	468	0.150[a]	10.00
	10	200000[a]	370	560	0.150[a]	10.00
Qiu *et al.* (2021)	2.8 $(\phi 3)$	180000	250	367	0.242	10.00
	7.7 $(\phi 8)$	200000	453	617	0.097	10.00

[a] Assumed values

Table 4.14 – Bond properties

Test specimen	Reinf. diameter	s_e	s_1	s_2	s_3	τ_e	τ_1	τ_3	Calibrated bond reduction
	mm	mm	mm	mm	MPa	MPa	MPa	MPa	
Ren *et al.* (2016)	6	0.15	1.21	3.00	4.80	11.00	22.40	6.16	0.18τ
	8	0.15	1.21	3.00	6.40	11.00	21.80	6.16	0.18τ
	10	0.15	1.21	3.00	8.00	11.00	21.19	6.16	0.18τ
Qiu *et al.* (2021)	2.8 $(\phi 3)$	0.15	0.95	1.50	2.24	10.00	18.24	4.81	0.63τ
	7.7 $(\phi 8)$	0.15	0.95	3.00	6.16	9.00	17.08	4.81	0.63τ

4.3.2.1 Load-displacement response

The numerical predictions compare well in general to the experimental data (Fig. 4.23), with the most visible differences observed for specimen S3, where a load drop is predicted by the proposed model at approximately 260mm of central displacement. This drop is considerably more significant than that observed experimentally, subsequently leading to a parallel offset of the linear load response within the tensile catenary/membrane stage. So as to investigate the reason behind the predicted load drop, the experimental result is further compared to the responses predicted by i) the same beam model but without the fracture of reinforcement, and ii) a beam-shell model also without the fracture of the reinforcement. The latter model involves a more detailed modelling of specimen S3, where the slab is explicitly represented via shell elements – *csl4* (Izzuddin *et al.*, 2004) – and connected to the *cbp3* beam elements (Izzuddin and Lloyd Smith, 2000) via rigid links. Models i) and ii) are herein termed as *si nsft* and *shell*, respectively.

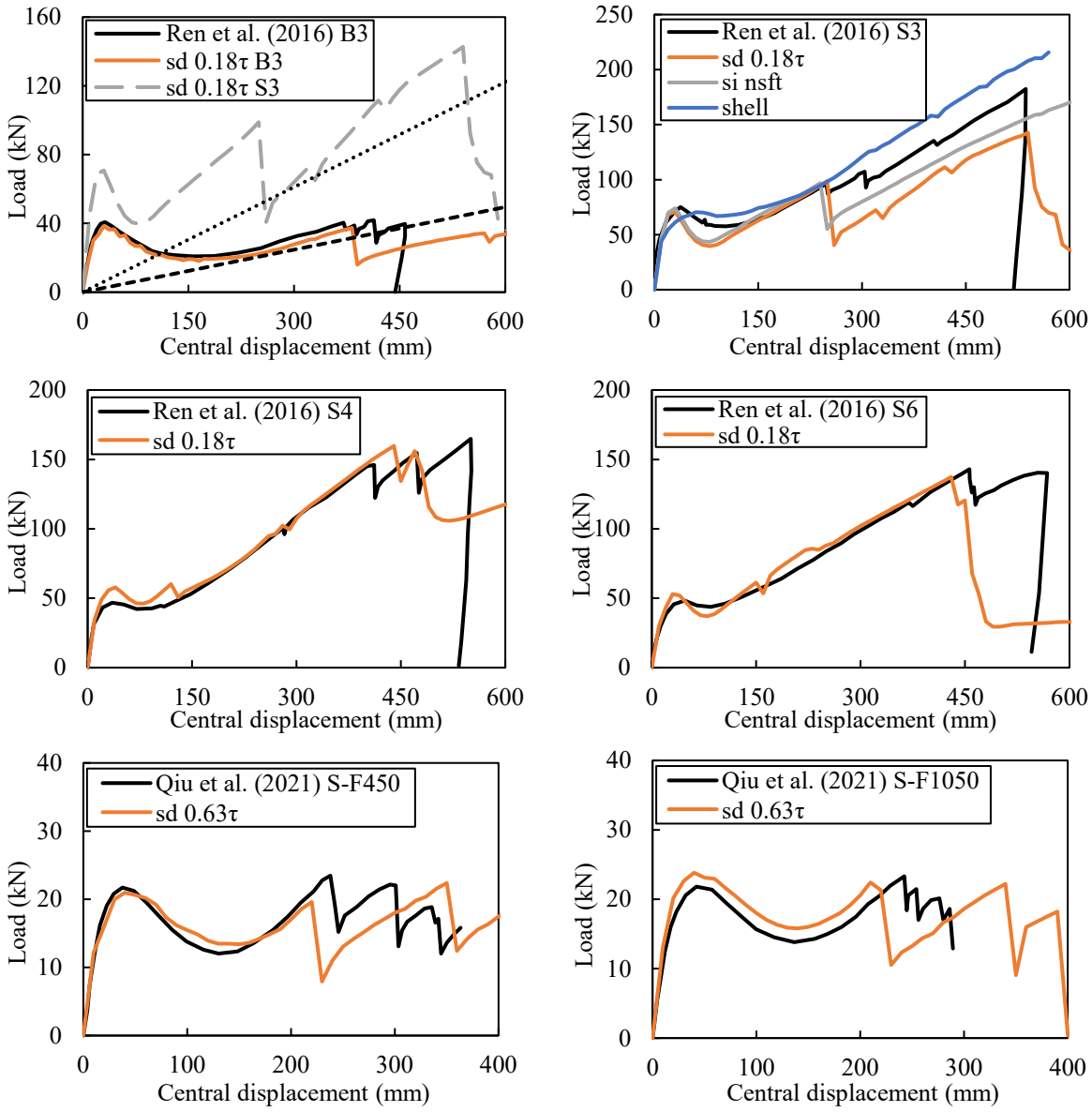


Fig. 4.23 – Validation of the proposed modelling approach: specimens with T-shaped section

The response predicted by the *si nsft* model shows that the load drop persists even when the fracture of reinforcement is deactivated, suggesting that the drop is related to damage mechanisms other than the fracture of reinforcement. Inspection of the incremental deformation predicted with the *sd 0.18τ* model at the considered central displacement reveals that a local hinge develops due to flexural cracking near the curtailment of the top beam and slab reinforcement, as illustrated in Fig. 4.24.

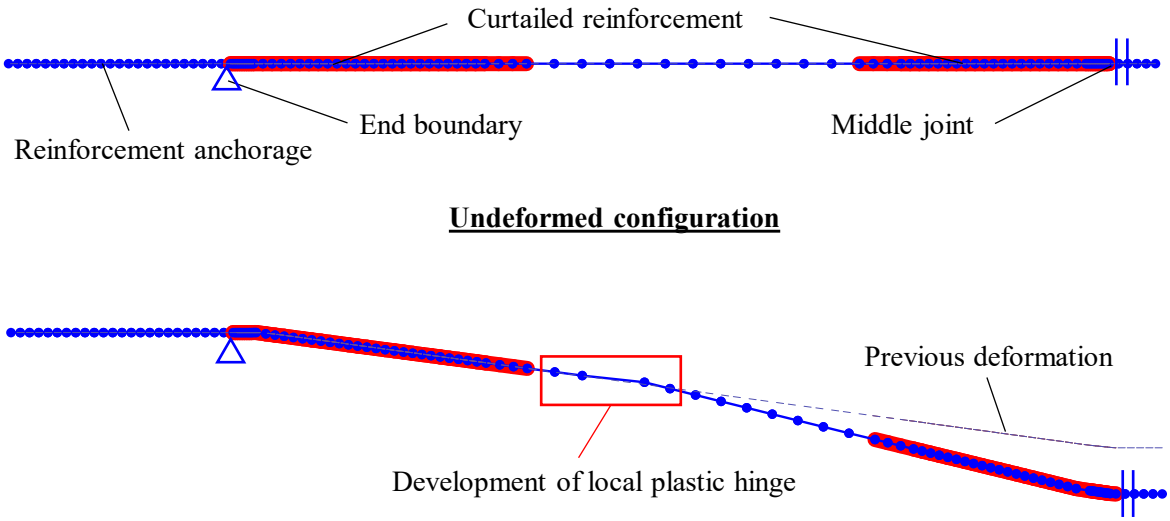
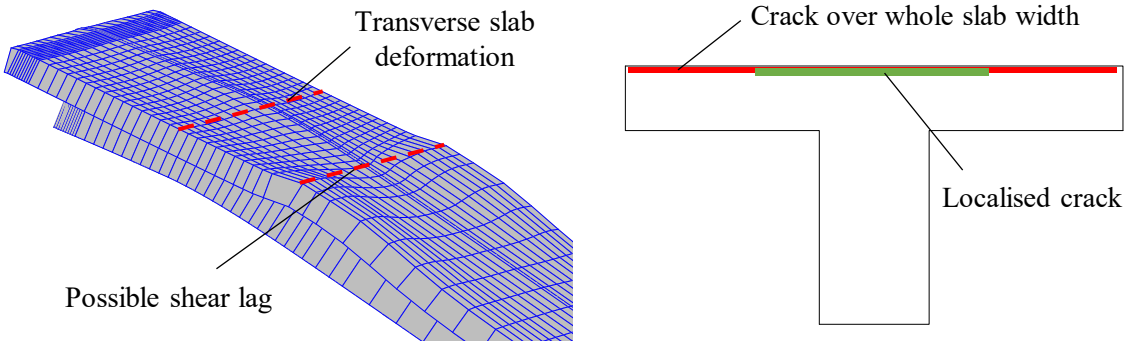


Fig. 4.24 – Development of local flexural hinge in specimen S3

The effect of this flexural crack is, however, less pronounced in the experimental test and the *shell* model. This observed difference can be explained based on the assumptions undertaken in the representation of T-section specimens via a beam element-only approach. Under this approach, the slab is assumed as the flange of the cross-section of the one-dimensional beam element, hence the approach is unable to reflect the transverse bending of the slab and the effects of shear lag, which are clearly visible in the *shell* model (see Fig. 4.25a).



(a) *shell* model (b) Difference in predicted flexural cracks

Fig. 4.25 – *shell* model of specimen S3

In this respect, whilst flexural cracks developed in the experimental test and the *shell* model are limited to an effective width directly above the beam, the *sd 0.18τ* model predicts a flexural crack over the entire slab width (see Fig. 4.25b). Accordingly, a more significant resistance loss due to the development of the local hinge is expected for the *sd 0.18τ* model. Furthermore, the beam element-only approach also represents the distributed slab reinforcement as a single

equivalent bar located at the symmetry axis of the beam cross-section, inherently augmenting the influence of reinforcement curtailment on the local resistance of the beam.

Notwithstanding the above, the discussed issue seems to be less significant for the models of specimens S4 and S6, as the predicted load-displacement responses compare well with the corresponding experimental responses. Compared to specimen S3, these entail a shallower beam, associated with a lower ratio of flexural resistances before and after cracking, which likely decreases the magnitude of the predicted load drop associated with the development of a local hinge at the locations of reinforcement curtailment. Also, unlike specimen S3, fracture of reinforcement is not predicted prior to the ductility limit of specimens S4 and S6. In specimen S3, the load drop associated to the fracture of reinforcement at approximately 260mm of central displacement is overestimated due to the assumption of a symmetric beam model, predicting the simultaneous fracture of all bottom beam reinforcement passing through the middle joint, whereas in the actual test specimen only a portion of this reinforcement fractured. Finally, it is worth noting that flexural hinges do not develop at regions other than the beam ends in specimens S-F450 and S-F1050, which comprise of continuous reinforcement only. In these cases, the accuracy of the proposed modelling approach in predicting the load-displacement response of T-section beam sub-systems should remain reasonably consistent.

Comparison of the load-displacement predictions for specimens B3 and S3 in Fig. 4.23 demonstrates the effectiveness of the proposed modelling approach in representing the general influence of the slab on the resistance of the beam sub-system under column loss. The slab strip enhances the resistance of the beam sub-system within both the CAA and CA stages. In the former stage, the resistance increase primarily originates from flexural enhancement of the beam, which is achieved with the additional slab reinforcement and the increase in lever arm. On the other hand, the enhancement achieved in the latter stage arises primarily from the additional contribution of the continuous slab reinforcement to tying. Indeed, through illustration of the analytically predicted tying response for both specimens (i.e. the linear relationships established with the horizontal tying force method presented in Chapter 5 of this thesis), it can be seen that the numerical predictions within the CA stage approximately follow such linear relationships. It is demonstrated in Chapter 5 that the difference in slope between these linear relationships corresponds to the additional contribution of continuous slab reinforcement to tying.

4.3.2.2 Local cracks and reinforcement strains

The local cracks and reinforcement strains predicted for specimen S6 are herein compared to the experimental observation. Fig. 4.26 illustrates the predicted deformation of the beam specimen at the ductility limit (approximately 430mm of central displacement), where the horizontal nodal displacements are scaled to highlight the location of the widest cracks. The figure also illustrates the location of the relevant reinforcement, along with its corresponding strain development with increasing central displacement. On the other hand, Fig. 4.27 provides a schematic illustration of the main cracks and reinforcement fracture developed in the experimental test (Ren *et al.*, 2016).

It can be seen that the proposed modelling approach offers a reasonable prediction of the crack locations and the fracture of the reinforcement, with the widest cracks developing at the beam-column interfaces and approximately at the reinforcement curtailment near the middle joint. However, the model fails to represent the damage developed at the reinforcement curtailment near the boundary beam. The predicted ductility limit of the beam sub-system is established by the fracture of the bottom beam reinforcement passing through the middle joint, which agrees well with the damage mechanism observed in the experiment. The proposed modelling approach also estimates reasonably well the central displacement at which this reinforcement fractures.

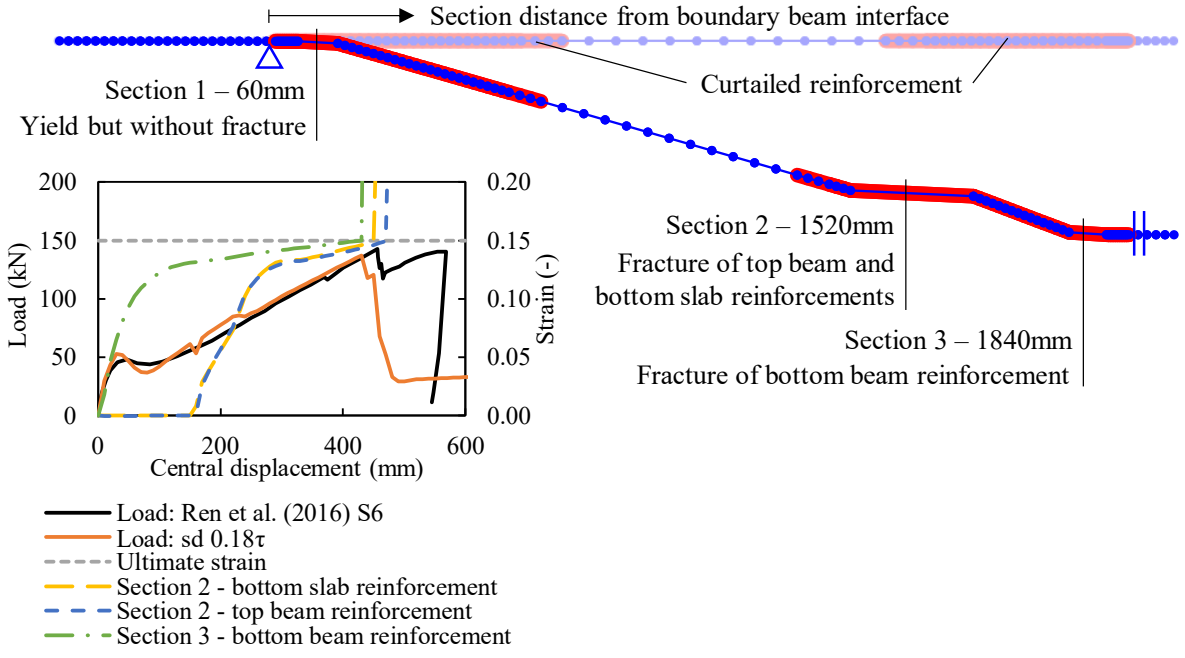


Fig. 4.26 – Damage mechanisms predicted for specimen S6 at its ductility limit

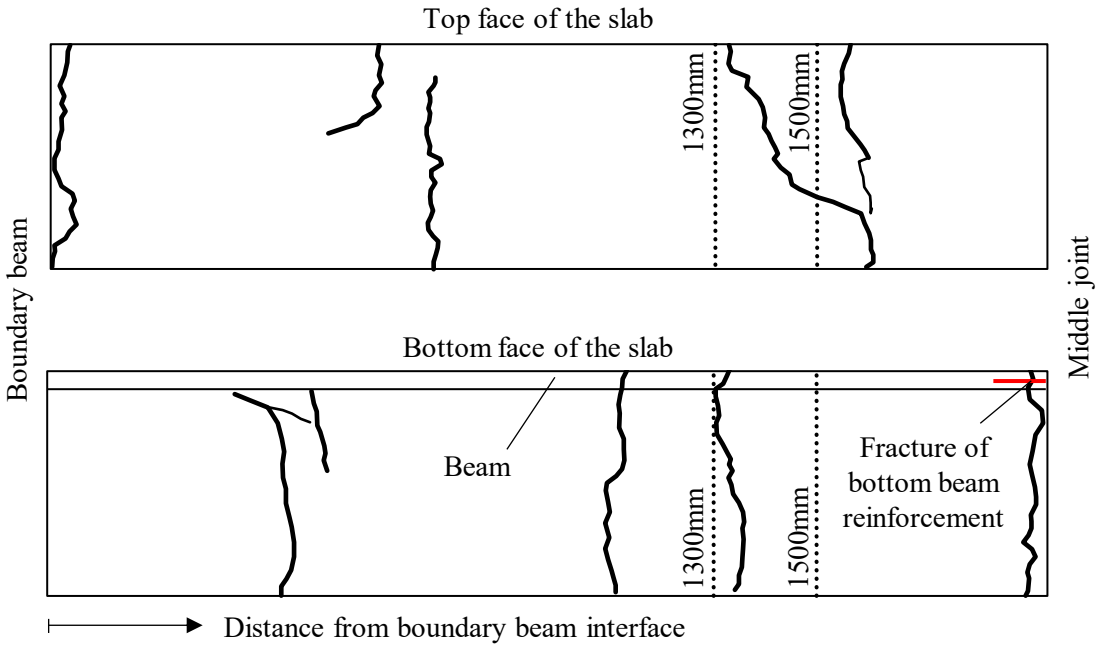


Fig. 4.27 – Experimental damage mechanisms from specimen S6 (data adapted from Ren *et al.*, 2016)

Table 4.15 lists the experimental and predicted locations for the fracture of reinforcement of the remaining specimens, along with the corresponding central displacement. The outcomes presented in this table again demonstrate reasonable predictions by the proposed modelling approach on the ductility limit of T-section RC beam sub-systems, noting that a higher variance between numerical and experimental results is expected (e.g. specimen S4) due to the previously discussed assumptions undertaken in the application of the modelling approach for such beam sub-systems.

Table 4.15 – T-section RC sub-systems: fracture of reinforcement

Typical damage	Central displacement (mm)					
	Ren *et al.* (2016)				Qiu *et al.* (2021)	
	B3	S3	S4	S6	S-F450	S-F1050
Experimental						
Initial fracture of MJBR	-	250	410	455	295	276
Second fracture of MJBR	-	305	474	462	-	-
Fracture of ECTR	371	-	-	-	237	242
Fracture of bottom slab reinforcement	-	-	-	565	-	-
Numerical						
Fracture of MJBR	383	250	-	430	350	340
Fracture of ECTR	-	-	-	-	220	210
Fracture at curtailed locations/slab reinforcement	-	540	440	460	-	-

'-' refers to inexistent and/or not observed

4.3.2.3 Discussion

The previous validation demonstrates the effectiveness of the proposed modelling approach to represent RC beam sub-systems with a T-shaped cross-section, with the most accurate predictions of the load-displacement response achieved for specimens with continuous reinforcement, where flexural hinges additional to those located at the beam ends are not expected to develop. Even in the presence of curtailed reinforcement, the proposed modelling approach still offers a reasonable prediction of the load-displacement response, specifically in the tensile catenary/membrane range, where flexural resistance contributions become less relevant. On the other hand, in the range where flexural resistance is still significant, the prediction is more accurate for RC sub-systems with shallow beams and a slab width limited to the effective width.

4.3.3 Beam models with sophisticated detailing

This section provides a brief demonstration of the practicality of the proposed modelling approach in representing RC beam sub-systems with more sophisticated reinforcement detailing, involving for example an offset layer of reinforcement and different bond conditions along a continuous reinforcement. Accordingly, specimens FR-R (Lim *et al.*, 2017b) and F3-PD (Yu and Tan, 2013b) are considered herein, with the geometry, material and modelling details provided in Appendix C. The FR-R specimen utilises smooth reinforcement, with the curtailed top reinforcement offset from the continuous ones by 25mm. The F3-PD specimen, on the other hand, involves deformed reinforcement, though sleeves are applied for the bottom reinforcement passing through the beam-column joints so as to locally debond the reinforcement from the concrete. These details can be represented via the proposed modelling approach by simply defining additional groups for the steel-bond elements, associated with a different distance d to the centroidal axis of the beam element for the former detailing and a significantly reduced bond resistance for the latter detailing (e.g. 0.05τ). The offset layer of reinforcement is then modelled by overlaying the additional group of steel-bond elements to the group representing the continuous reinforcement, whereas the partially debonded region can be simply realised by replacing the standard group elements within the specified region with the group elements having a significantly reduced bond strength.

Fig. 4.28 illustrates the comparison of the numerical and experimental load-displacement responses of the considered specimens.

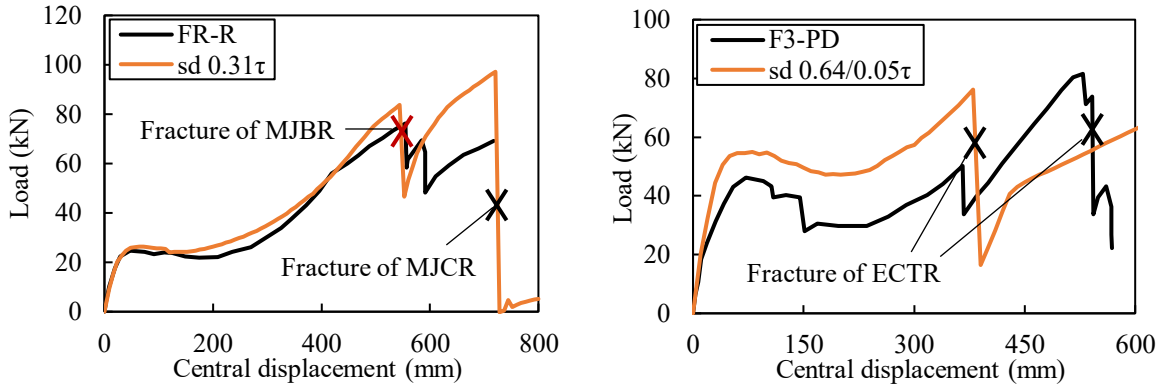


Fig. 4.28 – Specimens with sophisticated detailing (MJ – middle joint; EC – end-column; BR, TR and CR – bottom, top and curtailed reinforcement)

The numerical prediction for the two specimens demonstrates the ability of the proposed modelling approach to reasonably represent not only the reduction in bond strength (associated with either the use of smooth reinforcement or partial debonding), but also the inclusion of the offset reinforcement layer. Significantly, it can be seen in Fig. 4.28b that the partial debonding of the bottom reinforcement near the beam ends in specimen F3-PD prevented the fracture of this reinforcement, with the ductility limit of the specimen established as the fracture of the ECTR, which is reasonably represented by the numerical model. Notwithstanding, the numerical model consistently overestimates the resistance of specimen F3-PD with the difference primarily arising from the severe spalling of the concrete at the bottom face of the beam near the end-columns. As reported in Yu and Tan (2013b), the introduction of the sleeves weakened the compressive zones of the beam in such a way that the concrete was more likely to spall under compression, which in turn reduced the flexural resistance of the cross-section and the ability of the sub-system to develop CAA. In this respect, the numerical model is unable to represent such localised reduction in compressive strength of the concrete, hence the overestimation of the flexural resistance of the system. Furthermore, this limitation can also explain the predicted premature fracture of the top reinforcement at the end-columns. In the experiment, the spalling of the concrete reduced the effective cross-section of the beam sub-system, leading to a greater rotation capacity.

4.4 Sensitivity assessment

With reference to the review presented in Section 2.5.1, this section gives further consideration to the performance sensitivity of RC beam sub-systems under column loss to various material and geometric parameters, with emphasis on the ductility limit of the beam sub-system and on

additional findings not reported in the review. The control model is derived from specimen S4 of Yu and Tan (2012), employing the single joint approach for the modelling of the boundary restraints and considering the curtailed top reinforcement $(\phi 13)$ as a continuous reinforcement instead, leading to a total of $3\phi 13$ and $2\phi 13$ continuous top and bottom reinforcements, respectively.

4.4.1 Boundary restraint

The sensitivity assessment of the system response to the level of restraint stiffness (Fig. 4.29) confirm the observations noted in Section 2.5.1 in the sense that the mobilisation of CAA necessitates both axial and rotational restraint stiffness, whilst the mobilisation of CA primarily depends on the axial restraint stiffness. Then, once a sufficient level of restraint stiffness is reached, the sensitivity of the system response to further increase in restraint stiffness becomes negligible, under which the boundary restraints can be simply idealised as rigid supports.

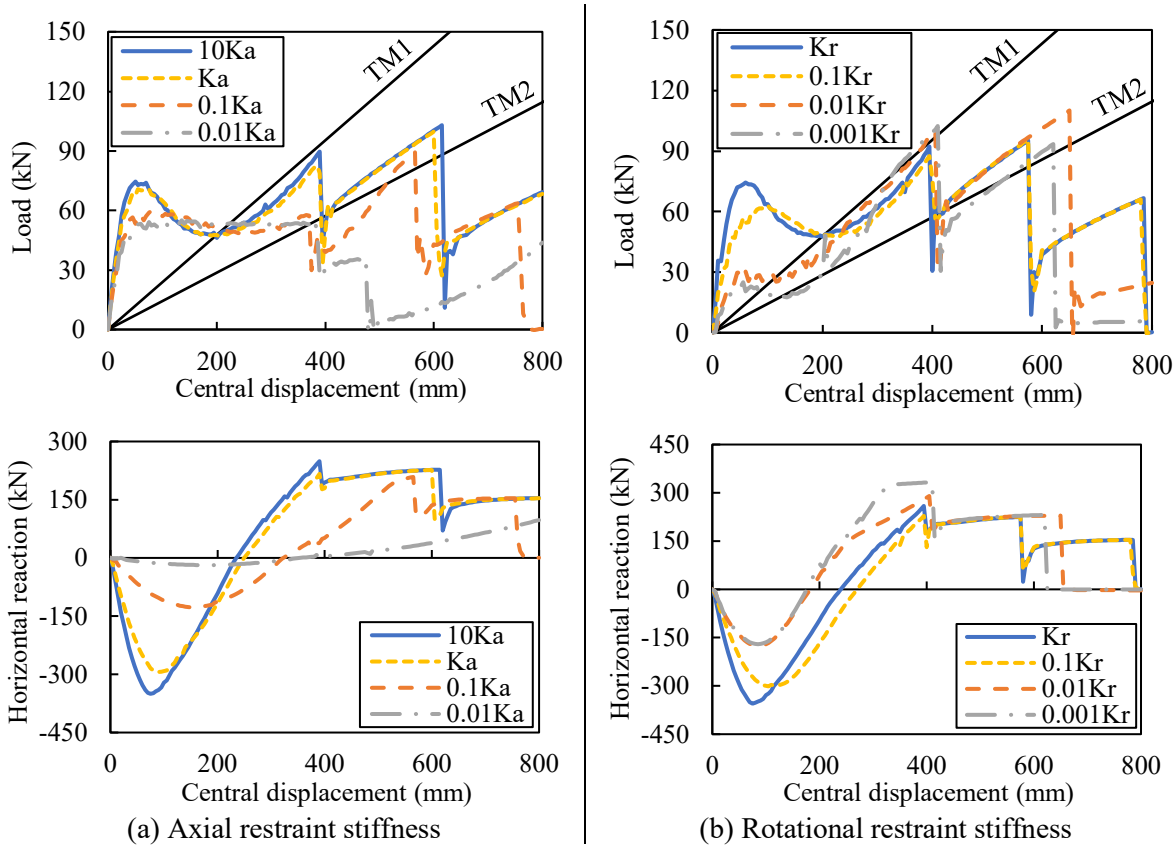


Fig. 4.29 – Sensitivity of the system response to the level of restraint stiffness

It also follows that the influence of restraint stiffness on the CA primarily corresponds to the deformation required before the activation of tying forces instead of the corresponding rate of

resistance gain. This is evidenced with the comparison of the numerical responses to the linear relationships depicted in black, which represent the tying resistance predicted by the horizontal tying force method presented in Chapter 5 considering (i) all reinforcement – TM1 and (ii) only the top reinforcement of the model – TM2. It can be seen that all numerical responses follow closely these linear relationships subsequent to the activation of tying.

Finally, the results suggest that the displacement at which the MJBR and ECTR fracture is practically insensitive to the surrounding restraint stiffness, with the exception of the case considering *0.01Ka* (Fig. 4.29a). Under an insufficient level of axial restraint stiffness, the planar beam sub-system resists gravity loads via flexure, the ductility limit of which differs from that established for tensile catenary action.

4.4.2 Reinforcement and span-to-depth ratio

The performance sensitivity of RC beam sub-systems is herein assessed to the quantity of reinforcement and to the span-to-depth ratio. The former parameter is represented by the mechanical ratio defined as:

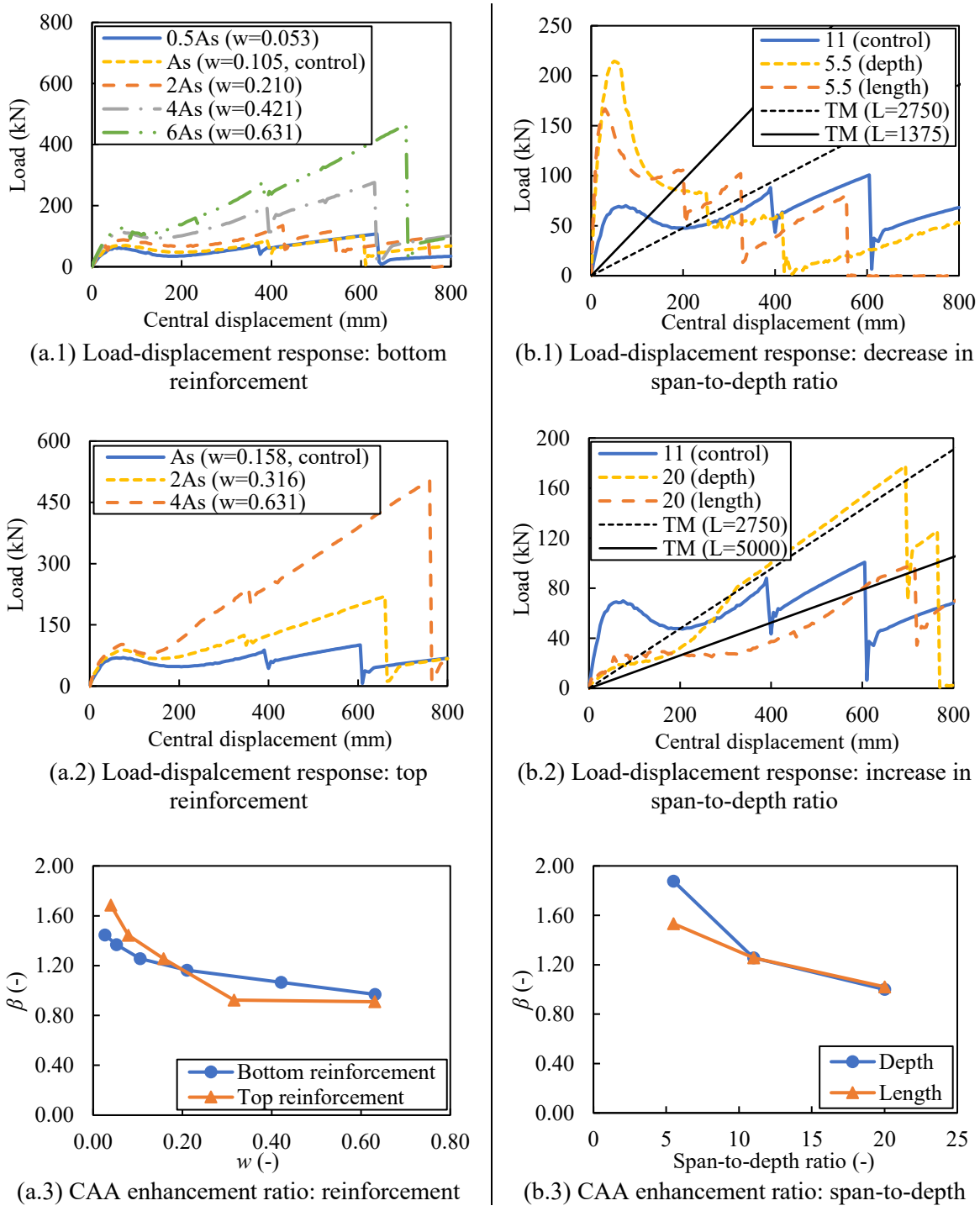
$$w = \frac{A_s}{b\,d}\frac{f_y}{f_c} \tag{4.5}$$

where A_s, b and d are respectively the area of bottom (top) longitudinal reinforcement, the width of the beam, and the distance from the geometric centre of the reinforcement to the top (bottom) face of the beam. On the other hand, f_y and f_c are respectively the yield strength of the steel and the concrete compressive strength.

The latter parameter is established as the ratio between the span of the beam sub-system and its corresponding beam depth. It is worth noting that the increase of longitudinal reinforcement and/or decrease of span-to-depth ratio may lead to shear-dominant damage mechanisms which are not reflected in the proposed modelling approach. Accordingly, the present sensitivity assessment assumes that shear failure mechanisms are avoided in all beam cases through appropriate design of the sub-system against shear failure. It is also worth noting that the change in mechanical ratio is herein achieved by adding/removing continuous longitudinal reinforcement, thus the subsequent results may not be representative of varying quantities of curtailed reinforcement, specifically within the CA stage.

Fig. 4.30 illustrates the sensitivity of the system load-displacement response to varying reinforcement and span-to-depth ratios, noting that the variation of the former parameter is

achieved via the variation of bottom or top reinforcement alone, whilst the latter is achieved via the variation of either the depth or the span length of the beam.



(a.1) Load-displacement response: bottom reinforcement

(b.1) Load-displacement response: decrease in span-to-depth ratio

(a.2) Load-dispalcement response: top reinforcement

(b.2) Load-displacement response: increase in span-to-depth ratio

(a.3) CAA enhancement ratio: reinforcement

(b.3) CAA enhancement ratio: span-to-depth

Fig. 4.30 – Sensitivity of the system response to varying reinforcement and span-to-depth ratios

Sensitivity to the quantity of reinforcement. The increase in reinforcement leads to an overall enhancement in system resistance associated with a higher peak resistance within the CAA

stage and a faster rate of resistance gain within the CA stage. It is worth noting though that similar to the observations reported in Su *et al.* (2009) and Yu and Tan (2014b) the peak resistance enhancement in the CAA stage with increasing reinforcement progressively arises from the increase in flexural resistance instead of the beneficial effects from the CAA mechanism. This is evidenced in Fig. 4.30a.3 by the decrease of β, which is defined as the CAA enhancement ratio:

$$\beta = \frac{P_{\text{CAA}}}{P_{\text{flexural}}} \tag{4.6}$$

where P_{CAA} and P_{flexural} are the CAA peak load and flexural resistances determined with the beam sub-system respectively considering and neglecting axial restraint.

Furthermore, Figs. 4.30a.1-a.2 also suggest that the uneven increase in reinforcement over the cross-section slightly improves the ductility limit of the system, independently of the location at which reinforcement is added (top or bottom). This can be due to the variation in position of the neutral axis at the critical sections of the beam sub-system, decreasing the strain demand on the MJBR and ECTR. Indeed, a separate sensitivity assessment involving the simultaneous increase in both top and bottom reinforcement demonstrates that the increase in ductility limit of the beam sub-system is less significant.

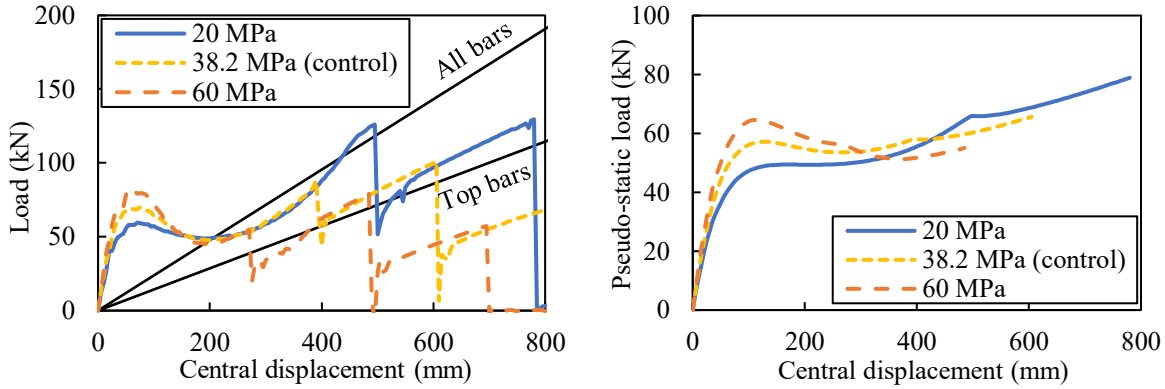
Sensitivity to the span-to-depth ratio. Similar to the results reported in Su *et al.* (2009), Yu and Tan (2012) and Ren *et al.* (2016), the span-to-depth ratio primarily defines the dominant mechanism via which the beam sub-system arrests disproportionate collapse – CAA and CA respectively for a low and high ratio. The outcomes in Figs. 4.30b.1-b.3 also suggest that the span-to-depth ratio is not unique to the variation of the depth and the span length of the beam, with a more effective CAA enhancement achieved via the increase in the beam depth (Fig. 4.30b.3).

Within the CA stage, the slope of the linear relationships illustrated in Figs. 4.30b.1-b.2 is insensitive to the beam depth but increases with shorter span lengths. In this respect, to maximise the load resistance gain under CA, an increase in span-to-depth ratio with reference to the control model should be achieved via reduction of the beam depth, whilst a decrease in span-to-depth ratio should be achieved via the shortening of the span length. Notwithstanding, given that lower span-to-depth ratios limit the ductility of the beam sub-system to the extent that CA cannot be fully activated, and that higher span-to-depth ratios encourage the resistance

of the gravity loads via CA instead of CAA, it is of more interest to maximise the resistance gain under CA by increasing the span-to-depth ratio through reduction of the beam depth.

4.4.3 Concrete strength

Consideration is given herein to the performance sensitivity of the beam sub-system to the concrete compressive strength, noting that a higher concrete strength also improves the bond conditions between the concrete and the reinforcement. The static load-displacement responses illustrated in Fig. 4.31a suggest that higher concrete compressive strengths promote the mobilisation of CAA, and thus the enhancement of the corresponding local peak resistance.



(a) Static system response (b) Pseudo-static system response

Fig. 4.31 – Sensitivity of the system response to the concrete strength

On the other hand, the rate of resistance gain within the CA stage is insensitive to the concrete strength as all the corresponding load-displacement responses converge to the linear relationships defined by the horizontal tying force method. It is worth noting though that the deterioration in bond conditions with weaker concrete strengths improves the ductility limit of the system, thus allowing the system to achieve greater deflections and thus resistance under CA. Similar observations have been reported in Deng *et al.* (2020). In this sense, the strength of the concrete also primarily defines the dominant mechanism via which the beam sub-system arrests disproportionate collapse – CAA and CA respectively for high and low strength concrete. Nonetheless, a general trend cannot be defined for the sensitivity of the pseudo-static resistance to the concrete compressive strength (Fig. 4.31b), as it is uncertain whether the resistance mobilised via CA of the beam sub-system with lower concrete strength would compensate for the loss of peak resistance within the CAA stage.

4.4.4 Bond strength and anchorage length

For the sensitivity assessment of RC beam sub-systems to the parameters of bond strength and anchorage length, the control specimen is further modified by deactivating the slip restraints at the end of the reinforcement anchorages. Furthermore, the anchorage at the middle joint is herein defined identical to the anchorages at the end columns. These considerations allow for the development of reinforcement pull-out as one of the damage mechanisms. A total of 9 models are generated for the present sensitivity assessment involving 3 levels of bond strength and 3 different end-anchorage lengths, as presented in Table 4.16.

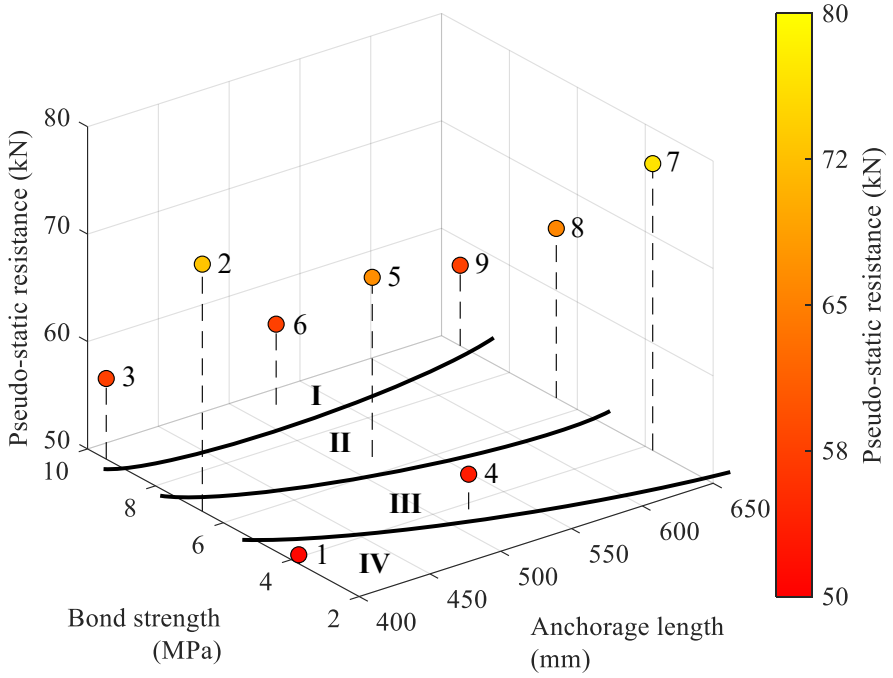
Table 4.16 – Anchorage lengths and bond strengths

Model	Maximum bond strength (MPa) Reference bond – 18.90 MPa	Anchorage length (mm)
1	3.78 (0.20τ)	400
2 (control)	6.62 (0.35τ)	400
3	9.45 (0.50τ)	400
4	3.78 (0.20τ)	520
5	6.62 (0.35τ)	520
6	9.45 (0.50τ)	520
7	3.78 (0.20τ)	650
8	6.62 (0.35τ)	650
9	9.45 (0.50τ)	650

The performance comparison between the considered cases is obtained based on the maximum pseudo-static resistance, as illustrated in Fig. 4.32, whilst the supplementary information on the fracture displacements of the reinforcement is provided in Appendix D. The outcomes demonstrate that four possible damage scenarios can occur for the considered cases, noting that the divisions defined in Fig. 4.32 for these types of damage scenarios are merely qualitative: i) premature fracture of the reinforcement preceding the activation of CA; ii) fracture of the reinforcement under CA; iii) pull-out of yielded reinforcement, and iv) pull-out of elastic reinforcement.

The pseudo-static resistance of the RC beam sub-system is maximised for a balanced design of bond strength and anchorage length (models 2, 5, 7 and 8), where the damage mechanisms ii) and iii) establish the ductility limit of the system, with the latter mechanism offering a relatively better performance owed to the slightly improved ductility limit. It is worth noting that further improvement in bond-slip conditions from this balanced design via the consideration of either an increased bond strength or greater anchorage length (model 3, 6 and 9) is detrimental to the system pseudo-static resistance as it encourages the premature fracture

of the reinforcement, under which the system is unable to mobilise resistance under CA. On the other hand, further deterioration in bond-slip conditions (models 1 and 4) is equally detrimental to the performance of the system due to the occurrence of complete reinforcement pull-out in the range of relatively small displacements, which limits the pseudo-static resistance of the system.



I – Premature fracture of reinforcements

II – Fracture of reinforcements within the CA stage

III – Pull-out of yielded reinforcement

IV – Pull-out of elastic reinforcement

Fig. 4.32 – Sensitivity of the pseudo-static resistance to the bond strength and anchorage length

4.4.5 Enhancement solutions

Several detailing techniques and solutions can be found in the literature to enhance the performance of RC beam sub-systems under the scenario of column loss including:

- External enhancement via strengthening of the sub-system with carbon-fibre reinforced polymers, typically applied at the critical sections of the sub-system (Orton *et al.*, 2009);
- Partial debonding of the bottom reinforcement (Yu and Tan, 2013b) and the use of smooth reinforcement (Lim *et al.*, 2017b), as previously discussed in Section 4.3.3, in

view of delaying the fracture of reinforcement, and thus allowing for a greater resistance gain via CA.

- Specially detailed partial hinges to concentrate damage from large rotations (Yu and Tan, 2013b), serving as fuses for the beam-column joint interfaces. Given the high rotation capacity of the partial hinges, tensile catenary action is expected to develop with little to no premature fracture of the longitudinal bars.
- Addition of a mid-layer reinforcement to the beam sub-system (Yu and Tan, 2013b; Alogla *et al.*, 2016a), which depending on its position within the section of the beam sub-system can offer resistance enhancement primarily under CA, with minimal contribution to the flexural resistance of the beam. This can be specifically useful for a compatible design of the sub-system under a multi-hazard perspective involving seismic and robustness assessments.

The use of smooth reinforcement and the addition of a mid-layer reinforcement can be considered the most practical amongst the solutions reviewed for robustness enhancement of RC beam sub-systems. Notwithstanding, the exclusive use of smooth reinforcement may not be ideal under service load conditions since it is less desirable for crack and deformation control compared to deformed reinforcement, typically resulting in a higher quantity of reinforcement to comply with the design requirements. In this respect, the solution involving an additional mid-layer reinforcement is assessed herein. Though, differently to the solution employed by Yu and Tan (2013b) and Alogla *et al.* (2016a), which considered deformed bars for the mid-layer reinforcement, the solution assessed herein involves the use of smooth bars instead, whilst the top and bottom reinforcements remain as deformed. Fig. 4.33 illustrates the three cases of mid-layer reinforcement considered for the current assessment.

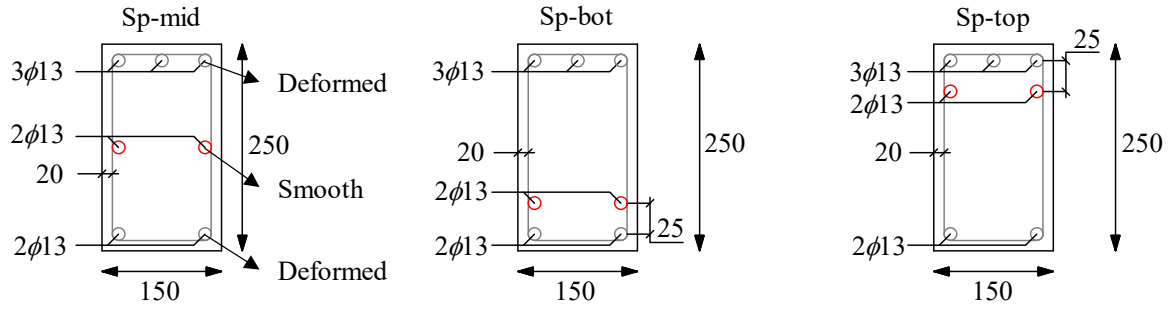


Fig. 4.33 – Detailing scheme for the three cases of mid-layer reinforcement

Fig. 4.34 presents the static and pseudo-static load-displacement responses of the control model and the three case models with the mid-layer reinforcement. The ductility limit of the models

is established here as the displacement at which all three layers of reinforcement (i.e. bottom, top and mid-layer) fracture at least once over their length. This is a conservative assumption neglecting the residual load resistance under CA after the interruption of all continuous reinforcement, as the continuity of the tie forces would then need to rely also on the stirrups to transfer the tensile force of the fractured reinforcement, the resistance mechanism of which is deemed less reliable.

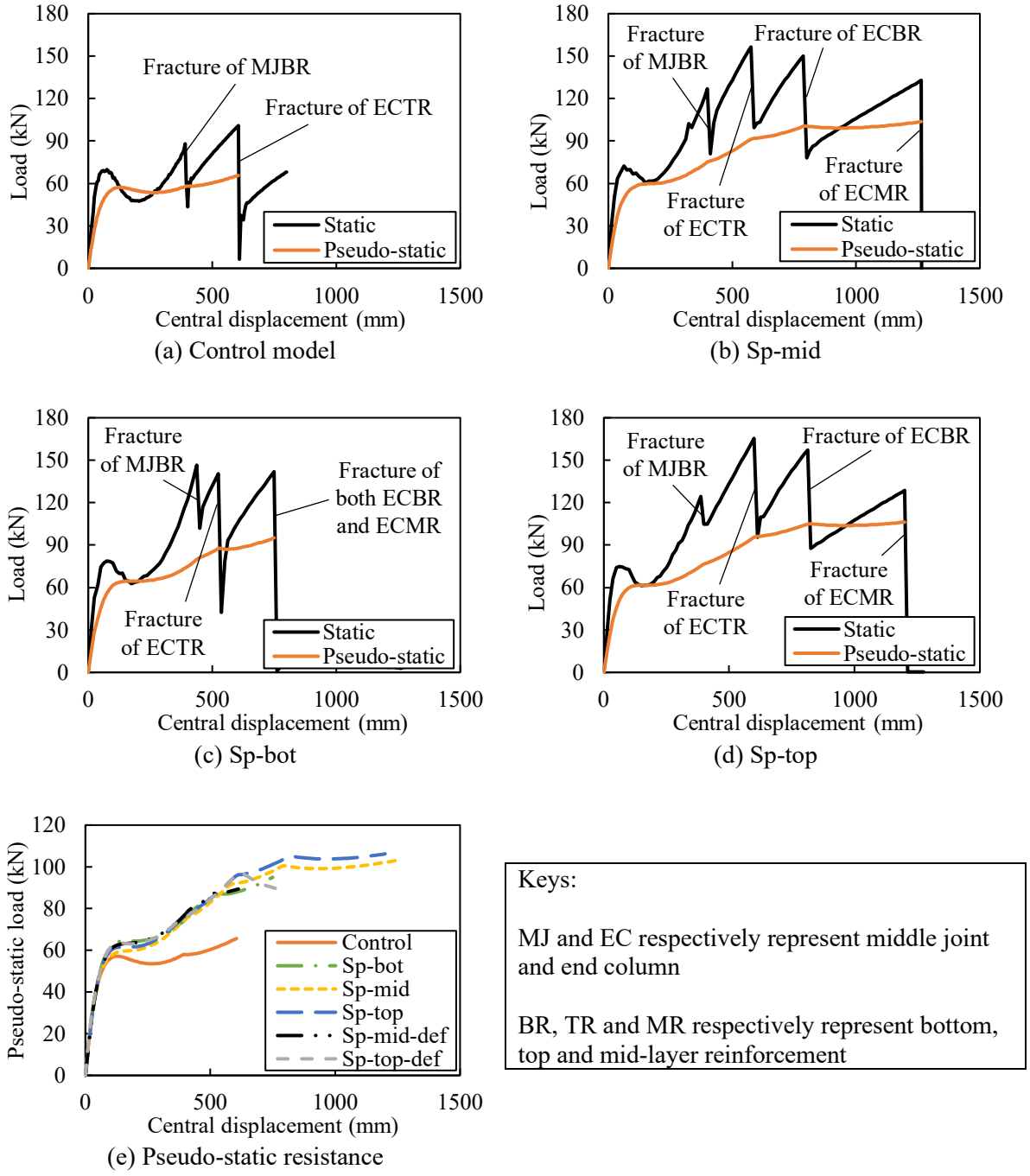


Fig. 4.34 – Load response of the control model and the three cases of mid-layer reinforcement

The influence of the additional mid-layer reinforcement on the performance of the beam sub-system is twofold. On one hand, the mid-layer reinforcement offers additional ties, resulting in a faster rate of resistance gain within the CA stage (i.e. steeper slope for the characteristic linear relationship), with such gain specifically significant in the early stages of CA, where the fracture of reinforcement is still limited. On the other hand, the ductility limit of the sub-system also increases, allowing for the fracture of the bottom reinforcement at both the middle joint and the end-column, as evidenced in the *Sp-mid* and *Sp-top* model results. With reference to the control model, where only a single fracture is predicted for the top and bottom reinforcements up to the established ductility limit, such improvement in ductility limit allows for a further gain in pseudo-static resistance via tensile catenary action (Fig. 4.34e). In this respect, both *Sp-top* and *Sp-mid* can be considered as suitable enhancement solutions, though from the perspective of multi-hazard design involving seismic considerations the latter provides the lowest enhancement to the flexural resistance of the beam sub-system.

Finally, so as to highlight the significance of using smooth bars for the mid-layer reinforcement, the pseudo-static responses of the *Sp-mid* and *Sp-top* models are compared to the responses of *Sp-mid-def* and *Sp-top-def*, which are models employing deformed bars for the mid-layer reinforcement instead. It is evident that the latter models present a reduced ductility limit, preventing further resistance gains under tying. In this respect, the practical consideration of smooth bars for the mid-layer reinforcement is beneficial, as it leads to a relative enhancement in pseudo-static resistance compared to its deformed counterpart.

4.5 Conclusion

The present chapter proposes a novel modelling approach aimed at accurate yet practical evaluation of the nonlinear static response and ductility limit of RC planar beam sub-systems under a column loss scenario, serving as a relevant complement to performance-based assessment frameworks for disproportionate collapse, such as the framework developed by Izzuddin *et al.* (2008). Significantly, the ability of the proposed modelling approach to quantify the ductility limit of the system also benefits simplified horizontal tying approaches, such as the method developed in the subsequent chapters (Izzuddin and Sio, 2022), in defining the maximum resistance mobilised by the system via tying and in verifying future simplified methods for the prediction of the ductility limit. In this respect, the proposed modelling approach features: i) the explicit representation of bond-slip behaviour throughout the beams of the sub-system; ii) practical representation of sophisticated reinforcement detailing,

involving curtailments and lap splices; and iii) computational savings compared to other explicit bond modelling approaches as it avoids elements that are specific for bond-slip and the requisite duplication of nodes.

Following the exposition of the model constituents, which include the various enhancements presented in Chapter 3, the validation of the proposed modelling approach against experimental tests available in literature, albeit with the calibration of the bond-slip parameters due to a lack of experimental data, demonstrates the effectiveness and practicality of the approach in predicting the nonlinear static response and ductility limit of RC planar beam sub-systems with a beam cross-section symmetric about its vertical axis. This validation also demonstrates the superiority of the strain-dependent bond-slip model, as it subsumes the strain-independent one due to its ability in representing yield penetration, requiring a moderate global reduction of bond strength for the calibration of the response. Nonetheless, regardless of the dependency of the bond-slip model on reinforcement strains, the proposed modelling approach effectively resolves the main shortcoming of conventional fibre-beam elements assuming infinite bond, which generally predict premature fracture of the reinforcement.

It is again worth noting that the validation of the proposed modelling approach relied on the calibration of the bond-slip parameters to match the experimental fracture displacements, as there is typically a lack, if not absence, of bond-slip properties from the experiments available in literature. Under the present framework for the modelling of RC beam sub-systems subject to a column loss scenario, there is a considerable need for future experimental work to provide detailed information on the bond-slip properties within the relevant sections of the sub-system, along with an accurate assessment of the ductility limit of the reinforcement, given that both the bond-slip and reinforcement ductility significantly influence the ductility limit of the sub-system. The proposed modelling approach can then readily employ such accurate data for further calibration of the strain-dependent bond-slip model.

The chapter culminates with a sensitivity assessment noting the main parameters influencing the resistance and ductility limit of RC planar beam sub-systems under a column loss.

Chapter 5: Rational horizontal tying force method for practical robustness design of building structures

5.1 Introduction

This chapter presents the rational horizontal tying force method developed by Izzuddin (Izzuddin and Sio, 2022), along with its validation, verification and application performed by the author of this thesis. Unlike current prescriptive tying force approaches, the newly developed method benefits from i) a rational association with local damage scenario consisting of the sudden loss of a column, load-bearing wall or floor support (e.g. punching shear failure), ii) the explicit consideration of dynamic amplification and system ductility and iii) supplementary methods for assessing the interaction of the affected floor system with the surrounding structure. The proposed method also allows for iv) a systematic combination of different types of loading and sources of tying based on common principles of superposition, including distributed tying, as may be developed via the reinforcement within the floor slab. Importantly, such relative benefits are realised within a practical framework, with consideration of the simplifications detailed below, rendering the method as a potential candidate to replace current prescriptive tying force requirements for robustness design.

- Under the sudden loss of a load-bearing member, the adequacy of tying is considered on an individual floor level, ignoring the interaction across the various storeys in resisting the overall gravity load. This is a conservative assumption provided that all floors exhibit similar deformation capacities and are adequately restrained in plane for tensile catenary/membrane action to develop.
- Resistance to gravity loading under the considered scenario of load-bearing member loss is established mainly from tying action, specifically catenary action of beams and/or membrane action of the floor slab. This is also a conservative assumption ignoring additional resistance contributions such as residual flexural resistances and

strain-hardening effects. Though, such contributions can be optionally considered via a load reduction factor included in the general tying formulation.

- The response of the affected floor system in the catenary/membrane stage is dominated by a single deformation mode.
- Assessment is undertaken for a floor panel substructure, the boundary of which are defined by the actual boundary of the building and/or column/wall gridlines surrounding the lost column/wall.
- The affected floor system has sufficient planar restraint and ductility to mobilise full tensile catenary/membrane action, the satisfaction of which can be checked with the provided supplementary methods.
- The surrounding structure has adequate capacity to resist the redistributed gravity loads, for which the dynamic amplification is established also from the provided supplementary methods.

Furthermore, the proposed method relies on the provision of the ductility limit of the affected floor system expressed in terms of chord rotation capacity. In this respect, it is worth noting that this limit is not the typical rotational capacity that is considered in flexural design, beyond which the flexural resistance drops significantly, but is rather the rotational capacity that can be achieved before a significant reduction in tying resistance. This is typically associated with the fracture of a joint, a reinforcement bar or a tying force component. For example, in the case of RC planar beams, the chord rotation capacity can be established based on the response of the numerical models proposed in Chapter 4, typically at the point of a significant drop in resistance.

5.2 General tying formulation

The general formulation presents a lower bound on tying in terms of the applied loading and is expressed by (5.1) based on principles of structural mechanics as elaborated in Sections 5.3-5.5:

$$T \geq \eta \, \rho \left(\frac{i_f}{\bar{\alpha}} \right) P, \quad \bar{\alpha} = \frac{\alpha}{0.2}, \quad (\alpha \text{ in rad}) \tag{5.1}$$

where $P = \sum P_j$ is the total equivalent load obtained as a superposition from all loads applied to the double-span beam/floor system; and $T = \sum T_k$ is the total equivalent tying force

obtained as a superposition from all active tying forces within the beam/floor system. The remaining parameters are as follows:

- i_f is a tying force intensity factor that depends on the system under consideration, and is established under a reference chord rotation of 0.2rad;
- $\bar{\alpha} = \alpha / 0.2$ is introduced to allow for different levels of chord rotation capacity α (rad), representing the system ductility limit;
- η is a dynamic amplification factor allowing for the influence of sudden column/load bearing member loss; and
- ρ is a reduction factor that allows for additional sources of resistance above and beyond tying action based on constant tying forces, including residual flexural resistance, strain-hardening effects and the contributions of through-column reinforcement for a punching shear local failure scenario. This chapter focuses mainly on tying action arising from constant tying forces, thus a default $\rho = 1$ is implied in the following sections. Notwithstanding, a brief discussion on the quantification of ρ is provided later in Section 5.7.

Equation (5.1) provides the basis for assessing the adequacy of the ties within the affected beam/floor system (as expressed by the equivalent tying force T) to resist the gravity loads (as expressed by the equivalent load P) for the maximum normalised rotation capacity of the system $\bar{\alpha}$, which as noted before, clearly requires the knowledge of the rotation capacity of the system α. Furthermore, the activation of tying requires a minimum value for α, which can be established via the supplementary method presented in Section 5.6.1. If the rotation capacity of the system is below this minimum threshold, (5.1) is no longer applicable and the assessment of the affected system in bridging the gravity loads would then necessitate a performance-based alternative load path approach.

In evaluating the tying force, it is proposed that this is conservatively based on the yield strength rather than the ultimate strength of the material since it is unlikely that all tying components would provide tying force at ultimate tensile strength when the rotation capacity of the system is reached. Nevertheless, the influence of strain-hardening can be considered via an appropriate reduction factor ρ, but with such reduction based on a small fraction of the increased strength beyond yield. On the other hand, the equivalent load P should be the factored load for accidental design situation as specified in relevant design codes.

In summary, the application of the proposed tying force method follows an assessment procedure where the loading, geometric and material details of the structural system are assumed to be known. Furthermore, the method also assumes that the surrounding structure offers sufficient resistance to the horizontal tying forces and that the affected system presents a minimum rotation capacity such that tying is effectively mobilised, the verification of which follows the procedure presented in Section 5.6.1. The dynamic amplification factor η is established according to Section 5.5. The adequacy of the affected floor system in bridging over the gravity loads is then assessed with (5.1), making use of the parameters derived in Sections 5.3 and 5.4. Finally, the adequacy of the surrounding structure in resisting the dynamically redistributed gravity loading can be checked according to Section 5.6.2.

Notwithstanding, despite an assessment procedure is to be followed, the proposed method can also be applied in design via a synthesis-assessment cycle, in which the assessment of an initial candidate design leads to the synthesis of an improved design candidate.

5.3 Tying via double-span beams

Consideration is given to the case where tying is provided via a double-span beam with negligible contribution from the floor slab. This applies for instance to precast reinforced concrete beams, where the slab panels lack planar continuity, or to other forms of construction where the main source of tying is from the beams.

Under the sudden loss of a column/load-bearing wall member, the dominant deformation of the double-span beam is assumed to follow a mechanism with three hinges, where deformation is concentrated, allowing for the cases of equal and unequal spans defined by the location of the internal hinge, as illustrated in Fig. 5.1.

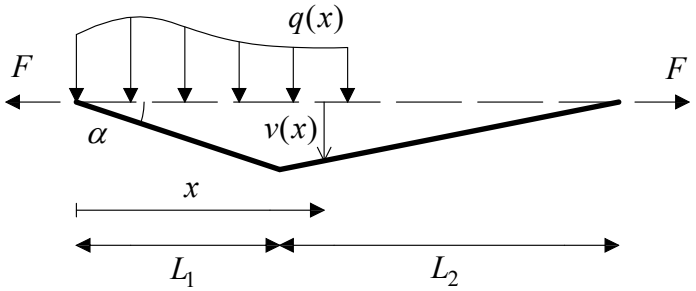


Fig. 5.1 – General case of tying via double-span beams

The relation between the tying force and the applied loading is derived based on discrete equilibrium, established in terms of equivalence between internal and external work in the deformed configuration:

$$\int_0^{L_1+L_2} F\,\delta\varepsilon(x)\,dx = \int_0^{L_1+L_2} q(x)\;\delta v(x)\,dx \tag{5.2}$$

where F is the tying force, and $q(x)$ is the distributed load per unit length. On the other hand, $v(x)$ is the transverse displacement and $\varepsilon(x)$ is the corresponding axial strain due to transverse displacements, as given by:

$$v(x) = \alpha\,\Phi(x), \quad \delta v(x) = \Phi(x)\,\delta\alpha, \quad \Phi(x) = \begin{cases} x & 0 \le x \le L_1 \\ \dfrac{L_1}{L_2}\left(L_1 + L_2 - x\right) & L_1 \le x \le L_1 + L_2 \end{cases} \tag{5.3}$$

$$\varepsilon(x) = \frac{1}{2}\left(\frac{\partial v(x)}{\partial x}\right)^2, \quad \delta\varepsilon(x) = \alpha\left(\frac{\partial \Phi(x)}{\partial x}\right)^2 \delta\alpha \tag{5.4}$$

in which α is the greater chord rotation at the end of L_1 span (assuming $L_1 \le L_2$). It is worth noting that the expression for $\varepsilon(x)$ is an approximation valid for the range of moderate displacements, as determined by ductility levels of typical forms of construction.

Combining (5.2)-(5.4), the equilibrium between the tying force and applied loads can be shown as:

$$T = \left(\frac{i_f}{\bar{\alpha}}\right) P, \qquad \bar{\alpha} = \frac{\alpha}{0.2} \quad (\alpha \text{ in rad}) \tag{5.5}$$

where T is an equivalent tying force corresponding to F, and P is an equivalent load corresponding to $q(x)$. It is worth noting that different types of loading (e.g. multiple concentrated loads with distributed load) can be easily combined via common principles of superposition in which the contributions of the different loading conditions to P are simply added up. It is also worth noting that for a given maximum chord rotation capacity of the double-span beam, the equilibrium condition in (5.5) becomes a lower bound on T, consistent with (5.1) which additionally accounts for dynamic effects via the amplification factor η. Table E.1 in Appendix E provides the intensity factor i_f, the equivalent tying force T and the equivalent load P for different loading conditions and for the symmetric/asymmetric double-

span configurations, with full details of the established values provided in Izzuddin and Sio (2022).

5.4 Tying via floor system

Consideration is given to the case where tying is provided via a floor system with distributed reinforcement and floor beams. Two scenarios are identified for such a case, specifically the development of two-way tying when the structure surrounding the affected floor system offers sufficient planar restraint in both directions, a scenario typically associated to an interior column loss, and the development of one-way tying when the surrounding structure offers sufficient planar restraint only in one of the directions, a scenario typically associated to a peripheral column loss.

5.4.1 Two-way tying

Under tensile catenary/membrane action, the affected floor system is assumed to follow a transverse deformed configuration described by a quadratic approximation in the two planar directions, as illustrated in Fig. 5.2.

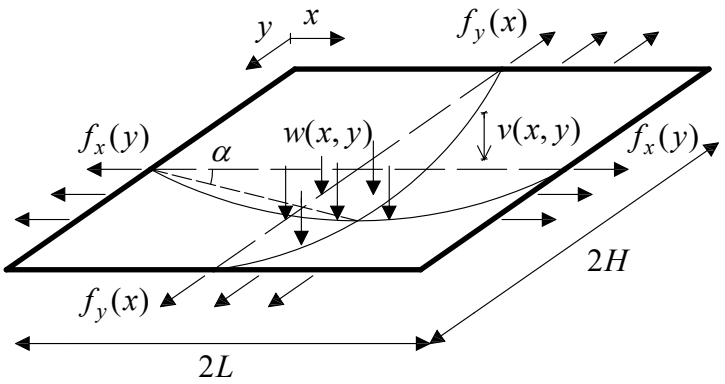


Fig. 5.2 – General case of tying via floor system: two-way tying

The equilibrium condition between the tying forces and the applied loading is again established in terms of equivalence between the internal and external work under the deformed configuration:

$$\int_0^{2H}\int_0^{2L} f_x(y)\ \delta\varepsilon_x(x,y)\,dxdy + \int_0^{2H}\int_0^{2L} f_y(x)\ \delta\varepsilon_y(x,y)\,dxdy = \int_0^{2H}\int_0^{2L} w(x,y)\ \delta v(x,y)dxdy \quad (5.6)$$

where $f_x(y)$ is the tying force acting in the x-direction per unit length along the y-direction, $f_y(x)$ is the tying force acting in the y-direction per unit length along the x-direction and

$w(x,y)$ is the distributed load per unit area. On the other hand, $v(x,y)$ is the transverse displacement, whilst $\varepsilon_x(x,y)$ and $\varepsilon_y(x,y)$ are the corresponding axial strains in the *x*-direction and *y*-direction, respectively, due to transverse displacements, as given for the case $(L \le H)$ by:

$$v(x,y) = \alpha\,\Phi(x,y), \quad \delta v(x,y) = \Phi(x,y)\,\delta\alpha, \quad \Phi(x,y) = x\left(2-\frac{x}{L}\right)\left(\frac{y}{H}\right)\left(2-\frac{y}{H}\right) \tag{5.7}$$

$$\varepsilon_x(x,y) = \frac{1}{2}\left(\frac{\partial v(x,y)}{\partial x}\right)^2, \quad \delta\varepsilon_x(x,y) = \alpha\left(\frac{\partial \Phi(x,y)}{\partial x}\right)^2 \delta\alpha \tag{5.8}$$

$$\varepsilon_y(x,y) = \frac{1}{2}\left(\frac{\partial v(x,y)}{\partial y}\right)^2, \quad \delta\varepsilon_y(x,y) = \alpha\left(\frac{\partial \Phi(x,y)}{\partial y}\right)^2 \delta\alpha \tag{5.9}$$

in which α is the chord rotation along the shorter L span (assuming here $L \le H$).

Combining (5.6)-(5.9), the equilibrium condition is again expressed consistently with (5.1) as:

$$T = \left(\frac{i_f}{\bar{\alpha}}\right)P, \quad \bar{\alpha} = \frac{\alpha}{0.2} \quad (\alpha \text{ in rad}) \tag{5.10}$$

where T is an equivalent tying force corresponding to $f_x(y)$ and $f_y(x)$, and P is an equivalent load corresponding to $w(x,y)$. Here again, different sources of tying and loading conditions can be easily combined by adding up its corresponding contributions to the equivalent tying force T and the equivalent load P, respectively. Table E.2 in Appendix E provides the intensity factor i_f, the equivalent tying force T and the equivalent load P for different sources of tying and load conditions, with full details of the established values provided in Izzuddin and Sio (2022).

5.4.2 One-way tying

The response derivation of one-way tying follows closely that of two-way tying, except that two alternative deformation modes are considered depending whether the peripheral edge of the affected system is restrained in torsion. The equilibrium between the tying forces and the applied loading can again be established with reference to Fig. 5.3 using the principle of virtual work.

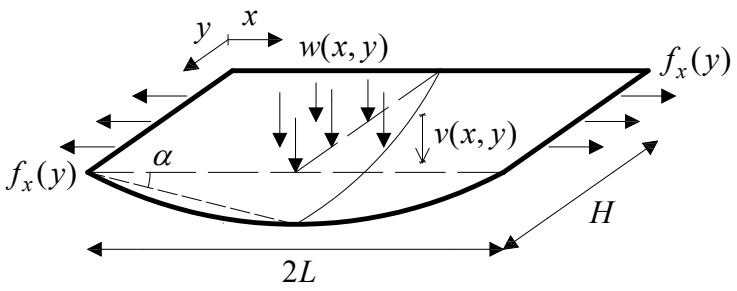


Fig. 5.3 – General case of tying via floor system: one-way tying

$$\int_0^H \int_0^{2L} f_x(y)\ \delta\varepsilon_x(x,y)\,dxdy = \int_0^H \int_0^{2L} w(x,y)\ \delta v(x,y)dxdy \tag{5.11}$$

with the individual terms as defined for the two-way tying scenario, noting the absence of the tying in the *y*-direction. It is also noted that the expressions for $v(x,y)$ and $\varepsilon_x(x,y)$ in (5.7) and (5.8), respectively, remain applicable, except that the deformation mode is adjusted to a linear variation in the *y*-direction for the case without torsional edge restraint:

$$\Phi(x,y) = \begin{cases} x\left(2-\dfrac{x}{L}\right)\left(\dfrac{y}{H}\right)\left(2-\dfrac{y}{H}\right) & \text{torsional edge restraint} \\ x\left(2-\dfrac{x}{L}\right)\left(\dfrac{y}{H}\right) & \text{no torsional edge restraint} \end{cases} \tag{5.12}$$

The ensuing equilibrium follows similar considerations previously discussed for two-way tying, with Table E.3 in Appendix E providing the intensity factor i_f, the equivalent tying force T for different tying sources, and the equivalent load P for various loading conditions.

5.5 Dynamic amplification

As noted before, the dynamic effect associated with the sudden loss of a column/load-bearing wall is encapsulated within the general formulation expressed in (5.1) via the amplification factor η:

$$\eta = \frac{P_s(\alpha)}{P_d} \tag{5.13}$$

where $P_s(\alpha)$ is the static resistance of the affected system as a function of chord rotation α, and P_d defines the dynamic resistance, so-called pseudo-static resistance (Izzuddin *et al.*, 2008; Izzuddin, 2010), as the average of the static resistance up to α.

$$P_d = \frac{1}{\alpha}\int_0^{\alpha} P_s(\alpha)\,\mathrm{d}\alpha \tag{5.14}$$

Equation (5.14) is established with the energy balance concept assuming a dominant deformation mode under the sudden loss of a vertical load bearing member.

It is worth noting that η is equal to 2 for a linear static response and may be reduced for nonlinear elasto-plastic systems depending on the ductility limit (Izzuddin, 2010). Considering the proposed tying approach, since the affected system would ultimately follow a linear static response, η would tend back to 2 subsequent to its initial reduction under the flexural elasto-plastic response of the system. This implies that $\eta = 2$ establishes an upper bound for the dynamic amplification, and thus can be conservatively assumed when the response preceding full tying action is unknown.

η can be further refined if the response preceding tying action is known. For the typical case involving an initial flexural response at lower levels of deflection/chord rotation, where the flexural resistance P_f is assumed to be achieved at relatively small deflections, as illustrated in Fig. 5.4, η can be shown for this case as (Izzuddin and Sio, 2022):

$$\eta = \frac{P_t}{P_d} = \begin{cases} \dfrac{2}{1+\lambda^2} & \text{if } \alpha_{min} \le \lambda\alpha \\ \dfrac{2}{1+\lambda^2 - \dfrac{1}{3}\left(\dfrac{\alpha_{min}}{\alpha} - \lambda\right)^2} & \text{if } \alpha_{min} > \lambda\alpha \end{cases} \tag{5.15}$$

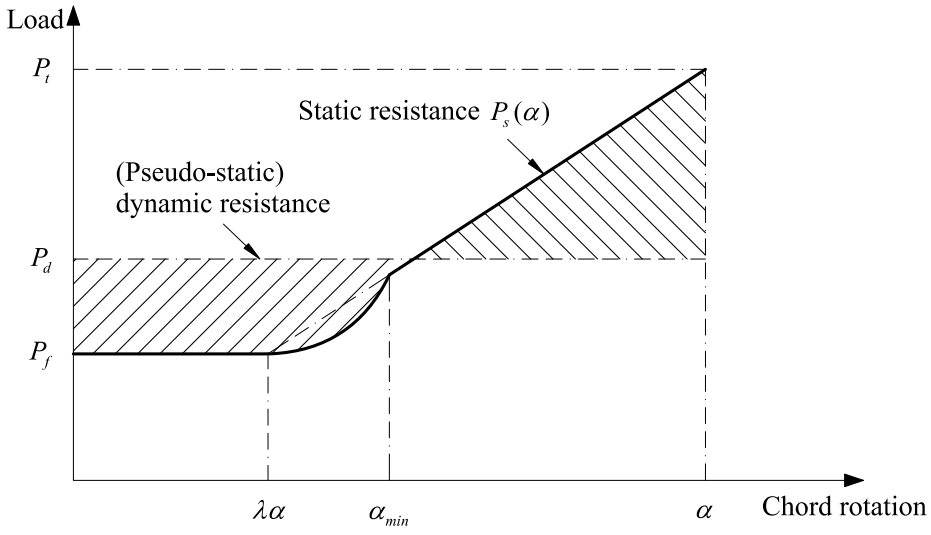


Fig. 5.4 – Development of flexural and tying resistance

In (5.15), α_{min} is the minimum chord rotation for full activation of tying, and λ represents the relative significance of flexural and tying resistance:

$$\lambda = \frac{\lambda_f}{\lambda_t} \tag{5.16}$$

where λ_f is the proportion of the total load that is resisted by flexural action:

$$\lambda_f = \frac{P_f}{P} \tag{5.17}$$

and λ_t is the proportion of the total load that is resisted by tying action under static conditions, which with reference to (5.1) is given by:

$$\lambda_t = \frac{P_t}{P} = \frac{(T\bar{\alpha})/(\rho i_f)}{P} \tag{5.18}$$

It is worth noting that if $\lambda_f \geq 1$ and assuming that the flexural resistance is achieved at relatively small deflections, the system under the sudden loss of a vertical load bearing member can resist the gravity loads fully through flexural resistance, hence not requiring horizontal tying.

5.6 Interaction with the surrounding structure

Consideration is given herein to the supplementary methods assessing the interaction of the affected system with the surrounding structure, specifically involving the requisite planar restraint stiffness for the mobilisation of full tying action and the amplification of redistributed gravity loading to the surrounding columns.

5.6.1 Planar interaction

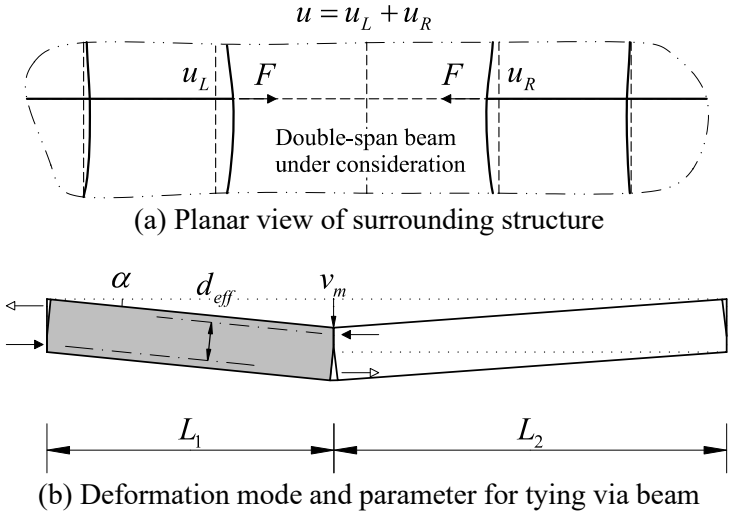
The development of horizontal tying depends on the planar restraint stiffness offered by the surrounding structure in the sense that a more flexible planar restraint leads to a higher chord rotation demand of the affected system before full tying action is mobilised.

5.6.1.1 Tying via beams

The interaction of a beam affected by the loss of a vertical load-bearing member with its surrounding structure can be shown, with reference to Fig. 5.5, to require the following condition for the full activation of tying (Izzuddin and Sio, 2022):

$$\frac{L_1}{2}\left(\alpha-\frac{d_{eff}}{L_1}\right)^2\left(1+\frac{L_1}{L_2}\right)\geq u+\delta \tag{5.19}$$

where α is the chord rotation determined as v_m/L_1; d_{eff} represents the distance over the cross-section between the centres of plastic rotation at the support and the interior hinges; u is the total pull-in of the surrounding structure; and δ is the elastic beam elongation.



(a) Planar view of surrounding structure

(b) Deformation mode and parameter for tying via beam

Fig. 5.5 – Interaction of tying beam with surrounding structure

Equation (5.19) is established considering that tying is fully mobilised when the incremental axial extension of the beam under the assumed deformation mode exceeds the plastic hinge extensions as well as the aggregate of the pull-in of the surrounding structure and the elastic beam elongation, both obtained under the full tying force F. Furthermore, (5.19) provides an upper bound on the pull-in of the surrounding structure at a specific level of chord rotation, where exceedance of this threshold implies that the planar restraint stiffness from the surrounding structure is insufficient to fully enable tying action at the considered chord rotation.

Alternatively, (5.19) can be re-written with respect to α as:

$$\alpha_{\min}=\frac{d_{eff}}{L_1}+\sqrt{\frac{2(u+\delta)}{L_1+L_2}\left(\frac{L_2}{L_1}\right)} \tag{5.20}$$

which for a specific level of pull-in (representative of the planar restraint stiffness from the surrounding structure) defines the minimum chord rotation that the affected double-span beam should undergo before activation of full tying forces. Accordingly, a less stiff planar restraint,

implied by a greater pull-in under the full tying force, would require an increased minimum chord rotation for the mobilisation of full tying forces.

5.6.1.2 Tying via floor system

The interaction of an affected floor system with the surrounding structure for the case of one-way tying (Fig. 5.3) can be shown to be governed by the following condition for the activation of tying (Izzuddin and Sio, 2022):

$$\left(\Delta = \alpha^2 L\right) \geq u_x + 4\varepsilon_y L \tag{5.21}$$

where u_x is the maximum pull-in of the surrounding structure in the *x*-direction at $y = H$ under the full tying forces. The above condition is established considering that full mobilisation of tying in the distributed reinforcement is achieved when the maximum strain exceeds twice the yield strain ε_y, allowing for the fact that the reinforcement strain varies over the floor system. The maximum reinforcement elongation is also conservatively established based on a bilinear deformation mode instead of the quadratic mode considered for the evaluation of tying resistance. Re-writing (5.21) with respect to u_x gives:

$$\left(\alpha^2 - 4\varepsilon_y\right) L \geq u_x \tag{5.22}$$

and can be further generalised to two-way tying (Fig. 5.2) as:

$$\left(\alpha^2 - 4\varepsilon_y\right) L \geq u_x, \quad \left(\left(\frac{L}{H}\right)^2 \alpha^2 - 4\varepsilon_y\right) H \geq u_y \tag{5.23}$$

Similar to tying via beams, (5.22) and (5.23) provide again an upper bound on the pull-in of the surrounding structure at a specific level of chord rotation. Finally, the corresponding conditions defining the minimum chord rotation for activation of full tying forces can be determined by re-writing the above expressions with respect to α, where this is expressed for one-way tying as:

$$\alpha_{\min} = \sqrt{\frac{u_x}{L} + 4\varepsilon_y} \tag{5.24}$$

and for two-way tying as:

$$\alpha_{\min} = \max\left(\sqrt{\frac{u_x}{L} + 4\varepsilon_y}, \frac{H}{L}\sqrt{\frac{u_y}{H} + 4\varepsilon_y} \right) \tag{5.25}$$

It is worth noting that further contribution to the planar restraint stiffness may be realised through compressive ring action, especially for the two-way tying scenario, though the neglect of such contribution would be conservative. This additional contribution is developed as an enhanced feature of the tying force method in Chapter 6.

5.6.2 Amplification of redistributed gravity loads

As noted in Section 5.5, the dynamic effects related to the affected system under the sudden loss of a vertical load-bearing member is encapsulated within the dynamic amplification factor η for the purpose of evaluating the maximum dynamic deformations. However, application of this amplification factor would be overconservative for the evaluation of the redistributed vertical loading to the surrounding structure, since the actual inertia forces follows a distribution that resembles more closely the governing deformation mode of the affected system, thus can differ from the distribution of the applied loading.

The amplification factor considered for the redistributed vertical loading can be derived based on work equivalence at the point of maximum dynamic displacement. Considering the case of a double-span beam subject to a distributed gravity load $q(x)$ (Fig. 5.1), at the maximum dynamic displacement, the static resistance exceeds the applied gravity loading, where the out-of-balance force $(\eta - 1)q(x)$ is effectively realised as inertia forces $m(x)a_m\Phi(x)$ responsible for the deceleration of the beam, with $m(x)$ representing the distributed mass which follows the same distribution as $q(x)$, a_m is an acceleration parameter, and $\Phi(x)$ is the governing deformation mode of the beam.

$$\int_0^{L_1+L_2} m(x)a_m\left(\Phi(x)\right)^2 dx = \int_0^{L_1+L_2} (\eta-1)q(x)\Phi(x)dx \Rightarrow a_m = \frac{\int_0^{L_1+L_2} (\eta-1)q(x)\Phi(x)dx}{\int_0^{L_1+L_2} m(x)\left(\Phi(x)\right)^2 dx} \tag{5.26}$$

The amplification of the redistributed gravity loading is then obtained by considering the inertia forces as follows:

$$\eta_L = \frac{\int_0^{L_1+L_2} \left[q(x) + m(x) a_m \Phi(x)\right] dx}{\int_0^{L_1+L_2} q(x) dx} \tag{5.27}$$

A similar approach is followed for the derivation of the amplification factors related to tying via floor system, where integration is performed over the (x, y) domain.

Tables E.4-E.6 in Appendix E provides the redistributed load amplification factors for typical loads considered for tying via beams and the floor system. It should be noted that the amplification factors are obtained for the single load that is dominant, under which its contribution to the equivalent load P is most significant. In this respect, amplification of other non-dominant loads is realised in an approximate way considering the amplification factor of the dominant load. Nevertheless, the redistributed amplification factor η_L can be refined for different loading conditions with comparable contribution to the equivalent load P again via determination of a_m and η_L respectively with (5.26) and (5.27). An alternative and practical approach is to define an equivalent η_L from the weighted average of the factors associated with each single loading condition, where the corresponding weight can be established based on the contribution of each loading condition to the total equivalent load P. Lastly, it is important to note that the amplification of redistributed loads should be considered only for the gravity loading directly applied to the affected double-span floor system.

5.7 Contributions additional to tying

For some forms of construction, the load resistance of the system under the loss of a column/load-bearing member can involve the activation of tying along with other sources of resistance above and beyond tying action based on pure tying forces, such as coexisting bending contributions, material strain hardening and the external resistance contribution from infill panels. As noted in Section 5.2, these additional resistance contributions can be indirectly reflected via the reduction factor ρ, thus allowing for a reduction in the required levels of tying forces.

The quantification of ρ can be either based on principles of mechanics or on a parametric study focused on specific forms of construction. As an illustration, the approach proposed by Izzuddin (2022) for quantifying ρ in the presence of a coexisting residual bending resistance in the catenary action stage is briefly presented herein. Consider tying via a beam in which the

maximum axial force F is governed by the middle joint in the double-span configuration, as illustrated in Fig. 5.6.

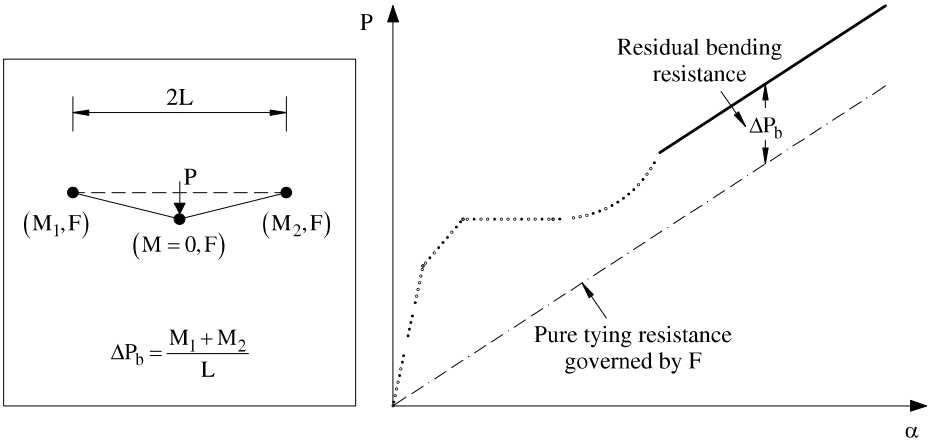


Fig. 5.6 – Influence of residual bending resistance in catenary stage (source: Izzuddin, 2022)

The bending moment in the middle joint would therefore vanish once the maximum axial force F is activated via catenary action. On the other hand, assuming that the end joints have a greater axial resistance, these can retain residual bending moments M_1 and M_2, respectively, at F. As such, the load resistance of the beam in the double-span configuration will comprise of the pure tying resistance along with a residual bending resistance ΔP_b determined as shown in Fig. 5.6. The reduction of the requisite tying resistance due to this residual bending resistance contribution can then be achieved via the reduction factor ρ, given for this example as:

$$\rho = 1 - \frac{\Delta P_b}{P} \tag{5.28}$$

5.8 Validation and verification

The proposed horizontal tying formulation along with its supplementary method are herein verified against nonlinear finite element analysis using ADAPTIC (Izzuddin, 1991). The applicability of ADAPTIC is first validated against an experimental test to demonstrate its validity for the considered verification. The proposed method is then verified for tying via beams and floor system.

5.8.1 Validation of numerical models for floor systems

The validation example considers specimen SE1 experimentally tested by Lu *et al.* (2017), which represents a peripheral reinforced concrete floor system subject to the loss of an edge

column. Fig. 5.7 illustrate the geometry of the floor system and the detailing of the reinforcement, where the thickness of the floor slab is 50mm and the cross-section of both the longitudinal and transverse beams measure 85mm in width and 170 mm in depth. The concrete cover for the floor slab and the beams is 5mm and 6mm, respectively. The rotational and planar restraints from the surrounding structure are realised via enlarged beams, which were shown to provide sufficient restraint stiffness for the mobilisation of compressive arching and tensile catenary actions (Lu *et al.*, 2017). Table 5.1 provides the material properties considered for the current verification, whilst the full details of specimen SE1 and the experimental testing procedure can be found in Lu *et al.* (2017).

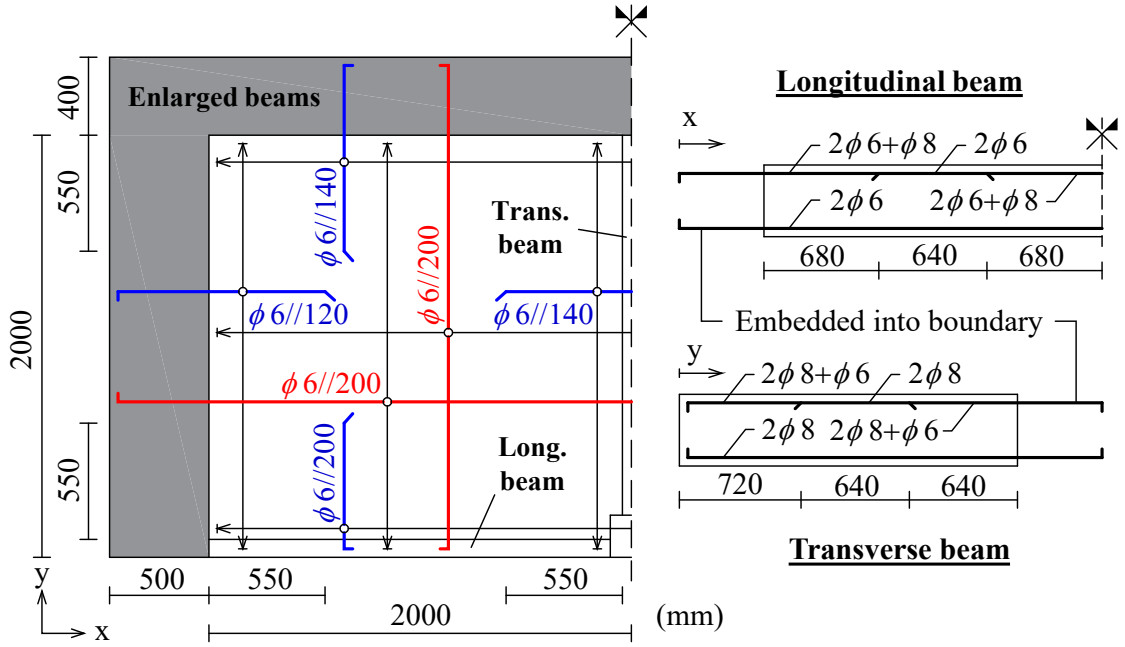


Fig. 5.7 – Geometry and detailing illustration of specimen SE1

Table 5.1 – Mechanical properties for the steel reinforcement and the concrete

Reinforcement properties (data from Lu *et al.*, 2017)

Diameter (mm)	Young's modulus (MPa)	Yield strength (MPa)	Ultimate strength (MPa)	Ultimate strain (-)
$\phi 6$	2.25×10^5	372	526	0.187
$\phi 8$	2.21×10^5	355	502	0.153

C30 concrete properties (mean compressive strength data from Lu *et al.*, 2017)

Stiffness modulus		Compressive properties		Tensile properties	
Initial (MPa)	Secant (MPa)	Mean strength (MPa)	Softening modulus (MPa)	Mean strength (MPa)	Softening modulus (MPa)
3.41×10^4	1.91×10^4	43	-1.50×10^2	1.00	-1.00×10^3

The corresponding numerical model of specimen SE1 is illustrated in Fig. 5.8, where the beams and the slab of the floor system are represented respectively via the cubic elasto-plastic beam element 'cbp3' (Izzuddin and Lloyd Smith, 2000; Izzuddin, 2016) and the enriched shell element 'csl4' (Izzuddin *et al.*, 2004). These elements account for the effects of geometric and material nonlinearity, hence they are suitable for modelling reinforced concrete floor systems under column loss scenarios. For the concrete response, the cubic elasto-plastic beam element employs a trilinear uniaxial model with tensile softening (Izzuddin, 2016), whereas the biaxial concrete model featured in Izzuddin *et al.* (2004) is considered for the shell element. For the steel response, both elements employ a uniaxial bilinear kinematic strain hardening model capped at the ultimate tensile strength.

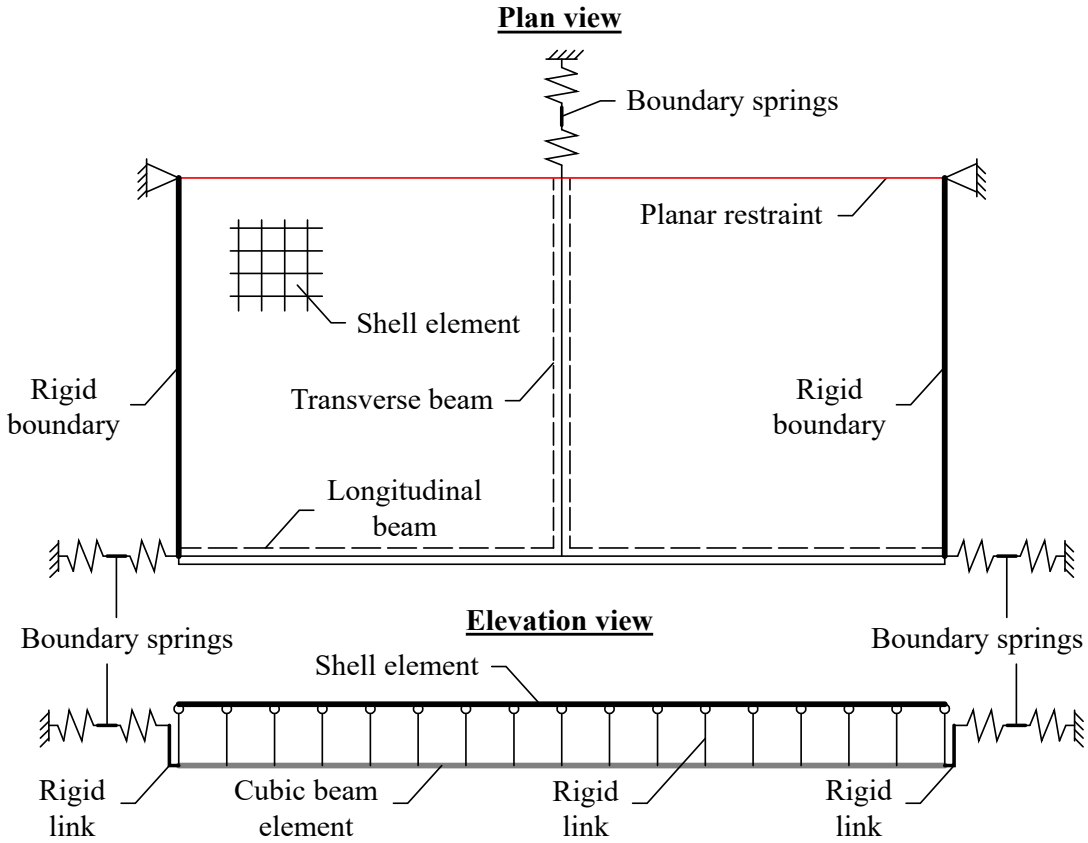


Fig. 5.8 – Schematic representation of the finite element model

The following assumptions are considered for the modelling of the boundary restraints, the reasoning of which is detailed in Izzuddin and Sio (2022):

- In the *y*-direction, the top border is simply restrained in plane along the mid-plane of the slab. However, elastic axial and rotational spring elements are defined for the transverse beam to allow for possible deformations at the beam support.

- In the *x*-direction, the two borders are assumed to exhibit a linear in-plane push-out/pull-in deformation, dependent on the restraint stiffness at the ends of the longitudinal beam.
- The restraints of the beams are applied at the geometric centroid of the equivalent T-section, which is considered to have a flange width equal to one-third of the corresponding slab development (i.e. 2/3m and 4/3m for the longitudinal and transverse beams, respectively). The additionally defined node at which the beam restraints are applied is then rigidly connected to the geometric centroid of the cubic elasto-plastic beam element via a rigid link, as illustrated in Fig. 5.8.
- Table 5.2 summarises the main boundary spring properties.

Table 5.2 – Main boundary spring properties

Boundary springs	Axial stiffness (N/mm)	Rotational stiffness (N.mm/rad)
Longitudinal beam (*x*-dir)	4.00×10^{5}	5.00×10^{9}
Transverse beam (*y*-dir)	4.00×10^{5}	5.00×10^{9}

Fig. 5.9 shows good agreement between the load-displacement response numerically predicted with ADAPTIC and the experimental response, thus demonstrating the applicability of ADAPTIC for the verification of the proposed horizontal tying method. The good agreement between numerical and experimental responses also suggests that the considered assumptions for the representation of the boundary restraints are reasonable.

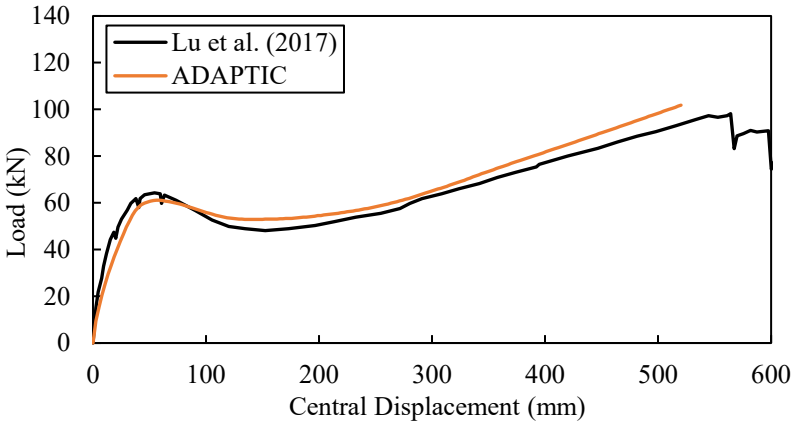


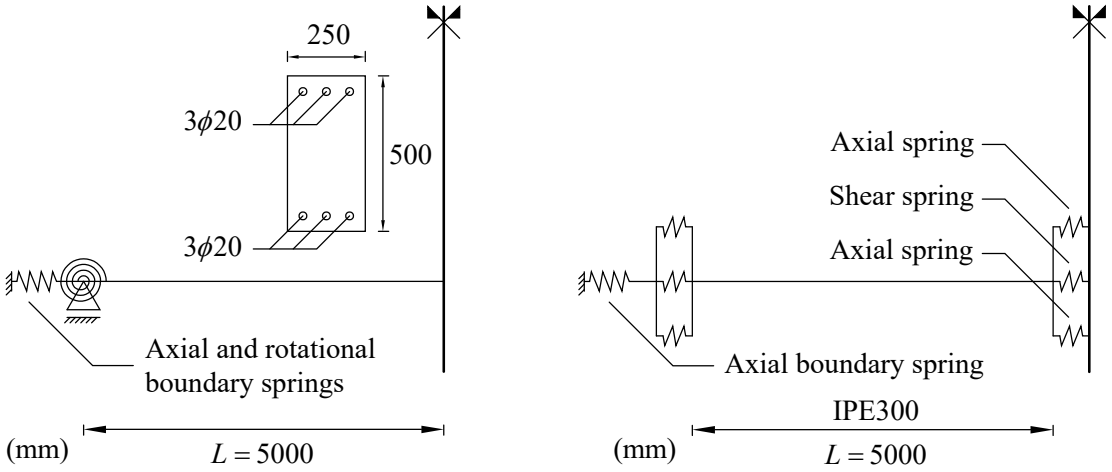
Fig. 5.9 – Validation of static response under concentrated load condition

5.8.2 Verification of tying via beams

Consideration is given herein to the verification of tying via beams with both reinforced concrete (RC) and steel beam examples. Verification proceeds with the consideration of the

static tying response, the minimum chord rotation for the activation of tying, the dynamic amplification of the loading response, and the amplification of the redistributed gravity loading.

Fig. 5.10 illustrates the typical geometry and reinforcement detailing of the RC and steel beam examples, whilst Tables 5.3 and 5.4 provide the corresponding material properties.



(a) Reinforced concrete beam (b) Steel beam

Fig. 5.10 – Typical geometry and reinforcement detailing of beam examples

Table 5.3 – RC beam properties

Mean concrete strength, f_{cm} (C30/37)	38 MPa
Concrete modulus, E_c	32837 MPa
Concrete section area, A_c	125000 mm^2
Continuous reinforcement (Top – $3\phi20$, Bottom – $3\phi20$), A_y	1884.94 mm^2
Steel strength (A500), f_y	500 MPa
Steel modulus, E_y	200000 MPa
Axial stiffness of RC beam (single span), $K_{a,1}^{RC} = E_c A_c / L$	8.21×10^5 N/mm
Axial stiffness of the reinforcement (single span), $K_{a,2}^{RC} = E_y A_y / L$	7.54×10^4 N/mm
Bending moment resistance of RC beam, M_{pl}^{RC}	2.23×10^8 N.mm

Table 5.4 – Steel beam properties

Steel strength (S355), f_s	355 MPa
Steel modulus, E_s	210000 MPa
IPE300 cross-section area, A_s	5188.06 mm^2
Axial stiffness of steel beam (single span), $K_a^{STL} = E_s A_s / L$	2.18×10^5 N/mm
Axial force resistance of the steel beam, N_{pl}^{STL}	1.84×10^6 N
Bending moment resistance of the steel beam, M_{pl}^{STL}	2.23×10^8 N.mm

The RC beam examples include elastic axial and rotational springs at the beam ends to simulate different boundary restraint conditions, whereas the ends of the steel beam examples are rigidly restrained in rotation, hence only allowing for axial flexibility from the surrounding structure. However, the steel beam examples further include idealised connections, simplified as two axial springs representing joint components connected with rigid links according to the representation illustrated in Fig. 5.10b. A rigid shear spring is also defined at the centre of the idealised connection, rendering the connection rigid in shear. An elastic-perfectly plastic relationship is assumed for the top and bottom axial springs, which resistance and the stiffness are defined based on the following:

$$\begin{aligned} F_{sprg} &= 0.5N' \\ K_{sprg} &= 0.5K'_a \end{aligned} \tag{5.29}$$

where N' and K'_a are the axial resistance and stiffness of the connection and are assumed as a percentage of the axial resistance and stiffness of the steel beam, respectively. Assuming equal ratios of connection to beam resistances for both axial force and bending moment, the distance between top and bottom axial springs of the connection can be shown as:

$$h = \frac{2M_{pl}^{STL}}{N_{pl}^{STL}} \tag{5.30}$$

A total of 3 and 4 verification cases are respectively conceived for the RC and steel beam examples, involving different boundary restraint stiffness and, specifically for the latter beam examples, different connection stiffness and resistances according to Tables 5.5 and 5.6. On the other hand, the application of the proposed tying method involves the following considerations:

- For the RC beam example, only the continuous reinforcement over the whole beam span contributes to the tying resistance, with steel stresses limited as the yield strength.
- For the steel beam example, tying resistance is limited by the lowest of the beam and connection resistances.
- In the determination of the minimum chord rotation for activation of tying as per (5.20), δ is the elastic elongation of the continuous reinforcement in the RC beam example, and the aggregate elongation from the beam and the connections of the steel beam example, determined based on the considered tying force. The pull-in u is established as the displacement of the axial boundary springs also under the considered tying force.

Lastly, the effective depth d_{eff} is defined as the distance between the top and bottom reinforcements in the RC beam example and as h in the steel beam example. The effective depth is halved for the cases with a pinned support at the ends of the double-span beam.

- In the determination of the amplification factor η as per (5.15)-(5.18), the load proportion resisted by flexural action λ_f is determined based on plastic limit analysis, assuming the same mechanism with three hinges as in tying. Accordingly, for the cases where the ends of the double-span beam are rotationally restrained, λ_f can be shown expressed as:

$$\lambda_f = \frac{4M_{pl}}{PL} \quad \text{with} \quad P = \begin{cases} Q & \text{concetrated load } Q \\ qL & \text{uniformly distributed load } q \end{cases} \tag{5.31}$$

where M_{pl} is the bending moment resistance of the RC beam or the minimum of resistances between the steel beam and the connections, and L is the span, as illustrated in Fig. 5.10. Otherwise, λ_f is halved for the cases where the ends of the double-span beam are pinned.

Table 5.5 – Verification cases for RC beam example

Case	Rotational boundary spring stiffness	Axial boundary spring stiffness
RC1	Rigid	100% of $K_{a,1}^{RC}$
RC2	Rigid	10% of $K_{a,1}^{RC}$
RC3	Pinned	100% of $K_{a,1}^{RC}$

Table 5.6 – Verification cases for steel beam example

Case	Axial boundary spring stiffness	Connection resistance, N'	Axial stiffness of the connection, K_a'
STL1	Rigid	50% of N_{pl}^{STL}	Rigid (3000% of K_a^{STL})
STL2	Rigid	50% of N_{pl}^{STL}	100% of K_a^{STL}
STL3	Rigid	50% of N_{pl}^{STL}	50% of K_a^{STL}
STL4	10% of K_a^{STL}	50% of N_{pl}^{STL}	Rigid (3000% of K_a^{STL})

The outcomes of the considered verification are illustrated in Fig. 5.11, noting that the central displacement is simply αL.

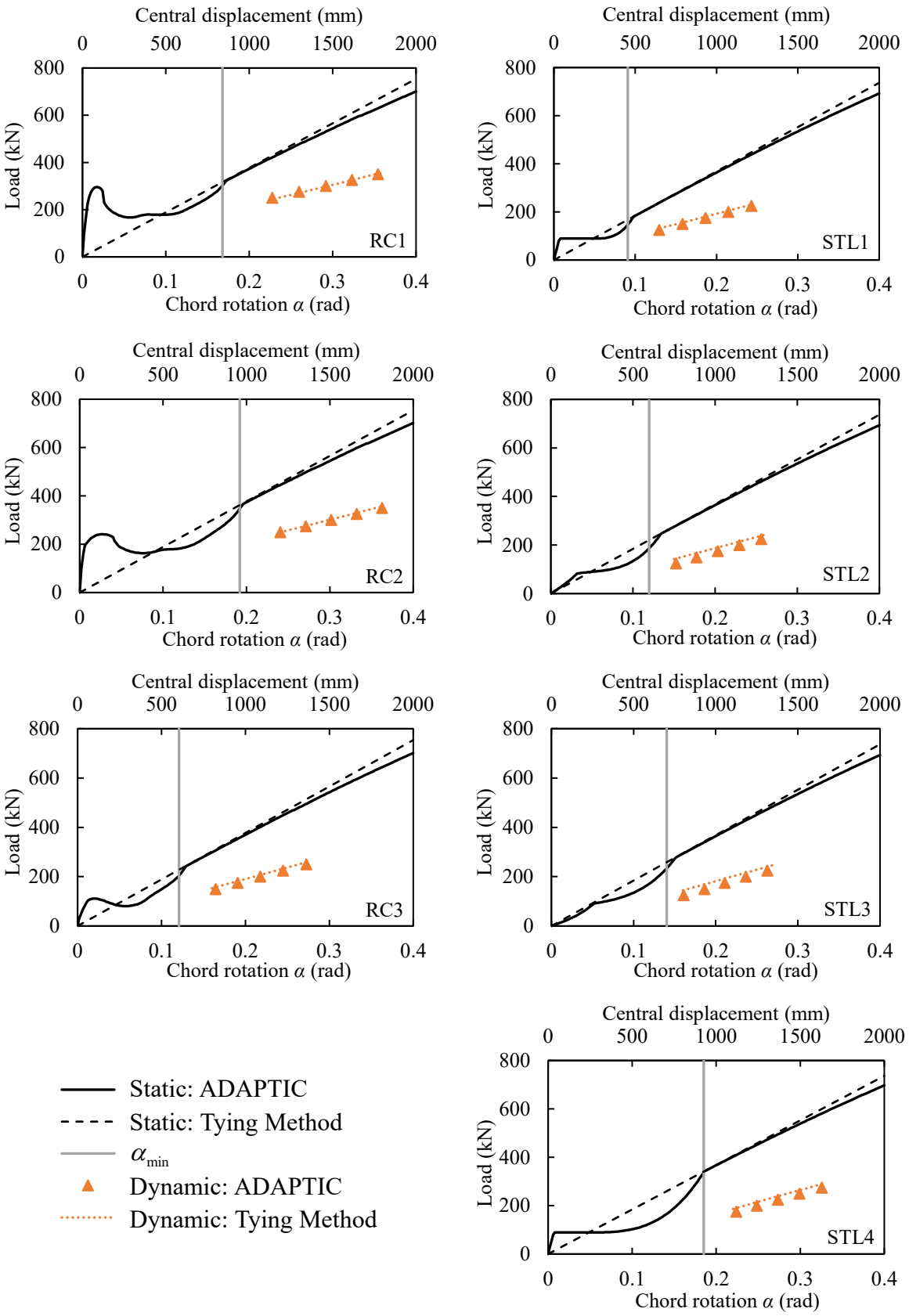


Fig. 5.11 – Static and dynamic responses of the beam examples under concentrated loading

Static tying response. The proposed tying method predicts the static tying response of all verification cases with satisfactory accuracy, in which a very good fit between numerical and predicted responses is achieved at the activation of tying. The predicted response then slightly overestimates the numerical response with increasing chord rotations due to large displacement considerations in the numerical response, which are neglected in the proposed method.

Minimum chord rotation for the activation of tying. A good fit between numerical and predicted $\alpha_{\min}$ is also achieved, hence demonstrating the effectiveness of the proposed method in representing the influence of the boundary restraints (encapsulated in the pull-in displacement u and the effective depth d_{eff}) and the deformation of the beam components (represented by δ) in the minimum chord rotation for the activation of tying. Specifically, the activation of tying is delayed for the cases with a less stiff planar restraint and involving additional deformable components such as the connections in the steel beam example, whereas the consideration of a pinned support condition at the ends of the double-span beam, represented by halving the effective depth, expedites the activation of tying.

Dynamic response and amplification factor. Verification of the dynamic response is undertaken at five discrete chord rotation levels, established from the maximum dynamic displacement of the numerical response under five discrete load levels. The predictions of the proposed method compare again very well against the numerical responses. Notwithstanding, the proposed method generally overestimates the dynamic resistance of the beam examples, specifically for the verification cases of STL2 and STL3. This overestimation can be explained by the fact that the actual flexural response of the beam examples at lower levels of chord rotation is characterised by a finite initial stiffness, hence slightly differing from the rigid assumption considered for the determination of η (see Fig. 5.4). In this respect, the discrepancy between predicted and numerical responses increases for beam examples exhibiting a less stiff initial flexural response, as observed in the cases of STL2 and STL3.

Redistribution of vertical gravity loads. The amplification factor predicted by the proposed method, as given in Table E.4 in Appendix E, is compared to the numerical amplification factor, which is determined as the ratio of maximum dynamic to static vertical reaction forces. In addition to the verification cases under concentrated loading applied at the mid-span of the beam examples (CL), two cases using RC1 and STL1 are presented to assess the amplification factor proposed for uniform distributed loading (UDL). Fig. 5.12 demonstrate a general good agreement between numerical and predicted amplification factors, noting that load levels are

reported in terms of equivalent load P. The minor discrepancies between numerical and predicted outcomes, which are most significant in STL2, can be correlated to the differences highlighted for the dynamic response.

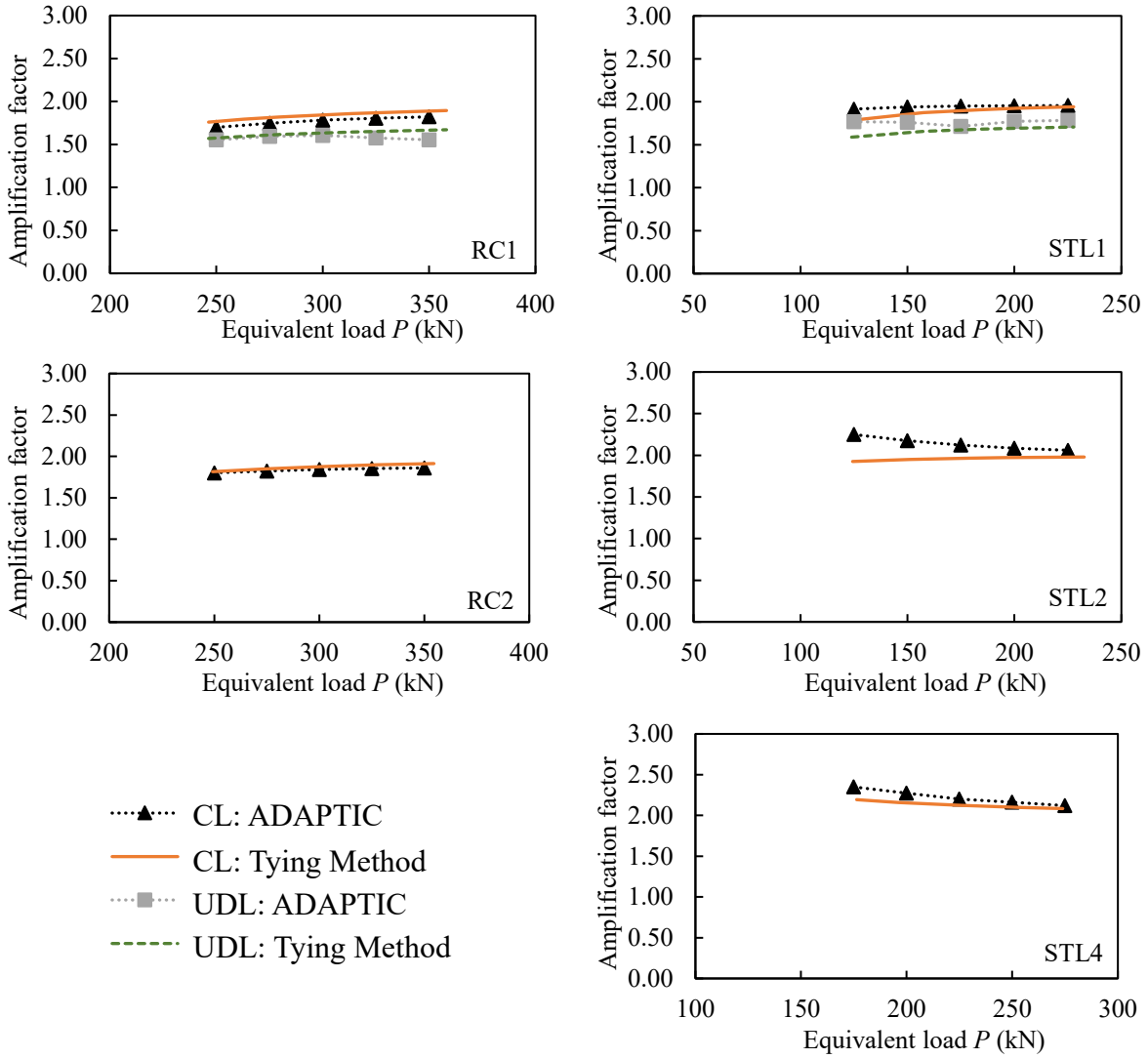


Fig. 5.12 – Redistribution of vertical gravity loads of the beam examples

5.8.3 Verification of tying via floor system

Verification of tying via floor system proceeds with the numerical model presented in Section 5.8.1, which is herein termed as initial model. This initial model is progressively modified to match four target responses predicted by the proposed method, thereby highlighting the underlaying assumptions of the method. The four target responses generated with the proposed method represent the tying response of the following scenarios: (i) beam-slab system with edge torsional restraint and subject to an applied concentrated load (CL); (ii) same as scenario (i) but subject to a uniformly distributed load (UDL); (iii) slab-only system with edge torsional

restraint and under UDL; (iv) same as scenario (iii) but without edge torsional restraint. These four tying response scenarios, respectively termed as TM1 to TM4 with reference to the proposed tying method, consider the tying resistance to be provided by the continuous reinforcement only, with the steel stress limited to the yield strength.

The modification of the initial model follows the scheme presented in Table 5.7, with the resulting models respectively termed as NM1 to NM4.

Table 5.7 – Model modification scheme

Loading condition	Case model	Reference model	Applied model modifications
Concentrated load (CL)	NM1a	Initial model	No offset between beam and slab centroids
	NM1b	NM1a	Concrete material set to linear elastic with $E_c = 1.0$ MPa ; removal of the transverse beam; prescription of displacements to match the deformation mode of a floor system with edge torsional restraint
	NM1c	NM1b	Removal of the curtailed reinforcement of the longitudinal beam; neglect of strain hardening for all reinforcement
Uniformly distributed load (UDL)	NM2	NM1c	Loading condition changed to UDL; removal of the curtailed slab reinforcement in the longitudinal direction
	NM3	NM2	Removal of the longitudinal beam
	NM4	NM3	Prescription of displacements to match the deformation mode of a floor system without edge torsional restraint

It is worth noting the need to prescribe the deformation modes considered for the proposed method when modifying the concrete material model to linear elastic with a significantly reduced stiffness, which intention is to focus only on the load resistance of the floor system that is realised via tying. Such a material assumption can lead to unrealistic deformation modes, associated to the overactivation of tying forces, since the concrete in compression, which is crucial for the geometric restraint of the floor system, is also neglected. Indeed, the contribution of the concrete in compression is not negligible, imposing deformation modes similar to those considered in the proposed method.

Figs. 5.13 and 5.14 demonstrate a general good agreement between the numerical responses of NM1 to NM4 and the predicted responses of TM1 to TM4 following the successive model modifications implemented according to Table 5.7. Considering that the main aim of such

modifications is to exclude additional contributions to tying (e.g. flexural resistance contributions from the concrete, the curtailed reinforcement and the transverse beam), it can be concluded that the proposed tying method predicts quite well the load resistance of the floor system that is exclusively associated with tying action. Indeed, any additional flexural contribution to the load resistance of the floor system cause in principle a parallel shift of the linear response within the tensile catenary/membrane action stage without changing its slope. This is clearly evidenced by comparing the responses of the initial model and scenario TM1.

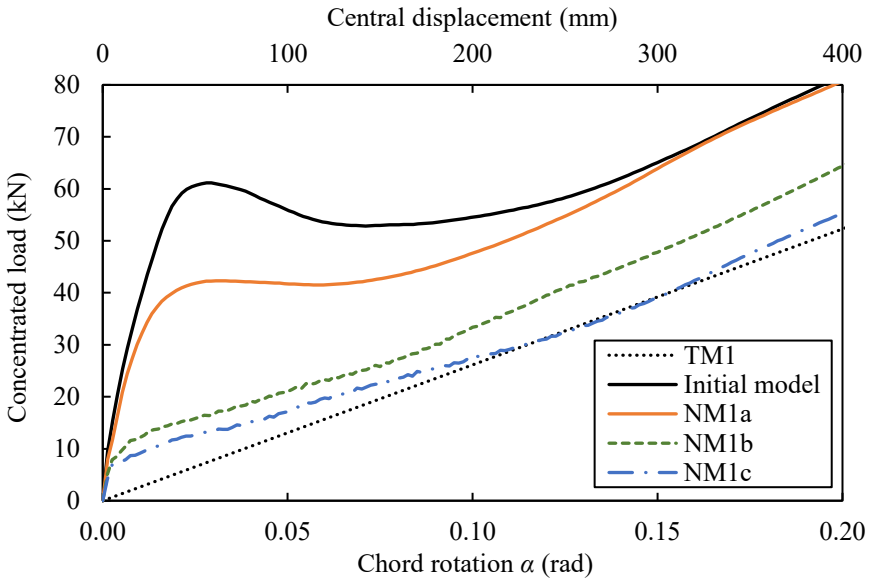


Fig. 5.13 – Static response of case models under applied concentrated load

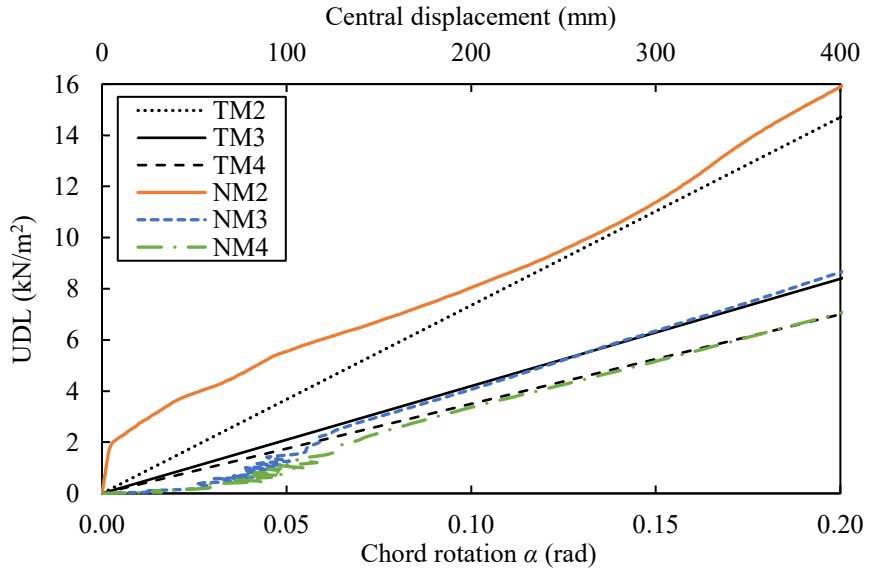


Fig. 5.14 – Static response of case models under applied uniformly distributed load

Another conclusion is that the development of strain hardening, manifested as a progressive increase in the rate of tying resistance gain with chord rotation, is limited under deformations up to typical chord rotation capacity levels (usually around 0.2rad). This can be again demonstrated by the similar load-displacement response slopes of the initial model and scenario TM1. In this respect, neglecting strain hardening in the proposed method is not only conservative but can be deemed appropriate. Notwithstanding, as discussed in Section 5.2, the effects of strain hardening can be considered via an appropriate reduction factor ρ in (5.1).

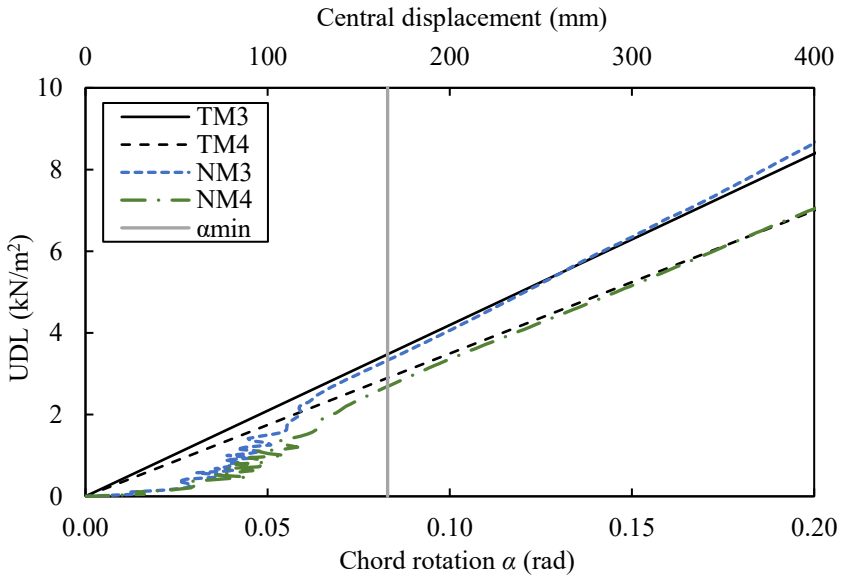
Consideration is next given to the verification of the minimum chord rotation for the activation of tying, the dynamic response and the amplification of redistributed gravity loads, where similar to tying via beams the following considerations are undertaken for the application of the supplementary methods:

- In the determination of $\alpha_{\min}$ as per (5.20) and (5.24) respectively for the longitudinal beam and the floor slab, the pull-in displacement u, measured at the ends of the peripheral edge of the floor system, is determined based on the aggregate tying resistance from the beam reinforcement and the distributed reinforcement of the floor slab.
- In the determination of the amplification factor η as per (5.15)-(5.18), the load proportion resisted by flexural action λ_f is determined based on yield line and plastic limit analysis assuming that the floor system follows a flexural mechanism involving the rotation of rigid plates and that the borders of the system which are shared with the surrounding structure are rotationally restrained.

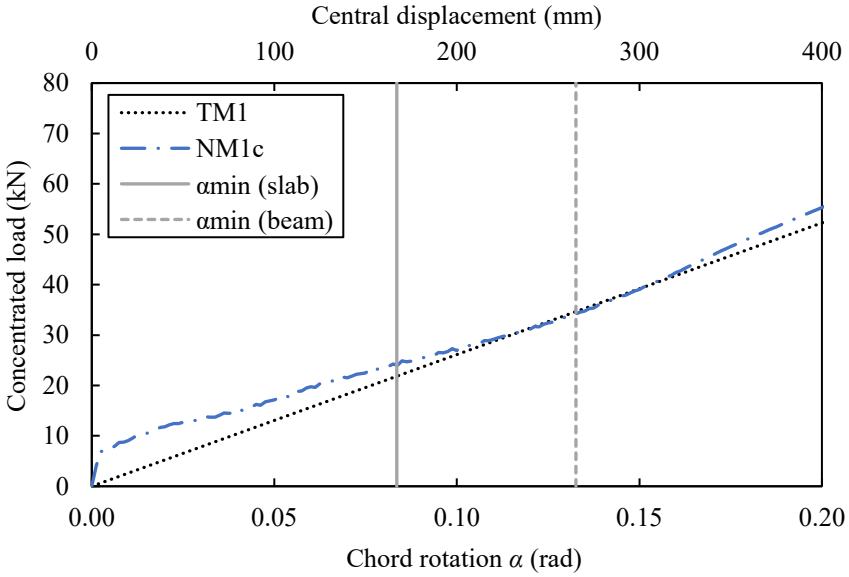
Minimum chord rotation for the activation of tying. The threshold proposed for slab-only systems (e.g. NM3 and NM4), determined according to (5.24), defines quite well the onset of tensile membrane action, independently of the condition of torsional restraint along the peripheral edge (Fig. 5.15a). Furthermore, since $\alpha_{\min}$ is slightly overestimated, the proposed threshold can be deemed conservative.

It is worth noting though that the sole application of (5.24) may not be sufficient to provide an accurate prediction on the activation of full tying forces within a beam-slab system, as demonstrated in Fig. 5.15b. This is because (5.24) only determines the onset of tensile membrane action within the slab. Tying of the beam reinforcement may not be fully activated at the chord rotation estimated with (5.24) due to a more significant presence of initial flexural

response within the beam, reflected via the effective depth d_{eff} in (5.20). Such presence of initial flexural response delays the activation of tying for the beam reinforcement.



(a) Slab-only systems



(b) Beam-slab systems

Fig. 5.15 – Verification of minimum chord rotation for the activation of tying

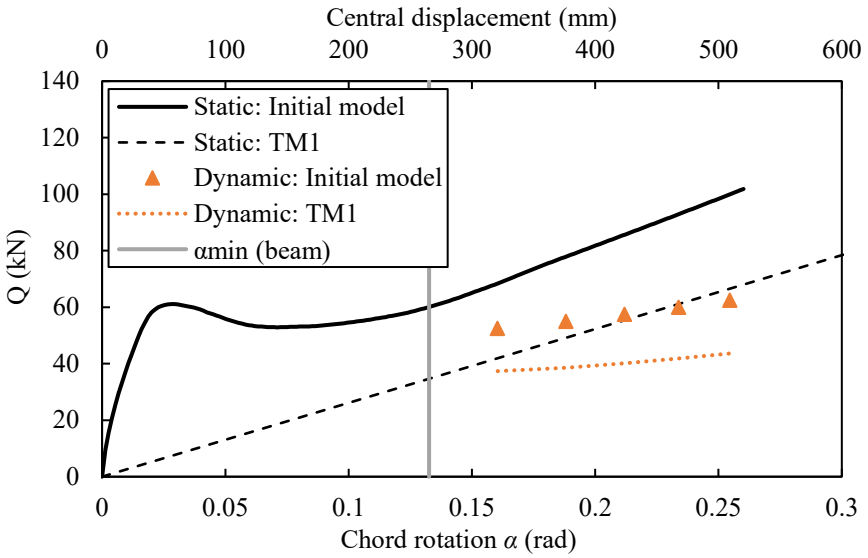
Indeed, comparing the numerical response of model NM1c to the minimum thresholds proposed for slabs and for beams (Fig. 5.15b), it can be seen that the onset of tensile catenary/membrane action of the beam-slab system occurs somewhere between these two thresholds, with the minimum chord rotation proposed for beams providing a more

conservative estimate in this case. It is therefore recommended for beam-slab systems that the minimum chord rotation for the activation of tying should be established as the maximum value of the two thresholds, thus ensuring that full tying action is mobilised once the chord rotation of the system surpasses the established value.

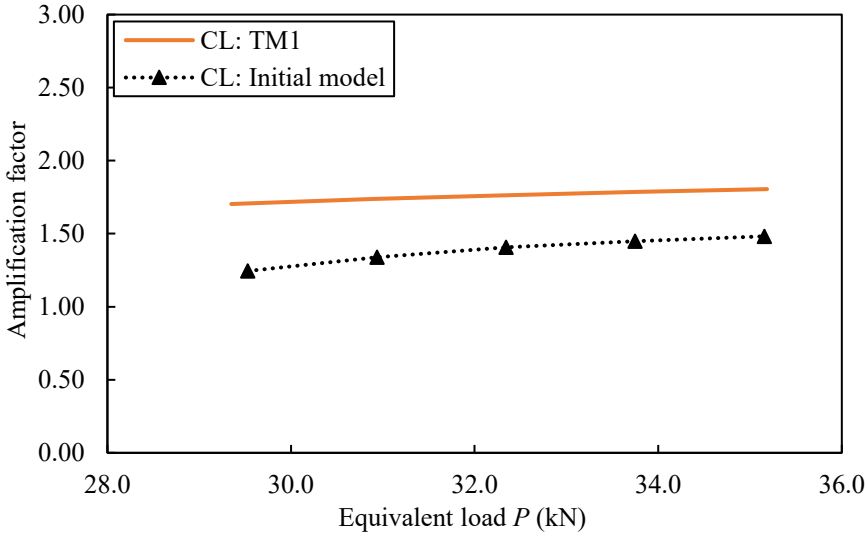
Dynamic response and amplification of redistributed gravity loads. Similar to the verification of tying via beams, the assessment of the dynamic response is again compared at five chord rotation levels, respectively established from the maximum dynamic displacement of the numerical response under five discrete load levels. On the other hand, the amplification of redistributed gravity loads is directly verified at the five discrete load levels, expressed in terms of equivalent load P.

Fig. 5.16a compares the dynamic response of the initial numerical model to the prediction of scenario TM1, noting that the static response of scenario TM1 only reflects the load resistance of the system that is exclusively associated to tying. Thus, the proposed method underestimates the dynamic resistance of the floor system, the difference of which is due to the previously discussed additional flexural contributions to the static response of the system as well as the amplification factor η, which differs from the value determined via (5.15)-(5.18) as a result of such flexural contributions. Though, an improved η can be established as per (5.13)-(5.14) considering a refinement of the static response illustrated in Fig. 5.4. Nonetheless, an improved agreement between the numerical and predicted dynamic responses is expected if the predicted response of scenario TM1 is compared to the numerical response of model NM1c, which excludes all additional flexural contributions to the load resistance of the system.

Fig. 5.16b assesses the amplification of the distributed gravity loads, where the proposed factor, determined according to the concentrated load case of Table E.6 in Appendix E, overestimates the actual amplification. It is worth noting that, given the significant difference in the dynamic responses, the chord rotations associated to the predicted amplification factors η_L are much higher than those defined for the assessment of the dynamic response η, as the verification of η_L proceeds at comparable levels of equivalent load P instead. It is also worth noting that such a conservative outcome (i.e. higher redistributed forces to the surrounding structure) may not be generalised since it depends on the amplification factor predicted for the dynamic response η, which as previously mentioned may not be appropriate for the current verification.



(a) Dynamic response

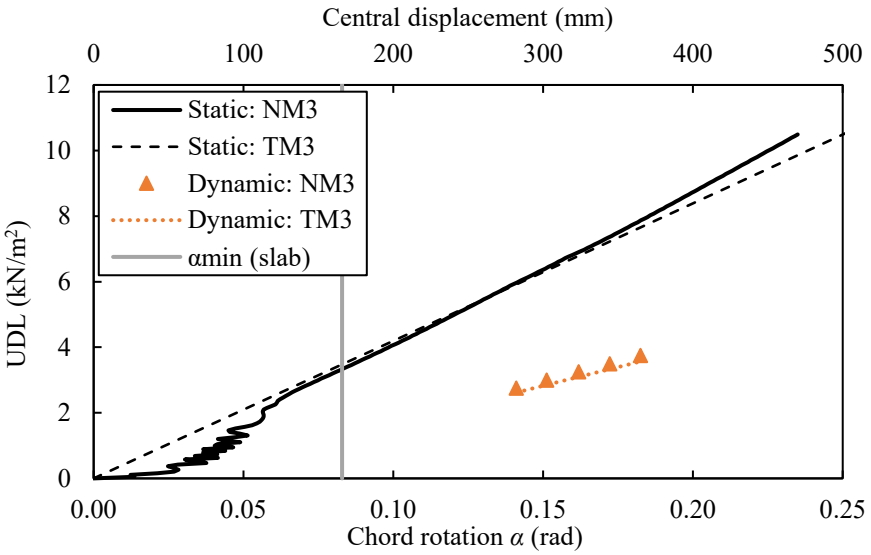


(b) Amplification of redistributed gravity loads

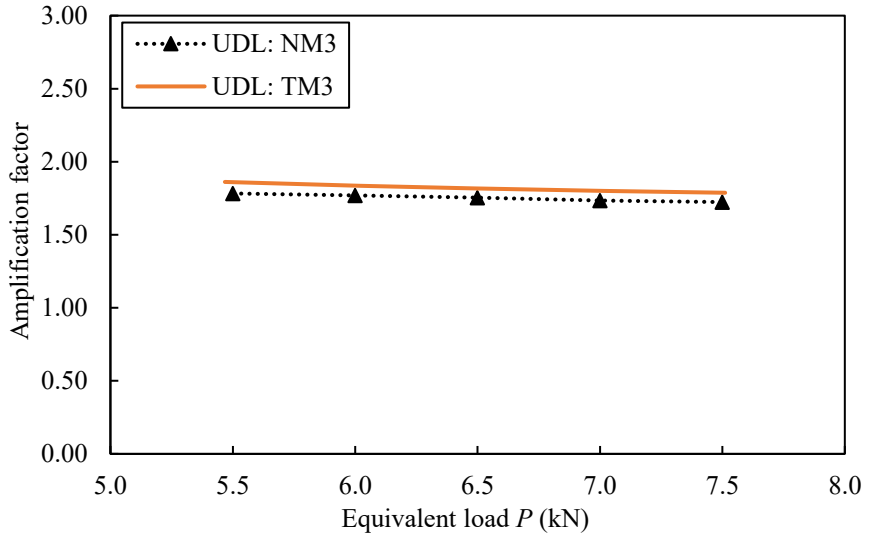
Fig. 5.16 – Verification with initial model under applied concentrated load

A more fitting verification of the dynamic response and amplification of redistributed gravity loads for tying via floor systems is considered with the numerical model NM3, which follows the considerations defined for scenario TM3, i.e. tying resistance of a slab-only system with edge torsional restraint and under uniformly distributed load. Since model NM3 excludes the contribution of the concrete, the resulting response presents negligible flexural resistance at relatively small chord rotations. In this respect, the determination of the amplification factor η assumes that the total load of the system is entirely resisted via tying action, leading to $\lambda = 0$. Lastly, the amplification of the redistributed gravity loads is determined according to the

uniformly distributed load case of Table E.6 in Appendix E. Fig. 5.17 illustrate the considered verification for the dynamic response and the amplification of redistributed gravity loads, where a very good agreement is achieved between numerical and predicted responses.



(a) Dynamic response



(b) Amplification of redistributed gravity loads

Fig. 5.17 – Verification with model NM3 under uniformly distributed load

5.9 Validation against experimental tests

Consideration is herein given to the validation of the proposed tying method against experimental tests, performed in collaboration with Ravasini *et al.* (2021). Whilst the full details on experimental data collection and general validation are provided in Ravasini *et al.*

(2021), the validation presented in this section focuses on the effectiveness of the method in predicting the tying response of reinforced concrete sub-systems involving the fracture of the reinforcement. The validation considers the following assumptions:

- Only experimental specimens meeting the requirements for activation of tying are assessed, i.e. specimens with sufficient planar restraint from the surrounding structure and adequate chord rotation capacity for the mobilisation of tying. This therefore excludes beam/floor systems under the loss of a corner or penultimate column.
- The reinforcement anchorages and lap-splices of the experimental specimens should provide an axial resistance higher than the ultimate axial resistance from the reinforcement so as to prevent reinforcement pull-out and to ensure reinforcement continuity under tying action.
- The proposed method is validated under static loading condition and considering pure tying action, thus excluding any dynamic effects and additional resistance contributions. Accordingly, the parameters ρ and η are considered as 1.
- The evaluation of the tying resistance according to the general formulation of (5.1) considers only the reinforcement that is continuous throughout the beam/floor system, along with the reinforcement stress limited to the yield strength.
- The experimental and predicted resistances of the beam/floor system are compared at the defined chord rotation capacity of the specimens rather than at 0.2rad as assumed in Ravasini *et al.* (2021).

5.9.1 Tying via beams

Two case scenarios are predicted for the tying response of the experimental beams, the first case involving the contribution of all continuous reinforcement to tying (TM wo/fracture) and the second case involving only the continuous reinforcement which has not fractured at the chord rotation capacity of the experimental beams (TM w/fracture). Table 5.8 presents the chord rotation capacity, the corresponding load resistance and the status of reinforcement fracture of selected beam specimens, along with the prediction of the two considered case scenarios, whilst Table E.7 in Appendix E lists the geometry, quantity of continuous reinforcement and steel strength of the selected specimens.

Table 5.8 – Validation of tying via beams against experimental tests

Specimen		Experimental data				TM wo/fracture		TM w/fracture	
		Δf,exp (mm)	θf,exp (rad)	Pf,exp (kN)	Remaining bars at θf	Pf,est (kN)	Ratio	Pf,est (kN)	Ratio
Qian *et al.* (2014)	P1	361.00	0.190	47.00	Top	52.17	1.11	26.08	0.55
	P2	291.00	0.224	59.00	Top	61.46	1.04	30.73	0.52
Lim *et al.* (2017b)	FR	547.00	0.246	70.90	Top	78.49	1.11	39.25	0.55
	FR-S	526.00	0.237	65.00	Top	75.48	1.16	37.74	0.58
	FR-R	555.00	0.250	76.00	All	72.88	0.96	72.88	0.96
Ren *et al.* (2016)	B2	421.00	0.222	58.00	All	34.75	0.60	34.75	0.60
	B3	413.00	0.217	42.00	All	34.09	0.81	34.09	0.81
	S2	467.9	0.246	93.00	All	58.05	0.62	58.05	0.62
	S3	536.79	0.283	181.00	All	109.39	0.6	109.39	0.6
	S4	551.25	0.290	164.00	All	134.28	0.82	134.28	0.82
	S5	530.84	0.279	186.00	All	108.18	0.58	108.18	0.58
	S6	567.88	0.299	140.00	All	115.72	0.83	115.72	0.83
Yu and Tan (2017)	F1-NS	467.50	0.170	46.27	Top	87.55	1.89	43.78	0.95
	F2-WS	526.00	0.191	43.46	Top	98.51	2.27	49.25	1.13
Yu and Tan (2012, 2013a)	S1	573.00	0.208	69.40	Top	66.90	0.96	33.45	0.48
	S2	605.00	0.220	67.40	Top	70.64	1.05	35.32	0.52
	S3	728.00	0.265	125.70	Top	110.52	0.88	69.43	0.55
	S4	614.00	0.223	104.84	Top	117.12	1.12	58.56	0.56
	S5	665.00	0.242	105.60	Top	158.56	1.50	63.42	0.60
	S6	578.00	0.210	142.00	Top	138.63	0.98	83.50	0.59
	S7	623.50	0.290	108.90	Top	152.12	1.40	76.06	0.70
Lew *et al.* (2014)	IMF	1098.00	0.204	539.00	All	433.00	0.80	433.00	0.80
	SMF	1202.90	0.230	1232.52	All	887.59	0.72	887.59	0.72
		Average	**0.236**				**1.04**		**0.68**
		CoV (%)	**14.55**				**38.80**		**24.30**

The comparison between predicted and experimental responses is herein presented as the ratio of predicted to experimental resistances, where a value below 1.0 indicates a conservative prediction of the tying resistance. In this respect, scenario TM wo/fracture provides a conservative estimate of the tying resistance for the specimens without any reinforcement fracture, with the comparative ratio varying around 0.6-1.0. Such underestimation can be attributed to the neglect of additional resistance contributions via the assignment of ρ equal to 1, as evidenced in Fig. 5.18 for specimens B3 and S3 of Ren *et al.* (2016), and specimens IMF and SMF of Lew *et al.* (2014).

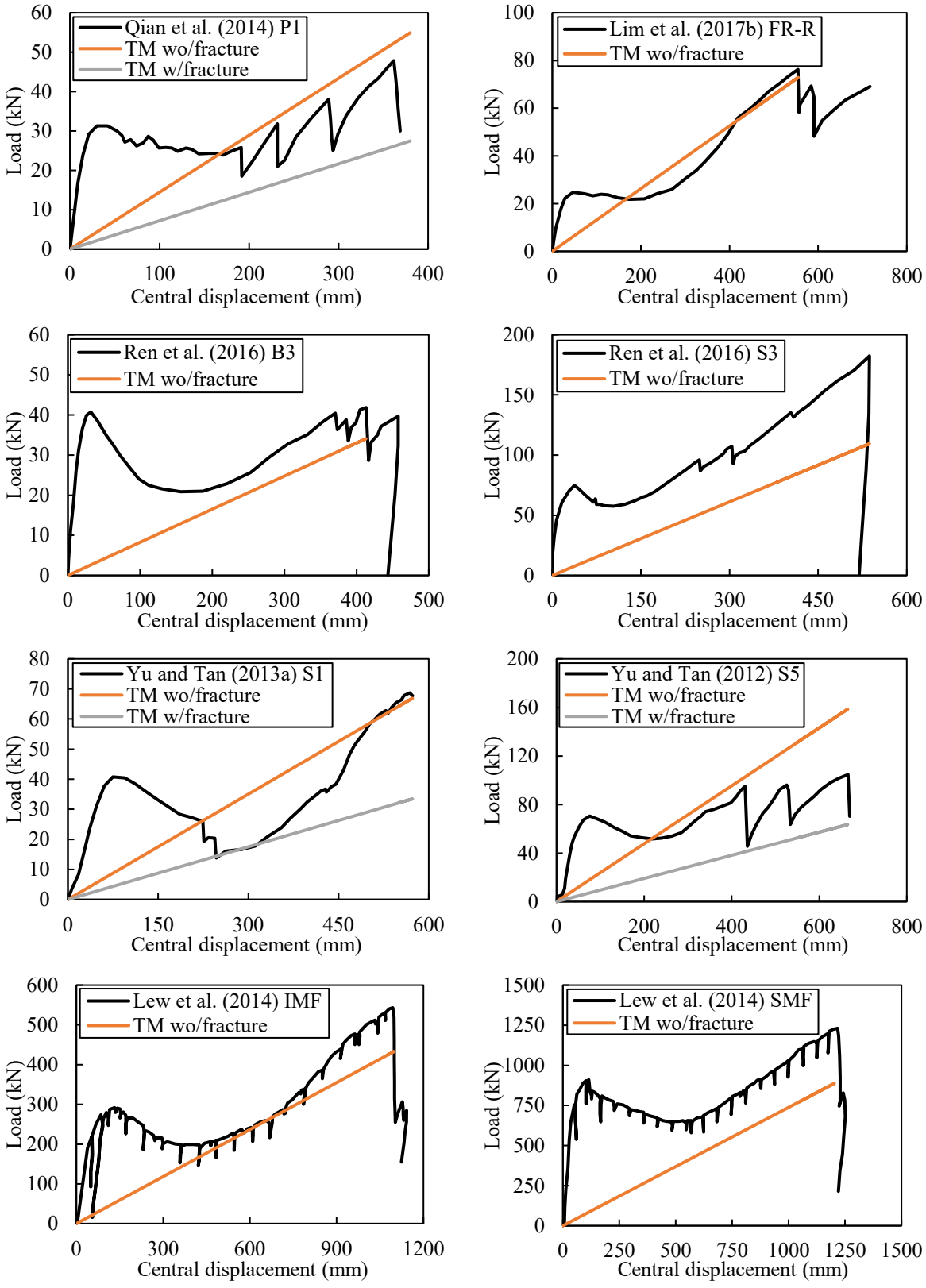


Fig. 5.18 – Validation of tying via beams against experimental tests

Scenario TM wo/fracture may overestimate the tying resistance of the beam specimens if any continuous reinforcement fractures preceding the established chord rotation/displacement capacity. Notwithstanding, the proposed method still offers a reasonable estimate of the tying resistance for the selected beam specimens, with the overpredicted resistance within 50% of the actual value except for specimens F1-NS and F2-WS of Yu and Tan (2017). Indeed, despite the initial load reduction due to the fracture of the reinforcement, such a load drop is partially compensated by the strain hardening of the reinforcement under yield and the additional flexural resistance contribution from the curtailed reinforcement, which are again neglected in the current prediction of the proposed method. This is evidenced in Fig. 5.18 for specimen P1 of Qian *et al.* (2014), and specimens S1 and S5 of Yu and Tan (2012, 2013a). On the other hand, with the additional conservative assumption of considering only the contribution of the intact reinforcement (i.e. without fracture) to the tying resistance, scenario TM w/fracture consistently underestimates the load resistance of the beam specimens, thus confirming the effectiveness and conservatism of the proposed horizontal tying method provided that the requirements for the activation of tying are satisfied.

Observing again the responses of specimen P1 (Qian *et al.*, 2014), and specimens S1 and S5 (Yu and Tan, 2012, 2013a) in Fig. 5.18, it follows that, following the initial fracture of any reinforcement, the experimental responses approximately locate between the two considered case scenarios. In this respect, a response transition from tying scenario TM wo/fracture to TM w/fracture can be established provided the knowledge of the chord rotation/displacement at which reinforcement fractures. The development of an analytical supplementary method to estimate such a chord rotation/displacement would be ideal, though this chord rotation/displacement can also be determined with the numerical approach proposed in Chapter 4 of this thesis. Furthermore, the proposed numerical approach can also serve as a verification means to the development of said analytical methods.

5.9.2 Tying via floor system

Tying via floor system is next validated against experimental test specimens, with Table 5.9 presenting the chord rotation capacity (of the direction with the shortest span) and the corresponding load resistance of the selected test specimens, along with the prediction of the proposed tying method, noting that all continuous reinforcement are considered for the tying resistance and the peripheral edge of 1-way tying floor specimens is assumed to be restrained in torsion. Table E.8 in Appendix E lists further details regarding the geometry, quantity of continuous reinforcement and steel strength of the selected floor specimens.

Once again, provided that the response of the floor system does not present any fracture of the reinforcement, the proposed method effectively offers a conservative means to predict the load resistance of the system under tying action, as evidenced by the comparative ratio, which is below 1, and by the comparison of the predicted and experimental responses illustrated in Fig. 5.19.

Table 5.9 – Validation of tying via floor system against experimental tests

Specimen		Experimental data				TM	
		Δf,exp (mm)	θf,exp (rad)	Pf,exp (kN)	Tying	Pf,est (kN)	Ratio
Qian *et al.* (2014)	S1	213	0.142	169.00	2-way	143.04	0.85
	S2	164	0.109	163.00	2-way	117.51	0.72
Lu *et al.* (2017)	SE1	563	0.282	99.00	1-way	73.69	0.74
	SE2	542	0.271	82.00	1-way	88.32	1.08
	SE3	573	0.287	87.00	1-way	75.00	0.86
	SE4	450	0.225	126.00	1-way	96.05	0.76
Yu *et al.* (2020a)	S1	348	0.193	253.00	1-way	214.38	0.85
	S2	299	0.166	221.00	1-way	237.00	1.07
	S3	418	0.232	251.00	1-way	218.50	0.87
		Average	**0.212**				**0.87**
		CoV (%)	**28.29**				**14.1**

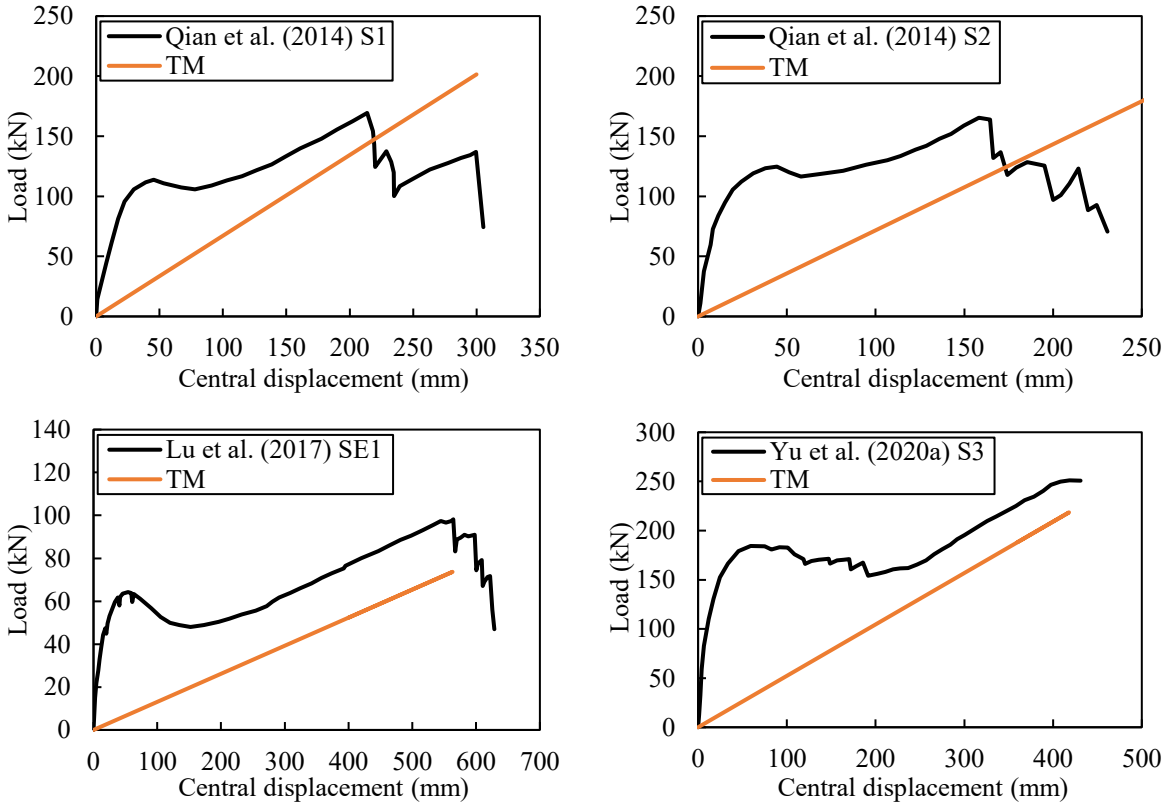


Fig. 5.19 – Validation of tying via floor system against experimental tests

5.10 Conclusion

This chapter presents the novel horizontal tying force method developed by Izzuddin (Izzuddin and Sio, 2022) for robustness building design, along with its validation and verification performed by the author of this thesis. Anchored within a rational framework considering the resistance of the structure under the sudden loss of a vertical load bearing member or support, the proposed method brings major benefits including i) the consideration of a variable ductility limit, ii) the incorporation of dynamic amplification associated with sudden local damage, iii) systematic combination of different sources of tying and types of loading, and iv) supplementary methods considering the interaction of the affected beam/floor system with the surrounding structure namely the requisite planar restraint and the amplification of redistributed gravity loads. Despite such relative benefits, the proposed method retains sufficient simplicity, rendering it suitable for practical design application and as a potential replacement to current prescriptive tying force requirements.

Following the description of the general formulation, along with the supplementary methods for dynamic amplification and interaction with the surrounding structure, extensive verification and validation of the proposed method is conducted using the nonlinear structural analysis program ADAPTIC as well as experimental test specimens. The outcome of such verification and validation demonstrates the effectiveness of the proposed method in predicting the load resistance that is exclusively associated to tying of a beam/floor system under the sudden loss of a vertical load bearing member. Notwithstanding, the proposed method allows for the optional consideration of additional contributions such as residual flexural resistance and strain hardening via the parameter ρ. Furthermore, the supplementary method establishing the requisite planar restraint from the surrounding structure can also be extended to account for the influence of the compressive ring formed under tensile membrane action, as developed in the subsequent chapter.

Finally, application of the proposed horizontal tying force method requires the knowledge of the chord rotation capacity of the beam/floor system, calling for the development of an additional supplementary method for this purpose. In this respect, the numerical modelling approach proposed in Chapter 4 provides an initial means to estimate the chord rotation capacity of RC beam/floor systems and potentially as a verification tool for future development of analytical methods.

Chapter 6: Planar interaction with compressive ring

6.1 Introduction

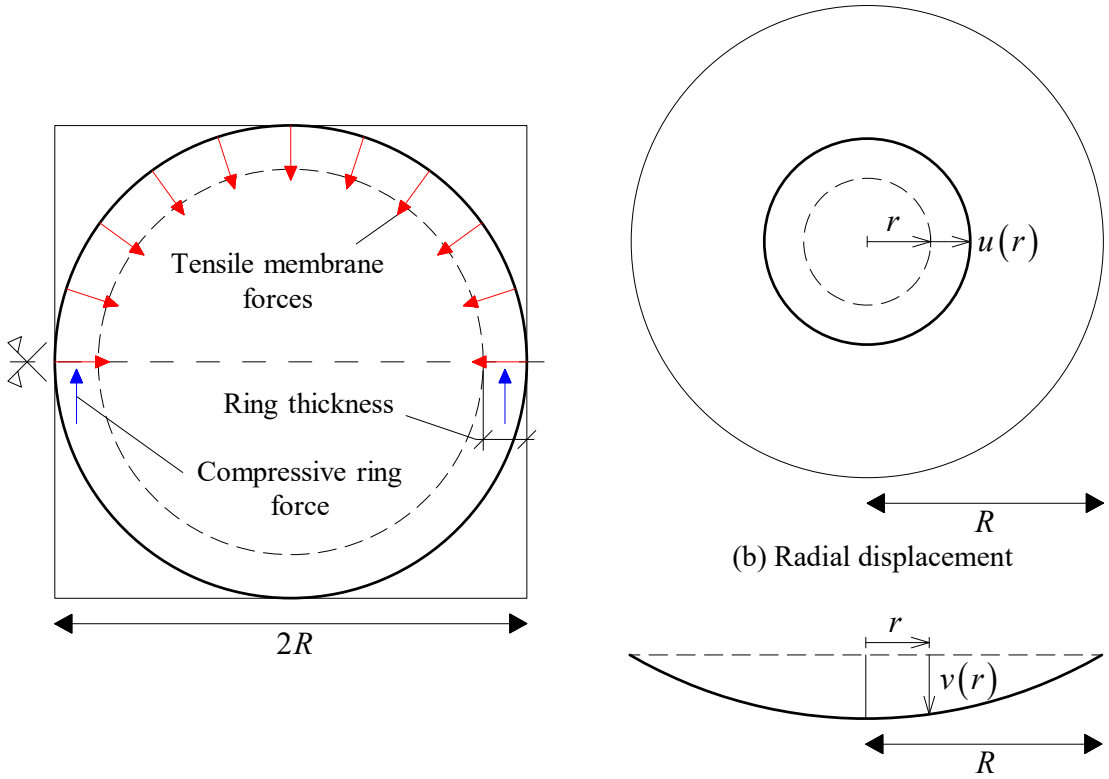
As detailed in the previous chapter, the compressive ring action can provide additional restraint stiffness necessary for the mobilisation of tying. Accordingly, the supplementary method for the assessment of planar interaction, which is first presented in Section 5.6.1.2, is extended in this chapter to include the influence of the compressive ring on the mobilisation of tying.

Herein, the extension of the supplementary method is initially considered for affected floor systems with a square aspect ratio, with the applicability of the resulting formulation to rectangular floor systems subsequently verified via numerical analysis. In this respect, the extension of the supplementary method commences with a tentative formulation established based on a circular floor system to quantify its planar pull-in with increasing transverse displacement, as the geometry associated to the compressive ring action within a square floor system is thought to be assimilated by a circular floor system under tensile membrane action. Notwithstanding, despite the prediction of the tentative formulation agreeing reasonably well with the numerical response of circular floor slabs, such a formulation is later demonstrated to offer an unsatisfactory representation of the pull-in predicted for square floor systems via nonlinear finite element analysis. An alternative formulation is therefore considered, involving the representation of the compressive ring similarly to a square hollow boundary region instead. The subsequent sub-sections detail the formulation and verification for the two considered approaches.

6.2 General formulation for circular slabs

With reference to Fig. 6.1a, the compressive ring action within a square floor system is first considered to be assimilated by the behaviour of a circular floor slab under tensile membrane action, with the outer ring in compression self-equilibrating the tensile forces imposed by the central region of the circular slab. In this respect, the primary aim of the formulation is to

establish, for a given level of transverse displacement/chord rotation and horizontal pull-in, the requisite thickness (or depth) of the ring such that the resultant compressive force effectively equilibrates the tying forces imposed by the central region of the slab.



(a) Circular slab analogy for compressive ring

(b) Radial displacement

(c) Transverse displacement

Fig. 6.1 – Circular formulation for compressive ring

6.2.1 Main assumptions

With the simplifying assumption of axisymmetric response, under which the circular slab is considered with radial and circumferential detailing of reinforcement, determination of the ring thickness requires in turn knowledge of the radial displacement $u(r)$ of the circular slab. With reference to Fig. 6.1b, this displacement establishes whether the circumference at a given radius r is shrinking or expanding, thereby defining the tensile and compressive regions of the circular slab.

Accordingly, the radial displacement field $u(r)$ is herein established assuming that the centroidal axial strains of the radial reinforcement within the axisymmetric plane is constant and that the transverse displacement $v(r)$ follows a quadratic approximation, as illustrated in Fig. 6.1c.

Lastly, for the equilibrium between the tensile membrane forces of the reinforcement and the resultant force of the compressive ring, the considered formulation assumes that the former forces are based on the tensile yield strength of the reinforcement, whilst the latter force is established based on the elastic response of the concrete.

6.2.2 Formulation

On the basis of the main assumptions outlined above and considering that the constant centroidal axial strains ε_{rad} relates to the radial displacement $u(r)$ and the transverse displacement $v(r)$ through:

$$\varepsilon_{rad} = \frac{\mathrm{d}u(r)}{\mathrm{d}r} + \frac{1}{2}\left(\frac{\mathrm{d}v(r)}{\mathrm{d}r}\right)^2 \tag{6.1}$$

the radial displacement $u(r)$ can be determined via integration of (6.1) as:

$$u(r) = \int \varepsilon_{rad} - \frac{1}{2}\left(\frac{\mathrm{d}v(r)}{\mathrm{d}r}\right)^2 dr + \mathrm{C} \tag{6.2}$$

where C is a constant of integration and $v(r)$ is given as:

$$v(r) = \delta\left[1 - \left(\frac{r}{R}\right)^2\right] \tag{6.3}$$

in which δ is the vertical displacement at the centre of the circular slab (also related to the chord rotation α through $\delta = \alpha R$) and R is the total radius of the circular floor system.

The constants ε_{rad} and C from (6.2) are determined by solving the boundary problems at $u(r=0)$ and $u(r=R)$, respectively.

$$\begin{aligned} u(r=0) = 0 \quad &\rightarrow \quad \mathrm{C} = 0 \\ u(r=R) = -\Delta \quad &\rightarrow \quad \varepsilon_{rad} = \frac{2\delta^2 - 3\Delta R}{3R^2} \end{aligned} \tag{6.4}$$

where Δ is the pull-in displacement at the boundary of the circular slab. It is worth noting the minus sign preceding Δ, which is considered so as to obtain a negative radial displacement $u(r=R)$ for a positive pull-in Δ.

The circumferential strain at a considered radius $\varepsilon_{cir}(r)$ can be then established as:

$$\varepsilon_{cir}(r)=\frac{u(r)}{r}=\frac{2\delta^2}{3R^2}\left[1-\left(\frac{r}{R}\right)^2\right]-\frac{\Delta}{R} \tag{6.5}$$

Accordingly, considering a second order approximation of Δ, the radius $r=r_0$ at which the tensile membrane forces transition to the compressive membrane forces is determined as:

$$\varepsilon_{cir}(r_0)=0 \quad \rightarrow \quad r_0=R\left(1-\frac{3}{4}\frac{\Delta R}{\delta^2}\right) \tag{6.6}$$

With the thickness of the compressive ring established, the resultant force of the compressive ring F, which is determined via integration of the elastic circumferential stresses within the ring region, should equilibrate the resultant force of the tying forces T, which can be determined with reference to Fig. 6.2:

$$F=t\int_{r_0}^{R}E_c\varepsilon_{cir}(r)\,dr=\int_{0}^{\pi/2}f\sin\theta\,R\,d\theta=T \tag{6.7}$$

where t is the thickness of the circular slab and E_c is the elastic modulus of the concrete. On the other hand, f is the distributed radial force assumed to act at the outer radius of the slab.

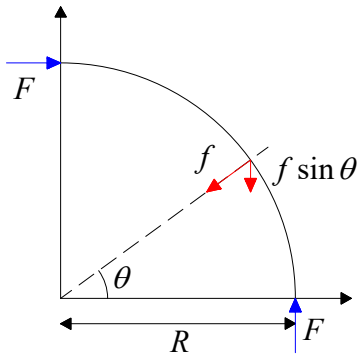


Fig. 6.2 – Force equilibrium of the circular formulation

Combining (6.5)-(6.7) and solving for the horizontal pull-in Δ leads to three solution branches, only one of which presents an actual physical meaning. Subsequent to the mathematical simplification of such a solution, the horizontal pull-in Δ is obtained:

$$\Delta=4\delta\sqrt{\frac{f}{6tE_c}} \tag{6.8}$$

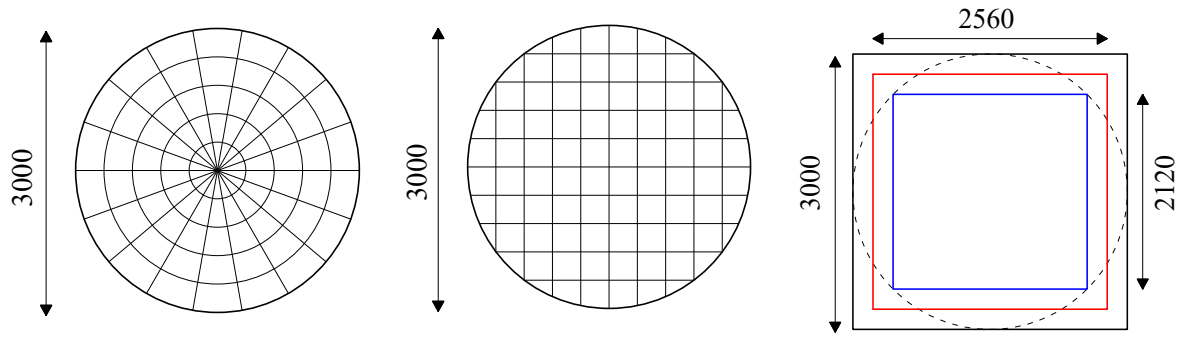
The above equation indicates that the pull-in at the boundary of the circular slab is linearly dependent on the central displacement/chord rotation.

It is also worth noting that, as it currently stands, the above equation evaluates the horizontal pull-in response of the floor slab based on its own planar restraint stiffness only, that is neglecting the interaction with the surrounding structure. The formulation can be further extended to include such an interaction for example by idealising the surrounding restraint stiffness as radial elastic springs located at the boundary perimeter of the circular slab. Notwithstanding, this has not been further developed as the formulation in (6.8) is subsequently demonstrated to not provide a reasonable representation for the horizontal pull-in of square slabs, under which an alternative formulation would be required as developed in Section 6.3.

6.2.3 Verification of the formulation and its applicability to square slabs

The verification of the formulation for circular slab proceeds with two circular slab models under uniformly distributed loading (UDL): one with radial and circumferential reinforcements (herein termed as Rad – Fig. 6.3a), and another with orthogonal reinforcements (herein termed as Ortho – Fig. 6.3b). Three additional square slab models, also subject to UDL, are then considered to assess the applicability of the circular formulation to square slabs (Sq – Fig. 6.3c). The length of these square slabs is chosen assuming the equivalency of the circular slab illustrated in Fig. 6.3b is established by either an inscribed square, a circumscribed square or an average of the former two squares, as illustrated in Fig. 6.3c.

All slab models, for which the geometry and reinforcement detailing are listed in Table 6.1, are simply supported and without planar restraint. The corresponding numerical models in ADAPTIC involve the biaxial rotating crack model with a linear elastic compressive response, ‘con9’ (Izzuddin, 2016), for the concrete response and the bilinear kinematic strain hardening model, ‘stl1’ (Izzuddin, 1991), for the steel response, with Table 6.2 presenting the associated material properties. Triangular and quadrilateral shell elements – ‘csl3’ (Grosman and Izzuddin, 2018) and ‘csl4’ (Izzuddin *et al.*, 2004) – are used respectively for the modelling of the circular and square slabs.



(a) Rad – circular slab w/radial reinforcement

(b) Ortho – circular slab w/orthogonal reinforcement

(c) Sq – square slabs w/orthogonal reinforcement

Fig. 6.3 – Verification of circular slabs (dimensions in mm)

Table 6.1 – Geometric and reinforcement details for the slab models

Slab	Circular w/radial reinforcement	Circular w/orthogonal reinforcement	Square w/orthogonal reinforcement
Slab radius, R /half-length, L	1500mm	1500mm	1060, 1280 and 1500mm
Slab thickness, t	55mm	55mm	55mm
Radial reinforcement, $A_{s,rad}$	ϕ6//250 (mm)	-	-
Circumferential reinforcement, $A_{s,cir}$	ϕ6//250 (mm)	-	-
Reinforcement spanning in x direction, $A_{s,x}$	-	ϕ6//250 (mm)	ϕ6//250 (mm)
Reinforcement spanning in y direction, $A_{s,y}$	-	ϕ6//250 (mm)	ϕ6//250 (mm)
Distance of reinforcement to mid-plane	0mm	0mm	0mm

Table 6.2 – Concrete and steel properties

Concrete	
Young's modulus	28355MPa
Poisson's ratio	0.2
Compressive strength	23.3MPa
Tensile strength	0.01MPa
Steel	
Young's modulus	185864MPa
Yield strength	355MPa

Considering that $t.E_c$ in (6.8) represents the planar resistance of the compressive ring, it is worth noting that the thickness of the slabs and the elastic stiffness modulus of the concrete are respectively reduced and scaled by 1000 for all cases. The aim of such adjustments is to reduce

the additional resistance contributions due to flexure whilst keeping the same resistance for the compressive ring, and thereby limiting the load response to tensile membrane action only. The value of $t.E_c$ in the control models is then scaled down by 100 to assess the response sensitivity of the floor slabs under a lower resistance of the compressive ring.

Figs. 6.4 and 6.5 illustrate the variation of the horizontal pull-in with central displacement for a planar resistance of $t.E_c$ and $0.01(t.E_c)$, respectively, noting that the keys 'TM' and 'NM' respectively represent the predictions of the proposed formulation and the numerical models.

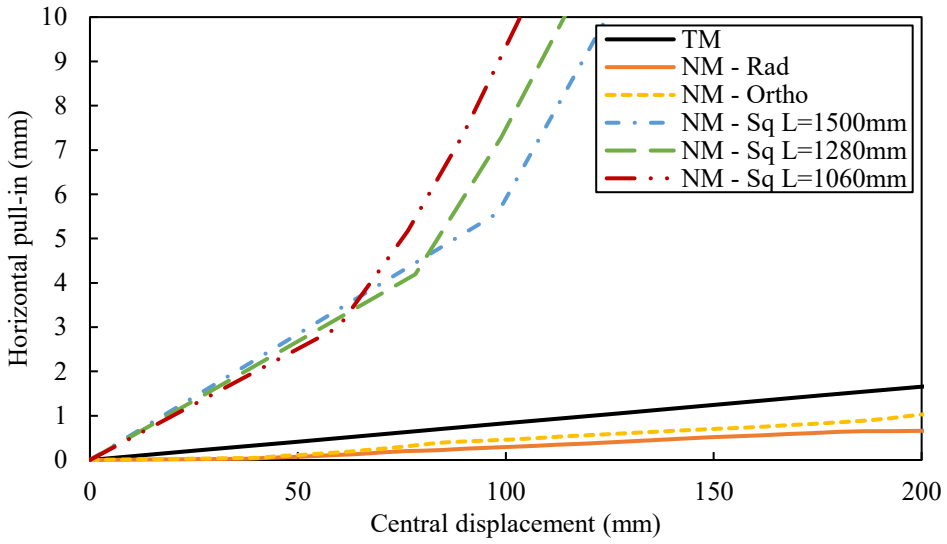


Fig. 6.4 – Verification of the circular formulation considering $t.E_c$

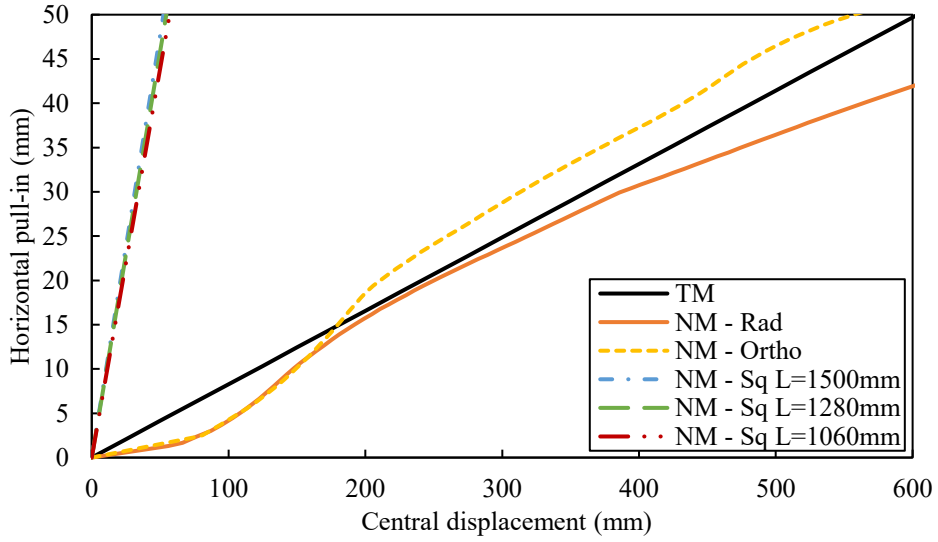


Fig. 6.5 – Verification of the circular formulation considering $0.01(t.E_c)$

The figures demonstrate a reasonable agreement between the circular formulation and the numerical response of the circular slab models, independently of its reinforcement detailing. The slightly overpredicted pull-in for the cases with a planar resistance of $t.E_c$ can be attributed to the residual flexural resistance which may still be significant.

Importantly, despite the reasonable agreement between the formulation and the numerical response of circular floor slabs, it is evident that such a formulation is not applicable to square slabs, as the corresponding variation of the horizontal pull-in with increasing central displacement follows more closely a higher-order function in the initial phases of loading as opposed to the linear increase predicted by the circular slab formulation. An alternative formulation is therefore considered in the subsequent sections.

6.3 General formulation for square slabs

The alternative formulation involves the equilibrium of the distributed pull-in forces from the central region of the square slab with the combined planar restraint stiffness contribution from the surrounding structure and a square hollow boundary region of concrete representing the compressive ring, as illustrated in Fig. 6.6. It is worth noting that, unlike the circular formulation, the resulting analytical expression simply provides the level of horizontal pull-in under full activation of the tensile membrane forces, which is independent of the central displacement of the floor slab.

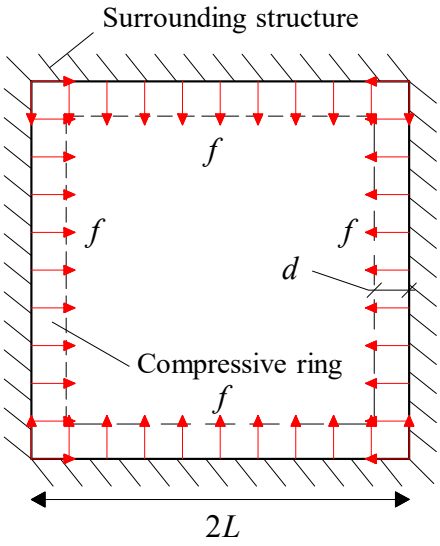
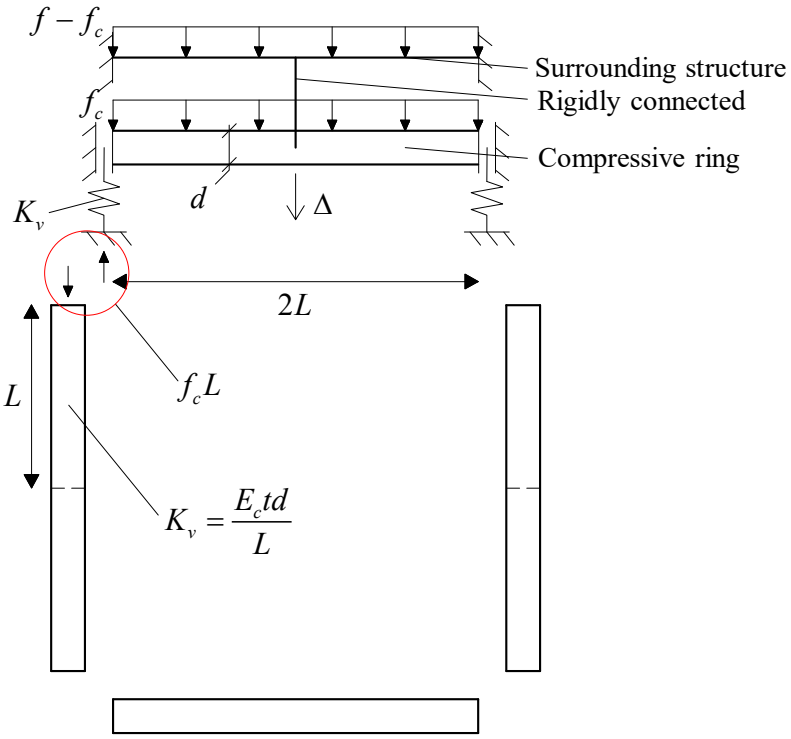


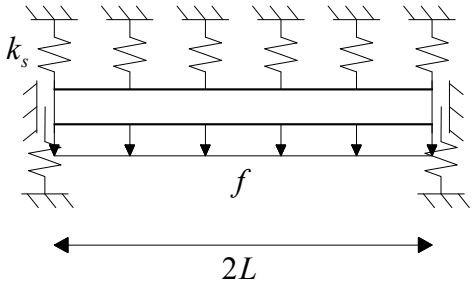
Fig. 6.6 – Idealisation of the compressive ring as a square hollow boundary region

6.3.1 Main assumptions

With reference to Fig. 6.6, provided the identical geometry and loading condition on all four edges of the floor system, the representation of the horizontal pull-in under tensile membrane action can be further idealised into a system of two fully fixed beams in a parallel configuration (Fig. 6.7a). The two fully fixed beams respectively represent the surrounding structure and the compressive ring for a single edge of the floor slab.



(a) Idealisation involving a system of two fully fixed beams in a parallel configuration



(b) Alternative idealisation of the surrounding structure involving distributed springs

Fig. 6.7 – Models associated with the compressive ring formulation for square slabs

In this respect, assuming an elastic response for both beams, the horizontal pull-in is simply the maximum elastic deflection of the system under a uniformly distributed load representing the tensile membrane forces. It is worth noting that the beam representing the stiffness from the surrounding structure can be alternatively substituted by equivalent springs with distributed

planar stiffness k_s (units in FL^{-2}) to allow for a more general configuration of the surrounding structure (Fig. 6.7b).

Notwithstanding the above, the tensile membrane forces also lead to a general inward deformation of the square hollow boundary region due to the axial compressive forces acting within its edges. As a result, an additional horizontal pull-in arises for the beam representing the compressive ring, which is idealised herein by replacing the rigid vertical supports of such beam with elastic supports, the stiffness of which is determined from the axial stiffness of the edges of the square hollow boundary region.

The remaining consideration required for the formulation is to establish the thickness of the square hollow boundary region d, in other words the depth of its representative beam. The present work assumes this depth to be a fraction of the span length, the ratio of which is chosen via calibration with the considered numerical outcomes.

6.3.2 Formulation

Given the parallel configuration of the two-beam system, their corresponding pull-in displacement must be identical:

$$\Delta = \Delta_c = \Delta_s \tag{6.9}$$

where Δ_c and Δ_s represent the pull-in displacement from the compressive ring and the surrounding structure, respectively.

According to the main assumptions, the pull-in displacement from the beam representing the compressive ring is established considering its elastic deflection under the portion of the tensile membrane force which is resisted by the compressive ring f_c, and the additional displacement arising from its vertical supports.

$$\Delta_c = \frac{f_c (2L)^4}{384 E_c \left(\frac{t d^3}{12} \right)} + \frac{f_c L^2}{E_c t d} \tag{6.10}$$

where L is the span of the beam (i.e. half-length of the edge of the floor system); t is the thickness of the slab (or the width of the representative beam); d is the considered thickness of the compressive ring (or the depth of the representative beam); and E_c is the elastic stiffness modulus of the concrete. The first term provides the elastic deflection of the fully fixed beam

under a uniformly distributed load f_c, whilst the second term adds the displacement due to the elastic vertical supports of the beam (Fig. 6.7a).

The pull-in displacement from the surrounding structure can be simply expressed with reference to the distributed planar stiffness k_s as:

$$\Delta_s = \frac{f - f_c}{k_s} \tag{6.11}$$

and considering a fully fixed beam to represent the surrounding structure, k_s can be further established as:

$$k_s = \frac{384 E_s I_s}{(2L)^4} \tag{6.12}$$

where $E_s I_s$ is the flexural stiffness of the considered beam representing the surrounding structure; and L is again the beam span.

Lastly, the level of pull-in under full activation of tensile membrane forces can be determined combining (6.9)-(6.11), solving for f_c and subsequently determining Δ with either (6.10) or (6.11):

$$\Delta = \frac{f L^2 \left(L^2 + 2d^2\right)}{2E_c t d^3 + k_s L^2 \left(L^2 + 2d^2\right)} \tag{6.13}$$

The above equation assumes that the thickness of the compressive ring (or the depth of the representative beam) d is defined a priori, which is herein assumed as a fraction of the span length ($0.1L$). Notwithstanding, the thickness can also depend on parameters such as the level of transverse and pull-in displacements and in the case of rectangular floor slabs on the form factor. In this respect, consideration of such effects can indeed improve the accuracy of the proposed formulation, though their quantification is not straightforward and may render the formulation without a closed form solution, thereby requiring an iterative solution procedure.

6.4 Verification against square models

Verification of the proposed formulation proceeds with square reinforced concrete slab models surrounded by elastic boundary steel beams which offer the surrounding planar restraint stiffness, as illustrated in Fig. 6.8.

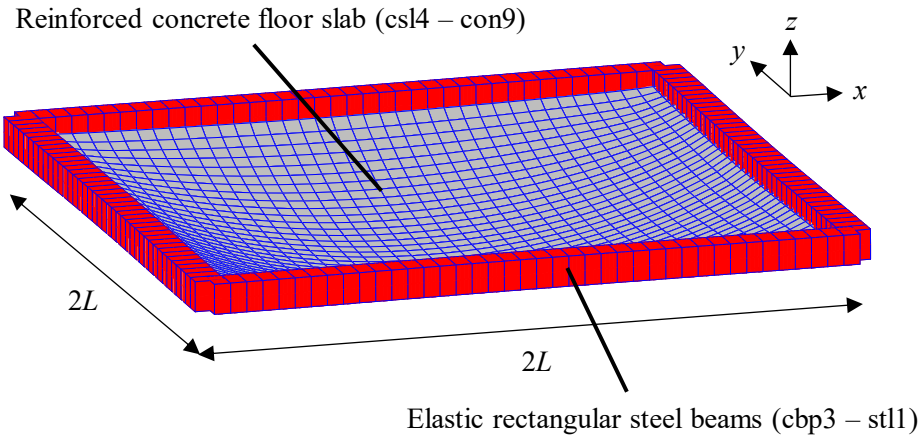


Fig. 6.8 – Verification of compressive ring model for square slabs

The boundary steel beams are continuously supported in the *z*-direction and present a square frame, the dimensions of which are subsequently defined based on the established distributed planar restraint stiffness k_s. As also indicated in Fig. 6.8, the concrete floor slab is modelled with the 'csl4' shell element, along with the 'con9' biaxial concrete model (with zero tensile strength), whereas the rectangular beams are modelled with the 'cbp3' beam elements, along with the 'stl1' steel model but with a very high resistance threshold to avoid yielding of the beams (Izzuddin, 1991; Izzuddin *et al.*, 2004; Izzuddin, 2016). The rigid connection between the beam and shell elements are then established via the 'cpl2' couple elements.

Identical to the assumptions undertaken for the circular slab models, the slab thickness and the concrete stiffness modulus are also reduced and scaled by a factor of 1000, respectively, to minimise the additional resistance contribution from flexure.

Two control models with span lengths L of 3000mm and 6500mm are first considered, with the floor system geometry, reinforcement detailing and material properties as provided in Tables 6.3 and 6.4, noting that the reinforcement is located at the mid-plane of the floor slab.

Table 6.3 – Geometric and reinforcement details for the control square slab models

Control model	3000mm	6500mm
Slab thickness	55mm	180mm
Steel beam depth	100mm	600mm
Steel beam width	100mm	600mm
Reinforcement spanning in x direction, $A_{s,x}$	ϕ6//250	2x ϕ12//125
Reinforcement spanning in y direction, $A_{s,y}$	ϕ6//250	2x ϕ12//125

Table 6.4 – Concrete and steel material properties for the control square slab models

Control model	3000mm	6500mm
Concrete		
Young's modulus	28355MPa	31476MPa
Poisson's ratio	0.2	0.2
Compressive strength	23.3MPa	33MPa
Tensile strength	0.0MPa	0.0MPa
Steel reinforcement		
Young's modulus	185864MPa	200000MPa
Yield strength	355MPa	435MPa
Yield strain	1.910‰	2.175‰
Surrounding steel beams		
Young's modulus	210000MPa	210000MPa

The control model with 6500mm span length is then modified to further verify the proposed formulation under varying parameters including slab thickness, span length, quantity of reinforcement, and restraint stiffness from the surrounding steel beams. Table 6.5 lists the various models considered for the current verification, noting that the reference distributed planar restraint stiffness k_s from each set, determined according to (6.12), is further scaled down by a factor of 0.1, 0.2, 0.4 and 0.6, rendering a total of 55 assessment cases.

Assuming the thickness of the compressive ring d as $0.1L$, the predicted analytical (TM) and numerical (NM) outcomes are first presented in terms of central displacement of the floor system versus the horizontal pull-in at one of its edges, as exemplified with the outcomes based on the reference k_s of the two control models in Figs. 6.9 and 6.10, respectively. It is worth noting that the continuous black line labelled '$\alpha_{\min}$ limit' represents the central displacement threshold beyond which tensile membrane forces is fully mobilised within the floor system, and is established by expressing (5.24) as follows:

$$v_{\min} = \alpha_{\min} L = L\sqrt{\frac{2\Delta}{L} + 4\varepsilon_y} \tag{6.14}$$

where $v_{\min}$ and $\alpha_{\min}$ are respectively the minimum central displacement and chord rotation for full activation of tying; L is the span length; Δ is the pull-in at one edge of the floor system; and ε_y is the yield strain of the reinforcement.

Table 6.5 – Numerical models for the verification of the square formulation

Set	Model description/varying parameter	Reference steel beam depth (mm)	Reference steel beam width (mm)	Reference k_s (N/mm^2)	Further scaling for k_s	Total number of cases
1	Control model with 3000mm span length	100	100	0.5185	0.1, 0.2, 0.4, 0.6	5
2	Control model with 6500mm span length	600	600	30.4930	0.1, 0.2, 0.4, 0.6	5
Sensitivity assessment of the control model with 6500mm span length						
2a	Quantity of reinforcement (0.5A_s, 2.0A_s)	600 600	600 600	30.4930 30.4930	0.1, 0.2, 0.4, 0.6	10
2b	Slab thickness (100mm and 300mm)	600 600	600 600	30.4930 30.4930	0.1, 0.2, 0.4, 0.6	10
2c	Span length (0.40L, 0.80L, 1.25L)	240 480 750	240 480 750	30.4930 30.4930 30.4930	0.1, 0.2, 0.4, 0.6	15
2d	Surrounding restraint stiffness (0.24k_s, 0.48k_s)	420 500	420 500	7.3214 14.7054	0.1, 0.2, 0.4, 0.6	10

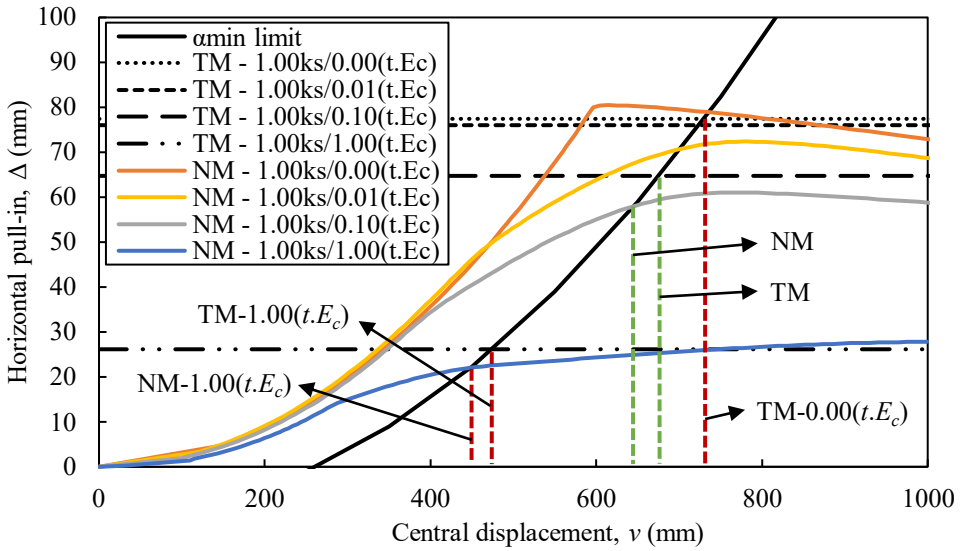


Fig. 6.9 – Predicted and numerical outcomes for control model (1) with 1.00k_s

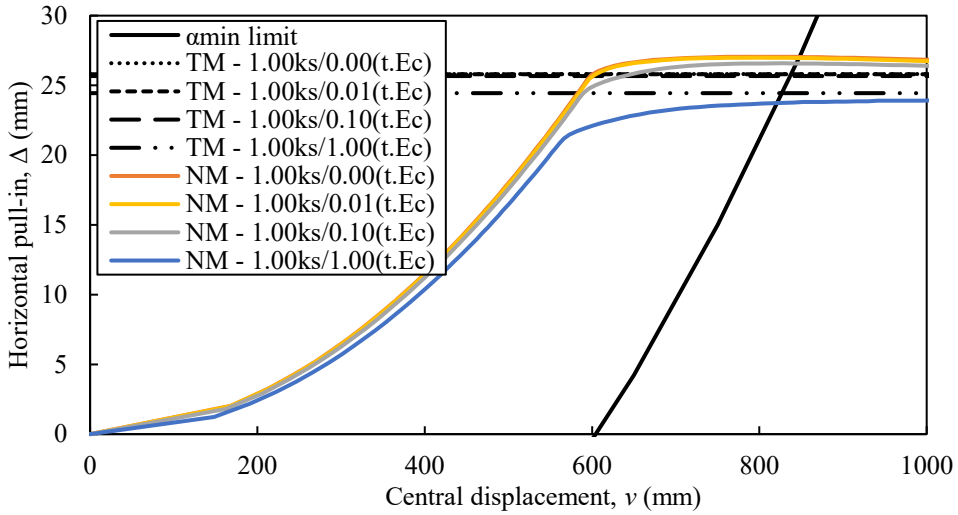


Fig. 6.10 – Predicted and numerical outcomes for control model (2) with $1.00k_s$

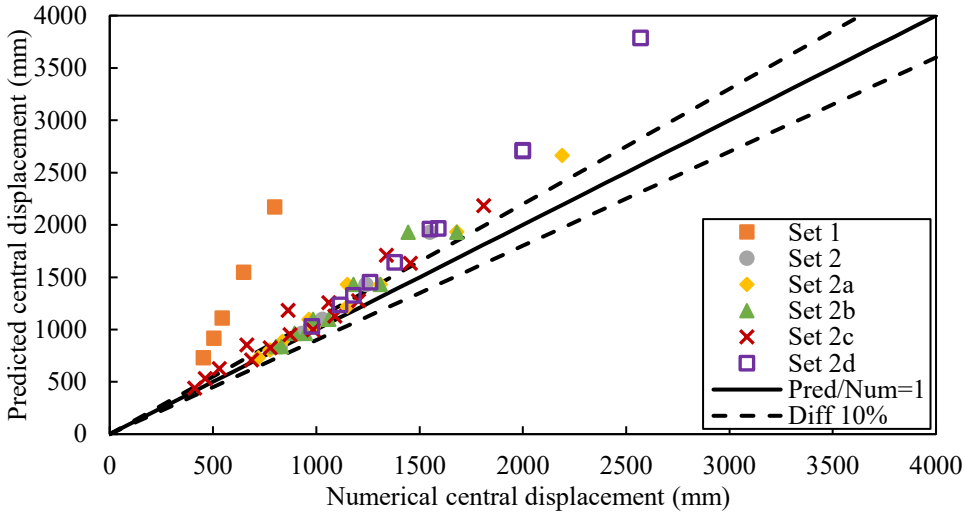
It is also worth noting that Figs. 6.9 and 6.10 also present the predicted and numerical outcomes for reduced compressive ring stiffness of 0.00, 0.01 and 0.10 of $t.E_c$, where t is the thickness of the slab and E_c is the compressive stiffness modulus. Specifically, $0.00(t.E_c)$ corresponds to the case neglecting the planar restraint stiffness contribution from the compressive ring. For the numerical model (NM), this condition is approximately realised by defining a compressive ring stiffness of $10^{-4}(t.E_c)$, whilst for the proposed analytical formulation (TM), the horizontal pull-in at one edge of the floor system is determined according to (6.11) considering f_c as zero.

The assessment between predicted and numerical outcomes is then established based on the corresponding intersection with the '$\alpha_{\min}$ limit' threshold and the subsequent comparison of the resulting central displacements, as demonstrated with the green dashed lines illustrated in Fig. 6.9 for one of the NM and TM curve sets, where it follows that the proposed analytical formulation predicts reasonably well the numerically determined central displacement beyond which tensile membrane action is fully activated, irrespective of the considered compressive ring stiffness. It is worth noting that the reference central displacement established for the NM curve is also approximate as it depends on the accuracy of the analytical expression for the '$\alpha_{\min}$ limit'. A fairer comparison between numerical and analytical predictions would be based on the point of the NM curve where the horizontal pull-in starts to plateau, under which it suggests that more conservative values would be determined for control model (2). Notwithstanding, given the typical conservatism of the analytical expression for the '$\alpha_{\min}$ limit' and the objective of the current verification to assess the improvement of the supplementary

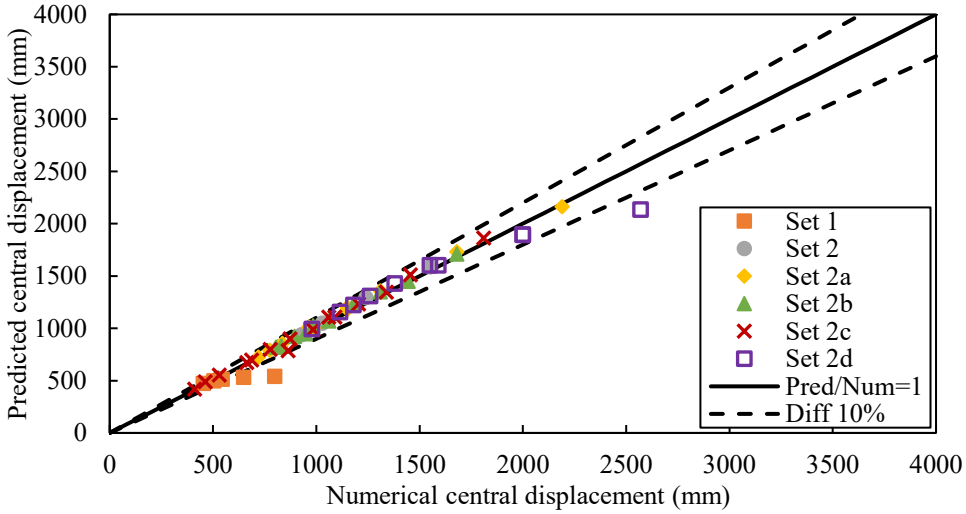
method considering compressive ring action, wherein comparison of the analytical predictions considering and neglecting the compressive ring can be established in a relative sense, the reference central displacement considered herein for the NM curve is deemed acceptable.

The subsequent verification based on all 55 assessment cases focuses on the accuracy improvement achieved with the formulation accounting for the planar restraint stiffness contribution from the compressive ring, i.e. TM-1.00($t.E_c$), with reference to the formulation neglecting the compressive ring action, i.e. TM-0.00($t.E_c$). In this respect, for each of the 55 assessment cases, the relevant outcomes selected from the central displacement versus horizontal pull-in plots, identical to those illustrated in Figs. 6.9 and 6.10, are the central displacements determined from the intersection of the '$\alpha_{\min}$ limit' threshold with the cases NM-1.00($t.E_c$), TM-1.00($t.E_c$) and TM-0.00($t.E_c$), as demonstrated by the red dashed lines illustrated again in Fig. 6.9. These cases represent the numerical outcome considering planar restraint contribution from the compressive ring, the corresponding prediction of the proposed formulation, and the prediction of the formulation neglecting the compressive ring, respectively. Accordingly, Figs. 6.11a-b compare the numerically determined central displacement for the full activation of tying to the prediction of the formulations respectively neglecting and considering the planar restraint stiffness contribution from the compressive ring.

The formulation neglecting the planar restraint contribution from the compressive ring offers a conservative estimate to the minimum central displacement of the floor system for full activation of tensile membrane action, with all analytical predictions higher than the numerical predictions (Fig. 6.11a). The average ratio between analytical and numerical outcomes is approximately 1.230 with a coefficient of variation of 26.14%. The most significant overestimation of the minimum central displacement derives from the predictions for Sets 1 and 2d, corresponding to the floor system cases with the lowest planar restraint stiffness from the surrounding steel beams k_s. The largest difference between analytical and numerical outcomes reaches +172.76% when ignoring compressive ring action. Such observations can be explained by the increasing relevance of the planar restraint stiffness contribution from the compressive ring with decreasing planar restraint stiffness from the surrounding steel beams. In this respect, with the neglect of compressive ring action in the analytical model, the analytical prediction of the minimum central displacement for full activation of tying becomes increasingly overconservative.



(a) Analytical prediction neglecting compressive ring action



(b) Analytical prediction considering compressive ring action

Fig. 6.11 – Verification of analytical compressive ring formulation for square slabs

On the other hand, the prediction accuracy improves significantly with the analytical formulation when considering the compressive ring action (Fig. 6.11b), with an average ratio between analytical and numerical outcomes limited to 1.004 and a corresponding coefficient of variation of 6.31%. This suggests that the assumed ring thickness of $d = 0.1L$ is reasonable. Notwithstanding, unlike the formulation neglecting the contribution from the compressive ring, which offers a conservative prediction for all 55 assessment cases, the improved formulation underpredicts marginally in some of the considered cases the minimum central displacement for full activation of tensile membrane action, with the most significant underpredicted displacements again observed for Sets 1 and 2d. The largest underestimated difference reaches -32.18%.

Further inspection of the difference between analytical and numerical minimum central displacements suggests that, provided the floor system presents a minimum level of planar restraint stiffness from the surrounding steel beams, the thickness of the compressive ring seems to be dependent on the span length only, as the assumption of a compressive ring thickness $d = 0.1L$ in the proposed formulation does not introduce a significant error variation in the predicted results. However, with the surrounding steel beams offering a relatively low distributed planar restraint stiffness, the results suggest that the thickness of the compressive ring may be further reduced depending on additional system parameters to offset the underprediction of the minimum displacement for activation of tying. Still, considering the purpose of the proposed formulation, which is to provide a practical means to quantify the planar interaction of the floor system with the surrounding structure and the compressive ring, the proposed formulation evidently establishes an improved alternative to predict the minimum chord rotation for the full activation of tying within square slabs.

6.5 Application to rectangular slabs

The proposed formulation is generalised herein for application to rectangular floor slabs, with the typical geometric configuration and surrounding planar restraint as illustrated in Fig. 6.12, noting that $L \leq H$.

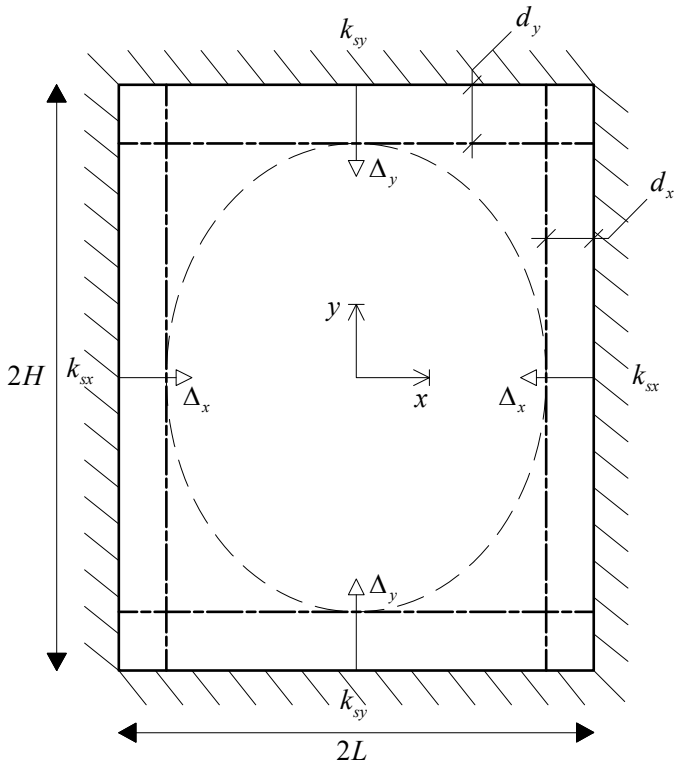


Fig. 6.12 – Idealisation of the compressive ring as a rectangular hollow section

6.5.1 Generalisation of the proposed formulation

The formulation for compressive ring action in rectangular floor systems follows that for square systems except that the pull-in is now distinguished for the shorter and the longer edges. On the basis of Fig. 6.12, this leads to:

$$\begin{aligned}
&\Delta_x = \Delta_{cx} = \frac{f_{cx}\left(2H\right)^4}{384E_c\left(\frac{t\,d_x^{\,3}}{12}\right)} + \frac{f_{cx}HL}{E_c t d_y} = \frac{f_x - f_{cx}}{k_{sx}} = \Delta_{sx} \\
&\Delta_x = \frac{f_x H\left(H^3 d_y + 2L d_x^{\,3}\right)}{2E_c t d_x^{\,3} d_y + k_{sx} H\left(H^3 d_y + 2L d_x^{\,3}\right)}
\end{aligned} \tag{6.15}$$

$$\begin{aligned}
&\Delta_y = \Delta_{cy} = \frac{f_{cy}\left(2L\right)^4}{384E_c\left(\frac{t\,d_y^{\,3}}{12}\right)} + \frac{f_{cy}LH}{E_c t d_x} = \frac{f_y - f_{cy}}{k_{sy}} = \Delta_{sy} \\
&\Delta_y = \frac{f_y L\left(L^3 d_x + 2H d_y^{\,3}\right)}{2E_c t d_y^{\,3} d_x + k_{sy} L\left(L^3 d_x + 2H d_y^{\,3}\right)}
\end{aligned} \tag{6.16}$$

where $\Delta_{x(y)}$, $\Delta_{cx(y)}$, $\Delta_{sx(y)}$ are the total, compressive ring and the surrounding structure pull-in displacement in the x (y) direction, respectively, whereas $f_{x(y)}$ and $f_{cx(y)}$ represent the total distributed tying force and the portion resisted via the compressive ring in the x (y) direction, respectively. On the other hand, $k_{sx(y)}$ is the distributed planar restrain stiffness from the surrounding structure in the x (y) direction, whereas $d_{x(y)}$ is the depth of the beam representing the compressive ring along the longer (shorter) edge, and is herein assumed as:

$$\begin{aligned}
d_x &= 0.1L \\
d_y &= 0.1H
\end{aligned} \tag{6.17}$$

It is worth noting that both (6.15) and (6.16) would result in (6.13) for a square floor system with identical distributed tying force and planar restraint stiffness in the x and y directions.

6.5.2 Verification against rectangular models

The verification of the rectangular formulation is based on the square control model (2) with 6500mm span length presented in Section 6.4 (with the geometric and material properties as listed in Tables 6.3 and 6.4), only modifying its span length in the y-direction to represent rectangular floor systems as well as the cross-section of the surrounding steel beams to keep the same distributed planar restraint stiffness. Table 6.6 lists the verification cases, along with

further sensitivity assessment of the floor system with a 1.25:1 form factor to different parameters. It is worth noting that the form factors of 2:1, 1.5:1, 1.25:1 correspond to rectangular floor systems involving a shorter edge with a span length of L=6500mm and a longer edge with a span length of H=13000mm, 9750mm and 8125mm, respectively. It is also worth noting that the further scaling for the surrounding restraint stiffness proceeds simultaneously in both x and y directions, resulting in a total of 45 assessment cases, ten of which are related to the control square model with the 6500mm span length presented in Section 6.4, but with different distributed tying force and restraint stiffness in the x and y directions.

Table 6.6 – Numerical models for the verification of the rectangular formulation

Set	Model description/ varying parameter	Cross-section for longer steel beam (mm^2)	Cross-section for shorter steel beam (mm^2)	Reference k_{sx} (N/mm^2)	Reference k_{sy} (N/mm^2)	Further scaling for $k_{sx(y)}$
3	Form factor 2:1	1200×1200	600×600	30.4930	30.4930	0.1, 0.2, 0.4, 0.6
4	Form factor 1.5:1	900×900	600×600	30.4930	30.4930	0.1, 0.2, 0.4, 0.6
5	Form factor 1.25:1	750×750	600×600	30.4930	30.4930	0.1, 0.2, 0.4, 0.6
Sensitivity assessment of the rectangular model with a form factor of 1.25:1						
5a	Global restraint stiffness ($0.24k_{sx(y)}$)	525×525	420×420	7.3214	7.3214	0.1, 0.2, 0.4, 0.6
5b	Restrain stiffness in the y-direction ($0.24k_{sy}$, $0.48k_{sy}$)	750×750 750×750	420×420 500×500	30.4930 30.4930	7.3214 14.7054	0.1, 0.2, 0.4, 0.6
5c	Quantity of reinforcement in the x-direction ($1.25A_{sx}$)	750×750	600×600	30.4930	30.4930	0.1, 0.2, 0.4, 0.6
Sensitivity assessment of the control square model with 6500mm span length						
2e	Quantity of reinforcement in the x-direction ($1.25A_{sx}$)	600×600	600×600	30.4930	30.4930	0.1, 0.2, 0.4, 0.6
2f	Restrain stiffness in the y-direction ($0.24k_{sy}$)	600×600	420×420	30.4930	7.3214	0.1, 0.2, 0.4, 0.6

The generation of the analytical and the numerical results follows the same procedure described for the verification of the square formulation, i.e. determining for each of the 45 cases i) the numerical minimum central displacement for full activation of tying forces, considering planar

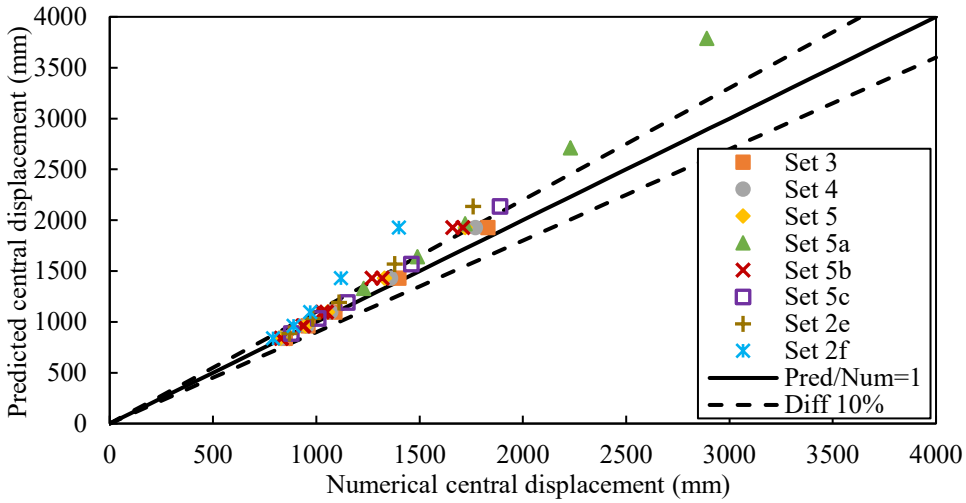
restraint contribution from the compressive ring, ii) the corresponding prediction of the rectangular formulation, and iii) the prediction of the formulation neglecting the compressive ring. The difference is that these outcomes are now established with a distinct '$\alpha_{\min}$ limit' threshold for each of the x and y directions. Consistently with (6.14), this leads to:

$$x\text{-direction} \quad v_{\min,x} = L\sqrt{\frac{2\Delta_x}{L} + 4\varepsilon_y} \tag{6.18}$$

$$y\text{-direction} \quad v_{\min,y} = H\sqrt{\frac{2\Delta_y}{H} + 4\varepsilon_y} \tag{6.19}$$

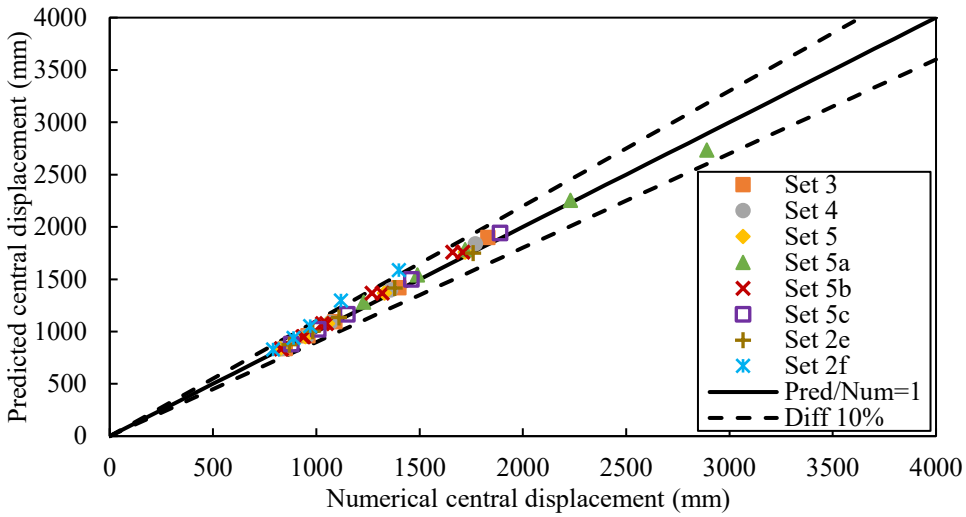
where $v_{\min,x(y)}$ is the minimum central displacement for full activation of tying in the x (y) direction; L and H are the shorter and longer span length, respectively; ε_y is the yield strain of the reinforcement; and $\Delta_{x(y)}$ is the pull-in of the longer (shorter) edge of the floor system determined according to (6.15) and (6.16).

Figs. 6.13 and 6.14 compare the prediction accuracy of the proposed analytical formulation considering and neglecting compressive ring action, respectively, in the x and y directions, where conclusions similar to the verification of the square formulation can be established. For the response in the x-direction (Fig. 6.13), the inclusion of the restraint stiffness contribution from the compressive ring improves the average ratio of predicted to numerical central displacements from 1.084 to 1.012, with the coefficient of variation correspondingly reduced from 7.81% to 3.71%.



(a) Analytical prediction neglecting compressive ring action

Fig 6.13 – Verification of analytical compressive ring formulation for rectangular slabs: response in the x-direction (cont'd)



(b) Analytical prediction considering compressive ring action

Fig. 6.13 – Verification of analytical compressive ring formulation for rectangular slabs: response in the *x*-direction

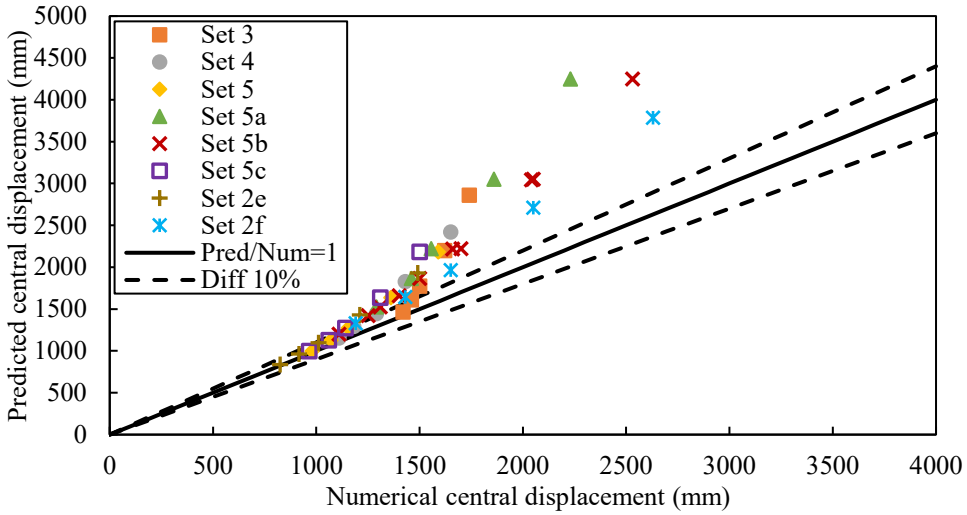
Once again, the analytical formulation neglecting the influence of the compressive ring generally offers a conservative estimate to the numerical central displacement, with the largest offset determined as +37.83%. On the other hand, the highest underestimated offset by the formulation considering the influence of the compressive ring is -5.42%.

For the response in the *y*-direction (Fig. 6.14), the average ratio of predicted to numerical central displacements improves from 1.253 to 0.995, with the coefficient of variation correspondingly reduced from 16.09% to 6.35%. The largest overestimated offset by the formulation neglecting the influence of the compressive ring is +90.49%, whilst the largest underestimated offset by the formulation considering such influence is -23.51%.

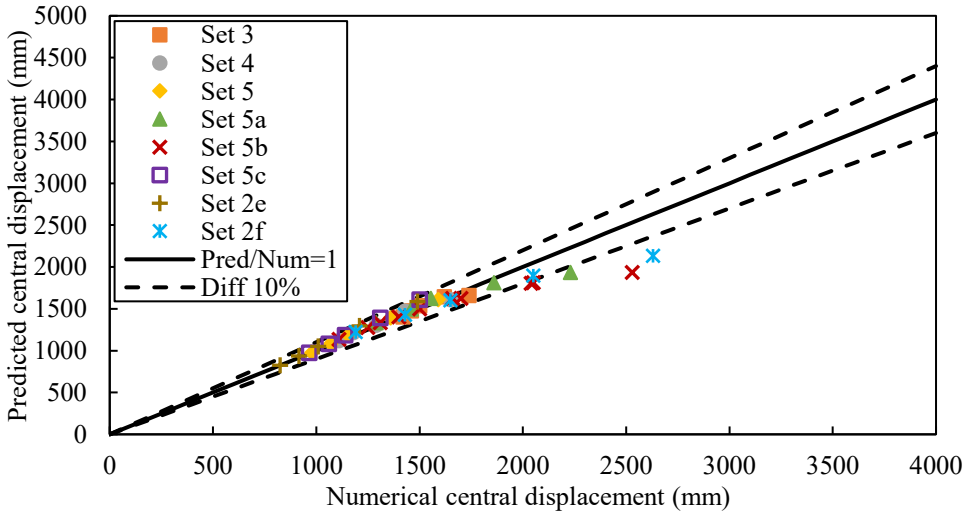
Such outcomes suggest that the assumptions undertaken for the thickness of the compressive ring (or the depth of the corresponding representative beams) are again reasonable. Furthermore, the largest offset between analytical and numerical results corresponds to the sets of assessment cases involving lowest planar restraint stiffness for the same reasons discussed in the verification of the square formulation.

It is worth noting that the average ratio of analytical to numerical central displacements in the *x*-direction determined with the formulation neglecting the influence of the compressive ring is within 10% of the unit value, suggesting that the actual restraint stiffness contribution from the compressive ring in the *x*-direction is already negligible due to the longer span. It is also worth noting that for increasing form factors the improvement achieved for the ratio of

analytical to numerical central displacements with the consideration of the compressive ring becomes less significant for the pull-in response in the *x*-direction and increasingly significant for the pull-in response in the *y*-direction. This suggests that the influence of the compressive ring progressively localises along the shorter edge of the floor system with increasing form factors.



(a) Analytical prediction neglecting compressive ring action



(b) Analytical prediction considering compressive ring action

Fig. 6.14 – Verification of analytical compressive ring formulation for rectangular slabs: response in the *y*-direction

In conclusion, the outcomes illustrated in Figs. 6.13 and 6.14 suggest that the proposed generalisation of the compressive ring formulation to cover rectangular floor system is reasonable from a practical application standpoint, though a more sophisticated relationship

can be established for the compressive ring thicknesses d_x and d_y to further improve prediction accuracy, ideally supported by experimental validation.

6.6 Conclusion

This chapter covers the extension of the supplementary method presented in Chapter 5 for the planar interaction of the floor system under sudden column loss with the surrounding structure. The extension includes the consideration of the restraint stiffness contribution from the compressive ring, which is not considered in the initial version of the supplementary method.

A tentative formulation assimilating the response of the compressive ring to that of a circular floor slab under large deformation, while working satisfactorily for circular floor slabs, failed to provide an accurate prediction for the planar pull-in of square slabs with an equivalent circular slab radius. In this respect, a simplified mechanical model involving two fully fixed beams configured in parallel is developed instead, with the two beams respectively representing the restraint contribution from the surrounding structure and the compressive ring along one edge of the square/rectangular floor system. Due simplifications are undertaken so as to retain the practicality of the proposed extension, specifically assuming an elastic response for the fully fixed beams and the predefinition of the compressive ring thickness as $0.1L$ and $0.1H$, respectively, for the longer and shorter edges of the rectangular floor system.

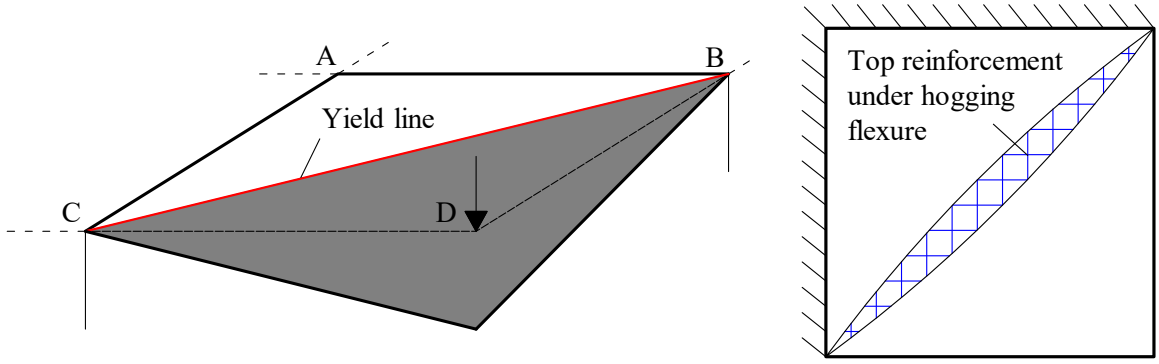
Verification of the proposed extension against numerical models demonstrates reasonable agreement between analytical and numerical outcomes for floor systems with form factors ranging from 1:1 to 2:1, suggesting that the thicknesses assumed for the compressive ring are appropriate. Importantly, the results also highlight the conservatism of the initial iteration of the supplementary method and the effectiveness of the proposed extension in improving the prediction provided that the surrounding structure offers a relatively low level of planar restraint stiffness. Otherwise, the proposed extension tends to underestimate the planar pull-in, and thus the minimum central displacement for the full activation of tying forces. Still, the proposed extension is deemed acceptable from a practical application standpoint, with possible improvement in prediction accuracy achieved via future elaboration of the expression for the compressive ring thickness.

Chapter 7: Rational horizontal tying force method for corner column loss scenario

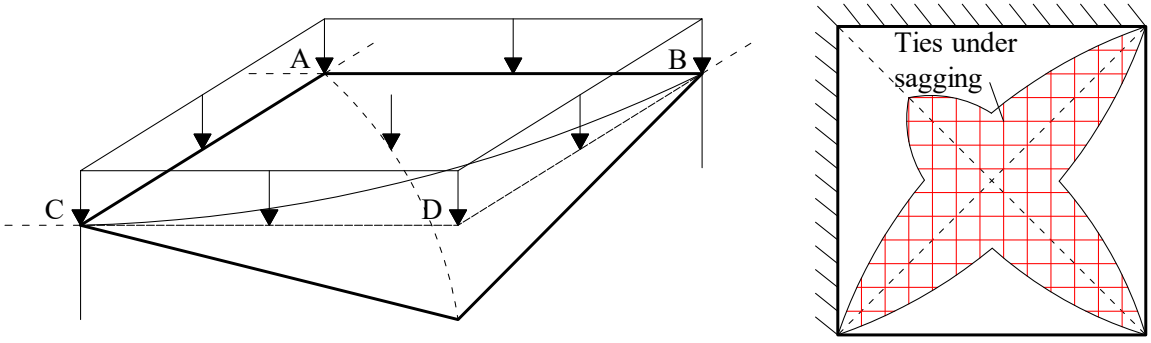
7.1 Introduction

Under a corner column loss scenario, the performance of typical floor systems involving the placement of reinforcement parallel to the edges of the system is generally limited to the flexural resistance, neglecting the beneficial enhancements from compressive arching action and tensile membrane action. This is specifically verified for floor systems where the top slab reinforcement is discontinued at mid-span and for systems under a dominant concentrated load applied at the free tip (Lim *et al.*, 2017a; Pham *et al.*, 2017a).

Notwithstanding, corner floor systems under uniformly distributed loading typically allow for a more significant activation of tensile membrane forces compared to systems under an applied concentrated load (Pham *et al.*, 2017a). Such further mobilisation of tensile membrane forces is primarily due to the different dominant mechanisms involved under the application of the two types of loading. Under a concentrated load applied at the free tip, the dominant mechanism is characterised by a hogging diagonal yield line BC, as illustrated in Fig. 7.1a, with the unsupported region of the floor slab rotating similarly to a rigid plate. Under this mechanism, the overall sagging of the corner floor system is limited (i.e. the deformation of the floor system along diagonal AD is similar to that of a cantilever beam). On the other hand, the presence of a uniformly distributed load imposes a dominant deformation mode where the corner floor system can undergo more significant sagging (Fig. 7.1b). Such sagging deformation is what allows for the potential formation of a tensile net via the bottom reinforcement within the central region of the corner floor system, as suggested in Pham *et al.* (2017a) and Qian *et al.* (2021). Nonetheless, even under uniformly distributed loading, typical current assumptions neglect the activation of tensile membrane forces due to inadequate planar restraint stiffness from the free edges of the corner floor system (Lim *et al.*, 2017a; Qian *et al.*, 2021).



(a) Concentrated load at the free tip



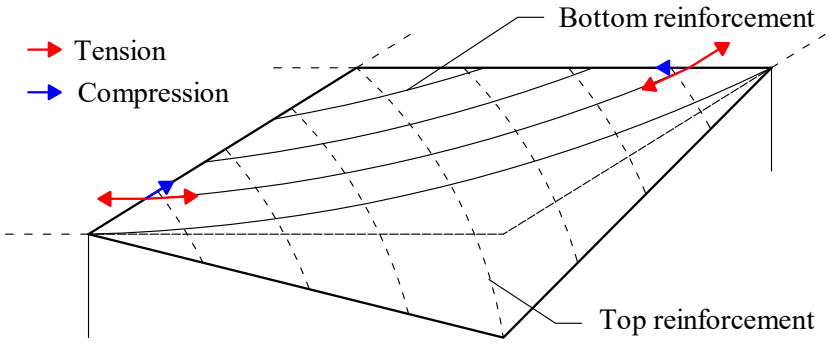
(b) Uniformly distributed load

Fig. 7.1 – Dominant mechanism for different loading conditions

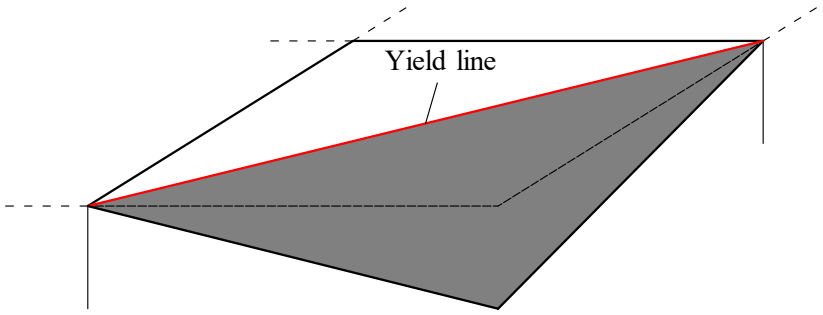
For a simplified analytical analysis of the floor system response under corner column loss, Zhang *et al.* (2018) developed an analytical model that is based on the virtual work principle, where the dominant applied loading is assumed to be the concentrated load at the free tip. The novelty of the analytical model is that, beyond the conventional work contribution from the flexural resistance at the plastic hinges and along the hogging yield line, consideration is also given to the work contribution from the local elongation of the reinforcement at the same locations. This consideration, which was first presented by Dong (2010), tentatively includes some effects associated with tensile membrane action. Nevertheless, given that the analytical model developed by Zhang *et al.* (2018) is limited to an applied concentrated load at the free tip, the underlying mechanism, which involves a rigid plate rotation of the outer part of the floor slab, still neglects the potential tensile membrane action developed under a deformation mode consistent with the application of a uniformly distributed load, noting that such a loading condition is generally dominant for actual building structures under a column loss scenario.

In recognition of the reduced activation of membrane forces currently considered for corner floor systems with typical placement of the reinforcement, the present thesis explores and proposes an alternative formulation under which both ends of the floor ties are anchored to the

restrained edges of the corner floor system, thereby exploiting a greater mobilisation of tensile membrane action. Consideration is initially given to a corner floor slab under a deformation mode as illustrated in Fig. 7.2 and involving two diagonal reinforcement layers, with a bottom layer spanning between the restrained edges and an orthogonal top layer spanning from the inner joint towards the outer unsupported corner. It clearly follows that the tensile forces from the bottom diagonal ties are equilibrated via the restraint offered by the surrounding structure and via the compression of the concrete along the supported edges. Indeed, the concept of an alternative resistance mechanism involving diagonal ties has been previously presented in *fib* Bulletin 63 (fib, 2012a) as a robustness strengthening strategy for precast concrete corner floor systems, though such recommendations remain at a qualitative level.



(a) Tying mechanism – equilibrium of diagonal ties



(b) Bending mechanism

Fig. 7.2 – Dominant deformation modes/mechanisms involved in the proposed method

Furthermore, provided that the planar pull-in of the floor slab can be reasonably quantified, resistance contributions additional to the tying of the bottom diagonal ties within the supported triangular region of the floor slab can also be considered, including the contribution from the bottom diagonal ties within the outer unsupported region and the orthogonal top reinforcement. It is also worth noting that the progressive mobilisation of tying of the bottom slab reinforcement with increasing deformation eventually leads to a change in mechanism due to

the exceedance of flexural resistance offered by the top reinforcement, with a deformation mode consisting of a rigid plate rotation of the unsupported region of the floor slab (Fig. 7.2b).

The tying method proposed herein, which is formulated based on the virtual work principle similar to Izzuddin and Sio (2022), effectively represents all the aforementioned dominant mechanisms and work contributions from the slab reinforcement, offering a rational means to assess a more significant mobilisation of tensile membrane action in floor systems under corner column loss. Importantly, unlike the formulation presented by Zhang *et al.* (2018), the proposed method considers the system response under uniformly distributed load, which is deemed a more realistic loading scenario for the robustness assessment of actual building structures. This chapter proceeds with the underlying assumptions for the proposed tying method. The formulation of the new method is then presented for the two fundamental deformation modes/mechanisms, followed by its verification against numerical models with varying quantities of reinforcement, span length and slab depth. The chapter culminates with a discussion on the applicability of the proposed method under typical placement of the slab reinforcement, i.e. parallel to the edges of the floor system, and on the additional resistance contribution from the beams in beam-slab corner floor systems.

7.2 General formulation

7.2.1 Rational basis and main assumptions

As a proposed extension to the horizontal tying force method developed by Izzuddin and Sio (2022), the tying method for corner column loss scenario also aims to provide an assessment framework that is anchored in the same rational basis utilised for alternate load path methods, as adopted in modern design codes such as the UFC code (DoD, 2009), whilst remaining sufficient practical for the robustness assessment and design of multi-storey buildings. For such a purpose, the following simplifications are considered within the current framework:

- The adequacy of tying under the sudden loss of a corner vertical load-bearing member is again considered on an individual floor level, ignoring interaction in resisting the gravity loads across the various storeys, such as the Vierendeel action of frames. This is a conservative approach provided that all floors have similar deformation mode, ductility limit and planar restraint conditions.
- As it currently stands, the assessment is undertaken for a square slab-only corner floor system, the boundaries of which are defined by the two free edges of the slab and two

supported edges representing the column/wall gridlines surrounding the lost column/wall. Notwithstanding, with the aim to implicitly represent the geometric restraint from eventual beams of a beam-slab floor system, the free edges are assumed to deform in a rigid manner. Implications of the boundary beams on the robustness performance of the corner floor system is qualitatively assessed at the end of the present chapter.

- The response of the corner floor system is represented with two dominant deformation modes: i) a tying mechanism where the corner floor system follows a bilinear transverse deformation mode (Fig. 7.2a); and ii) a bending mechanism where the unsupported region of the corner floor system displaces similarly to a rigid plate (Fig. 7.2b). The critical deformation mode depends on the ratio of top-to-bottom reinforcement and on the extent of the tying forces mobilised under the tying mechanism.
- Resistance to gravity loading under the tying mechanism is achieved mainly via two contributions (Fig. 7.2a): i) the elongation of the diagonal bottom reinforcement and ii) the elongation of the orthogonal top reinforcement. It is worth noting that both bottom and top reinforcements are continuous throughout the slab. It is also worth noting that the elongation of the diagonal bottom reinforcement is mainly due to tying, with specific adjustment considered for the reinforcement strains within the unsupported triangular part of the floor slab since the free edges are unrestrained in-plane and the resulting planar pull-in would affect such strains. On the other hand, the elongation of the top reinforcement is mainly due to flexure of the floor slab in the considered direction, behaving like a cantilever beam, though a more significant mobilisation of tying can be observed near the corners of the floor system due to the imposed in-plane deformation. Such assumptions are deemed conservative as the method neglects the additional contribution from other residual flexural resistances.
- Resistance to gravity loading under the bending mechanism is achieved mainly via flexure of the slab along the diagonal hogging yield line illustrated in Fig. 7.2b. The proposed method considers the flexural resistance to be established based on an undeformed yield line, and hence a flat rectangular cross-section. This is again a conservative assumption given that the actual transverse deformation of the floor slab leads to a deformed ‘U’ cross-section along the diagonal yield line with an increased flexural resistance.

- The affected floor system presents sufficient ductility as well as planar restraint at the supported edges to mobilise tensile membrane action.
- The surrounding columns/walls have sufficient capacity to resist the redistributed gravity loading. The dynamic amplification of the redistributed gravity loading associated to sudden column loss can be determined via an approach similar to the supplementary method also provided in Izzuddin and Sio (2022).

Lastly, it is worth noting that the proposed tying method for corner column loss scenario also relies on the provision of the ductility limit for the corner floor system, which is herein expressed as the chord rotation of the unsupported edges.

7.2.2 Tying mechanism

Consideration is given herein to the case where the corner floor slab is under the tying mechanism, the governing deformation mode of which follows a bilinear approximation (Fig. 7.3a). Such a mechanism is considered to be dominant for corner slab systems where the resistance of the top reinforcement is adequate to prevent the development of the bending mechanism. The discrete equilibrium between the tying forces and the applied load is established with the principle of virtual work:

$$T_1 + T_2 + T_3 = \int_0^L \int_0^L w(x,y)\ \delta v(x,y)\, dxdy \tag{7.1}$$

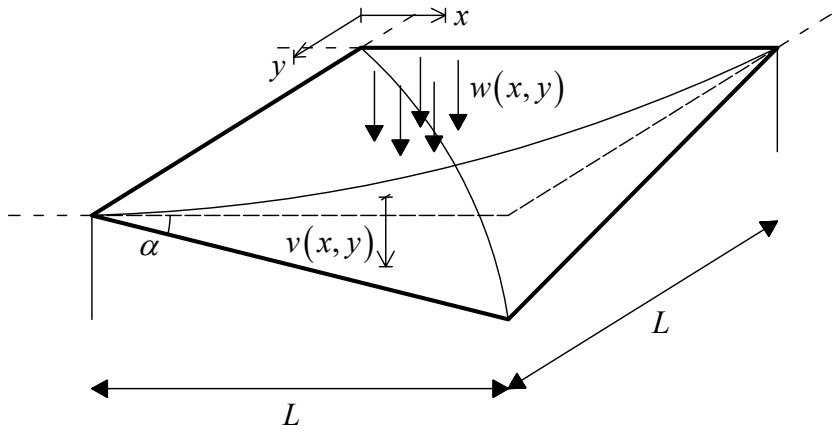
with the right side of the equality representing the external virtual work of the applied load $w(x,y)$ under the transverse displacement $v(x,y)$, as given by:

$$v(x,y) = \alpha\, \Phi(x,y), \quad \delta v(x,y) = \Phi(x,y)\, \delta\alpha, \quad \Phi(x,y) = \frac{xy}{L} \tag{7.2}$$

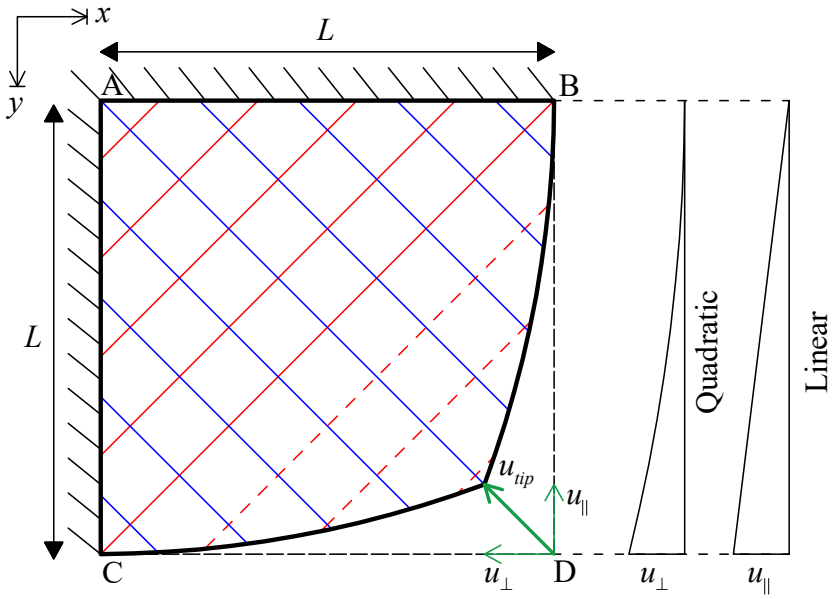
where α is the chord rotation of the unsupported/free edge of the corner floor system.

On the other hand, the left side of the equality represents the internal work from the reinforcement, comprising of three main contributions (Fig. 7.3b): the top reinforcement spanning in the direction AD (T_1) – depicted as blue lines; the bottom reinforcement spanning in the direction CB and within the supported region of the corner slab (T_2) – depicted as red solid lines; and the bottom reinforcement spanning in the direction CB and within the

unsupported region of the corner slab (T_3) – depicted as red dashed lines. The following sub-sections provide the derivation for such contributions.



(a) Transverse deformation and general loading case



(b) In-plane deformation and considered resistance contributions

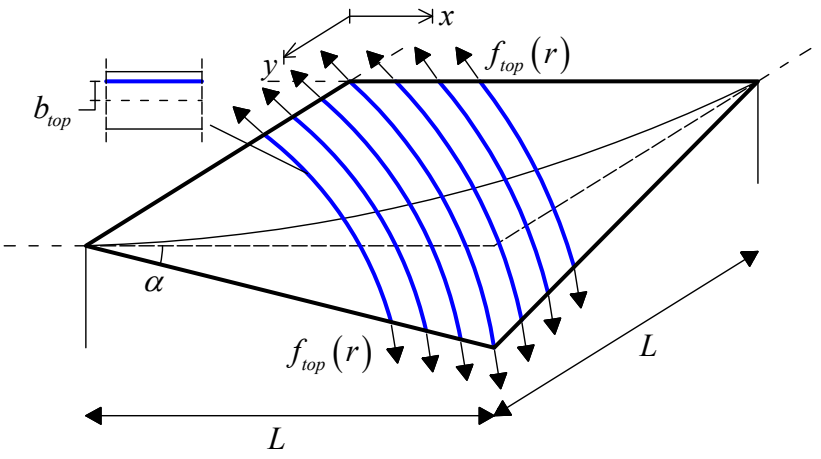
Fig. 7.3 – General case under tying mechanism

7.2.2.1 Derivation for T_1

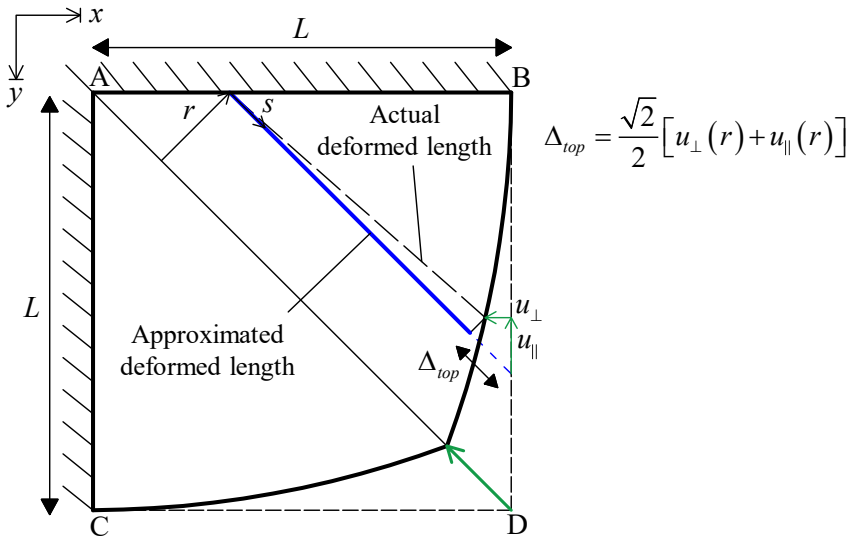
According to Fig. 7.4, the internal virtual work done by the distributed force of the top slab reinforcement $f_{top}(r)$ is given by:

$$T_1 = 2\left(\int_0^{R=\sqrt{2}L/2}\int_0^{S} f_{top}(r)\,\delta\varepsilon(x,y)\,ds\,dr\right) \tag{7.3}$$

where $\varepsilon(x,y)$ is the axial strain of the top slab reinforcement due to the considered deformation mechanism.



(a) Transverse deformation



(b) In-plane deformation

Fig. 7.4 – Tying contribution from the top reinforcement

The above equation first determines the elongation of a single line of top reinforcement via the integration over *ds*, which represents the direction in which the reinforcement is spanned. The equation then proceeds to integrate over *dr*, adding up the contribution from the distributed reinforcement. It is worth noting though that the integrations over *ds* and *dr* provide the internal virtual work of the top reinforcement for only half of the corner floor system, hence assuming that the top reinforcement is symmetric about segment AD illustrated in Fig. 7.4 the factor of 2 in (7.3) provides the full contribution of the top reinforcement to the internal virtual work. It is also worth noting that, despite the integration of (7.3) being performed over a

reference rotated by 45 degrees from the x and y axis, the axial strain $\varepsilon(x,y)$ is demonstrated subsequently to be partially defined as a function of x and y, hence requiring a parametrisation of these variables.

In this respect, considering the parametrisation of x and y along a diagonal straight segment at distance r, starting at the supported edge $(t=0)$ and ending at the free edge $(t=1)$ of the corner floor system, (7.3) can be expressed as:

$$T_1 = 2\left(\int_0^{\sqrt{2}L/2} \int_0^1 f_{top}(r)\, \delta\varepsilon(x,y) \sqrt{\left(\frac{\partial x}{\partial t}\right)^2 + \left(\frac{\partial y}{\partial t}\right)^2}\, dt dr \right) \tag{7.4}$$

with the parametrised function given as:

$$\begin{bmatrix} x \\ y \end{bmatrix} = (1-t)\begin{bmatrix} r\sqrt{2} \\ 0 \end{bmatrix} + t\begin{bmatrix} L \\ L\left(1-\dfrac{r\sqrt{2}}{L}\right) \end{bmatrix} \tag{7.5}$$

The strain of a single top reinforcement at distance r is herein established as:

$$\begin{aligned} \varepsilon(x,y) &= \left[\frac{1}{l_{top}(r)} \int_0^1 \frac{1}{2}\left(\frac{\partial v(x,y)}{\partial s}\right)^2 \sqrt{\left(\frac{\partial x}{\partial t}\right)^2 + \left(\frac{\partial y}{\partial t}\right)^2}\, dt \right] \\ &\quad + \left[b_{top} \frac{\partial^2 v(x,y)}{\partial s^2} \right] - \left[\frac{1}{l_{top}(r)} \frac{\sqrt{2}}{2} \left[u_{\perp}(r) + u_{\parallel}(r) \right] \right] \\ \delta\varepsilon(x,y) &= \left[\frac{1}{l_{top}(r)} \int_0^1 \alpha \left(\frac{\partial \Phi(x,y)}{\partial s}\right)^2 \delta\alpha \sqrt{\left(\frac{\partial x}{\partial t}\right)^2 + \left(\frac{\partial y}{\partial t}\right)^2}\, dt \right] \\ &\quad + \left[b_{top} \frac{\partial^2 \Phi(x,y)}{\partial s^2} \delta\alpha \right] - \left[\frac{1}{l_{top}(r)} \frac{\sqrt{2}}{2} \left[\delta u_{\perp}(r) + \delta u_{\parallel}(r) \right] \right] \end{aligned} \tag{7.6}$$

where $l_{top}(r)$ is the length of the top reinforcement at distance r, given as:

$$l_{top}(r) = \int_0^1 \sqrt{\left(\frac{\partial x}{\partial t}\right)^2 + \left(\frac{\partial y}{\partial t}\right)^2}\, dt = \sqrt{2}L - 2r \tag{7.7}$$

It is worth noting that (7.6) provides an average strain along a single line of top reinforcement at distance r, which depends on three contributions according to Fig. 7.4. The first term of the equation represents the strains due to the transverse displacement $v(x,y)$, considering that the reinforcement is located at the mid-plane of the floor slab and that there is no pull-in. This term is an approximation valid in the range of moderate displacement, as determined by typical ductility levels. The second term considers the additional strain due to the actual offset of the top reinforcement with reference to the mid-plane of the floor slab, which is established as the product between the curvature of the diagonal tie $\partial^2 v/\partial s^2$ and its distance to the mid-plane b_{top}. The third term corrects the strains to cover the planar pull-in along the unsupported edges of the corner slab. In this respect, the strain to be subtracted is established based on the assumed in-plane deformation mode. According to Fig. 7.3b, the in-plane deformation presents the largest pull-in at the free tip of the corner slab, defined as u_{tip}, with the pull-in progressively decreasing along the free/unsupported edges until it reaches zero displacement at the adjacent corners. The proposed method considers a quadratic variation for the pull-in component that is perpendicular to the free edges $u_{\perp}(r)$, whilst a linear variation is assumed for the component parallel to the free edges $u_{\parallel}(r)$:

$$
\begin{aligned}
&u_{\perp}(r)=\frac{\sqrt{2}}{2}u_{tip}\left(1-\frac{r}{R}\right)^2, \quad \delta u_{\perp}(r)=\frac{\sqrt{2}}{2}\delta u_{tip}\left(1-\frac{r}{R}\right)^2 \\
&u_{\parallel}(r)=\frac{\sqrt{2}}{2}u_{tip}\left(1-\frac{r}{R}\right), \quad \delta u_{\parallel}(r)=\frac{\sqrt{2}}{2}\delta u_{tip}\left(1-\frac{r}{R}\right) \\
&R=\frac{\sqrt{2}}{2}L
\end{aligned}
\tag{7.8}
$$

The total shortening for the diagonal top reinforcement at distance r is then given as the projection of the perpendicular and parallel in-plane displacements onto the initial direction of the reinforcement, as expressed in the third term of (7.6). It is worth noting that this is a conservative simplification compared to the actual difference between initial and final reinforcement lengths because the assumption overestimates the shortening of the reinforcement (see Fig. 7.4).

With the variation of the pull-in displacement defined as per (7.8), the remaining component yet to be quantified is the pull-in displacement at the free tip u_{tip}. Considering that the centre diagonal slab strip (segment AD) is mainly under flexure, with a deformation similar to a

cantilever, it is appropriate under large deflections to assume that the centre of rotation is located at the bottom fibre of the slab strip, where the condition of zero strain applies. Accordingly, the pull-in should be such that it cancels out the elongation at the bottom fibre due to the transverse displacement $v(x,y)$:

$$\begin{aligned} u_{tip} &= \left[\int_0^1 \frac{1}{2} \left(\frac{\partial v(x,y)}{\partial s} \right)^2 \sqrt{\left(\frac{\partial x}{\partial t} \right)^2 + \left(\frac{\partial y}{\partial t} \right)^2} \, dt \right] - \left[l_{top}(r=0) \frac{h}{2} \frac{\partial^2 v(x,y)}{\partial s^2} \right] \\ \delta u_{tip} &= \left[\int_0^1 \alpha \left(\frac{\partial \Phi(x,y)}{\partial s} \right)^2 \delta\alpha \sqrt{\left(\frac{\partial x}{\partial t} \right)^2 + \left(\frac{\partial y}{\partial t} \right)^2} \, dt \right] - \left[l_{top}(r=0) \frac{h}{2} \frac{\partial^2 \Phi(x,y)}{\partial s^2} \delta\alpha \right] \end{aligned} \tag{7.9}$$

where h is the thickness of the slab and $l_{top}(r=0)$ is the length of the top reinforcement determined with (7.7) for $r=0$. Here again, the strains are expressed in an average sense, with the first term representing the elongation at mid-plane due to the transverse displacement, in which x and y are evaluated from (7.5) at $r=0$, whereas the second term represents the difference in elongation between the mid-plane and the bottom fibre of the floor slab. It is worth noting that $\partial^2 v / \partial s^2$ is constant for the assumed deformation mode.

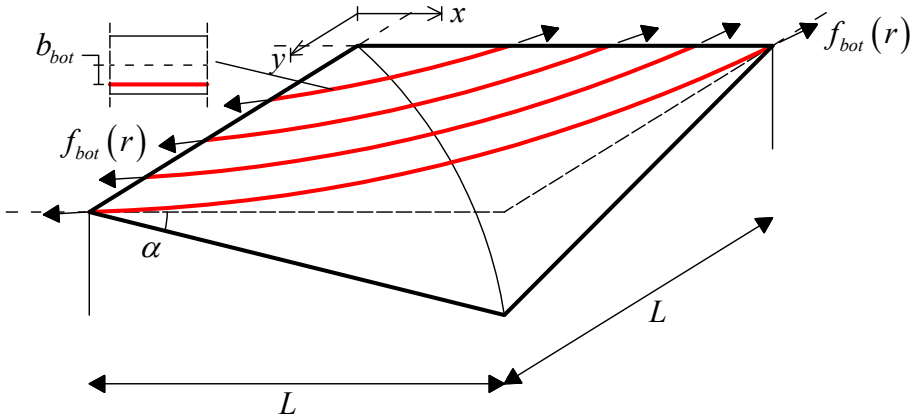
Lastly, it follows that (7.6)-(7.9) require differentiation of the transverse displacement $v(x,y)$ over the direction of the diagonal top reinforcement, which can be obtained via the directional differentiation using the corresponding vector:

$$ds = \left\langle \frac{\sqrt{2}}{2} \quad \frac{\sqrt{2}}{2} \right\rangle^{\mathrm{T}}, \quad \frac{\partial \Phi(x,y)}{\partial s} = \frac{\sqrt{2}(x+y)}{2L}, \quad \frac{\partial^2 \Phi(x,y)}{\partial s^2} = \frac{1}{L} \tag{7.10}$$

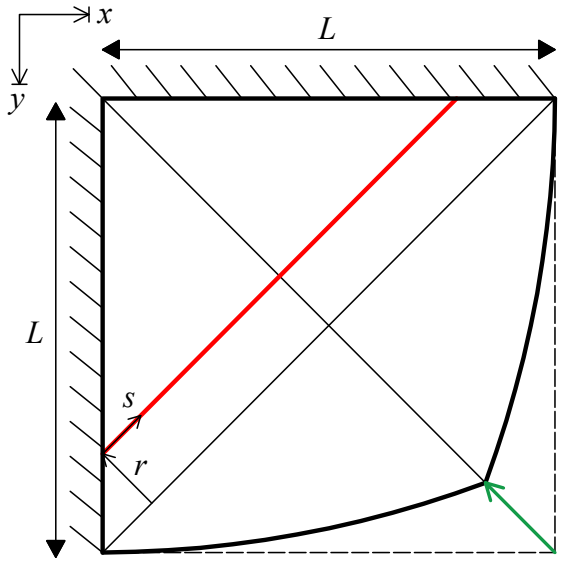
7.2.2.2 Derivation for T_2

Considering the reference system illustrated in Fig. 7.5, the internal virtual work of the bottom reinforcement within the supported region of the corner slab is given as:

$$T_2 = \left(\int_0^{R=\sqrt{2}L/2} \int_0^S f_{bot}(r)\, \delta\varepsilon(x,y)\, ds dr \right)$$
$$= \left(\int_0^{\sqrt{2}L/2} \int_0^1 f_{bot}(r)\, \delta\varepsilon(x,y) \sqrt{\left(\frac{\partial x}{\partial t}\right)^2 + \left(\frac{\partial y}{\partial t}\right)^2}\, dt dr \right) \tag{7.11}$$



(a) Transverse deformation



(b) In-plane deformation

Fig. 7.5 – Tying contribution from the bottom reinforcement within the supported region

The parametrised functions of x and y in (7.11) are now established based on a diagonal straight segment at distance r, starting at the supported edge parallel to the y axis $(t=0)$ and ending at the supported edge parallel to the x axis $(t=1)$:

$$\begin{bmatrix} x \\ y \end{bmatrix} = (1-t)\begin{bmatrix} 0 \\ L\left(1-\dfrac{r\sqrt{2}}{L}\right) \end{bmatrix} + t\begin{bmatrix} L\left(1-\dfrac{r\sqrt{2}}{L}\right) \\ 0 \end{bmatrix} \tag{7.12}$$

Furthermore, given that the ends of this reinforcement are anchored at the restrained edges, i.e. unaffected by the planar pull-in, the strain of the reinforcement is established only based on the transverse displacement and the additional contribution due to the offset of the reinforcement in relation to the mid-plane:

$$\begin{aligned} \varepsilon(x,y) &= \left[\frac{1}{l_{bot}(r)}\int_0^1 \frac{1}{2}\left(\frac{\partial v(x,y)}{\partial s}\right)^2 \sqrt{\left(\frac{\partial x}{\partial t}\right)^2+\left(\frac{\partial y}{\partial t}\right)^2}\,dt\right] \\ &\quad -\left[b_{bot}\frac{\partial^2 v(x,y)}{\partial s^2}\right] \\ \delta\varepsilon(x,y) &= \left[\frac{1}{l_{bot}(r)}\int_0^1 \alpha\left(\frac{\partial \Phi(x,y)}{\partial s}\right)^2 \delta\alpha\sqrt{\left(\frac{\partial x}{\partial t}\right)^2+\left(\frac{\partial y}{\partial t}\right)^2}\,dt\right] \\ &\quad -\left[b_{bot}\frac{\partial^2 \Phi(x,y)}{\partial s^2}\delta\alpha\right] \end{aligned} \tag{7.13}$$

where b_{bot} is the distance of the bottom reinforcement to the mid-plane of the corner slab. On the other hand, $l_{bot}(r)$ is given as:

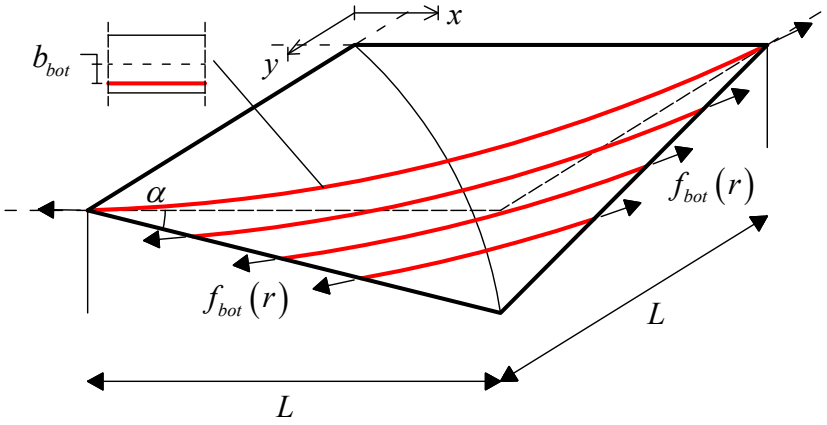
$$l_{bot}(r) = \int_0^1 \sqrt{\left(\frac{\partial x}{\partial t}\right)^2+\left(\frac{\partial y}{\partial t}\right)^2}\,dt = \sqrt{2}L - 2r \tag{7.14}$$

It is worth noting the minus sign for the additional contribution due to the offset of the bottom reinforcement in relation to the mid-plane, which corrects the sign determined from the curvature of the reinforcement, i.e. second derivative of the transverse displacement. Lastly, directional differentiation of the transverse displacement $v(x,y)$ is obtained over the direction of the bottom reinforcement, presenting the following directional vector:

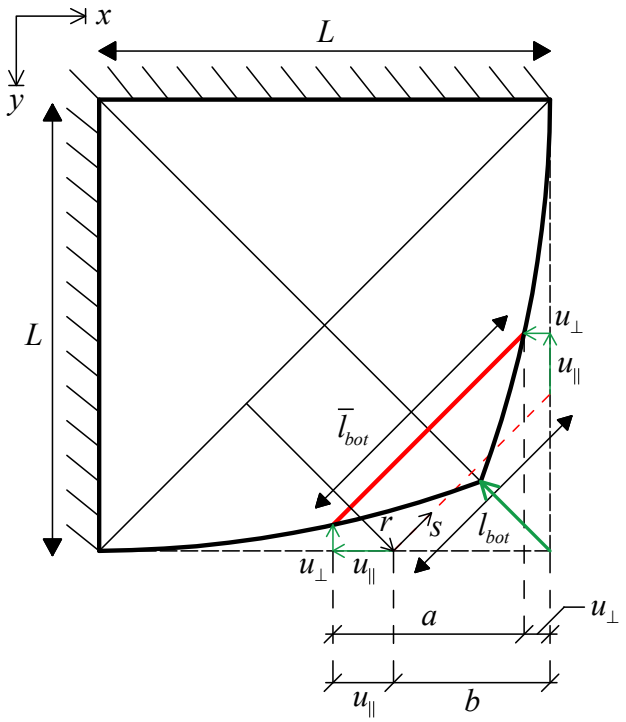
$$ds = \left\langle \frac{\sqrt{2}}{2} \quad -\frac{\sqrt{2}}{2} \right\rangle^{\mathrm{T}}, \quad \frac{\partial \Phi(x,y)}{\partial s} = \frac{\sqrt{2}(y-x)}{2L}, \quad \frac{\partial^2 \Phi(x,y)}{\partial s^2} = -\frac{1}{L} \tag{7.15}$$

7.2.2.3 Derivation for T_3

The reference system for the derivation of the internal virtual work from the bottom reinforcement within the unsupported triangular region is defined as illustrated in Fig. 7.6.



(a) Transverse deformation



$$\varepsilon(r) = \frac{\bar{l}_{bot}(r) - l_{bot}(r)}{l_{bot}(r)}$$

$$\bar{l}_{bot}(r) = \sqrt{2}a$$

$$a = b + u_{\parallel}(r) - u_{\perp}(r)$$

$$b = \left(1 - \frac{r}{R}\right)L$$

$$R = \frac{\sqrt{2}}{2}L$$

(b) In-plane deformation

Fig. 7.6 – Tying contribution from bottom reinforcement within the unsupported region

Accordingly, the internal virtual work is established as:

$$\begin{aligned} T_3 &= \left(\int_0^{R=\sqrt{2}L/2} \int_0^S f_{bot}(r)\ \delta\varepsilon(x,y)\, ds dr \right) \\ &= \left(\int_0^{\sqrt{2}L/2} \int_0^1 f_{bot}(r)\ \delta\varepsilon(x,y) \sqrt{\left(\frac{\partial x}{\partial t}\right)^2 + \left(\frac{\partial y}{\partial t}\right)^2}\, dt dr \right) \end{aligned} \tag{7.16}$$

The parametrised functions of x and y in (7.16) are now established based on a diagonal straight segment at distance r, starting at the unsupported edge parallel to the x reference $(t=0)$ and ending at the unsupported edge parallel to the y reference $(t=1)$:

$$\begin{bmatrix} x \\ y \end{bmatrix} = (1-t) \begin{bmatrix} r\sqrt{2} \\ L \end{bmatrix} + t \begin{bmatrix} L \\ r\sqrt{2} \end{bmatrix} \tag{7.17}$$

Further to the strain contributions from the transverse displacement and the offset of the reinforcement in relation to the mid-plane of the slab, the bottom reinforcement within the unsupported region should again consider the influence from the planar pull-in, which under the assumed approximation for the in-plane deformation mode, as illustrated in Fig. 7.6, leads to an additional contribution of reinforcement elongation:

$$\begin{aligned} \varepsilon(x,y) &= \left[\frac{1}{l_{bot}(r)} \int_0^1 \frac{1}{2} \left(\frac{\partial v(x,y)}{\partial s} \right)^2 \sqrt{\left(\frac{\partial x}{\partial t}\right)^2 + \left(\frac{\partial y}{\partial t}\right)^2}\, dt \right] \\ &\quad - \left[b_{bot} \frac{\partial^2 v(x,y)}{\partial s^2} \right] + \left[\frac{\bar{l}_{bot}(r) - l_{bot}(r)}{l_{bot}(r)} \right] \\ \delta\varepsilon(x,y) &= \left[\frac{1}{l_{bot}(r)} \int_0^1 \alpha \left(\frac{\partial \Phi(x,y)}{\partial s} \right)^2 \delta\alpha \sqrt{\left(\frac{\partial x}{\partial t}\right)^2 + \left(\frac{\partial y}{\partial t}\right)^2}\, dt \right] \\ &\quad - \left[b_{bot} \frac{\partial^2 \Phi(x,y)}{\partial s^2} \delta\alpha \right] + \left[\frac{\delta\bar{l}_{bot}(r)}{l_{bot}(r)} \right] \end{aligned} \tag{7.18}$$

where b_{bot} is again the distance of the bottom reinforcement to the mid-plane of the corner slab. On the other hand, the length of the bottom reinforcement at distance r, $l_{bot}(r)$, is given as:

$$l_{bot}(r)=\int_0^1\sqrt{\left(\frac{\partial x}{\partial t}\right)^2+\left(\frac{\partial y}{\partial t}\right)^2}\,dt=\sqrt{2}L-2r \tag{7.19}$$

whilst $\bar{l}_{bot}(r)$ represents the elongated length of the reinforcement at distance r, which is established based on Fig. 7.6 as:

$$\begin{aligned}
&\bar{l}_{bot}(r)=\sqrt{2}\left[\left(1-\frac{r}{R}\right)L+u_{\parallel}(r)-u_{\perp}(r)\right]\\
&\delta\bar{l}_{bot}(r)=\sqrt{2}\left[\delta u_{\parallel}(r)-\delta u_{\perp}(r)\right]\\
&R=\frac{\sqrt{2}}{2}L
\end{aligned} \tag{7.20}$$

with the variation of the planar pull-in in the orthogonal and parallel directions re-defined for the current reference as:

$$\begin{aligned}
&u_{\perp}(r)=\frac{\sqrt{2}}{2}u_{tip}\left(\frac{r}{R}\right)^2,\quad \delta u_{\perp}(r)=\frac{\sqrt{2}}{2}\delta u_{tip}\left(\frac{r}{R}\right)^2\\
&u_{\parallel}(r)=\frac{\sqrt{2}}{2}u_{tip}\left(\frac{r}{R}\right),\quad \delta u_{\parallel}(r)=\frac{\sqrt{2}}{2}\delta u_{tip}\left(\frac{r}{R}\right)
\end{aligned} \tag{7.21}$$

where u_{tip} is again the planar pull-in at the free tip and remains that determined with (7.9).

Here again, the derivatives of the transverse displacement $v(x,y)$ in (7.18) can be obtained via the directional differentiation of $v(x,y)$ over the directional vector:

$$ds=\left\langle\frac{\sqrt{2}}{2}\quad -\frac{\sqrt{2}}{2}\right\rangle^{\mathrm{T}},\quad \frac{\partial\Phi(x,y)}{\partial s}=\frac{\sqrt{2}(y-x)}{2L},\quad \frac{\partial^2\Phi(x,y)}{\partial s^2}=-\frac{1}{L} \tag{7.22}$$

7.2.2.4 Equilibrium

As the main verification case for this chapter, equilibrium is established for the case considering constant distributed reinforcement and uniformly distributed load applied over the corner slab. Other sources of tying and loading configurations can be simply worked out via (7.1), (7.3), (7.11) and (7.16) considering appropriate functions for $f_{top}(r)$, $f_{bot}(r)$ and $w(x,y)$.

Accordingly, for the case of constant top and bottom reinforcement distributed over the entire corner slab $\left(f_{top}, f_{bot}\right)$, the three contributions to the internal work, as determined per (7.3), (7.11) and (7.16), results in:

$$\begin{aligned} T_1 &= \frac{f_{top} L\left(\alpha L + 36 b_{top} + 15h\right)}{36} \delta\alpha \\ T_2 &= \frac{f_{bot} L\left(\alpha L + 12 b_{bot}\right)}{24} \delta\alpha \\ T_3 &= \frac{f_{bot} L\left(11\alpha L + 36 b_{bot} - 6h\right)}{72} \delta\alpha \\ T_1 + T_2 + T_3 &= \frac{L}{36}\left[f_{bot}\left(7\alpha L + 36 b_{bot} - 3h\right) + f_{top}\left(\alpha L + 36 b_{top} + 15h\right)\right]\delta\alpha \end{aligned} \tag{7.23}$$

On the other hand, the external virtual work done by the uniformly distributed load w over the assumed transverse deformation mode results in:

$$\int_0^L \int_0^L w(x,y)\ \delta v(x,y)\, dx dy = \frac{w L^3}{4} \delta\alpha \tag{7.24}$$

Thus, discrete equilibrium provides the following relationship between load w and chord rotation α :

$$w = \frac{1}{9L^2}\left[f_{bot}\left(7\alpha L + 36 b_{bot} - 3h\right) + f_{top}\left(\alpha L + 36 b_{top} + 15h\right)\right] \tag{7.25}$$

7.2.3 Bending mechanism

Consideration is given herein to the formulation of the resistance associated with the alternative bending mechanism, with a deformation mode defined by conventional yield line analysis, i.e. the development of a diagonal yield line along segment BC and subsequent rigid plate rotation of the unsupported region of the slab, as illustrated in Fig. 7.7. Such a mechanism is dominant when the top reinforcement becomes insufficient to resist the hogging flexure imposed by the applied loads. The discrete equilibrium between the flexural resistance about the hogging yield line and the applied loads can be established with the virtual work principle:

$$\int_{-\sqrt{2}L/2}^{\sqrt{2}L/2} m_{rr}(s)\, \delta\theta\, ds = \int_0^{\sqrt{2}L/2} \int_{-\sqrt{2}L/2+r}^{\sqrt{2}L/2-r} w(x,y)\ \delta v(r)\, ds\, dr \tag{7.26}$$

where $m_{rr}(s)$ and θ are respectively the flexural moment resistance and the rotation about the hogging yield line. On the other hand, $w(x,y)$ is the applied load and $v(r)$ is the transverse displacement approximation for the bending mechanism.

$$\theta = \frac{2}{\sqrt{2}}\alpha, \quad \delta\theta = \frac{2}{\sqrt{2}}\delta\alpha \tag{7.27}$$

$$v(r) = \alpha\Phi(r), \quad \delta v(x,y) = \Phi(r)\delta\alpha, \quad \Phi(r) = \left(\frac{2r}{\sqrt{2}}\right) \tag{7.28}$$

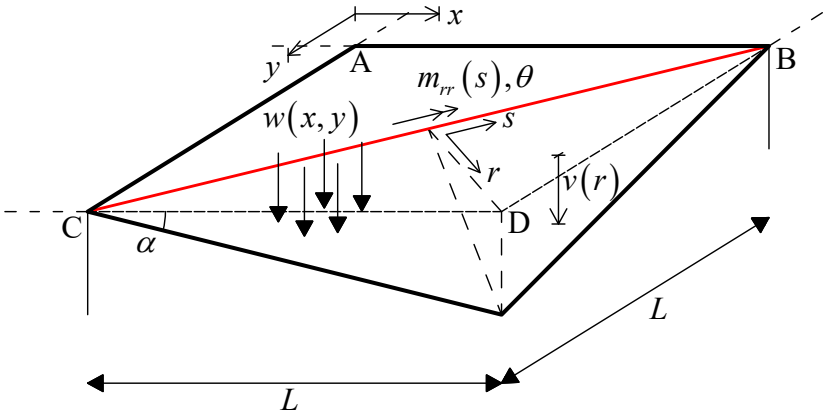


Fig. 7.7 – General case under bending mechanism

Accordingly, for the case of constant distributed top reinforcement, thus constant flexural resistance m_{rr}, and a uniformly distributed load w applied over the entire corner floor slab, the discrete equilibrium condition presented in (7.26) provides this limiting condition on w:

$$\begin{cases} W_{int} = 2m_{rr}L\delta\alpha \\ W_{ext} = w\dfrac{L^3}{6}\delta\alpha \end{cases} \Rightarrow W_{int} = W_{ext} \Rightarrow w = \frac{12m_{rr}}{L^2} \tag{7.29}$$

7.3 Verification of the proposed tying method

Consideration is given herein to the verification of the proposed method against the response predicted by numerical models in ADAPTIC (Izzuddin, 1991), noting that the validity of the nonlinear finite element analysis program in representing the nonlinear response of RC floor systems has been previously demonstrated in Chapter 5.

7.3.1 Verification cases and model description

The verification of the proposed method proceeds with two slab-only control specimens, for which the geometric and reinforcement details are summarised in Table 7.1, whilst the relevant concrete and steel properties are provided in Table 7.2. The detailing of the reinforcement is that illustrated in Fig. 7.3b, entailing top reinforcement spanning in the direction AD and bottom reinforcement spanning in the orthogonal direction.

Table 7.1 – Geometric and reinforcement details for the control corner floor systems

Span length of the floor system, L	4500mm	6500mm
Slab depth, h	120mm	180mm
Top reinforcement, $A_{s,top}$	ϕ8//250 (mm)	ϕ12//125 (mm)
Distance to mid-plane, b_{top}	49mm	64mm
Bottom reinforcement, $A_{s,bot}$	ϕ8//250 (mm)	ϕ12//125 (mm)
Distance to mid-plane, b_{bot}	49mm	64mm

Table 7.2 – Concrete and steel properties

Span length of the floor system, L	4500mm	6500mm
Concrete		
Young's modulus	28355MPa	31476MPa
Poisson's ratio	0.2	0.2
Compressive strength	23.3MPa	33MPa
Tensile strength	0.0MPa	0.0MPa
Steel		
Young's modulus	185864MPa	200000MPa
Yield strength	355MPa	435MPa

Since the aim of the current verification is to assess the accuracy of the proposed method specifically in predicting the tensile membrane response of the presented control specimens, i.e. the system response at large displacements, the modelling assumptions and simplifications are accordingly considered for such a purpose.

In this respect, the material laws considered for the concrete and the reinforcement entail respectively a biaxial rotating crack model with a linear elastic compressive response, con9 (Izzuddin, 2016), and an elastic-perfectly plastic bilinear model, stl1 (Izzuddin, 1991). Specifically, the former model neglects the tensile strength of the concrete, which is a reasonable assumption under large displacements, since the concrete should be extensively cracked, with the resistance contribution primarily arising from the reinforcement. On the other

hand, the latter model simply limits the resistance of the steel reinforcement to the yield strength.

The restraints of the supported and free edges of the corner slab are as illustrated in Fig. 7.8. The supported edges are unrestrained in rotation and consider planar restraint only in the direction orthogonal to these edges. Such assumptions neglect the resistance contributions that are additional to tying and the compressive membrane action that develops during the initial phase of loading. The free edges of the floor slab, on the other hand, are assumed to deform rigidly, resulting in a linear variation of the transverse displacement along the edges. This idealisation is achieved via the application of rigid links, which are coupled to the free edges of the slab, as illustrated in Fig. 7.8. Although the proposed method as it currently stands focuses solely on the tying contribution from the floor slab, hence neglecting the resistance developed by the beams of the corner floor system, the idealised restraint is considered so as to emulate the geometric restraint imposed by the beams. Furthermore, it also approximates the transverse deformation of the numerical model to the bilinear approximation assumed in the proposed method.

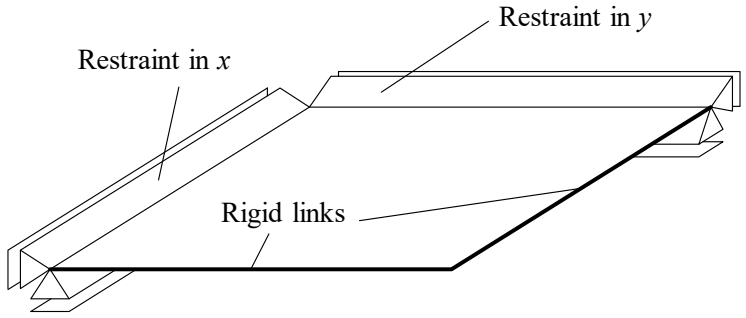


Fig. 7.8 – Boundary assumptions for the numerical models

7.3.2 Pull-in at the free tip and average reinforcement strains

With reference to (7.9), the pull-in at the free tip of a corner floor system is predicted via the proposed method as:

$$u_{tip} = \frac{v}{L}\left[\frac{\sqrt{2}}{3}v - \frac{\sqrt{2}}{2}h\right] \tag{7.30}$$

where v is the transverse displacement at the free tip; L is the span length; and h is the slab depth. The above equation indicates that, the pull-in at the free tip varies quadratically with the transverse displacement and solely depends on the geometry of the floor slab, thus insensitive to the amount of top and bottom reinforcement.

Fig. 7.9 demonstrates a good agreement between the predicted (TM) and numerical (NM) pull-in at the free tip of the considered control specimens, with the proposed method slightly underestimating the pull-in for the case with a span length of 6500mm. Such a good agreement suggests that the assumption of zero stain at the bottom fibre of the slab strip along segment AD (Fig. 7.4) is realistic.

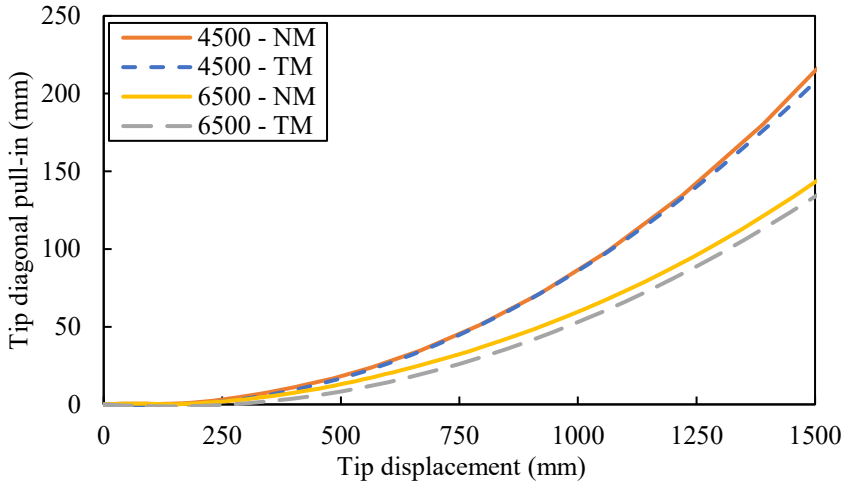


Fig. 7.9 – Verification of the planar pull-in at the free tip for the control specimens

The appropriateness of the predicted pull-in is further assessed against i) the equal variation of top and bottom reinforcement in Fig. 7.10, ii) the variation of the bottom reinforcement only in Fig. 7.11, and iii) the variation of the top reinforcement only in Fig. 7.12. The control specimen with a span length of 6500mm is considered for the current verification, with the variation of the reinforcement obtained via multiplication of the control quantity of reinforcement by a factor of 0.25, 0.50, 2.00 and 4.00.

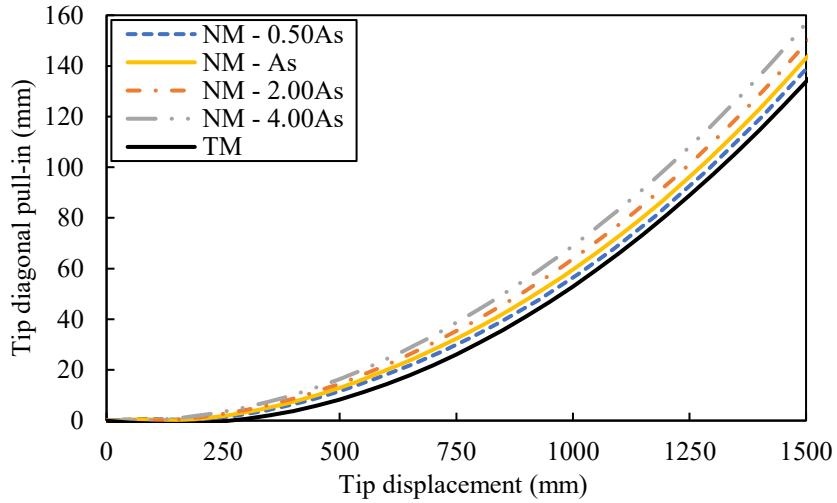


Fig. 7.10 – Control specimen 6500mm: Sensitivity of the pull-in to the equal variation of the top and bottom reinforcement

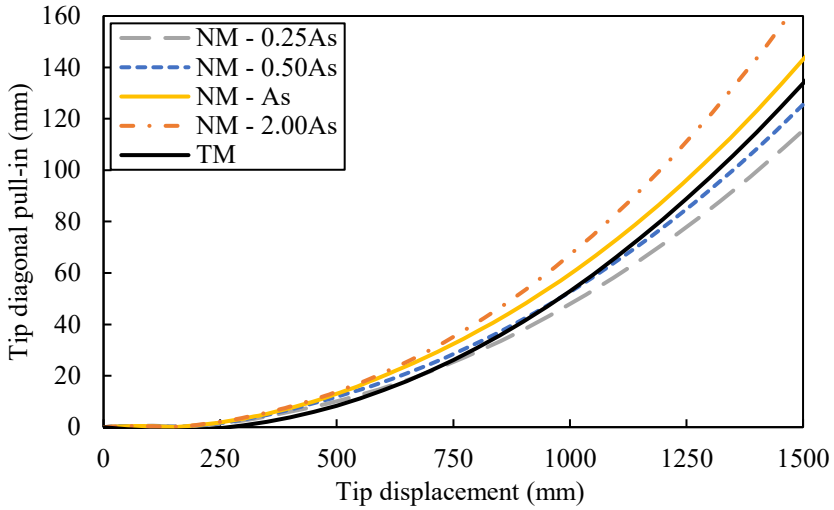


Fig. 7.11 – Control specimen 6500mm: Sensitivity of the pull-in to the variation of the bottom reinforcement only

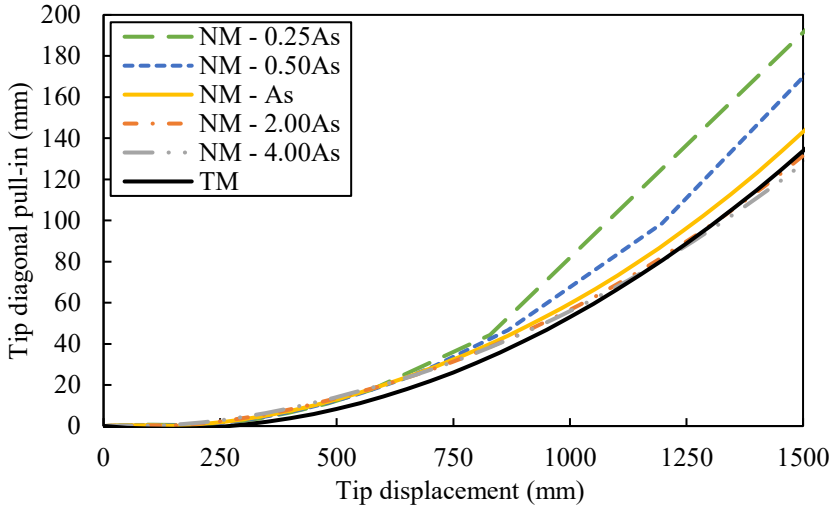


Fig. 7.12 – Control specimen 6500mm: Sensitivity of the pull-in to the variation of the top reinforcement only

For an equal variation of top and bottom reinforcement, the numerical pull-in at the free tip slightly increases with the amount of reinforcement, thus leading to an increased underestimation error by the proposed method. Notwithstanding, at 1300mm tip displacement (0.2rad), the deviation of the predicted pull-in is limited to 20% for the case where the quantity of reinforcement is four-fold. The increased underestimation of the proposed method with increasing quantity of the reinforcement can be partly explained by the resulting upward shift of the neutral axis. Indeed, considering that $h/2$ in (7.30) represents the distance of the neutral axis to the mid-plane of the slab, a reduction in this distance leads to a greater pull-in. The implications on the load-deflection response due to the underestimation of the pull-in is later discussed in the comparison of the analytical and numerical response predictions.

As also demonstrated later in the assessment of the load-deflection response, unlike the equal variation of top and bottom reinforcements, which does not influence the dominant mechanism, the variation of either the bottom or top reinforcement only can expedite the change in critical mechanism that the corner slab undergoes under column loss. Specifically, for higher ratios of bottom to top reinforcement, the reduced quantity of top reinforcement leads to an earlier development of the bending mechanism, where the assumptions considered for the determination of the pull-in at the free tip are no longer applicable.

In this respect, it follows that for decreasing bottom reinforcement (Fig. 7.11) and increasing top reinforcement (Fig. 7.12) the corner slab remains governed by the tying mechanism and the difference between the numerical and predicted responses can be deemed limited. On the other hand, for increasing bottom reinforcement (2.00 times the quantity) and decreasing top reinforcement (0.25 and 0.50 times the quantity), the same figures illustrate that, beyond a certain level of tip displacement, the numerical pull-in significantly diverges from the prediction of the proposed method, which is evidence of the change in dominant mechanism to the bending one. In summary, provided that the corner slab is under the tying mechanism, the assumed insensitivity of the pull-in at the tip to the quantity of reinforcement can be deemed appropriate.

Fig. 7.13 compares the analytical and numerical pull-in for varying depth and span length of the floor slab, noting that such parameters are assessed independently, with all other parameters including the offset of the reinforcement to the mid-plane remaining unchanged.

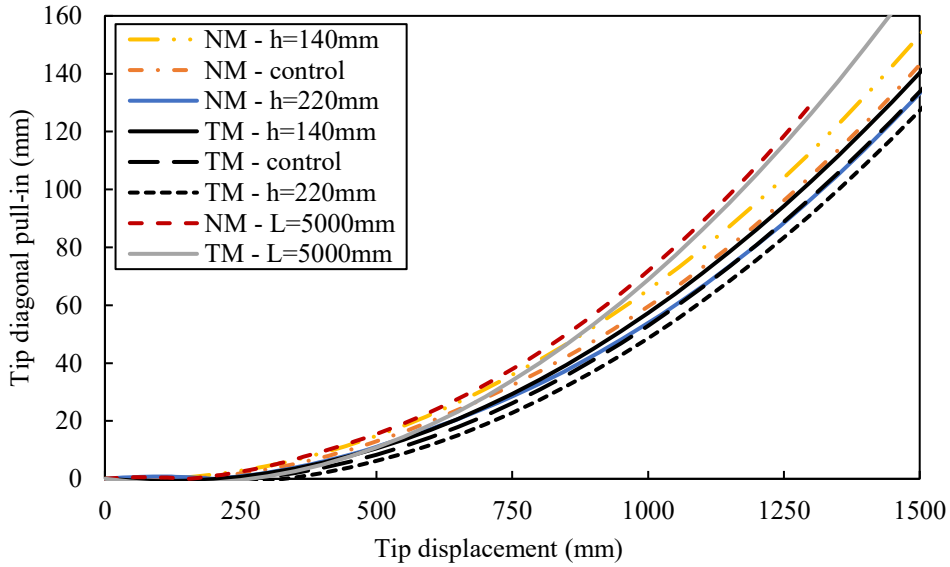
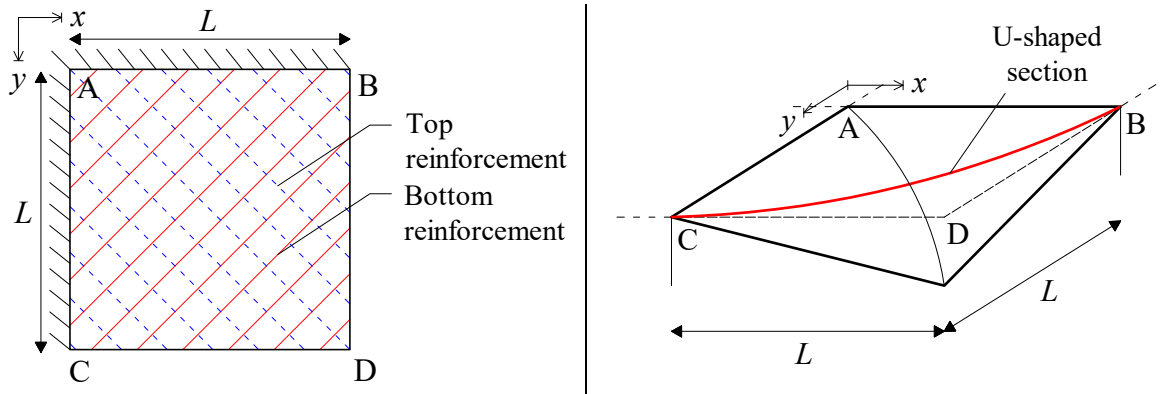


Fig. 7.13 – Control specimen 6500mm: Sensitivity of the pull-in to the depth and span length of the slab

A good agreement can again be seen between the analytical and numerical outcomes, specifically when the parameter under consideration is the span length of the floor slab. The proposed method reflects reasonably well the numerical trend to varying depths of the floor slab, in the sense that the method predicts a decrease in pull-in with increasing slab depths, though it consistently underestimates the numerical pull-in. Notwithstanding, such an underestimation can also be deemed within acceptable limits.

The numerical and predicted reinforcement strains within the corner slab are compared next. Since the proposed method determines the reinforcement strains in an average sense, the strains directly determined from the analysis of the numerical models must also be firstly averaged for a coherent comparison between numerical and predicted outcomes. This is achieved via averaging of the reinforcement strains along the span direction of the considered reinforcement. Fig. 7.14a illustrates the floor system reference and the indication of corners for the assessment of all subsequent outcomes presented in this Section 7.3. Figs. 7.15 and 7.16 illustrate the numerical and predicted average strains at specifically selected levels of tip displacement of the control specimens with 4500mm and 6500mm span lengths, respectively. The selected level of tip displacements, i.e. 668mm for the control specimen with 4500mm span length and 906mm for the control specimen with 6500mm span length, can be demonstrated with the corresponding load-deflection responses to be within the range where tying of the reinforcement is already mobilised. Further average strain contours at levels of tip displacement representative of the initial mobilisation of tensile membrane action (i.e. 400mm and 611mm respectively for the corner slab with 4500mm and 6500mm of span length) are provided in Appendix F, presenting similar conclusions as subsequently discussed.



(a) System reference and indication of corners

(b) General deformation under tying

Fig. 7.14 – Supplementary illustrations for the assessment of predicted and numerical outcomes

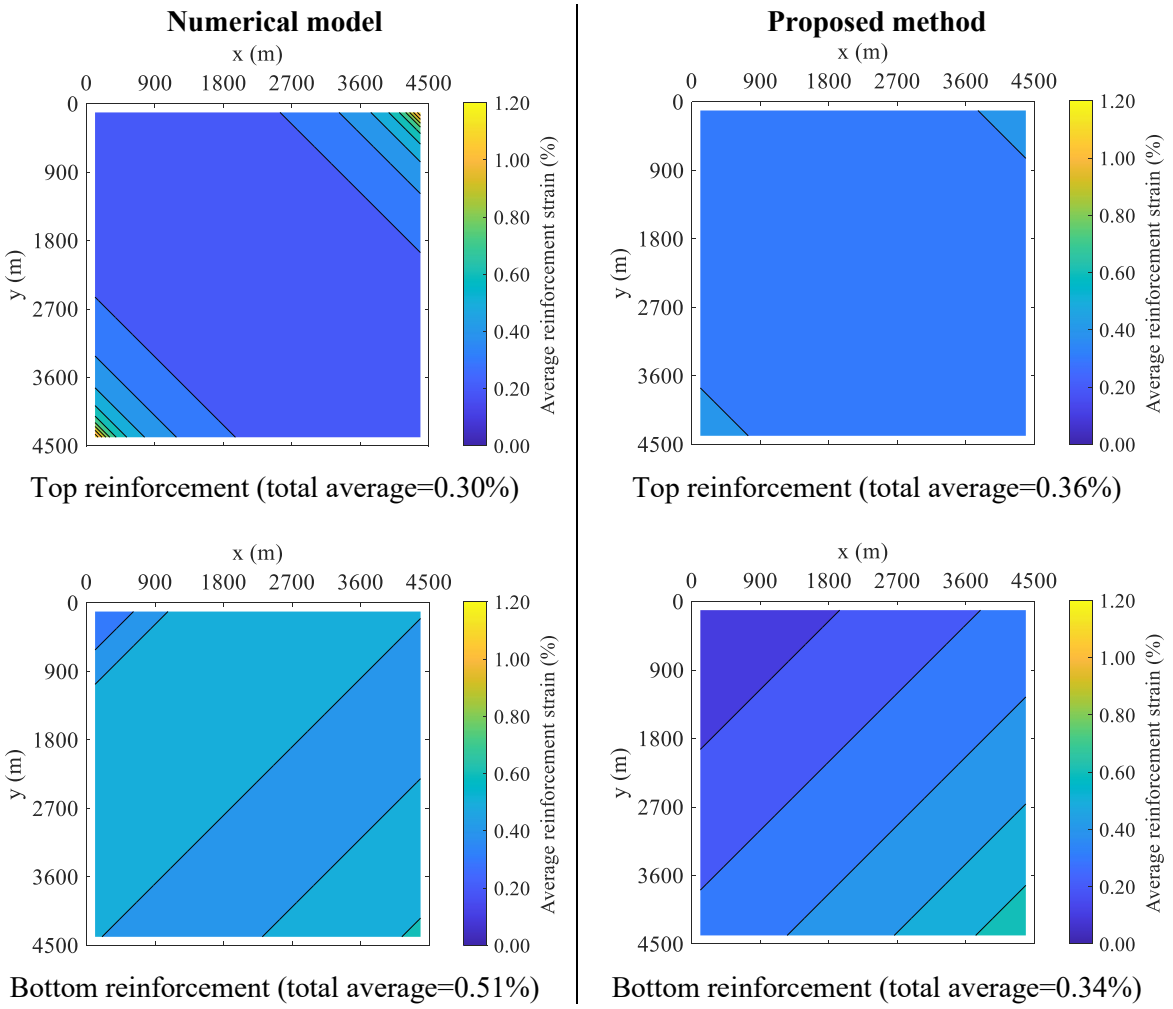


Fig. 7.15 – Average reinforcement strains at 668mm tip displacement of the control specimen with 4500mm span length

The predicted trend of the average strains agrees reasonably well with the numerical outcomes though the magnitude of the strains differs more significantly. For the top reinforcement, the numerical models clearly present a higher gradient of average strain variation, decreasing from the highest tensile strain at the corners B and C to the central part of the slab. Indeed, the proposed method does not consider the additional influence that the hogging flexure along segment AD imposes to the strains (Fig. 7.14b). This flexural bending is resisted via the top reinforcement under a U-shaped configuration, which results from the sagging of the slab in the direction BC. In turn, such a U-shaped cross-section implies that the top reinforcement near corners B and C present the highest tensile strains, positively contributing to the overall resistance of the top reinforcement, whilst the reinforcement at the central part of the corner slab should be under compressive strains, thus reducing its contribution to the overall resistance.

In this respect, the neglect of such influence renders the average strain gradient predicted by the proposed method less representative.

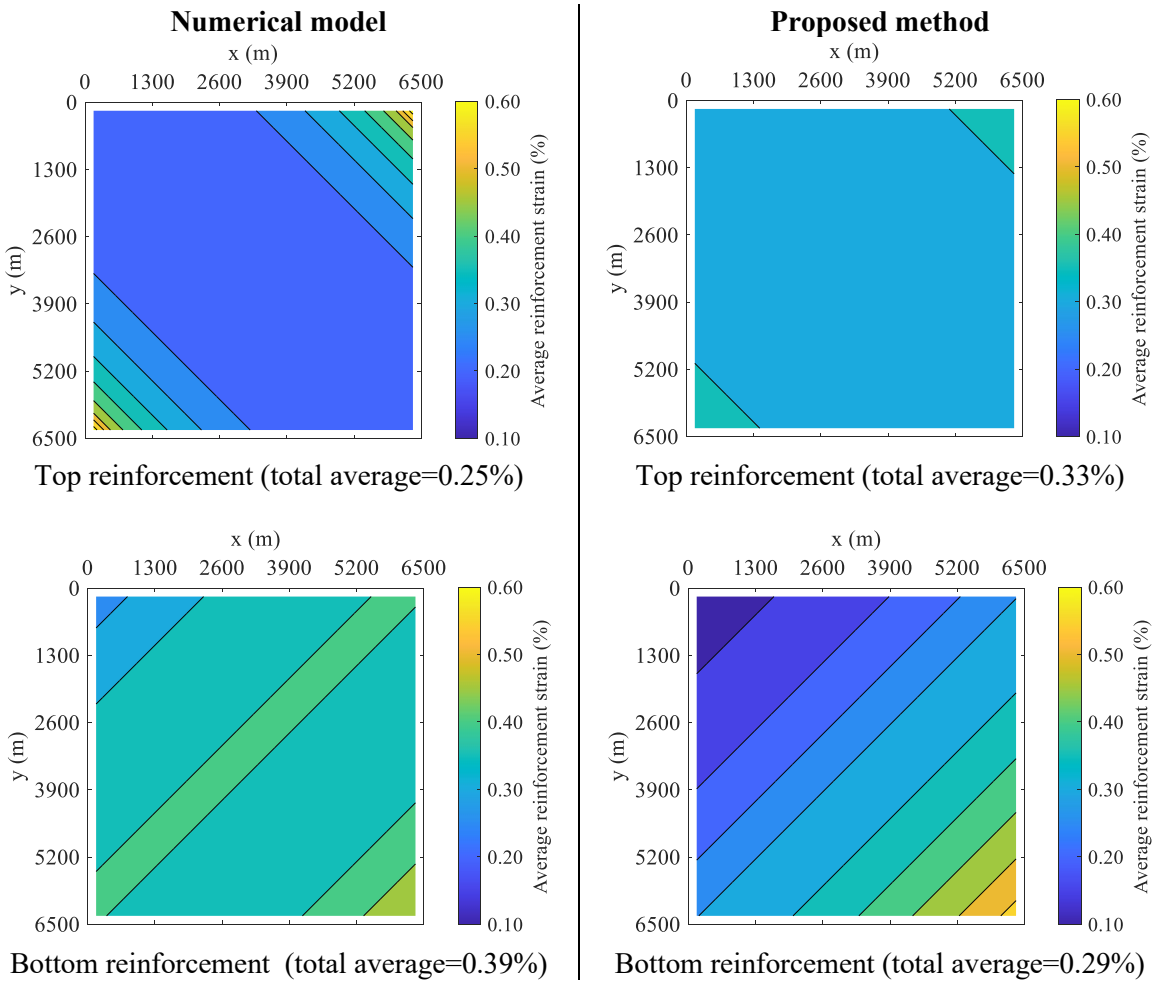


Fig. 7.16 – Average reinforcement strains at 906mm tip displacement of the control specimen with 6500mm span length

On the other hand, the proposed method consistently underestimates the strains of the bottom reinforcement within the supported region of the slab, suggesting that the transverse displacement within the interior part of the slab is more significant compared to the assumed bilinear approximation. In this respect, the proposed method offers a conservative prediction on the tying resistance of the bottom reinforcement within the supported region. This underestimation is, however, partly compensated by the overpredicted strains near the free tip of the corner slab, which is due to the assumptions considered for the variation of the planar pull-in along the unsupported edges, i.e. the in-plane displacement that is orthogonal and parallel to such edges, which follows herein quadratic and linear approximations, respectively.

The implications on the load-deflection response of alternative pull-in displacement approximations are discussed in Section 7.4.

The above phenomena and assumptions therefore lead to a general overestimation by the proposed method of the total average strain for the top reinforcement and an underprediction of the total average strain for the bottom reinforcement (also presented in Figs. 7.15 and 7.16), with the difference ranging between 20-40%. Nevertheless, despite such deviations when considering the top and bottom reinforcement separately, the proposed method offers, in an average sense, a reasonable estimate of the tensile reinforcement strains under the tying mechanism when the combined contribution of the top and bottom reinforcement is considered instead.

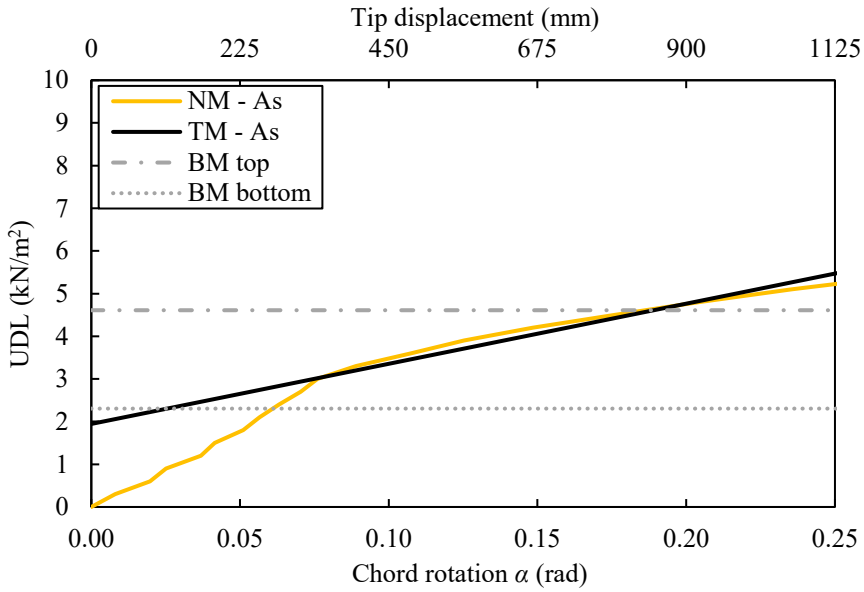
7.3.3 Verification of the load-deflection response of the control models

Fig. 7.17 illustrates the comparison of the numerical and predicted load-deflection responses of the considered control models, where the keys 'NM', 'TM', 'BM top' and 'As' respectively represent the numerical model, the proposed tying mechanism model, the proposed bending mechanism model and the reference quantity of reinforcement.

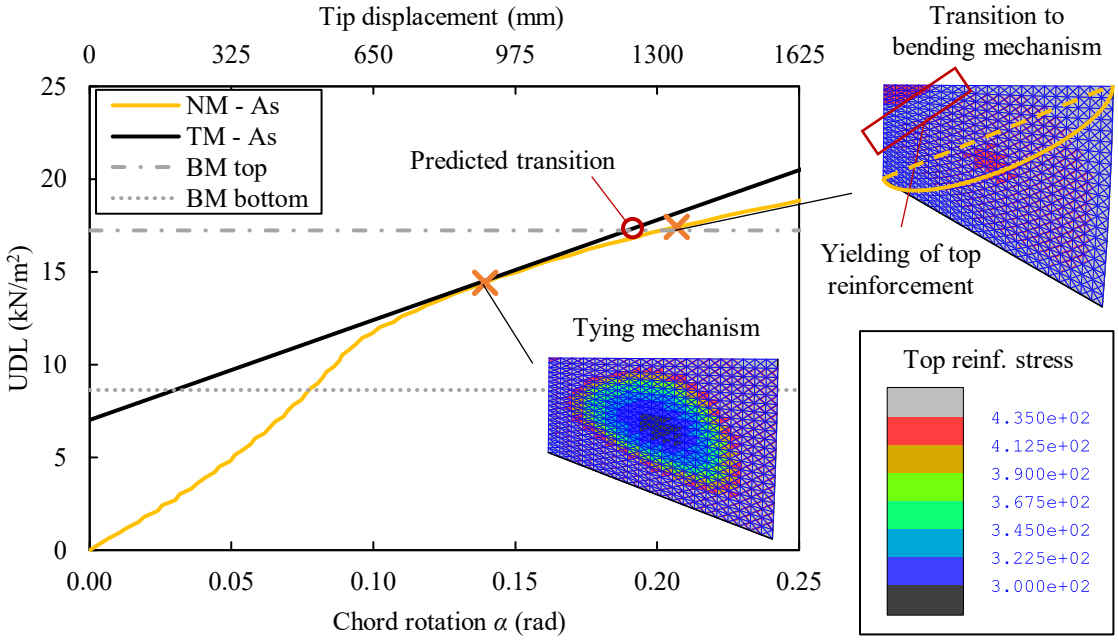
For the appreciation of the beneficial contributions from the tying of reinforcement to the robustness of the corner slab, a further load resistance prediction, established as per (7.31), is depicted in Fig. 7.17 as 'BM bottom', representing the yield line analysis of the corner slab under the development of a sagging yield line along segment AD (see Fig. 7.14a). Such a mechanism involving the flexure of the bottom reinforcement is critical for corner slabs with an adequate quantity of top reinforcement but which are unrestrained in-plane:

$$\begin{cases} W_{int} = 2m_{rr} L \delta\alpha \\ W_{ext} = w\dfrac{L^3}{3}\delta\alpha \end{cases} \Rightarrow W_{int} = W_{ext} \Rightarrow w = \frac{6m_{rr}}{L^2} \tag{7.31}$$

The numerical load-deflection responses clearly exceed the resistances predicted as per the above equation, suggesting that the planar restraint at the supported edges of the corner slab enables the mobilisation of tying of the reinforcement.



(a) Model with 4500mm span length

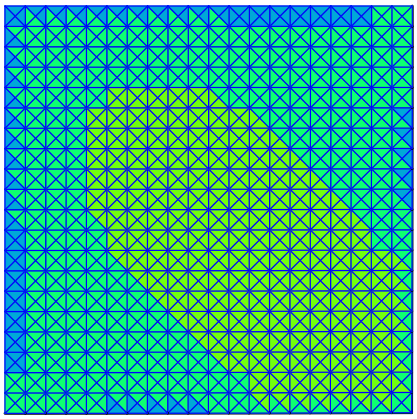


(b) Model with 6500mm span length

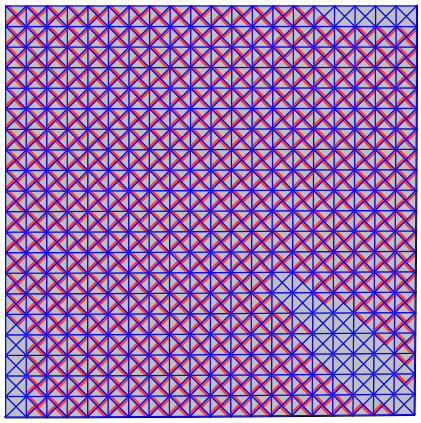
Fig. 7.17 – Verification of the load-deflection response of the control models

Fig. 7.18, which illustrates the evolution of the bottom reinforcement stresses for the corner slab with 6500mm span length, also evidences the activation of tying. At a tip displacement of 454mm, the stress of the bottom reinforcement approximately follows the typical quadratic stress gradient along segment BC (see Fig. 7.14a) observed in simply supported beams under a uniformly distributed load, with highest stresses within the central region of the slab. The applied load is primarily resisted via flexure of the corner slab at this stage. With further loading,

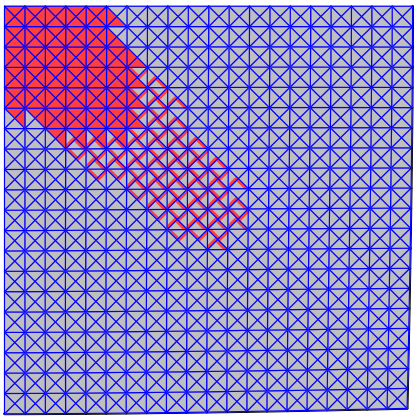
the reinforcement at the central region of the slab yields, where the yield is expected to remain limited within the central region of the slab if the planar restraints were inadequate. However, the stress contour at 906mm and 1340mm tip displacements shows that reinforcement yield propagates to almost the entirety of the slab, confirming the mobilisation of tensile membrane forces within the system.



(a) 454mm tip displacement



(b) 906mm tip displacement



(c) 1340mm tip displacement

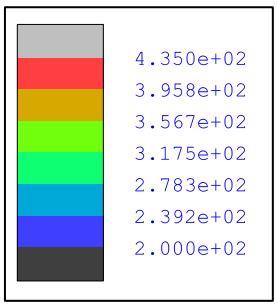


Fig. 7.18 – Evolution of the bottom reinforcement stresses with tip displacement

Within the range of loading where the tying mechanism is dominant, Fig. 7.17 demonstrates a good agreement between the prediction of the proposed method and the numerical response independently of the considered control model. It is worth noting the contour of the top reinforcement stresses illustrated for the control model with 6500mm of span length (Fig. 7.17b), which again shows the stress gradient of the top reinforcement due to the flexural resistance of the U-shaped cross-section, as previously discussed in Section 7.3.2.

It is also worth noting that the numerical response deviates from the analytical response at later stages of loading, with the proposed method overestimating the numerical resistance. Indeed,

the chord rotation/tip displacement at which such deviation initiates is seen to be well defined by the intersection of the load-deflection response predicted by the tying mechanism 'TM' and the limiting resistance determined by the bending mechanism 'BM top'. In this respect, the observed deviation represents the transition of the dominant deformation mode from the tying mechanism to the bending mechanism, where the transverse deformation differs from the assumed bilinear approximation. This is supported by the inspection of the top reinforcement stresses at approximately 0.2rad of chord rotation, where a yield region marked with a red box in Fig. 7.17b is clearly visible, contributing to a local increase in rotation analogous to the development of a plastic hinge in beams.

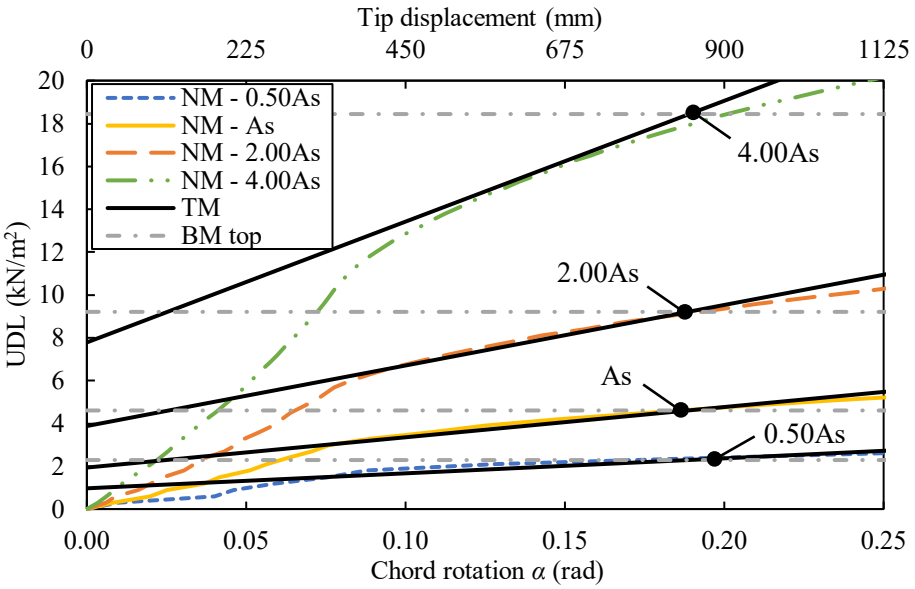
Despite defining reasonably well the chord rotation/displacement at which the corner slab transitions its dominant mechanism, the proposed formulation provides a lower bound estimate of the load resistance under the bending mechanism, as the flexural resistance about the hogging yield line is established based on a flat rectangular cross-section that neglects the transverse displacement of the slab (yellow dashed line in Fig. 7.17b). On the other hand, the actual U-shaped cross-section, illustrated as the yellow full line in the same figure, leads to an increased flexural resistance. In this sense, even when the floor system is under the bending mechanism, the system can indeed develop load resistance exceeding the limit predicted via conventional yield line analysis, which is typically the upper bound resistance considered in experimental tests and analytical approaches available in literature for the robustness assessment of corner floor slabs. The horizontal tying method proposed in this work can be extended to include such resistance enhancement from the U-shaped cross-section, though it would then involve the interaction of several effects, the quantification of which adds to model complexity. One such effect depends on the ratio of top-to-bottom quantities of reinforcement. This ratio affects the height of the U-shaped cross-section achieved preceding the transition to the bending mechanism, and hence defines the level of flexural resistance available following this transition.

Lastly, considering that the control model with 6500mm span length is representative of a corner floor system from an actual RC building under a static gravity load between 8-10kN/m^2, and that a dynamic amplification factor of 2.0 is conservatively assumed, the outcomes illustrated in Fig. 7.17b suggest that typical flexural resistance under the 'BM bottom' mechanism would not be able to resist the sudden loss of the corner column. On the other hand, the activation of tying within the corner floor system can provide the requisite resistance under

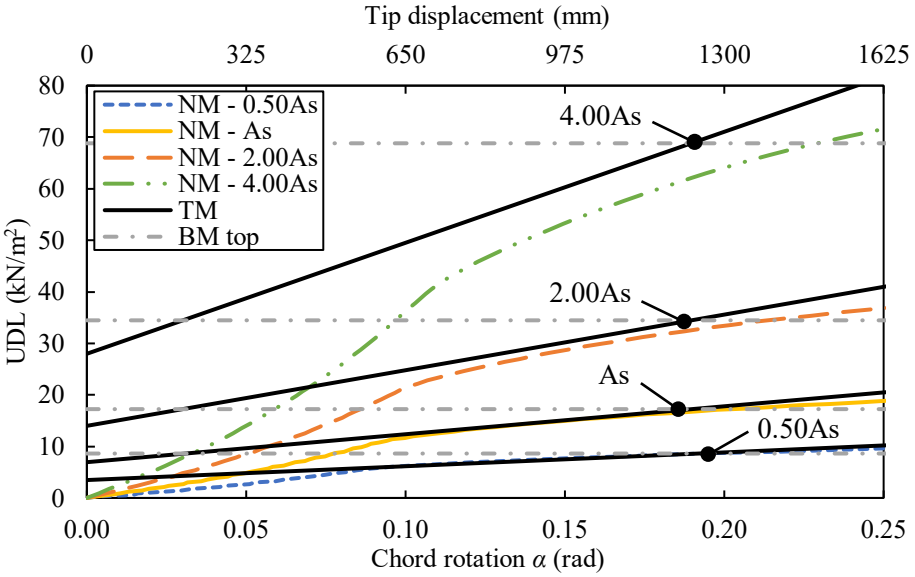
a chord rotation range within 0.2rad, thus demonstrating the feasibility in considering such beneficial contribution to the resistance of the corner floor system.

7.3.4 Sensitivity to equal variation of top and bottom reinforcement

Consideration is given herein to the equal variation of top and bottom reinforcement, where the results are provided in Figs. 7.19a-b for the control specimen with 4500mm and 6500mm span lengths, respectively.



(a) Corner slab with 4500mm



(b) Corner slab with 6500mm

Fig. 7.19 – Equal variation of top and bottom reinforcement

The figures demonstrate a general good agreement between numerical and predicted load-deflection responses, though the proposed method overestimates the numerical response with increasing quantity of reinforcement, with the greatest deviation observed for the case with 6500mm of span length and four-fold the reference quantity of reinforcement (Fig. 7.19b, model NM-4As). This deviation can be partly correlated to the underestimation of the planar pull-in at the free tip u_{tip}, as previously discussed in Section 7.3.2. In this respect, the internal virtual work, expressed in total displacements, can be shown as:

$$T = u_{tip}\frac{\sqrt{2}}{12}L\left(f_{bot} - 5f_{top}\right) + \frac{v^2}{24}\left(f_{bot} + 7f_{top}\right) + v\left(f_{bot}b_{bot} + f_{top}b_{top}\right) \tag{7.32}$$

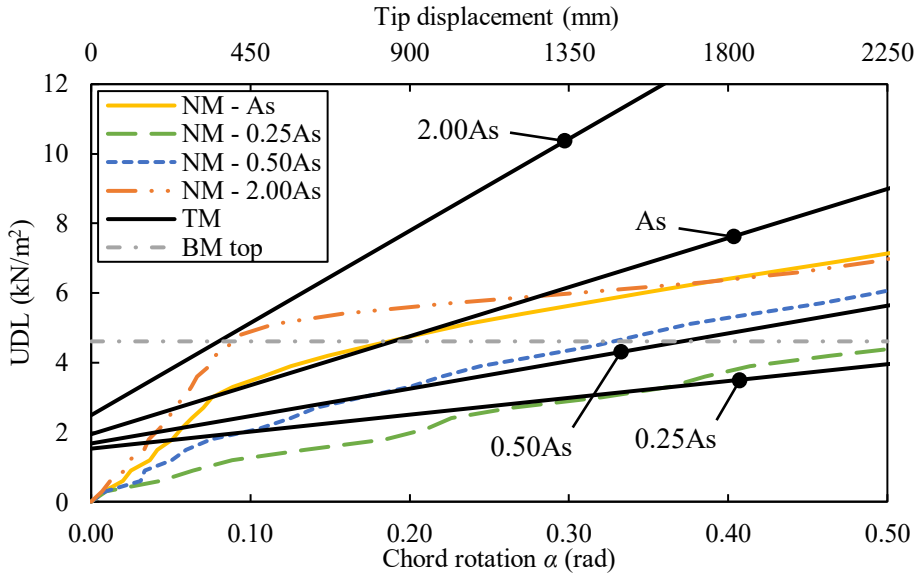
Inspection of the above equation reveals that the first term represents the influence of the planar pull-in on the tying resistance of the system. With equal quantities of top and bottom reinforcement, this term becomes increasingly detrimental to the resistance of the system with higher pull-in displacement u_{tip}. In this sense, an underestimation of the planar pull-in would result in an overpredicted tying response with respect to the numerical outcome. Notwithstanding, it is worth noting that the case NM-4As of the model with 6500mm span length presents a total slab reinforcement ratio of just over 4%, which exceeds the maximum area of reinforcement recommended in the Eurocode 2 (CEN, 2004b), hence such a case can be deemed as uncommon in typical RC buildings.

The good agreement between numerical and predicted responses for all the considered cases of reinforcement can also be credited to the fact that the variation in the quantity of reinforcement is applied equally for the top and bottom surfaces of the slab. As a result, the ensuing numerical models should predict similar transverse and planar deformation modes, and the bilinear approximation assumed for the proposed method should also remain appropriate for all the considered cases. Indeed, it can be seen in Figs. 7.19a-b that the displacements at which the tying force is fully mobilised in the reinforcement and at which the floor slab transitions to the bending mechanism are approximately insensitive to the equal variation of the top and bottom reinforcement.

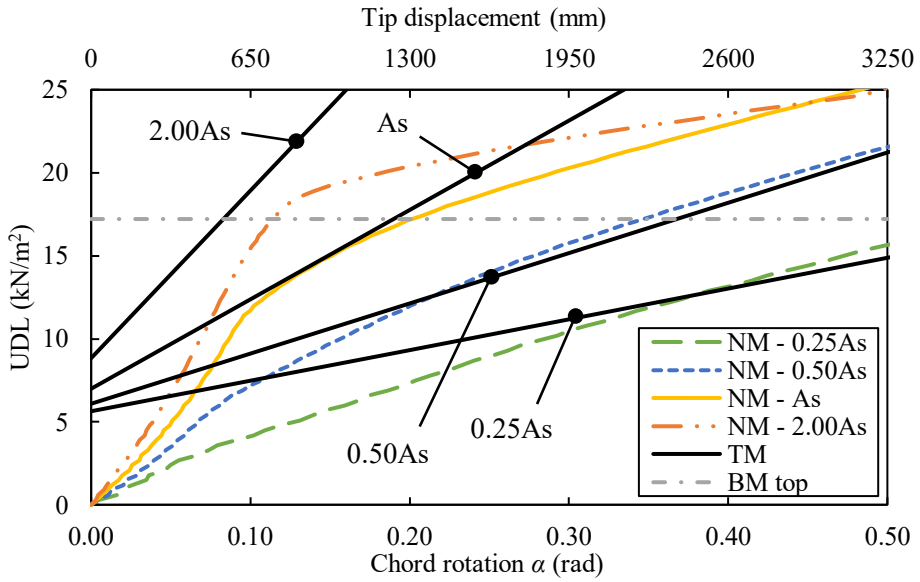
7.3.5 Sensitivity to variation of bottom or top reinforcement alone

Unlike the case of equal variation of top and bottom reinforcement, the variation of the top or the bottom reinforcement alone influences more significantly the deformation mode of the corner slab, and hence the trend of the corresponding load-deflection response. This is

illustrated in Fig. 7.20 for the variation of the bottom reinforcement only. The predicted load resistance under bending mechanism is identical for all the considered cases since it does not depend on the bottom reinforcement. In this respect, the increase in bottom reinforcement expedites the transition of the corner slab to the bending mechanism, as a faster rate of resistance increase is achieved under the tying mechanism.



(a) Corner slab with 4500mm span length



(b) Corner slab with 6500mm span length

Fig. 7.20 – Variation of the bottom reinforcement only

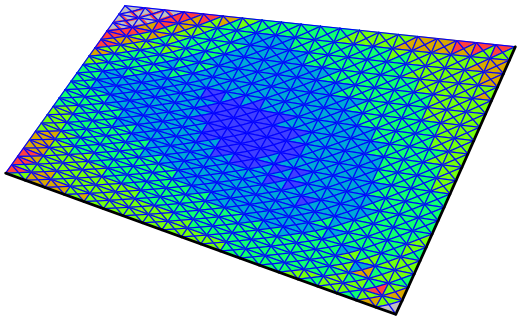
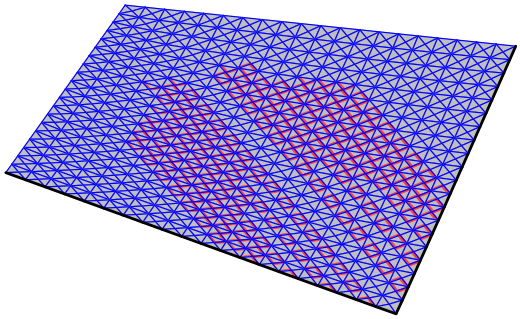
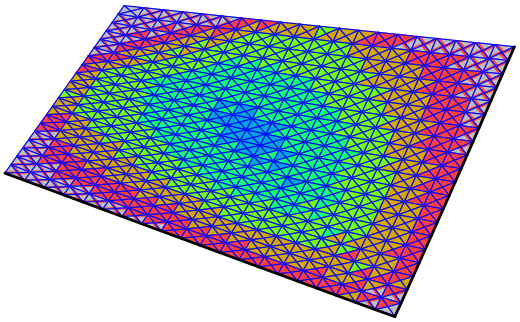
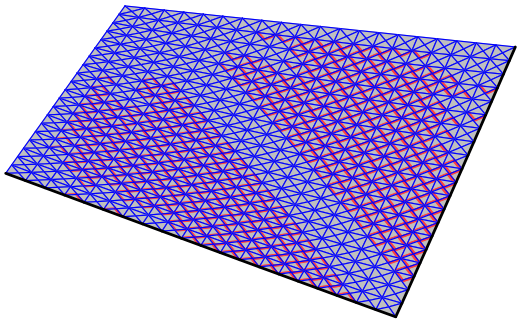
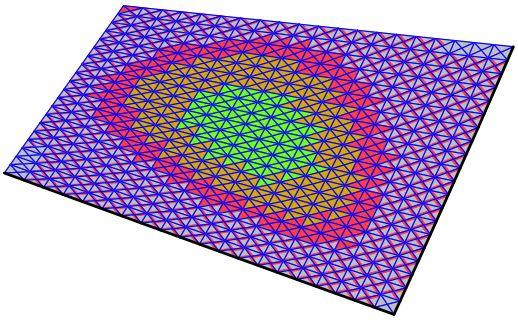
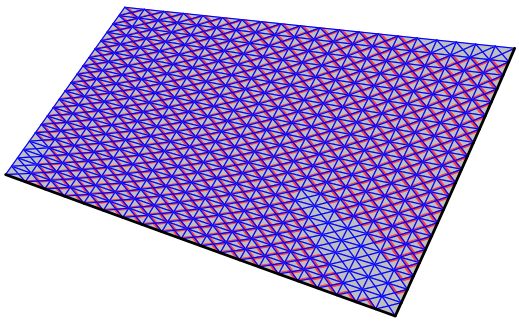
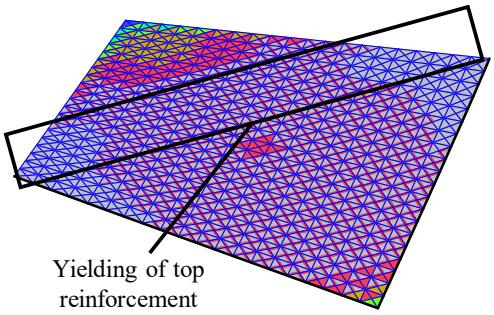
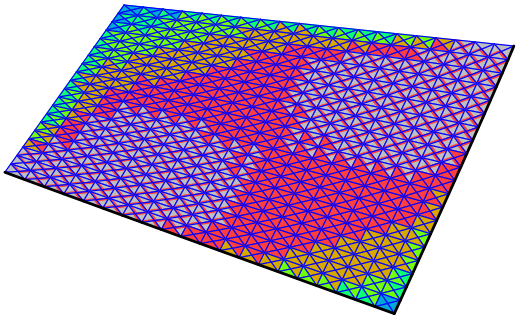
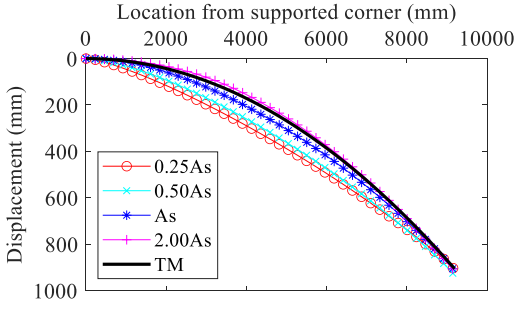
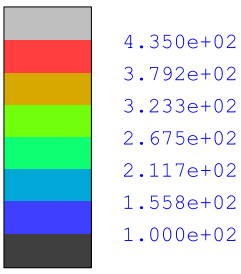
Furthermore, as discussed in Section 7.3.3, given that the chord rotation/tip displacement under tying mechanism influences the resistance offered by the U-shaped cross-section following the

transition to the bending mechanism, the numerical load-deflection response under the bending mechanism also depends on the ratio of top-to-bottom reinforcement. Specifically, the numerical outcomes in Fig. 7.20 suggest that, despite an initial enhancement in system stiffness and resistance at lower levels of chord rotation/tip displacement, increasing the amount of bottom reinforcement can be rather detrimental to the robustness of the corner floor system at large displacements. This is because the delay in transition to the bending mechanism allows the floor system to undergo a more significant sag and develop a U-shaped cross-section with increasing height, enhancing the flexural resistance under such a mechanism. Indeed, irrespective of the control model, the slope of the load-deflection response under the bending mechanism is shallower for the case considering twice the reference quantity of bottom reinforcement. Further increase in this reinforcement would lead to a load-deflection response with an approximately flat slope, with the corresponding deformation mode approximating to that assumed for the proposed method.

On the other hand, higher top-to-bottom reinforcement ratios via a decreasing quantity of bottom reinforcement promote the sag of the corner slab, which increases the displacement at which the system transitions to the bending mechanism, as conformed by the results of Fig. 7.20, besides leading to a slower rate in resistance increase under the tying mechanism.

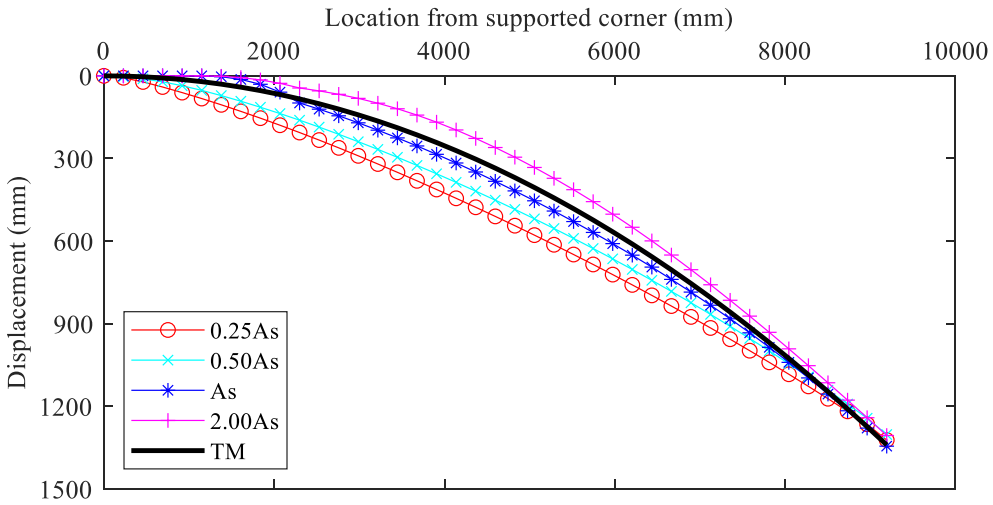
The above observations can be better visualised and explained with the deformation and stress contours of the considered corner floor cases at similar levels of tip displacement. In this respect, Table 7.3 provides illustrations at an approximate tip displacement of 906mm, as well as the transverse displacement profile along the diagonal AD (see Fig. 7.14a). Once again, the gradient of the top reinforcement stresses that is defined by the flexural resistance of the U-shaped cross-section is clearly visible in the contours of the cases with lower quantities of bottom reinforcement. It is worth noting though that this gradient becomes less representative with the increase in the quantity of bottom reinforcement, to the extent where the top reinforcement yields instead, as highlighted in the contour of NM – 2.00As. Correspondingly, in the case of NM – 2.00As, there is no clear development of a sagging yield line for the bottom reinforcement. This suggests that the curvature along the diagonal AD is greater than that along the orthogonal diagonal, which is characteristic of the assumed deformation mode for the bending mechanism. The opposite is observed for lower quantities of bottom reinforcement, where the diagonal AD presents a lower curvature instead.

Table 7.3 – Stress contours at approximately 900mm tip displacement for the corner slab with 6500mm span length

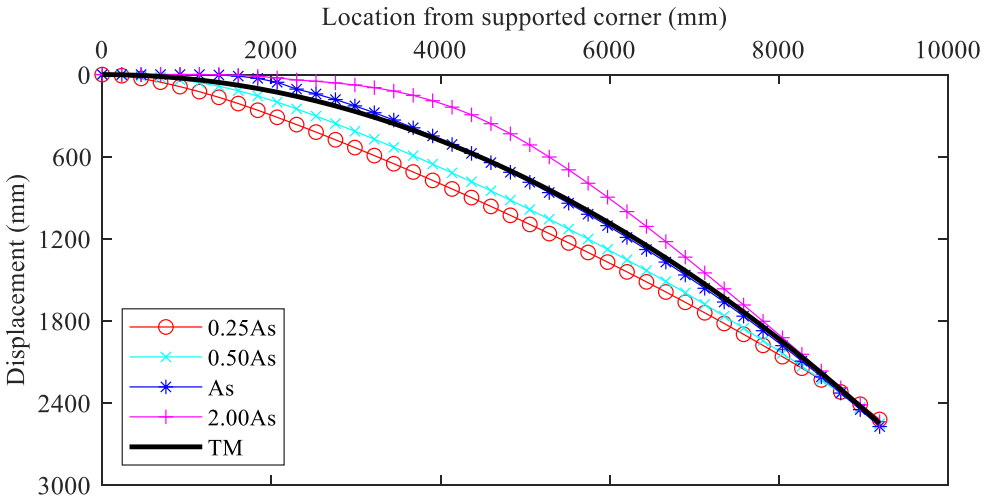
	Top reinforcement stresses	Bottom reinforcement stresses
NM – 0.25As at 903mm		
NM – 0.50As at 925mm		
NM – As at 906mm		
NM – 2.00As at 906mm		
Disp. along diagonal AD		

The reduced curvature along diagonal AD also explains the delay of the numerical responses in achieving the resistance predicted by the proposed method (Fig. 7.20), as the associated top reinforcement stresses are also less significant. The proposed method considers the resistance from both top and bottom reinforcement based on the yield strength. As such, given that the top reinforcement stresses for the cases NM – 0.25As and NM – 0.50As are mostly still below the yield strength (150-380MPa), it clearly follows that the top reinforcement are yet to be fully activated primarily in flexure.

The transverse displacement profile along diagonal AD of the corner slab with 6500mm span length is provided for two further levels of tip displacement, at approximately 1340mm (Fig. 7.21a) and 2570mm (Fig. 7.21b).



(a) At approximately 1340mm tip displacement



(b) At approximately 2570mm tip displacement

Fig. 7.21 – Displacement profile along the diagonal AD with 6500mm span length

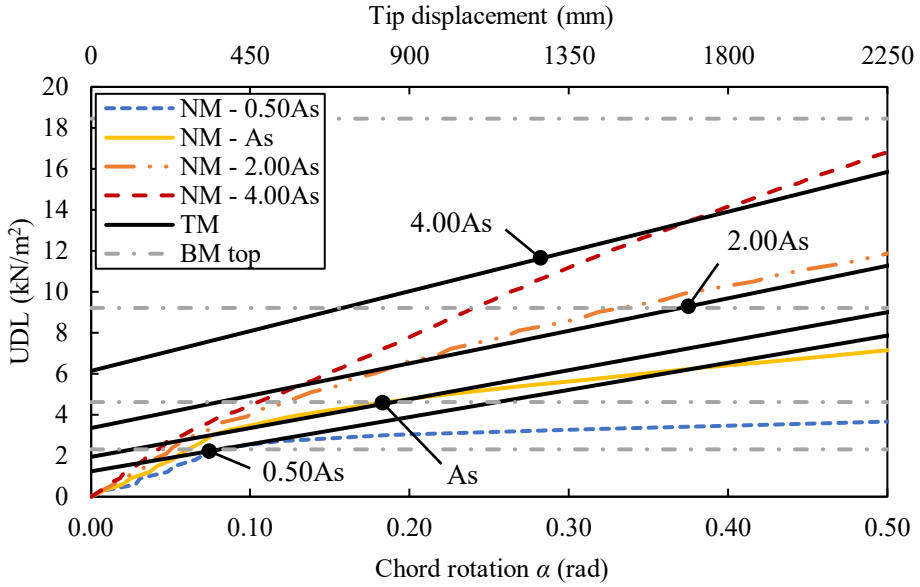
The figures demonstrate the evolution of the deformation mode with tip displacement. Firstly, at the approximate tip displacement of 906mm (Table 7.3), only the case of NM – 2.00As presents a curvature greater than that predicted by the proposed method (TM), demonstrating again the transition of the floor system to the bending mechanism. With further tip displacement, there is evident development of a localised rotation along the diagonal due to the continued transition of case NM – 2.00As to the bending mechanism. Interestingly, the location of such localised rotation progressively shifts towards the mid-length of the diagonal. This is a result of the progressive vertical resistance gain from the tying of the bottom reinforcement. Indeed, the response of the diagonal can be viewed as a cantilever beam over an elastic foundation, where the springs represent the resistance from the tying of the bottom reinforcement.

On the other hand, the diagonal of the remaining cases (NM – 0.25As, 0.50As and As) initially present, at approximately 906mm tip displacement, a curvature smaller than that predicted by the proposed method (TM). With further tip displacements, the diagonal of the case NM – As also develops a localised rotation as the corner slab transitions to the bending mechanism. Importantly, the diagonal of the cases NM – 0.25As and 0.50As, for which the deformation initially follows more closely a linear transverse approximation, progressively tends to the assumed approximation due to the gain in vertical resistance from the tying of the bottom reinforcement.

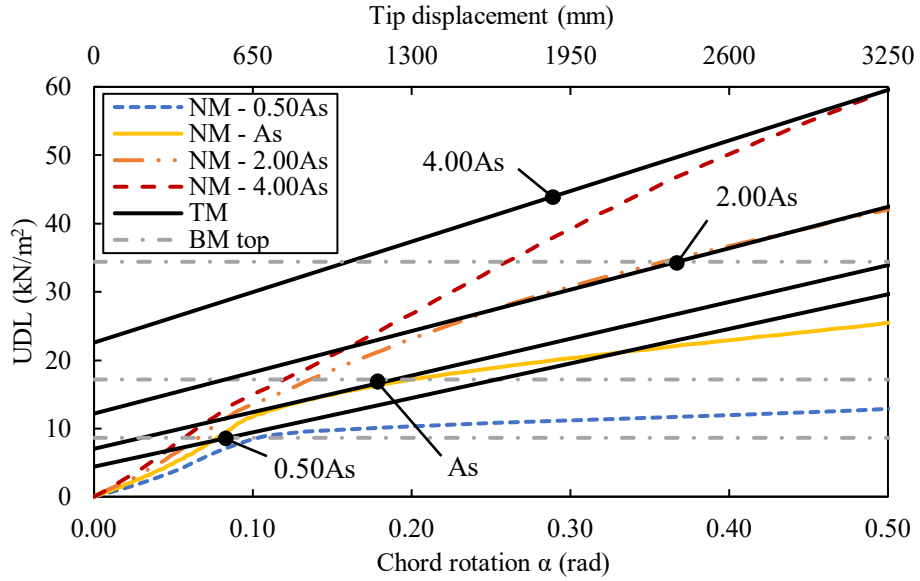
Notwithstanding, even though the numerical load resistance of the cases NM – 0.50As and 0.25As has reached the tying resistance predicted by the proposed method at approximately 1340mm and 2570mm tip displacement, respectively (see Fig. 7.20), Figs. 7.21a-b suggest that the proposed method is still overestimating the curvature along diagonal AD and hence the axial strains of the top reinforcement. However, because of this overestimation in curvature, the predicted average transverse displacement along this diagonal is generally lower. Correspondingly, the proposed method underestimates the strains along the orthogonal diagonal BC (i.e. the bottom reinforcement). This is in agreement with the conclusions undertaken in Section 7.3.2 for the average reinforcement strain contours.

Similar conclusions to the variation of bottom reinforcement can be applied to the variation of the top reinforcement, though in a reverse sense (Fig. 7.22), where the decrease in the quantity of top reinforcement expedites the transition of the corner slab to the bending mechanism,

whilst its increase leads to a more significant sag of the floor slab and to the delay of the numerical response in achieving the resistance predicted by the proposed method.



(a) Corner slab with 4500mm span length



(b) Corner slab with 6500mm span length

Fig. 7.22 – Variation of the top reinforcement only

Assessing the sensitivity of the load-deflection response predicted by the proposed method to the variation of the top and the bottom reinforcement (Figs. 7.20 and 7.22, respectively), it is evident that the slope of this response is more sensitive to the variation of the latter reinforcement, whilst the primary effect in varying the former relates to the parallel shift of the predicted load response. It can therefore be concluded that the bottom reinforcement primarily

contributes to the load resistance via tying, whilst the top reinforcement offer resistance under flexure.

In summary, the preceding detailed discussion highlights the effectiveness of the proposed model in offering a reasonably good comparison against the numerical results even under the variation of top or bottom reinforcement alone. Furthermore, considering the detrimental effects associated with the increase of the bottom reinforcement only (as it expedites the transition to the bending mechanism), it is recommended based on Fig. 7.23 that the robustness enhancement of a corner floor system is most effectively achieved via either the increase of the top reinforcement alone or the equal increase in top and bottom reinforcement in case an earlier mobilisation of full tying forces is required.

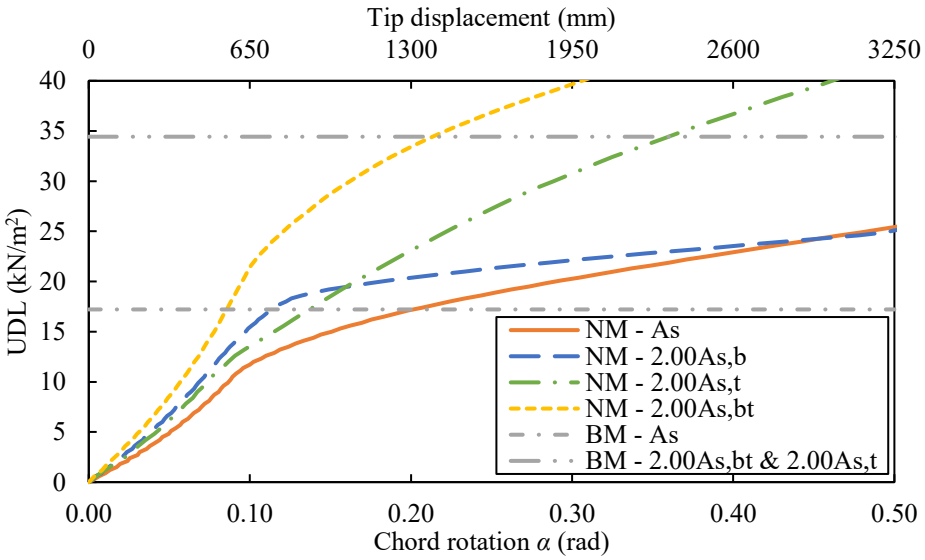


Fig. 7.23 – Models with 6500mm span length: comparison of load-deflection responses between equal increase of bottom and top reinforcement (As,bt), increase of bottom reinforcement only (As,b), and increase of top reinforcement only (As,t)

7.3.6 Sensitivity to depth and span length of floor slab

The prediction accuracy of the proposed method is further assessed under the independent variation of the depth and the span of the floor slab, as shown in Figs. 7.24 and 7.25, respectively.

It is evident from Fig. 7.24 that the variation in slab depth results in a parallel shift of the predicted load-deflection response, as the slab depth only influences the intercept of the linear function according to (7.25). Furthermore, the proposed method reflects reasonably well the trend of the load-deflection response under varying depths of the slab, though it underestimates the corresponding magnitude of load variation (Fig. 7.24). The more significant load variation

determined numerically can be explained by the additional resistance contribution from the concrete in compression, which is neglected in the proposed method. It is worth noting though that since the offset of the reinforcement from the mid-plane is not readjusted with the decrease of the slab depth to 140mm, the resulting floor system does not entail concrete cover, and thus considered as an unrealistic case example. A separate assessment is conducted involving such an adjustment in the offset of the reinforcement, though the difference between the numerical and predicted load-deflection responses remains.

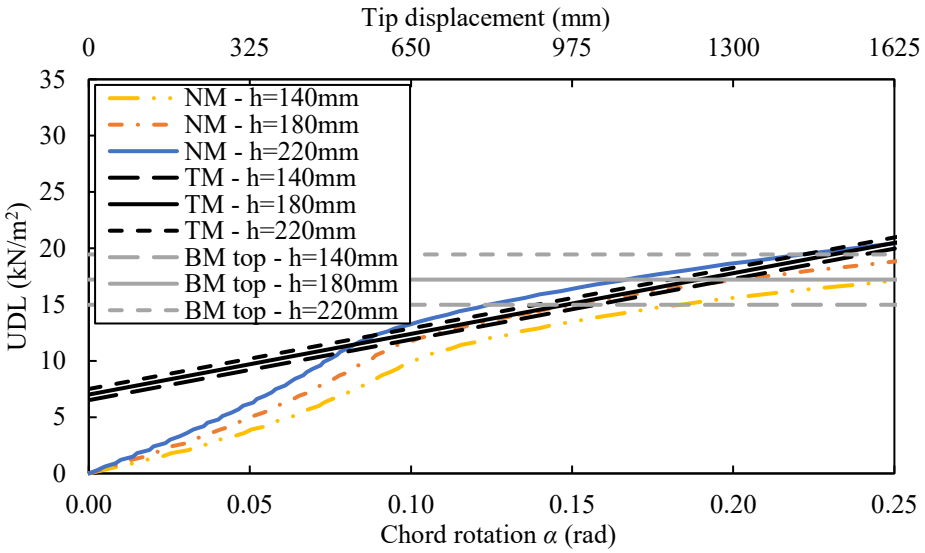


Fig. 7.24 – Sensitivity of the load-deflection response to the depth of the slab

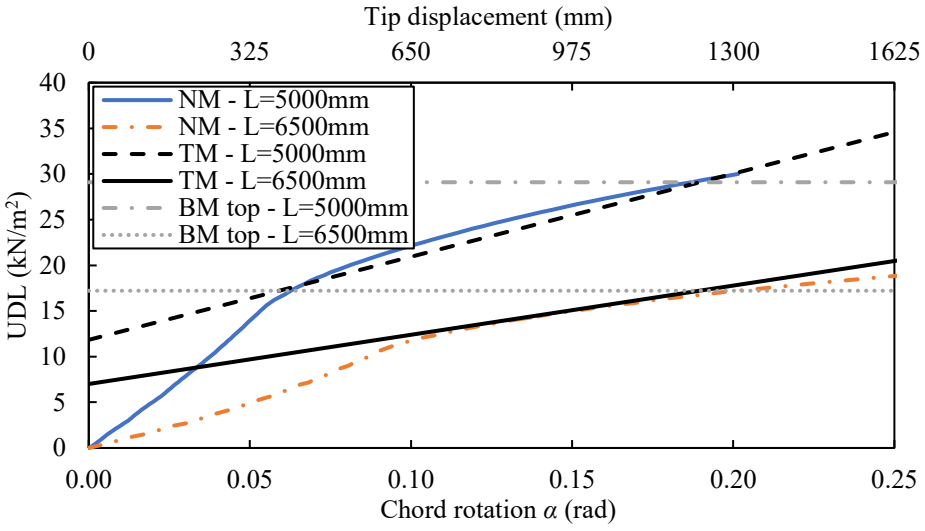


Fig. 7.25 – Sensitivity of the load-deflection response to the span length of the slab

Fig. 7.25 suggests that the prediction accuracy of the proposed method remains satisfactory for varying span lengths, under which it follows that not only the predicted and numerical tying

response agree reasonably well but the displacement at which the predicted responses of the tying and bending mechanisms intersect also represents reasonably well the transition of the numerical response from the tying mechanism to the bending mechanism.

7.4 An alternative planar displacement approximation

Consideration is given to the assessment of the load-deflection response prediction under an alternative planar displacement approximation so as to demonstrate the final selection of the quadratic and linear approximations, respectively, for the pull-in component that is orthogonal and parallel to the edges (herein termed as QD-LN). The alternative approximation involves a quadratic variation for both the orthogonal and the parallel pull-in components (herein termed as QD-QD). This approximation results in a decreased contribution of the bottom reinforcement to the internal virtual work, as the elongation of the reinforcement within the unsupported region becomes dependent only on the transverse displacements and the offset of the reinforcement from the mid-plane, with the contribution from the in-plane displacement nullified under such an approximation. Conversely, the contribution of the top reinforcement to the internal virtual work increases due to a generally smaller pull-in. This can be demonstrated by comparing the discrete equilibrium of (7.25), which is established assuming the QD-LN approximation for the planar pull-in, and the discrete equilibrium established assuming the QD-QD approximation instead:

$$w = \frac{1}{9L^2}\left[f_{bot}\left(3\alpha L + 36 b_{bot}\right) + f_{top}\left(5\alpha L + 36 b_{top} + 12h\right)\right] \tag{7.33}$$

It follows from this comparison that the rate of resistance gain, as represented by the values that are multiplying the term αL in (7.25) and (7.33), increases five-fold and reduces by a factor of 2.33 (i.e. 7/3) for the top and bottom reinforcement, respectively, when considering the QD-QD approximation for the planar pull-in. This suggests that the resistance contribution of the top reinforcement under the tying mechanism becomes more significant with the QD-QD approximation. On the other hand, an inverse variation is observed for the intersect of the load-deflection responses, as represented by the terms independent of α in (7.25) and (7.33), with the QD-QD approximation predicting at zero chord rotation a lower and higher initial flexural resistance contribution from the top and bottom reinforcement, respectively.

Figs. 7.26-7.28 compare the two in-plane displacement approximations respectively for the equal variation of the top and bottom reinforcement, the variation of the bottom reinforcement only and the variation of the top reinforcement only. Under an equal variation of the top and

bottom reinforcement (Fig. 7.26), the two approximations result in an identical tying response prediction.

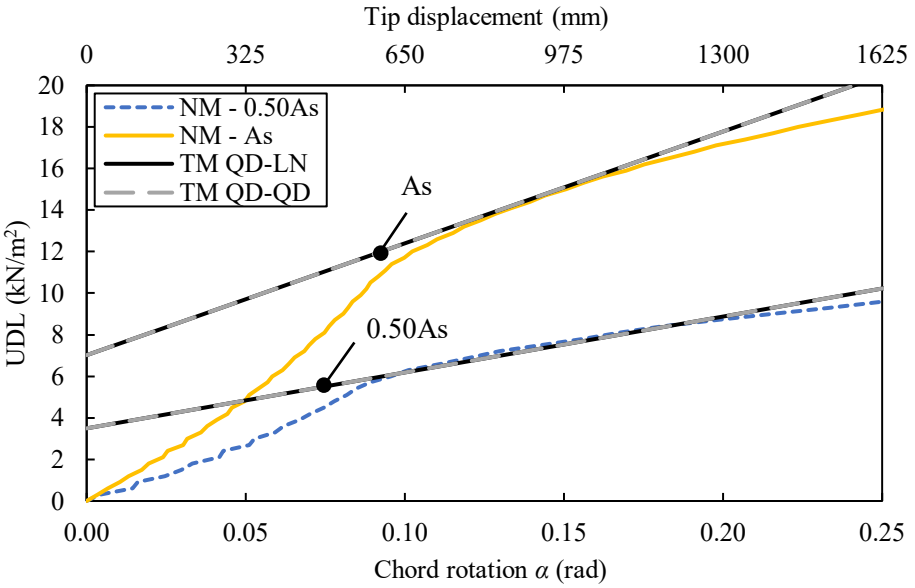


Fig. 7.26 – Sensitivity of the displacement approximation to the equal variation of the top and bottom reinforcement

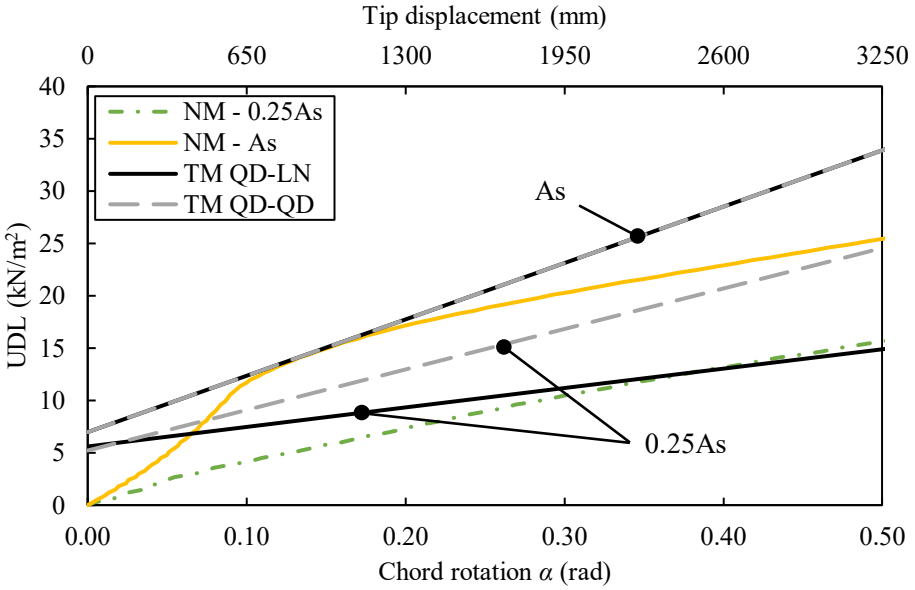


Fig. 7.27 – Sensitivity of the displacement approximation to the variation of the bottom reinforcement only

Notwithstanding, the load responses of the two approximations differ under the variation of either the bottom or the top reinforcement alone (Figs. 7.27 and 7.28). Specifically in the case where the variation of reinforcement promotes the tying mechanism as the dominant mechanism (i.e. the decrease of the bottom reinforcement or the increase of the top

reinforcement), the QD-QD approximation increasingly overestimates the numerical tying response compared to the QD-LN approximation, which can be attributed to the aforementioned variations in rate of resistance gain under tying of the top and bottom reinforcements.

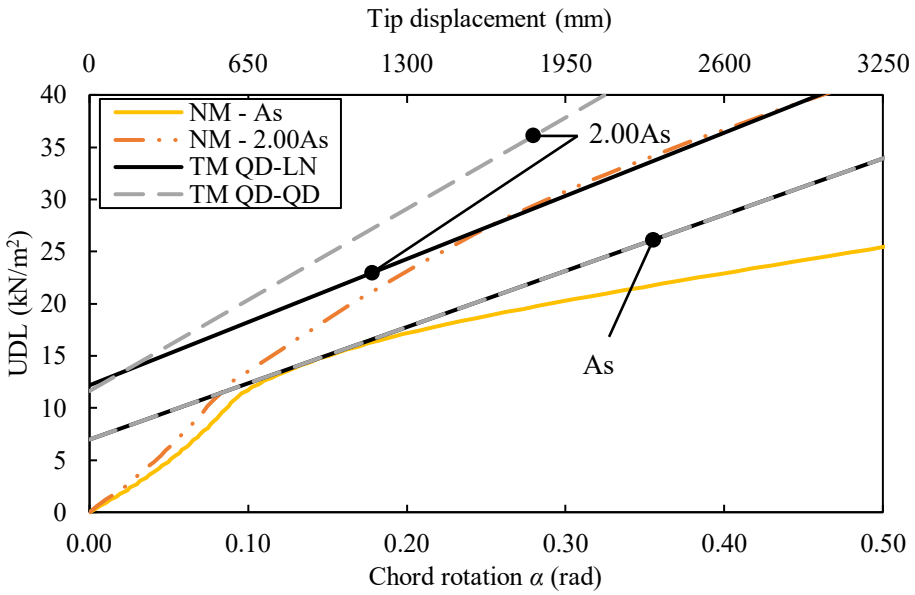


Fig. 7.28 – Sensitivity of the displacement approximation to the variation of the top reinforcement only

Furthermore, considering that the assumption of higher-order approximations for the orthogonal and parallel components of the planar pull-in displacement would lead to further overestimation of the numerical load response, even for the case where the top and bottom reinforcements are equally varied, and that the assumption of a linear-linear approximation would, on the other hand, lead to a significant underestimation of the response, the QD-LN approximation is deemed most suitable for the proposed method.

7.5 Applicability of proposed method to conventional reinforcement layout

This section assesses the applicability of the proposed method to corner floor systems with conventional reinforcement detailing with reinforcement parallel to the edges of the floor system. As noted previously, while such floor systems are typically considered to resist the gravity loads under the sudden loss of the corner column primarily via flexure, due to the inadequate planar restraint of the reinforcement, it may well be possible to achieve the alternative load resistance mechanism described in the current work (i.e. involving a resultant tying force over the end-restrained diagonal) with conventional reinforcement, provided that the reinforcement is continuous over the whole corner floor system. Such similarity in the

resistance mechanism can be demonstrated via a strut and tie model, where the axial force of the orthogonal reinforcement is projected onto the considered diagonals, and with the concrete equilibrating the remaining force components under compression.

In order to assess whether such an observation is valid, the load-deflection response under corner column loss of the control model with 6500mm span length is compared to that of a floor system with identical geometry but with a conventionally detailed reinforcement mesh at both the top and bottom face of the slab (Fig. 7.29, layout b). The quantity of conventionally detailed reinforcement should be appropriately defined so as to provide a comparable assessment between the two detailing layouts.

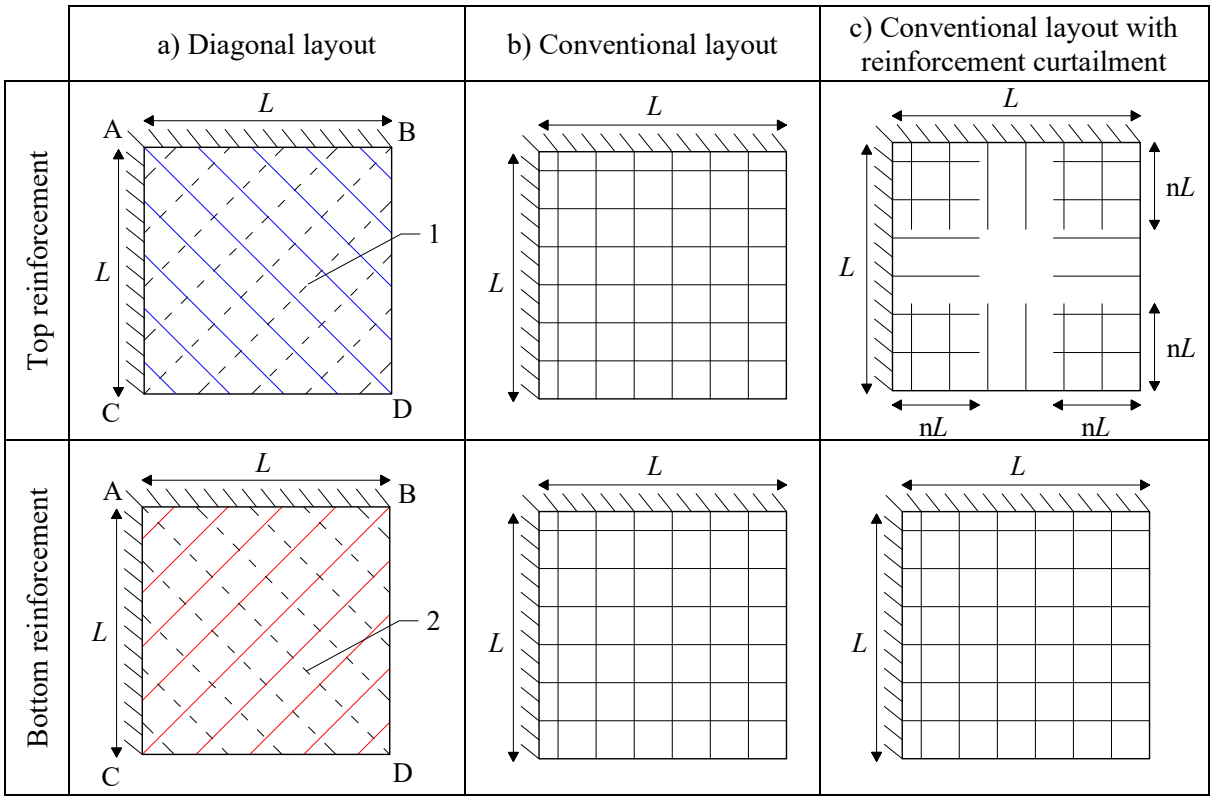


Fig. 7.29 – Diagonal and conventional reinforcement layout

Under the loss of a corner column, the critical yield lines expected to develop within the corner floor system would be the diagonals AD and BC (Fig. 7.29a), respectively, due to sagging and hogging flexure. Accordingly, the relevant reinforcement for such a design scenario is the reinforcement directly orthogonal to the aforementioned yield lines, specifically the bottom and top reinforcements spanning in the directions BC and AD, respectively, as considered in the proposed method. In this respect, it is demonstrated in Fig. 7.30, illustrating the transformation of forces between conventionally and diagonally detailed reinforcement along

a critical yield line, that the consideration of conventionally detailed reinforcement involving isotropic meshes at both the top and bottom parts of the floor slab would necessitate in each direction of each individual mesh the same quantity of distributed reinforcement required in the direction orthogonal to the yield line.

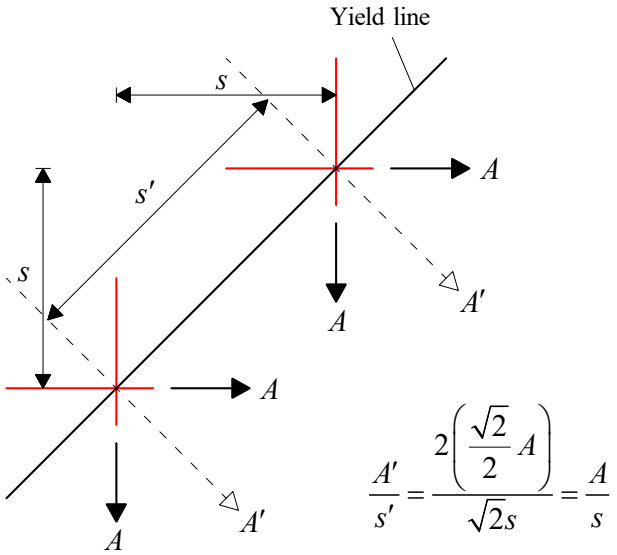


Fig. 7.30 – Equivalence between diagonal and conventional reinforcement layouts

For example, if the quantity of top reinforcement required for the diagonal layout is ϕ12//125mm, then the top reinforcement mesh under the conventional layout would require ϕ12//125mm reinforcement in each of the orthogonal directions. The same applies for the bottom layer of reinforcement. Thus, on the sole basis of the considered resistance contributions under the tying mechanism, it is expected that the conventional reinforcement layout would necessitate twice the quantity of reinforcement required in the diagonal layout to achieve similar levels of load resistance under the tying mechanism.

Notwithstanding, in the general design of the corner floor system for the ultimate limit states (ULS) in the original configuration excluding the corner column loss, the system undergoes the alternative collapse mechanism illustrated in Fig. 7.31.

Under such a mechanism, the diagonal reinforcement considered for the proposed method alone are clearly inadequate to equilibrate the gravity loads. This is because there would not be any bottom reinforcement covering for the sagging yield line along segment BC. Furthermore, contrary to the mechanisms developed under the scenario of corner column loss, the hogging yield lines developed along the edges of the floor system under ULS imply that the conventional layout now presents reinforcement that is orthogonal to such yield lines, whilst

the reinforcement forces from the diagonal layout now requires transformation. Considering that the transformation process is again that illustrated in Fig. 7.30, the consideration of the top reinforcement spanning along diagonal AD alone only offers half of the resistance at the hogging yield lines compared to the reinforcement of the conventional layout. An additional set of top reinforcement that are orthogonal to diagonal AD and a set of bottom reinforcement that are orthogonal to diagonal BC should be included in the diagonal layout so as to provide similar levels of load resistance achieved by the conventional layout under ULS.

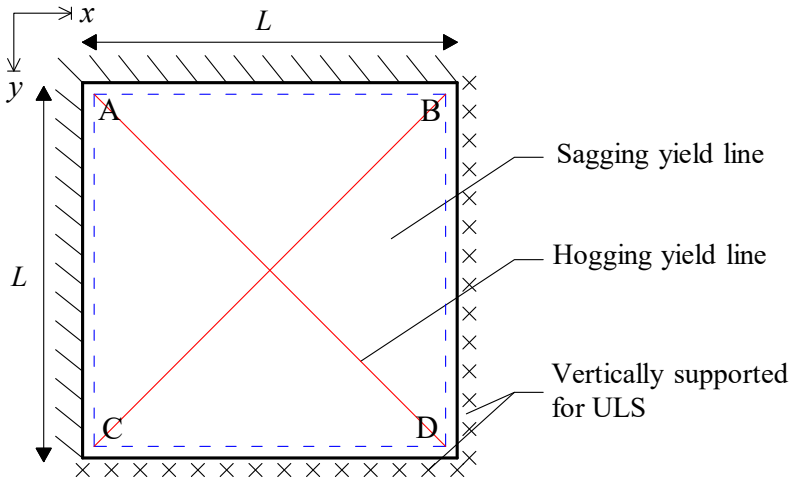


Fig. 7.31 – Yield line analysis for ULS design of the corner slab

It can therefore be concluded based on the actual design of the corner floor system, which involves the scenarios of ULS and the sudden loss of a corner column, that the equivalence between the conventional and diagonal reinforcement layouts should be established provided that both of the layouts present orthogonal meshes with identical quantity of distributed reinforcement at the top and bottom parts of the slab.

Accordingly, the corner floor system with the conventional reinforcement layout herein presents top and bottom meshes with ϕ12//125mm reinforcement in each orthogonal direction. Three additional cases are also considered with reference to the control model with 6500mm span length for the verification of the above observations. These are illustrated in Fig. 7.29 (layout a) and involve the addition to the existing reinforcement within the control model of i) set 1 reinforcement alone, ii) set 2 reinforcement alone, and iii) both sets, with sets 1 and 2 each entailing ϕ12//125mm reinforcement.

Fig. 7.32 compares the load-deflection responses for the proposed assessment cases, noting that the keys '+1', '+2' and '+1&2', respectively, represent the addition to the existing

reinforcement within the control model of set 1, set 2 and both sets of reinforcement. Interestingly, the outcomes demonstrate that the corner slab with conventional detailing presents a load resistance surpassing that of the control model, suggesting that such a floor system can indeed also mobilise tensile membrane action effectively. The lower resistance achieved by the control model can be explained by the exclusion of set 1 and set 2 reinforcement.

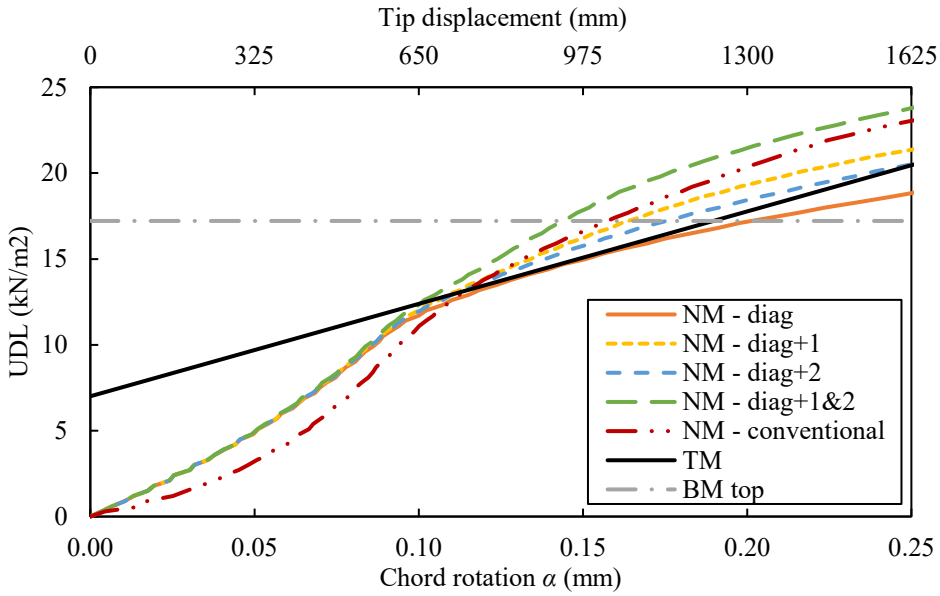


Fig. 7.32 – Load-deflection response of the diagonal and conventional reinforcement layouts

Indeed, besides the reinforcement forces required in the two most relevant diagonals of the floor system under corner column loss, the conventional reinforcement layout can also be providing resistance equivalent of the reinforcement sets excluded from the control model, as the load-deflection response of the conventionally detailed corner floor system is closer to that of the diagonal layout including both sets 1 and 2 reinforcement. This confirms that the conventional reinforcement layout is equivalent to the diagonal layout that presents orthogonal meshes at both the top and bottom part of the slab. Furthermore, the proposed method is demonstrated to be conservatively applicable for corner systems with a conventional reinforcement layout, provided that the corresponding reinforcement is continuous over the span of the floor slab.

Despite confirmation of the equivalence between conventional and diagonal layouts of reinforcement, hence suggesting under the backdrop of practical detailing that the former layout of reinforcement would suffice for the application of the proposed horizontal tying method, it is worth appreciating the diagonal placement of reinforcement. As previously

discussed, considering that most of the load resistance of the floor slab under the scenario of corner column loss is achieved from the top and bottom reinforcements spanning respectively in the direction AD and BC, the diagonal placement of reinforcement can lead to approximately 50% saving in the quantity of reinforcement compared to the conventional layout. In this respect, the robustness design of corner floor systems can make use of diagonal reinforcement as localised enhancements additional to the conventional reinforcement meshes, which are previously detailed for ULS. The proposed tying method is readily available for such a design scenario, where the tying contribution from the conventional reinforcement meshes can be established based on the demonstrated equivalence to the diagonal reinforcement, whilst the contribution from individual diagonal reinforcement can be determined also based on the presented formulation, but rather than performing an integration over the whole domain of the floor slab, the tying resistance is evaluated for each diagonal reinforcement at the corresponding distance r.

Lastly, a qualitative assessment on the influence of top reinforcement curtailment is presented. The assessment involves floor systems with reinforcement layout c, as illustrated in Fig. 7.29, where two different lengths are considered for the curtailed reinforcement, with n defined as 0.25 and 0.35. With reference to the load-deflection response of the model with continuous reinforcement, Fig. 7.33 clearly shows that the curtailment of the top reinforcement significantly reduces the resistance of the corner floor system under the loss of a corner column, to the extent of being even lower than the resistance of the control model.

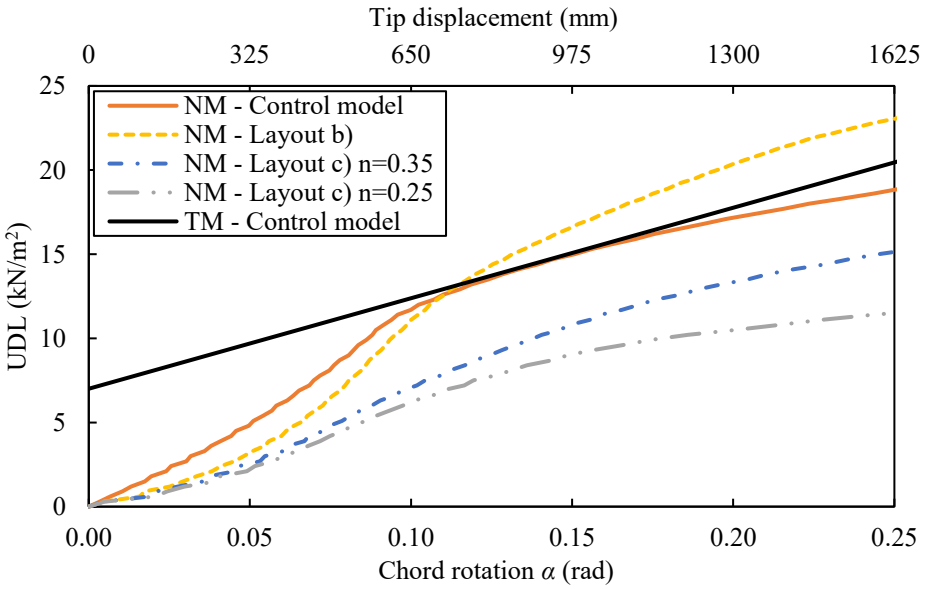


Fig. 7.33 – Load-deflection response of the conventional layout with curtailed top reinforcement

Notwithstanding, the load-deflection response for the cases with curtailed reinforcement still demonstrates some development of tensile membrane action. This ability of the floor system with curtailed top reinforcement to still offer some mobilisation of tying action can be related to the partial mobilisation of resistance within the parts of the slab where the top curtailed reinforcement still forms local orthogonal meshes (Fig. 7.29, layout c). In this respect, the initial reduction of the load-deflection response (n=0.35) is primarily flexural because the missing top reinforcement due to curtailment is located in the centre of the slab, and this would contribute to the load resistance primarily under flexure, as evidenced in Fig. 7.33 by the similar slope of the load-deflection responses of the n=0.35 model and the model with continuous reinforcement. On the other hand, the reinforcement near the corners is contributing more significantly to the tying resistance, as also evidenced in Fig. 7.33 by the shallower slope of the n=0.25 load-deflection response, leading to a more significant diminishing of tensile membrane action.

Nonetheless, it is worth noting that the above conclusions are established on the basis that the curtailed reinforcement is fully bonded with the concrete. In a more realistic scenario, where the bond strength is finite, the curtailed reinforcement may not reach the level of stresses determined numerically because of reinforcement pull-out, rendering the load resistance of the corner floor system much lower than that illustrated in Fig. 7.33. In conclusion, it is more appropriate and conservative to consider floor systems with top curtailed reinforcement unsuitable for the mobilisation of tensile membrane action.

7.6 Potential formulation including resistance contribution from beams

This section discusses some implications arising from the explicit inclusion of beams in corner floor systems and presents a potential extension of the proposed method accounting for the tying resistance of these beams. It is worth noting though that this simply involves an illustrative example where the associated formulation is verified against a specific case, and by no means establishes a final proposal. An extensive verification of the formulation under the variation of several parameters would be required before its general application.

Under the tying mechanism and considering again the deformation of the floor system to follow the assumed transverse and planar displacement approximations illustrated in Fig. 7.3, the peripheral beams follow a linear transverse displacement, similar to a hinged cantilever beam, with the pull-in at its free end dependent on the pull-in at the free tip of the floor system, u_{tip}.

Accordingly, the internal work contributions from the reinforcement of the peripheral beam in the x and y directions are respectively established as:

$$T_4 = \int_0^L F_x \delta\varepsilon(x,L)\,dx \tag{7.34}$$

$$T_5 = \int_0^L F_y \delta\varepsilon(L,y)\,dy \tag{7.35}$$

F_x and F_y in the above equation are the axial force of the beam reinforcement under yield in the x and y direction, respectively, whereas $\varepsilon(x,L)$ and $\varepsilon(L,y)$ are the corresponding reinforcement strains, as given by:

$$\varepsilon(x,L) = \frac{1}{2}\left(\frac{\partial v(x,L)}{\partial x}\right)^2 - \frac{\sqrt{2}}{2}\frac{u_{tip}}{L}, \quad \delta\varepsilon(x,L) = \alpha\left(\frac{\partial \Phi(x,L)}{\partial x}\right)^2 \delta\alpha - \frac{\sqrt{2}}{2}\frac{\delta u_{tip}}{L} \tag{7.36}$$

$$\varepsilon(L,y) = \frac{1}{2}\left(\frac{\partial v(L,y)}{\partial y}\right)^2 - \frac{\sqrt{2}}{2}\frac{u_{tip}}{L}, \quad \delta\varepsilon(L,y) = \alpha\left(\frac{\partial \Phi(L,y)}{\partial y}\right)^2 \delta\alpha - \frac{\sqrt{2}}{2}\frac{\delta u_{tip}}{L} \tag{7.37}$$

with $v(x,L)$, $\Phi(x,L)$, $v(L,y)$ and $\Phi(L,y)$ given as per (7.2) but evaluated at the indicated locations, whereas u_{tip} is determined according to (7.9).

Combining (7.36) and (7.37) respectively with (7.34) and (7.35) gives:

$$T_4 = \frac{F_x(2\alpha L + 3h)}{6}\delta\alpha \tag{7.38}$$

$$T_5 = \frac{F_y(2\alpha L + 3h)}{6}\delta\alpha \tag{7.39}$$

Thus, the additional resistance contribution from the peripheral beams under tying is established for the case under applied uniformly distributed loading w as:

$$T_4 + T_5 = \frac{wL^3}{4}\delta\alpha \quad \Rightarrow \quad w = \frac{2}{3L^3}(F_x + F_y)(2\alpha L + 3h) \tag{7.40}$$

The control model with 6500mm span length is again considered for the present verification, but the boundary conditions along the edges of the floor slab are now realised via the explicit modelling of reinforced concrete beams with 'cbp3' elements (Izzuddin, 2016), with vertical supports applied only at the corners of the floor system. All four beams supporting the floor

slab entail a 500×250mm^2 cross-section and are rigidly connected, with the beam top surface flushed against the top surface of the floor slab, rendering a vertical offset of 160mm between the centroidal axis of the beams and the mid-plane of the slab. The beam nodes and the slab nodes are connected via the rigid 'lnks' elements (Izzuddin, 2016), but allowing the slab to freely rotate in relation to the beams. The two supported interior beams entail $2\phi16+\phi12$ reinforcement as the top and bottom layers, whilst the two unsupported peripheral beams entail $3\phi12$ reinforcement as the top and bottom layers. The associated material properties are identical as those presented in Table 7.2. The concrete response of the beams is, however, modelled with the trilinear concrete model 'con1' (Izzuddin, 2016) with a negligible tensile strength and without a softening response subsequent to the attainment of the compressive strength.

Fig. 7.34 illustrates the predicted and numerical pull-in at the free tip of the beam-slab floor system with increasing vertical displacements (respectively represented by the keys 'TM' and 'NM'), noting that the predicted pull-in is again determined according to (7.30). It follows that the predicted pull-in also agrees reasonably well with the numerical pull-in of the beam-slab floor system, though the difference between these outcomes becomes increasingly significant at displacements exceeding 1000mm.

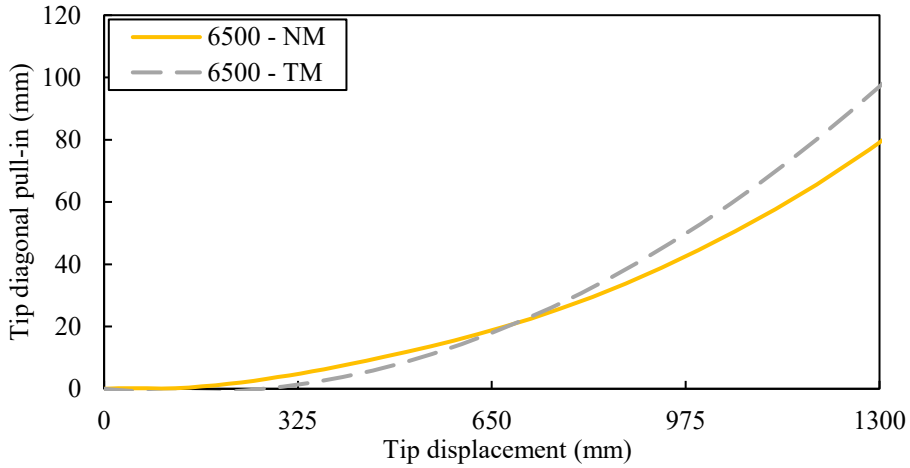
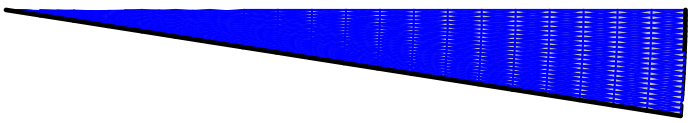


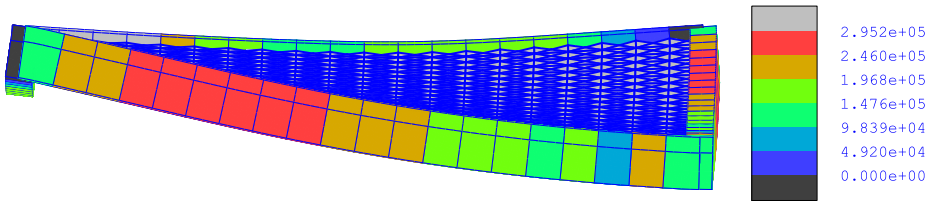
Fig. 7.34 – Verification of the planar pull-in at the free tip for the beam-slab floor model

Comparing the deformation mode of the slab-only model (Fig. 7.35a) and the beam-slab model (Fig. 7.35b) at a tip displacement of around 1000mm, it can be seen that the floor slab undergoes a more significant sag in the latter model. In this respect, the strain contribution of the top and bottom diagonal slab reinforcement to the internal virtual work is respectively reduced and increased with reference to the slab-only model. Such outcomes can also be

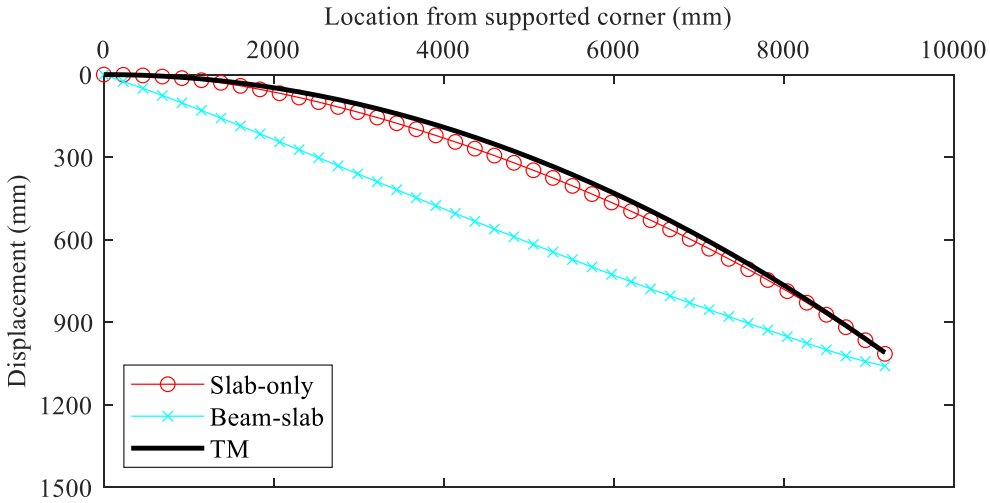
established via the assessment of the transverse displacement profile of the beam-slab model along diagonal AD (Fig. 7.14a), which follows closely a linear variation instead of the quadratic variation consistent with the bilinear approximation (Fig. 7.35c). It is worth noting though that the abovementioned observations depend on the stiffness of the beams, where with increasing beam stiffness the transverse deformation of the beam-slab model approximates that of the slab-only model.



(a) Slab-only model



(b) Axial forces of the beams in the beam-slab model (units in N)



(c) Comparison of transverse displacement profile along diagonal AD

Fig. 7.35 – Comparison of transverse deformation between the slab-only model and the beam-slab model at approximately 1000mm of tip displacement

Inspection of the axial force contours plotted for the beam-slab model in Fig. 7.35b reveals that the peripheral beams of the floor system can indeed develop significant tensile axial forces within the considered deformation range (up to 0.2rad), with a significant portion of the peripheral beams reaching tensile axial forces close to the yield resistance threshold, thus providing an additional tying resistance contribution to the floor system under corner column

loss. In this respect, such an observation suggests that the assumption of the tying forces being evaluated at the yield strength is reasonable for the extension of the proposed method.

Lastly, Fig. 7.36 demonstrates a good agreement between the analytical (TM) and numerical (NM) load-deflection responses of the beam-slab model, suggesting that the formulation outlined in this section offers a potential extension of the proposed method to include the tying resistance contribution from the peripheral beams. It is worth noting again, however, that such a good agreement is still verified only for the specific case presented herein, hence the extended method should be further verified before its general application via a sensitivity assessment to several relevant parameters such as the amount of beam reinforcement and beam depth.

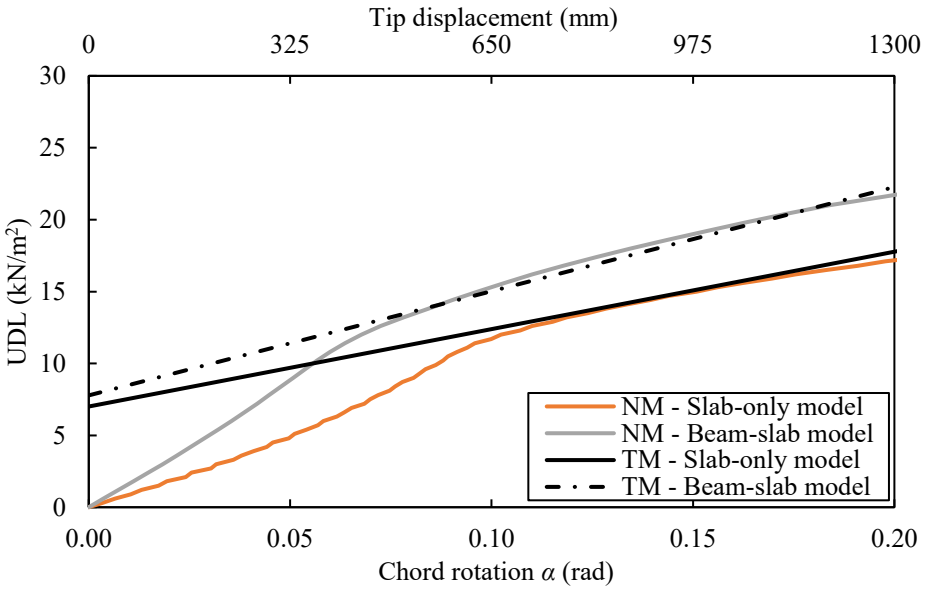


Fig. 7.36 – Verification of the analytical and numerical load-deflection responses of the beam-slab model

7.7 Conclusion

This chapter presents a newly developed horizontal tying force method for RC floor systems under the loss of a corner column. The proposed method is posited within a rational yet practical framework as an extension of the original method developed for floor systems with adequate planar restraint (Izzuddin and Sio, 2022). Accordingly, it is also suitable for consideration in future robustness design guidance to replace the prescriptive tying force requirements.

Importantly, the novelty of the proposed method is that it quantifies the mobilisation of tensile membrane action within the corner floor system, the load resistance contribution of which has

been commonly neglected due to the uncertainty in the adequacy of planar restraint to mobilise tensile membrane forces under a conventional reinforcement layout. Instead, the mobilisation of tensile membrane forces is herein realised based on the assumption of an alternative resistance mechanism, for which the ties are considered to be adequately anchored at the supported edges of the corner floor system.

The formulation of the proposed method involves two dominant mechanisms: i) a tying mechanism with a bilinear approximation for the transverse displacement, along with an additional planar displacement approximation to account for the pull-in of the unsupported edges of the corner floor system, and ii) a bending mechanism which formulation follows that of conventional yield line analysis.

Subsequent to the exposition of its formulation, the proposed method is extensively verified against numerical models in ADAPTIC under varying quantities of reinforcement, slab depth and span length. A generally good agreement is achieved between numerical and predicted load-deflection responses for the considered parameters, demonstrating the effectiveness of the proposed method in predicting the tying resistance of floor systems under the loss of a corner column. Lastly, the equivalence between conventional and diagonal reinforcement layouts is successfully established, demonstrating that corner floor systems with a conventional reinforcement detailing can indeed also mobilise tensile membrane action provided that both top and bottom slab reinforcements are continuous. The corresponding resistance can then be conservatively predicted by the proposed method.

These outcomes offer a novel view on the current state of research dealing with floor systems under the loss of a corner column, encouraging further validation of the proposed method against experimental tests. In this respect, there is a lack of experimental data specifically for such a purpose, which is recommended for future research to validate the underlying hypotheses of the proposed method. Other lines of research work would be i) to further extend the formulation of the bending mechanism to account for the additional flexural resistance from the U-shaped cross-section, and ii) to further verify the formulation accounting for the resistance contribution from the peripheral beams.

Chapter 8: Summary and conclusions

8.1 Summary

With the aim of further shifting the assessment of disproportionate collapse from the qualitative towards the quantifiable, the present thesis presents further contributions to the rational methods recently developed for the two main strategies of current robustness design regulations. These rational methods are the simplified multi-level assessment framework for the direct assessment of building structures under the sudden loss of a load-bearing member and the novel horizontal tying force method as a potential replacement for the prescriptive tying force requirements, with the associated research work primarily focused on reinforced concrete building structures.

8.1.1 Notional member removal

For the requirements of notional member removal, the multi-level assessment framework previously developed at Imperial College London offers a practical means to assess building structures under the sudden loss of a column/load-bearing member, where the assessment only requires the nonlinear static response of a planar beam sub-system extracted from the building structure, provided the regularity of the building structure allows for its highest level of idealisation. The dynamic nature of sudden loss is then considered via the conversion of the nonlinear static response into the so-called pseudo-static response based on the principle of energy balance, whilst the global response of the affected bay can be established from the assembly of the individual beam sub-systems.

In this respect, the present thesis proposes a novel approach for the modelling of reinforced concrete beam-column sub-systems involving geometric and material nonlinearity, with the benefit compared to alternative strategies currently available in literature of explicitly representing the bond-slip behaviour between the concrete and the reinforcement continuously throughout the whole beam member.

This is achieved by employing the bond-modelling elements developed by Khalid (2011) with enhancements proposed in this thesis such that these elements become readily suitable for the assessment of beam-column sub-systems under the loss of a column/load-bearing member. These enhancements include, at the material level, a nonlinear strain-dependent bond-slip model and a kinematic strain hardening steel model with an exponential tensile softening branch. On the other hand, at the section level, the formulation of the bond-modelling elements is extended to allow for I- and T-shaped cross-sections.

Subsequent validation and verification of several numerical models against experimental outcomes, including beam-column sub-systems entailing a T-shaped cross-section, demonstrate the reasonable accuracy of the proposed modelling approach in representing the bond-slip between the reinforcement and the concrete, the development of crack and the fracture of the reinforcement. The proposed approach also presents itself as a practical means to assess beam-column sub-systems with relatively sophisticated reinforcement detailing, for example involving a mixture of deformed and smooth reinforcement bars.

Furthermore, given its ability to predict the ductility limit of reinforced concrete planar frame sub-systems, the proposed approach can supplement more simplified assessment methods, such as the novel horizontal tying force method also presented in this thesis, in establishing the limit of tying resistance, or alternatively, as a verification means for the development of simplified approaches to estimate such a limit.

Notwithstanding, it should be noted that the reasonable agreement between numerical and experimental outcomes is achieved via calibration of the bond-slip properties, and its validity may still be relatively limited. Still, the proposed modelling approach is readily available for further calibration of the nonlinear bond-slip material model once detailed data on the ductility limit of the reinforcement and the bond between the reinforcement and the concrete are provided in experimental tests.

A sensitivity assessment is subsequently undertaken focused on the ductility limit of the system under the loss of a column/load bearing member, noting that the improvement of this measure alone does not necessarily lead to a performance enhancement of the beam-column sub-system against disproportionate collapse. It is found that the ductility limit of the system primarily improves with lower concrete strength and higher span-to-depth ratios. Furthermore, the assessment involving the variation of both the bond strength and the embedment length of the

reinforcement suggests that the ductility limit of the system is highest for a damage mechanism involving the pull-out of the reinforcement under yield.

8.1.2 Rational horizontal tying force method

The horizontal tying force method recently proposed by Izzuddin (Izzuddin and Sio, 2022) as a candidate replacement for the current prescriptive tying requirements is validated and verified in this thesis, demonstrating its effectiveness in predicting the load resistance under sudden column loss that is exclusively associated to tying. Importantly, unlike current prescriptive tying requirements, the basis of which is rather inconsistent and does not account for the ductility limit of the system, the novel method presents a similar rationale to alternative load paths in terms of i) explicitly relating the tying resistance to the ductility limit of the system and ii) accounting for the dynamic nature of sudden column loss via the amplification factor η. The method, which is established based on the principles of virtual work, also offers a practical combination of different sources of tying and loading condition, including distributed ties and loads of the floor slab. This offers a major improvement over other tying force methods currently available in literature, as the novel method accurately addresses tying forces developed within 1D and 2D systems, contrary to the typical reliance of the available methods on equivalent 1D beam systems to represent the response of 2D systems indirectly.

Despite mainly predicting the load resistance that is exclusively associated to tying, the formulation of the novel method allows for additional contributions such as material strain hardening of the ties, interaction with infill panels and residual flexural resistance via the reduction factor ρ, with a simple example provided in Izzuddin (2022) for the quantification of ρ associated to the residual flexural resistance in beams.

Along with the ductility limit of the system, the novel method necessitates adequate resistance and planar restraint stiffness from the surrounding structure for the mobilisation of full tying forces, with supplementary assessment methods also proposed for its corresponding compliance. Specifically, the original supplementary method for assessing the adequacy of the planar restraint stiffness does not consider the additional restraint stiffness contribution from the compressive ring developed within the affected floor system.

In this respect, the present thesis extends the supplementary method to include such a contribution. This is achieved with an analytical expression established based on the equilibrium of a simplified mechanical model under the application of the tying forces

mobilised within the central part of the floor system. The simplified mechanical model entails two fully fixed beams acting as a parallel system, where the beams respectively represent the surrounding structure and the compressive ring along one of the edges of the floor system. The fully-fixed beam representative of the surrounding structure can be alternatively replaced by springs with a corresponding distributed stiffness k_s for a more generic idealisation of the surrounding structure. The mechanical model also requires prior assumptions to the thickness of the compressive ring (depth of the corresponding fully-fixed beam). Considering a square/rectangular floor slab where the span lengths follow $L \leq H$, the ring thicknesses (beam depths) along the shorter and longer edges of the floor slab are assumed as $0.1H$ and $0.1L$, respectively. The subsequent verification of the analytical expression against numerical models demonstrates the adequacy of the assumed ring thicknesses. Furthermore, the consideration of the compressive ring in the supplementary method reduced the inherent conservatism of the original method.

Another line of research work under the backdrop of the novel horizontal tying force method consists in extending the applicability of the method to deal with column/load-bearing member loss scenarios where the planar restraint stiffness from the surrounding structure is typically thought to be negligible, namely corner, penultimate interior and penultimate exterior column/load-bearing member loss scenarios.

The present thesis focuses on the formulation for the tying of floor systems under corner column/load-bearing member loss. The premise is that tensile membrane action within corner floor systems can be more extensively mobilised under an alternative resistance mechanism, with the bottom ties spanned diagonally to the supported edges of the corner floor system, thereby being anchored to the surrounding structure instead of the unsupported peripheral beams, which provide negligible planar restraint stiffness. On the other hand, additional top slab reinforcement orthogonal to these ties should also be defined to prevent the premature development of a flexural failure mechanism.

Thus, this leads to the formulation of two resistance mechanisms based on the principles of virtual work: the tying mechanism and the bending mechanism. The transverse deformation mode of the former mechanism is assumed to follow a bilinear approximation, whilst the transverse deformation of the latter mechanism follows that typically considered in yield line analysis, involving the rigid-plate rotation of the unsupported region of the floor system. Specifically for the former mechanism, an additional in-plane displacement approximation is

assumed, established based on the diagonal pull-in at the free tip, which in turn relates to the level of transverse displacement at the same location. Along with the transverse displacement approximation, this in-plane displacement approximation is necessary to reflect the influence of the general pull-in of the floor system on the strain of the reinforcement.

The proposed method is verified against numerical models with varying amount of reinforcement, span length and slab thickness, with a reasonable agreement achieved between the predicted and numerical tying resistance as well as the point of transition from the tying mechanism to the bending mechanism. The predicted resistance under the bending mechanism is also conservative since the actual transverse deformation of the floor system renders the cross-section resisting the hogging flexure with an increased flexural resistance (U-shaped) compared to the cross-section assumed for the bending mechanism (a flat rectangular cross-section). Furthermore, the results also suggest that, under the bending mechanism, corner floor systems presenting a delayed transition from the tying mechanism to the bending mechanism can develop a more significant resistance gain compared to floor systems with a premature transition.

An equivalence between floor systems with conventional and diagonal layout of reinforcement is then tentatively established to assess the applicability of the proposed method to corner floor systems of typical buildings structures. An equivalence is successfully established between floor systems with conventional and diagonal layout of reinforcement provided that these layouts present a continuous and identical orthogonal reinforcement mesh at both the top and bottom part of the floor slab. This demonstrates the ability of corner floor systems with a conventional layout of reinforcement to also mobilise tensile membrane forces.

Accordingly, provided that both top and bottom reinforcement meshes are continuous, the tying resistance of a floor system with a conventional layout of reinforcement can be determined by first establishing its equivalence to a diagonal layout of reinforcement and subsequently employing the proposed method to predict the corresponding tying resistance. Such a prediction is conservative since the method neglects the resistance contribution from the top and bottom slab reinforcements spanned in the less relevant diagonals. It is worth noting the necessity of continuous reinforcement, as additional assessment involving curtailed top reinforcement suggests that the load resistance of corner floor systems significantly diminishes with increasing curtailment, even when assuming full-bond condition between the reinforcement and the concrete. In a more realistic scenario where the corner floor system

allows for the slip of the reinforcement, such load resistance would be even more questionable. This also explains the common perception of negligible mobilisation of tensile membrane forces within corner floor systems as typical experimental tests only entailed discontinued top slab reinforcement.

The research work culminates with a potential extension of the proposed method to consider the resistance contribution from the tying of the unsupported peripheral beams, under which a reasonable prediction is again established, though further research should be conducted prior to its general application.

Overall, the present work offers a novel view on the current state of research and design of floor systems under the sudden loss of a corner column/load-bearing member, where the corresponding performance against disproportionate collapse is typically limited to the flexural resistance of the system, as indeed, the prescriptive tying requirements from current robustness design regulations do not include any rational reference for the tying of corner floor systems. In this respect, the horizontal tying force method proposed in this thesis offers a pioneering design approach for such floor systems, relying on the load resistance exclusively associated to tying, and hence encourages future validation of the proposed method with experimental tests.

8.2 Recommendations for future research

The following lines of work can form part of the future research for the contributions presented in this thesis.

8.2.1 Modelling approach for RC planar frame sub-systems under a column loss

The proposed modelling approach is limited to planar frame sub-systems not exhibiting shear related damage within the beam members and with negligible deformation within the beam-column joint panels. In this respect, the modelling approach can be extended to represent such behaviours via the inclusion of additional links and spring elements with appropriately validated constitutive relationships.

The fibre beam elements with bond-modelling feature employed within the proposed approach is also limited to planar beam assessments, and thus can be further formulated for its application under more general 3D assessments. Along with the extended formulation to represent beam members with a T-shaped section, such a development would enable the modelling of reinforced concrete (RC) beam-slab floor systems as an equivalent grillage system, despite still

neglecting secondary mechanisms mobilised within the floor slab (i.e. compressive and tensile membrane action). Alternatively, the extension of the bond-modelling fibre beam elements to a 3D framework would also allow its application together with shell elements, similar to the floor system models presented throughout this thesis, with the connection between the two types of elements established via rigid links. Since under column loss scenario the slab reinforcement is less likely to fracture compared to the beam reinforcement, the joint application of the fibre beam elements with bond-modelling feature and the shell elements 'csl3' (Grosman and Izzuddin, 2018) or 'csl4' (Izzuddin *et al.*, 2004) would be sufficient to represent the load-deflection response and the ductility limit of RC beam-slab floor systems.

Notwithstanding, a further realism can be considered by replicating the bond-modelling feature from the fibre beam elements onto the shell elements. The ensuing shell elements would be specifically convenient for the representation of floor systems involving flat slabs, where the slab reinforcement necessarily fracture. Evidently, flat slab floor systems would also involve punching shear failure, hence requiring further modelling considerations to reflect this damage mechanism.

Under the sensitivity assessment of RC beam sub-systems, the addition of mid-layer smooth reinforcement within the beam members presents itself as an effective yet practical robustness enhancement solution for RC beam sub-systems, subsuming the solution entailing the addition of deformed reinforcement bars instead. This encourages the confirmation of the numerical outcomes with experimental tests, comparing between the solutions with smooth and deformed mid-layer reinforcement.

8.2.2 Tying force method for column loss scenarios with adequate planar restraint

As previously noted, the novel horizontal tying force method provides the option to consider additional resistance contribution to tying via the reduction factor ρ, with Izzuddin (2022) providing a simple example for the case involving residual flexural resistances at the ends of a double-span beam under column loss. Future research can establish a practical means to quantify such residual flexural resistances given the geometric and material properties of the beam sub-system, i.e. the connection of the steel beams and the reinforcement of RC beams.

The quantification of ρ for material strain hardening would necessitate the assessment of the corresponding average resistance gain beyond yield within the sub-system under column loss, as it is unlikely that all tying components would provide tying force at ultimate tensile strength when the ductility limit of the sub-system is reached. In this respect, the modelling approach

proposed in this thesis for RC planar frame sub-systems can be employed to evaluate the reinforcement stresses of the sub-system and thus aid the development of a supplementary analytical method for ρ. Other additional resistance contributions to tying can involve the unrestrained transverse beam from a floor system under 1-way tying and the interaction of a planar frame with infill panels. It is worth noting that the consideration of additional resistance contributions to tying influence the predicted dynamic response of the sub-system under column loss, hence the dynamic amplification factor η would also require corresponding adjustment.

Lastly, given that the design tying resistance directly depends on the chord rotation capacity of the system under consideration, there is also the need to develop supplementary methods establishing the ductility limit for beam/floor sub-systems.

8.2.3 Tying force method for other column loss scenarios

The promising outcomes from the verification of the proposed tying force method for corner floor systems against numerical models encourage its validation against experimental tests. These tests should ideally involve a uniformly distributed loading procedure since not only it is the dominant load assumed for the proposed method but also, as discussed in Chapter 7, the corner floor system is expected to mobilise tensile membrane action more extensively under such a loading condition. On the other hand, it is recommended that the experimental floor systems entail continuous reinforcement at both top and bottom parts of the floor slab, and that both conventional and diagonal layouts of reinforcement are assessed.

With respect to the formulation of the horizontal tying force method for corner column loss, future research can deal with further assessment of the extension that includes the tying resistance contribution from the peripheral beams. The proposed method can then proceed to assess additional resistance contributions to tying, specifically the flexural resistance from curtailed top reinforcement if the supported edges of the floor system are rotationally restrained. The current formulation would also need to be extended for rectangular corner floor systems, where it would be interesting to assess the sensitivity of the load-deflection response to different bar orientations. Finally, the supplementary methods presented in Chapter 5 would also need to be accordingly modified for application to corner floor systems.

Another line of research work would be to assess the significance of compressive membrane action within the corner floor system, as the corresponding resistance mechanism is simply the inverse of that presented for tensile membrane action. In this respect, unlike in the case under

tensile membrane action, where the compression along the supported edges of the floor system is directly equilibrated by the concrete slab in compression, the equilibrium of the tensile forces along the edges of the floor system under compressive membrane action necessitates adequate axial restraint from both the supporting beams and the adjacent columns, the absence of which renders the compressive membrane action negligible.

Lastly, the concept of diagonal resistance mechanism can also be applied to floor systems under penultimate interior and penultimate exterior column/load-bearing member loss scenarios, the formulation of which would be established based on transverse and planar displacement approximations appropriate for such column/load-bearing member loss scenarios.

References

Adam, J. M., Parisi, F., Sagaseta, J. & Lu, X. (2018) Research and practice on progressive collapse and robustness of building structures in the 21st century. *Engineering Structures*. 173, 122-149. Available from: https://doi.org/10.1016/j.engstruct.2018.06.082

Agarwal, J. & England, J. (2008) Recent developments in robustness and relation with risk. *Proceedings of the Institution of Civil Engineers-Structures and Buildings*. 161 (4), 183-188.

Alogla, K., Weekes, L. & Augusthus-Nelson, L. (2016a) A new mitigation scheme to resist progressive collapse of RC structures. *Construction and Building Materials*. 125, 533-545. Available from: https://doi.org/10.1016/j.conbuildmat.2016.08.084

Alogla, K., Weekes, L. & Augusthus-Nelson, L. (2016b) Progressive collapse resisting mechanisms of reinforced concrete structures. In: Silva Gomes, J. F. & Meguid, S. A. (eds.) *Proceedings of the 5th International Conference on Integrity-Reliability-Failure*, *24-28 July 2016*, *Porto, Portugal*. Porto, INEGI/FEUP. pp. 392-397.

Bailey, C. G. (2001) Membrane action of unrestrained lightly reinforced concrete slabs at large displacements. *Engineering Structures*. 23 (5), 470-483. Available from: https://doi.org/10.1016/S0141-0296(00)00064-X

Baldridge, S. M. & Humay, F. K. (2003) Preventing progressive collapse in concrete buildings. *Concrete international*. 25 (11), 73-79. Available from: http://baseengr.com/images/uploads/01-news-publications/whitepaper/03.11_PreventingProgressiveCollapse.pdf [Accessed 5 March 2019].

Bao, Y., Kunnath, S. K., El-Tawil, S. & Lew, H. S. (2008) Macromodel-based simulation of progressive collapse: RC frame structures. *Journal of Structural Engineering*. 134 (7), 1079-1091. Available from: https://doi.org/10.1061/(ASCE)0733-9445(2008)134:7(1079)

Bao, Y., Lew, H. S. & Kunnath, S. K. (2012) Modeling of reinforced concrete assemblies under column-removal scenario. *Journal of Structural Engineering*. 140 (1), 04013026. Available from: https://doi.org/10.1061/(ASCE)ST.1943-541X.0000773

Bathe, K.-J. (1996) *Finite element procedures*. Prentice-Hall, Inc.

Beconcini, M. L., Croce, P. & Formichi, P. (2008) Influence of bond-slip on the behaviour of reinforced concrete beam to column joints. In: Walraven & Stoelhorst (eds.) *Proceedings of International fib Symposium "Taylor Made Concrete Structures: New Solutions for our Society"*, *May 2008*. London, Taylor & Francis Group. pp. 533-539.

Bermejo, M., Santos, A. P. & Goicolea, J. M. (2017) Development of practical finite element models for collapse of reinforced concrete structures and experimental validation. *Shock and Vibration*. 2017. Available from: https://doi.org/10.1155/2017/4636381

Biondini, F., Frangopol, D. M. & Restelli, S. (2008) On structural robustness, redundancy, and static indeterminacy. In: *Structures Congress 2008: Crossing Borders*. pp. 1-10.
BSI (British Standards Institute). (1972) CP110. *Code of Practice for the Structural Use of Concrete*. London, UK, British Standards Institute.
BSI (British Standards Institute). (1985a) BS 5950-1:1985. *Structural use of steelwork in building - Code of practice for design in simple and continuous construction: hot rolled sections.* London, UK, British Standards Institute.
BSI (British Standards Institute). (1985b) BS 8110-1:1985. *Structural use of concrete - Code of practice for design and construction.* London, UK, British Standards Institute.
Burnett, E. F. P. (1975) *The Avoidance of Progressive Collapse: Regulatory Approaches to the Problem*. National Bureau of Standards. Report number: NBS-GCR 75-48.
Byfield, M. & Paramasivam, S. (2007) Catenary action in steel-framed buildings. *Proceedings of the Institution of Civil Engineers-Structures and Buildings*. 160 (5), 247-257.
Casanova, A., Jason, L. & Davenne, L. (2012) Bond slip model for the simulation of reinforced concrete structures. *Engineering Structures*. 39, 66-78. Available from: https://doi.org/10.1016/j.engstruct.2012.02.007
CEN (European Committee for Standardisation). (2002) EN1990:2002. *Eurocode - Basis of structural design*. Brussels, Belgium.
CEN (European Committee for Standardisation). (2004a) EN1998-1:2004. *Eurocode 8: Design of structures for earthquake resistance - Part 1: General rules, seismic actions and rules for buildings*. Brussels, Belgium.
CEN (European Committee for Standardisation). (2004b) EN1992-1-1:2004. *Eurocode 2: Design of concrete structures - Part 1-1: General rules and rules for buildings*. Brussels, Belgium.
CEN (European Committee for Standardisation). (2006) EN1991-1-7:2006. *Eurocode 1 - Actions on structures - Part 1-7: General actions Accidental actions*. Brussels, Belgium.
Choi, H. & Kim, J. (2011) Progressive collapse-resisting capacity of RC beam–column sub-assemblage. *Magazine of concrete research*. 63 (4), 297-310. Available from: https://doi.org/10.1680/macr.9.00170
Corley, W. G., Sozen, M. A., Thornton, C. H. & Mlakar, P. F. (1996) *The Oklakoma City Bombing: Improving Building Performance Through Muilti-Hazard Mitigation*. Federal Emergency Management Agency, United States.
Corley, W. G., Sr, P. F. M., Sozen, M. A. & Thornton, C. H. (1998) The Oklahoma City bombing: Summary and recommendations for multihazard mitigation. *Journal of Performance of Constructed Facilities*. 12 (3), 100-112. Available from: https://doi.org/10.1061/(ASCE)0887-3828(1998)12:3(100)
Dat, P. X. & Hai, T. K. (2013) Membrane actions of RC slabs in mitigating progressive collapse of building structures. *Engineering Structures*. 55, 107-115. Available from: https://doi.org/10.1016/j.engstruct.2011.08.039
Dat, P. X. & Tan, K. H. (2013) Experimental study of beam–slab substructures subjected to a penultimate-internal column loss. *Engineering Structures*. 55, 2-15. Available from: https://doi.org/10.1016/j.engstruct.2013.03.026
Dat, P. X. & Tan, K. H. (2014) Experimental response of beam-slab substructures subject to penultimate-external column removal. *Journal of Structural Engineering*. 141 (7), 04014170. Available from: https://doi.org/10.1061/(ASCE)ST.1943-541X.0001123
Deng, X.-F., Liang, S.-L., Fu, F. & Qian, K. (2020) Effects of high-strength concrete on progressive collapse resistance of reinforced concrete frame. *Journal of Structural Engineering*. 146 (6), 04020078.
Diao, M., Li, Y., Guan, H., Lu, X. & Gilbert, B. P. (2020) Influence of horizontal restraints on the behaviour of vertical disproportionate collapse of RC moment frames. *Engineering*

Failure Analysis. 109, 104324. Available from: https://doi.org/10.1016/j.engfailanal.2019.104324
DoD (Department of Defense). (2005) UFC 4-023-03:2005. *Unified Facilities Criteria - Design of buildings to resist progressive collapse*. Washington, D.C., Department of Defense.
DoD (Department of Defense). (2009) UFC 4-023-03:2009. *Unified Facilities Criteria - Design of buildings to resist progressive collapse*. Change 3, November 2016, Washington, D.C., USA.
Dong, Y. L. (2010) Tensile membrane effects of concrete slabs in fire. *Magazine of concrete research*. 62 (7), 497-505.
Dusenberry, D. O. & Hamburger, R. O. (2006) Practical means for energy-based analyses of disproportionate collapse potential. *Journal of Performance of Constructed Facilities*. 20 (4), 336-348.
Elghazouli, A. Y. & Izzuddin, B. A. (2004) Failure of lightly reinforced concrete members under fire. II: Parametric studies and design considerations. *Journal of Structural Engineering*. 130 (1), 18-31. Available from: https://doi.org/10.1061/(ASCE)0733-9445(2004)130:1(18)
Eligehausen, R., Popov, E. P. & Bertero, V. V. (1983) *Local bond stress-slip relationships of deformed bars under generalized excitations*. Earthquake Engineering Research Center, University of California Berkeley. Report number: UCB/EERC-83/23.
Ellingwood, B. R., Smilowitz, R., Dusenberry, D. O., Duthinh, D., Lew, H. S. & Carino, N. J. (2007) *Best practices for reducing the potential for progressive collapse in buildings*. National Institute of Standards and Technology, United States.
Encyclopædia Britannica. *September 11 attacks.* Available from: https://www.britannica.com/topic/World-Trade-Center#/media/1/648633/60121 [Accessed 12 October 2022].
Encyclopædia Britannica. *Oklahoma City bombing.* Available from: https://www.britannica.com/event/Oklahoma-City-bombing#/media/1/735994/70968 [Accessed 6 January 2023].
Favvata, M. J., Izzuddin, B. A. & Karayannis, C. G. (2008) Modelling exterior beam–column joints for seismic analysis of RC frame structures. *Earthquake Engineering & Structural Dynamics*. 37 (13), 1527-1548. Available from: https://doi.org/10.1002/eqe.826
Felippa, C. A. (2004) *Introduction to Finite Element Methods*. Department of Aerospace Engineering Sciences and Center for Aerospace Structures, University of Colorado Boulder, Colorado 80309-0429, USA.
Fernández Ruiz, M., Muttoni, A. & Gambarova, P. G. (2007) Analytical modeling of the pre- and postyield behavior of bond in reinforced concrete. *Journal of Structural Engineering*. 133 (10), 1364-1372. Available from: https://doi.org/10.1061/(ASCE)0733-9445(2007)133:10(1364)
Ferraioli, M. (2016) Dynamic increase factor for pushdown analysis of seismically designed steel moment-resisting frames. *International Journal of Steel Structures*. 16 (3), 857-875. Available from: https://doi.org/10.1007/s13296-015-0056-6
fib (Fédération Internationale Du Béton). (2012a) *Bulletin 63. Design of precast concrete structures against accidental actions*. Fédération Internationale Du Béton.
fib (Fédération Internationale Du Béton). (2012b) *CEB-FIP Model Code 2010*. Lausanne, Fédération Internationale Du Béton.
Fintel, M. & Schultz, D. M. (1976) A philosophy for structural integrity of large panel buildings. *PCI Journal*. 21 (3), 46-69.

Fintel, M. & Schultz, D. M. (1979) Structural integrity of large panel buildings. *ACI Journal*. 76 (5), 583-620. Available from: https://www.concrete.org/publications/internationalconcreteabstractsportal/m/details/id/6960 [Accessed 20 January 2020].

Foster, S. J., Bailey, C. G., Burgess, I. W. & Plank, R. J. (2004) Experimental behaviour of concrete floor slabs at large displacements. *Engineering structures*. 26 (9), 1231-1247. Available from: https://doi.org/10.1016/j.engstruct.2004.04.002

Frangopol, D. M. & Curley, J. P. (1987) Effects of damage and redundancy on structural reliability. *Journal of structural engineering*. 113 (7), 1533-1549.

Gouverneur, D., Caspeele, R. & Taerwe, L. (2013) Effect of reinforcement curtailment on deflections, strain and crack development in RC slabs under catenary action. *Magazine of Concrete research*. 65 (22), 1336-1347. Available from: https://doi.org/10.1680/macr.13.00141

Gouverneur, D., Caspeele, R. & Taerwe, L. (2015) Strain and crack development in continuous reinforced concrete slabs subjected to catenary action. *Structural Engineering and Mechanics*. 53 (1), 173-188. Available from: https://doi.org/10.12989/sem.2015.53.1.173

Griffiths, H., Pugsley, A. & Saunders, O. A. (1968) *Report of the inquiry into the collapse of flats at Ronan Point, Canning Town: presented to the Minister of Housing and Local Government*. HM Stationery Office.

Grosman, S. & Izzuddin, B. A. (2018) Realistic modelling of irregular slabs under extreme loading. *Proceedings of the Institution of Civil Engineers-Engineering and Computational Mechanics*. 171 (2), 49-64. Available from: https://doi.org/10.1680/jencm.18.00020

Gross, J. L. & McGuire, W. (1983) Progressive collapse resistant design. *Journal of Structural engineering*. 109 (1), 1-15.

GSA (General Services Administration). (2003) *Progressive Collapse Analysis and Design Guidelines for New Federal Office Buildings and Major Modernization Projects*. Washington, D.C., General Services Administration.

GSA (General Services Administration). (2013) *Alternative Path Analysis and Design Guidelines for Progressive Collapse Resistance*. Revision 1, January 2016, Washington, D.C., USA.

Gu, J. (2018) *Nonlinear Dynamic Analysis of Large Scale Structures.* PhD thesis. Imperial College London (University of London).

Gudmundsson, G. & Izzuddin, B. (2010) The 'sudden column loss' idealisation for disproportionate collapse assessment. *The Structural Engineer*. 88 (6), 22-26.

Hayes, B. (1968) Allowing for membrane action in the plastic analysis of rectangular reinforced concrete slabs. *Magazine of Concrete Research*. 20 (65), 205-212. Available from: https://doi.org/10.1680/macr.1968.20.65.205

Izzuddin, B. A. (1991) *Nonlinear dynamic analysis of framed structures.* PhD thesis. Imperial College London (University of London).

Izzuddin, B. A. & Elnashai, A. S. (1993a) Adaptive space frame analysis. Part I: A plastic hinge approach. *Proceedings of the Institution of Civil Engineers-Structures and Buildings*. 99 (3), 303-316.

Izzuddin, B. A. & Elnashai, A. S. (1993b) Adaptive space frame analysis. Part II: A distributed plasticity approach. *Proceedings of the Institution of Civil Engineers-Structures and Buildings*. 99 (3), 317-326.

Izzuddin, B. A. & Lloyd Smith, D. (2000) Efficient nonlinear analysis of elasto-plastic 3D R/C frames using adaptive techniques. *Computers & Structures*. 78 (4), 549-573.

Izzuddin, B. A. (2002) Advanced large displacement analysis of composite floor slabs. In: *Proc. 15 th ASCE Engineering Mechanics Conference*.

Izzuddin, B. A. & Elghazouli, A. Y. (2004) Failure of lightly reinforced concrete members under fire. I: Analytical modeling. *Journal of Structural Engineering*. 130 (1), 3-17. Available from: https://doi.org/10.1061/(ASCE)0733-9445(2004)130:1(3)

Izzuddin, B. A., Tao, X. Y. & Elghazouli, A. Y. (2004) Realistic modeling of composite and reinforced concrete floor slabs under extreme loading. I: Analytical method. *Journal of Structural Engineering*. 130 (12), 1972-1984. Available from: https://doi.org/10.1061/(ASCE)0733-9445(2004)130:12(1972)

Izzuddin, B. A. (2005) An enhanced co-rotational approach for large displacement analysis of plates. *International Journal for Numerical Methods in Engineering*. 64 (10), 1350-1374.

Izzuddin, B. A., Vlassis, A. G., Elghazouli, A. Y. & Nethercot, D. A. (2007) Assessment of progressive collapse in multi-storey buildings. *Proceedings of the Institution of Civil Engineers-Structures and Buildings*. 160 (4), 197-205.

Izzuddin, B. A., Vlassis, A. G., Elghazouli, A. Y. & Nethercot, D. A. (2008) Progressive collapse of multi-storey buildings due to sudden column loss—Part I: Simplified assessment framework. *Engineering structures*. 30 (5), 1308-1318. Available from: https://doi.org/10.1016/j.engstruct.2007.07.011

Izzuddin, B. A. & Nethercot, D. A. (2009) Design-Oriented Approaches for Progressive Collapse Assessment: Load-Factor vs. Ductility-Centred Methods. In: *Structures Congress 2009: Don't Mess with Structural Engineers*, *30 April-02 May 2009*, *Austin, Texas, United States*. ASCE. pp. 1791-1800.

Izzuddin, B. A. (2010) Robustness by design–Simplified progressive collapse assessment of building structures. *Stahlbau*. 79 (8), 556-564. Available from: https://doi.org/10.1002/stab.201001350

Izzuddin, B. A. (2012) Mitigation of progressive collapse in multi-storey buildings. *Advances in Structural Engineering*. 15 (9), 1505-1520. Available from: https://doi.org/10.1260/1369-4332.15.9.1505

Izzuddin, B. A. (2016) *ADAPTIC - User Manual Revision 1.5e*. Department of Civil and Environmental Engineering, Imperial College London (internal document).

Izzuddin, B. A. & Liang, Y. (2016) Bisector and zero-macrospin co-rotational systems for shell elements. *International Journal for Numerical Methods in Engineering*. 105 (4), 286-320.

Izzuddin, B. A. (2022) Rational Robustness Design of Multistory Building Structures. *Journal of Structural Engineering*. 148 (3), 04021279.

Izzuddin, B. A. & Sio, J. (2022) Rational horizontal tying force method for practical robustness design of building structures. *Engineering Structures*. 252, 113676.

Jahromi, H. Z., Vlassis, A. G. & Izzuddin, B. A. (2013) Modelling approaches for robustness assessment of multi-storey steel-composite buildings. *Engineering structures*. 51, 278-294. Available from: https://doi.org/10.1016/j.engstruct.2013.01.028

Jahromi, H. Z. Z. (2009) *Progressive collapse of building structures - Influence of membrane action in floor slabs.* MSc thesis. Imperial College London (University of London).

Jian, H. & Zheng, Y. (2014) Simplified models of progressive collapse response and progressive collapse-resisting capacity curve of RC beam-column substructures. *Journal of Performance of Constructed Facilities*. 28 (4), 04014008. Available from: https://doi.org/10.1061/(ASCE)CF.1943-5509.0000492

Kang, S.-B., Wang, S. & Gao, S. (2020) Analytical study on one-way reinforced concrete beam-slab sub-structures under compressive arch action and catenary action. *Engineering Structures*. 206, 110032.

Karayannis, C. G., Izzuddin, B. A. & Elnashai, A. S. (1994) Application of adaptive analysis to reinforced concrete frames. *Journal of Structural Engineering*. 120 (10), 2935-2957.
Kazemi-Moghaddam, A. & Sasani, M. (2015) Progressive collapse evaluation of Murrah Federal Building following sudden loss of column G20. *Engineering Structures*. 89, 162-171. Available from: https://doi.org/10.1016/j.engstruct.2015.02.003
Khalid, H. (2011) *Objective modelling of reinforced concrete structures.* PhD thesis. Imperial College London (University of London).
Lew, H., Bao, Y., Pujol, S. & Sozen, M. A. (2014) Experimental Study of Reinforced Concrete Assemblies under Column Removal Scenario. *ACI Structural Journal*. 111 (4).
Lew, H. S., Bao, Y., Sadek, F., Main, J. A., Pujol, S. & Sozen, M. A. (2011) *An experimental and computational study of reinforced concrete assemblies under a column removal scenario*. National Institute of Standards and Technology, Gaithersburg. Report number: NIST Technical Note 1720.
Li, M. & Sasani, M. (2015) Integrity and progressive collapse resistance of RC structures with ordinary and special moment frames. *Engineering Structures*. 95, 71-79. Available from: https://doi.org/10.1016/j.engstruct.2015.03.050
Li, Y., Lu, X., Guan, H. & Ye, L. (2011) An improved tie force method for progressive collapse resistance design of reinforced concrete frame structures. *Engineering Structures*. 33 (10), 2931-2942. Available from: https://doi.org/10.1016/j.engstruct.2011.06.017
Li, Y., Lu, X., Guan, H. & Ye, L. (2014) Progressive Collapse Resistance Demand of Reinforced Concrete Frames under Catenary Mechanism. *ACI Structural Journal*. 111 (5), 1225-1234.
Li, Y., Lu, X., Guan, H. & Ren, P. (2016) Numerical investigation of progressive collapse resistance of reinforced concrete frames subject to column removals from different stories. *Advances in Structural Engineering*. 19 (2), 314-326. Available from: https://doi.org/10.1177/1369433215624515
Li, Z.-X., Zhong, B., Shi, Y., Ding, Y. & Hao, Y. (2019) A computationally efficient numerical model for progressive collapse analysis of reinforced concrete structures. *International Journal of Protective Structures*. 10 (3), 330-358. Available from: https://doi.org/10.1177/2041419619854768
Lim, N. S., Tan, K. H. & Lee, C. K. (2017a) Experimental studies of 3D RC substructures under exterior and corner column removal scenarios. *Engineering Structures*. 150, 409-427. Available from: https://doi.org/10.1016/j.engstruct.2017.07.041
Lim, N. S., Tan, K. H. & Lee, C. K. (2017b) Effects of rotational capacity and horizontal restraint on development of catenary action in 2-D RC frames. *Engineering Structures*. 153, 613-627. Available from: https://doi.org/10.1016/j.engstruct.2017.09.059
Livingston, E., Sasani, M., Bazan, M. & Sagiroglu, S. (2015) Progressive collapse resistance of RC beams. *Engineering Structures*. 95, 61-70. Available from: https://doi.org/10.1016/j.engstruct.2015.03.044
Lowes, L. N. & Altoontash, A. (2003) Modeling reinforced-concrete beam-column joints subjected to cyclic loading. *Journal of Structural Engineering*. 129 (12), 1686-1697. Available from: https://doi.org/10.1061/(ASCE)0733-9445(2003)129:12(1686)
Lowes, L. N., Mitra, N. & Altoontash, A. (2004a) *A beam-column joint model for simulating the earthquake response of reinforced concrete frames*. Pacific Earthquake Engineering Research Center, College of Engineering, University of California, Berkeley.
Lowes, L. N., Moehle, J. P. & Govindjee, S. (2004b) Concrete-steel bond model for use in finite element modeling of reinforced concrete structures. *ACI Structural Journal*. 101 (4), 501-511.
Lu, X., Lin, K., Li, Y., Guan, H., Ren, P. & Zhou, Y. (2017) Experimental investigation of RC beam-slab substructures against progressive collapse subject to an edge-column-

removal scenario. *Engineering Structures*. 149, 91-103. Available from: https://doi.org/10.1016/j.engstruct.2016.07.039

Marchis, A. G., Moldovan, T. S. & Ioani, A. M. (2013) The influence of the seismic design on the progressive collapse resistance of mid-rise RC framed structures. *Acta Tehnica Napocensis: Civil Engineering & Architecture*. 56 (2), 222-234. Available from: https://constructii.utcluj.ro/ActaCivilEng/download/atn/ATN2013(2)_19.pdf [Accessed 5 March 2019].

Marjanishvili, S. & Agnew, E. (2006) Comparison of various procedures for progressive collapse analysis. *Journal of Performance of Constructed Facilities*. 20 (4), 365-374. Available from: https://doi.org/10.1061/(ASCE)0887-3828(2006)20:4(365)

Marjanishvili, S. M. (2004) Progressive analysis procedure for progressive collapse. *Journal of Performance of Constructed Facilities*. 18 (2), 79-85. Available from: https://doi.org/10.1061/(ASCE)0887-3828(2004)18:2(79)

Marti, P., Alvarez, M., Kaufmann, W. & Sigrist, V. (1998) Tension chord model for structural concrete. *Structural Engineering International*. 8 (4), 287-298.

McKay, A., Marchand, K. & Diaz, M. (2012) Alternate path method in progressive collapse analysis: Variation of dynamic and nonlinear load increase factors. *Practice Periodical on Structural Design and Construction*. 17 (4), 152-160. Available from: https://doi.org/10.1061/(ASCE)SC.1943-5576.0000126

MHCLG (Ministry of Housing, Communities and Local Government). (2013) *The Building Regulations 2010, Structure: Approved Document A: A3 Disproportionate Collapse*. London, UK.

Mitchell, D. & Cook, W. D. (1984) Preventing progressive collapse of slab structures. *Journal of Structural Engineering*. 110 (7), 1513-1532. Available from: https://doi.org/10.1061/(ASCE)0733-9445(1984)110:7(1513)

Naji, A. & Irani, F. (2012) Progressive collapse analysis of steel frames: Simplified procedure and explicit expression for dynamic increase factor. *International Journal of Steel Structures*. 12 (4), 537-549. Available from: https://doi.org/10.1007/s13296-012-4008-0

Nakamura, H. & Higai, T. (1999) Compressive Fracture Energy and Fracture Zone Length of Concrete. In: *Seminar on Post-Peak Behavior of RC Structures Subjected to Seismic Loads*, *1999*. pp. 259-272.

Orton, S., Jirsa, J. O. & Bayrak, O. (2009) Carbon Fiber-Reinforced Polymer for Continuity in Existing Reinforced Concrete Buildings Vulnerable to Collapse. *ACI Structural Journal*. 106 (5), 608-616. Available from: https://www.concrete.org/publications/internationalconcreteabstractsportal.aspx?m=details&i=51663101 [Accessed 5 March 2019].

Osteraas, J. D. (2006) Murrah building bombing revisited: A qualitative assessment of blast damage and collapse patterns. *Journal of performance of Constructed Facilities*. 20 (4), 330-335. Available from: https://doi.org/10.1061/(ASCE)0887-3828(2006)20:4(330)

Park, R. (1964a) Tensile membrane behaviour of uniformly loaded rectangular reinforced concrete slabs with fully restrained edges. *Magazine of Concrete Research*. 16 (46), 39-44. Available from: https://doi.org/10.1680/macr.1964.16.46.39

Park, R. (1964b) Ultimate strength of rectangular concrete slabs under short-term uniform loading with edges restrained against lateral movement. *Proceedings of the Institution of Civil Engineers*. 28 (2), 125-150. Available from: https://www.icevirtuallibrary.com/doi/pdf/10.1680/iicep.1964.10109

Park, R. (1965) The lateral stiffness and strength required to ensure membrane action at the ultimate load of a reinforced concrete slab-and-beam floor. *Magazine of concrete Research*. 17 (50), 29-38. Available from: https://doi.org/10.1680/macr.1965.17.50.29

Pearson, C. & Delatte, N. (2005) Ronan point apartment tower collapse and its effect on building codes. *Journal of Performance of Constructed Facilities*. 19 (2), 172-177. Available from: https://doi.org/10.1061/(ASCE)0887-3828(2005)19:2(172)

Pereira, M. F. D. F. (2012) *Robustness of multi-storey steel-composite buildings under column loss: rate-sensitivity and probabilistic framework.* PhD thesis. Imperial College London (University of London).

Pham, A. T., Lim, N. S. & Tan, K. H. (2017a) Investigations of tensile membrane action in beam-slab systems under progressive collapse subject to different loading configurations and boundary conditions. *Engineering Structures*. 150, 520-536. Available from: https://doi.org/10.1016/j.engstruct.2017.07.060

Pham, A. T. & Tan, K. H. (2017) A simplified model of catenary action in reinforced concrete frames under axially restrained conditions. *Magazine of Concrete Research*. 69 (21), 1115-1134. Available from: http://dx.doi.org/10.1680/jmacr.17.00009

Pham, A. T., Tan, K. H. & Yu, J. (2017b) Numerical investigations on static and dynamic responses of reinforced concrete sub-assemblages under progressive collapse. *Engineering Structures*. 149, 2-20. Available from: https://doi.org/10.1016/j.engstruct.2016.07.042

Pham, A. T. & Tan, K. H. (2019a) Analytical model for tensile membrane action in RC Beam-Slab structures under internal column removal. *Journal of Structural Engineering*. 145 (6), 04019040.

Pham, A. T. & Tan, K. H. (2019b) Static and dynamic responses of reinforced concrete structures under sudden column removal scenario subjected to distributed loading. *Journal of Structural Engineering*. 145 (1), 04018235. Available from: https://doi.org/10.1061/(ASCE)ST.1943-541X.0002214

Qian, K. & Li, B. (2012) Slab effects on response of reinforced concrete substructures after loss of corner column. *ACI Structural Journal*. 109 (9), 845-856. Available from: https://www.concrete.org/publications/internationalconcreteabstractsportal.aspx?m=details&i=51684128 [Accessed 30 April 2019].

Qian, K., Li, B. & Ma, J.-X. (2014) Load-carrying mechanism to resist progressive collapse of RC buildings. *Journal of Structural Engineering*. 141 (2), 04014107. Available from: https://doi.org/10.1061/(ASCE)ST.1943-541X.0001046

Qian, K., Cheng, J.-F., Weng, Y.-H. & Fu, F. (2021) Effect of loading methods on progressive collapse behavior of RC beam-slab substructures under corner column removal scenario. *Journal of Building Engineering*. 44, 103258.

Qiu, L., Lin, F., Wu, K. & Gu, X. (2021) Progressive collapse resistance of RC T-beam cable subassemblages under a middle-column-removal scenario. *Journal of Building Engineering*. 42, 102814.

Ravasini, S., Sio, J., Franceschini, L., Izzuddin, B. A. & Belletti, B. (2021) Validation of Simplified Tying Force Method for Robustness Assessment of RC structures. *Engineering Structures*. 249, 113291.

Ren, P., Li, Y., Lu, X., Guan, H. & Zhou, Y. (2016) Experimental investigation of progressive collapse resistance of one-way reinforced concrete beam–slab substructures under a middle-column-removal scenario. *Engineering Structures*. 118, 28-40. Available from: https://doi.org/10.1016/j.engstruct.2016.03.051

Russell, J. M., Sagaseta, J., Cormie, D. & Jones, A. E. K. (2019) Historical review of prescriptive design rules for robustness after the collapse of Ronan Point. *Structures*. 20, 365-373. Available from: https://doi.org/10.1016/j.istruc.2019.04.011

Sadek, F., Main, J. A., Lew, H. S. & Bao, Y. (2011) Testing and analysis of steel and concrete beam-column assemblies under a column removal scenario. *Journal of Structural*

Engineering. 137 (9), 881-892. Available from: https://doi.org/10.1061/(ASCE)ST.1943-541X.0000422

Shima, H., Chou, L.-L. & Okamura, H. (1987) Micro and macro models for bond in reinforced concrete. *Journal of the Faculty of Engineering, The University of Tokyo*. 39 (2), 133-194. Available from: http://www.infra.kochi-tech.ac.jp/shima/paper/1987/Bond%20models%20(U%20Tokyo).pdf

Smith, P. P. (2016) *An Investigation into tensile membrane action as a means of emergency load redistribution.* PhD Thesis. University of Southampton.

Sozen, M. A., Thornton, C. H., Corley, W. G. & Sr, P. F. M. (1998) The Oklahoma City bombing: structure and mechanisms of the Murrah Building. *Journal of Performance of Constructed Facilities*. 12 (3), 120-136. Available from: https://doi.org/10.1061/(ASCE)0887-3828(1998)12:3(120)

Starossek, U. (2006) Progressive collapse of structures: Nomenclature and procedures. *Structural engineering international*. 16 (2), 113-117. Available from: https://doi.org/10.2749/101686606777962477

Starossek, U. (2007a) Typology of progressive collapse. *Engineering Structures*. 29 (9), 2302-2307. Available from: https://doi.org/10.1016/j.engstruct.2006.11.025

Starossek, U. (2007b) Disproportionate collapse: a pragmatic approach. In: *Proceedings of the Institution of Civil Engineers-Structures and Buildings*. Thomas Telford Ltd. pp. 317-325.

Starossek, U. & Haberland, M. (2008) Measures of structural robustness—Requirements and applications. In: *Structures Congress 2008: Crossing Borders*. pp. 1-10.

Starossek, U. & Haberland, M. (2010) Disproportionate collapse: terminology and procedures. *Journal of performance of constructed facilities*. 24 (6), 519-528.

Stevens, D., Crowder, B., Hall, B. & Marchand, K. (2008) Unified progressive collapse design requirements for DOD and GSA. In: *Structures Congress 2008: Crossing Borders*. pp. 1-10.

Stylianidis, P. M., Nethercot, D. A., Izzuddin, B. A. & Elghazouli, A. Y. (2016) Study of the mechanics of progressive collapse with simplified beam models. *Engineering Structures*. 117, 287-304. Available from: https://doi.org/10.1016/j.engstruct.2016.02.056

Su, Y., Tian, Y. & Song, X. (2009) Progressive Collapse Resistance of Axially-Restrained Frame Beams. *ACI Structural Journal*. 106 (5), 600-607.

Taylor, R. (1965) A note on a possible basis for a new method of ultimate load design of reinforced concrete slabs. *Magazine of concrete research*. 17 (53), 183-186. Available from: https://doi.org/10.1680/macr.1965.17.53.183

Taylor, R., Maher, D. R. H. & Hayes, B. (1966) Effect of the arrangement of reinforcement on the behaviour of reinforced concrete slabs. *Magazine of concrete research*. 18 (55), 85-94. Available from: https://doi.org/10.1680/macr.1966.18.55.85

The National Archives. *Ronan Point Tower.* Available from: http://www.nationalarchives.gov.uk/education/resources/sixties-britain/ronan-point-tower/ [Accessed 12 April 2019].

Tsai, M. H. & Lin, B. H. (2009) Dynamic amplification factor for progressive collapse resistance analysis of an RC building. *The Structural Design of Tall and Special Buildings*. 18 (5), 539-557. Available from: https://doi.org/10.1002/tal.453

Tsai, M. H. & Chang, Y. T. (2015) Collapse-resistant performance of RC beam–column sub-assemblages with varied section depth and stirrup spacing. *The Structural Design of Tall and Special Buildings*. 24 (8), 555-570. Available from: https://doi.org/10.1002/tal.1199

Viwathanatepa, S., Popov, E. P. & Bertero, V. V. (1979) *Effects of generalized loadings on bond of reinforcing bars embedded in confined concrete blocks*. Earthquake Engineering Research Center, University of California Berkeley. Report number: UCB/EERC-79/22.

Vlassis, A. G. (2007) *Progressive collapse assessment of tall buildings.* Imperial College London (University of London).

Vlassis, A. G., Izzuddin, B. A., Elghazouli, A. Y. & Nethercot, D. A. (2008) Progressive collapse of multi-storey buildings due to sudden column loss—Part II: Application. *Engineering Structures*. 30 (5), 1424-1438. Available from: https://doi.org/10.1016/j.engstruct.2007.08.011

Vlassis, A. G., Izzuddin, B. A., Elghazouli, A. Y. & Nethercot, D. A. (2009) Progressive collapse of multi-storey buildings due to failed floor impact. *Engineering structures*. 31 (7), 1522-1534. Available from: https://doi.org/10.1016/j.engstruct.2009.02.009

Vrouwenvelder, T. (2008a) Treatment of risk and reliability in the Eurocodes. *Proceedings of the Institution of Civil Engineers-Structures and Buildings*. 161 (4), 209-214.

Vrouwenvelder, T. 2008b. EN1991-1-7 Eurocode 1 Accidental Actions.

Wang, K. Q., Fang, C., Li, G. Q. & Izzuddin, B. A. (2011) An analytical model for evaluating axial boundary stiffness of steel beam restrained by neighboring floor systems. *International Journal of Steel Structures*. 11 (4), 457-466. Available from: https://doi.org/10.1007/s13296-011-0001-2

Wang, S. & Kang, S.-B. (2019) Analytical investigation on catenary action in axially-restrained reinforced concrete beams. *Engineering Structures*. 192, 145-155. Available from: https://doi.org/10.1016/j.engstruct.2019.05.008

Xavier, F. B., Macorini, L. & Izzuddin, B. A. (2014) Robustness of multistory buildings with masonry infill. *Journal of Performance of Constructed Facilities*. 29 (5), B4014004. Available from: https://doi.org/10.1061/(ASCE)CF.1943-5509.0000684

Xiao, H. & Hedegaard, B. (2017) Flexural, compressive arch, and catenary mechanisms in pseudostatic progressive collapse analysis. *Journal of Performance of Constructed Facilities*. 32 (1), 04017115. Available from: https://doi.org/10.1061/(ASCE)CF.1943-5509.0001110

Xu, L. (2013) *Numerical study on reinforced concrete beam-column frames in progressive collapse.* PhD thesis. Nanyang Technological University.

Yi, W.-J., He, Q.-F., Xiao, Y. & Kunnath, S. K. (2008) Experimental study on progressive collapse-resistant behavior of reinforced concrete frame structures. *ACI Structural Journal*. 105 (4), 433-439. Available from: https://www.concrete.org/publications/internationalconcreteabstractsportal.aspx?m=details&i=19857 [Accessed 5 March 2019].

Yu, J. (2012) *Structural behavior of reinforced concrete frames subjected to progressive collapse.* PhD thesis. Nanyang Technological University.

Yu, J. & Tan, K. H. (2012) Structural behavior of RC beam-column subassemblages under a middle column removal scenario. *Journal of Structural Engineering*. 139 (2), 233-250. Available from: https://doi.org/10.1061/(ASCE)ST.1943-541X.0000658

Yu, J. & Tan, K. H. (2013a) Experimental and numerical investigation on progressive collapse resistance of reinforced concrete beam column sub-assemblages. *Engineering Structures*. 55, 90-106. Available from: https://doi.org/10.1016/j.engstruct.2011.08.040

Yu, J. & Tan, K. H. (2013b) Special detailing techniques to improve structural resistance against progressive collapse. *Journal of Structural Engineering*. 140 (3), 04013077. Available from: https://doi.org/10.1061/(ASCE)ST.1943-541X.0000886

Yu, J. & Tan, K. H. (2014a) Numerical analysis with joint model on RC assemblages subjected to progressive collapse. *Magazine of Concrete Research*. 66 (23), 1201-1218. Available from: http://dx.doi.org/10.1680/macr.14.00100

Yu, J. & Tan, K. H. (2014b) Analytical model for the capacity of compressive arch action of reinforced concrete sub-assemblages. *Magazine of Concrete Research*. 66 (3), 109-126. Available from: http://dx.doi.org/10.1680/macr.13.00217

Yu, J. & Tan, K. H. (2017) Structural behavior of reinforced concrete frames subjected to progressive collapse. *ACI Structural Journal*. 114 (1), 63-74. Available from: https://doi.org/10.14359/51689424

Yu, J., Luo, L.-z. & Fang, Q. (2020a) Structure behavior of reinforced concrete beam-slab assemblies subjected to perimeter middle column removal scenario. *Engineering Structures*. 208, 110336. Available from: https://doi.org/10.1016/j.engstruct.2020.110336

Yu, J., Tang, J.-h., Luo, L.-z. & Fang, Q. (2020b) Effect of boundary conditions on progressive collapse resistance of RC beam-slab assemblies under edge column removal scenario. *Engineering Structures*. 225, 111272. Available from: https://doi.org/10.1016/j.engstruct.2020.111272

Zhang, J.-Z., Li, G.-Q. & Jiang, J. (2018) Modeling structural behavior of reinforced concrete beam–slab substructures subject to side-column loss at large deflections. *Advances in Structural Engineering*. 21 (7), 1051-1071.

Zhou, B., Wu, R. & Feng, J. (2017) Two models for evaluating the bond behavior in pre-and post-yield phases of reinforced concrete. *Construction and Building Materials*. 147, 847-857. Available from: https://doi.org/10.1016/j.conbuildmat.2017.04.067

Zienkiewicz, O. C. & Taylor, R. L. (2000a) *The Finite Element Method Volume 2: Solid Mechanics*. Linacre House, Jordan Hill, Oxford OX2 8DP, Butterworth-Heinemann.

Zienkiewicz, O. C. & Taylor, R. L. (2000b) *The Finite Element Method Volume 1: The Basis*. Linacre House, Jordan Hill, Oxford OX2 8DP, Butterworth-Heinemann.

Appendix A: Properties of structural robustness

Continuity

As noted by Starossek and Haberland (2008), continuity refers to the provision of "continuous connection of components as well as the continuous reinforcement of concrete components" and is one of the first properties advocated for structural robustness following the collapse of Ronan Point in 1968. The provision of continuity, typically via the prescription of ties within structural members and connections, generally enhances the robustness of the structure by enabling secondary load-carrying mechanisms for the redistribution of the gravity load to the surrounding structure. These mechanisms can be in the form of cantilever action of beams/walls, Vierendeel action of frames and tensile catenary/membrane action via double-span beams/floor systems. Emphasis should also be given, however, to the verification of the surrounding structure so as to ensure that its structural members do not fail under the redistributed gravity load. Otherwise, the provision of continuity becomes counterproductive (Starossek, 2007b), with the prescribed ties assuming the means to promote the propagation of collapse. In this respect, Starossek (2007b) highlights the segmentation approach to mitigate disproportionate collapse, which is based on a concept opposite to continuity, consisting in dividing the structure into individual sections/compartments such that, in an unforeseen event leading to an initial local damage at any of the divided sections, propagation of collapse is limited to the section initially affected by the local damage.

Redundancy

Biondini *et al.* (2008) defines structural redundancy as "the ability of a system to redistribute among its members the load which can no longer be sustained by some other members due to their damage". The provision of redundancy is often associated with the increase in the degree of static indeterminacy of the structure, in the sense that it adds more members for load redistribution. However, such an observation should not be generalised as redundancy can be demonstrated to depend on other factors such as the structural typology, material properties

and applied loads (Frangopol and Curley, 1987). Furthermore, structures with lower static indeterminacy can be more redundant than structures with higher static indeterminacy (Biondini *et al.*, 2008). Biondini *et al.* (2008) also note that the allocation of static indeterminacy for structural robustness should be a function of the expected amount of damage since the enhancement in structural robustness becomes negligible with increasing static indeterminacy beyond the required level.

Izzuddin *et al.* (2008) suggest that the benefits of redundancy are guaranteed only in conventional strength-based plastic design, where the plastic strength of the components is typically achieved at relatively small displacements. In structural robustness assessment, reliance is placed on the ultimate strength of the components, which is difficult to achieve simultaneously for all components before a ductility limit is reached. On this basis, Izzuddin *et al.* (2008) demonstrate with determinate and redundant floor systems that, for certain ductility limits of the former system, its corresponding robustness can decrease when the system is made redundant.

Ductility

Ductility allows a structural system to sustain large plastic deformations without significant loss of resistance, aiding the load-redistribution of the system. As noted by Ellingwood *et al.* (2007), such property can be achieved by: (i.a) using high toughness steel in steel structures; (i.b) for concrete structures, providing adequate concrete confinement with stirrups and ensuring reinforcement continuity with adequate lap splices; and (ii) designing connections which resistance exceeds that of the members. Ductility has been previously considered in the design of structures against earthquake. Notwithstanding, it is worth noting the substantial differences in the loading nature and demand of ductility under seismic and disproportionate collapse scenarios (Vlassis, 2007). In seismic design, the demand of ductility relates, at the global level, to the ability of the structure to undergo hysteretic loading and lateral sway within set deformation limits and, at the local level, to the low-cycle fatigue of the joints (Pereira, 2012). In disproportionate collapse, although the sudden unbalance in gravity loading is dynamic in its nature, the extent of load reversal is limited, hence ductility demand can be considered monotonic. Furthermore, ductility demand is rather focused at the local system level, where emphasis is given to the development of the required level of tie forces before failure of a critical component, even at the expense of significant local deformations (Pereira, 2012).

In general terms, ductility is considered beneficial for structural robustness, specifically because it supports the activation of secondary mechanisms in redundant systems, allowing for the mobilisation of full system resistance before failure of a critical component (Vlassis, 2007). Notwithstanding, similar to redundancy, ductility should not be considered as a measure of structural robustness alone (Izzuddin *et al.*, 2008; Starossek and Haberland, 2008), as the benefits of ductility to structural robustness is also shown by Izzuddin *et al.* (2008) to be dependent of the system configuration, where greater robustness performance of a system can be achieved at a lower level of ductility.

Energy absorption

Recent publications on energy-based assessment methods for disproportionate collapse (e.g. Dusenberry and Hamburger, 2006; Izzuddin *et al.*, 2008) have led to the appreciation of energy absorption as an attractive measure for structural robustness. The property derives from the principle of energy balance between the external work done by the applied loads and the internal strain energy. Notwithstanding, on the basis of the aforementioned principle, Izzuddin *et al.* (2008) note that the consideration of energy absorption as a measure for structural robustness alone suffers from a fundamental flaw in that energy absorption depends not only on the applied loads but also on the response of the structure. It follows that structural systems offering the same amount of internal strain energy can be associated to remarkably different structural responses, i.e. different load resistances and ductility limits. Thus, even if the available strain energy is adequate to absorb the external work done by the applied loads, the structure may not mobilise the required level of load resistance within its ductility limit, noting that compliance of the structure against disproportionate collapse involves the equilibrium of the suddenly unbalanced forces after the initial local damage. Furthermore, for a structural response with softening behaviour following the peak load resistance, an increase in deformation ductility beyond the threshold corresponding to this peak load would enhance the energy absorption of the structural system but would not benefit its resistance against disproportionate collapse.

Local load resistance

In contrast to methods presuming an initial local damage (e.g. alternative load path and segmentation), provision of local load resistance aims at preventing an initial local damage to key elements of the structure. As noted by Starossek (2007b), such a provision does not aim at enhancing structural robustness, but rather focuses on the improvement of collapse resistance, where key elements are identified and designed to withstand specific types of accidental action.

The provision of local load resistance is preferable for small structures, where the number of key elements are generally limited and well-identified, and the assumed extent of accidental damage is small (Starossek, 2007b). However, the quantification of accidental actions for the design of key elements is often challenging because the probability of occurrence of such actions is very low, hence difficult to predict, and the corresponding extent of damage can vary significantly. Furthermore, since the provision of local load resistance does not aim at increasing the robustness of the structure, avoidance of collapse is not guaranteed once a key element fails. Nonetheless, the provision of local load resistance can be used in combination with methods presuming an initial local damage (alternative load path method or segmentation) to cover a wider range of design objectives against disproportionate collapse (Starossek, 2007b). Indeed, the combination of key element provision and alternative load path establishes the 'direct design approach' in current design regulations for structural robustness.

Appendix B: Background of prescriptive tying requirements

Requirements for horizontal tying

Table B.1 – Horizontal tying for framed structures

Regulation	Internal ties	Peripheral ties
Eurocode 1 – Part 1-7	$0.8(g_k + \psi q_k)sL \geq 75\,\text{kN}$	$0.4(g_k + \psi q_k)sL \geq 75\,\text{kN}$
Eurocode 2	$q_3(L_1 + L_2)/2 \geq Q_4$ $q_3 = 20\,\text{kN/m}$, $Q_4 = 70\,\text{kN}$	$L_i\, q_1 \geq Q_2$ $q_1 = 10\,\text{kN/m}$, $Q_2 = 70\,\text{kN}$
Eurocode 2 + UK National Annex	$\frac{(g_k + q_k)}{7.5}\frac{L_r}{5}F_t \geq F_t$ (kN/m) $F_t = 20 + 4n_0 \leq 60\,\text{kN/m}$	$L_i\, q_1 \geq Q_2$ $q_1 = (20 + 4n_0)L_i\,\text{kN/m}$, $Q_2 = 60\,\text{kN}$
UFC 4-023-03:2009	$F_i = 3w_f L_r$ (kN/m)	$F_p = 6w_f s_p L_r + 3W_c$ (kN)

Table B.2 – Horizontal tying for load-bearing wall constructions

Regulation	Internal ties	Peripheral ties
Eurocode 1 – Part 1-7	$\frac{(g_k + \psi q_k)}{7.5}\frac{z}{5}F_t \geq F_t$ (kN/m) $F_t = 20 + 4n_0 \leq 60\,\text{kN/m}$ $z = \min(5h_w, L)$	$20 + 4n_0 \leq 60\,\text{kN/m}$
UFC 4-023-03:2009	Two-way panels $F_i = 3w_f L_r$ (kN/m) One-way panel $F_i = 3w_f L_3$ (kN/m)	Two-way panels $F_p = 6w_f s_p L_r + 3W_c$ (kN) One-way panel $F_p = 6w_f s_p L_4 + 3W_c + 3W_w$ (kN)

Considering the general form of the tying force requirements as:

$$F = i_f wL \tag{B.1}$$

where F is the required tying force; i_f is denoted as the force intensity factor; L is the longest service span in the direction of tying; and w is the distributed area load.

Thus, the intensity factor i_f given by Eurocode 1 – Part 1-7 for internal and peripheral ties can be shown to be 0.8 and 0.4, respectively, whereas in the UFC code the corresponding intensity factors are 3.0 and 6.0. The requirements of the UFC code are clearly more conservative because not only the resulting requisite tying force is higher under the same distributed area load, but the peripheral tying requirements also considers the dead loads from claddings along the perimeter of the building structure.

It also follows that, whilst in Eurocode 1 – Part 1-7 the requisite tying force of peripheral ties is half of that required for internal ties, the UFC code doubles the requisite tying forces for peripheral ties, revealing significant inconsistencies across different design regulations. Even within the same design regulation, the tying requirements of Eurocode 2 differ from those of Eurocode 1 – Part 1-7, with the basis of the requirements even less clear given the use of pre-established design loads q_1 and q_3. Notwithstanding, similarly to Eurocode 1 – Part 1-7, the requisite force of peripheral ties in Eurocode 2 can also be shown as half of the force required for internal ties if L_1 and L_2 are assumed as L_i.

The UK National Annex of Eurocode 2 adopts expressions first appeared in the Code of Practice 110 following the partial collapse of the Ronan Point Tower, remaining practically unchanged since then. Initially proposed for precast large panel structures, these expressions also establish the requirements for load-bearing wall constructions in Eurocode 1 – Part 1-7. According to Smith (2016), the term $20 + 4n_0$ is an empirical value intended to reflect the susceptibility of the building to disproportionate collapse with increasing number of storeys. However, Li *et al.* (2011) claims that this empirical assumption is flawed by showing that the redundancy of the damaged structure (following the loss of a column/load-bearing member) increases with the number of stories above the lost column since more remaining beams are available to carry the applied load. On the limiting value of 60 kN, Burnett (1975) suggests that this is established from the moment equilibrium of a double-span beam with a service span of $L = 5$ m (Fig. B.1), at a central deflection Δ of $0.2L$, between the tying force F_t and an

imposed distributed load of $q = 4.8$ kN/m, the value of which derives from a typical service floor load of 7.2kN/m^2 whereby the characteristic dead and live loads are each taken at 3.6kN/m^2, under an accidental load case of $1.0g_k + 0.33q_k$ (Smith, 2016):

$$F_t \cdot 0.2L = \frac{q \cdot (2L)^2}{8} \quad (q \text{ in kN/m}) \tag{B.2}$$

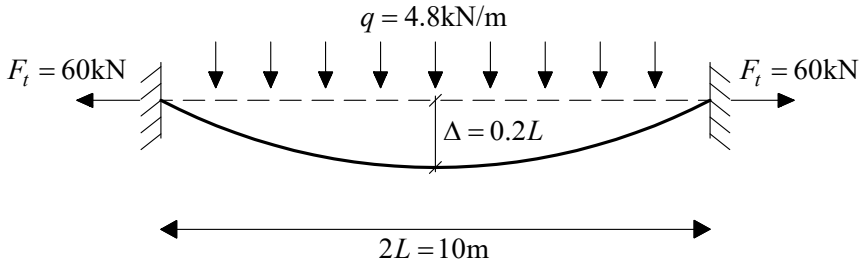


Fig. B.1 – Equilibrium model considered for the tying force requirement in the UK National Annex of Eurocode 2

Rearranging (B.2) and evaluating the terms of the equation gives:

$$F_t = 60 \text{ kN} \tag{B.3}$$

An effort has been made to extend the formulation for general application by proportionally adjusting F_t with factors accounting for the load and span length under consideration. This is evidenced in the internal tying requirements for framed structures in the UK National Annex of Eurocode 2 and for load-bearing wall constructions in Eurocode 1 – Part 1-7. The value of F_t is adjusted by the factors $(g_k + q_k)/7.5$ and $z/5$. These values are in accordance with the load and span considered in the derivation of $F_t = 60$ kN, with the denominator of 7.5kN/m^2 being approximately equal to the typical service floor load of 7.2kN/m^2, and the denominator of 5 m being the span length. However, as noted by Smith (2016), the described extension has not been considered in the initial iterations of the peripheral tying requirements, not even in the current requirements for load-bearing wall constructions in Eurocode 1 – Part 1-7. Along with the initial limitation of the tying forces to $F_t = 60$ kN, this suggests that peripheral ties may have not been intended to sustain catenary action but rather conceived as anchorages for the internal ties (Smith, 2016). Despite posterior consideration of the term $20 + 4n_0$ as a multiple of the end span length L_i and the use of $F_t = 60$ kN as a lower limit in the UK National Annex

of Eurocode 2, the amendment remains inconsistent in relation to the requirements for interior ties.

The deflection of $0.2L$ assumed in the definition of $F_t = 60$ kN is believed to be adequate for the mobilisation of catenary action. Indeed, it follows that the tying requirements of the current UFC code are also derived based on a deflection of $0.2L$, along with a derivation procedure similar to that illustrated in Fig. B.1 but assuming a generalised distributed floor load w and service span length L instead.

$$F = \frac{w \cdot (2L)^2}{8 \cdot 0.2L} = 2.5\, wL \text{ (in kN/m)} \tag{B.4}$$

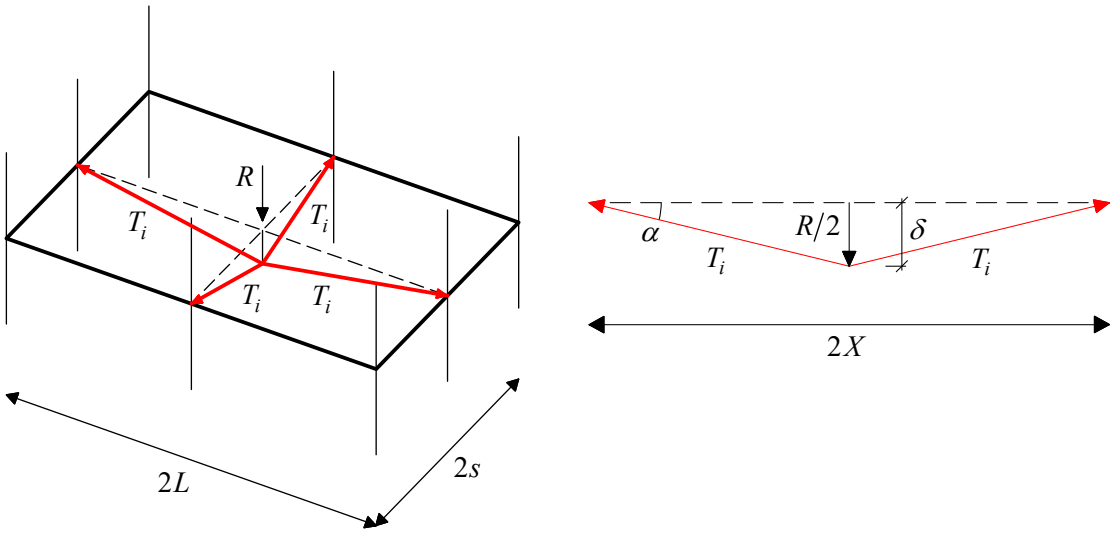
where the intensity factor of 2.5 approximates the intensity factor of internal tying requirements provided in the UFC code $(i_f = 3.0)$. The confirmation of the assumed derivation method with generalised floor loads and span lengths eradicates much of the confusion surrounding the requirements initially provided in the Code of Practice 110. Furthermore, (B.2) and (B.4) indicate that structural members undergoing catenary action should develop at least a rotation of 0.2rad so as to mobilise the required tying force, hence justifying the rotation capacity imposed by the UFC code and highlights the serious shortcoming of the UK building regulation and the Eurocode in not providing any statement concerning the rotation capacity of the structural members under tying.

Considering further inspection of the tying requirements in Eurocode 1 – Part 1-7 for framed structures, Vrouwenvelder (2008b) presented a possible derivation for the expression of internal ties. Fig. B.2 illustrates a framed structure with the span length of the service bays in the orthogonal directions equal to s and L. Under the loss of the central column, the framed structure is assumed to undergo a vertical deflection δ equal to approximately 16% of the sum of the orthogonal span lengths:

$$\delta = \frac{s + L}{6} \tag{B.5}$$

The corresponding vertical equilibrium under this deformed state is established based on Fig. B.2b:

$$R = 4\, T_i \sin\alpha \tag{B.6}$$



(a) Spatial response (b) Equivalent planar equilibrium

Fig. B.2 – Equilibrium model considered for the tying force requirement in the Eurocode 1: Part 1-7 for framed structures (adapted from Vrouwenvelder, 2008b)

Inspection of the above equation suggest that both directions contribute the same level of vertical resistance via tying (i.e. contribution of $2T_i \sin\alpha$ from each orthogonal direction). Note that this is an approximated assumption when s differs from L. Rearranging (B.6) leads to:

$$\sin\alpha = \frac{R}{4T_i} \approx \frac{\delta}{X} \tag{B.7}$$

where X is the average length of the orthogonal spans:

$$X = \frac{s+L}{2} \tag{B.8}$$

On the other hand, R can be determined by the product of the uniformly distributed load and the corresponding vertical tributary area of the lost column.

$$R = (g_k + \psi q_k)\, s\, L \tag{B.9}$$

The internal tying force requirement is obtained by combining (B.5)-(B.9):

$$T_i = 0.75R \approx 0.8R = 0.8(g_k + \psi q_k)\, s\, L \tag{B.10}$$

There is no clear justification on the choice of central deflection, which can be shown unrealistically large: if the orthogonal spans are assumed equal, the central deflection δ will

be $L/3$ as per (B.5), corresponding to a beam chord rotation of 0.33 rad. This implies that the structural member under tying must exhibit a chord rotation capacity of at least 0.33 rad, which is even higher than that required in the UFC code.

If the derivation procedure proposed by Vrouwenvelder (2008b) is again utilised to seek the expression for peripheral ties, the vertical equilibrium should be:

$$R = 2T_p \sin\alpha \tag{B.11}$$

The above equation assumes that tying forces are mobilised in the axially retrained direction alone. Assuming that the central deflection δ is equal to $L/3$, (B.11) can be rearranged into:

$$\sin\alpha = \frac{R}{2T_p} = \frac{\delta}{L} = \frac{1}{3} \tag{B.12}$$

The total load from the tributary area is:

$$R = (g_k + \psi q_k)\frac{s}{2}L \tag{B.13}$$

The peripheral tying force is obtained by combining (B.11)-(B.13):

$$T_p = 1.5R \approx 0.8(g_k + \psi q_k)\,s\,L \tag{B.14}$$

Although the above demonstration may not be the actual derivation procedure considered for the peripheral tying expression in Eurocode 1 – Part 1-7, it is worth noting that the ensuing intensity factor i_f clearly differs from 0.4 and suggests that the required force for peripheral ties should be at least equal to that required for internal ties. In this respect, further to the unrealistic rotation capacity of 0.33 rad, the assumption of halving the required force for peripheral ties can be even unsafe. It is therefore highly doubtful whether the requirements in Eurocode 1 – Part 1-7 and Eurocode 2 for peripheral ties ensure the capability of the structural members in bridging the gravity load via tying action.

Requirements for vertical tying

Both European and US codes recommend that all columns and walls should be tied continuously from the foundations to the roof level. For framed structures, 'the columns and walls carrying vertical actions should be capable of resisting an accidental design tensile force equal to the largest design vertical permanent and variable load reaction applied to the column from any one storey'. This statement is translated as (Vrouwenvelder, 2008b):

$$T_v = (g_k + \psi q_k)\, s\, L \tag{B.15}$$

where $(g_k + \psi q_k)$ is the load combination with dead and live loads; and sL is the tributary area of the vertical element under consideration. According to Eurocode 1 – Part 1-7, the accidental design loading given in (B.15) 'should not be assumed to act simultaneously with permanent and variable actions that may be acting on the structure'.

For load bearing wall construction, Eurocode 1 – Part 1-7 recommends that vertical tying may be considered effective if it is designed to sustain the following tying force:

$$T = \max \left\{ \begin{array}{l} \dfrac{34A}{8000}\left(\dfrac{H}{t}\right)^2 \text{ (in N)} \\ 100 \text{ kN/m of wall} \end{array} \right\} \tag{B.16}$$

where A is the cross-sectional area in mm^2 of the wall measured on plan. Equation (B.16) seems to be obtained following a derivation procedure similar to Fig. B.1, but considering a central deflection equal to one slab depth $(\delta = t)$. Such observation suggests that the design distributed load is $34kN/m^2$, which corresponds to the estimated pressure of the gas explosion that led to the partial collapse of Ronan Point. Indeed, despite vertical tying is primarily aimed to suspend the floor system above the loss column, Fintel and Schultz (1976) note that such ties can also be provided to avoid the 'kicking out' of the columns and walls in the event of an explosion, potentially justifying the basis for (B.16). In this sense, it seems more appropriate to view (B.16) as a key element provision instead, where the load-bearing wall is designed to resist an explosion with an associated pressure of $34kN/m^2$. However, the consideration of a pre-specified design pressure restricts the use of the expression, which may be unsafe if the actual pressure associated to the explosion exceeds the considered design value.

Appendix C: Modelling considerations for beam sub-systems with sophisticated reinforcement detailing

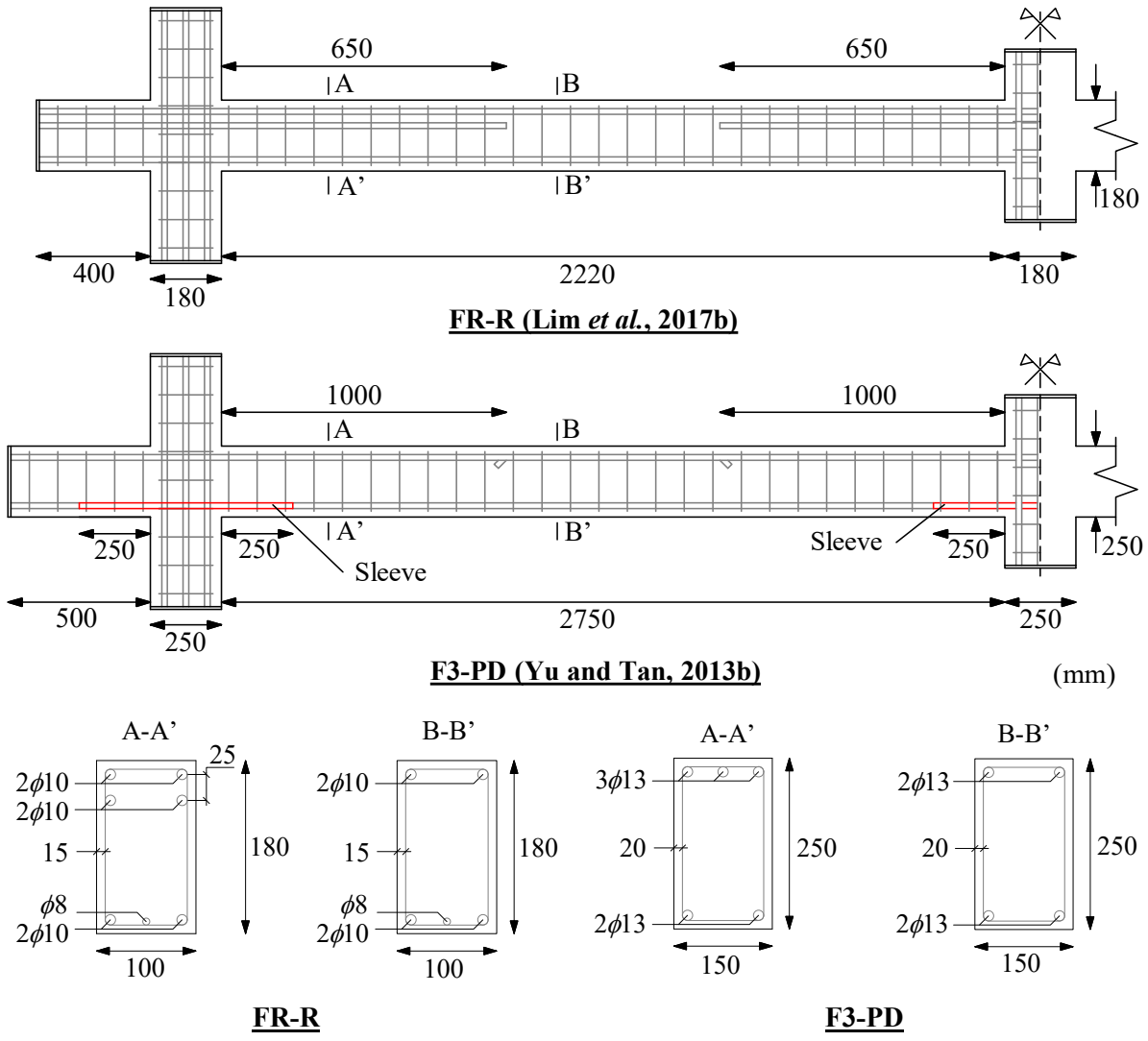


Fig. C.1 – Specimens with sophisticated reinforcement detailing

Table C.1 – Stiffness of boundary springs (assumed values)

Test specimen		Spring stiffness		
		Axial (10^4 N/mm)		Rotation (10^9 N.mm/rad)
		K^+	K^-	K_θ
Lim *et al.* (2017b)	FR-R	0.50	0.80	4.26
Yu and Tan (2013b)	F3-PD	11.20	2.59	32.30

Table C.2 – Concrete properties

Test specimen	Compressive				Tensile		
	Secant stiffness[b]	Strength[a]	G_{fc}	Residual strength[c]	Initial stiffness	Strength	G_{ft}
	MPa	MPa	N.mm	MPa	MPa	MPa	N.mm
Lim *et al.* (2017b)	15612	32.00	34.06	1.00	26600[a]	3.70[a]	0.1362
Yu and Tan (2013b)	14825	29.69	67.20	1.00	30493[b]	2.33[b]	0.1344

[a] Values from paper
[b] Values determined based on Eurocode 2 (CEN, 2004b)
[c] Assumed values

Table C.3 – Steel properties

Test specimen	Reinforcement diameter	Young's modulus	Yield strength	Ultimate strength	Ultimate strain	Softening parameter[a]
	mm	MPa	MPa	MPa	-	-
Lim *et al.* (2017b)	R8	200000	300	395	0.150[a]	50.00
	R10	200000	400	500	0.150[a]	50.00
Yu and Tan (2013b)	T13	170125	488	586	0.110	10.00

[a] Assumed values

Table C.4 – Bond properties

Test specimen	Reinf. diameter	s_e	s_1	s_2	s_3	τ_e	τ_1	τ_3	Calibrated bond reduction
	mm	mm	mm	mm	mm	MPa	MPa	MPa	MPa	
Lim *et al.* (2017b)	R8	0.14	1.03	3.00	6.40	9.60	18.59	5.25	0.31τ
	R10	0.15	1.03	3.00	8.00	9.50	18.07	5.25	0.31τ
Yu and Tan (2013b)	T13	0.12	1.00	3.00	10.40	8.00	16.66	5.06	0.64τ
	T13 debonded	0.12	1.00	3.00	10.40	8.00	16.66	5.06	0.05τ

Appendix D: Supplementary information for the sensitivity assessment of the system response on the bond strength and anchorage length

Table D.1 – Damage mechanism and corresponding vertical displacement (in mm)

Model	MJBR damage	ECTR damage
1	Pull-out of elastic reinforcement, 72.50	Pull-out of elastic reinforcement, 117.00
2 (control)	Pull-out of yielded reinforcement, 455.00	Pull-out of yielded reinforcement, 595.00
3	Fracture of reinforcement, 235.00	Fracture of reinforcement, 440.00
4	Pull-out of yielded reinforcement, 220.00	Pull-out of yielded reinforcement, 305.00
5	Fracture of reinforcement, 430.00	Fracture of reinforcement, 605.00
6	Fracture of reinforcement, 235.00	Fracture of reinforcement, 440.00
7	Pull-out of yielded reinforcement, 500.00	Pull-out of yielded reinforcement, 635.00
8	Fracture of reinforcement, 430.00	Fracture of reinforcement, 600.00
9	Fracture of reinforcement, 230.00	Fracture of reinforcement, 440.00

Appendix E: Supplementary tables for the rational horizontal tying force method

Table E.1 – Tying parameters for double-span beams

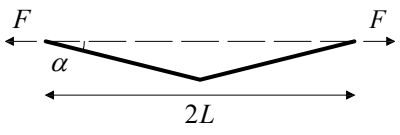
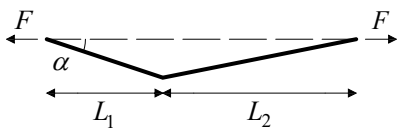
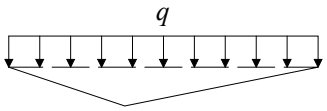
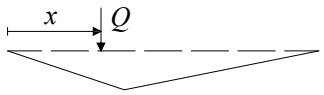
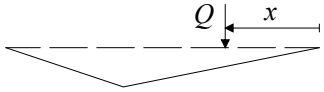
	Equal spans 	Unequal spans $(L_1 \le L_2)$ 
Intensity factor: i_f	2.5	$5.0\left(\frac{L_2}{L_1+L_2}\right)$
Equivalent tying force: T	F	F
Equivalent load: P		
	qL	$q\left(\frac{L_1+L_2}{2}\right)$
	$Q\left(\frac{x}{L}\right)$	$Q\left(\frac{x}{L_1}\right)$
	$Q\left(\frac{x}{L}\right)$	$Q\left(\frac{x}{L_2}\right)$

Table E.2 – Tying parameters for two-way floor tying

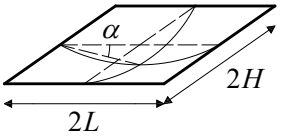
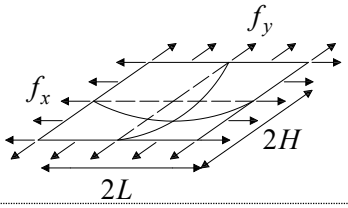
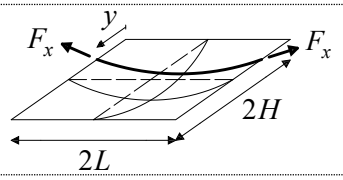
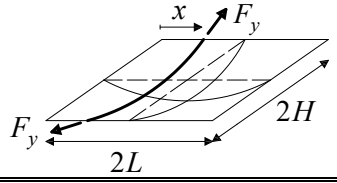
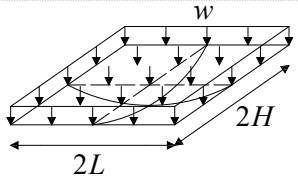
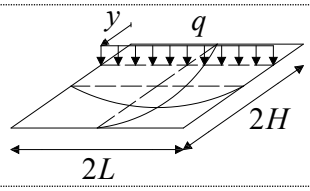
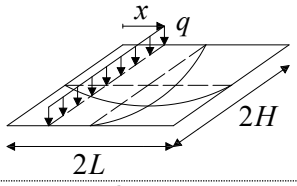
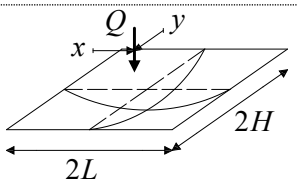
	Two-way tying $(L \le H)$ 
Intensity factor: i_f	3.125
Equivalent tying force: T	
	$f_x H + f_y L\left(\frac{L}{H}\right)$
	$0.9375F_x\left[\left(\frac{y}{H}\right)\left(2-\frac{y}{H}\right)\right]^2$
	$0.9375F_y\left(\frac{L}{H}\right)\left[\left(\frac{x}{L}\right)\left(2-\frac{x}{L}\right)\right]^2$
Equivalent load: P	
	wLH
	$0.75qL\left[\left(\frac{y}{H}\right)\left(2-\frac{y}{H}\right)\right]$
	$0.75qH\left[\left(\frac{x}{L}\right)\left(2-\frac{x}{L}\right)\right]$
	$0.5625Q\left[\left(\frac{x}{L}\right)\left(2-\frac{x}{L}\right)\right]\left[\left(\frac{y}{H}\right)\left(2-\frac{y}{H}\right)\right]$

Table E.3 – Tying parameters for one-way floor tying

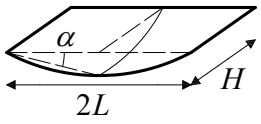
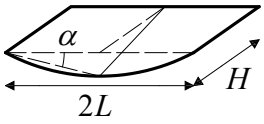
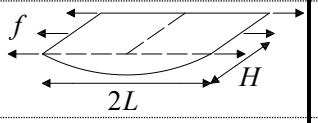
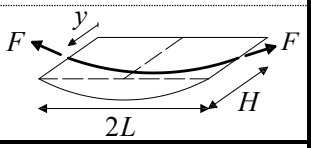
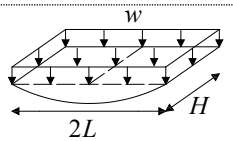
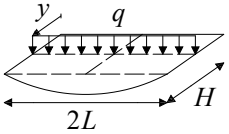
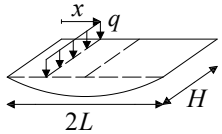
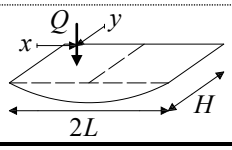
	One-way tying (torsional edge restraint) 	One-way tying (no torsional edge restraint) 
Intensity factor: i_f	3.125	3.75
Equivalent tying force: T		
	$\frac{f\,H}{2}$	$\frac{f\,H}{2}$
	$0.9375F\left[\left(\frac{y}{H}\right)\left(2-\frac{y}{H}\right)\right]^2$	$1.5F\left(\frac{y}{H}\right)^2$
Equivalent load: P		
	$\frac{w\,L\,H}{2}$	$\frac{w\,L\,H}{2}$
	$0.75\,q\,L\left[\left(\frac{y}{H}\right)\left(2-\frac{y}{H}\right)\right]$	$q\,L\left(\frac{y}{H}\right)$
	$0.375\,q\,H\left[\left(\frac{x}{L}\right)\left(2-\frac{x}{L}\right)\right]$	$0.375\,q\,H\left[\left(\frac{x}{L}\right)\left(2-\frac{x}{L}\right)\right]$
	$0.5625Q\left[\left(\frac{x}{L}\right)\left(2-\frac{x}{L}\right)\right]\left[\left(\frac{y}{H}\right)\left(2-\frac{y}{H}\right)\right]$	$0.75Q\left[\left(\frac{x}{L}\right)\left(2-\frac{x}{L}\right)\right]\left(\frac{y}{H}\right)$

Table E.4 – Amplification of redistributed vertical gravity loading for double-span beams

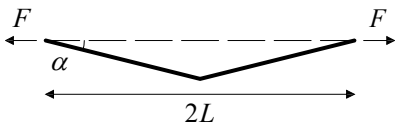
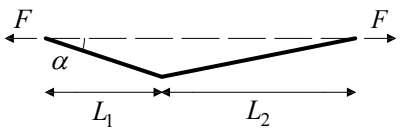
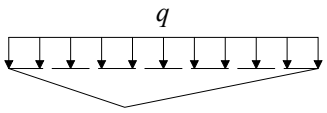
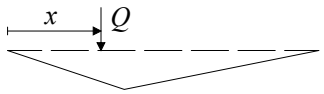
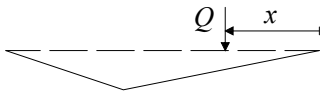
	Equal spans	Unequal spans ($L_1 \le L_2$)
		
Redistributed gravity load amplification		
	$0.25 + 0.75\eta$	
	η	
	η	

Table E.5 – Amplification of redistributed vertical gravity loading for two-way floor tying

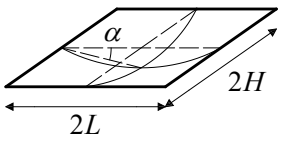
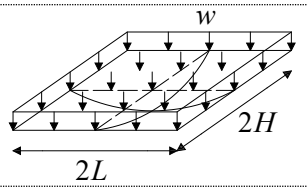
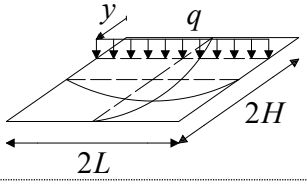
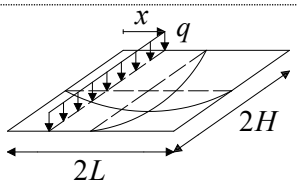
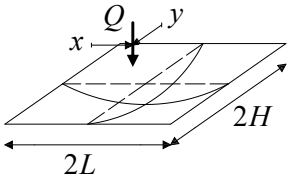
Redistributed gravity load amplification	Two-way tying $(L \le H)$ 
	$0.3056 + 0.6944\eta$
	$0.1667 + 0.8333\eta$
	$0.1667 + 0.8333\eta$
	η

Table E.6 – Amplification of redistributed vertical gravity loading for one-way floor tying

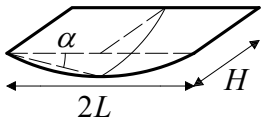
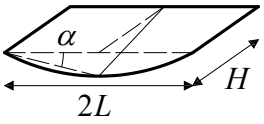
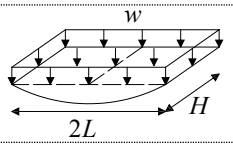
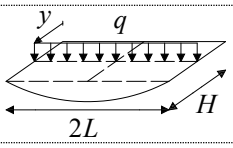
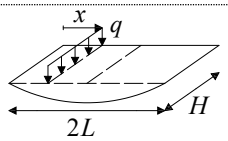
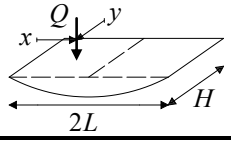
	One-way tying (torsional edge restraint) 	One-way tying (no torsional edge restraint) 
Redistributed gravity load amplification		
	$0.3056 + 0.6944\eta$	$0.375 + 0.625\eta$
	$0.1667 + 0.8333\eta$	$0.1667 + 0.8333\eta$
	$0.1667 + 0.8333\eta$	$0.25 + 0.75\eta$
	η	η

Table E.7 – Properties of the specimens selected for the validation of tying via beams

Specimen		Span length L (mm)	Beam			Slab	
			Continuous top reinforcement (mm^2)	Continuous bottom reinforcement (mm^2)	Yield strength (MPa)	Continuous reinforcement (mm^2)	Yield strength (MPa)
Qian *et al.* (2014)	P1	1900	157.08	157.08	437	-	-
	P2	1300	157.08	157.08	437	-	-
Lim *et al.* (2017b)	FR	2220	157.08	157.08	507	-	-
	FR-S	2220	157.08	157.08	507	-	-
	FR-R	2220	157.08	207.34	400	-	-
Ren *et al.* (2016)	B2	1900	100.53	100.53	390	-	-
	B3	1900	100.53	100.53	390	-	-
	S2	1900	100.53	100.53	390	101.94	387
	S3	1900	100.53	100.53	390	297.62	387
	S4	1900	157.08	157.08	370	297.62	387
	S5	1900	100.53	100.53	390	297.62	387
	S6	1900	100.53	100.53	390	297.62	387
Yu and Tan (2017)	F1-NS	2750	265.46	265.46	485	-	-
	F2-WS	2750	265.46	265.46	485	-	-
Yu and Tan (2012, 2013a)	S1	2750	157.08	157.08	511	-	-
	S2	2750	157.08	157.08	511	-	-
	S3	2750	265.46	157.08	494	-	-
	S4	2750	265.46	265.46	494	-	-
	S5	2750	265.46	398.19	494	-	-
	S6	2750	402.12	265.46	494	-	-
	S7	2150	265.46	265.46	494	-	-
Lew *et al.* (2014)	IMF	5385	1013.41	1284.85	462	-	-
	SMF	5230	2026.83	2026.83	476	-	-

Table E.8 – Properties of the specimens selected for the validation of tying via floor system

Specimen		L (mm)	H (mm)	Continuous beam reinforcement			Continuous slab reinforcement		
				x-dir (mm^2)	y-dir (mm^2)	Yield (MPa)	x-dir (mm^2/mm)	y-dir (mm^2/mm)	Yield (MPa)
Qian *et al.* (2014)	S1	1500	1900	314.15	314.15	437	0.1131	0.1131	355
	S2	1500	1500	314.15	314.15	437	0.1131	0.1131	355
Lu *et al.* (2017)	SE1	2000	2000	113.09	-	372	0.1414	-	372
	SE2	2000	2000	113.09	-	372	0.2020	-	372
	SE3	2000	2000	113.09	-	372	0.1414	-	372
	SE4	2000	2000	314.16	-	372	0.1414	-	372
Yu *et al.* (2020a)	S1	1800	1800	201.06	-	488	0.1767	-	511
	S2	1800	1800	314.15	-	481	0.1767	-	511
	S3	1800	1800	201.06	-	364	0.1767	-	493

Appendix F: Average strain contours at initial stages of tensile membrane action

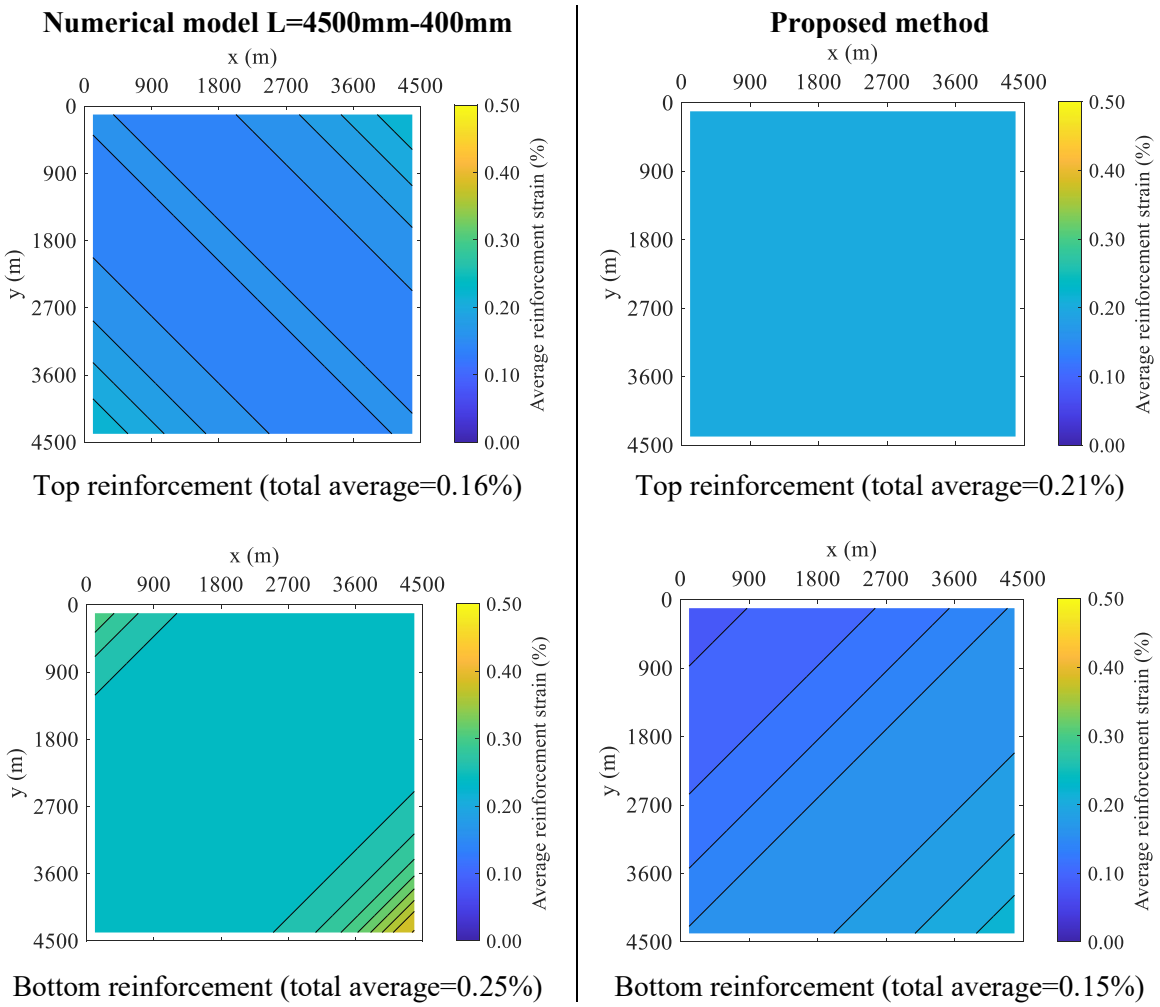


Fig. F.1 – Average reinforcement strains at 400mm tip displacement of the control specimen with 4500mm span length

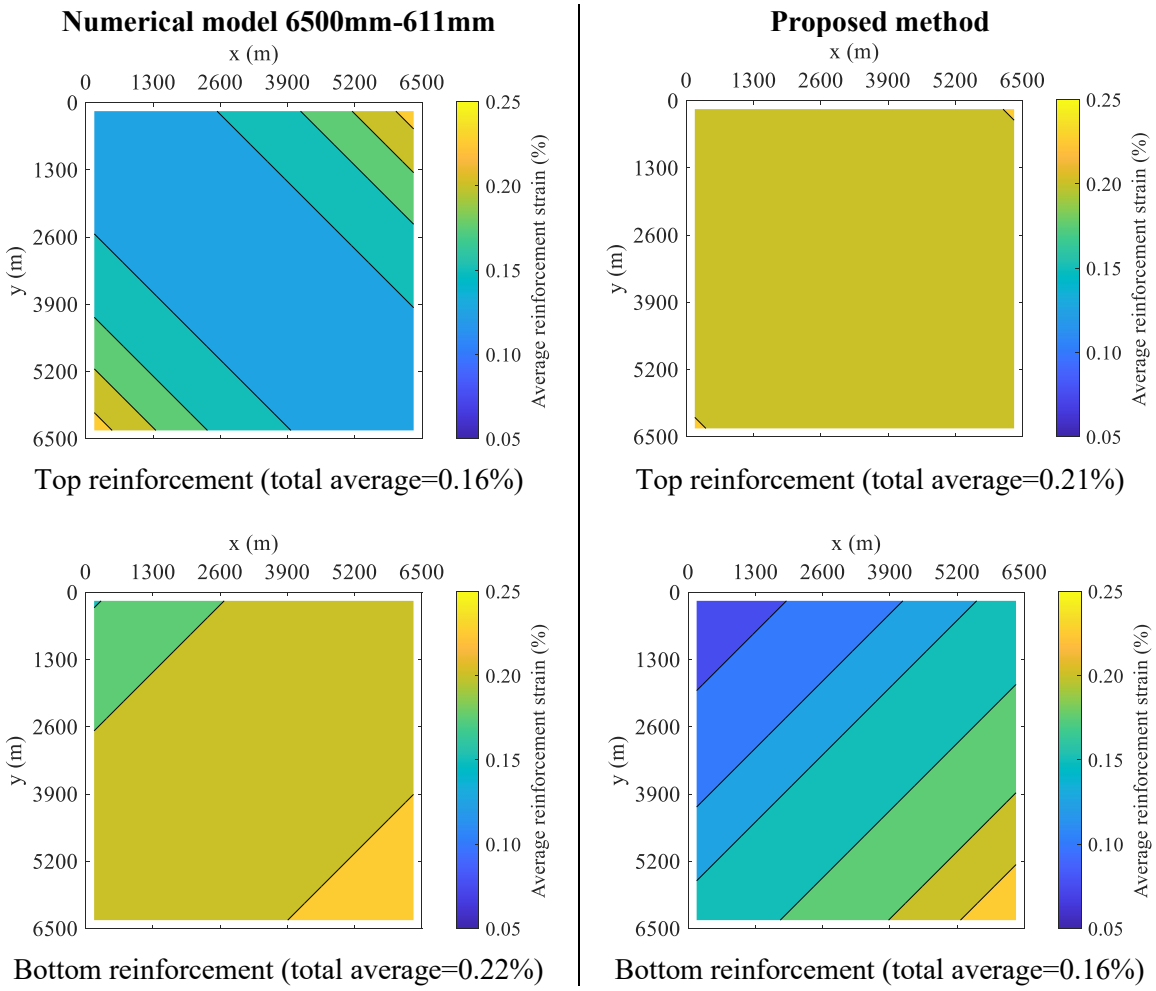


Fig. F.2 – Average reinforcement strains at 611mm tip displacement of the control specimen with 6500mm span length

Appendix G: Permission to reuse figures from other publications

Page no.	Figure	Source	Copyright holder	Permission request date	I have permission yes/no	Permission note
28	Fig. 1.1	http://www.nationalarchives.gov.uk/education/resources/sixties-britain/ronan-point-tower/	The National Archives	4 January 2023	yes	via email
29	Fig. 1.2a	https://www.britannica.com/event/Oklahoma-City-bombing#/media/1/735994/70968	AP Images	5 January 2023	yes	via email, paid permission
29	Fig. 1.2b	https://www.britannica.com/topic/World-Trade-Center#/media/1/648633/60121	Chao Soi Cheong/AP Images	5 January 2023	yes	via email, paid permission
52	Fig. 2.1	Izzuddin, B. A., Vlassis, A. G., Elghazouli, A. Y. & Nethercot, D. A. (2008) Progressive collapse of multi-storey buildings due to sudden column loss—Part I: Simplified assessment framework. Engineering structures. 30 (5), 1308-1318. Available from: https://doi.org/10.1016/j.engstruct.2007.07.011	Elsevier	4 January 2023	yes	online request via Copyright Clearance Center, Inc. ("CCC")
53	Fig. 2.2	Izzuddin, B. A., Vlassis, A. G., Elghazouli, A. Y. & Nethercot, D. A. (2008) Progressive collapse of multi-storey buildings due to sudden column loss—Part I: Simplified assessment framework. Engineering structures. 30 (5), 1308-1318. Available from: https://doi.org/10.1016/j.engstruct.2007.07.011	Elsevier	4 January 2023	yes	online request via Copyright Clearance Center, Inc. ("CCC")

66	Fig. 2.7	Dat, P. X. & Hai, T. K. (2013) Membrane actions of RC slabs in mitigating progressive collapse of building structures. Engineering Structures. 55, 107-115. Available from: https://doi.org/10.1016/j.engstruct.2011.08.039	Elsevier	4 January 2023	yes	online request via Copyright Clearance Center, Inc. ("CCC")
68	Fig. 2.8	Pham, A. T., Lim, N. S. & Tan, K. H. (2017) Investigations of tensile membrane action in beam-slab systems under progressive collapse subject to different loading configurations and boundary conditions. Engineering Structures. 150, 520-536. Available from: https://doi.org/10.1016/j.engstruct.2017.07.060	Elsevier	4 January 2023	yes	online request via Copyright Clearance Center, Inc. ("CCC")
201	Fig. 5.6	Izzuddin, B. A. (2022) Rational Robustness Design of Multistory Building Structures. Journal of Structural Engineering. 148 (3), 04021279.	ASCE	4 January 2023	yes	online request via Copyright Clearance Center, Inc. ("CCC")